ISSN 2434-9488

KURNS Progress Report 2023

Institute for Integrated Radiation and Nuclear Science,
Kyoto University

KURNS Progress Report 2023

APRIL 2023 – MARCH 2024

Published by
Institute for Integrated Radiation and Nuclear Science,
Kyoto University,
Kumatori-cho, Sennan-gun, Osaka 590-0494, Japan

Preface for the KURNS Progress Report 2023

It is our pleasure to announce that the KURNS Progress Report 2023 has been published. This report contains all of the accomplishments of research and related activities at the Institute for Integrated Radiation and Nuclear Science, Kyoto University (KURNS) during the fiscal year 2023 (hereafter called as FY2023). A large number of research subjects have been enrolled in FY2023, which covers various fields of nuclear science and technology, materials science, radiation life science and radiation medical science. It means that our institute continues to play a distinctive role as a Joint Usage/Research Center, promoting an extensive range of studies from fundamental to applied research with research reactors and accelerators.

In FY2023, the country was completely out of the COVID-19 pandemic, and research activities have largely returned to their pre-pandemic status. In FY 2023, KUR was operated for 904 hours and KUCA was for 0 hours. In total, we accepted 3464 man-day researchers and students for using research facilities and for attending scientific meetings.

We strive for safe and stable operations for nationwide use, making it our primary mission to provide scientists the opportunity to conduct research and education. We are happy to dedicate our support to enable users conduct significant interdisciplinary research at KURNS.

Kumatori, July 12, 2024

Ken Kurosaki

Director, KURNS

CONTENTS

5. Geochemistry and Environmental Science

6. Life Science and Medical Science

7. Neutron Capture Therapy

I. ANNUAL SUMMARY OF EXPERIMENTAL RESEARCH ACTIVITIES

I-1. PROJECT RESEARCHES

Project 1

Project Research on Advances in Isotope-Specific Studies Using Muti-Element Mössbauer Spectroscopy

M. Seto
Institute for Integrated Radiation and Nuclear Science, Kyoto University

OBJECTIVES OF RESEARCH PROJECT:

Irreplaceable feature of the Mössbauer spectroscopy is to extract several information such as electronic states and magnetic properties for a specific isotope. The main objectives of this project research are the investigation in the frontier of the materials science and the development of advanced experimental methods by using multi-element Mössbauer spectroscopy. Promotion of variety of Mössbauer isotope provides useful and valuable methods in modern materials science even for complicated systems.

In this project research, each group performed their research by specific isotopes:

^{197}Au in R5P1-1; ^{61}Ni in R5P1-2; ^{57}Fe in R5P1-3, R5P1-4, R5P1-5, R5P1-6, R5P1-7, R5P1-8, R5P1-9; and other developments in R5P1-10, R5P1-11

MAIN SUBJECTS AND RESULTS OF THIS REPORT:

Main subjects and results are as follows:

(R5P1-1, H. Ohashi) Temperature Dependence of ^{197}Au Mössbauer Spectra for Au(III) Ions Adsorbed on MnO_2

H. Ohashi *et al*. investigated Au(III) catalyst supported by MnO_2 synthesized from using $HAuCl_4$. The temperature-dependent ^{197}Au Mössbauer spectroscopy was performed to confirm the existence of Au(III) component.

(R5P1-2, T. Kitazawa) ^{61}Ni Mössbauer spectroscopy of Fe-Ni Hofmann-type complex

K. Kitase *et al.* investigated spin-crossover phenomenon in Fe-Ni Hofmann-type complex, Fe(Allyl Isonicotinate)$_2$[Ni(CN)$_4$]. The ^{61}Ni Mössbauer spectra of the compound shows similar singlet spectrum to $Fe_{86}V_{14}$ alloy. The recoilless fraction was smaller due to organic ligands and flexible framework.

(R5P1-3, K. Shinoda) Mössbauer Spectra and Intensity Tensors for Fe^{3+} and Fe^{2+} of Bridgmanite

K. Shinoda *et al.* measured single crystals of bridgmanite by using the microscopic Mössbauer spectroscopy. The intensity tensors of quadrupole doublets for both Fe^{3+} and Fe^{2+} sites were successfully evaluated.

(R5P1-4, I. Mashino) Electrical conductivity and the valence state of iron in silicate glasses up to Mbar pressures

I. Mashino *et al.* evaluated the valence state of iron bearing enstatite glass to investigate high pressure studies for understanding the behavior of iron silicate melts at the bottom of the mantle.

(R5P1-5, M. Tabuchi) Fe valence control for Fe and Ni substituted Li_2MnO_3 positive electrode material during charge and discharge reactions using ^{57}Fe Mössbauer spectroscopy

M. Tabuchi *et al*. investigated Fe and Ni substituted Li_2MnO_3 electrode for Li-ion battery with Fe:Ni:Mn ratios of 15:15:70. Fe valence components were evaluated by Mössbauer spectroscopy to improve its charge and discharge characteristics.

(R5P1-6, K. Yonezu) Experimental Preliminary Approach on the Precipitation Mechanism of Banded Iron Formation (BIF): Precipitation Behavior of Iron in the Absence and Presence of Silicic Acid

K. Yonezu *et al.* investigated the role of silicic acid in precipitation process to investigate precipitated sedimentary rock at Precambrian age. The results suggested magnetite was formed even at high silicic acid concentrations.

(R5P1-7, Y. Kamihara) Research on Magnetism and Electronic Phase in a H-doped Iron-based Superconductor II

Y. Kamihara *et al.* are investigating H-doped SmFeAsO and F-doped SmFeAsO, iron-based superconductor with high transition temperature of around 55K. The temperature-dependent Mössbauer spectroscopy was performed to clarify its electronic and magnetic properties.

(R5P1-8, K. Okada) Magnetic Measurememts of Irons in Soda-lime Glass by Mössbauer Spectroscopy (2)

K. Okada *et al.* performed Mössbauer Spectroscopy of soda-lime glass to evaluate Fe^{2+} and Fe^{3+} components.

(R5P1-9, Y. Kobayashi) ^{57}Fe Mössbauer Study of Fe-Si Magnetic Materials

Y. Kobayashi *et al.* studied magnetic properties of Fe-Si alloy to reveal Fe-Si disordered phase and Fe_3Si phase.

(R5P1-10, R. Masuda) Mössbauer study of nanoparticles synthesized in Y-type Zeolite

R. Masuda *et al.*measured temperature-dependent Mössbauer spectra of nanoparticles in HY-type zeolite to evaluate the Debye temperature for the information of size of the particle.

(R5P1-11, S. Kitao) ^{166}Er Mössbauer Study of ErB_4

S. Kitao *et al.* investigated ^{166}Er Mössbauer spectra of ErB_4 to evaluate magnetic properties. The results showed the relaxation phenomena were observed above the antiferromagnetic transition temperature.

Temperature Dependence of ^{197}Au Mössbauer Spectra for Au(III) Ions Adsorbed on MnO_2

H. Ohashi, R. Tawatari, K. Arata[1], A. Nakayama[1], T. Ishida[1], T. Murayama[1], H. Wang[1], Y. Kobayashi[2], S. Kitao[2]

Faculty of Symbiotic Systems Science, Fukushima University

[1] Department of Applied Chemistry for Environment, Tokyo Metropolitan University
[2]Institute for Integrated Radiation and Nuclear Science, Kyoto University

INTRODUCTION: Gold catalysts have been very famous as heterogeneous catalysts. When preparing gold catalysts from Au(III) compounds, it was known that the preparation conditions differ depending on the support metal oxides. Preparation of Au/MnO_2 from $HAuCl_4$ compounds was known to be difficult. This was because Au(III) ions were partially reduced to Au(0) on the surface of MnO_2.

We have investigated the mechanism of this automatic reduction to Au(0)[1]. As a conclusion, the Au(III) component with relatively high IS and QS values was important. However, there remained doubts whether this component was really trivalent gold. In this study, we aimed to solve the above problem by measuring the ^{197}Au Mössbauer spectra for Au(III) ions adsorbed on MnO_2 with varying temperature.

EXPERIMENTS: Manganese dioxide was added to the $HAuCl_4$ aqueous solution to adjust the pH 9, and the mixture was stirred. The suspension solution was filtered using 0.45 μm membrane filter, and the filtrate was dried at 30°C for 12 hours. The amount of gold was approximately 10wt%.

^{197}Au Mössbauer spectra were measured at Kyoto University Research Institute of Nuclear Science. The ^{197}Pt isotope ($T_{1/2}$ = 18.3 h), γ-ray source feeding the 77.3 keV Mössbauer transition of ^{197}Au, was prepared by neutron irradiation of isotopically enriched ^{196}Pt metal at the Kyoto University Reactor. The measurement temperature was 20-60 K, and the measurement was performed by the transmission method.

RESULTS: Figure 1 shows ^{197}Au Mössbauer spectra at 20 - 60 K for the sample of Au(III) adsorbed on MnO_2. The spectra were divided into three peaks and analyzed temperature changes in the areas of peaks with relatively high IS and QS values using the same method as previously reported[2]. The results showed that it behaved similarly to other Au(III) compounds. It was estimated that the peak was Au(III).

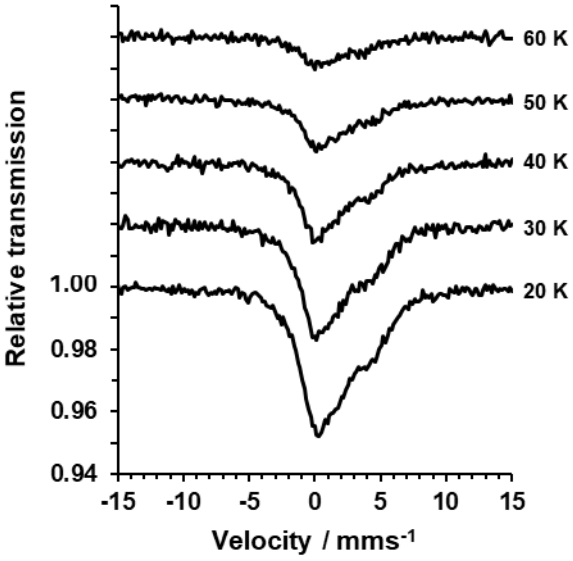

Fig. 1. ^{197}Au Mössbauer spectra at 20-60 K for the sample of Au(III) adsorbed on MnO_2.

REFERENCES:

[1] H. Ohashi *et.al.,* Anal. Sci., **37** (2021) 1321-1330.
[2] Y. Kobayashi *et.al.*, Interactions, **245** (2024) 42.

^{61}Ni Mössbauer spectroscopy of Fe-Ni Hofmann-type complex

K. Kitase[1], C. Ohshima[1], H. Tanabe[1], T. Chiba[1], T. Kitazawa[1, 2], S. Kitao[3], Y. Kobayashi[3], T. Kubota[4], M. Seto[3].

[1]*Department of Chemistry, Faculty of Science, Toho University, Japan*
[2]*Research Centre for Materials with Integrated Properties, Toho University*
[3]*Institute for Integrated Radiation and Nuclear Science, Kyoto University*
[4]*Agency for Health, Safety and Environment, Kyoto University*

INTRODUCTION: Spin-crossover (SCO) phenomenon is a reversible spin transition between high-spin and low-spin state. Hofmann-type complex is the one of coordination polymer which consist of center metal ion, bridging ligand [M(CN)$_4$], pyridine-type ligand. In Hofmann-type SCO complex, SCO phenomenon usually occurs in Fe center. ^{57}Fe Mössbauer spectroscopy is useful tool to investigate Hofmann-type SCO complex since the isomer shift (IS), quadrupole splitting (QS), and spectrum shape of ^{57}Fe Mössbauer spectroscopy are sensitive to the coordination environments or spin state of Fe sites, so ^{57}Fe Mössbauer spectroscopy is widely used by many researchers to investigate SCO phenomenon of Fe center in Hofmann-type complex. Hofmann-type complex contains other Mössbauer active nuclei such as Ni, Au. Nevertheless, other type of Mössbauer spectroscopy such as ^{61}Ni Mössbauer spectroscopy is much less resarched than ^{57}Fe Mössbauer spectroscopy. Now we synthesized Fe-Ni Hofmann-type complex Fe(Allyl Isonicotinate)$_2$[Ni(CN)$_4$] and researched the properties of this complex by ^{61}Ni Mössbauer spectroscopy.

EXPERIMENTS: The complex was synthesized using Mohr's salt $Fe(NH_4)_2(SO_4)_2 \cdot 6H_2O$, citric acid, $K_2[Ni(CN)_4] \cdot H_2O$, and pyridine-type ligand ethyl nicotinate. First, Mohr's salt and ligand were dissolved into water. Then aqueous solution of $K_2[Ni(CN)_4]$ was dropped into this solution. The powder sample was obtained as two types of colors, large amount of yellow powder and small amount of orange powder. We can separate yellow powder from orange powder. We confirmed that both types of powder are same formula and isostructural by elemental analysis and powder X-ray diffraction measurement. We charged 1.969 g of powder of this complex into a 10 mm diameter holder for ^{61}Ni Mössbauer spectroscopy. The thickness of Ni atom in this sample is c.a. 0.282 g cm^{-2}..

RESULTS: Fig. 1 shows ^{61}Ni Mössbauer spectroscopy of $Ni_{86}V_{14}$ alloy and Fe(Allyl Isonicotinate)$_2$[Ni(CN)$_4$]. Both spectra has singlet peak. The parameter of former spectrum is IS = 0 (definition), FWHM = 0.96 mm s^{-1}, and relative peak area is 0.0411 whereas that of latter spectrum is IS = -0.002 mm s^{-1}, FWHM = 1.07 mm s^{-1}, and relative peak area is 0.0326. The thickness of the Fe(Allyl isonicotinate)$_2$[Ni(CN)$_4$] sample (c.a. 0.282 g cm^{-2} for Ni atom) is thicker than the $Ni_{86}V_{14}$ alloy sample (0.0907 g cm^{-2}, c.a. 0.0794 g cm^{-2} for Ni atom). Nevertheless, the absorption intensity of the spectrum of Fe(Allyl isonicotinate)$_2$[Ni(CN)$_4$] is smaller than $Ni_{86}V_{14}$ alloy. This result could be explained as Hofmann-type coordination polymers contains organic long ligands and flexible framework. As result, the recoil fraction in Fe(Allyl isonicotinate)$_2$[Ni(CN)$_4$] is smaller than that of $Ni_{86}V_{14}$ alloy.

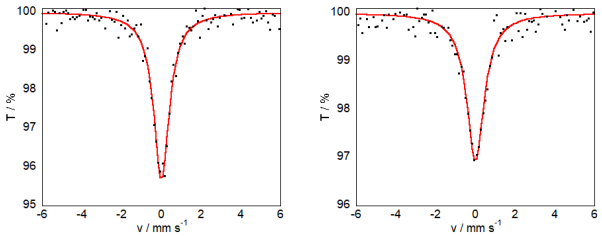

Fig. 1. ^{61}Ni Mössbauer spectroscopy of $Ni_{86}V_{14}$ alloy (left) and Fe(Allyl isonicotinate)$_2$[Ni(CN)$_4$] (Right).

PR1-3

Mössbauer Spectra and Intensity Tensors for Fe^{3+} and Fe^{2+} of Bridgmanite

K. Shinoda[1], Y. Kobayashi[2], T. Okuchi[2]

[1]*Department of Geosciences, Graduate School of Science, Osaka Metropolitan University*
[2]*Institute for Integrated Radiation and Nuclear Science, Kyoto University*

INTRODUCTION: Bridgmanite is a high-pressure mineral that is supposed to the major mineral in the Earth's lower mantle. Bridgmanite belongs to orthorhombic system. Crystal structure of bridgmanite is based on the perovskite structure. Although bridgmanite is a nominally ahhydrous mineral, bridgmanite incorporates hydrogen as OH^- in the crystal structure and supposed to act as 'water reserver' of Earth's mantle. Purevjav et al. (2023) synthesized high-quality single crystal of bridgmanite with a composition of $(Mg_{0.88}\ Fe^{2+}_{0.05}\ Fe^{3+}_{0.05}\ Al_{0.03})\ (Si_{0.88}\ Al_{0.11}\ H_{0.01})\ O_3$, evaluated the crystallographic position of hydrogen by single crystal neutron diffraction and infrared spectroscopy. In Purevjav et al. (2023), the ratio of ferrous to ferric irons was determined by Mössbauer spectra of the single crystal of the synthesized bridgmanite. In the analyses of Mössbauer spectra, two quadrupole doublets due to Fe^{2+} and Fe^{3+} and either doublet of the same intensity of lower and higher Doppler velocities were assumed. However, the lower (I_l) and higher peak's intensity (I_h) of quadrupole doublets due to Fe ions in a single crystal generally show different intensities. The peak intensity (I) defined as $I_h/(I_h+I_l)$ depends on the angle between crystallographic axes and direction of γ-ray. To analyze Mössbauer spectra of single crystal bridgmanite, intensity tensors for Fe^{3+} and Fe^{2+} of bridgmanite necessary as indicated by [2]. In this study, crystallographically oriented crystals of bridgmanite were prepared by X-ray diffraction, and Mössbauer spectra of single crystal of bridgmanite were measured to examine intensity tensors.

EXPERIMENTS and RESULTS: Two single crystals of bridgmanite, which were synthesized by [1], were used to measure Mössbauer spectra. Mössbauer measurements were carried out in transmission mode on a constant acceleration spectrometer with an Si-PIN semiconductor detector (XR-100CR, AMPTEK Inc.) and multi-channel analyzer of 1024 channels. A 3.7GBq ^{57}Co/Rh of 4mmϕ in diameter was used as γ-ray source. An ^{57}Fe-enriched iron foil was used as velocity calibrant. The two symmetric spectra were folded and velocity range was ± 7mm/s. Nine Mössbauer spectra of crystallographically oriented single crystals of bridgmanite were measured. The incident γ-ray directions were chosen to uniformly distribute against crystal axes. By normalizing all spectra and averaging the normalized spectra, an averaged Mössbauer spectrum of bridgmanite was obtained. Isomer shift and quadrupole splitting for Fe^{3+} and Fe^{2+} were obtained from the averaged spectrum by fixing peak intensity as 0.5 during peak analyses using Mosswinn program. Figure 1 shows Mössbauer spectrum of bridgmanite measured under γ-ray parallel to the ***c***-axis, where black dots are raw data, broken line is due to Fe^{3+} and dotted line is due to Fe^{2+}. Peak separations were done by fixing isomer shift and quadrupole splitting as obtained from the averaged spectrum. According to Zimmermann (1975) [3], three tensors' components (I_{XX}, I_{YY}, I_{ZZ}) for Fe^{3+} and Fe^{2+} of bridgmanite were obtained from nine spectra as (0.461, 0.468, 0.571) for Fe^{3+} and (0.587, 0.449, 0.464) for Fe^{2+}, respectively.

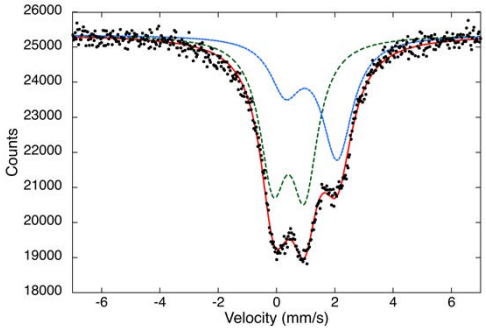

Fig.1. Mössbauer spectrum of bridgmanite measured under γ-ray parallel to the ***c***-axis.

REFERENCES:

[1] Purevjav, N. *et al.,* (2023) American Mineralogist. (doi) 10.2138/am-2022-8680.
[2] Fukuyama, D. *et al.,* (2022) J. Mineral. Petrol. Sci., (doi) 10.2465/jmps.220506.
[3] Zimmermann, R., Nucl. Instr. and Meth., **128** (1975) 537-543.

Electrical conductivity and the valence state of iron in silicate glasses up to Mbar pressures

I. Mashino, T. Yoshino, S. Kitao[1], T. Mitsui[2], M. Seto[1]

Institute for Planetary Materials, Okayama University
[1]Institute for Integrated Radiation and Nuclear Science, Kyoto University
[2]Synchrotron Radiation Research Center, Kansai Photon Science Institute, Quantum Beam Science Research Directorate, National Institutes for Quantum and Radio-logical Science and Technology

INTRODUCTION: Silicate melt is expected to exist at the bottom of the mantle, but its stability is still under debate. Previous studies [1,2] showed that the iron partition coefficient between the melt and solid changes at around ~80 GPa, which would produce a denser melt with negative buoyancy. They suggested that the observed discontinuity of the iron partition coefficient could be explained by spin transition of iron in the melts or the change in crystal chemistry of the co-existing mineral. The spin transition of iron affects not only the partitioning behavior but also the physical properties such as density, electrical and thermal conductivities. To understand the valence/spin states of iron in silicate melts, we are conducting high-pressure electrical conductivity measurements of iron-bearing enstatite glass which has a representative composition of the mantle, because silicate glasses have been considered as good analogues of silicate melts.

EXPERIMENTS: Iron-bearing enstatite glass (hereafter Fe-glass) was synthesized from reagent MgO, Fe_2O_3 and SiO_2 powders. The mixtures of oxides were placed in a platinum foil capsule and melted in air using an electric furnace at 1650 ℃. The sample was subsequently quenched by immersing the base of the crucible in water. The conventional ^{57}Fe-Mössbauer spectroscopy was performed using a ^{57}Co source in Rh matrix with nominal activity of 1.85 GBq at Institute for Integrated Radiation and Nuclear Science, Kyoto University. The velocity scale is referenced to α-Fe.

RESULTS: Fig. 1 shows the Mössbauer spectrum of Fe-glass. The obtained spectrum was fitted using a two-doublet model, one with higher center shift (CS) (doublet#1) and one with lower CS (doublet#2). According to our previous measurements of iron-bearing glass, we fixed the quadrupole splitting (QS) value of doublet#2 to 1.2 (mm/s) (Table 1). Compared with hyperfine parameters in silicate glasses previously reported at ambient condition [3,4], doublets#1 and #2 can be assigned to Fe^{2+} and Fe^{3+} in octahedral site. We are now proceeding with the high-pressure experiments and then will discuss the effects of the valence/spin states of iron on the conductivity.

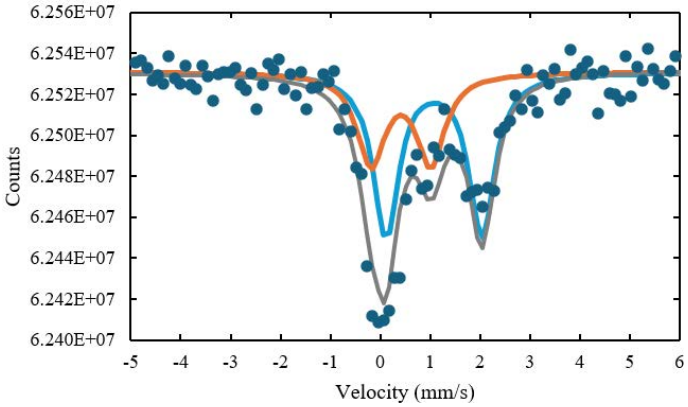

Fig.1. Mössbauer spectrum of Fe-glass. Blue and orange curves represent doublets#1 and #2 respectively

Table 1.
Fitting results of the ambient conventional Mössbauer spectrum of Fe-glass

	IS (mm/s)	QS (mm/s)	FWHM (mm/s)	Aria (%)
Doublet 1 ($Fe2^+$)	1.08±0.03	1.93±0.07	0.62±0.11	62±8
Doublet 2 ($Fe3^+$)	0.41±0.07	1.2(fix)	0.67±0.23	38±8

REFERENCES:

[1] R. Nomura *et al.*, Nature, **473** (2011) 199.
[2] S. Tateno *et al.*, J. Geophys. Res. Solid Earth, **119** (2014) 4684–4694.
[3] M. Dyar, Am Min, **70** (1985) 304–316.
[4] B. Mysen & P. Richet, *Silicate glasses and melts* (Elsevier, 2018).

PR1-5

Fe valence control for Fe and Ni substituted Li_2MnO_3 positive electrode material during charge and discharge reactions using ^{57}Fe Mössbauer spectroscopy

M. Tabuchi and Y. Kobayashi[1]

Research Institute of Electrochemical Energy, Advanced Industrial Science and Technology (AIST)
[1]Institute for Integrated Radiation and Nuclear Science, Kyoto University

INTRODUCTION: Lithium-ion battery (LIB) is utilized as large power source for electrical vehicle (EV) and Energy storage system (ESS). Further development for such applications, minimizing Co and Ni contents in positive electrode is necessary, because both elements are recognized as rare metals. Present Fe and Ni substituted Li_2MnO_3 has features of Co-free and minimizing Ni content (<20% per total transition metal content) [1]. However, precise Fe valence state analysis is important for further improve charge and discharge characteristics. Therefore, ^{57}Fe Mössbauer spectroscopy was selected.

EXPERIMENTS: Target materials were prepared by coprecipitation-calcination method [2]. The Fe:Ni:Mn ratio was set to 15:15:70, $(Li_{1+x}(Fe_{0.15}Ni_{0.15}Mn_{0.70})_{1-x}O_2$, $0<x<1/3)$. First and second (final) calcination atmospheres are air and nitrogen, respectively. Calcination temperatures of 1st and 2nd ones were 650 and 900 ºC for 5 h, respectively. Products were characterized by XRD, charge and discharge data and ^{57}Fe Mössbauer spectroscopy.

RESULTS: XRD data for as-prepared sample showed formation of single-phase with monoclinic Li_2MnO_3 type structure. Its ^{57}Fe Mössbauer spectrum can be fitted by a symmetric doublet (isomer shift (IS) = +0.33 mm/s). Only high-spin Fe^{3+} ion was contained. Fig. 1 (left) showed ^{57}Fe Mössbauer spectrum for first charged electrode. In addition to trivalent iron (A) component (71%), B and C ones were observed, both had highly negative IS values (29%, see left figure). The IS value for B component was close to pentavalent one (-0.4 mm/s), whereas that for C one corresponded to intermediate (4.5+) between tetravalent (-0.1 mm/s) and pentavalent irons. Fig. 1 (left) showed ^{57}Fe Mössbauer spectrum for fifth charged electrode. The fraction of high valence state B component (IS=-0.39 mm/s, 5+ state) was changed to small (5.6%), indicating that Fe reduction was occurred on deep charging. However, no high valence component was detected for the sample with lower 2nd calcination temperature (850 ºC). The fact means that present calcination condition is a suitable for utilizing Fe as 3+/5+ redox center.

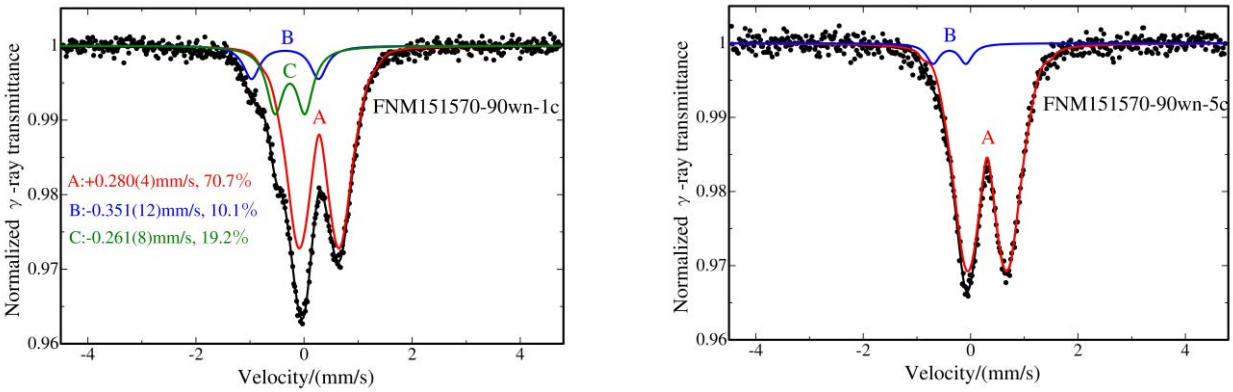

Fig. 1 ^{57}Fe Mössbauer spectra for first (left) and fifth charged (right) electrodes. First and fifth charged states correspond to 80mAh/g delithiation and 4.8 V charging, respectively.

REFERENCES: [1] M. Tabuchi *et al*., J. Power Sources, **196** (2011) 3611-3622.
[2] M. Tabuchi *et al*., Mat. Res. Bull., **149** (2022) 11743.

Experimental Preliminary Approach on the Precipitation Mechanism of Banded Iron Formation (BIF): Precipitation Behavior of Iron in the Absence and Presence of Silicic Acid

K. Yonezu[1], H. Hirano[1], S. Juhri[1], R. Terashi[1], Y. Kobayashi[2] and T. Yokoyama[3]

[1]*Department of Earth Resources Engineering, Faculty of Engineering, Kyushu University*
[2] *Institute for Integrated Radiation and Nuclear Science, Kyoto University*
[3]*Department of Chemistry, Faculty of Sciences, Kyushu University*

INTRODUCTION: Banded Iron Formation (BIF) is chemically precipitated sedimentary rock at Precambrian age. Current iron resource widely used in our industries largely depends on BIF. The formation of BIF was closely related with seafloor hydrothermal activity. In addition, the hydrothermal water, anoxic water was mixed with oxic seawater (e.g., Otake and Otomo, 2021). However, there are many mysteries remained on the formation mechanism of BIF. One of the biggest issues are the alternation of iron bearing mineral and silicate minerals. Therefore, this study aims to under-stand the formation mechanism, especially redox condition during the formation of BIF. Here, we would like to report the precipitation behavior of iron in the absence and presence of silicic acid. For further understanding of the formation mechanism, comprehensive analyses on the precipitates are necessary.

EXPERIMENTS: The sample solutions were prepared by the iron chloride and silicic acid stock solutions. Initial concentration of Fe and silicic acid is adjusted by the dilution with ultra pure water to be 50 – 1500 ppm and 0 – 10 ppm, respectively. In case of the absence of silicic acid, the sample solution was adjusted to pH 8 after the dilution and this timing was regarded as T=0. Precipitation reaction was allowed for 15 minutes with stirring and the monitoring of redox potential and dissolved oxygen concentration. After 15 minutes, the suspension was filtered by 0.45 μm membrane filter. Filtrate was immediately kept in acidic condition and used for the determination of Fe by ICP-AES and the residue on the filter was kept for solid characterization. This time, we focused on the results from filtrate.

RESULTS: As shown in Fig. 1(a), precipitation % of Fe was almost 100 % when initial concentration was low. Under such condition, precipitated iron species was amorphous phase. In contrast, when initial concentration of Fe was high and precipitation % is less than 30 %, the iron species precipitated was mostly magnetite based on XRD analysis, suggesting that magnetite is more likely to form under conditions where there is a certain limit to the amount of oxygen. Fig. 1(b) showed more effective precipitation of Fe (major solid phase by XRD was magnetite) in the presence of silicic acid. These results may imply that it is possible that magnetite was formed even at high silicic acid concentrations because silicic acid can be adsorbed on iron hydroxide since iron hydroxide is formed at the same timing of magnetite formation. Further evidence will be obtained from Mossbauer analysis at KURNS.

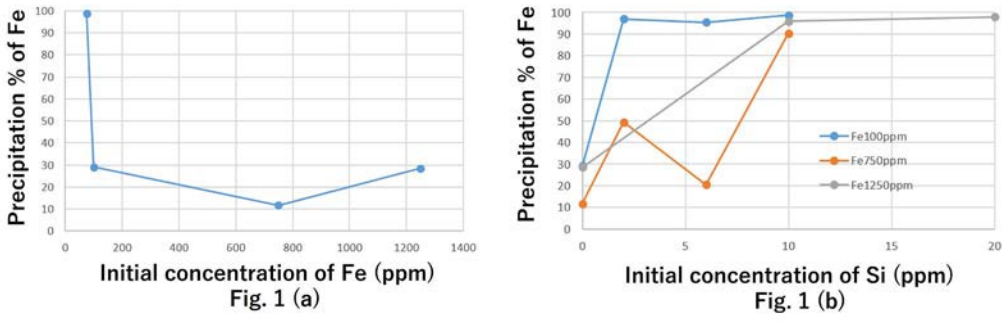

Fig. 1. Precipitation behavior of Fe as a function of the initial concentration of (a) Fe and (b) silicic acid contained with fixed Fe concentration of Fe.

REFERENCES:

[1] T. Otake *et al.*, Shi-gen-Chishitsu, **71** (2021) 57-73.

Research on Magnetism and Electronic Phase in a H-doped Iron-based Superconductor II

Y. Kamihara, R. Hotchi, M. Matoba, Y. Kobayashi[1], S. Kitao[1], and M. Seto[1]

Department of Applied Physics and Physico-Informatics , Faculty of Science and Technology, Keio University
[1]Institute for Integrated Radiation and Nuclear Science, Kyoto University

INTRODUCTION: The research in 2023 is the second year of a three-year plan to clarify the bulk electrical and magnetic properties of polycrystalline $SmFeAsO_{1-x}H_x$ (H-doped Sm1111) prepared by high temperature and high pressure synthesis as a preliminary step for Mossbauer spectroscopy in 2024.
Among the Fe-SC, $SmFeAsO_{1-x}F_x$ (F-doped Sm1111) and H-doped Sm1111, whose mother compound is an antiferromagnetic (AFM) metal SmFeAsO, exhibit T_c ~55 K under ambient pressure. This feature is similar to an electronic and magnetic phase diagram for high-T_c cuprate superconductors, whose mother compound exhibit antiferromagnetic phase of copper sublattice. [1-6] A novel ^{57}Fe Mössbauer spectra of H-doped Sm1111 will appear during 2024-2025.

EXPERIMENTS: The phase purity, lattice constants, and crystal structure of the sintered powders were examined by powder x-ray diffraction (XRD) Rigaku Rint2500 using Cu K alpha radiation from a rotating anode. The magnetic moment (M) of polycrystalline H-doped Sm1111 was measured using a SQUID magnetometer (Quantum Design MPMS) at several temperatures (T) and magnetic fields (H). ^{57}Fe Mössbauer spectroscopy was performed at a low temperature.

RESULTS: Figure 1 exhibits lattice constants and volume as a function of the H-doped Sm1111 samples. The F contents are determined using Volume Vegard's rule. [7]

REFERENCES:

[1] For a review, M. Fujioka, Ph. D thesis (Keio University, 2012).
[2] Y. Kamihara *et al.*, New J. Phys. **12** (2010) 033005 .
[3] Y. Kamihara *et al.*, American Physical Society March Meeting, Dallas, USA (2011).
[4] K. Miyazawa *et al.*, Appl. Phys. Lett. **96** (2010) 072514.
[5] P. M. Shirage *et al.*, Phys. Rev. Lett. **105** (2010) 037004.
[6] Y. Muraba *et al.*, Inorg. Chem. **54** (2015) 11567-11573 .
[7] A. Cox, and M. J. L. Sangster, J. Phys. C: Solid State Physics, **18** (1985) L1123-L1126.

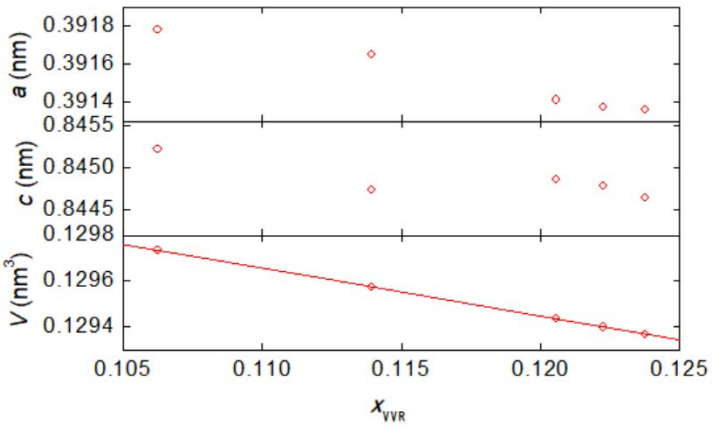

Fig. 1. Lattice constant (a, c) and lattice volume for the H-doped Sm1111.

Magnetic Measurememts of Irons in Soda-lime Glass by Mössbauer Spectroscopy (2)

K. Okada, and Y. Kobayashi[1]
SPring-8/JASRI
[1]Graduate School of Engineering, Kyoto University

INTRODUCTION: Glass is used in many applications in our every-day lives and has exciting new applications related to the energy. Soda-lime glass is made of mainly silica (SiO_2) and additive many other materials, such as magnesium, sodium, calcium, aluminum, iron, sulfur, and so on. Our reference glass composition, in percent by weight (wt%), was 72.25 SiO_2, 1.75 Al_2O_3, 4.00 MgO, 8.00 CaO, 14.00 Na_2O as basic components, and 0.015-5 iron in terms of Fe_2O_3 as coloring components. Iron contaminants of less than 0.0005-0.01 wt% from raw materials, and iron injection up to 1.5-5 wt%. The iron oxides in a glass composition are thought to be present in forms of Fe^{3+} and Fe^{2+}. The control parameters for irons are two: (1) the total iron mass weight percent in terms of Fe_2O_3, and (2) the ratio of $Fe^{2+}$to total iron ions (Fe^{2+}/Σ_nFe). The Fe^{3+} component adds a light yellow tint to the glass and absorption in the ultraviolet and visible band, while the Fe^{2+} component adds a blue tint to the glass and absorption in the near-infrared band (1 μm). The transmission from ultraviolet to infrared in glass cannot be explained by simple Fe^{2+} and Fe^{3+} structures. Then, to reveal the exact local structures of irons (Fe^{2+} and Fe^{3+}) is necessary. Many scientists proposed many new theories and local structures [1-2], but they did not resolve it completely.

We have prepared reference glass samples with using the Mössbauer isotope ^{57}Fe (natural abundance is about 2.119 %) and sample glass with natural Fe for measurements. The chemical composition of iron oxide in the ^{57}Fe enrichment glass was from 0.015 to 5 wt%, and the Fe^{2+}/Σ_nFe was from 0 to 0.6. We have investigated these samples by nuclear resonant inelastic scattering and XAFS methods at synchrotron radiation to reveal the local atomic structure around and neighboring iron atoms in sub-nanometer region [3]. And then we have investigated No. 100 sample glass with 30 wt% chemical composition of natural iron oxide by Mössbauer experiments to reveal the magnetic property in glass under recycled process.

EXPERIMENTS: The measurements were performed using conventional Mössbauer spectrometer. The specimens for Mössbauer measurements were tuned to 10 mm-phi pellet. We investigated two samples with 30 wt% chemical composition of natural iron oxide.

RESULTS: There were difference between the data of the 1st and the 3rd recycled samples as shown in Fig. 1, and the six line structures in the data of recycle 1st indicated the alpha-Fe_2O_3, which was not melted completely.

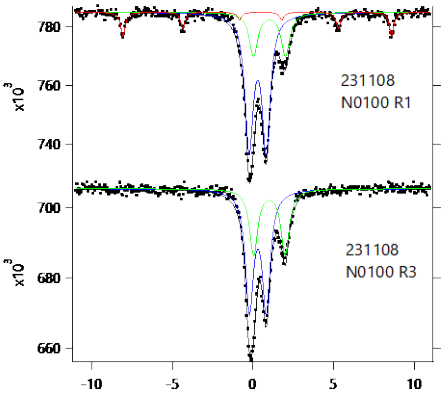

Fig. 1. Mössbauer spectra of the 1st (upper panel) and the 3rd (lower panel) recycled in-flight-melting glass with No. 100. The measurements were performed at room temperature.

REFERENCES:
[1] C. Ruessel *et al.*, *Phys. Chem. Glasses*, **47** (2006) 563.
[2] F. Farges *et al.*, *Physica Scripta*, **T115** (2005) 957.
[3] K. Okada *et al.*, X-ray Spectrometry, **47** (2018) 359-371.

^{57}Fe Mössbauer Study of Fe-Si Magnetic Materials

Y. KOBAYASHI[1], K. YUASA[2] and M.SETO[1]

[1]*Institute for Integrated Radiation and Nuclear Science, Kyoto University*
[2]*Corporate Research & Development Center, Daido Steel Co., Ltd.*

INTRODUCTION: Fe-Si alloy is a soft magnetic material used in many devices, such as transformers. A method of pressing powdered alloys is used to produce complex shapes, such as transformer cores. The alloy powders are prepared using the gas atomization method, in which the melted alloy is splayed into gas. We performed Mössbauer spectroscopy to investigate the state of the powder created using the gas atomization method.

EXPERIMENTS: The Fe-Si powder samples were prepared using the atomizing process with nitrogen gas. Base alloys were Fe-6.5wt%Si. The powder samples were annealed at 850°C for 3 hours for homogenization. ^{57}Fe Mössbauer measurements were performed at room temperature using the conventional Mössbauer spectrometer. About 30 mg of sample and about 100 mg of boron nitride were mixed and put in the sample holder with a diameter of 10 mm for Mössbauer transmission measurement. α-Fe was used for velocity calibration. The Mossbauer spectra were fitted with a MossWinn [1] program.

RESULTS: Two Fe sits in Fe_3Si ordered phase ($D0_3$ structure): the A site, where four of the eight nearest neighbors in the bcc structure are Si, and the B site, where all the nearest neighbors are Fe. The Fe atomic ratio of each site is 2:1. Figure 1 shows the Mössbauer spectra of Fe_3Si and Fe-6.5wt%Si powder samples. The spectrum of Fe_3Si consists of two magnetic components. The component with the large internal magnetic field is due to the B site, whose nearest neighbors are all Fe, and the component with the small internal magnetic field is due to the A site, whose four nearest neighbors are Si, and their area ratio is approximately 1:2.

The spectrum of the Fe-6.5wt%Si sample can be analyzed with four components whose internal magnetic fields are 34~24T and two components with almost the same parameters as the Fe_3Si sample (bold solid lines in the spectrum). The former four components are derived from the Fe-Si disordered phase of the bcc structure [2]. The previous work shows that the composition is divided according to how many Si atoms are present in the nearest or the second-nearest neighbor of Fe atoms. As the number of adjacent Si increases, the internal magnetic field becomes smaller, and the proportion of each component can be estimated from the binomial distribution of the Si concentration. The area ratios estimated from calculations generally agreed with those determined from the spectra.

Analysis of these spectra revealed that the Fe-6.5wt%Si powder sample consists of a Fe-Si disordered alloy and a small amount (6%) of Fe_3Si ordered phase.

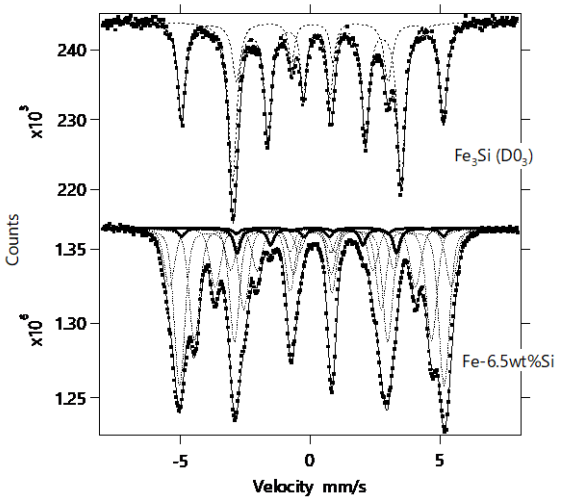

Fig. 1 Mössbauer spectra of Fe_3Si and Fe-6.5wt%Si samples.

REFERENCES:

[1] Z. Klencsar *et al.,* J. Radioanal. Nucl. Chem., **210** (1996) 105.
[2] G. Rixecker *et al.,* Phys. Stat. Sol. (a), **139** (1993) 309.

Mössbauer study of nanoparticles synthesized in Y-type Zeolite

R. Masuda, T. Kato, Y. Suzuki, S. Kitao[1], Y. Kobayashi[1], and M. Seto[1]

Graduate School of Science and Technology, Hirosaki University
[1]Institute for Integrated Radiation and Nuclear Science, Kyoto University

INTRODUCTION: Mössbauer studies sometimes requires energy standard, especially for the determination of the isomer shift. In the Mössbauer spectroscopy by ^{57}Fe nuclide, which is the most common case, it is the center of the absorption profile of Fe metal foil. Such energy standards also exist in the Mössbauer spectroscopy by nuclides other than ^{57}Fe. However, those for some nuclides are not perfectly agreed by researchers as Fe foil for ^{57}Fe is [1]. This is because some of the following desirable conditions are not satisfied: i) high recoilless fraction (i. e. strong Mössbauer effect), ii) no hyperfine splitting or clearly split hyperfine structure, and iii) chemical stability in the air. Considering these conditions, nanoparticles might be also candidates for such energy standard because the superparamagnetic property often cancel the magnetic hyperfine structure.

Recently we focused on the nanoparticles synthesized chemically using the zeolite, which is porous in nanometers scale. Large amount of nanoparticles in the size of its cage of the zeolite framework can be synthesized chemically. Furthermore, if the γ-ray energy used in Mössbauer spectroscopy is in the hard X-ray region, zeolite framework is relatively transparent because the framework includes only light elements, such as Al, Si, and O. Here, to study the nanoparticles synthesized by this method, we measured their Mössbauer spectra of the Fe nanoparticles.

EXPERIMENTS: The sample was prepared by the chemical displacement of cations in HY-type zeolite by Fe. The resultant chemical composition was $Si_{149.9}Al_{52.3}Na_{1.6}Fe_{4.3}$, evaluated by electron probe micro analyzer (EPMA). The Mössbauer spectra were measured under temperatures down to 100 K through a cryostat using liquid N_2 in KURNS. Velocity was calibrated by enriched Fe foil at room temperature.

RESULTS: The temperature dependence of the Mössbauer spectra of the nanoparticles were shown in Fig. 1. They showed quadrupole splitting of typically 0.8 mm/s, center shift of typically 0.4 mm/s. From these Mössbauer parameters, the chemical composition of the nanoparticles would be close to hematite, α-Fe_2O_3. Even the hematite nanoparticles with the diameter of approximately 5 nm showed magnetic splitting in 120 K [2], the diameter of the nanoparticles in this study would be less than that. If we assume that the absorption area is proportional to the recoilless fraction, the characteristic temperature under the Debye model for the fraction was 2.8 (±0,6) × 10^2 K, which is much less than that of bulk hematite. From these results, we successfully evaluate both the absence of magnetic hyperfine splitting down to 100 K, which also yields the information of the size of the particles and the recoilless fraction of the nanoparticles.

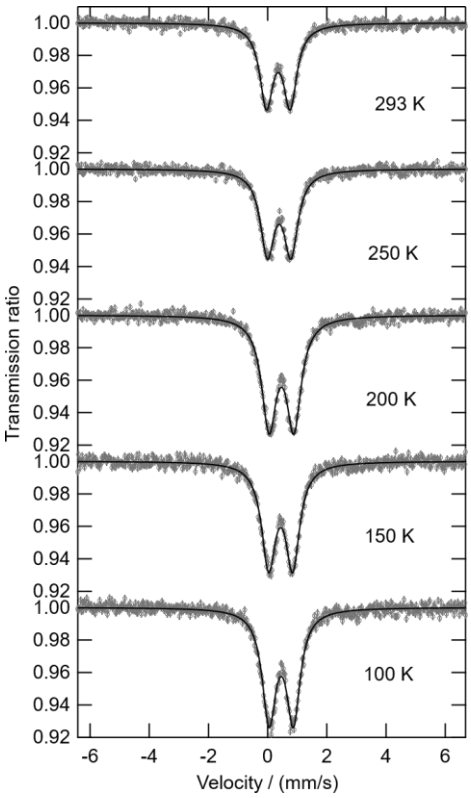

Fig. 1. Temperature dependence of the Mössbauer spectra of iron nanoparticles synthesized using HY-type zeolite.

REFERENCES:

[1] G. Concas *et al.,* Z. Naturforsch., **56a** (2001) 789.
[2] T. Nakamura *et al.*, Phys. Lett., **12** (1964) 178.

^{166}Er Mössbauer Study of ErB_4

S. Kitao[1], Y. Kobayashi[1], M. Kurokuzu[1], T. Kubota[2], H. Tajima[3], H. Yamashita[3], H. Ota[3], R. Masuda[4], and M. Seto[1]

[1]*Institute for Integrated Radiation and Nuclear Science, Kyoto University*
[2]*Agency for Health, Safety, and Environment, Kyoto University*
[3]*Graduate School of Science, Kyoto University*
[4]*Faculty of Science and Technology, Hirosaki University*

INTRODUCTION:

The Mössbauer spectroscopy is one of the most powerful methods to investigate electronic states and magnetic properties by extracting the information of a specific isotope. Mössbauer spectroscopy in general is performed for quite limited isotopes, such as ^{57}Fe and ^{119}Sn. On the contrary, the neutron irradiation facility at Kyoto University Reactor (KUR) at KURNS can be used to product various radioactive isotopes (RIs) for the Mössbauer sources. Moreover, some RIs
can be complementarily produced by high-energy γ-ray irradiation converted from electron beam from the electron linear accelerator (KURNS-LINAC). We have been developing practical methods for Mössbauer spectroscopy for various isotopes. Available Mössbauer isotopes at present are as follows (source nuclides in parentheses): ^{61}Ni(^{61}Co), ^{125}Te(^{125m}Te), ^{129}I(^{129}Te,^{129m}Te), ^{161}Dy(^{161}Tb), ^{166}Er(^{166}Ho), ^{169}Tm(^{169}Er), ^{170}Yb(^{170}Tm), ^{197}Au(^{197}Pt), etc.

Among these isotopes, ^{166}Er Mössbauer spectroscopy is one of the most useful methods for studies of electronic or magnetic state for Er compounds. For some former studies, $HoAl_2$ was used as a Mössbauer source [1]. However, the measurement temperature had not to be cooled below around 40 K, since $HoAl_2$ has magnetic transition at 25 K. To overcome this disadvantage, another source material, $Ho_{0.4}Y_{0.6}H_2$ had been successfully synthesized with similar meth-od in the references [2,3] and confirmed a single-line ^{166}Er Mössbauer spectra as low as 18K [4].

In this report, the study of a typical Er compound, ErB_4 is described. ErB_4 is expected as a compound with high re-coilless fraction. Since it has an antiferromagnetic transition temperature, T_N of 15 K, the spectrum is expected as a sin-gle-line above T_N. However, the temperature dependence of Mössbauer spectra of ErB_4 has not been known around the transition temperature.

EXPERIMENTS AND RESULTS:

The source material $Ho_{0.4}Y_{0.6}H_2$ has been synthesized by hydridation of $Ho_{0.4}Y_{0.6}$ alloy. The neutron irradiation was performed at pneumatic tube of KUR for 150 minutes at 1MW operation or 30 minutes at 5MW operation. The ^{166}Ho source with a half-life of 26.8 h was obtained and used for the ^{166}Er Mössbauer measurement for 2 or 3 days. The source material can be irradiated repeatedly if it is kept in a vacuum desiccator after using to avoid deterioration. The ErB_4 was purchased from Mitsuwa Chemicals Co., Ltd. The measurement temperature was controlled by keeping both the source and the absorber in a He-gas filled space using a closed cycle He-refrigerator.

The obtained spectra of ErB_4 at 22K and 50K are shown in Fig. 1. The spectrum at 22 K was apparently magnetically split. The internal magnetic field was evaluated as about 790 T. In the spectrum at 22 K, a small line with large broadening has been observed. In the spectrum at 50 K, the magnetically-split component was reduced and the line with large broadening has been mainly observed. The results showed the antiferromagnetic phase was observed even above the transition temperature of 15 K. Moreover, a broad component was observed above the transition temperature possibly due to a relaxation phenomenon. These information will be useful for the studies for related several erbium borides.

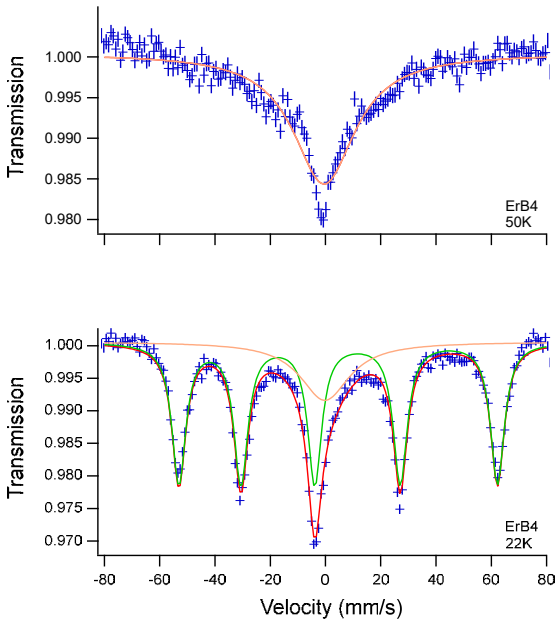

Fig. 1. ^{166}Er-Mössbauer spectrum of ErB_4 using $^{166}Ho_{0.4}Y_{0.6}H_2$ source at 50 and 22 K.

REFERENCES:

[1] S. Nakamura *et al.,* Hyperfine Interact., **240** (2019) 75.
[2] J. Stöhr and J. D. Cashion, Phys. Rev. B, **12** (1975) 4805.
[3] D. B. Prowse *et al.,* J. Phys. D:Appl. Phys., **6** (1973) 646.
[4] S. Kitao *et al.,* Hyperfine Interact., **244** (2023) 10.

I-1. PROJECT RESEARCHES

Project 2

PR2

Preclinical studies for applying BNCT to veterinary medicine

M. Suzuki

Institute for Integrated Radiation and Nuclear Science, Kyoto University

In this research project, six research projects were included. The four researches were planned by veterinarians. Details of six projects are referred to each progress report.

P2-1. The Basic Study Aimed at Performing the Boron Neutron Capture Therapy for Canine Hemangiosarcoma

In this study project, the possibility of applying BNCT to canine hemangiosarcoma (HAS) using the three canine HSA cell lines were investigated. In conclusion, BNCT can be applied to canine HSA because enough ^{10}B uptake and the anti-tumor effect of BNCT were confirmed in this study.

P2-2. Preparation of Rabbit-Dog Chimeric Anti-BSH Antibody and Comparison with Caninized Anti-BSH Antibody

In this study, since the yield and purity of caninized anti-BSH antibodies were low, creating a rabbit-dog chimeric anti-BSH antibody in which only the constant region was canonized were attempted. Since chimeric anti-BSH antibody (chBSH IgG) has high binding ability and excellent production efficiency, usage of chBSH IgG to produce a bispecific antibody against Her2 and BSH will be attempted to estimate an antitumor effect on canine cancer cells.

P2-3. Preparation of immunoliposomes comprising hydrophobic boron cluster via exchanging reaction.

In this study, applicability of immunoliposome comprising highly concentrated carborane that is prepared by exchanging reaction as a boron agent for BNCT was investigated. The developed im-munoliposome exhibited higher BNCT activity *in vitro* study and high accumulation in the tumor tissue *in vivo* study. The immunoliposome system are promising candidate for BNCT.

P2-4. Investigation of the relationship between the therapeutic efficacy of boron neutron cap-ture therapy and the residence of boron drugs in tumors

In this study, the effects of tumor tissue diversity (stromal volume and blood flow distribution) on BPA retention and response to BNCT were investigated. It was observed that BNCT inhibited tumor growth regardless of the amount of stroma, suggesting that macroscopic BPA uptake alone does not predict therapeutic efficacy.

P2-5. The basic study of the effect of BNCT for squamous cell carcinoma of the head and neck in dogs

In this study, the efficacy of boron neutron therapy using a tumor-bearing model of canine tonsillar squamous cell carcinoma (TSCC) was investigated. Tumor growth curves for each group indicates that BNCT has the potential to be a treatment for NTSCC.

P2-6. Boron Delivery to Brain Cells via Cerebrospinal Fluid (CSF) Circulation for BNCT in a Rat Glioma Model

In the previous study, use of the boron CSF administration method resulted in the same amount of BPA accumulation in the brain tumor as that achieved using the intravenous (IV) administration method. In this study, the therapeutic effect by the CSF administration method was almost equiva-lent to that following the IV administration method, even though the dose of BPA in the CSF ad-ministration method was quite low.

The Basic Study Aimed at Performing the Boron Neutron Capture Therapy for Canine Hemangiosarcoma

R. Iwasaki, S. Uchida, R. Yoshikawa, T. Mori, Y. Sakurai[1] and M. Suzuki[1]

Faculty of Applied Biological Sciences, Gifu University
[1]Institute for Integrated Radiation and Nuclear Science, Kyoto University

INTRODUCTION: Hemangiosarcoma (HSA) is one of the most major malignant cancers in dogs. Canine HSA occurs frequently in the spleen, liver, heart and skin and can easily rupture, subsequently causing serious local problem. Furthermore, HSA is known to be highly metastatic. Thus, it is important to prevent the progression of metastatic lesions as well as local control of primary lesion. Although doxorubicin-based chemotherapy has been shown to prolong prognosis, long-term survival in not expected, with a median survival time of 4–7 months. Therefore, new treatment strategies are needed.

Boron neutron capture therapy (BNCT) is a therapeutic method that selectively destroys the tumor while leaving normal tissues almost unharmed by utilizing the nuclear reaction with neutron and boron, which tends to accumulate in the cancer cells. In human, LAT1, an amino acid transporter that has been found to be particularly involved in the intracellular transport of boron compound, is shown to be overexpressed in many malignant tumor cells.

In this study project, we investigated the possibility of applying BNCT to canine HSA by examining the LAT1 expression, the intracellular boron concentration, and the survival after the neutron irradiation using the canine HSA cell lines.

EXPERIMENTS: Three cell lines derived from canine HSA, JuB2, Ud6 and Re21, were used for this study. As boron compound, p-boronophenylalanine (BPA) was prepared at a dose of 30 mg/ml.

RT-PCR Total RNA was isolated from each cell line using the RNA extraction solution (NucleoSpin RNA, Macherey-nagel, Germany). RT-PCR amplification was performed using the One-step RT-PCR kit (QIAGEN, Germany). A mixture of RT-PCR products and loading buffer (Takara Bio Inc., Japan) was electrophoresed in a 2% agarose gel. RP19 primer was used as a housekeeping gene.

Inductively coupled plasma atomic emission spectrometry (ICP-AES) 1×10^6 cells of JuB2, Ud6 and Re21 were co-incubated with BPA for 0.5, 1 and 2 h. The boron-10 (^{10}B) concentrations in BPA solution were adjusted with culture medium to 28 ppm. Each sample was digested by heating overnight in nitric acid (60%), then diluted with distilled water and divided into three test tubes. After measuring the boron concentration in these tubes using ULTIMA2 (HORIBA, Ltd., Kyoto, Japan), their average was taken as the amount of the sample and expressed in "ng ^{10}B / 10^6 cells."

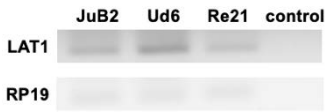

Fig. 1. Expression of LAT1 mRNA by RT-PCR.

Irradiation In the neutron group, 1×10^5 cells of JuB2, Ud6 and Re21 were irradiated with thermal neutron at a power of 1 MW for 15, 30, and 45 minutes (fluence: 7.35–23.5 $\times$ 10^{11} n / cm^2) at KURNS. In the BNCT group, cells were co-incubated with 28 ppm ^{10}B of BPA for 8 hours before irradiation. In the X-ray group, cells were irradiated with 1, 2, 4, 8, and 12 Gy of X-ray at a dose rate of 250 cGy / min at Gifu University. After irradiation, each survival rate was evaluated by colony formation assay.

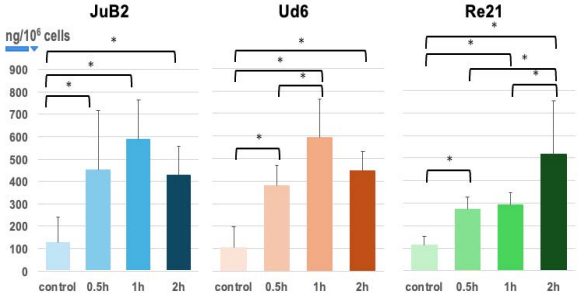

Fig. 2. Intracellular ^{10}B concentrations by BPA co-incubation time using ICP-AES.

RESULTS: The mRNA expressions of LAT1 were seen in all three cell lines (Fig. 1). Fig. 2 shows the intracellular ^{10}B uptake measured by the ICP-AES. In JuB2 and Ud6, there were peaks in ^{10}B uptake for 1-h co-incubation, whereas the peak was seen for 2-h co-incubation in Re21. The amount of ^{10}B uptake at the peak was highest in Ud6, followed by JuB2 and Re21. The colony formation assay showed that the cell survival rate was significantly lower in the BNCT group than in the neutron group in all three cell lines (Fig. 3). Furthermore, the effect of BNCT among cell lines was dependent on the amount of ^{10}B uptake.

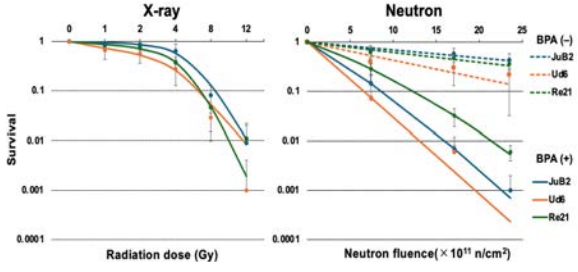

Fig. 3. Survival curves for each cell line after X-ray or neutron irradiation by colony forming assay.

CONCLUSION: Our results indicate that BNCT can be applied to canine HSA because enough ^{10}B uptake and the anti-tumor effect of BNCT were confirmed in this study.

Preparation of Rabbit-Dog Chimeric Anti-BSH Antibody and Comparison with Caninized Anti-BSH Antibody

N. Ueda, N. Yasukawa, R. Kawasaki[1], Y. Sakurai[2], Y. Sanada[2], N. Kondo[2], M. Suzuki[2], and T. Nagasaki

Graduate School of Engineering, Osaka Metropolitan University
[1] Graduate School of Advanced Science and Engineering, Hiroshima University
[2]Institute for Integrated Radiation and Nuclear Science, Kyoto University

INTRODUCTION: It has been reported that 39% of deaths in long-lived dogs were due to age-related diseases, especially cancer [1]. Boron neutron capture therapy (BNCT) is expected to be a new treatment strategy for canine cancer [2]. In our laboratory, bispecific antibodies against BSH and Her2 have previously prepared as boron delivery tool [3]. It is composed of rabbit-derived IgG that bins BSH and llama VHH antibody that binds Her2, typical tumor antigen. In order to use this bispecific antibody against BSH and Her2 for canine BNCT, we have successfully produced a caninized anti-BSH IgG antibody. Unfortunately, it was found that the efficiency of the antibody production was too low to apply *in vivo* estimation [4]. Since the yield and purity of caninized anti-BSH antibodies were low, we herein attempted to create a rabbit-dog chimeric anti-BSH antibody in which only the constant region was caninized.
****

EXPERIMENTS: The heavy chain expression vector of a bispecific antibody against BSH and Her2 and the heavy chain expression vector of canine anti-PD-1 IgG antibody were digested with restriction enzymes Eco RI and Nhe I and ligated. In this way, a rabbit-dog chimeric anti-BSH heavy chain expression vector (pCAGEN chBSH HC) was constructed. On the other hand, PCR was performed using the rabbit anti-BSH light chain expression vector (pCAGEN caBSH LC) and the light chain expression vector of canine anti-PD-1 IgG antibody as templates to produce 1st PCR products. Using the 1st PCR product as a template, 2nd PCR was performed to produce a 2nd PCR product. The 2nd PCR product was digested with restriction enzymes Eco RI and Not I and ligated to pCAGEN caBSH LC, which had been previously digested with the same enzymes, to create a rabbit-dog chimeric anti-BSH light chain expression vector (pCAGEN chBSH LC). Using ExpiCHO cells as a host, rabbit-dog chimeric anti-BSH heavy chain and light chain expression vectors (pCAGEN chBSH HC and LC) were cotransfected to produce rabbit-dog chimeric anti-BSH antibody (chBSH IgG). ELISA was performed using an HRP-labeled secondary antibody to evaluate the BSH-binding ability of the produced antibody (Fig.1).
****

RESULTS: The amount of antibody produced per a liter of culture medium was 0.94 mg for the caninized antibody, whereas it was 10.1 mg for the chimeric antibody. The ELISA results are shown in Fig.1. As the concentration of antibody increased, the absorbance value at 450 nm also increased. Therefore, it was confirmed that both the caninized antibody (caBSH IgG) and the chimeric antibody (chBSH IgG) had the ability to bind to BSH. Furthermore, when comparing caBSH IgG and chBSH IgG, chBSH IgG had higher absorbance at any concentration, and chBSH IgG was found to have higher antigen binding than caBSH IgG.
Since chimeric anti-BSH antibody (chBSH IgG) has high binding ability and excellent production efficiency, we will use chBSH IgG to produce a bispecific antibody against Her2 and BSH, and estimate an antitumor effect on canine cancer cells.
****

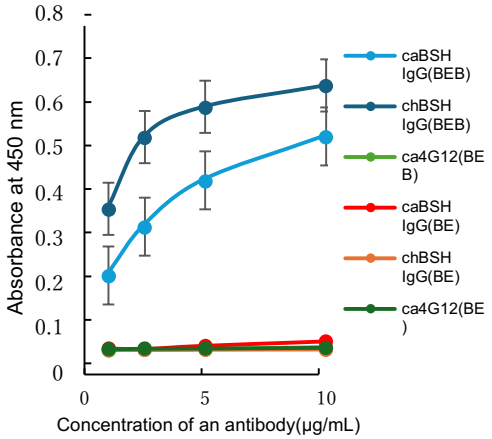

Fig. 1. Evaluation of antigen binding ability of canonized and chimeric anti-BSH IgG.

REFERENCES:

[1] R.T. Bronson, Am. J. Vet. Res., **43**(1982) 2057.
[2] A. E. Schwint *et al.,* Biol., **9** (2000) 327.
[3] T. Kanai *et al*., KURNS Prog. Rep., (2020) 31P6-6.
[4] N. Ueda *et al*., KURNS Prog. Rep., (2023) R4P4-2.

PR2-3

Preparation of immunoliposomes comprising hydrophobic boron cluster via exchanging reaction

Riku Kawasaki,[1] Ayano Oshige,[1] Keita Yamana,[1] Yu Sanada,[2] Kaori Bando,[3] Takushi Takata,[2] Yoshinori Sakurai,[2] Hiroki Tanaka,[2] Tomoki Kodama,[4] Seiji Kawamoto,[4] Takeshi Nagasaki,[3] Atsushi Ikeda[1]

[1]*Program of Applied Chemistry, Graduate School of Advanced Science and Engineering, Hiroshima University*
[2]*Institute for Integrated Radiation and Nuclear Science, Kyoto University*
[3]*Department of Applied Chemistry and Bioengineering, Graduate School of Engineering, Osaka Metropolitan University*
[4]*Program of Bioengineering, Graduate School of Integrated Science for Life, Hiroshima University*

INTRODUCTION: Liposomes has been widely used nanoplatform for drug delivery system since the system can encapsulate both hydrophilic and hydrophobic pharmaceuticals in internal water phase and lipid bilayer, respectively. Moreover, the functionalization such as tumor targeting and controlled release properties can be achieved by surface modification. For these fascinating properties of liposomes, this nanomaterial is the first example which was approved in clinical. In our group, drug loading technique based on supramolecular chemistry for hydrophobic compounds was developed, that is exchanging reaction. The strategy consists of two steps. Initially, liposomes are mixed with interests dispersed in water using natural products such as cyclodextrins, polysaccharides, and polypeptides. Next, the complex of hydrophobic compounds with natural products were decomposed by inducing heat stress and released cargo molecules were trapped by liposomes. The system could introduce much larger amount of pharmaceuticals to lipid bilayer compared with conventional drug loading method for liposomes. In this work, we demonstrated applicability of immunoliposome comprising highly concentrated carborane that is prepared by exchanging reaction as a boron agent for BNCT.
EXPERIMENTS: Lipids comprising maleimide conjugated polyethylene glycol were used as antibody presenting units and PEGylated liposomes were prepared by extrusion method. Carboranes were introduced to the PEGylated liposomes via exchanging reaction and the proceeding of the reaction was monitored by ^{1}H-NMR. Antibody was introduced to the PEGylated liposome loading carborane and the conjugated amount of antibody was quantified by protein detection reagents after purification with ultracentrifugation. We demonstrated BNCT activity *in vitro* using HER-2 targeting antibody. Here, we employed human cervical cancer cell (SK-OV-3) which overexpress HER-2 on the cellular membrane. Finally, we demonstrated deliverability of current system *in vivo* using tumor xenograft model mice.
RESULTS: After mixing of PEGylated liposomes and carborane-cyclodextrin complex, H-NMR measurement was carried out and representative proton peak of carborane was gradually broadened with time, indicating the kinetics of carborane including molecular rotation got decreased. Moreover, the exchanging reaction could load larger amount of carborane in each liposomes.Then, carborane was trapped by PEGylated liposomes by just heating dispersion. Afterward, antibody was introduced to the system. After 24 h incubation, almost all the maleimide groups were consumed and over 80% of antibody was successfully conjugated with liposomes. During these procedures, changes in size and formulation of aggregates were not found. When HER-2 targeted antibody was introduced to the immunoliposomes, the immunoliposomes exhibited higher BNCT activity toward SK-OV-3 cells than L-BPA-fructose complex. This is why the cellular uptake amount of boron was significantly boosted by antibody conjugation. We next investigated deliverability of current system *in vivo* using tumor xenograft model mice established by transplantation of SK-OV-3 to nude mouse. After administration, our system could accumulate to the tumor tissue with high selectivity. For these results, our immunoliposome systems are promising candidate for BNCT.
REFERENCES: [1] R.Kawasaki *et al.,* Chem. Eur. J., **5** (2023) 3857.

PR2-4

Investigation of the relationship between the therapeutic efficacy of boron neutron capture therapy and the residence of boron drugs in tumors

Y. Wada[1,2], M. Suzuki[2].

[1] *Veterinary Medical Center, Osaka Prefecture University*

[2]*Particle Radiation Oncology Research Center, Institute for Integrated Radiation and Nuclear Science, Kyoto University*

INTRODUCTION: The decision to use BNCT depends on the ratio of tumor uptake of 18FBPA to normal tissue (T/N ratio) on 18F-BPA-PET scans. However, it has recently been reported that prolonged residence time of BPA in tumors contributes to improved therapeutic efficacy of BNCT.[1] Therefore, BPA uptake alone may not be sufficient to predict therapeutic efficacy. In this study, we investigate the effects of tumor tissue diversity (stromal volume and blood flow distribution) on BPA retention and response to BNCT.

EXPERIMENTS: Capan-1cells and PSN1 cells(5.0 ×106/100 μL in 0.1 ml PBS) were injected into the subcutaneous femoral of mice (six-week-old female BALB/c nude mice), and the mice were divided into the cold control (no treatment, no neutron irradiation), hot control (neutron irradiation only), BPA administration only and BNCT (intraperitoneal BPA administration and neutron irradiation) groups. . Irradiation was performed 48 days after the injection of Capan-1cells and PSN1 cells at the heavy water facility of Kyoto University Research Reactor for 12 min at a power of 5 MW. BPA was injected subcutaneously at a dose of 250 mg/kg 1 h before irradiation. Tumor size in the four groups was investigated.

RESULTS: Tumor growth curves for each group are shown in Fig1, where X-axis indicates the number of days after irradiation and Y-axis indicates the tumor growth rate. The results showed that both of the two cell types showed tumor growth inhibition in the BNCT group.

Conclusion: It was observed that BNCT inhibited tumor growth regardless of the amount of stroma, suggesting that macroscopic BPA uptake alone does not predict therapeutic efficacy.

Fig. 1.
Tumor growth curves for Capan-1 and PSN1 treated with the combination of BPA and radiation.

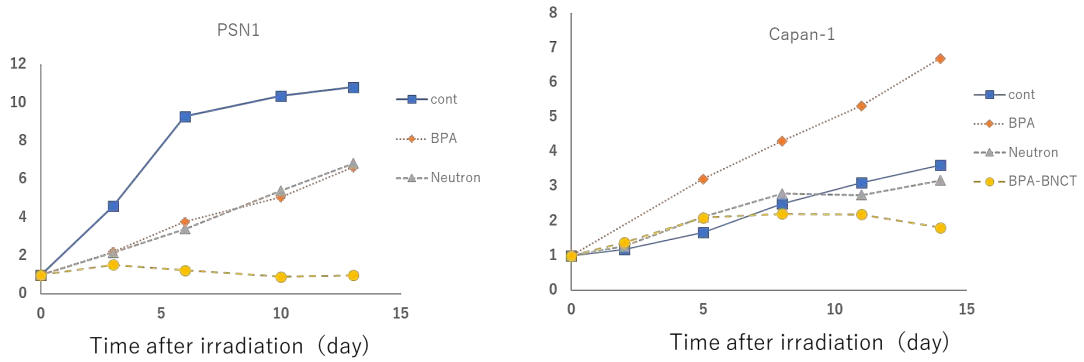

REFERENCES:

[1] T. Nomoto *et al.,* Sci Adv., **6** (2020) 1722.

PR2-5

The basic study of the effect of BNCT for squamous cell carcinoma of the head and neck in dogs

Y. Wada[1,2], M. Suzuki[2].

[1] Veterinary Medical Center, Osaka Metropolitan University

[2]*Particle Radiation Oncology Research Center, Institute for Integrated Radiation and Nuclear Science, Kyoto University*

INTRODUCTION: The disadvantage of boron neutron capture therapy is that the neutron beam cannot be absorbed deeply into the body. However, for companion animals, almost all malignant tumors in dogs and cats are applicable because of their size. In this study, we focused on canine tonsillar squamous cell carcinoma. Canine oral squamous cell carcinoma is the second most frequently occurring tumor in the canine oral cavity. Canine tonsillar squamous cell carcinoma (TSCC) has a high rate of metastasis and a short prognosis even with surgical treatment, radiation therapy, and chemotherapy. In a report of a patient treated with radiotherapy and chemotherapy, CR was temporarily observed, but most of the patients died due to local recurrence.[1] Therefore, there is a need for a treatment method that can provide strong local control of TSCC. If BNCT is an effective treatment for canine TSCC, it may be effective against both localized and metastatic lesions and improve prognosis. This study is designed to investigate the efficacy of boron neutron therapy in a tumor-bearing model of TSCC.

EXPERIMENTS: TSCCLN-5 cells (5.0×10^6/100 μL in 0.1 ml PBS) were injected into the subcutaneous femoral of seven-week-old female BALB/c nude mice, and the mice were divided into the cold control (no treatment, no neutron irradiation), hot control (neutron irradiation only), BPA administration only and BNCT (intraperitoneal BPA administration and neutron irradiation) groups. Irradiation was performed 48 days after the injection of TSCCLN-5 cells. at the heavy water facility of Kyoto University Research Reactor for 12 min at a power of 5 MW. BPA was injected subcutaneously at a dose of 250 mg/kg 1 h before irradiation. Tumor size in the four groups was investigated.

RESULTS: Tumor growth curves for each group are shown in fig1, where X-axis indicates the number of days after irradiation and Y-axis indicates the tumor growth rate. The results show proliferation inhibition in the BNCT group. The results indicate that BNCT has the potential to be a treatment for NTSCC.

Fig.1.
Tumor growth curves for TSCCLN-5 treated with the combination of BPA and radiation.

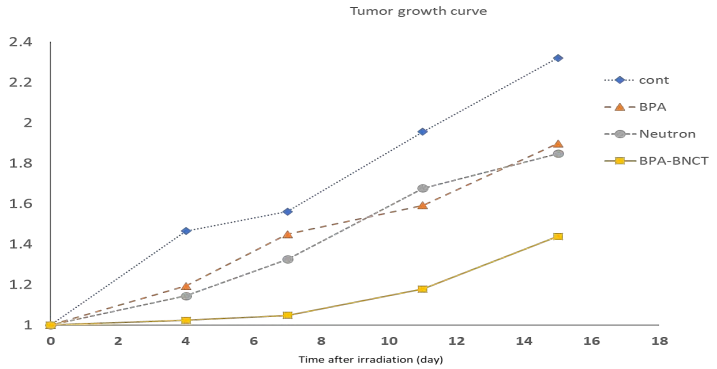

REFERENCES:

[1] M.B Brooks *et al.*, J Vet Intern Med., **4** (1988) 206-211 .

PR2-6

Boron Delivery to Brain Cells via Cerebrospinal Fluid (CSF) Circulation for BNCT in a Rat Glioma Model

S. Kusaka[1], N.Voulgaris[1], K. Onishi[2], J. Ueda[2], S. Saito[2], I. Murata[1], Y. Tamari[3], T. Takata[3], M. Suzuki[3]

[1] *Graduate School of Engineering, Osaka University*
[2] *Graduate School of Medicine, Osaka University*
[3] *Institute for Integrated Radiation and Nuclear Science, Kyoto University*

INTRODUCTION: Recently, some drug delivery systems to bypass blood brain barrier (BBB) have been developed for brain tumor therapy. Our laboratory has been developing a system for boron delivery to brain cells using cerebrospinal fluid (CSF) circulation in boron neutron capture therapy (BNCT), which we call the "boron CSF administration method"[1][2][3]. The understanding of CSF circulation has changed since meningeal lymphatic vessels were first described in 2015. We have obtained important results that use of the boron CSF administration method resulted in a level of a boron accumulation in the brain cells of normal rats that was equal to that achieved using the intravenous (IV) administration method, even though the dose of BPA was quite low (around 1/90 of the BPA dose used in the IV administration method) [4].Based on the results, we designed a CSF-based administration protocol of BNCT for rat glioma models and a thermal neutron irradiation experiment was conducted in Kyoto University Reactor.

****

EXPERIMENTS: The C6 rat glioma models were supplied for the present experiment 10 days after implantation. Sixteen models were randomly divided into the following four groups: untreated control group (non- irradiated), neutron-irradiated control group (irradiation only), the group subjected to thermal neutron irradiation after the end of the infusion of BPA via IV route and the group subjected to thermal neutron irradiation after the end of the infusion of BPA via CSF route. In the IV administration group, 350 mg/kg of BPA was administered to four rats via the tail vein for 1.5 h. In the CSF administration group, BPA was administered to four rats via the intracisterna magna at a rate of 8.0 mg/kg/h for 2 h. The C6 glioma rats were irradiated at a 5 MW reactor with a heavy water irradiation facility for 20 min (3.8×10^{12} neutrons/cm^2 on average). After the thermal neutron irradiation, all rats remained under the same experimental conditions as the control groups for seven days. The therapeutic effects of BNCT were evaluated using MRI.

****

RESULTS: As shown in Fig. 1, we demonstrated that the therapeutic effect by the CSF administration method was almost equivalent to that following the IV administration method, even though the dose of BPA in the CSF administration method was quite low.

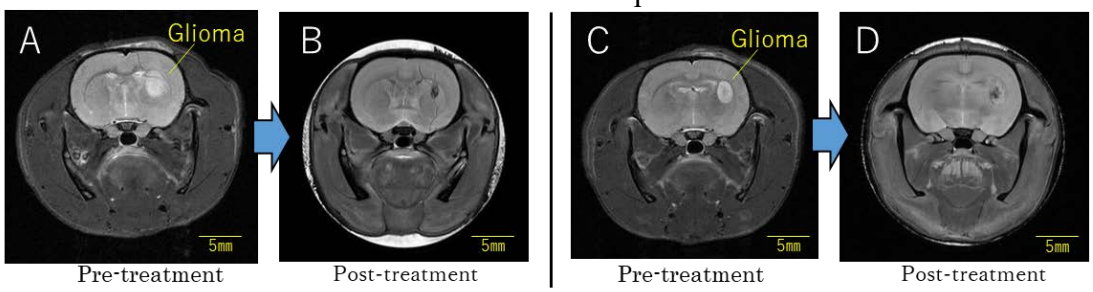

Fig. 1. Representative T2 images of rat brain in IV administration group (A, B) and CSF administration group (C, D).

REFERENCES:

[1] S. Kusaka *et al.*, Research in Veterinary Science, **148** (2022) 1-6.
[2] S. Kusaka *et al.*, Life, **12(11)** (2022) 1-14
[3] Y. Miyake, S. Kusaka *et al.*, Life, Mass Spectrometry, **11** (2022) A0105.
[4] S. Kusaka *et al.*, Biology, **11**, 397 (2022) 1-10.

I-1. PROJECT RESEARCHES

Project 3

PR3

The effect of BNCT on normal tissues

M. Suzuki

Institute for Integrated Radiation and Nuclear Science, Kyoto University

In this research project, four research projects were included. One research was not performed. Details of three projects are referred to each progress report.

P3-1. The investigation of early and late effects of Boron Neutron Capture Therapy (BNCT) on a mouse pelvis

In previous study, anti-tumor effect of Boron Neutron Capture Therapy (BNCT) for a mouse mod-el of pelvic recurrence of colorectal cancer (CRC) was reported. In this study, early and late adverse effects in pelvic BNCT was investigated. In BNCT study, animals were divided into three groups (6-7 animals per group); the cold control (no treatment, no neutron irradiation), hot control (neutron irradiation only), and BNCT (intraperitoneal BPA administration and neutron irradiation) groups in early stage (about 1 month) and late stage (about 6 month). All mice did not have symp-toms such as diarrhea and survived until the endpoint. Although remarkable weight loss was not observed in three groups at the endpoint in early stage, significant weight loss was observed in BNCT group of late stage compared with cold control.

P3-3. Effect of BNCT on trans-endothelial electric resistance in blood brain barrier kits

Radiation necrosis is accompanied by chronic inflammation, which is an irreversible late effect, and there is no effective treatment. Assuming that the damage on blood vessel by BNCT plays im-portant role, in this study, the blood brain barrier sensitivity in BNCT was investigated in this study. Measurement of trans-endothelial electric resistance (TEER) was measured by Millicell-ERS2 on 2 and 10 days after irradiation. TEER did not make significant changes at 2 days after irradiation in all groups compared with the non-irradiated control. And at 7 days after irradiation, in the higher dose irradiated group (8-17 Gy), the TEER decreased compared with the non-irradiated control.

P3-4. The effect of boron neutron capture therapy (BNCT) on stomach in mice.

For accelerated BNCT to be recognized as a new radiotherapy, the indication of BNCT should be extended to many malignancies. In case of the treatment with multiple liver tumors by BNCT, stomach should be dealt with one of the organs at risk. The aim of this study is to investigate the effects of BNCT on the stomach.

Thermal neutron was irradiated to upper abdomen including stomach of C3H mouse after admin-istration of BPA at the dose of 500 mg/kg. At the 7days after boron neutron capture irradiation, the stomach was extracted and processed for preparation of the section and hematoxylin-eosin (HE) staining. The histopathological studies demonstrated the gastric mucosa of 15-,20-minutte irradiated mice were severely damaged compared with that of control, 5-, 10- minutes irradiated mice.

PR3-1

The investigation of early and late effects of Boron Neutron Capture Therapy (BNCT) on a mouse pelvis

S. Hagihara[1], J. Arima [1], K. Taniguchi[1,2], Y. Inomata[1], A. Miyamoto[1], M. Suzuki[3], and Sang-Woong Lee [1]

[1] *Department of General and Gastroenterological Surgery, Osaka Medical and Pharmaceutical College, Osaka, Japan*
[2] *Translational Research Program, Osaka Medical and Pharmaceutical College, Osaka, Japan*
[3] *Department of Particle Radiation Oncology, Research Reactor Institute, Kyoto University, Kumatori, Osaka, Japan.*

INTRODUCTION: Previously, we reported the anti-tumor effect of Boron Neutron Capture Therapy (BNCT) for a mouse model of pelvic recurrence of Colorectal cancer (CRC). On the other hand, we could not fully evaluate side effects in terms of immune response or the later complications, because we examined the effectiveness of BNCT in the nude mouse model only a month after treatment. This study investigates early and late effect of pelvic BNCT. **********

EXPERIMENTS: We used Boronophenylalanine (BPA) as a boron compound. Also, we used seven-week-old female BALB/c mouse. The boron concentrations in blood, skin and various pelvic organs (rectum, bladder, uterus, iliopsoas, vagina and cecum) at 2h, 4h, 6h after 50 mg 10B/kg BPA administration intraperitoneally. (**Figure.1**) According to this result, we decided to inject BPA intraperitoneally at 4h before irradiation. In BNCT study, animals were divided into three groups (6-7 animals per group); the cold control (no treatment, no neutron irradiation), hot control (neutron irradiation only), and BNCT (intraperitoneal BPA administration and neutron irradiation) groups in early stage (about 1 month) and late stage (about 6 month).
****

RESULTS: All mice did not have symptoms such as diarrhea and survived until the endpoint. Although remarkable weight loss was not observed in three groups at the endpoint in early stage, significant weight loss was observed in BNCT group of late stage compared with cold control. (**Figure.2,3)**
****

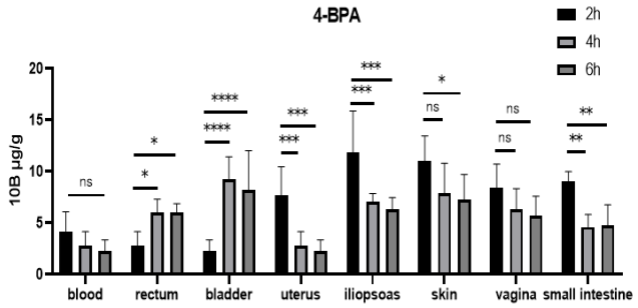

Fig.1. At 2 hours after BPA administration,
high peaks of boron concentration were observed in several organs,
including the uterus, iliopsoas, and vagina.
(****P<0.0001, ***P<0.001, **P<0.01, *P<0.05)

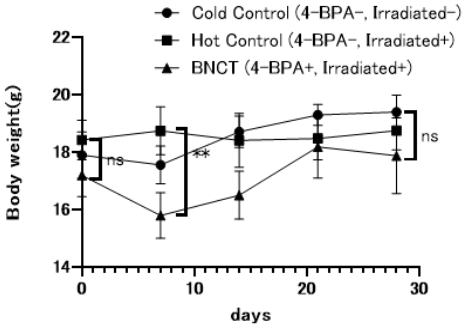

Fig.2. Body weight loss were observed a week after irradiation in BNCT group.
There were not a significant difference in body weight four weeks after irradiation. (**P<0.01) .

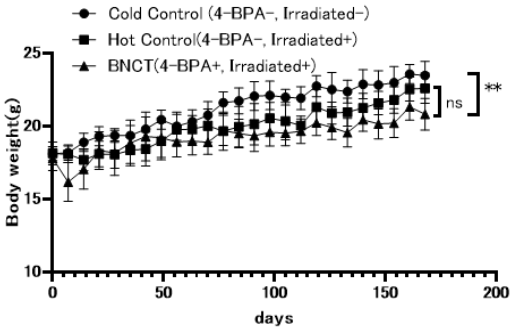

Fig.3. Body weight loss was observed six months after irradiation in BNCT group compared with Control group. (**P<0.01) .

Ongoing study: Using HE staining, western blot analysis, enzyme-linked immunosorbent assay (ELISA) and RNA-sequence, we intend to investigate characterization of early and late effect of pelvic organs.
We will continue this study and the results will be published in the future.

REFERENCES:
[1] J. Arima *et al.,* Biomed. Pharmacother., **154** (2022) (doi) 10.1016/j.biopha.2022.113632.

PR3-2

Effect of BNCT on trans-endothelial electric resistance in blood brain barrier kits

Natsuko Kondo[1], Yoshinori Sakurai[1], Takushi Takata[1], and Minoru Suzuki[1]

[1] *Particle Radiation Oncology Research Center, Institute for Integrated Radiation and Nuclear Science, Kyoto University (KURNS)*

INTRODUCTION:

The effects on the reactions and functions that occur in normal cranial nerve tissues after BNCT are often unknown. Radiation brain necrosis (RN) often occurs after BNCT for recurrent malignant brain tumors. RN is accompanied by chronic inflammation, which is an irreversible late effect, and there is no effective treatment (medication approved by insurance. RN accompanies with edema and micro-bleedings in pathology. We assume that the damage on blood vessel by BNCT plays im-portant role. In order to perform safer BNCT on cranial nerve tissues, we will investigate the blood brain barrier sensitivity in this study.

EXPERIMENTS:

Cells:

We cultured the brain-blood barrier kit (vascular endothelial cells, pericytes, and astrocytes) in DMEM in a 5 % CO_2 incubator.

Boronophenylalanine (BPA) Treatment:

A stock solution of the *p*-^{10}B-para-boronophenylalanine (BPA)- fructose complex was used. The ^{10}B concentrations was approximately 1000 ± 4.55 ppm. BPA was dissolved in the cell culture medium at a concentration of 25 ppm 2 hours before irradiation.

Thermal Neutron Irradiation:

The vascular endothelial cells and pericytes on the both sides of inserts in the kits were irradiated using a neutron beam at the Heavy Water Neutron Irradiation Facility installed in the Kyoto University Reactor (KUR-HWNIF). The operating power of the reactor was 1 MW. After irradiation, the cells were placed in the original wells in the kit.

Measurement of trans-endothelial electric resistance (TEER):

TEER was measured by Millicell-ERS2 on 2 and 10 days after irradiation.

RESULTS:

TEER did not make significant changes at 2 days after irradiation in all groups compared with the non-irradiated control. And at 7 days after irradiation, in the higher dose irradiated group (8-17 Gy), the TEER decreased compared with the non-irradiated control.

PR3-3

The effect of boron neutron capture therapy (BNCT) on stomach in mice

M. Suzuki, H. Tanaka, Y. Sakurai, T. Takata

Institute for Integrated Radiation and Nuclear Science Kyoto University

INTRODUCTION: Boron neutron capture therapy (BNCT) has been applied to head and neck cancer as an insured therapy at the medical institutes where accelerator-based BNCT system has been installed. Only head and neck cancer is approved as an insured therapy. My laboratory has been engaged in the basic study for applying BNCT to malignancies in body trunk such as liver or lung cancers [1-3]. For accelerated BNCT to be recognized as a new radiotherapy, the indication of BNCT should be extended to many malignancies. In case of the treatment with multiple liver tumors by BNCT, stomach should be dealt with one of the organs at risk. The aim of the present study is to investigate the effects of BNCT on the stomach.

EXPERIMENTS:

Mice: Ten- to twelve-week-old female C3H/He mice were used. The mice were purchased from Japan SLC, Inc.

BNCT and measurement of thermal neutron and γ-ray: In this study, BPA was administered subcutaneously at the dose of 500 mg/kg before the upper thorax irradiation. At the each BNCR, three mice were held within a specially designed acrylic box. LiF plates (5-mm thick) were used to shield the whole body except for chest. Neutron fluences were measured by radio activation of gold foils (3mm diameter; 0.05 mm thick) on the anterior and dorsal surface of the mice. Chemi-luminescent dosimeters were used for γ-ray dosimetry.

Histopathological evaluation of gastric mucosa: The stomachs were extracted at the 7 days after BNCT. The extracted stomachs were fixed in the 10% neutral formaldehyde. The fixed samples were processed for preparation of the section and hematoxylin-eosin (HE) staining.

RESULTS: Figure 1 shows the HE stained histopathological specimen including control, 5-, 10-, 15- and 20-minutes irradiation. The specimen of 15-,20-minutte irradiation were severely damaged compared with control, 5-, 10- minutes irradiation.

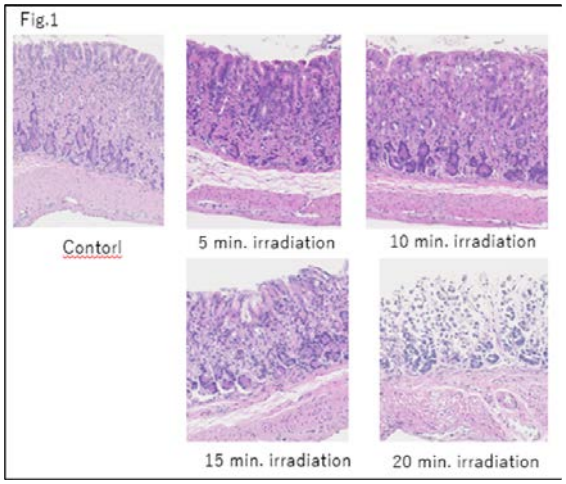

Further studies will be performed to compare the effects of thermal neutron irradiation without BPA and X-ray irradiation.

REFERENCES:

[1] M. Suzuki *et al.*, Int. Cancer. Conference J., **1** (2012) 235-238.
[2] M. Suzuki *et al.*, Radiotherapy and Oncology, **92** (2009) 89-95.
[3] M. Suzuki *et al.*, Radiotherapy and Oncology, **88** (2009) 192-195.

I-1. PROJECT RESEARCHES

Project 4

PR4

Production of medical RI by reactor irradiation

T. Yamamura, Y. Nakamoto[1], H. Kimura[2], Y. Shimizu[3], K. Washiyama[4]

KURNS, Kyoto University

[1]*Department of Diagnostic Imaging and Nuclear Medicine, Graduate School of Medicine, Kyoto University*
[2]*Research Center for Experimental Modeling of Human Disease, Kanazawa University*
[3]*Division of Clinical Radiology Service, Kyoto University Hospital*
[4]*Advanced Clinical Research Center, Fukushima Medical University*

INTRODUCTION: Remarkable results have been achieved in the treatment of metastatic cancer with β-ray emitting radionuclides such as ^{177}Lu, which can be easily produced in nuclear reactors. In recent theranostics, the incidentally emitted gamma rays can also be used for diagnosis. Extraction chromatography is widely used technique for chemical separation of Ytterbium (Yb) and medically relevant Lutetium-177 (^{177}Lu); however, chemical similarity between Lu and Yb require a larger column size and more eluent for gram-scale Yb target separation.
Kimura et al. has studied theranostics as a new medical technology that combines therapeutics and di- agnostics. The key to the realization of theranostics is a drug known as theranostic probes. In this study, we will utilize the theory of creation of unit-coupling molecular probes to develop drugs that can ultimately be applied clinically. First, a basic study of the production of ^{177}Lu in the KUR was conducted. Next, we developed radiotheranostics probes targeting EphA2, which is expressed in cancer. Erythropoietin-producing hepatocellular receptor A2 (EphA2) is overexpressed in cancer cells and causes abnormal cell proliferation. Therefore, it has attracted attention as a target for radiotheranostics probes.

RESULTS AND DISCUSSIONS:
Recovery of ^{177}Lu by LN2 extraction chromatograph: In this study, a CZT detector measuring the gamma-ray spectrum was installed in the eluent part of the chromatography, allowing in-line, in-situ observation of the separation situation. Irradiation of ^{176}Yb enriched isotopes has two well-separated peaks and the production of ^{177}Lu, which is far larger than the target-derived radioactive impurity, is observed. The separation ratio shows that the separation of ^{177}Lu from $^{169/175}$Yb using natural Yb improved significantly from approximately 1.2 in the ratio of elution times to approximately 1.6 when using the ^{176}Yb enriched isotope. This indicates that the use of ^{176}Yb enriched isotope targets improves chromatographic overload conditions. This result is expected to be used for the precise separation and recovery of ^{177}Lu fractions in the process of highly radioactive ^{177}Lu separation while reducing the exposure of workers to large amounts of separation in a hot cell.
Development of radiotheranostics probes: In this study, the EphA2-57-1 monoclonal antibody (EphA2-57-1) was labeled with [^{111}In]In and evaluated as an imaging tracer for single-photon emission computed tomography (SPECT) of EphA2.
Development of radiotheranostics probes: EphA2-57-1 was conjugated with *p*-SCN-BnDTPA and then labeled with [^{111}In]In. [^{111}In]In-DTPA-EphA2-57-1 was evaluated in cell-binding, biodistribution, and SPECT studies. In the biodistribution study, a high uptake of [^{111}In]In-DTPA-EphA2-57-1 was observed in tumor tissue (8.8 ± 2.2% injected dose/g at 96 h). The accumulation of [^{111}In]In-DTPA-EphA2-57-1 in tumors was also confirmed using SPECT. Therefore, [^{111}In]In-DTPA-EphA2-57-1 has potential as a radiotheranostics probe for EphA2.

REFERENCES:
[1] A. Dash *et al.,* Nucl Med Mol Imaging., **49** (2015) 85-107.

PR4-1

Development of tumor-targeted radiotheranostics probes and its clinical application

H. Kimura[1], T. Yamamura[2], K. Shirasaki[3]

[1]*Research Center for Experimental Modeling of Human Disease, Kanazawa University*
[2]*Institute for Integrated Radiation and Nuclear Science, Kyoto University*
[3]*Institute for Materials Research, Tohoku University*

INTRODUCTION: Theranostics is a new medical technology that combines therapeutics and diagnostics. The key to the realization of theranostics is a drug known as theranostic probes. The characteristic of the radiotheranostics probes we are developing is that we consider a single molecule as an aggregate of target recognition units, linker units, and chelating units, and design molecular probes based on the concept of "unit-coupling molecular probes," in which independently developed units are freely combined. This drug design theory is not only effective for designing molecular probes with relatively large molecules such as antibodies and other proteins and bioactive peptides as the nucleus, but also can also be applied to organic small molecular compounds. In this study, we will utilize the theory of creation of unit-coupling molecular probes to develop drugs that can ultimately be applied clinically. First, a basic study of the production of ^{177}Lu in the KUR was conducted. Next, we developed radiotheranostics probes targeting EphA2, which is expressed in cancer. Erythropoietin-producing hepatocellular receptor A2 (EphA2) is overexpressed in cancer cells and causes abnormal cell proliferation. Therefore, it has attracted attention as a target for radiotheranostics probes.

EXPERIMENTS: *^{177}Lu Production*: To obtain ^{177}Lu, Lu_2O_3 and Yb_2O_3 were irradiated at 1 MW for 24 hours and 5 MW for 6 hours.
Development of radiotheranostics probes: In this study, the EphA2-57-1 monoclonal antibody (EphA2-57-1) was labeled with [^{111}In]In and evaluated as an imaging tracer for single-photon emission computed tomography (SPECT) of EphA2.

RESULTS: *^{177}Lu Production*: This year, we attempted to produce ^{177}Lu by an indirect method. Optimization of separation and purification conditions for post-irradiation samples is underway.
Development of radiotheranostics probes: EphA2-57-1 was conjugated with *p*-SCN-BnDTPA and then labeled with [^{111}In]In. [^{111}In]In-DTPA-EphA2-57-1 was evaluated in cell-binding, biodistribution, and SPECT studies. In the biodistribution study, a high uptake of [^{111}In]In-DTPA-EphA2-57-1 was observed in tumor tissue (8.8 ± 2.2% injected dose/g at 96 h). The accumulation of [^{111}In]In-DTPA-EphA2-57-1 in tumors was also confirmed using SPECT. Therefore, [^{111}In]In-DTPA-EphA2-57-1 has potential as a radiotheranostics probe for EphA2.

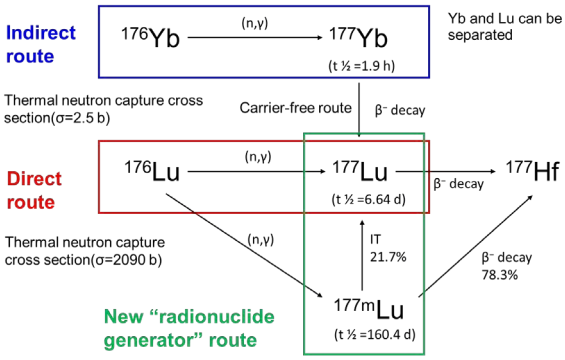

Two different routes for reactor production of ^{177}Lu

REFERENCES:
[1] A. Dash *et al.,* Nucl Med Mol Imaging., **48** (2015) 85-107.

The development of the online monitoring system for column separation of ^{177}Lu from enriched ^{176}Yb irradiated target

K. Washiyama[1], R. Okumura[2], K. Shirasaki[3], K. Ogawa[4], T. Yamamura[2]

[1]*Advanced Clinical Research Center, Fukushima Medical University*
[2]*Institute for Integrated Radiation and Nuclear Science, Kyoto University*
[3]*Institute for Materials Research, Tohoku University*
[4]*Institute for Frontier Science Initiative, Kanazawa University*

INTRODUCTION: Extraction chromatography is widely used technique for chemical separation of Ytterbium (Yb) and medically relevant Lutetium-177 (^{177}Lu); however, chemical similarity between Lu and Yb require a larger column size and more eluent for gram-scale Yb target separation. Therefore, it is essential to fully understand the process of separating Yb and Lu in the column and to extract only the required ^{177}Lu fraction to improve the efficiency of the chemical separation operation. CZT detectors are small and can be powered by USB, making them suitable for online remote measurements. In the previous study, we preliminary evaluated the online measurement of a column separation using a CZT detector with $^{169, 175}$Yb and ^{177}Lu tracers produced by irradiating the ^{nat}Yb target; however, the 238keV γ-ray of ^{177}Lu could not be identified because it was covered by the Compton component derived from the high-energy γ-ray of $^{169, 175}$Yb. Therefore, in this study, enriched ^{176}Yb, which is used for commercial production of ^{177}Lu, was used for online monitoring evaluation.

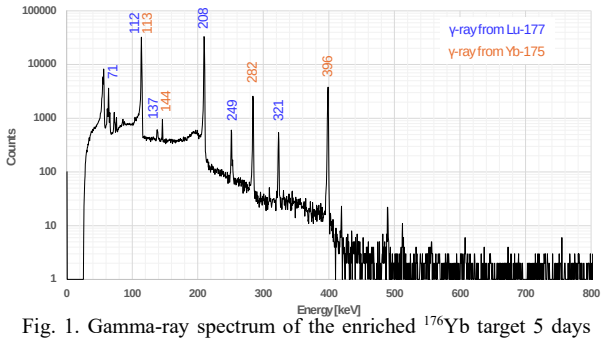

Fig. 1. Gamma-ray spectrum of the enriched ^{176}Yb target 5 days after neutron irradiation.

EXPERIMENTAL: The CZT detector used for the measurements was a RadAngel manufactured by Kromek. A Ge detector (ORTEC) was used to confirm the elution profile. Enriched $^{176}Yb_2O_3$ powder was purchased from Isoflex and has a 99.14% enrichment of ^{176}Yb. A $^{176}Yb_2O_3$ sample (^{176}Yb, 1.0 mg) was irradiated for 6 hours at a power of 5 MW at the Kyoto University research reactor KURR. Irradiated $^{176}Yb_2O_3$ was dissolved and adjusted to 4M HNO_3. Then, the solution was added into a jacketed 11 mmφ x 240 mm glass column (Kiriyama Chemical) containing extraction LN2-Resin (Eichrom) and about 500 mL of 1.5 M HNO_3 was added to separate the Yb target and ^{177}Lu. The tube containing the eluted solution from the column was brought into contact with the CZT detector for online measurement. The eluent was collected as each fraction containing 250 drops, which were subjected to γ-ray spectroscopy using a Ge detector and compared with the elution curve obtained with the CZT detector monitoring.

RESULTS: A Ge detector measurement confirmed only the production of high radioactivity ^{177}Lu, and low radioactivity ^{175}Yb in the irradiated sample after 5 days irradiation (Figure 1). Figure 2 shows the elution curves obtained with a Ge detector (Left), and a CZT detector (Right), which set the ROI to the channel between the 396 keV of ^{175}Yb and 208 keV of ^{177}Lu photoelectric peaks. The elution curves of ^{175}Yb and ^{177}Lu obtained with the CZT and Ge detectors showed the same trend. In addition, online measurements using a CZT detector confirmed that the column length used in the experiment was sufficient to separate ^{175}Yb and ^{177}Lu.

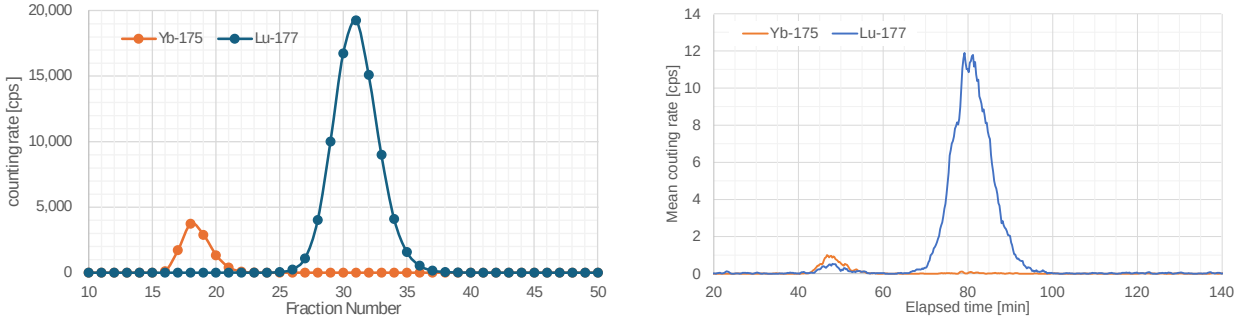

Fig. 2. Elution profile of extraction chromatography with an 11 mmφ × 240 mmL column packed with LN2 resin measured with a Ge detector (Left) and a CZT detector (Right)

CONCLUSION: In this study, online monitoring of γ radiation was performed using a CZT detector for column separation of an enriched ^{176}Yb target and ^{177}Lu. The use of enriched isotope made it possible to distinguish between the low-energy high radioactivity γ-rays from ^{177}Lu and the high-energy low radioactivity γ-rays from ^{175}Yb. This result is expected to be used for the precise separation and recovery of ^{177}Lu fractions in the process of highly radioactive ^{177}Lu separation while reducing the exposure of workers to large amounts of radioactivity in a hot cell.

I-1. PROJECT RESEARCHES

Project 5

PR5

Chemical and electronic properties of Actinide compounds and their applications

T. Yamamura, Y. Haga[1], M. Abe[2], M. Nakase[3], K. Shirasaki[4], S. Kambe[1], N. Ishikawa[5], T. Suzuki[6], M. Nogami[7], T. Kobayashi[1]

KURNS, Kyoto University, [1] Advanced Science Research Center, JAEA, [2] Graduate School of Advanced Science and Engineering, Hiroshima University, [3] Institute of Innovative Research, Tokyo Institute of Technology, [4] Institute for Materials Research, Tohoku University, [5] Department of Chemistry, Graduate School of Science, Osaka University, [6] Ngaoka University of Technology, [7] Graduate school of Electronic Eng., Kindai University

INTRODUCTION: Actinide compounds shows a unique chemical and electronic nature due to the partial and insufficient shield of 5f orbital electrons as inner transition elements. We have a deep interest in the aspect of the electronic properties of the actinide compounds and formed the group consisting of three major fields: (1) inorganic and coordination chemistry, (2) electronic properties and (3) theoretical chemistry and its users. Such research environments to handle actinides elements are extremely difficult to build in ordinary university institutes. The hot laboratory of the KURNS offers unique opportunities for the above-mentioned characteristic re-search activities.

EXPERIMENTS and RESULTS: The first fiscal year of the project has been devoted to the setting up the experimental environment and initial test experiments. Each of research fields has made their progress as followings: (1) S. Kambe has investigated ”Hidden ordering” in URu_2Si_2 by NMR spectroscopy (^{101}Ru NQR) under zero field without uni-axial stress indicating that 4-fold crystal symmetry remains in the hidden ordered state. (2) Y. Haga et al. has investigated $ThRh_6Ge_4$ identified as $LiRh_6P_4$-type structure. The electronic structure of $ThRh_6Ge_4$ was experimentally determined from the quantum oscillation measurements. This information will help understanding the electronic structure of a correlated material $CeRh_6Ge_4$ where a phase transition from Ce^{3+} to Ce^{4+} is assumed across the quantum phase transition [1]. (3) M. Abe et al. has developed new programs for calculating electronic states and properties of actinide compounds with high accuracy, based on the X2C relativistic Hamiltonian. the initial development of the CASPT2/RASPT2 program and are preparing to make our code publicly available on the GitHub webpage free of charge [2]. We conducted benchmark calculations for the ground and excited states of the UO_2^{2+} molecule using our software. (4) M. Nakase et al. selected phthalocyanine (Pc) as the basic structure for extractants according to the CHON principle and scrutinized its properties. With regard to solubility prediction, a basic regression model for solubility prediction using other chemical parameters was tested this year using HSPiP software based on Hansen Solubility Parameters (HSP). (5) K. Shirasaki et. al. has synthesized some uranium(III) BDI complexes through synthesis of BDI potassium salt. (6) N. Ishikawa et al. has measured temperature and magnetic-field-dependent magnetic circular dichroism (HT-VH-MCD) spectroscopy. Similar interaction was confirmed in the sandwich bilayer complex [Pc_2Ln] and the monolayer complex [PcLn(cyclen)].[3] The peak top of the absorption spectrum in the visible region shifted to the short wavelength side by addition of salen. Otained compound showed a typical spectrum of metal phthalocyanines with a sharp characteristic band, Q-band, at λmax = 687nm. (7) The dissolution method of ThO_2 by thermochemical conversion has been studied by T. Suzuki et al. The removal of thorium from the precipitate is not sufficient because the amount of thorium is higher than that of radium. An additional method for separating radium from thorium needs to be added before the precipitation method. (8) M. Nogami et al. has examined diamide compounds and synthesize a resin with a diamide structure, *N,N,N',N'*-tetramethylmalonamide (TMMA) as the functional group. [3]

REFERENCES:

[1] Y. Haga *et al.,* International Conference on Strongly Correlated Electron Systems 2023.
[2] The software will be downloadable from https://github.com/RQC-HU/dirac_caspt2
[3] K. Kizaki *et al.,* Inorg. Chem. Front., **10** (2023) 915-925.

PR5-1

Electronic structure of $ThRh_6Ge_4$ with non-centrosymmetric crystal structure

Y. Haga[1], E. Yamamoto[1], A. Nakamura[2], F. Honda[3], D. Aoki[2], Y. Matsumoto[4], T. Yamamura[5], K. Shirasaki[2], H. Yamagami[6]

[1]*Advanced Science Research Center, Japan Atomic Energy Agency*
[2]*Institute for Materials Research, Tohoku University*
[3]*Central Institute of Radioisotope Science and Safety Management, Kyushu University*
[4]*Department of Physics, University of Toyama*
[5]*Institute for Integrated Radiation and Nuclear Science, Kyoto University*
[6]*Kyoto Sangyo University*

INTRODUCTION: Actinide intermetallic compounds have long been studied because of their unusual physical properties. In the context of condensed matter physics, electron correlations between charge carriers responsible for electrical transport and those carrying magnetic moments, and local symmetry of those electrons play crucial roles. In this study we demonstrate that the electronic structure of a thorium compound with the characteristic symmetry can precisely be determined by quantum oscillations experiments and the band structure calculations. $ThRh_6Ge_4$ crystallizes in the hexagonal $LiRh_6P_4$-type structure. It belongs to the space group P-6m2 which lacks center of inversion. It is also isostructural to an intriguing compound $CeRh_6Ge_4$ which undergoes ferromagnetic to heavy fermion quantum phase transition under hydrostatic pressure [1]. It is therefore important to identify the electronic structure of this compounds.

EXPERIMENTS : We tried to synthesize $ThRh_6Ge_4$ using arc-melting the stoichiometric mixture of each element. Czochralski-pulling technique was successfully applied to grow single crystals. Electron microprobe analysis and X-ray diffraction for both powder and single crystals successfully identified $LiRh_6P_4$-type structure. The sample was characterized by electrical resistivity, specific heat and magnetization measurements. The quantum oscillation was measured using the field-modulation technique at low temperatures. Theoretical band structure calculations were performed using the software package Elk.

RESULTS: The electronic structure of $ThRh_6Ge_4$ was experimentally determined from the quantum oscillation measurements. The results are well described by the band structure calculations. These results define the electronic structure of the compounds with a tetravalent actinide site. This imformation will help understanding the electronic structure of a correlated material $CeRh_6Ge_4$ where a phase transition from Ce^{3+} to Ce^{4+} is assumed across the quantum phase transition. Further investigation is in progress on this respect. [2]

REFERENCES:

[1] H. Kotegawa *et al.,* J. Phys. Soc. Jpn., **88** (2019) 093702.
[2] Y. Haga *et al.,* International Conference on Strongly Correlated Electron Systems 2023.

PR5-2

Development of relativistic multireference electron correlation methods for actinide compounds

M. Abe,[1] Y. Masuda,[1] S. Toda,[1] T. Yamamura[2]

[1] *Department of Chemistry, Hiroshima University*
[2] *Institute for Integrated Radiation and Nuclear Science, Kyoto University*

INTRODUCTION: Understanding the properties of actinide compounds is crucial for both engineering and academic research. Theoretical calculations, alongside experimental approaches, play a vital role in elucidating their characteristics and facilitating safe verification studies. However, accurately handling relativistic and electron correlation effects is essential for theoretical investigations of actinide compounds. As the atomic number Z increases, the relativistic effect becomes significant, challenging the accuracy of conventional scalar relativistic treatments or perturbative corrections of spin-orbit interactions. Rigorous relativistic effects demand the application of four-component Dirac or exact two-component (X2C) relativistic Hamiltonians. Moreover, because all s, p, d, and f orbitals serve as valence orbitals for actinide atoms, static electron correlation cannot be neglected, limiting the efficacy of conventional single reference methods like density functional theories. Multi-reference electron correlation theory becomes necessary but poses computational challenges due to its complexity. Our group has developed new quantum chemistry programs based on the X2C relativistic Hamiltonian to accurately calculate electronic states and properties of actinide compounds. Specifically, we have created a program for the CASPT2/RASPT2 method, employing multiconfigurational wave functions (CASCI/RASCI) as the 0th-order state of perturbation. CASPT2/RASPT2 is a well-established perturbation theory in the non-relativistic framework [1].

METHODS: The Hartree-Fock and molecular orbital integral transformation with the X2C relativistic Hamiltonian can be executed using the free software DIRAC [2,3]. Consequently, we have developed a CASPT2/RASPT2 program that utilizes molecular orbital information computed by the DIRAC software.

RESULTS: This year, we have nearly completed the initial development of the CASPT2/RASPT2 program and are preparing to make our code publicly available on the GitHub webpage free of charge [4]. We conducted benchmark calculations for the ground and excited states of the UO_2^{2+} molecule using our software. Fig. 1 illustrates the potential energy curves obtained at the RASPT2 level. Although no experimental data exist for this system, numerous previous calculation reports are accessible. Overall, our optimized U-O bond length and excitation energies align with some prior works, indicating successful program implementation. Consequently, we plan to utilize our program for other actinide molecules to explore the electronic state properties further.

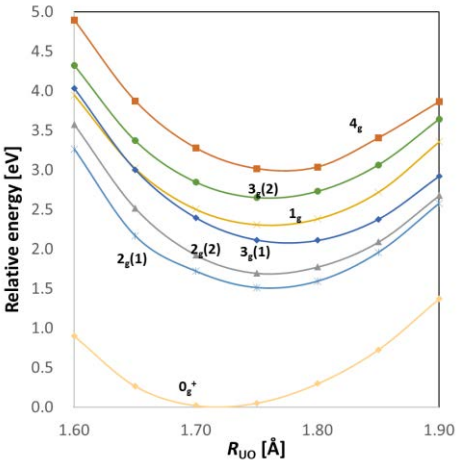

Fig. 1. Potential energy curves for the ground and low-lying excited states for UO_2^{2+}

REFERENCES:

[1] K. Anderson *et al.,* J. Phys. Chem., **94** (1990) 5483–5488.
[2] H. J. Aa. Jensen *et al.,* DIRAC, a relativistic ab initio electronic structure program, Release DIRAC22 (2022).
[3] T. Saue *et al.,* J. Chem. Phys., **152** (2020) 204104.
[4] The software will be downloadable from https://github.com/RQC-HU/dirac_caspt2

PR5-3

Synthesis of novel phthalocyanine derivatives and effect of substituent on recognition of light actinide and chemical property-4

M. Nakase[1], F. Ikhwan[1], T. Yamamura[2]

Graduate School of Science, Kyoto University
[1]Institute of Innovative Research, Tokyo Institute of Technology
[2]Institute for Integrated Radiation and Nuclear Science, Kyoto University

INTRODUCTION: Understanding actinide chemistry is crucial in areas like nuclear fuel reprocessing, Fukushima waste treatment, and medical uses of actinium. My focus is on the thorium (Th) fuel cycle, which avoids producing heavy actinides like americium (Am) and curium (Cm), instead dealing with lighter actinides such as Th, protactinium (Pa), and uranium (U). This cycle requires separating U from Th and other fission products in spent Th fuel. Recently, CHON principle-compliant extractants like monoamides have been explored for U/Th separation. We chose phthalocyanine (Pc) as the base extractant structure and studied its properties. Efforts are ongoing to make Pc soluble in organic solvents and develop a purification method.

EXPERIMENTS: The experimental setup for distillation purification of Pc-U was upgraded, as shown in **Fig. 1**. The aluminum frame was newly installed to reinforce and enhance safety in experiments. The electric power supply was installed on the top, and the pump was set under the tube, making the space needed for experiments smaller. Such ingenuity is essential for experiments in a limited controlled area.

Figure 1 Updated distillation apparatus

SOLUBILITY PREDICTION: Predicting the solubility of the complexes in an organic solvent for solvent extraction is an essential step for minimizing experimental tests and reducing waste generation. Hence, our efforts have been directed towards constructing prediction models based on complex structures, as we started last year. We tested a basic regression model for solubility prediction utilizing HSPiP software, which can predict the physicochemical properties of chemicals based on the Hansen Solubility Parameter (HSP). The HSP is a set of empirical parameters that predict the solubility behavior of substances in different solvents. HSP characterizes the three primary forces involved in solvation: dispersion forces (related to London dispersion forces), polar forces (related to dipole-dipole interactions), and hydrogen bonding forces. Each substance and solvent can be assigned a set of HSP values corresponding to these forces. By comparing the HSP values of solvents, we can predict whether the substance can dissolve in that solvent. The HSP values are typically represented as points in a three-dimensional space, with axes corresponding to the three forces. Solvents close together in the space are expected to dissolve similar substances. Conversely, substances with HSP values distant from those of a solvent are less likely to dissolve well in that solvent. The HSP parameters can be predicted from chemical structures such as SMILES, where characters represent atoms and bonds. Atoms are represented by their atomic symbols (e.g., C for carbon, O for oxygen), and bonds between atoms are indicated by various symbols (e.g., single bonds are usually implicit, double bonds are represented by "=," triple bonds by "#"). We tested such a scheme and tested it shortly.

PLANS: In the next fiscal year, our efforts will extend to validating the prediction model regarding the solubility of U-Pc complexes, emphasizing rigorously testing its predictive capabilities. Additionally, we plan to incorporate supplementary data from pertinent literature sources to enhance our understanding and prediction of complex characteristics.

Fundamental preparation study to access functional uranium(III) complexes: Investigation of β-diketoiminate ligand preparation

K. Shirasaki, K. Miyahara, T. Yamamura[1]

Institute for Materials Research, Tohoku University
[1]Institute for Integrated Radiation and Nuclear Science, Kyoto University

INTRODUCTION: The electron configuration of uranium(III) is $5f^3$ whose electrons are influenced by the shielding effects of 5*s* and 5*p* less than 4*f*, thus the complexes with uranium(III) often have unique properties in contrast to other oxidation states. In 2013, King et al. synthesized uranium(III) β-diketoiminate (BDI) complex such as $(BDI)UI_2$ [1] and in 2020, Boreen et al. reported that the single molecule magnet (SMM) behavior was observed in low temperature using $(BDI)U(OAr)_2$ (OAr = 2,6-Diisopropylphenyl) [2]. Because of the steric hindrance of BDI ligands, low-coordination complexes with BDI ligands are relatively easy to achieve. The purpose of this study is to investigate suitable preparation method of uranium complexes with BDI ligands and its derivatives and to characterize low valent uranium BDI complexes. Here, we synthesized a commercially unavailable BDI derivative potassium salt for the starting materials of uranium(III) complexes.

Fig. 1. Dean- Stack apparatus used for preparation of BDI and its derivatives.

EXPERIMENTS: The procedure to synthesize BDI potassium salt was followed by the one reported by Cleg with fine modifications regarding stoichiometry and reflux time [3] and described as follows. The BDI ligand was synthesized by dehydration reaction using a Dean-Stark apparatus (Fig. 1). Acetylacetone 15 ml and 2,6-diiso- propylaniline were dissolved in 150 ml of toluene. The volume of 2,6-diisopropylaniline was 55 ml for condition 1 and 30 ml for condition 2. In addition, about 1 g of *p*-toluenesulfonic acid was mixed as a catalyst. After the freeze-pump-thaw method (3 times), refluxing was carried out as heating for 48 h (condition 1) or 1.5 h (condition 2). After that, the reaction mixture was distilled under reduced pressure and obtained residuals. Recrystallization was performed for the target substance. Hexane was used as the solvent, and the compound was recovered after being dissolved at 30°C and allowed to stand at -15°C for 2 days for condition 1 and 2 weeks for condition 2. $KN(SiMe_3)_2$ (toluene solution, 0.5 mol/L) was added at one stoichiometric ratio to the compound obtained in both conditions.

RESULTS: The precipitate from condition 1 was identified as $C_{29}H_{41}N_2K$ (molecular weight 391.375) using ICP-AES and CHN elemental analysis (Table 1). The compound weight was 0.83 g and the yield throughout the experiment was 47.7%. Addition of $KN(SiMe_3)_2$ to the precipitate obtained under experimental condition 2 yielded a derivative of KBDI, $C_{17}H_{24}NOK$ (molecular weight 298.29). The yield of the compound in total was 64.8%.

Table 1 Elemental analysis results of KBDI salt

	Calculated [%]	Obtained(Difference) [%]
C	73.60	73.30(-0.30)
H	9.26	8.52(-0.74)
N	7.15	7.24(+0.09)
K	9.98	8.54(-1.44)

REFERENCES:

[1] D.M. King *et al.*, Angew. Chem. Int. Ed., **52** (2013) 4921-4924.
[2] M.A. Boreen *et al.*, Dalton Trans., **49** (2020) 7938-7944.
[3] W. Clegg *et al.,* Inorg. Chem., **37 (**1998) 2317-2319.

Study of Heavy Fermion Superconductor URu_2Si_2 ^{101}Ru-NQR study

S. Kambe, Y. Haga, H. Sakai, T. Ishitobi, Y. Tokunaga, S. Kitagawa[1], K. Ishida[1] and T. Yamamura[2]

Advanced Science Research Center, Japan Atomic Energy Agency
[1]Department of Physics, Kyoto University
[2]Institute for Integrated Radiation and Nuclear Science, Kyoto University

INTRODUCTION: Understanding of "Hidden ordering" in URu_2Si_2 is fairly progressed recently [1], whereas the definitive answer is still missing. This issue is very exciting since the hidden ordering is supposed to be new spontaneous symmetry breaking. Considering the recent experimental results, few possible space groups of hidden order symmetry have been selected previously [2,3]. If the hidden order symmetry is once determined, corresponding multipolar order parameter is spontaneously determined.

EXPERIMENTS: In this study, the local symmetry of Ru site is determined in the hidden order state without uni-axial stress and with uni-axial stress along the [100] and [110] directions [4], by means of precise Ru-NQR measurements. These measurements again support the 4-fold symmetry at Ru site in the hidden order state without uni-axial stress. Furthermore, certain cases can be excluded from the previously proposed possible ones. In this year, the Ru-NQR measurements without uni-axial stress are performed.

****

RESULTS: As shown in Fig. 1, ^{101}Ru NQR spectra under zero field without uni-axial stress in the hidden ordered state at 4.2K. There is no splitting of spectra under uniaxial pressure, indicating that there is no internal magnetic field appearing in the hidden ordered state. As ^{101}Ru is I=5/2 nuclei, there are two NQR peaks are observed *i.e.* ν_{1Q} ($I = \pm 3/2 \Leftrightarrow I = \pm 1/2$) and ν_{2Q} ($I = 5/2 \Leftrightarrow I = \pm 3/2$). In the present case, the ratio ν_{2Q}/ν_{1Q} is exactly 2 within the experimental errors, indicating that the 4-fold symmetry at Ru site holds in the hidden order state, which also indicates that 4-fold crystal symmetry remains in the hidden ordered state.

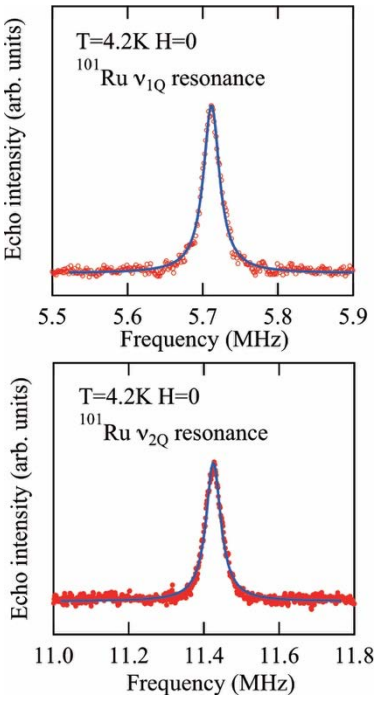

Fig. 1. ^{101}Ru NQR spectra at 4.2 K under zero field. Two resonance spectra: ν_{1Q} ($I = \pm 3/2 \Leftrightarrow I = \pm 1/2$) and ν_{2Q} ($I = 5/2 \Leftrightarrow I = \pm 3/2$) have been observed.

REFERENCES:

[1] J. Mydosh *et al.,* J. Phys.:Condens. Matter, **32** (2020) 143002.
[2] S. Kambe *et al.,* Phys. Rev. B., **97** (2018) 235142.
[3] S. Kambe *et al.,* JPS Conf. Proc. **30** (2020) 011035.
[4] See experimental methods: K. Karube *et al.,* J. Phys. Soc. Jpn. **83** (2014) 084706 .

PR5-6

Exploration of new interactions between actinide 5f electron systems and photo-excited organic π-electron systems

N. Ishikawa, Ryo Akiyama

Department of Chemistry, Graduate School of Science, Osaka University

INTRODUCTION: Metal complexes of actinide as well as those of lanthanide have high magnetic anisotropy due to the orbital angular momentum component in the total angular momentum of the f-electronic systems. In contrast to 4f electrons, 5f electrons are characterized by a large covalency involved in chemical bonding.
Another type of electronic angular momentum is known to be generated on a cyclic π-conjugated system of macrocyclic ligands, such as phthalocyanines (Pc) or porphyrins, by photo-excitation into degenerate π-π* excited states.
Previously, our group revealed the existence of a magnetic interaction between these two angular momenta (J-L interaction) in rare-earth Pc complexes by temperature- and magnetic-field-dependent magnetic circular dichroism (HT-VH-MCD) spectroscopy [1][2]. This interaction has been observed in sandwich-type bilayer complexes [Pc_2Ln] (Ln=Tb, Dy) and monolayer complexes [PcLn(cyclen)]. Similar interaction was confirmed in the sandwich bilayer complex [Pc_2Ln] and the monolayer complex [PcLn(cyclen)].[3][4]
Last year, we reported measurement of VT-VH-MCD in the visible energy region for the monolayer Pc complex of U(IV) as well as that of Th(IV) to investigate magnetic interaction between the $(5f)^2$ system and the ligand π-conjugate system in a photo excited state.
This year, we conducted preliminary experiments for the synthesis of a new type of Pc-uranium complex having a different second ligand, namely salen (N,N'-Bis(2-hydroxybenzylidene)ethylenediamine).

EXPERIMENTS: The precursor $[PcUCl_3]Li(THF)_4$ was synthesized according to Ref [5]. Dilithium phthalocyanine, UCl_4, and dehydrated triglyme were placed in a flask in a glove box and THF was added. The mixture was heated outside the glove box in a sealed condition using an oil bath. After cooling to room temperature, hexane was added, and the precipitate was collected by filteration. Salen was dissolved in DMSO and Triethylamine was added. To this solution, a DMSO solution of $[UPcCl_3]Li(THF)_4$ was mixed a small amount at a time, and the mixture was shaken well.

RESULTS: The peak top of the absorption spectrum in the visible region shifted to the short wavelength side by addition of salen. The addition was stopped when the absorption peak of salen increased. Thus obtained compound showed a typical spectrum of metal phthalocyanines with a sharp characteristic band, Q-band, at λ_{max} = 687nm.

REFERENCES:
[1] K. Kizaki *et al.,* Chem. Commun. **53** (2017) 6168-6171.
[2] T. Fukuda *et al.,* Chemistry A European Journal, **23(64)** (2017) 16357-16363.
[3] K. Kizaki *et al.,* Inorg. Chem., **60(3)** (2021) 2037-2044.
[4] K. Kizaki *et al.,* Inorg. Chem. Front, **10** (2023) 915-925.
[5] W. Zhou *et al.,* Chem.-Eur. J., **26(51)** (2020) 1027-1031.

PR5-7

Fundamental Study on Extraction/Separation of Actinides and Their Decay Products for Medical Nuclide Production - Precipitation Method by using Magnecium Carbonate -

T. Suzuki[1], F. Yin[1], S. Fukutani[2], M. Toyama[2], and T. Yamamura[2]

[1]*Department of Nuclear System Safety Engineering, Nagaoka University of Technology*
[2]*Institute for Integrated Radiation and Nuclear Science, Kyoto University*

INTRODUCTION: Many amounts of decay products are generated from uranium and/or thorium chemicals which are stored in long term. If these decay products are extracted and/or transmuted, we can obtain the several kinds of nuclides and can apply them to many fields such as medicine. While, concern of nuclear therapy using α-nuclides recently increases. Especially, ^{225}Ac is one of the most concerning α-nuclides. However, since ^{225}Ac don't exist in nature, it must be generated artificially. We have proposed ^{229}Th/^{225}Ac generator, ^{229}Th is generated by ^{228}Ra(n,γ) reaction. Our plain of obtaining ^{228}Ra is recovery of decay products from Th. We have plan to use the residue of rare earth ore and/or long storage ThO_2. For obtaining this type generator, development of the dissolution method of thorium compounds, extraction of Ra-228 from thorium and other decay products, manufacturing of stable target, irradiation of neutron, and separation of ^{229}Th, etc. are required. In the last year, we investigated the dissolution method of ThO_2 by thermochemical conversion. In this year, we investigated the precipitation methods for the radium extraction from solution. We carried out the co-precipitation experiment of radium in thorium solution by magnesium carbonates.

EXPERIMENTS: We use 4 types of thorium solutions; dissolution of ThO_2 in HCl or HNO_3 after thermochemical conversion using CCl_3CCl_3 or CBr_4. The chemical conversion was carried out by heating of capsule within 0.1g of ThO_2 and 1g of halides at 300°C in 12h. The chemical converted thorium samples were dissolved 30mL of concentrated HCl or HNO_3. The solutions were filtrated using 20mL of deionized water. The obtained solutions were neutralized by adding Na_2CO_3, after neutralization, we added 8mL of 1M Na_2CO_3, and finally added 2mL of 1M $MgCl_2$. We immediately obtained white precipitation after adding $MgCl_2$ solution. After waiting 1 hour, the precipitations were filtrated. The filtrates were measured by Ge γ-ray spectrometer and ICP-MS. The determination of activity of ^{228}Ra was evaluated by using the measurement of radioactivity of ^{228}Ac under the radiation equilibrium. ^{232}Th was detected and measured by ICP-MS.

RESULTS: The precipitation ratios of ^{228}Ra were calculated the activity difference between before and after precipitation experiment. We confirmed that almost all of ^{228}Ra was coprecipitated regardless of sample solutions. The amounts of ^{232}Th in solution before and after precipitation experiments and the percent precipitation of ^{232}Th were shown in Fig. 1. The precipitation amounts of Th in the case of the dissolution of chemical converted Th with CCl_3CCl_3 by HCl is the least among the all cases. The dependence of the chemical reagents for thermochemical conversion is speculated that the counter anion of the reagent used in the thermochemical conversion may have affected thorium precipitation formation. Although the separation of radium from thorium is available by the coprecipitation method, the removal of thorium from precipitate is not enough since there are much amounts of thorium in comparison with radium. We would have to add the further separation methods of radium from thorium before the precipitation method.

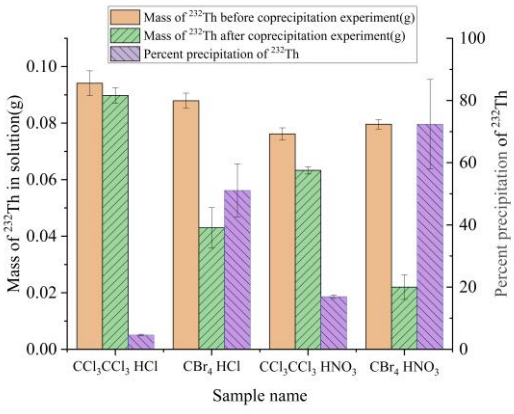

Fig. 1. Mass change of ^{232}Th in the solution before and after the precipitation experiments, and the percent precipitation of ^{232}Th

Consideration of Another Candidate Resins Containing Monoamide Structure with Selectivity for Actinyl Ions

M. Nogami and T. Yamamura [1]

Faculty of Science and Engineering, Kindai University
[1]*Institute for Integrated Radiation and Nuclear Science, Kyoto University*

INTRODUCTION: Development of highly selective compounds for actinyl ions has been important. We have been focusing on monoamide compounds as promising candidates. Earlier we have considered two factors for interaction between monoamides and actinyl ions; one is "chelating effect" of the ring formed by polymer monoamides and actinyl ion(s), and the other is "flexibility" of monoamide. For our synthetic organic resins with a monoamide structure as the functional group, however, we have not found any clear tendency between the chemical structure of functional monoamide and the adsorptivity to uranium(VI) (UO_2^{2+}) species[1]. Separately, last year we mentioned another preferable factor for compounds with selectivity for U(VI), *i.e.*, UO_2^{2+} ions prefer to form "planner five-coordinated complexes" which are scarcely seen in other metal ions[2]. Based on the above knowledge, this year a novel type of resin structure was suggested.

RESULTS: Our main target solvent for using monoamide compounds is nitric acid, and as already discussed, a typical coordination style of a monoamide compound to UO_2^{2+} in HNO_3 media is shown in Fig. 1, *i.e.*, one UO_2^{2+} ion is surrounded by two carbonyl oxygen atoms of two monoamide molecules and in total four oxygen atoms of two nitrate ions, forming a six-coordinated complex[2]. In the past, we have been sticking to the exclusive utilization of monoamide compounds. In case of resins, however, forming such six-coordinated structures or the above-mentioned five-coordinated ones might be difficult spatially. Our novel idea is to use the combination of monoamide and diamaide compounds as the bifunctional groups. Diamide compounds are famous for the separation of actinide(III) and lanthanide(III) species as well as actinide(IV) and (VI) ones, and we have already had an experience to synthesize a resin with a diamide structure, *N,N,N',N'*-tetramethylmalonamide (TMMA : Fig. 2) as the functional group[3]. We expect higher possibility of interaction between amide oxygen atoms and U(VI), and also lower possibility of interaction between amide oxygen atoms and lanthanide(III) species by combining monoamide and diamaide structures in one resin. In the former case, it may be possible that either of the two amide oxygen atoms in one diamide group is involved in the bonding with U(VI).

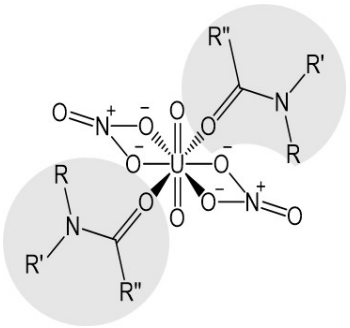

Fig. 1. Typical coordination style of a monoamide compound to UO_2^{2+} in HNO_3 .

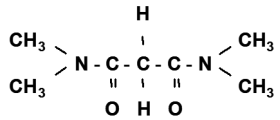

Fig. 2. Chemical structure of TMMA.

REFERENCES:

[1] M. Nogami *et al.*, KURNS Progress Report 2019 (2020) PR13-5.
[2] M. Nogami *et al.*, KURNS Progress Report 2022 (2023) PR7-8.
[3] M. Nogami *et al.*, KURNS Progress Report 2021 (2022) PR4-8.

I-1. PROJECT RESEARCHES

Project 6

PR6

Fundamental Research on Decommissioning of Reactor Facility

J. Hori

Institute for Integrated Radiation and Nuclear Science, Kyoto University

OBJECTIVES and RESEARCH SUBJECTS:

The main objective of this research project is to improve the method and the fundamental information on decommissioning of KUR and the Fukushima-Daiichi NPPs. This project consists of seven research subjects from four institutions, as follows.

R5P6-1: Neutron Flux Measurement for Activation Modeling of KUR facility (T. Sano *et al*., Kindai Univ.)
R5P6-2: Measurement of Activation in the Structure Materials of Reactor for decommissioning Process (K. Takamiya *et al*., Kyoto Univ.)
R5P6-3: Fundamental Research about Radioactive Contamination Survey on Nuclear Reactor Facility (S. Fukutani *et al*., Kyoto Univ.)
R5P6-4: Neutron Capture Cross-Section Measurements with TC-Pn in KUR for Same Nuclides targeted for Decommissioning (S. Nakamura *et al*., JAEA)
R5P6-5: Identification of Nuclear Material in Spent Fuel (Y. Nauchi *et al*., Central Research Institute of Electric Power Industry)
R5P6-6: External Neutron Source for Non-destructive Analysis of Fuel Debris (Y. Nauchi *et al*., Central Research Institute of Electric Power Industry)
R5P6-7: Study on Non-destructive Analysis Method for Fuel Debris using Neutron Resonance Absorption (J. Hori *et al*., Kyoto Univ.)

One research project (R5P6-2) could not be reported in this fiscal year since a sampling inspection of the object is under way.

MAIN RESULTS and CONTENTS of this REPORT:

T. Sano *et al.* (R5P6-1) evaluated the neutron flux distribution in the KUR sub-pile room during 5-MW operation for the decommissioning of KUR.
S. Fukutani *et al.* (R5P6-3) measured stable nuclide by INAA (Instrumental neutron activation analysis) for decommissioning the KUR stack made of RC (Reinforced Concrete). About 100 mg core samples were irradiated with standard samples by using Pn-2 and Pn-3 of KUR.
S. Nakamura *et al.* (R5P6-4) performed the activation experiments by using the thermal column pneumatic tube (TC-Pn) of KUR. The tentative thermal-neutron capture cross-sections of ^{58}Fe, ^{170}Er and ^{180}Hf selected from the viewpoint of clearance level in decommissioning were obtained.
Y. Nauchi *et al.* (R5P6-5) measured the gamma-ray spectrum from short-lived FPs from fission of ^{235}U induced by thermal neutrons at the pulsed neutron source in the KURNS-LINAC. The out-of-phase event spectroscope (OOPS) newly developed was applied.
Y. Nauchi *et al.* (R5P6-6) measured the background gamma rays were measured with good energy resolution using a fusion neutron source in an inertial electrostatic confinement device (IEC source) as an external source to apply a neutron induced gamma ray spectroscopy (NIGS) to non-destructive quantification technique of ^{235}U enrichment of irradiated nuclear material.
J. Hori *et al.* (R5P6-7) performed the verification experiment with a self-indication method for applying to the non-destructive assay of nuclear material such as fuel debris using a pulsed neutron source in the KURNS-LINAC. It was confirmed that the estimation of the reduction rate can be used for the determination of the areal density of fuel material.

PR6-1

Neutron flux measurement for KUR facility activation modeling

T. Sano, J. Hori[1], Y. Yashima[1], Y. Takahashi[1], K. Tera-da[1], Z. Zhang[1] and Y. Fujihara[1]

Atomic Energy Research Institute, Kindai University
[1]Institute for Integrated Radiation and Nuclear Science, Kyoto University

INTRODUCTION: For the decommissioning of the KUR, it is important to evaluate the amount of radioactivation in the generated waste. In particular, it is important to evaluate the radioactivation in the equipments around the biological shield and the neutron tubes. In general, the evaluation of the activation dose is mainly based on numerical calculations (deterministic or probabilistic models), although some part of the activation dose is measured. In numerical calculations, the neutron spectrum and absolute neutron flux are important in-put information. In recent years, the performance of computers has improved to the point where it is now possible to calculate neutron flux for the entire facility, including buildings, and to evaluate the injected neutron spectrum into facilities and equipment. However, the absolute values often differ by several 10% or more between the calculated and measured values. In the 2022, the neutron flux on the KUR biological shielding surface was measured using the EneRgY selective Neutron detector containment device for thermal Group neutron InterruptIon "ERYNGII" neutron detector [1].
In 2023, neutron shielding calculations were performed using Monte Carlo method to predict the neutron flux in the sub-pile room under the KUR.

CALCULATIONS: Neutron flux calculations in the KUR subpile room were performed in the following two steps: 1) A core calculation of KUR was performed using the Monte Carlo calculation code MVP3 [2] and JENDL-5 [3] to obtain the neutron spectrum in the KUR core. 2) Using the neutron spectrum as input, a neutron transport calculation was performed using PHITS2 version 3.31 [4] and JENDL-5 to obtain the neutron flux in the KUR sub-pile room.
Here, the core conditions of the KUR were adopted for the core in 2023 year. In addition, for simplification of the calculation model, each irradiation facilities and neutron tubes were not taken into account in the calculations.

RESULTS: Figure 1 shows the neutron flux distribution in the KUR calculated by PHITS2. The value of neutron flux is relative. Neutron flux at the top of the reactor are well shielded by the cooling water. On the other hand, the neutron flux in the sub-pile room during 5 MW operation was evaluated to be about 100 n/cm/sec.

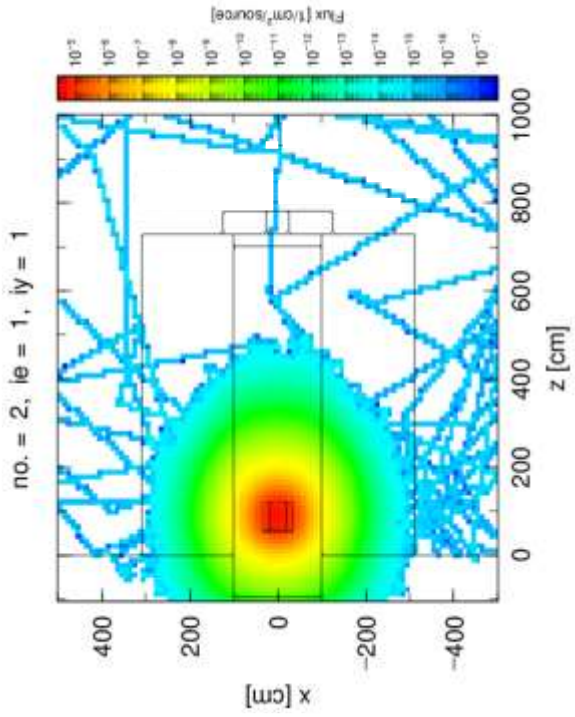

Fig. 1. Calculated neutron flux distribution

REFERENCES:
[1] T. Sano, *et al.,* KURNS-Progress report 2022 (2023) 71.
[2] Y. Nagaya, *et al.*, JAEA-Data/Code 2016-018 (2016).
[3] O. Iwamoto, *et al.,* J. Nucl. Sci. Technol., **60** (2023) 1-60.
[4] T. Sato, *et al.,* J. Nucl. Sci. Technol., **55** (2018) 684-690.

PR6-2

Fundamental Research about Radioactive Contamination Survey on Nuclear Reactor Facility

S. Fukutani[1)], R. Tsuchiya[2)], J. Hori[1)] and K. Takamiya[1)]

1) Institute for Integrated Radiation and Nuclear Science, Kyoto University
2) Graduate School of Engineering, Kyoto University

INTRODUCTION: It is important to survey radioactive contamination for decommission of nuclear reactor facilities. The KUR stack, which was built in 1963, made of RC (Reinforced Concrete) was demolished in 2013. In this study, we used the KUR stack core [1] and measured stable nuclide by INAA for fundamental estimate of activation amount in concrete.

EXPERIMENTS: Instrumental neutron activation analysis (INAA) was conducted for KUR stack core samples, which was made of RC (Reinforced Concrete). Pn-2 and Pn-3 of KUR facilities were used. For the experiment by using Pn-2, about 100mg core samples were irradiated with standard samples, which were BCR-176 (from Commission of the European Communities, city waste incineration ash) and JB-2 (from National Institute of Advanced Industrial Science and Technology, Basalt). At 5MW thermal power of KUR, samples were irradiated for 60 minutes. After about 6 days and 40 days cooling time, γ spectrometry was made by the HPGe semiconductor detector (ORTEC GEM25185). The experiment by using Pn-3 was conducted for measuring chlorine (Cl), and Cl-38 was measured. Standard sample for Cl was used LiCl solution (1003mg-Li / L). At 1MW thermal power of KUR, samples were irradiated for 30 seconds. Cl-38 is short half-life nuclide (half-life is about 37.2 minutes), so after irradiation, the measurement by γ spectrometry with the HPGe semiconductor detector (ORTEC GEM25185) was made Immediately. Quantitative of each element was conducted by comparative method

RESULTS: Main measurement results by INAA ware shown in the Table 1. Arsenic (As) is short half-life nuclide, so it may be not important as radioactive nuclide. But as element, because of its toxicity, it is necessary to be careful. As for chlorine, Cl-38 is made by neutron activation from stable nuclide Cl-37, abundance: 24.24%, (n, γ) cross section: 0.433b. Cl-38 is very short half-life nuclide, it is not important for radioactive waste treatment and disposal. But, chlorine has another stable nuclide Cl-35. Abundance and (n, γ) cross section of Cl-35 are 75.76% and 43.6b. Cl-36 made from Cl-35 is long half-life (3×10^5 year), pure beta emitter nuclide. It is difficult to detect and measure. Cl-38 wad detected by neutron activation, and it means Cl-35 was made at the same time. And chlorine is thought to be negative ion form and to be easy mobility, it is necessary to be careful.

Table 1 Measuring Results by INAA

Element	As	Ce	Cr	Co	Eu
Nuclide	As-76	Ce-144	Cr-51	Co-60	Eu-152
Half-life	1.1d	285d	28d	5.3y	13y
Conc. (mg/kg)	8.38 ± 1.7	6.80 ± 1.07	5.56E+1 ± 4.0	8.75 ± 7.6E-2	0.44 ± 3.4E-2
Element	Mn	Sb	Zn	Cl	
Nuclide	Mn-54	Sb-124	Zn-65	Cl-38	
Half-life	312d	60d	244d	37m	
Conc. (mg/kg)	7.17E+2 ± 7.3E+1	5.69 ± 0.15	3.40E+2 ± 4.8	2.34E+2 ± 1.1E+2	

REFERENCES:

[1] S. Fukutani *et al.,* KURNS Prog. Report 2022 (2023) 72.

Neutron Capture Cross-Section Measurements at TC-Pn in KUR for Nuclides of Concern in Decommissioning

S. Nakamura[1], S. Endo[1], R. Gerard[1], A. Kimura[1], Y. Shibahara[2]

[1]*Nuclear Data Center, Japan Atomic Energy Agency*
[2]*Institute for Integrated Radiation and Nuclear Science, Kyoto University*

INTRODUCTION: As nuclear facilities are dismantled in decommissioning, of course, various and large amounts of waste are generated, for instance, structural materials, concrete pieces, pipes, electric cables and so on. Even more inconveniently, they are radioactive waste due to neutron activation. In decommissioning, it is necessary to predict and evaluate the amount of radioactivity generated. Thus, the present study aims to measure accurate neutron capture cross-sections for nuclides of concern in decommissioning. We have performed measurements using the thermal column pneumatic tube (TC-Pn) of KUR [1, 2]. From the viewpoint of clearance level [3] in decommissioning, the present work selected the following nuclides and measured their thermal-neutron capture cross-sections: ^{58}Fe, ^{170}Er and ^{180}Hf nuclides.

EXPERIMENTS: High purity metal samples were prepared for irradiation. A gold-aluminum alloy wire and a cobalt foil were used to monitor the neutron flux at the irradiation position. **Fig. 1** draws a rough sketch of irradiation targets and TC-Pn. Two targets were prepared, (a) and (b). To make use of the well-thermalized neutron field, two dummy capsules were sent into TC-Pn in advance, and then followed by the one target capsule. The target was irradiated for 1 hour under 1-MW operation of KUR. The other target capsule was irradiated in the same condition next day. After irradiation, the samples and flux monitors were enclosed in a thin vinyl bag one by one. The sample was subjected to γ-ray measurement with a high-purity Ge detector. A sample was placed at a distance of 100 mm from the front surface of the Ge detector. The γ-ray peak efficiencies of the Ge detector were measured with a gamma reference source of ^{152}Eu and a mixed γ-ray source.

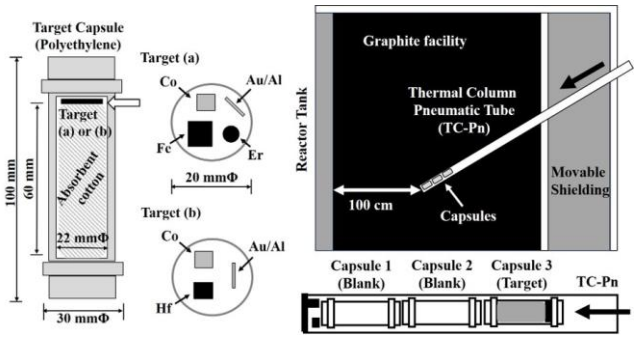

Fig.1 Rough sketch of targets and TC-Pn facility.

ANALYSIS AND RESULTS: The reaction rates of the samples and flux monitors were obtained from their γ-ray yields. Using the reaction rates of monitors, the thermal-neutron flux component was derived on the basis of *Westcott*'s convention [4]. The obtained rection rates for samples divided by the thermal-neutron flux component present the thermal-neutron capture cross-sections. Details of the analysis are given in Ref. [1]. The tentative results were obtained as follows: 1.23±0.03 barn for the ^{58}Fe(n,γ)^{59}Fe reaction, 8.19±0.35 barn for the ^{170}Er(n,γ)^{171}Er reaction and 13.57±0.14 barn for the ^{180}Hf(n,γ)^{181}Hf reaction. As a by-product, 0.427±0.006 barn for the ^{179}Hf(n,γ)^{180m}Hf reaction was obtained. The authors currently proceed with the analysis toward derivation of the final results of the thermal-neutron capture cross-sections for those reactions.

REFERENCES:

[1] S. Nakamura *et al*., J. Nucl. Sci. Technol., **58(10)** (2021) 1061.
[2] S. Nakamura *et al*., J. Nucl. Sci. Technol., **59(11)** (2022) 1388.
[3] IAEA; 2004. (No. RS-G-1.7).
[4] C.H. Westcott *et al.,* "*Proc.2nd Int. Conf. Peaceful Use of Atomic Energy, Geneva*", **16** (1958) 70.

Identification of Nuclear Material in Spent Fuel (2)

Y. Nauchi, J. Hori[1], K. Terada[1], T. Sano[2]

Energy Transformation Research Laboratory, Central Research Institute of Electric Power Industry
[1]Institute for Integrated Radiation and Nuclear Science, Kyoto University
[2]Atomic Energy Research Institute, Kinki University

INTRODUCTION: The delayed gamma ray assay would be useful to estimate fission rate ratio of nuclides in nuclear fuel. For the assay, nuclear data of yield and decay of fission products (FPs) are essential. To evaluate those with better accuracy, we have measured γ rays from short-lived FPs radiated from fission of ^{235}U induced by thermal neutrons at the pulsed source in the KURNS-LINAC facility [1]. For that, the **o**ut-**o**f-**p**hase event **s**pectroscopy (OOPS) has been newly developed where γ ray spectra are measured after thermal neutron decays out. In the present work, pulse frequency F is surveyed to enhance the counting efficiency.

EXPERIMENTS: The measurement set up was almost as same as that applied in the previous work [1]. Uranium (U)-Aluminum (Al) alloy samples was irradiated by the pulsed neutron and the γ ray was measured with a HPGe of the 35% relative efficiency. Data of pulse height of a signal in the HPGe and timing of the signal were accumulated event by event for OOPS. The length of the OOP time region for a neutron pulse is $(1/F - d)$ where d is the time required for decay out of the thermal neutrons. d should be longer than 16 ~ 20 ms [1] but longer d is not preferable since $(1/F - d)$ becomes less. The summation of the time length per second for OOPS counting is $F(1/F - d)$ and the neutron fluence per second on the U-Al sample is proportional to F. We chose F = 30 Hz since an index for γ ray count, $F^2(1/F - d)$, is larger for d = 16~20 ms, as shown in Fig. 1.

RESULTS: The measured spectrum in the OOP time region is shown in Fig. 2. Here, d = 20 ms. The measurement time was 17 hours. Thanks to the survey of F, counting statistics has been gradually enhanced compared to the previous work [1] so that the discrete peaks have been distinguished for γ ray energy region from 1.0 to 5.5 MeV. Based on the JENDL/FPY&FPD-2011 data [2], activities of the FPs were calculated by solving Bateman's formular and intense γ rays from the FPs were selected. By comparing the selected intense γ rays and the measured spectrum, the FPs radiating the γ rays are identified as shown in Fig. 2.

REFERENCES:

[1] Y. Nauchi *et al.,* KURNS Progress Report 2022 (2023) PR8-4.
[2] J. Katakura, JAEA-Data/Code 2011-025, 2012.

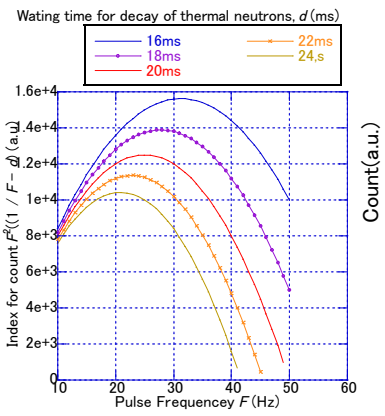

Fig. 1. Optimum Pulse frequency .

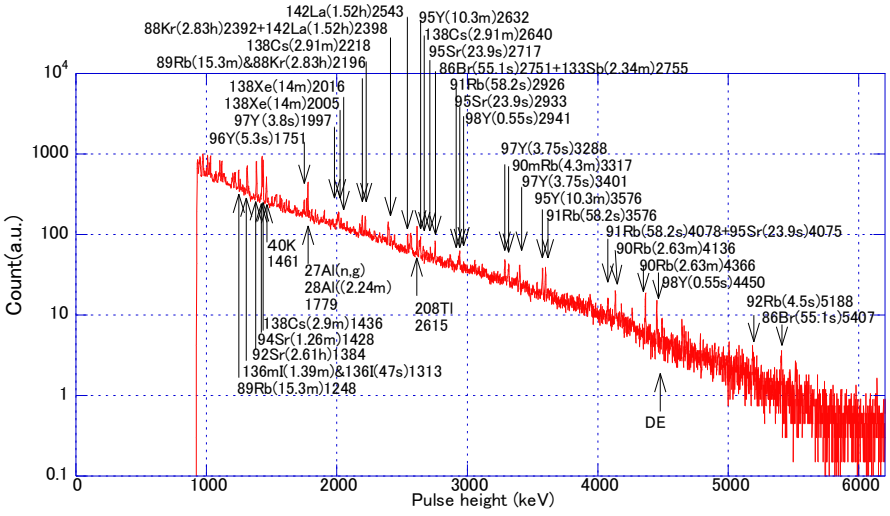

Fig. 2. Measured γ ray spectrum in OOP time region.

External Neutron Source for Non-Destructive Analysis of Fuel Debris (2)

Y. Nauchi, Y. Takahashi[1]

Energy Transformation Research Laboratory, Central Research Institute of Electric Power Industry
[1]Institute for Integrated Radiation and Nuclear Science, Kyoto University

INTRODUCTION: As a non-destructive quantification technique of ^{235}U enrichment of irradiated nuclear material, neutron induced gamma ray spectroscopy (NIGS) has been studied [1]. For NIGS, we need an external neutron source. In the previous work, we had measured the γ ray background (BG) spectra inherent to three types of neutron sources, ^{252}Cf, ^{241}Am-Be, and a fusion neutron source in an inertial electrostatic confinement device (IEC source), by employing BGO scintillator. Among them, the IEC source is considered preferable since BG γ rays are not so intense in the energy region from 2.7~5.5 MeV where signature γ rays of ^{235}U, ^{238}U and ^{239}Pu are radiated [2]. In the current work, the BG γ rays were measured with good energy resolution.

EXPERIMENTS: Schematic view of the measurement is given in Fig. 1. Uranium (U) metal plates were loaded in rectangular aluminum pipe column with polyethylene plates. They were irradiated by neutrons from the ^{252}Cf or the IEC source. γ rays are measured with a HPGe of the 35% relative efficiency. From the U sample, γ rays of energy less than 100 keV was intense. To shield them, lead (Pb) plate and Pb-Bismuth (Pb-Bi) plates were placed. To increase the neutron flux in the U plates, polyethylene blocks and plates were placed surrounding the U plates. The measured pulse height was calibrated to energy referring ^{35}Cl(n, γ) γ ray spectrum measured additionally.

RESULTS: The measured pulse height spectra were shown in Fig. 2. With the ^{252}Cf source with intensity of 3 x 10^5 n/s, ^{238}U(n,γ) 4060 keV γ ray peak was identified within 2.5 hours of measurement. In the measurement, peaks corresponding to the neutron separation energy of $^{71, 74, 75}$Ge were measured. In the case where the U sample was irradiated by neutron from the IEC source, the neutron flux in the sample is less. Although we confirmed increment of count rate from 2.3 to 4 MeV mainly by the fission events, we could not identify the 4060 keV γ ray peak within 2 hours of measurement. When the IEC source was employed, ^{56}Fe(n,γ) 7631 and 7645 keV γ rays from the wall of the IEC device were identified. However, the count rates of them were less than those of γ rays from the $^{71, 75}$Ge(n,γ) reactions. That means major BG γ rays in this geometry were the neutron induced events in HPGe. To identify the ^{238}U(n,γ) 4060 keV γ ray peak with the IEC source, more than a hundred hours of measurement would be required in the current geometry.

REFERENCES:

[1] Y. Nauchi, H. Ohta *et al.,* Proc. ICNC2023, Sendai, Oct. 2023.
[2] Y. Nauchi *et al.,* KURNS progress report 2022, PP8-5.

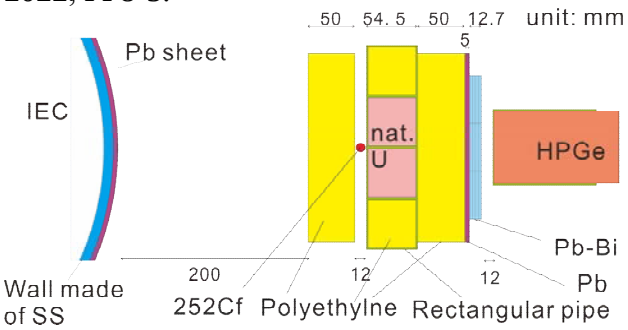

Fig. 1. Horizontal geometry.

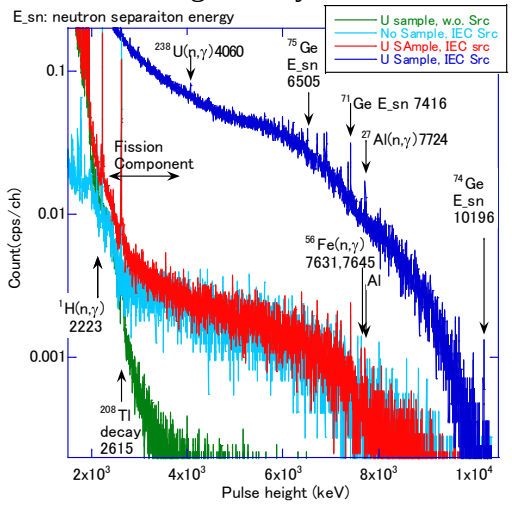

Fig. 2. Measured γ ray spectra.

Study of Non-destructive Analysis Method for Fuel Debris using Neutron Resonance Absorption

J. Hori, K. Terada, T. Takahashi, H. Yashima and T.Sano[1]
Institute for Integrated Radiation and Nuclear Science, Kyoto University
[1]*Atomic Energy Research Institute, Kindai University*

INTRODUCTION: In the units 1 to 3 of Fukushima Daiichi Nuclear Power Plant (1F), the fuel, the metal cladding and the control rods were melted and large amount ware re-solidified in the bottom of the pressure vessel as fuel debris. In the decommission plan of 1F, the fuel debris will be collected and analyzed in the near future. Non-destructive nuclide assay is one of the important issues for nuclear material accountancy. We have studied the Neutron Resonance Densitometry (NRD) as a method of non-destructive nuclear assay. In the study, we proposed to apply a self-indication method to analysis of the fuel debris [1]. In the self indication method, an indicator consisting of the target nuclide is placed at the neutron beam downstream from a sample. The transmitted neutron though the sample can be measured indirectly by detecting the reaction products from the indicator with the neutron time-of-flight (TOF) method. We carried out the verification experiment.

EXPERIMENTS: The experiment was performed at the Institute for Integrated Radiation and Nuclear Science, Kyoto University (KURNS-LINAC). The linac was operated with a repetition rate of 200 Hz, a peak current of about 5 A, and an electron energy of about 30 MeV. We used a flight path in the direction of 135 degree with respect to the linac electron beam. A Cd sheet of 0.5 mm in thickness was inserted into the TOF beam line to suppress overlap of low energy neutrons due to the previous pulse. A natural uranium sheet as a indicator was set in the neutron beam line at a distance of about 12 m from the neutron target. Capture gamma-rays from the indicator were measured by a 4π $Bi_4Ge_3O_{12}$ spectrometer. On the other hands, three kinds of uranium samples with different thickness were set in the upper beam.

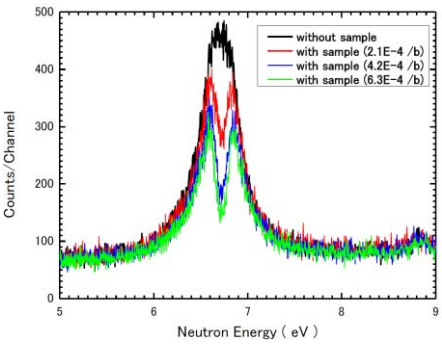

Fig. 1 TOF spectra for the 6.7-eV resonance of ^{238}U with and without the samples.

RESULTS: Figure 1 shows the TOF spectra for the 6.7–eV resonance of ^{238}U. The reduction of the resonance peak of the indicator was observed by inserting the sample in the upper beam. The reduction ratio has a relationship with the areal density of ^{238}U in the sample. We estimated the reduction ratio by using a Monte Carlo simulation code MCNP-6.3 with JENDL-5. The comparison between the experimental and the calculated reduction rates are shown in Fig. 2. The reduction ratios estimated by simple calculation reproduce the experimental ones. It was confirmed that the estimation of the reduction rate can be used for the determination of the areal density of fuel material.

In the future, we are going to perform the verification experiment using a realistic sample to simulate the fuel debris.

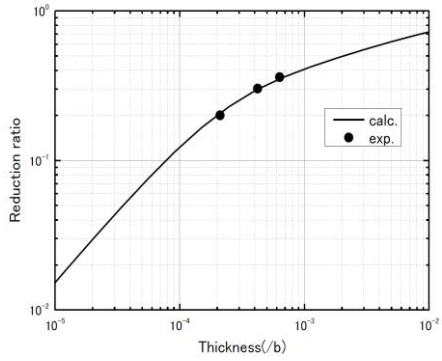

Fig. 2 Comparison between the experimental and the calculated reduction rates for the 6.7-eV resonance of ^{238}U.

REFERENCES:

[1] J. Hori *et al.,* EPJ Web of Conferences **146** (2017) 09042 .

I-1. PROJECT RESEARCHES

Project 7

PR7

Development on Neutron Imaging Application

Y. Saito

Institute for Integrated Radiation and Nuclear Science, Kyoto University

OBJECTIVES and ALLOTED RESEARCH SUBJECT: Neutron imaging provides valuable information which cannot be obtained from an optical or X-ray imaging. The purpose of this project is to develop the imaging method itself and the experimental environment for expanding the application area of the neutron imaging. The allotted research subjects are as follows:

ARS-1: Measurements of Multiphase Dynamics by Neutron Radiography (Y. Saito et al.)
ARS-2: Visualization of Liquid Water Behavior in a Polymer Electrolyte Fuel Cell under High Temperature Operation (H. Asano et al.)
ARS-3: Trial Visualization of Quenching Phenomena in Vertical Hole (H. Umekawa et al.)
ARS-4: Evaluation of Meltwater Penetration During Defrosting Process (R. Matsumoto et al.)
ARS-5: Effect of the water content of concrete on the spalling phenomenon (M. Kanematsu et al.)
ARS-6: Neutron Radiography on the Effects of a Mixer with an Inserted Tube in a Flow-type Supercritical Hydrothermal Reactor (S. Takami et al.)
ARS-7: Visualization of plant roots in media containing organic matter using neutron CT (U. Matsushima et al.)
ARS-8: Development of a method for quantitative estimation of neutron imaging (M. Kitaguchi et al.)
ARS-9: In-situ Observation of Electrolyzed Lithi-um-ion Conductor through Neutron Radiography (S. Takai et al.)
ARS-10: Flow Visualization of Coolant inside Layered Rod Array (Kaneda et al.)

MAIN RESULTS AND THE CONTENTS OF THIS REPORT:

ARS-1 performed visualization of boiling two-phase flow by high-speed imaging. The dynamics of the two-phase flow pattern in a tube were analyzed based on its spatio-temporal distribution.

ARS-2 applied to neutron imaging to water accumulation in Polymer Electrolyte Fuel Cell (PEFC). In this study, the water content and its distribution were visualized at a cell temperature of 105 °C.

ARS-3 investigated the quenching phenomena. Results expresses the influence of the restriction caused by the counter current flow limitation (CCFL) condition clearly.

ARS-4 evaluates the meltwater penetration during defrosting process, which is one of the important phenomena to enhance the energy efficiency of the air conditioning system.

ARS-5 applied the spalling phenomenon of concrete from the perspective of its internal moisture.

ARS-6 proposed a mixer for the instantaneous heating of the reactant solution and performed neutron radiography measurements to confirm how the fluids mixed in the proposed mixer.

ARS-7 applied neutron CT to visualization of plant roots in media containing organic matter. It was demonstrated that root distribution can be observed by supplying D_2O to the roots.

ARS-8 applies the electric field to the model cell to observe the lithium migration in the solid electrolyte employing the NR.

ARS-9 was not performed due to the difficulties to set up experiments in 2023.

ARS-10 performed the visualization of coolant inside the layered rod array. From the experimental results, it was found the profile of the coolant inside the structure depends on the pouring liquid temperature and flowrate rather than the applied heat on the structure.

Measurements of multiphase flow dynamics using neutron radiography

Y. Saito, D. Ito and N. Odaira

Institute for Integrated Radiation and Nuclear Science, Kyoto University

INTRODUCTION: Neutron radiography (NRG) is useful for visualizing multiphase flow. It can also measure the flow structure and dynamics of boiling two-phase flow. This study aims to investigate changes in the flow pattern of boiling two-phase flow in a heated pipe using NRG and to clarify its dynamics by analyzing temporal fluctuations. NRG proves effective in understanding thermal-hydraulic phenomena in metallic pipes due to its high transmissivity and has been applied in various applications. While most previous studies have focused on average characteristics [1], measuring spatio-temporal characteristics can provide new insights using a high-speed imaging system.

EXPERIMENTS: Experiments were conducted in the B-4 facility of KUR. A high-speed imaging system comprising an optical image intensifier and a high-speed camera was employed to acquire sequences of neutron transmission images of boiling flow at 1000 fps. The test section featured a stainless-steel tube with an inner diameter of 10 mm, heated by Joule heating. The cross-sectional average void fraction was calculated from the instantaneous void fraction distribution estimated from the transmission images. The dynamics of the flow pattern in the tube were analyzed based on its spatio-temporal distribution.

RESULTS: A typical result of the spatio-temporal distribution of measured void fraction is shown in Fig. 1. In the middle of the heated section, bubble generation begins, and the rise of bubbles is observable in the distribution. In the upper part of the tube, the flow changes to the annular flow, and the movement of the liquid film appears as stripes. Thus, understanding the dynamic characteristics of the flow structure and identifying the pattern can be achieved by estimating characteristic quantities from it.

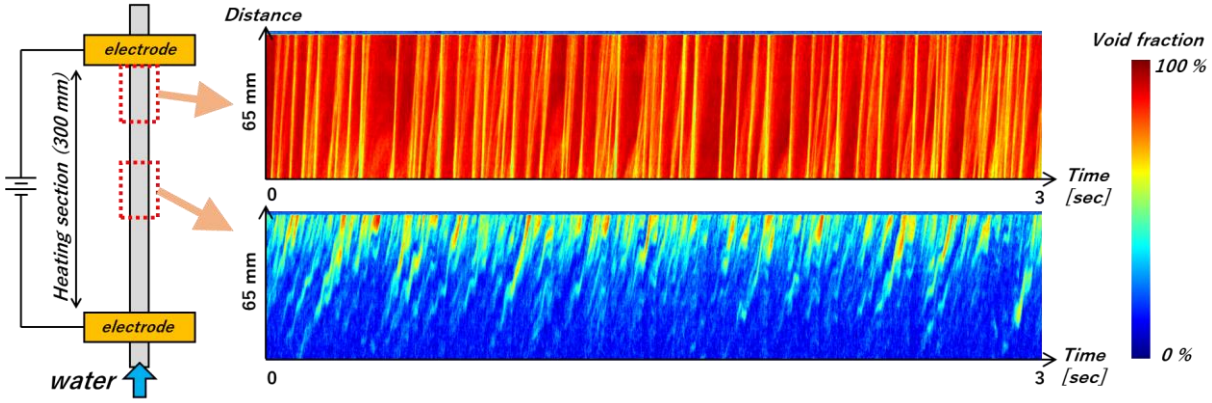

Fig. 1 Spatio-temporal distributions of cross-sectional averaged void fraction in a heated tube (q = 290 kW/m^2, G = 200 kg/s, ΔT_{sub} = 20 K)

REFERENCES:

[1] T. Ami *et al.*, Exp. Therm Fluid Sci., **141** (2023) 110799.

PR7-2

Visualization of Liquid Water Behavior in a Polymer Electrolyte Fuel Cell under High-Temperature Operation

H. Murakawa, Y. Obayashi, K. Nakagawa, K. Sugimoto, H. Asano, Y. Shirase[1], C. Schreiber[1], S. Wakolo[1], E. Dzramado[1], J. Inukai[1], D. Ito[2] and Y. Saito[2]

Department of Mechanical Engineering, Graduate School of Engineering, Kobe University
[1]Hydrogen and Fuel Cell Nanomaterials Center, University of Yamanashi
[2]Institute for Integrated Radiation and Nuclear Science, Kyoto University

INTRODUCTION: Polymer electrolyte fuel cells (PEFCs) are expected to be used in the electrification of heavy-duty vehicles (HDVs), but higher operating temperatures are required to accommodate higher power outputs and smaller cooling systems. Currently, the practical realization of fuel cells with an operating temperature of about 120 °C is being considered [1], but in this case, to prevent dryout, the saturation temperature of the water must be increased, i.e., the pressure in the fuel cell must be increased. The formation of liquid water in a fuel cell is determined by humidity, temperature and the amount of water produced by the cell reactions, which may depend on their spatial distribution when accompanied by cell reactions. In this study, the water content and its distribution were visualized at a cell temperature of 105 °C under various pressure condition by neutron radiography.

EXPERIMENTS: A small single-cell PEFC with a reaction area of 20×20 mm^2 was used. Humidified hydrogen gas and air were supplied to the anode and cathode through ten parallel straight channels with the cross-section of 1×1 mm^2, respectively. The width of ribs was 1 mm. The thickness of the PEM including the catalyst layer was 200 μm and the thickness of the GDL was 235 μm. The pressure in the anode and cathode of the PEFC was maintained by regulating valves in the exhaust line. The PEFC was placed in the vertical plane and the gas flows in the anode and cathode formed counter-current flow. The air flow in the cathode was a vertical downward flow. Hydrogen gas and air were supplied to the anode and cathode at a humidification temperature of 74.6 °C and a flow rate of 200 cc, respectively. The imaging was carried out with an exposure time of 30 s during the reactor operation at 1 MW output.

RESULTS: The cell voltage was measured when the current density was varied from 0, 0.4, 0.6, 0.8 and 1.0 mA/m^2 under the condition of the pressure in the PEFC of 250 kPa. The relative humidity of the supplied gas was 34.2 % at the inlet of the PEFC. Steady-state conditions were obtained up to a current density of 0.8 mA/m^2, but at 1.0 mA/m^2, a decrease and fluctuation of the cell voltage was observed. The measured results of water thickness are shown in Fig. 1(a) to (c). At 80 minutes after the measurement start, just before the current density was increased to 1.0 mA/m^2, little increase in the water film thickness was observed. At 88 minutes, Liquid water began to drain into the channel from the corner at the base of the ribs, and then, the liquid water in the channels gradually increased. At 100 minutes, it was confirmed that some liquid water plugs were formed in the channels. Such liquid water plugs interfered with the supply of the reaction gas and led to a drop in the cell voltage.

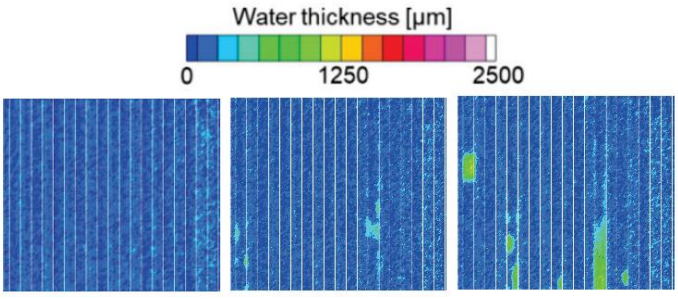

(a) 80 minutes (b) 88 minutes (c) 100 minutes

Fig. 1. Water thickness distribution.

REFERENCES:

[1] J. Zhang *et al.,* Electrochimica Acta, **52**(15) (2007) 5095-5101.

Trial Visualization of Quenching Phenomena in Vertical Hole

H. Umekawa, T. Ami, R. Tujimoto, Y.Saito[1], D.Ito[1] and N.Odaira[1]

Department of Mechanical Engineering Kansai University
[4]Institute for Integrated Radiation and Nuclear Science, Kyoto University

INTRODUCTION: The continuous feeding of cool water to the hot surface is one of the key points of the quenching phenomena. These phenomena are widely observed in several industrial instrument, and also in the sever accident of nuclear reactor. Especially in the case of the sever accident, the water must be feed through the complex structure to the hot surface as like as the case of TMI. In this trial, the visualization of the cooling of the hot closed bottom end tube was conducted. Results expresses the influence of the restriction caused by CCFL condition at the channel inlet clearly.

EXPERIMENTS: Figure 1 is the schematic diagram of the experimental apparatus. Firstly, the test section is heated up a.800 deg.C by installing into the electric farness. When the temperature reached the predetermined value, testsection is pull up, and the Head tank water enter to the receiver by opening of Electric valve. During the quenching, flow structure is recorded by using the highspeed camera (250fps exposure period 1/900). Sheathed thermocouples is fixed upon the test section surface by using wire, and the data is recorded by data logger (10Hz). The example of cooling curve is shown in Fig.2, and succeed visualization images are shown in Figs. 3(a) and (b). Owing to the restriction at the tube inlet in small diameter tube, liquid is kept at the top region. As the results, quenching period of small diameter tube takes the longer period compared with the large tube. Even in the case of the large diameter tubes, the restriction caused by the CCFL condition at the inlet of the tube, but This restriction is intermitted and the inverted annular flow is observed in the visualization results.

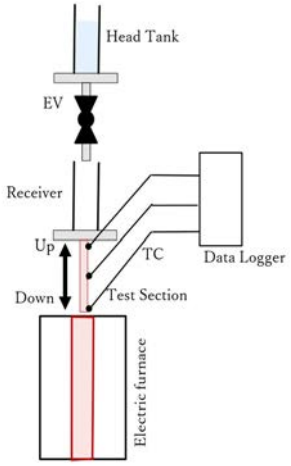

Fig.1 Experimental apparatus

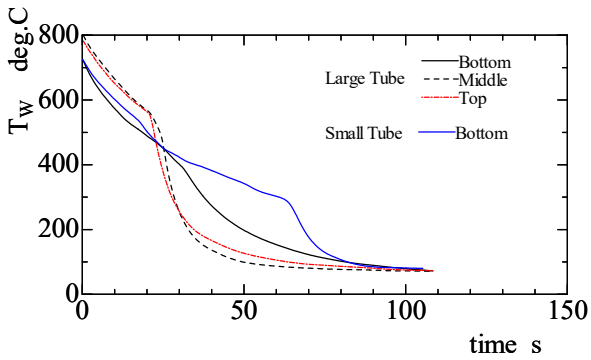

Fig 2 Example of Cooling curves

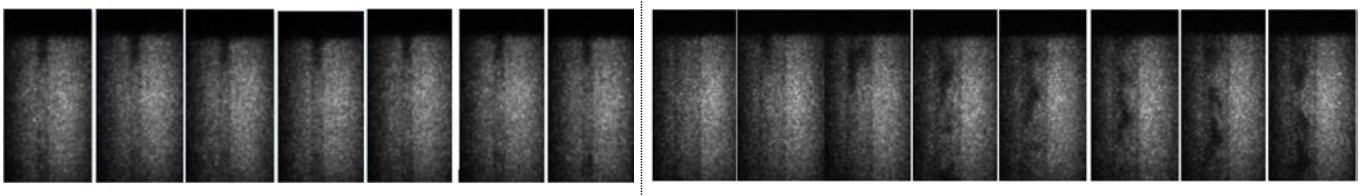

(a) Small Tube (b) Large Tube

Fig.3 Example of flow Visualization (250fps)

PR7-4

Evalulation of Meltwater Penetration During Defrosting Process

S. Kimura, R. Matsumoto [1], K. Kida, Y. Shirotani[1], K. Kobayasi[1], Y. Saito[2] D. Ito[2] and N. Odaira[2]

Graduate School of Science and Engineering, Kansai University
[1]Faculty of Engineering Science, Kansai University
[2]Institute for Integrated Radiation and Nuclear Science, Kyoto University

INTRODUCTION: Frost formation on the heat exchangers of the air conditioning system causes the serious problem on the heat transfer performance. In order to recover the performance of the heat exchanger, a defrosting operation is performed periodically to remove the frost from the heat exchanger by flowing hot gas through the heat transfer tubes. Matsumoto et al. [1] reported the removal of meltwater by penetrating into the remaining frost layer. By using this phenomenon, effective defrosting can be achieved. However, the relationship between the penetration speed of the meltwater and the temperature distribution on the frosting plate is not clear. In this study, the behavior of meltwater was estimated by neutron radiography.

EXPERIMENTS AND RESULTS: Frost was formed on the aluminum plate with a thickness of 0.5 mm by cooling it down to -25 °C. A temperature gradient was applied by raising the temperature at one edge of the plate to 5°C, thus, the defrosting was performed in one direction. The defrosting duration was 15 min. The water penetration image at 7 min after the start of defrosting is shown in Fig.1, where defrosting was occurred from left to right, and melted water can be seen in the center of the plate with a water penetration width of approximately 5 mm. The water distribution of the rectangular area indicated by the orange line was extracted and rearranged for each defrosting time in Fig. 2. The vertical axis in Fig. 2 is the direction of meltwater penetration and the horizontal axis is the time elapsed since defrosting. Figure 2 shows that defrosting occurs at a constant speed while increasing the penetration width, and that the frost layer in the penetration zone can hold up to about twice its own water content. The visually observed penetration front, indicated by the circle plot, is in agreement with the results of the neutron radiography observation. The temperature distribution was measured by 11 thermocouples attached to the back of the aluminum plate. The temperature of the penetration front shows 0°C.

REFERENCES:

[1] R. Matsumoto *et al.,* Transactions of the Japan Society of Refrigerating and Air Conditioning Engineers, **37(3)** (2020) 249.

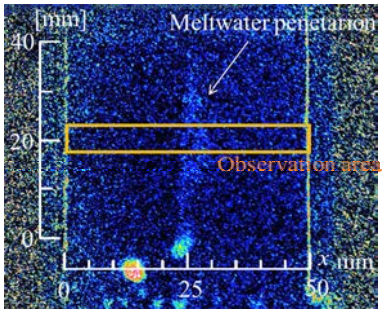

Fig. 1 Water penetration image.

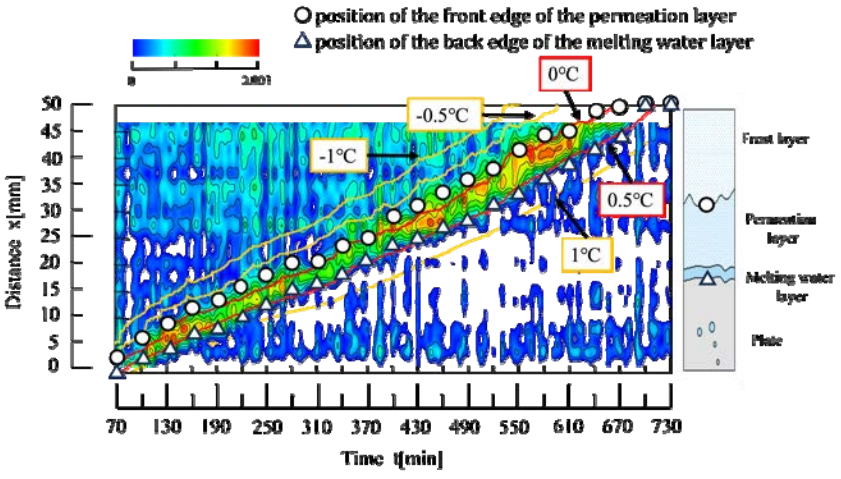

Fig. 2 Spatio-temporal distribution of meltwater penetration .

Effect of the water content of concrete on the spalling phenomenon

M. Kanematsu[1], Y. Nishio[2], J. Kim[1], N. Odira[3], D. Ito[3], Y. Saito[3]

[1]*Department of Architecture, Tokyo University of Science*
[2]*Building Research Institute*
[3]*Institute for Integrated Radiation and Nuclear Science, Kyoto University*

INTRODUCTION: This study aimed to understand the spalling phenomenon of concrete from the perspective of its internal moisture. Capturing detailed moisture movement in concrete under fire is essential to understanding the spalling mechanism [1]. Therefore, the explosion tendency according to the change in the internal moisture state is identified, and the effect of the change in the pressure state due to the condensation of moisture on the explosion is examined by using neutron radiography.

EXPERIMENTS: The size of the test specimen is 100 × 70 × 30 mm, shown in Fig.1. Additionally, to measure the internal pressure, the pipes for pressure measurement and thermocouples were molded at 10mm and 20mm from the heating surface. Neutron radiography was performed at TNRF in the B-4 port of KUR.

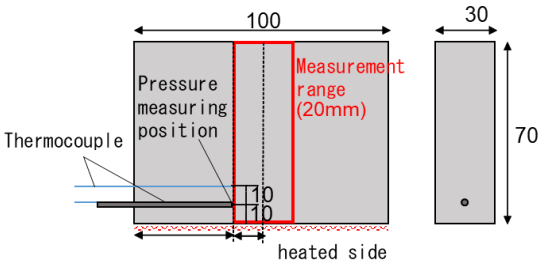

Figure 1. Pressure and temperature measurement location of the specimen

RESULTS: Our findings, as depicted in Figure 2, reveal the relative moisture content distribution after 5 minutes of heating for concrete with varying initial moisture contents. Notably, at the 53% and 87% initial relative moisture content levels, we observed the moisture clog phenomenon, where the moisture content exceeded the initial moisture content, in areas distant from the heated surface. Considering that spalling was observed in specimens with an initial moisture content of 40-95% in excess of 90%, we can infer that the moisture clog is linked to the spalling tendency of these specimens.

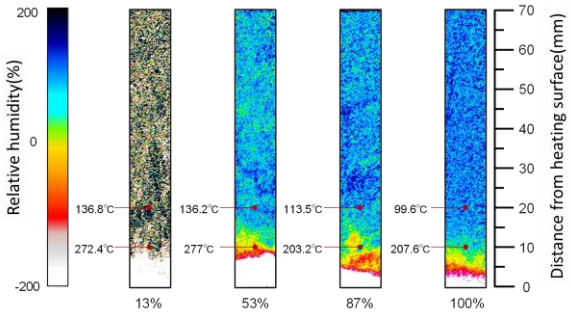

Figure 2. Moisture content after 5 minutes of heating in concrete with different initial moisture contents.

Figure 3 shows the maximum pressure values after 10 minutes of heating. The pressure at 10 mm from the heating surface was mostly less than 1 MPa. This trend is similar to the previous report [2], confirming that the maximum pressure inside the specimen where spalling did not occur was less than 1 MPa

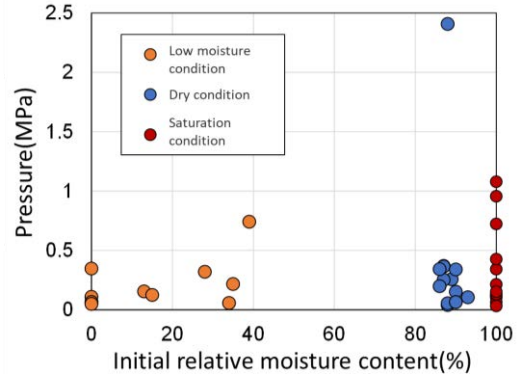

Figure 3. Relationship between maximum pressure and relative moisture content at 10mm from the heating surface

REFERENCES:

[1] JCI-TC-154A (2017). "Committee Reports:"
[2] T. Tanibe, (2014). "Ring restraining testing and spalling index of concrete at high temperature"

Neutron Radiography on the Effects of a Mixer with an Inserted Tube in a Flow-type Supercritical Hydrothermal Reactor

R. Sasaki, T. Kurono, S. Takami, M. Kubo[1], K. Sugimoto[2], N. Odaira[3], D. Ito[3] and Y. Saito[3]

Graduate School of Engineering, Nagoya University
[1]Graduate School of Engineering, Tohoku University
[2]Graduate School of Engineering, Kobe University
[3]Institute for Integrated Radiation and Nuclear Science, Kyoto University

INTRODUCTION: Supercritical hydrothermal synthesis is a method to produce metal oxide nanoparticles in supercritical water. During supercritical hydrothermal synthesis using flow-type reactors, a stream of metal ion aqueous solution was instantaneously heated by mixing with a stream of heated water in a mixer. The previous studies indicated that a mixer with an inserted tube promoted faster mixing of reactant solutions with a stream of heated water. In this study, we tired various sizes of inserted tubes to observe how supercritical water and room-temperature water mixed in the mixer.

EXPERIMENTS: In this study, we conducted neutron radiography measurements to visualize the mixing behavior in a flow-type reactor under operation. The measurements were performed at the B4 port of the Kyoto University Reactor (KUR). The KUR was operated at a 1 or 5 MW output with a neutron flux of ca. 1 or 5×10^7 n/cm^2 s at the beam exit of the B4 neutron guide tube. The experimental setup was similar to that used in previous studies.[1-4] The neutron radiography images were processed to obtain images of the average water density in the mixer.

RESULTS: Figs. 1a, 1c, and 1e show the shape of the mixers with an inserted tube. In this study, we used 1/4-inch T-junction component (Fig. 1a) and a tube with the diameter of 1/8 or 1/16 inch was inserted (Figs. 1c and 1e) from side to supply room temperature water. The observed averaged water density water was shown in Fig. 1b, 1d, and 1f. In the original 1/4-inch T-junction, the room temperature water flowed from side went downward on the right side of the tube (Fig. 1b). When a 1/8-tube was inserted (Fig. 1c), the room temperature water was released from the end of the tube and mixed with the heated water from the top. On the other hand, the insertion of a 1/16-inch tube resulted in the collision of the room temperature water with the left side of wall in the mixer. These results showed that the mixing of the heated water and room temperature water is controlled by the size of side tube and the insertion of 1/8-inch tube realized the most uniform mixing.

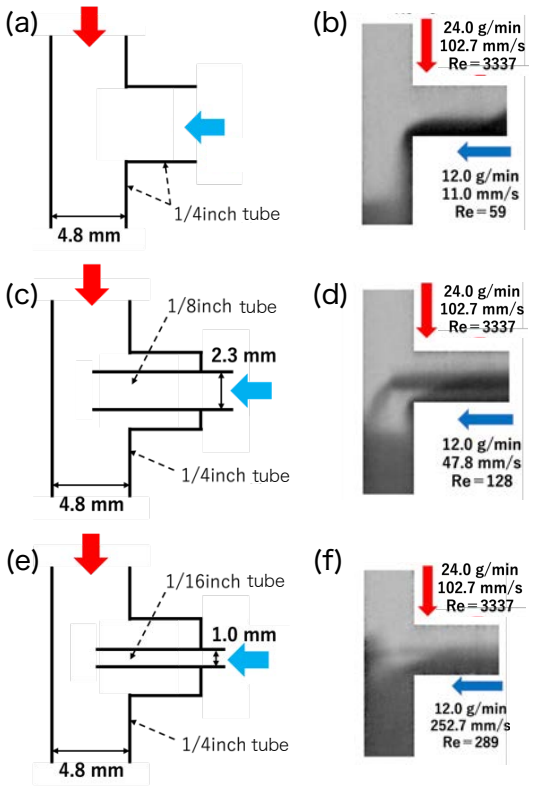

Fig. 1. (a, c, e) Shape of the mixers and (b, d, f) averaged water density in the mixer.

REFERENCES:

[1] K. Sato *et al.*, Chem. React. Eng., **8** (2023) 1449-1456.
[2] R. Sasaki *et al.*, J. Phys.: Conf. Ser., **2605** (2023) 012029.
[3] K. Sugioka *et al.*, AIChE J., **60** (2014) 1168-1175.
[4] S. Takami *et al.*, Phys. Proc., **69** (2015) 564-569.

PR7-7

Visualization of plant roots in media containing organic matter using neutron CT

U. Matsushima[1], N. Odaira[2], D. Ito[2], Y. Saito[3]

Iwate University
Graduate School of Science, Kyoto University

INTRODUCTION: Heavy water (D_2O), which can be readily absorbed by plant roots and creates a contrast between the water in the soil, can be used to visualize roots. This study aimed to utilize heavy water (D_2O) as a contrast agent to visualize plant roots in soil with high organic matter con-tent using neutron computed tomography (CT).

EXPERIMENTS: A rice husk medium containing organic matter (rice husk: soil = 3:1 by volume) was used as the medium, which filled inside aluminum growing containers and planted with a plant sample of komatsuna (*Brassica rapa*). Neutron CT images were acquired using a neutron CT imag-ing system installed in the B4 experimental hole in the KUR research reactor at the Institute for Integrated Radiation and Nuclear Science, Kyoto University. Neutron CT was performed before and after introducing deuterium oxide (D_2O) into the experimental setup. D_2O was supplied only to the roots extending beyond the boundaries of the growing container.

RESULTS: In the image of neutron CT volume data sliced vertically on the surface of the medium (surface image), a shape resembling that of the plant roots observed in the surface image of the medium was observed (Fig. 1-A-a). In contrast, the central image, which is a vertical slice of the volume data at the center of the container, displays a circular image of red-brick soil grains and a filament-like image of the plant roots or surrounding rice husks (Fig. 1-B-a). However, it was chal-lenging to determine whether the filament-like images originated from rice husks or plant roots. Upon introducing D_2O to the roots, a decrease in the pixel values was observed in the region from the bottom to approximately one-third of the vertical direction in both the surface and central images (Fig. 1-A-b, Fig. 1-B-b). In particular, the root image (arrow 1) became invisible after the heavy water supply. In this region, the water content of the roots was replaced by D_2O due to the absorption of water by the plant, which may have increased neutron permeability. A re-gion exhibiting increased neutron transmission was also observed from the bottom of the container to the maximum height of 50 mm (Fig. 1-A-d a, 1-B-d). It was demonstrated that root distribution can be observed in a medium containing organic materials by supplying D_2O to the roots, thereby preventing its diffusion in the medium.

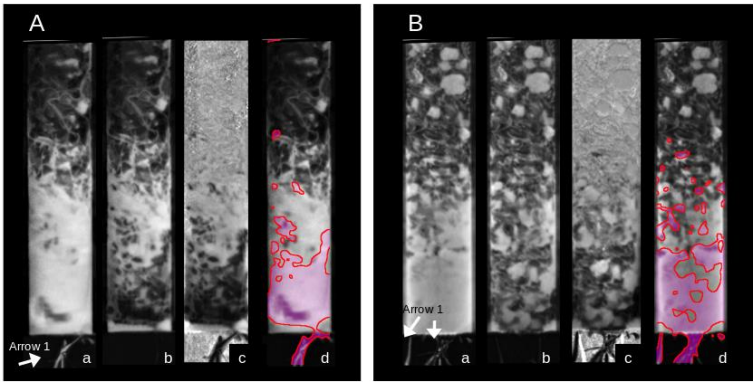

Fig. 1: Slice image of CT volume data of rice husk culture planted with komatsuna. A: surface image, B: central im-age, a, b: pre- and post-D_2O supply, c: The difference be-tween the pre- and post-D_2O supply, d: The difference im-age was binarized and superimposed on the image before introducing D_2O

In-situ Observation of Electrolyzed Lithium-ion Conductor through Neutron Radiography

S. Takai[1], H. Takagi[1], T. Yabutsuka[1], T. Yao[2], D. Ito[3], and Y. Saito[3]

[1]*Graduate School of Energy Science, Kyoto University*
[2]*Kyoto University*
[3]*Institute for Integrated Radiation and Nuclear Science, Kyoto University*

INTRODUCTION: Lithium-ion conductors are presently attracting much interest for the application of solid electrolytes for All-solid-state batteries. While the Li+ ions migrate from the anode to the cathode through the electrolyte during working, the diffusion of lithium-ion is hardly detectable due to the light element. We have carried out the lithium diffusion coefficient measurement using the neutron radiography (NR) technique. Utilizing the large difference in the neutron attenuation factors between ^{6}Li and ^{7}Li, we have measured the diffusion coefficient from the isotope diffusion profiles of the annealed samples.

In the present study, we applied the electric field to the model cell to observe the lithium migration in the solid electrolyte employing the NR.

EXPERIMENTS: ^{7}Li-LAGP ($Li_{1.5}Al_{0.5}Ge_{1.5}(PO_4)_3$ using ^{7}Li) solid electrolyte and ^{6}Li-LMO ($LiMn_2O_4$ using ^{6}Li) electrode material were prepared by the conventional solid-state reaction method. Test cell with Cu/^{6}Li-LMO/PEO/^{7}Li-LAGP/PEO/^{6}Li-LMP/Al was constructed, which were heated up to 140°C and electrolyzed by using a galvanostat with 28.8 – 86.4 μA of current. The mounted amount of cathode and anode materials are 3 and 6 mg, respectively. Before, after, and during the electrolysis, NR data were collected by CCD camera at the B4 guide tube in IIRNS, Kyoto University.

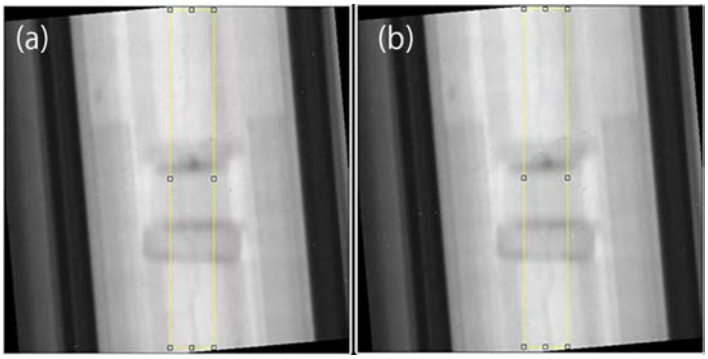

Fig. 1 NR images of test cell consisting of ^{7}Li-LAGP (a) before and (b) after the electrolysis.

RESULTS: Fig. 1 shows the NR images of (a) before and (b) after the electrolysis. The dark area indicates the ^{6}Li-containing part (electrode) in the test cell and the intermediate area between the electrodes corresponds to the electrolyte. Fig. 2 (a) shows the neutron-transmitted intensities of the image before and after the electrolysis. Since the difference is relatively small, the data before the electrolysis are divided by those after the electrolysis in (b). A large deviation is observed around the anode interface, indicating that ^{6}Li is extracted from the anode and migrated into the electrolyte around the anode side.

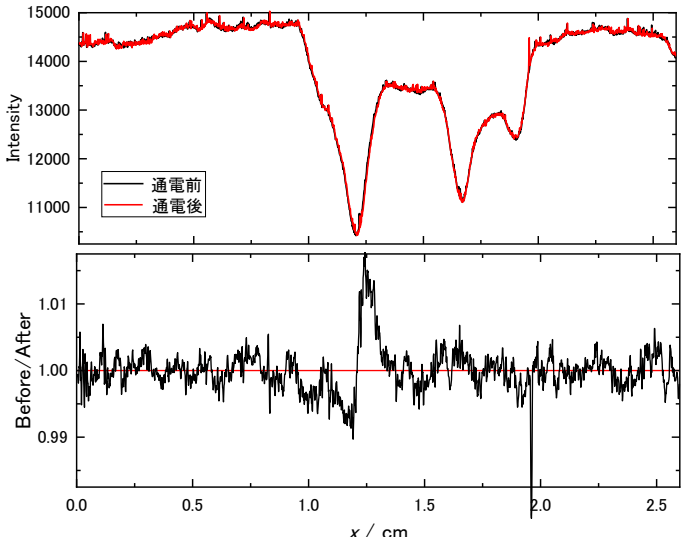

Fig. 2 (a) Neutron intensity profiles for the test cell before and after the electrolysis. (b) Division intensities of the cell.

Flow Visualization of Coolant inside Layerd Rod Array

M. Kaneda[1], Y. Uemura[2] and K. Suga[1]

[1]*Department of Mechanical Engineering, Osaka Metropolitan University*
[2]*Faculty of Mechanical Engineering, Osaka Prefecture University*

INTRODUCTION: Trend of electric motors in electric and hybrid vehicles is higher rotation speed, more power, and compactness [1]. This leads higher heat density due to Joule heating of electric coil in the compact motor package. One of present cooling techniques is so-called direct cooling that the coolant is poured directly onto the coil from a nozzle above. Wetting and profile of the coolant are crucial for the cooling efficiency. We experimented the visualization of the coolant liquid inside the layered structure last year. We found the profile of the coolant inside the structure depends on the pouring liquid temperature and flowrate rather than the applied heat on the structure. In this study, effects of the liquid temperature and flowrate on the liquid profile are further investigated by the neutron radiography.

EXPERIMENTS: The coolant liquid (Automatic Transmission Oil) pumped up from the bath was poured onto the horizontal simplified coil structure. The coolant temperature and flowrate are controlled constant by thermostatic bath and electric pump. The coil structure was presumed by the four-layered accumulated serpentine aluminum plates. The coolant temperature at the nozzle was set at 35 and 50 deg.C and the flowrates of the coolant were tested at 500 and 650 mL/min. The neutron radiography was conducted in B-4 room and visualized inside the structure from the horizontal direction.

RESULTS: The representative visualized images are shown in Fig. 1. The poured liquid spreads as it goes down through the layer. As the liquid temperature increases under the constant coolant flowrate, the liquid profile inside the structure shrinks due to the lower viscosity. As the flowrate becomes larger at the constant liquid temperature, the liquid inside the structure becomes large since the liquid at the uppermost layer spreads. The results obtained have good agreement with our previous trial.

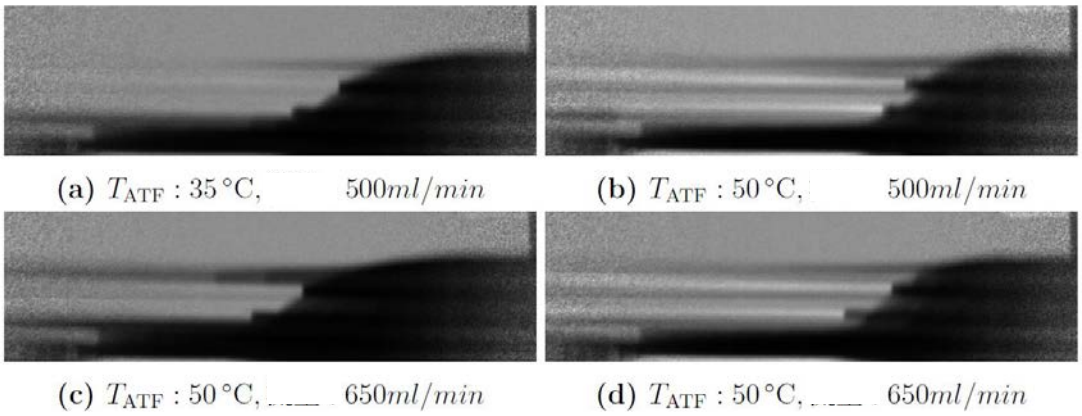

Fig. 1. Visualized images of the coolant inside the layered structure.

REFERENCES:

[1] N. Kobayashi and T. Ikegami, Thermal Sci. Eng., **15(2)** (2007) 49-54.

I-1. PROJECT RESEARCHES

Project 8

PR8

Estimation for 3D Distribution of Biological and Chemical Doses for BNCT

Y. Sakurai

Institute for Integrated Radiation and Nuclear Science, Kyoto University

BACKGROUNDS AND PURPOSES: For the further advancement of BNCT, it is important to improve the estimation for biological effect due to neutrons. At Heavy Water Neutron Irradiation Facility of Kyoto University Reactor (KUR-HWNIF), the fundamental studies for BNCT in the fields of medicine, biology, chemistry and pharmacology, etc., have been performed. Through these studies, the difficulty in the estimation for neutron biological effects is being acutely realized. In the BNCT irradiation field, it is difficult to monochromatically generate neutrons with a specific energy, and neutrons with the various energy ranges such as thermal, epi-thermal and fast neutrons, and also gamma rays are mixed. Furthermore, the neutron energies and the types and energies of secondary charged particles due to the nuclear reactions in living body are different. The biological effect estimation for BNCT are being studied by multiple groups in the world, but the consistent estimations have not been possible due to the difficulty of estimation for the biological effects, particularly regarding neutrons. The final goal of this project research is to develop a consistent estimation method of the biological effects for BNCT. In 2023, the estimation method for the 3D dose distribution, focused on the biological effects, and the chemical effects as precursors to the biological effects.

RESEARCH SUBJECTS: The collaboration and allotted research subjects (ARS) were organized as follows;

ARS-1 (R5P8-1): "Establishment of beam-quality estimation method in BNCT irradiation field using dual phantom technique (VII)", Y. Sakurai, *et al.*.
ARS-2 (R5P8-2): "Effect of co-culture of astrocytes and gliomas using spheroids on the efficacy of BNCT", N. Kondo and Y. Sakurai.
ARS-3 (R5P8-3): "The effect of BNCT on cancer associated fibroblasts using 3D oral cancer model", K. Igawa, *et al.*.
ARS-4 (R5P8-4): "Verification of BNCT effect on hematological cancer cells and dosimetry for expansion of BNCT cases", S. Yoshihashi, *et al.*.
ARS-5 (R5P8-5): "Imaging measurements of 478 keV prompt gamma rays of the boron neutron capture reaction at the KUR-HWNIF and the E-3 Facility", T. Mizumoto, *et al.*.
ARS-7 (R5P8-7): "Development and evaluation of 3D gel dosimeter for the measurement of dose distribution in BNCT", S. Hayashi, *et al.*.
ARS-8 (R5P8-8): "Establishment of three-dimensional dose distribution estimation method for BNCT using radiochromic gel dosimeter", Y. Sakurai, *et al.*.
ARS-9 (R5P8-9): "Survey of luminescent material with varied wavelength-dependence for beam quality measurement in BNCT", K. Tanaka, *et al.*.
ARS-10 (R5P8-10): "The study for development and application of tissue equivalent dosimeter - feasibility of proton magnetic resonance analysis of Fricke dosimeter -", M. Oita, *et al.*.
ARS-11 (R5P8-11): "Comparison of measurement of contamination gamma-ray dose using thermo-luminescence dosimeter and glass dosimeter", S. Nakamura, *et al.*.
ARS-12 (R5P8-12): "Influence of tissue water content in dose calculation for BNCT", T. Takata, e*t al.*.

ARS-6 (R5P8-6) could not be performed mainly because of the lack of budget.

PR8-1

Establishment of Beam-quality Estimation Method in BNCT Irradiation Field using Dual Phantom Technique (VII)

Y. Sakurai, N. Kondo, T. Takata, H. Tanaka and M. Suzuki

Institute for Integrated Radiation and Nuclear Science, Kyoto University

INTRODUCTION: Before the start of treatment with BNCT, the relative biological effectiveness (RBE) for the fast neutrons incident to the irradiation field must be estimated. Measurements of RBE are typically performed by biological experiments with a phantom. Although the dose deposition due to secondary gamma rays is dominant, the relative contributions of thermal and fast neutrons are virtually equivalent in a water and/or acrylic phantom. Uniform contributions to the dose deposited from thermal and fast neutrons are based in part on relatively inaccurate dose information for fast neutrons. The aim of this study is to establish the accurate beam-quality estimation method mainly for fast neutrons by using two phantoms made of different materials [1]. In 2023, verification experiments for the dual phantom technique were performed using Heavy Water Neutron Irradiation Facility installed in Kyoto University Reactor (KUR-HWNIF) as in the previous year [2].

MATERIALS AND METHODS: Figure 1 shows the experimental setup using the dual phantom technique. One of the dual solid phantoms was made of polyethylene with natural lithium fluoride for 30 weight percent (LiF-polyethylene phantom), and the other phantom was made of polyethylene with 95%-enriched lithium-6 fluoride for 30 weight percent (^{6}LiF-polyethylene phantom). Glioblastoma cells were divided in two groups. One was treated group using p-boronophenylalanine (BPA, containing B-10) for B-10 concentration of 25 ppm, and the other was non-treated group. The depth dose distributions for the thermal neutron, fast neutron and gamma-ray components were determined based on the simulation calculation results normalized referring to the measured values. The epi-thermal neutron irradiation mode was used for the phantom experiments.

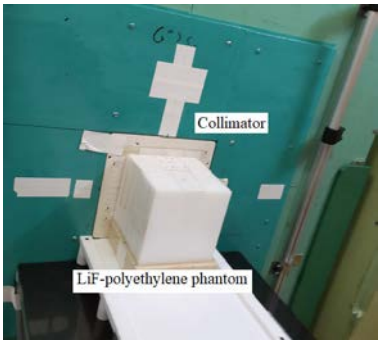

Fig. 1. Experimental setup for the dual phantom technique.

RESULTS: It was confirmed that the survival fraction became smaller as the thermal neutron flux became larger in the LiF-polyethylene phantom. The survival fraction for the non-treated cell was higher than that in BPA-treated cell. In the ^{6}LiF-polyethylene phantom, the survival fraction showed no difference between non-treated and BPA-treated cells. The ^{6}LiF-polyethylene phantom absorbs thermal neutrons although it has not significant effect in fast neutron dose. No difference in survival fractions between non-treated and BPA-treated cells with ^{6}LiF-polyethylene phantom indicated fast neutrons might not effect cell survival. On the other hand, due to mixture of thermal neutron in LiF-polyethylene phantom, BPA-treated cells were killed effectively compared with non-treated cells through n-alpha reactions.

ACKNOWLEDGMENT: This work was supported by JSPS KAKENHI Grant Number JP 16H05237.

REFERENCES:

[1] Y. Sakurai, *et al.*, Med. Phys., **42** (2015) 6651-6657.
[2] Y. Sakurai and T. Kobayashi, Nucl. Instr. Meth. A., **453** (2000) 569-596.

PR8-2

Effect of co-culture of astrocytes and gliomas using spheroids on the efficacy of BNCT

Natsuko Kondo[1] and Yoshinori Sakurai[1]

[1] *Particle Radiation Oncology Research Center, Institute for Integrated Radiation and Nuclear Science, Kyoto University (KURNS)*

INTRODUCTION:

Until now, BNCT evaluations for brain tumors have used two-dimensional cultures of only tumor cells when evaluating in vitro. Actual tissue contains many types of cells in addition to tumor cells, so it is not sufficient to evaluate biological effects. Furthermore, when evaluating in vivo, small animals (mice) have been used. However, because the size is significantly different from that of an actual human, there is a large gap in the spatial dose distribution. Therefore, we will use 3D co-culture of tumor cells and other cells to construct a more realistic irradiation system and evaluate its biological effects.

EXPERIMENTS:

Cells:

We used astrocytes that were derived from fetal C57BL/6 mouse brain and GL261 mouse glioma cells. They were cultured in DMEM with 10% heat-inactivated fetal bovine serum in 5 % CO_2 incubator. They were cultured separately in ultra-low attachment T75 flasks. One day before thermal neutron irradiation, astrocytes and gliomas were counted and co-cultured in ultra-low attachment 6-wells at the ratio of 1:1 (co-culture group). The number of cells were 2×10^5 respectively. The mono-culture group consisted of 2×10^5 astrocytes or GL261 cells alone, respectively.

Boronophenylalanine (BPA) Treatment:

A stock solution of the p-^{10}B-para-boronophenylalanine (BPA)- fructose complex was used. The ^{10}B concentrations was approximately 1000 ± 4.55 ppm. The day before irradiation, BPA was dissolved in the cell culture medium at a concentration of 25 ppm.

Thermal Neutron Irradiation:

The collected spheroids in 1.5-ml plastic tubes were irradiated for 10 or 20 min at room temperature using a neutron beam at the Heavy Water Neutron Irradiation Facility installed in the Kyoto University Reactor (KUR-HWNIF). The operating power of the reactor was 1 MW. After irradiation, half of the spheroids were spread in each ultra-low attachment 6-well.

Cell count:

The spheroids were collected after centrifugation and rinsed with PBS. They were trypsinized and the cells were counted 9-11 days after irradiation.

RESULTS:

Compared with the non-irradiated control group, the cell numbers of the BNCT-treated groups tended to smaller in all the GL261 alone, astrocytes alone and the co-culture groups. However, that of co-culture group tended to be larger than GL261 alone or astrocytes alone group.

PR8-3

The effect of BNCT on cancer associated fibroblasts using 3D oral cancer model

K.Igawa, I.Yamamoto[1], N.Kondo[2], M.Suzuki[2] and Y.Sakurai[2]

Neutron Therapy Research Center, Okayama University

[1]Department of Oral and Maxillofacial Surgery, Okayama University Graduate School of Medicine, Dentistry and Pharmaceutical Sciences

[2]Institute for Integrated Radiation and Nuclear Science, Kyoto University, Particle Radiation Oncology Research Center

INTRODUCTION: It has been reported that cancer associated fibroblasts (CAFs), one of the important cells that form the tumor microenvironment, govern local invasion and metastasis of cancer and are involved in cancer cell proliferation and resistance to cancer therapy, and that the prognosis is poor when CAFs are abundant in the stroma, and that the tumor microenvironment has a significant impact on the grade and progression of oral cancer. Therefore, focusing on CAFs, we will apply the evaluation of cancer therapy [1] to an oral cancer model consisting of normal oral fibroblasts (NOFs) and human squamous cancer cells (HSCs), and examine the prognosis of BNCT by seeding CAFs in cancer stroma.

EXPERIMENTS: At first the 3 D cancer models using oral CAFs and HSC-4 (JCRB0624) were fabricated as a control used oral NOFs. CAFs and NOFs were provided by Niigata University. Collagen matrix solutions containing either NOFs or CAFs (2.0×10^5 cells/mL) in a 12-well tissue culture insert were incubated for 7 days. After 7 days, HSC-4 cells (2.0×10^5 cells/well) were seeded on the top surface of the collagen matrix in which NOFs and CAFs are embedded. Then the 3D cancer models were cultured at the air–liquid interface from day 14. On day 15, 10 % BPA of medium was added for 24 hours and neutron beam was irradiated at Heavy Water Neutron Irradiation Facility of KUR on day 16. On day 21, the 3D oral cancer models were fixed and the sections were stained with HE staining for histological evaluation.

RESULTS: The 3D oral cancer model was irradiated with .neutron beams for 0, 20, 40, and 60 mins in the direction from the cancer cell layer to the cancer stromal layer. As shown in the Figure1, a decrease in the cancer cell layer was observed in both the NOF and CAF groups as the neutron irradiation dose increased. In the cancer stromal layer, the number of NOFs were not decreased with increasing irradiation dose, but the number of CAFs were decreased.

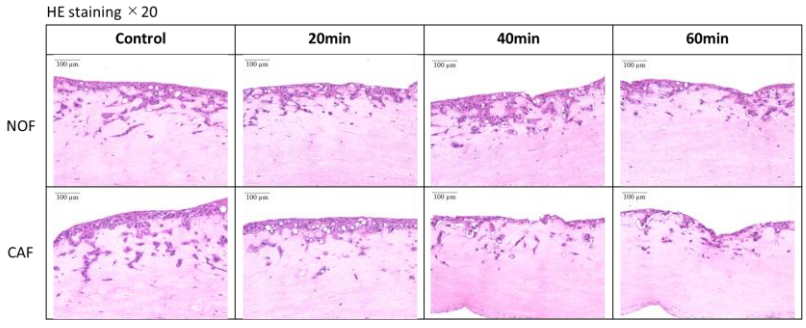

Fig. 1. HE staining of 3D oral cancer model.

REFERENCES:

[1] Igawa, K., K. Izumi, and Y. Sakurai, BioTech., **12**(2) (2023) 35.

PR8-4

Verfication of BNCT Effect on Hematological Cancer Cells and Dosimetry for Expansion of BNCT Cases

S. Yoshihashi, T. Kasai[1], M. Suzuki[2], Y. Sakurai[2], N. Kondo[2], A. Uritani, A. Yamazaki, K. Tsuchimoto, I. Suzuki, T. Fukutomi, K. Tsuchida, T. Nishitani, Y. Ichikawa and S. Furuya

Graduate School of Engineering, Nagoya University
[1]Neutron Therapy Research Center, Okayama University
[3]Institute for Integrated Radiation and Nuclear Science, Kyoto University

INTRODUCTION: The number of newly diagnosed patients with major hematologic cancers (malignant lymphoma, multiple myeloma, and leukemia) in Japan was 58,547 in 2019 [1], and 5,853 hematopoietic stem cell transplants were performed in FY2022 as the last treatment option for these refractory hematologic cancer patients [2]. While autologous transplantation is a desirable medical technique for patients because it does not require long-term administration of immunosuppressive drugs and prevents immune reactions (GVHD) caused by HLA incompatibility, the grafts contain tumor cells, which must be removed and treated with chemotherapy and radiotherapy, which are pre-treatment procedures. We are now conducting basic research to remove tumor cells in grafts by Ex Vivo BNCT. The target will initially be acute promyelocytic leukemia (APL) patients who have developed resistance to anticancer drugs, but allogeneic transplant recipients waiting for an HLA-matched donor and patients with poor post-transplant performance will also be treated.

EXPERIMENTS: In this study, to verify the applicability of Ex Vivo BNCT, we first evaluate boron uptake in a cell line of multiple myeloma (MM) and a hematopoietic stem cell model. We use a new boron agent OKD-001 which was discovered by Okayama University. Then, we evaluate the applicability of Ex Vivo BNCT to blood cancers by measuring the cell survival rate of cells with and without boron drug exposure and irradiating them with thermal neutrons. The neutron distribution in the moderator is measured using a gold foil, and the boron dose in the cell back-up will be evaluated together with the boron uptake evaluation results. Next, by neutron irradiation we evaluate the feasibility of Ex Vivo BNCT for blood cancer cells by evaluating the cell viability of the boron-induced cells for MM model and stem cell model. The neutron distribution in the moderator is measured using a gold foil, and the boron dose in the cell bag is evaluated together with the results of the boron uptake.

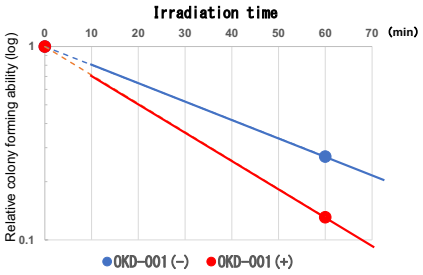

Fig. 1. Cell survival rates by neutron irradiation for MM cells with and without OKD-001.

RESULTS: When the cells of multiple myeloma (MM) cell line are exposed to the boron agent OKD-001 and then irradiated with neutrons, tumor cells tend to die, as shown in Figure 1, while cells do not tend to die without the boron agent. On the other hand, we have confirmed that hematopoietic stem cells are not killed by neutron irradiation after exposure to OKD-001. We are currently testing the efficacy of Ex Vivo BNCT on various tumor cell lines and developing a test method to determine its effectiveness.

REFERENCES:

[1] National Cancer Center (Japan), Current Cancer Statistics, https://ganjoho.jp/reg_stat/statis-tics/stat/summary.html (2024.02.19).
[2] Japan Hematopoietic Cell Transplantation Center (JDCHCT): Hematopoietic Cell Transplantation in Japan Annual Report of Nationwide Survey 2022, http://www.jdchct.or.jp/data/report/2022/(2024.02.19).

Imaging Measurement of 478 keV Prompt Gamma Rays of the Boron Neutron Capture Reaction at the KUR-HWNIF

T. Mizumoto, S. Komura, Y. Sakurai[1], T. Takata[1], T. Tanimori[1] and A.Takada[2]

J-BEAM Inc.
[1]*Institute for Integrated Radiation and Nuclear Science, Kyoto University*
[2]*Graduate School of Science, Kyoto University*

INTRODUCTION: We have been developing electron-tracking Compton cameras (ETCCs) for application to the monitoring of prompt 478 keV gamma rays from boron neutron capture reaction in BNCT by imaging. In this report, we present the results of experiments at the Heavy Water Neutron Irradiation Facility (HWNIF) with an ETCC based on previous studies [1].

EXPERIMENTS: To demonstrate the effectiveness of the ETCC in a real BNCT environment, we performed 478 keV prompt gamma-ray image monitoring of boron solution phantoms installed in the irradiation room of the HWNIF during neutron irradiation in epithermal mode under 5 MW operation. The phantom consisted of a 10 cm cubic acrylic container filled with a boric acid solution with a ^{10}B concentration of 100 ppm and 230 ppm. The 478 keV prompt gamma rays emitted from the phantom passed through a cylindrical hole in the ceiling and were measured by the ETCC placed directly above the hole, facing downward. A schematic view of the experimental setup is shown in Fig. 1.

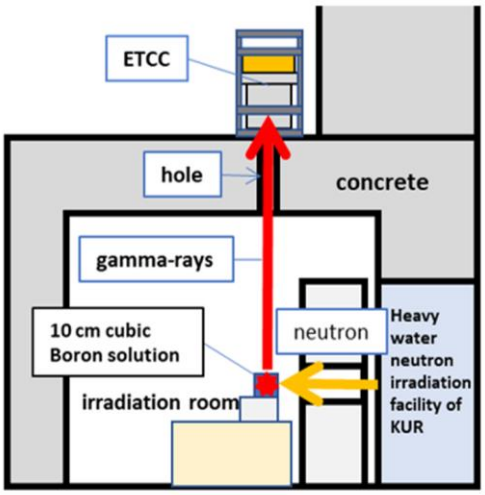

Fig.1. Schematic of the measurement setup.

RESULTS: We have successfully measured images of 478keV gamma rays from a boron solution phantom with a ^{10}B concentration of 230 ppm, irradiated for the first time with neutrons under the conditions of the 5 MW epithermal mode using ETCC as shown in Fig. 2. Even with a short exposure time of 10 minutes, the location of the phantom appears bright enough in the image. On the other hand, the clear image was not obtained from the phantom with a ^{10}B concentration of 100 ppm. There is a possibility that clearer images could be obtained by shielding the front of the ETCC with thin lead sheet to sup-press the incidence of low-energy gamma rays. In addition, quantitative evaluation remains a future task.

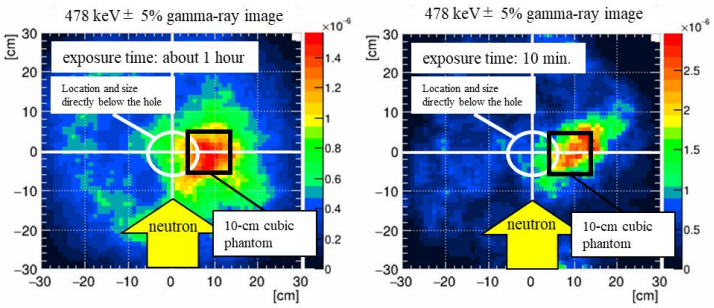

Fig.2. Measured 478 keV gamma-ray images of a boron solution phantom with a ^{10}B concentration of 230 ppm irradiated neutrons under 5 MW epithermal mode operation. The exposure times of left and right images are approximately 1 hour and 10 minutes, respectively.

REFERENCES:

[1] S. Komura *et al.*, KURNS Progress Re-port 2022.

Imaging Measurement of 478 keV Prompt Gamma Rays of the Boron Neutron Capture Reaction at the E-3 Facility

T. Mizumoto, S. Komura, T. Mitani, H. Kakesu, Y. Sakurai[1], T. Takata[1], T. Tanimori[1], H.Kimura[2] and A.Takada[3]

J-BEAM Inc.
[1]Institute for Integrated Radiation and Nuclear Science, Kyoto University
[2]Kanazawa University
[3]Graduate School of Science, Kyoto University

INTRODUCTION: In BNCT, quantitative imaging measurements of 478keV prompt gamma rays are effective for determining the distribution of boron concentration in the body and the boron dose during neutron irradiation. To achieve quantitative imaging in the neutron environment, we have been developing electron-tracking Compton cameras (ETCCs). In this report, we present the results of experiments at the E-3 irradiation port facility with ETCCs based on previous studies [1].

EXPERIMENTS: In the E-3 beamline, two phantoms with ^{10}B concentrations of 500 ppm and 1000 ppm were placed on the neutron beam to demonstrate the measurement of 478 keV prompt gamma rays. The phantoms were exposed to thermal neutron beams under 1 MW operation.

We also performed a test of stereo imaging measurement of 478 keV prompt gamma rays from neutron irradiated BPA-dosed cancer bearing mice using two ETCCs (ETCC1 and ETCC2) installed orthogonally to each other at E-3. Nude mice bearing MeWo tumors of approximately 1 cm diameter on the shoulder received BPA by subcutaneous injection at a rate of 400 mg/kg/h for two hours. Each mouse was anesthetized, fixed in an acrylic container, placed just above one of the ETCCs (ETCC1), and exposed to thermal neutron beams at the tumor site for 3 hours at E-3 under 5 MW operation.

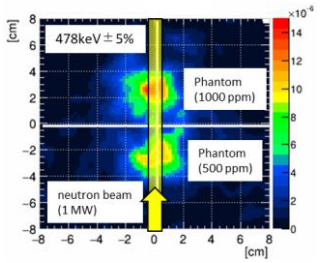

Fig.1: Measured 478 keV gamma-ray image of two phantoms.

RESULTS: Fig.1 shows the images of ETCC1 measurements when the two phantoms were irradiated simultaneously. This is the first time that the multiple-phantom separated 478 keV gamma-ray image has been successfully obtained with an ETCC.

As shown in Fig.2, both ETCCs successfully generated back-projection images of the mice viewed from two different directions. The bright areas in both images corresponded well to the areas of the mice irradiated with neutrons. We also obtained measurement results from ETCC1 indicating that the detection rate of 478keV gamma rays remained generally constant during the first 3 hours after administration. While the validity of the results needs to be investigated, we demonstrate the potential for measuring dynamic changes in mice administered sustained doses.

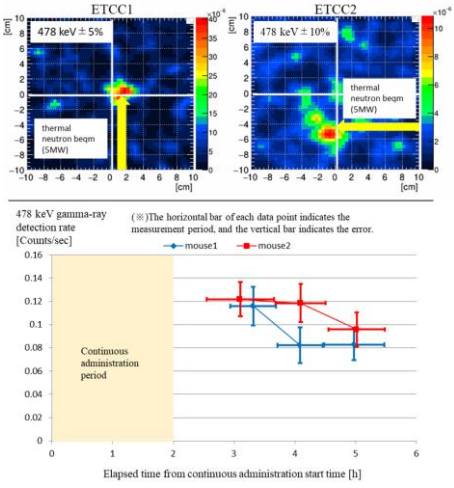

Fig.2: Measurement results of mice. (Top): 478 keV gamma-ray images taken by ETCC1 and ETCC2. (Bottom): Time variation of the detection rate of 478 keV gamma rays measured by ETCC1.

REFERENCES:

[1] S. Komura *et al.*, KURNS Progress Report 2022.

Development and evaluation of 3D gel dosimeter for the measurement of dose distribution in BNCT

S. Hayashi, Y. Sakurai[1], M. Suzuki[1], T. Takata[1], and R. Narita[2]

Department of Clinical Radiology, Hiroshima International University
[1] Institute for Integrated Radiation and Nuclear Science, Kyoto University
[2] Graduate school of Engineering, Kyoto University

INTRODUCTION: Three-dimensional (3D) gel dosimeters have been developed for the 3D dose measurement of the complex conformal dose distributions in radiation therapy [1]. These de-vices are composed of radio-sensitive substances and an aqueous gel matrix to preserve spatial in-formation about the absorbed dose. The 3D absorbed dose distribution is deduced from the distribu-tion of the reaction products measured by 3D imaging modalities such as MRI and Optical CT. In previous studies, we have developed a PVA-GTA-I radiochromic gel dosimeter that utilizes red col-or development due to the complex formation of polyvinyl alcohol (PVA) and iodide [2, 3].

In this work, as a preliminary experiment for evaluating the 3D dose distribution using optical CT, we evaluated the depth dose distribution in response to neutron beams from a nuclear reactor by combining small gel dosimeters with different compositions into blocks.

EXPERIMENTS: The PVA-GTA-I gel dosimeter is composed of partially saponified PVA, potassium iodide (KI), potassium nitrate (KNO_3), glutaraldehyde, fructose, glucono-δ-lactone, and water. As a thermal neutron sensitizer, boric acid ($B(OH)_3$) naturally containing ^{10}B of 20% was added into some gel dosimeters. The resulting solution was subdivided by pouring into PMMA cuvettes (4.5 mL, 1 cm path length). The neutron irradiations were performed using the HWNIF of KURR (1 MW). The samples were irradiated in the air at room temperature. The three different modes (thermal neutron-rich, fast neutron-rich, and mixed modes) of neutron beams made by heavy water spectrum shifter and cadmium thermal-neutron filters were applied to the samples.

RESULTS: Fig. 1. shows the result in mixed mode as an example. The beam was delivered from the left side of the pictures. In the pictures, asterisks (*) indicate gel dosimeters containing boron. As a result, the color development attenuates from the surface (left) to the deeper parts (right) in all sets and the coloring becomes locally deeper in samples containing boron. Therefore, it is shown that the PVA-GTA-I gel dosimeter is ef-fective for depth dose measurement and can measure sensitization due to boron against neutron irradiation. Similar results were confirmed in other modes. The results demonstrate the potential of the PVA-GTA-I gel dosimeter for future 3D dosimetry using optical CT. The comparison with Mon-te-Carlo simulations will be also performed as a next step.

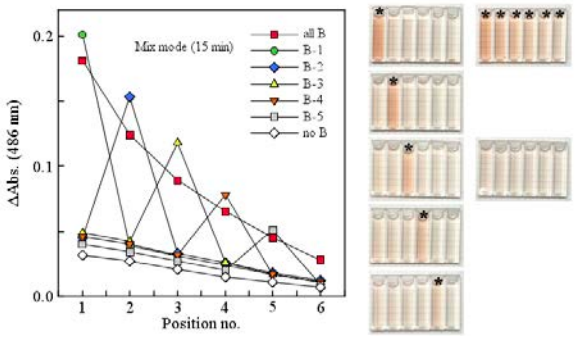

Fig. 1. The change of absorbances in depth (corresponding to relative depth dose distribution) in mixed mode, and the irradiated PVA-GTA-I radiochromic gel dosimeters. The asterisks (*) in the pictures indicate the samples with boron.

REFERENCES:

[1] Y. De Deene, Gels., **8** (2022) 599.
[2] S. Hayashi *et al.*, Radiat. Meas., **131** (2020) 106226.
[3] S. Hayashi *et al.*, J. Phys.; Conf. Ser., **2167** (2022) 012014.

Establishment of Three-dimensional Dose Distribution Estimation Method for BNCT using Radiochromic Gel Dosimeter

Y. Sakurai, R. Narita[1], J. Prateepkaew[1] and T. Takata

Institute for Integrated Radiation and Nuclear Science, Kyoto University
[1]Graduate School of Engineering, Kyoto University

INTRODUCTION: Development in accelerator-based irradiation systems for BNCT is underway. BNCT using newly developed accelerator systems is being implemented at multiple facilities around the world. However, there are still issues that need to be improved for further advancement of BNCT. The advancement of dose estimation is one of these, and the estimation of biological dose is particularly important. As part of the advancement of biological dose estimation for BNCT, we focus on chemical effects, which are the precursor to biological effects. We are studying on the estimation method using chemical dosimeters, especially gel dosimeters [1]. Gel dosimeters are made of materials similar to living tissue and can be formed into any shape. Using a phantom made from gel dosimeter that models human body, three-dimensional dose distribution estimation becomes possible. Among the various types of gel dosimeters, we are especially focusing on "radiochromic gel dosimeters" that can be read out using optical CT, etc.. The purpose of this study is to establish three-dimensional dose distribution estimation method for BNCT using multiple types of radiochromic gel dosimeters. In 2023, the characteristic estimation for micellar gel dosimeters containing leuco crystal violet (LCV) was performed [2].

MATERIALS AND METHODS: The compositions of the LCV micellar gel dosimeters were determined based on the simulation calculation. The experiments for the characterization were mainly performed using Heavy Water Neutron Irradiation Facility of Kyoto University Reactor (KUR-HWNIF) [3] and Cobult-60 Gamma-ray Irradiation Facility in KURNS. Three irradiation modes were used in the experiments using KUR-HWNIF: standard mixed neutron irradiation mode, standard epi-thermal neutron irradiation mode, and standard thermal neutron irradiation mode. The absorbance of the gel dosimeters after the irradiation was measured at the peak wavelength of 600 nm using a spectrophotometer. Figure 1 shows the experimental setup using Cobult-60 Gamma-ray Irradiation Facility. Figure 2 shows the micellar gel dosimeters after the gamma-ray irradiation.

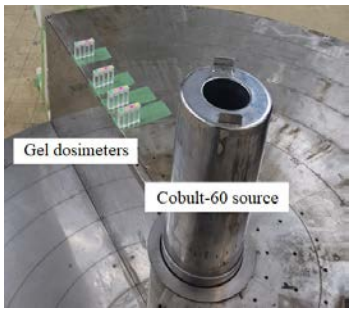

Fig. 1. Experimental setup using Cobult-60 Gamma-ray Irradiation Facility.

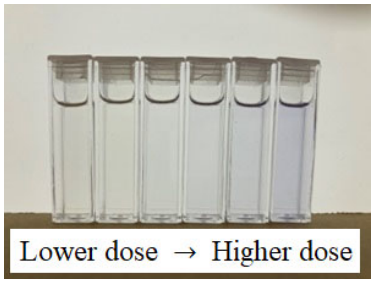

Fig. 2. Micellar gel dosimeters after the gamma-ray irradiation.

RESULTS: The experimental results confirmed that boric acid is particularly effective as a neutron sensitizer. Those also confirmed that the dose response of each gel dosimeter depended on the linear energy transfers (LETs) of the particles produced in each dosimeter. The experimental data analysis is currently underway to evaluate parameters for each gel dosimeter and each radiation component.

REFERENCES:

[1] R. Narita and Y. Sakurai, J. Phys: Conf. Ser., **2630** (2023) 012016.
[2] S. Babic, *et al.,* Phys. Med. Biol., **54** (2009) 6791-6808.
[3] Y. Sakurai and T. Kobayashi, Nucl. Instr. Meth. A, **453** (2000) 569-596.

Survey of luminescent material with varied wavelength-dependence for beam quality measurement in BNCT

Kenichi Tanaka, Yoshinori Sakurai[1], Hiroki Tanaka[1], Takushi Takata[1]

Division of Liberal Arts Sciences, Kyoto Pharmaceutical University
[1]Institute for Integrated Radiation and Nuclear Science, Kyoto University

INTRODUCTION: Measurement of beam fluence spatial distribution is required for quality assurance in the irradiation field, in boron neutron capture therapy. The imaging plate has been tested for usage in this purpose[1]. In imaging plate, the light for excitation and luminescence are investigated with respect to a single constant range of wavelength. However, BaFBr:Eu, *i.e.*, the luminescence material for imaging plate, has multiple peaks in its excitation spectrum[2]. Each peak corresponds to a excited state of electron and ion BaFBr:Eu. The efficacy in excitation to each level is expected to depend on the beam quality of the irradiated radiation, which deposits energy on the luminescence material. In this case, the dependence of the quantity of the luminescence on the wavelength of the excitation light, or possibly luminescence, will specify the beam quality. Also, one can predict the absorbed dose by using the quantity of the luminescence. Thus, this study investigated the use of the luminescence for measurement of both quantity and quality of the radiation. The preliminary survey for the suitable luminescence material is reported.

EXPERIMENTS: As an initial candidate, the imaging plate (Fujifilm Corporation, BAS-TR) is used for this study. In this imaging plate, BaFBr:Eu is embed in blue-colored film. In this study, BaFBr:Eu was also fabricated and utilized as a sample, in case the blue film distort the influence of the beam quality of the dependence of the luminescence quantity of wavelength. The samples were irradiated with gamma rays from ^{60}Co, and neutrons and gamma rays at the standard mixed neutron irradiation mode of Kyoto University Reactor Heavy Water Neutron Irradiation Facility at 1 MW of the power. In the latter, the samples were driven with Irradiation Rail Device. The fluorescence spectrofluorometer (Hitachi corporation, F-2700) was used to measure the dependence of the fluorescence quantity on the wavelength.

RESULTS: An example of the excitation spectrum is shown in Fig. 1 for BAS-TR. The ratio of the luminescence quantity by excitation at 630 nm to that at 650 nm is 7% lower for KUR than that for Co, where the uncertainty of the measured ratio is about 5%. These aspects suggest that the dependence of the quantity of the luminescence on the wavelength is a promising indicator of the beam quality. The attempt to measure the beam quantity by using the luminescence dependence on wavelength is undergoing for usage of BAS-TR and fabricated BaFBr:Eu.

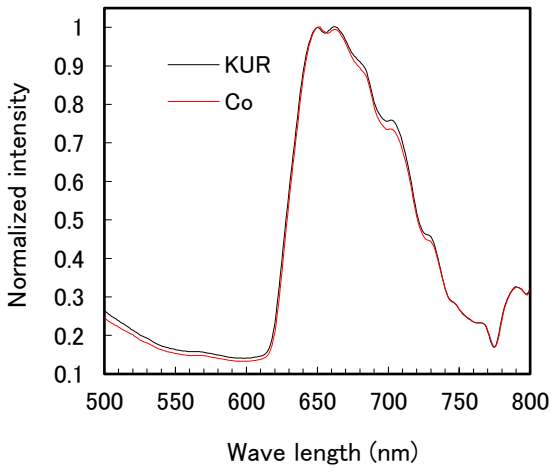

Fig. 1. Excitation spectrum of BAS-TR

REFERENCES:

[1] K. Tanaka *et al.*, Appl. Rad. Isot., **115** (2016) 212-220.
[2] K. Abe, Rad., **25** (1999) 31-49. (in Japanese)

PR8-10

The Study for Development and Application of Tissue Equivalent Dosimeter - Feasibility of Proton Magnetic Resonance Analysis of Fricke Dosimeter -

M. Oita[1], T. Kamomae[2], K. Sugimoto[3], T. Takada[4], K. Sakurai[4]

[1]*Graduate School of Interdisciplinary Science and Engineering in Health Systems, Okayama University*
[2]*Graduate School of Medicine, Department of Radiology, Nagoya University*
[3]*Faculty of Health Science and Technology, Department of Radiological Technology, Kawasaki University of Medical Welfare*
[4]*Research Reactor Institute, Kyoto University*

INTRODUCTION: In recent years, the clinical application of Accelerator-Based Boron Neutron Capture Therapy (AB-BNCT) has been introduced to make significant contributions to the treatment of intractable cancer such as glioblastoma multiforme, superficial head and neck cancer, and melanoma in Japan. In clinical situations, a radiochromic film (RCF) is one of the most helpful dosimetry tools in the advantages of high spatial resolution and tissue equivalence[1,2]. However, there are some limitations for mapping 3D dose distribution, so there has been increasing interest in gel or liquid dosimeters recently. Although the Fricke dosimeter[3] is rare among these findings, the authors have recently developed a new approach expected to lead to new developments.

EXPERIMENTS: A ferrous sulfate solution using a ^{60}Co gamma source was evaluated. To make a total of 500 ml of sulfuric acid solution, 197 ml of 1N dilute sulfuric acid and 303 ml of distilled water were mixed. To this solution, 30 mg sodium chloride and 200 mg ferrous ammonium sulfate hexahydrate were added to prepare an aqueous solution of the average concentration of ferrous ammonium sulfate. Each cylindrical polyethylene bottle contained 25 ml of this solution. For irradiation, polypropylene boxes containing a set of three bottles were placed 20 to 70 cm from the 60Co source. Then, all of the boxes, ranging from 0 to 873 Gy, were irradiated in the KUR ^{60}Co gamma-ray irradiation facility. After irradiation, all bottles were subjected to proton magnetic resonance (1.5T clinical MRI system, Avantofit, Siemens Inc.).

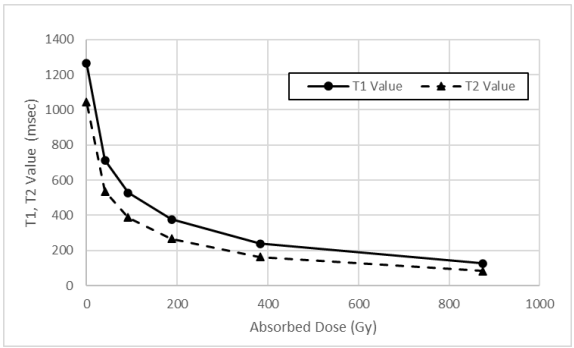

Fig. 1. Change of T1 and T2 values irradiated by the KUR ^{60}Co gamma-ray source. The variation of T1 and T2 value is higher at low-dose region.

RESULTS: Fig.1 shows the T1 and T2 values change irradiated by the KUR ^{60}Co gamma-ray. The average change in T1 and T2 values per Gy ranged from 0-40 Gy were approximately 13.5 and 12.4 msec, respectively. The dose resolution was relatively higher than that of the conventional analysis method. Further approaches could be feasible for using low-dose regions, neutron components, and contributions of gamma rays using Monte Carlo simulation and additional experiments with a cadmium filter.

REFERENCES:

[1] Niroomand-Rad, Azam *et al.,* Medical physics **25** (1998) 2093-2115.
[2] B. V. Casanova *et al.,* J. Appl. Clin. Med. Phys., **14(2)** (2013) 4111.
[3] Fricke H, Hart EJ: Chemical dosimetry. In: Attix FH, Roesch WC, Tochilin E eds. Radiation do-simetry: Instrumentation., (1966) 167-239, Academic Press, New York.

Comparison of Measurement of Contamination Gamma-ray Dose using Thermo luminescence Dosimeter and Glass Dosimeter

S. Nakamura, M. Yonemura, Y. Kobayashi, H. Igaki[1], T. Takata[2], H. Tanaka[2], M. Suzuki[2], Y. Sakurai[2]

Division of Radiation Safety and Quality Assurance, National Cancer Center Hospital
[1] Department of Radiation Oncology, National Cancer Center Hospital
[2] Institute for Integrated Radiation and Nuclear Science, Kyoto University

INTRODUCTION: Several types of accelerator-based neutron source can achieve the sufficient neutron flux for performing boron neutron capture therapy (BNCT). Thus, it is expected that BNCT will be widely used at hospitals because those sources can be implemented easier than the research reactor. Neutron beam from those sources has contamination gamma-rays as well as that from the research reactor. However, evaluations of contamination gamma-rays has been conventionally performed with a specially designed thermoluminescence dosimeter (TLD) of beryllium oxide (BeO) powder enclosed in a quartz glass tube [1], and it may be one of the problems limiting the widespread. Therefore, this study aims to discuss the evaluations of contamination gamma-rays in the neutron beam emitted from the research reactor using the commercial radiophtoluminescence glass dosimeter (RPLD), which was generally utilized in conventional radiotherapies [2], through comparing those using the TLDs.

EXPERIMENTS: The commercial RPLD (GD-302M, AGC Techno Glass Co., Ltd. Tokyo, Japan) was utilized in this study, and the custom-made TLD consisted of BeO powder and quartz glass was utilized for the comparison. To eliminate the effect of thermal neutrons to reading value on RPLD, RPLD was encapsulated with ^{6}LiF capsule of which thickness was 2 mm and actual density was 85% of the ideal density for LiF (2.24 g/cc). Relationship between the reading value and the delivered dose in the RPLD had been acquired using 6 MV-X ray emitted from the medical linear accelerator (TrueBeam, Varian, Palo Alto, CA). To compare the dose of contamination gamma-ray evaluated by the TLD and RPLD, we carried out the measurements at the edge of irradiation port without a phantom at the Heavy Water Neutron Irradiation Facility of Kyoto University Research Reactor. The thermal irradiation mode was applied in this study, and the irradiation time was 0, 5, 10, and 15 min.

RESULTS: As shown in Fig. 1, the dose evaluations of contamination gamma-ray using the TLD and the RPLD were comparable, and the linearity between the irradiation time and the dose was observed in both the TLD and the RPLD. Discrepancies of the dose evaluations between the TLD and the RPLD were within 7.3%, and decreased with increasing the irradiation time. At the irradiation time of 15 min, the discrepancy was 1.2%. Therefore, this study indicated the feasibility of the dose evaluation for the contamination gamma-ray using RPLD.

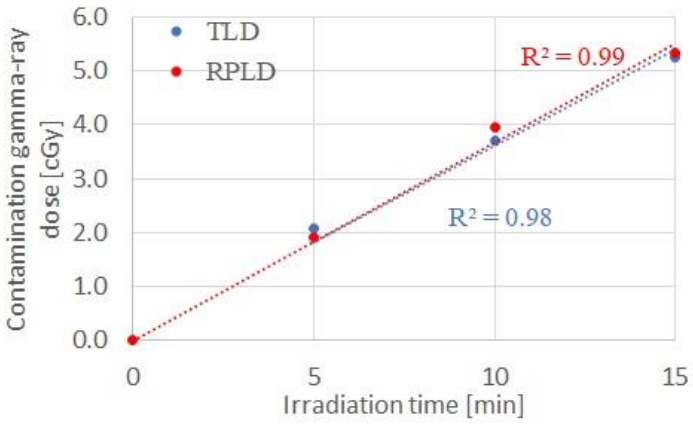

Fig. 1: Comparison of gamma-ray dose evaluations using TLD and RPLD.

REFERENCES:

[1] N. Hu *et al.*, Radiat. Oncol., **16** (2021) 243.
[2] JSMP, Guideline for radiophtoluminescence glass dosimeter. (2022).

Influence of Tissue Water Content in Dose Calculation for BNCT

T. Takata[1], Y. Tamari[1,2], Y. Sakurai[1], H. Tanaka[1], M. Suzuki[1]

[1]*Institute for Integrated Radiation and Nuclear Science, Kyoto University*
[2]*Department of Radiology, Kyoto Prefectural University of Medicine*

INTRODUCTION: A Monte Carlo method is commonly employed in dose calculations for BNCT, where radiation transport calculations are performed by specifying material information corresponding to each tissue in the body, such as density and elemental composition. Conventionally, typical values described in literature such as ICRU Report 46 are assigned as fixed values [1]. However, this method cannot reflect the details of material information, such as differences among patients or a detailed water content distribution in tissue. In this study, we aim to establish a method for quantitative evaluation of material density and water content by using data acquired by multi-energy X-ray CT, and to reflect the material information in the dose calculation. To confirm the importance of this method, the effect of tissue water content on dose calculations was examined.

MATERIALS AND METHODS: The dose calculations were performed to simulate irradiation for brain tumors. A voxel phantom was constructed from the CT images of the head phantom, and brain tissue, skull, and soft tissue were specified as the material of each voxel. For skull and soft tissue, elemental compositions and densities described in the ICRU report were assigned [1]. For brain tissue, the composition was based on the ICRU report, whereas the water content was varied in a range of ±2% from the reference value of 78.5% [2]. A negative correlation between water content and specific gravity of brain tissue, reported in studies of vasogenic cerebral edema, was assumed to derive the density from the water content [3]. The thermal neutron flux and gamma-ray dose rate were derived by using PHITS code [4], where the epi-thermal neutron irradiation of the phantom from the parietal region was simulated assuming the neutron source of the Heavy Water Neutron Irradiation Facility at KUR [5].

RESULTS: The depth profiles of the thermal neutron flux and gamma-ray dose rates relative to the reference water content are shown in Fig. 1. For a water content of 80.5% (+2% of the reference value), the thermal neutron flux and the gamma-ray dose rates increased up to about 4-cm and 6-cm depths, respectively. At the greater depths, decreases in both values were observed. The opposite trend was observed for a water content of 76.5% (-2% of the reference value) as for 80.5%. These reflect changes in the moderating and thermalizing ability of the epi-thermal neutrons and the absorption/capture reaction rate of the thermalized neutrons due to the increase or decrease in hydrogen density.

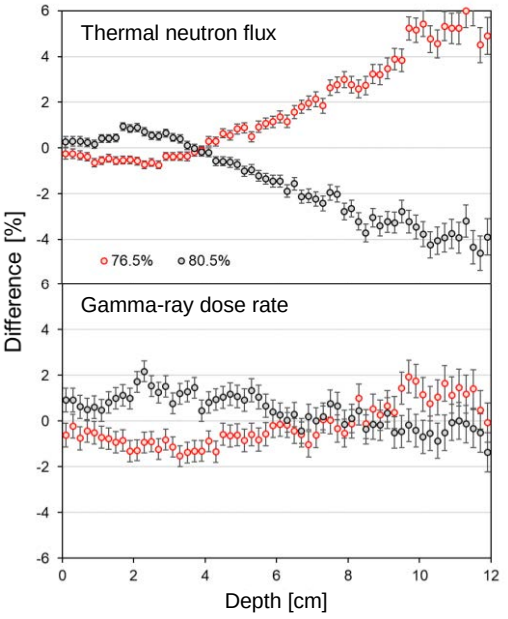

Fig. 1. Depth profiles of thermal neutron flux and gamma-ray dose rates relative to reference water content.

REFERENCES:

[1] ICRU Report 46 (ICRU, Bethesda, MD, 1992).
[2] E. M. Widdowson *et al.,* Biochem J., **77** (1960) 30-43.
[3] H. W. Bothe *et al.,* Acta Neuropathol., **64** (1984) 37-42.
[4] T. Sato *et al.,* J. Nucl. Sci. Technol., **55** (2018) 684-690.
[5] Y. Sakurai, T. Kobayashi, Med. Phys., **29** (2002) 2328-2337.

I-1. PROJECT RESEARCHES

Project 9

PR9

Sophistication of radiation detectors aimed at application in accelerator BNCT

H. Tanaka

Institute for Integrated Radiation and Nuclear Science, Kyoto University

BACKGROUNDS AND PURPOSE: Insurance treatment using the accelerator BNCT system has been started at medical institutions, and the number of BNCT cases is expected to increase in the future. As a quality assurance and quality control for treatment, it is required to measure thermal neutron flux and gamma dose before irradiation, and the gold activation method and thermoluminescence dosimeters used in reactor BNCT have been followed. The method is complicated and thermoluminescence dosimeters will not be available in the future, and medical institutions are hoping for a simple and highly accurate measurement method.

In addition, there is a growing need for research and development of radiation detectors related to BNCT, such as epithermal and fast neutron flux, prompt gamma rays, and neutron energy spectrum. Therefore, the objective of this project is to upgrade radiation detectors for application in accelerator BNCT.

RESEARCH SUBJECTS:

R5P9-1: Measurements of Neutron Fluence and Gamma ray Distribution using Thermoluminescence Slabs(K. Shinsho *et al.*)

R5P9-2: Comparison of optical observation of boron dose distributions using different types of boron-added liquid scintillators(A. Nohtomi *et al.*)

R5P9-3: Development and Demonstration of a Bonner Sphere Spectrometer for Intense Neutron Measurements(A. Masuda *et al.)*

R5P9-4: Study on neutron monitor using Li glass scintillator and gamma-ray measurement system for BNCT(S. Yoshihashi *et al.*)

R5P9-5: Establishment of Characterization Estimation Method in BNCT Irradiation Field using Bonner Sphere and Ionization Chamber (VII)(Y. Sakurai *et al.*)

R5P9-6: Development of Real-time Boron-concentration Estimation Method using Gamma-ray Telescope System for BNCT (II)(Y. Sakurai *et. al,*)

R5P9-7: Experimental Investigation of A Real-time Epi-thermal Neutron Absolute Flux Intensity Monitor Using Scintillation Detectors (I. Murata *et al.*)

R5P9-8: Neutron Image Sensor for Boron Neutron Capture Therapy(V. T. Ha *et al.*)

R5P9-9: Improvement of the SOF detector system for energy-dependent discrimination and long-term stability(M. Ishikawa *et al.*)

R5P9-10: Fast Neutron Dosimetry Using Solid-State Nuclear Track Detector for BNCT(T. Takata *et al.*)

R5P9-11: Fiber-reading Radiation Monitoring System with an Optical Fiber and Red-emitting Scintillator at the ^{60}Co Radiation Facility and KUR(S. Kurosawa *et al.*)

R5P9-12: Improvement To Increase Accuracy of Absolute Fast Neutron Flux Intensity Monitor for BNCT(I. Murata *et al.)*

R5P9-13: Study on Hybrid Radiation Detector for BNCT(N. Matsubayashi *et al.*)

R5P9-14: Measurement of Thermal Neutron-Induced Soft Error Rates in Semiconductor Memories(H. Tanaka *et al.*)

Research subjects R5P9-1,10, and 12 are research and development on methods to measure thermal and fast neutrons and γ-rays. R5P9-2 and 6 propose methods to obtain boron distributions in real-time. R5P9-3,5, and 9 propose new methods for measuring neutron spectra. R5P9- 4, 7, 8, 11,13 have succeeded in obtaining real-time measurements of gamma rays, thermal and epithermal neutrons in the irradiation field of BNCT. All of them are expected to be applied to accelerator BNCT.

PR9-1

Measurements of Neutron Fluence and Gamma ray Distribution using Thermoluminescence Slabs

K. Shinsho, E. Sasaki, M.Kawane, H. Tanaka[1], T. Takata[1], S. Matsumoto, G. Wakabayashi[2], G. Okada[3], Y. Koba[4]

Graduate School of Human Health Science, Tokyo Metropolitan University
[1] Research Reactor Institute, Kyoto University
[2] Graduate school of Science and Engineering Research, Kindai University
[3]Co-creative Research Center of Industrial Science and Technology, Kanazawa Institute of Technology
[4]Center for Radiation Protection Knowledge, QST-NIRS

INTRODUCTION: Boron Neutron Capture Therapy (BNCT) is one of the radiation therapies using neutrons and ^{10}B drugs which are attracted to tumors. BNCT is expected to be next-generation cancer therapy which will improve the QOL of patient because it is able to irradiate a cancer cell at the molecular level selectively. However, dosimetry techniques in mixed neutron-gamma fields have not been established yet. Therefore, we focused on neutron and gamma ray measurements using two- dimensional thermoluminescence dosimeter (2D-TLD). We have reported that the thermoluminescence (TL) of a Cr-doped Al_2O_3 ceramic plate sandwiched between Cd plates can selectively measure only the thermal neutron fluence at the BNCT irradiation field without being affected by mixed γ-rays [1,2], and that the TL characteristics of a high thermal conductivity type BeO ceramic plate (Na undoped BeO ceramic plate) can be used to selectively measure the γ-ray fluence at the BNCT irradiation field without being affected by neutrons [2,3]. In this study, we will clarify the mechanism by which these techniques can selectively measure the objective radiation and establish a method to measure neutron fluence distribution selectively and accurately and γ dose distribution with high spatial resolution in a BNCT irradiation field.

EXPERIMENTS: A large-area TL distribution measurement system (Fig.1) was developed to measure γ-ray dose distribution in BNCT irradiation field. 114 mm square BeO ceramic plates were used.

RESULTS: Figure 2 shows the γ-ray dose distribution using the TL characteristics of 114 mm square BeO ceramics. The γ dose was obtained with a spatial resolution of 50 μm/pixel. However, optimization of correction methods for higher accuracy, such as two-dimensional sensitivity correction, flatness correction, and conversion to dose, has not been done. In particular, due to the low sensitivity, it is necessary to work on improving sensitivity and accuracy, including consideration of γ dose measurement using pre-irradiation and OSL characteristics.

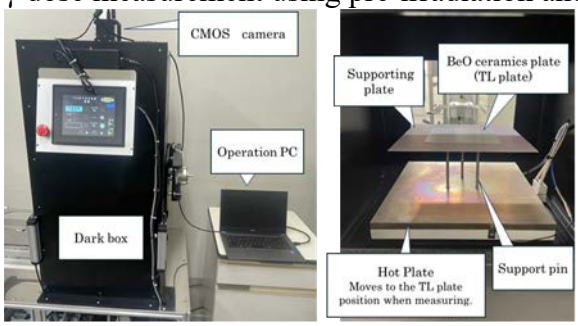

Fig.1. A large-area TL distribution measurement system

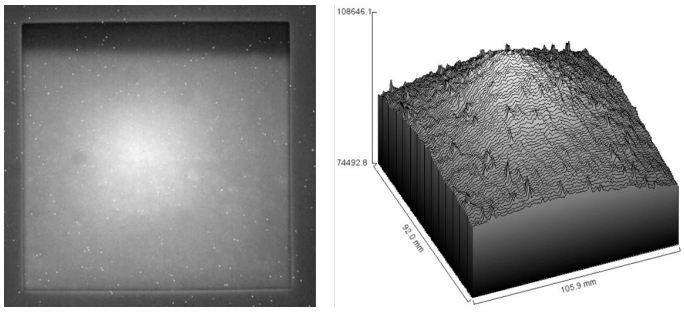

Fig.2. TL distribution (γ dose distribution) with 114 mm square BeO ceramic plates without correction

REFERENCES:

[1] R. Oh, K. Shinsho *et al.*, Sens. and Mater., **33(6)** (2021) 2129-213.
[2] K. Shinsho *et al.*, Jpn. J. Appl. Phys., **62** (2023) 010502.
[3] M.Tanaka, K. Shinsho *et al.*, J. Mater. Sci.: Mate. Elec., **33** (2022) 20271–20279.

Comparison of optical observation of boron dose distributions using different types of boron-added liquid scintillators

A. Nohtomi, H. Maeda, T. Yamane, Y. Kojima, G. Wakabayashi[1], Y. Sakurai[2], H. Tanaka[2] and T. Takata[2]

Graduate School of Medicine, Kyushu University
[1]Atomic Energy Research Institute, Kindai University
[2]Institute for Integrated Radiation and Nuclear Science, Kyoto University

INTRODUCTION: For boron-neutron capture therapy (BNCT), the information of boron dose distribution plays a significant role. In our previous work [1], a boron-added liquid scintillator has been proved to be very useful for the direct evaluation of boron dose distribution by observing the luminescence with a CCD camera during the neutron irradiation. In that work, as an attempt, we dissolved trimethyl borate in a commercially-available liquid scintillator, Insta-Gel Plus, approximately 1 wt%. However, other types of liquid scintillators have not been examined yet. In the present work, in addition to the Insta-Gel Plus, another two types of commercially-available liquid scintillators were examined as boron-added liquid scintillator for comparison.

EXPERIMENTS: We dissolved trimethyl borate in three types of commercially-available liquid scintillator (Insta-Gel Plus, Ultima Gold XR and Ultima Gold F: Perkin Elmer) approximately 1 wt% in natural boron concentration. The main component of Insta-Gel Plus is pseudocumene with a certain amount of addition of alkylphenol polyglycol ether as emulsifier. The main component of Ultima Gold XR is diisopropyl naphthalene isomers with a certain amount of addition of alkylphenol polyglycol ether as emulsifier. On the other hand, Ultima Gold F is made of almost diisopropyl naphthalene isomers solely. The boron-added liquid scintillator was filled in a quartz bottle phantom and was irradiated by thermal neutrons (~10^5 n/cm^2/s) during 150, 300 and 600 seconds at E-3 irradiation port [2]. Luminescence of each boron-added liquid scintillator was observed by a cooled CMOS camera (Bitran, CS-67M) during the irradiation in a black box.

RESULTS: The luminescence distributions were clearly observed for all types of boron-added liquid scintillators for 600 seconds irradiation. The luminance was proportional to the irradiation time as indicated in Fig. 1 for all types of boron-added liquid scintillators. However, the luminance was different for each type of liquid scintillator. The luminescence of Ultima Gold F was the brightest among the three and approximately 1.6 times higher than that of Insta-Gel Plus. The luminescence of Ultima Gold XR was approximately 82 % of that of Insta-Gel Plus.

From the facts mentioned above, it has been revealed that the image quality of boron dose distribution will be able to be improved by the optimization of choice of liquid scintillator without emulsifier.

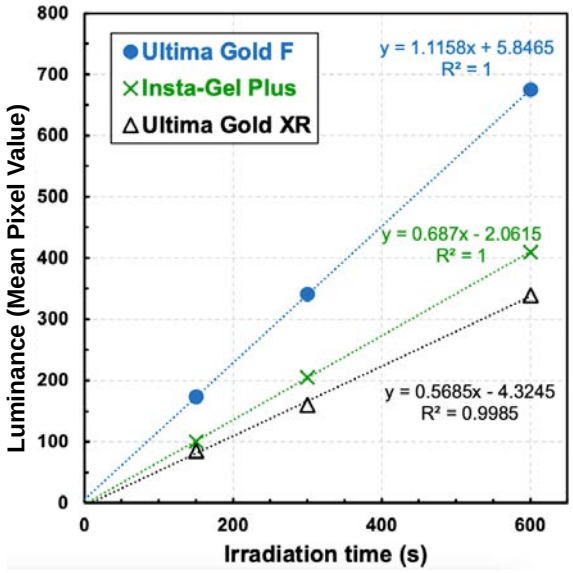

Fig. 1. Luminance value for different types of boron-added liquid scintillators as a function of neutron irradiation time.

REFERENCES:

[1] A. Nohtomi *et al.*, Radiol. Phys. Technol., **15** (2022) 37-44.
[2] T. Kobayashi and, K. Kanda. Nucl. Instrum. Meth., **204** (1983) 525-531.

PR9-3

Development and Demonstration of a Bonner Sphere Spectrometer for Intense Neutron Measurements

A. Masuda, T. Matsumoto, S. Manabe, K. Watanabe[1], A. Ishikawa[2], H. Tanaka[3], Y. Sakurai[3], H. Harano, T. Takata[3], A. Uritani[4] and H. Kumada[5]

National Metrology Institute of Japan, National Institute of Advanced Industrial Science and Technology
[1]*Graduate School of Engineering, Kyushu University*
[2]*Nuclear Science Research Institute, Japan Atomic Energy Agency*
[3]*Institute for Integrated Radiation and Nuclear Science, Kyoto University*
[4]*Graduate School of Engineering, Nagoya University*
[5]*Proton Medical Research Center, University of Tsukuba*

INTRODUCTION: Neutron spectral fluence measurement techniques are required in boron neutron capture therapy (BNCT). Bonner sphere spectrometer (BSS) is one of the best known and proven solutions [1]. A BSS for intense neutron beams is developed in this study. A small lithium-glass scintillator is adopted to the Bonner sphere detectors to accommodate the neutron intensity of 10^9 cm^{-2} s^{-1}. Demonstration measurements of the assembled BSS were performed at the Kyoto University Research Reactor (KUR).

EXPERIMENTS: The Bonner sphere detectors with the small lithium-glass scintillator coupled with an optical fiber [2] and a photomultiplier (PMT, Hamamatsu R9880U-21) were set and irradiated by the standard mixed neutrons in rotation at the measurement position of the heavy water irradiation facility of the KUR [3]. Diameter of HDPE moderators for BSS were 3”, 3.5”, 4”, 4.5”, 5”, 6”, 7” and 8”. Output signals from PMT were processed using a preamplifier (ORTEC 113) and a signal processing and acquisition system (Amptek PX5).

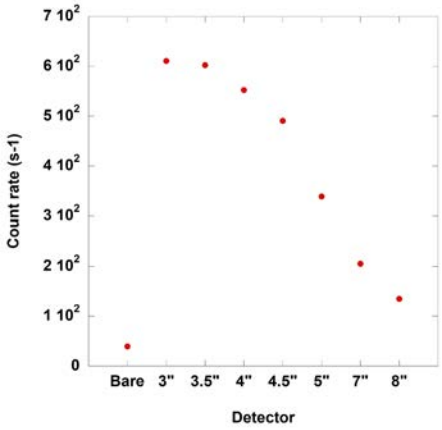

Fig. 1. Results of Bonner sphere measurements.

RESULTS: The results of the measurements are shown in Fig. 1. A reasonable dependence of the count rate on the detector is observed. Response functions of the developed BSS are shown in Fig. 2, that were calculated by Monte Carlo simulations using MCNP 6.2. The statistical fluctuations will be resolved by improving statistics. The neutron spectral fluence will be derived from the measurement results and improved response functions.

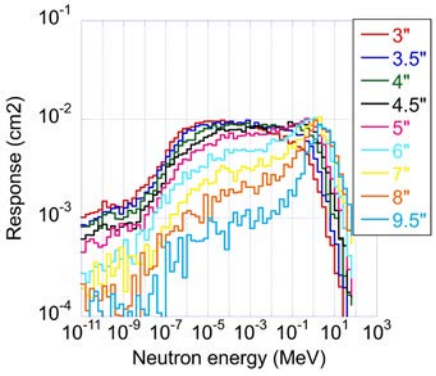

Fig. 2. Calculated response functions of Bonner spheres.

REFERENCES:

[1] A. Masuda *et al.,* Appl. Radiat. Isot., **127** (2017) 47-51.
[2] A. Ishikawa *et al.,* Sensors and Materials, **32** (2020) 1489-1495.
[3] Y. Sakurai and T. Kobayashi, Nucl. Instrum. Meth-ods Phys. Res. A, **453** (2000) 569-596.

This study is supported by Grant-in-Aid for Scientific Research, Japan Society for the Promotion of Science (JSPS KAKENHI Grant Number JP22K12667).

PR9-4

Study on neutron monitor using Li glass scintillator and gamma-ray measurement system for BNCT

S. Yoshihashi, K.Watanabe[1], A. Uritani, A. Yamazaki, I. Suzuki, T. Fukutomi, K. Tsuchimoto, Y. Oshima[1], S. Hasegawa[1], Y. Sakurai[2] and H. Tanaka[2]

Graduate School of Science, Kyoto University
[1]Graduate School of Engineering, Kyushu University
[2]Institute for Integrated Radiation and Nuclear Science, Kyoto University

INTRODUCTION: Boron neutron capture therapy (BNCT) is one of the radiotherapies. This is a combined modality of radiotherapy and chemotherapy for cancer treatment. Recently, an accelerator-driven neutron source has actively been developed instead of nuclear reactors, owing to its simplicity of management. It is important to characterize an irradiation field of BNCT facility.
In this study, we are developing a novel neutron detector using an optical fiber. So far, in order to realize the optical fiber type neutron detector showing a neutron peak in the pulse height spectrum, bright neutron scintillators, such as Eu:$LiCaAlF_6$ or LiF/Eu:CaF_2 eutectics, have been used [1]. Recently, we attempted to replace them with the faster Li glass scintillator [2]. For both cases, we have never controlled a shape of scintillators because the scintillator size has been too small. Since they had random shapes, the Monte-Carlo simulation-based study was difficult to be conducted. To evaluate the accurate detector response, the scintillator shape is required to be controlled. We proposed that a transparent composite Li glass scintillator, in which fine Li glass scintillator powder and resin are mixed. This type of scintillator is expected to be easily shaped because it is a resin-based material. In this study, we fabricate the optical fiber type neutron detector using the transparent composite Li glass scintillator and evaluate its response to thermal neutron irradiation.
EXPERIMENTS: We fabricated the optical fiber type neutron detectors using the transparent composite Li glass scintillator. First, fine powder of the Li glass and UV curable resin were mixed. The mixed resin was attached on a tip of an optical fiber using PC controlled fabrication system to control the attached resin amount. The resin was spontaneously shaped to a hemispherical shape by surface tension. And then, the mixed resin was irradiated with UV light to solidify it. The two fabricated detectors were irradiated with thermal neutron.
RESULTS: Figure 1 shows the signal pulse height spectra obtained from the two fabricated optical-fiber-based neutron detectors when they were irradiated with thermal neutron. The fabricated optical fiber type neutron detector shows a clear neutron peak in the signal pulse height spectrum. In addition, both detectors show almost the same response. By using the PC controlled fabrication system, we can control the attached amount of the mixed compound resin on a tip of an optical fiber.

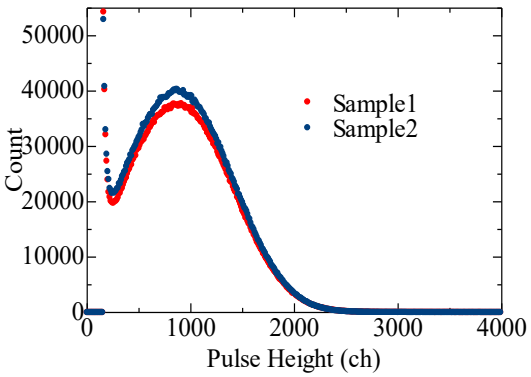

Fig. 1. Pulse height spectra obtained from the two fabricated optical-fiber-based neutron detectors. They were fabricated using the PC controlled fabrication system.

REFERENCES:
[1] K. Watanabe *et al.*, Nucl. Instrum. Methods Phys. Res. Sect. A., **802** (2015) 1-4.
[2] A.1 Ishikawa *et al.*, Sensors and Materials, **32** (2020) 1489-1495.

PR9-5

Establishment of Characterization Estimation Method in BNCT Irradiation Field using Bonner Sphere and Ionization Chamber (VII)

Y. Sakurai, J. Prateepkaew[1], R. Narita[1], T. Takata and H. Tanaka

Institute for Integrated Radiation and Nuclear Science, Kyoto University
[1]Graduate School of Engineering, Kyoto University

INTRODUCTION: Development in accelerator-based irradiation systems for BNCT is underway. BNCT using newly developed accelerator systems is being implemented at multiple facilities around the world. Considering this situation, it is important that the estimations for dose quantity and quality are performed consistently among several irradiation fields, and that the equivalency of BNCT is guaranteed, within and across BNCT systems. Then, we are establishing QA/QC system for BNCT. As part of the QA/QC system, we are developing estimation method for neutron energy spectrum using Bonner-sphere technique [1]. In our spectrometer, liquid such as pure water and/or boric acid solution is used as the moderator. A multi-layer case with multiple moderator layers is prepared. The moderator and its thickness are changeable without entering the irradiation room, by the remote supply and drainage of liquid moderator in the several layers. For the detector, activation foils are remotely changed, or online measurement is performed using SOF detector, etc. As a new type of spectrometer, we are developing the Cylindrical Hemisphere Accurate Remote Multilayer Spectrometer (CHARMS) [2]. In 2023, experiments using Simple Multilayer Spectrometer (SMS) were performed at Heavy Water Neutron Irradiation Facility of Kyoto University Reactor (KUR-HWNIF) in order to confirm the effectiveness of CHARMS [3].

MATERIALS AND METHODS: The shape of the SMS is a square, which is easy to prepare. It consists of three-layer acrylic square containers, with external dimensions of each container: 5 cm × 5 cm × 15 cm, 10 cm × 10 cm × 15 cm, and 15 cm × 15 cm × 15 cm. Pure water and boric acid water (^{10}B 0.14%wt) are used as the liquid moderators. The empty layers are also used. Activated foil is chosen as the neutron detector. In this study, bare and cadmium-covered gold foils were used. The response function for SMS and initial guess spectrum were calculated using PHITS 3.33. The MAXED and GRAVEL unfolding codes were used in the spectrum unfolding procedure. Figure 1 shows the experimental setup for SMS measurements at KUR-HWNIF. In this study, the standard epi-thermal neutron irradiation mode was selected.

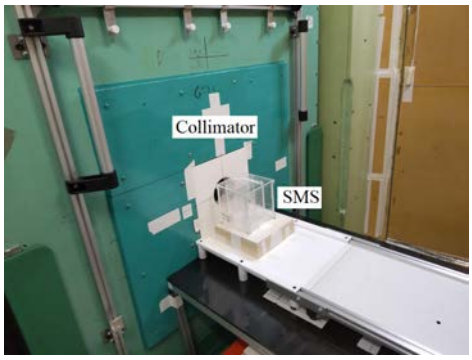

Fig. 1. Experimental setup for SMS measurements at KUR-HWNIF.

RESULTS: The effectiveness of the multi-layer neutron spectrometer with liquid moderators was experimentally confirmed using SMS. The neutron energy spectrum in the epi-thermal neutron irradiation mode of KUR-HWNIF was evaluated with an uncertainty of less than 15% by SMS. It is expected that the use of CHARMS will further reduce the uncertainty in the evaluation of the neutron energy spectrum.

REFERENCES:
[1] S. Shiraishi, *et al.*, Appl. Radiat. Isot. **163** (2020) 109213.
[2] J. Prateepkaew, *et al.*, Nucl. Instr. Meth. A., **1059** (2024) 168948.
[3] Y. Sakurai and T. Kobayashi, Nucl. Instr. Meth., **453** (2000) 569-596.

Development of Real-time Boron-concentration Estimation Method using Gamma-ray Telescope System for BNCT (II)

Y. Sakurai, J. Prateepkaew[1], T. Takata, H. Tanaka and M. Suzuki

Institute for Integrated Radiation and Nuclear Science, Kyoto University
[1]Graduate School of Engineering, Kyoto University

INTRODUCTION: It is important to decide the boron concentrations for tumor and normal parts in the dose estimation for BNCT. The on-line and real-time estimation method for the spatial distribution of boron concentration is expected for the advancement. The information about the boron concentration distribution can be obtained using the prompt gamma-ray analysis (PGA) for the prompt gamma rays from boron-10 (B-10). The improved gamma-ray telescope system is settled at Heavy Water Neutron Irradiation Facility of Kyoto University Reactor (KUR-HWNIF) [1-3]. This system consists of an HPGe semiconductor detector and a collimation system including two lead collimators. The gamma rays through these collimators can be detected, and the telescope view-filed can be changed by moving the two collimators independently. The experimental verification for the ability to distinguish between tumor and normal parts was continued in 2023 as well.

MATERIALS AND METHODS: Figure 1 shows the improved gamma-ray telescope system. A rectangular liquid phantom of 20 cm in width 20 cm in length and 40 cm in depth was used in the experiment. An acrylic hollow sphere with an outer diameter of 5 cm filled with boric acid with a B-10 concentration of 200 ppm was placed as the tumor part inside of the phantom. The phantom liquid was pure water or boric acid water with a B-10 concentration of 25 ppm. The epi-thermal neutron irradiation was performed in an irradiation field with a diameter of 12 cm. The initial position of the center of the tumor sphere was set on the beam axis at the center of the telescope view-field, and was moved to the right from 0 to 6 cm from the viewpoint on the beam aperture side. The positions of the two telescope collimators were fixed at the lowest position. At these positions, the effective telescope field on the beam axis is no more than 3 cm wide to the right in viewing from the beam aperture side. The prompt gamma rays from the neutron reaction with B-10 and hydrogen (H-1) from the tumor sphere and its surroundings during the neutron irradiation were measured.

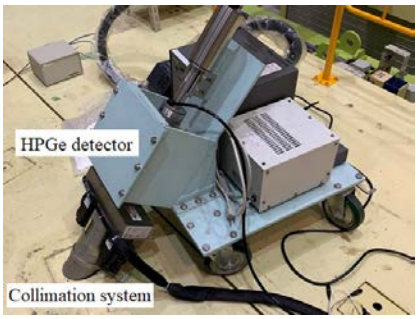

Fig. 1. Gamma-ray telescope system.

RESULTS: It was confirmed that the closer the tumor sphere center is to the beam axis, that is, the closer to the center of the effective telescope view-field, the larger the B/H count ratio becomes. It was also confirmed that the B/H count ratio was higher in the boric acid water phantom than in the pure water phantom. This is because the B-10 gamma rays from the boric acid water with a B-10 concentration of 25 ppm within the telescope view-field further contribute to the B-10 gamma ray count. If the B-10 concentration ratio between the tumor and normal parts is almost the same as this experiment, it is expected to be possible to distinguish between tumor and normal parts by comparing the counting ratio for the tumor positions inside and outside of the telescope view-field.

REFERENCES:

[1] Y. Sakurai, *et al.*, Appl. Radiat. Isot., **61** (2004) 829-833.
[2] Y. Sakurai, *et al.*, Appl. Radiat. Isot., **165** (2020) 109256.
[3] Y. Sakurai and T. Kobayashi, Nucl. Instr. Meth. A., **453** (2000) 569-596.

Experimental Investigation of A Real-time Epi-thermal Neutron Absolute Flux Intensity Monitor Using Scintillation Detectors

I. Murata[1], J. Qiu[1], Y. Ge[1, 2], N. Voulgaris[1], K. Sagara[1], D. Hatano[1], S. Tamaki[1], S. Kusaka[1] and T. Takata[3]

[1]*Graduate School of Engineering, Osaka University*
[2]*Sino-French Institute of Nuclear Engineering and Technology, Sun Yat-sen University, China*
[3]*Institute for Integrated Radiation and Nuclear Science, Kyoto University*

INTRODUCTION: In boron Neutron Capture Therapy (BNCT), epi-thermal neutrons (0.5 eV to 10 keV) are irradiated and converted into thermal neutrons that have a larger neutron capture reaction cross-section before reaching the tumor by slowing down process in a human body. Therefore, it is significantly required to develop a real-time monitor for measuring epi-thermal neutron flux intensity on the body surface of a patient during the irradiation to evaluate the therapeutic effect of BNCT. We have proposed a measurement system that has a constant response to incident epi-thermal neutrons using multiple detectors covered by neutron absorbers such as boron with various thicknesses. LiCAF glass scintillator [1] based on ^{6}Li(n, α)^{3}H reaction, and EJ-254 plastic scintillator [2] based on ^{10}B(n, α)^{7}Li reaction, were considered as potential detection elements. T-Yield tally of PHITS code is used to calculate the reaction rate and evaluate the detection response.

EXPERIMENTS: In this study, we conducted an irradiation experiment using the standard epi-thermal irradiation mode (1 MW) of Heavy Water Neutron Irradiation Facility in Kyoto University Research Reactor (KUR) [3] to verify the performance of our fabricated monitor. We constructed a prototype detector with a scintillator crystal glued to the tip of an optical fiber. And some cylindrical neutron absorbers were fabricated by using a powder molding press. The measurement circuit contains photomultiplier tube, pre-amplifier, linear amplifier, and multi-channel analyzer. Furthermore, we placed gold foils near the scintillator during irradiation, and measured the radioactivity of the activated foils to estimate the neutron flux intensity.

RESULTS: The pulse height spectrums of two scintillators were obtained successfully from the experiment, as shown in Fig. 1. In the actual irradiation field, the contribution of scattered neutrons from various directions to the scintillator is too large to be ignored, so we analyzed the components of front incident and scattered neutrons using the neutron flux intensity measured by gold foils, and evaluated the performance of the monitor. In summary, we demonstrated the feasibility of a real-time epi-thermal neutron absolute flux intensity monitor with a constant response to epi-thermal neutrons from a measurement experiment in the BNCT neutron irradiation field.

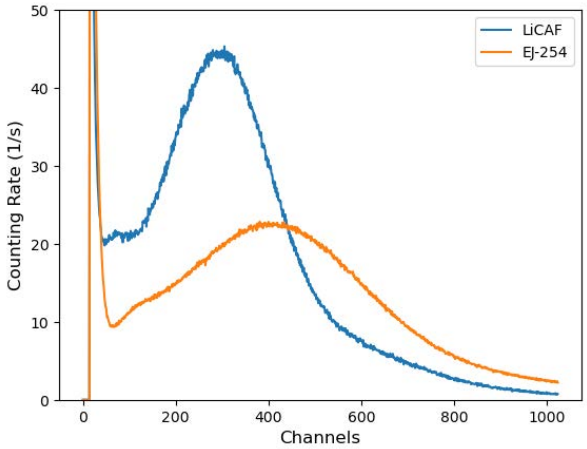

Fig.1 The measured pulse height spectrum

REFERENCES:

[1] T. Yanagida *et al.*, Appl. Phys. Express, **4(10)** (2011) 106401.
[2] G. Gabella *et al.*, IEEE Trans. Nucl. Sci., **68(1)** (2021) 46–53.
[3] H. Tanaka *et al.*, Nucl. Instrum. Methods Phys. Res. B, **267(11)** (2009) 1970–1977.

PR9-8

Neutron Image Sensor for Boron Neutron Capture Therapy

V. T. Ha[1], T. Meguro[1], H. Tanaka[2], and S.-I. Kuroki[1]

1Research Institute for Semiconductor Engineering, Hiroshima University
2 Institute for Integrated Radiation and Nuclear Science,
Kyoto University Graduate School of Science, Kyoto University

INTRODUCTION: Boron neutron capture therapy (BNCT) has been attracting attention as an advanced treatment method on cancer because this therapy has a great advantage on a minimally invasive and selective treatment. In the BNCT, for making this therapy more accurate one, it is better to measure the position of neutron beam profile. On the other hand, silicon carbide (SiC) semiconductor has a strong radiation hardness [1], and then is expected as radiation hardened devices. The purpose of this study is to develop a neutron image sensor with SiC devices [2].

EXPERIMENTS: The structure of our neutron sensor is based on a three- and four-transistor type image sensor pixel. The neutron sensor is based on an image sensor pixel using SiC, which has been developed in our laboratory, focusing on stable operation under neutron irradiation for a long time. The neutron sensors are equipped with boron-10 layer as a neutron conversion layer. In this layer, the injected neutrons have a reaction with boron-10, and then, alpha and lithium particles are emitted. The alpha particles penetrate the device, and generate electron-hole pairs, electrons are collected at gate electrode of SF(source-follower) transistor, and then the induced charge is detected as the output voltage from the sensor. For the highly sensitive neutron sensor, we designed the structure of the device, and design the device layout for next fabrication.

RESULTS: Figure 1 shows the result of our device designing and shows the chip layout of the device. We designed 4-transistor pixel devices in addition to former 3-transistor type. With this new device layout data, we'll fabricate new neutron 2D image sensors.

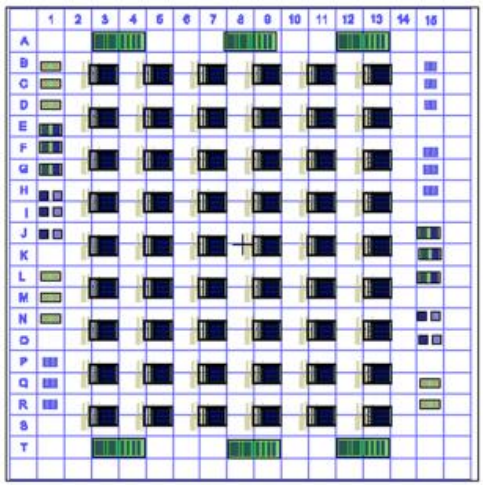

Fig. 1. Chip layout of the neutron sensors. This is a test chip with active pixel sensors.

REFERENCES:

[1] M. Tsutsumi *et al.,* IEEE Electron Device Lett., **44(1)** (2023) 100.
[2] M. Taniguchi, *et al.,* The Interna-tional Symposium on Biomedical Engineering 2022, (2022) 66 .

Improvement of the SOF detector system for energy-dependent discrimination and long-term stability

M. Ishikawa[1,2], Y. Ikeda[2], K. Takamiya[3] and Y. Sakurai[3]

[1]*Faculty of Health Sciences, Hokkaido University*
[2]*Graduate School of Biomedical Science and Engineering, Hokkaido University*
[3]*Institute for Integrated Radiation and Nuclear Science, Kyoto University*

INTRODUCTION: We have been conducting research on SOF detectors as thermal neutron flux monitors in BNCT for many years. [1,2] However, degradation of the SOF detector due to long-term irradiation has been reported.[3] As anti-degradation methods, we have replaced plastic optical fibers, which cause degradation, with quartz fibers, and developed degradation monitors using blue laser source. In addition, since epithermal neutron irradiation has become mainstream in recent years, it is desirable to be able to measure the epithermal neutron flux. In this study, we conducted to estimate the neutron energy spectrum at KUR HWNIF (Heavy Water Neutron Irradiation Facility).

EXPERIMENTS: In the degradation acceleration experiment using the slant-hole irradiation facility, it was found in last year's experiment that effective degradation monitoring could not be performed because fluorescence was generated in areas other than the scintillator as a problem with the degradation monitoring mechanism using a UV light source. Therefore, this year we attempted to monitor degradation using blue laser light source. However, the expected results could not be obtained because the degradation mechanism did not function effectively due to the failure of the blue laser source or the failure of the probe itself.

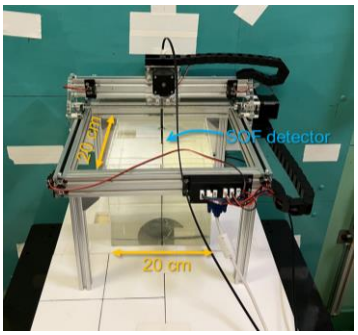

Fig. 1. Measurement geometry for neutron energy spectrum estimation using MLEM unfolding method.

For flux estimation in each energy region using SOF detectors, energy spectrum estimation using the MLEM (Maximum Likelihood Expectation Maximization) method from 1D thermal neutron flux profile data using SOF detectors was performed in experiments up to last year, but sufficient estimation results could not be obtained. Therefore, this year we attempted to estimate the energy spectrum using the MLEM method by extending the previous 1D scanning to 2D scanning data. Figure 1 shows the 2D scanning measurement experiment at KUR-HWNIF, where the SOF detector probe was located at a pitch of 1 cm in the lateral direction and 5 mm in the depth direction inside a 20 x 20 x 20 cm^3 PMMA phantom, and measurements were performed at each point for 20 sec. The PHITS simulation showed a relatively good estimation of the energy spectra of the 11 groups, as shown in Fig. 2 (a). However, as shown in Fig. 2(b), the estimation using the measured data shows a rather large deviation in the fast energy region.

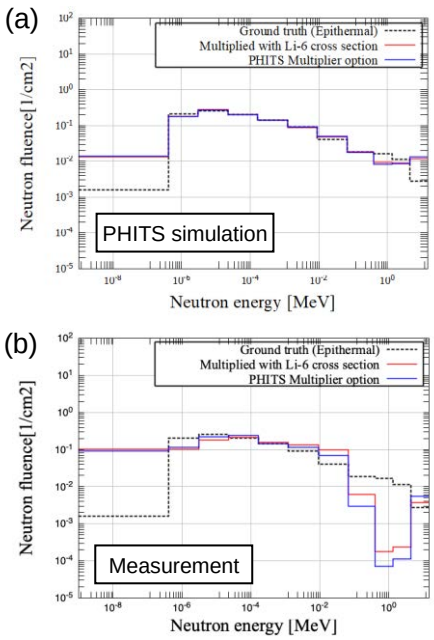

Fig. 2. Estimated neutron energy spectrum by SOF detector.

REFERENCES:

[1] M. Ishikawa *et al.*, Appl. Radiat. Isot., **61** (2004) 775-779.
[2] M. Ishikawa *et al.*, Nucl. Instr. Meth., A, **551** (2005) 448-457.
[3] M. Komeda *et al.*, Appl. Radiat. Isot., **67** (2009) 254-257.

PR9-10

Fast Neutron Dosimetry Using Solid-State Nuclear Track Detector for BNCT

T. Takata, Y. Sakurai, H. Tanaka and M. Suzuki

Institute for Integrated Radiation and Nuclear Science, Kyoto University

INTRODUCTION: In dosimetry of boron neutron capture therapy (BNCT), separate measurements of doses from thermal neutrons, fast neutrons, and gamma rays are required. In such a mixed neutron and gamma-ray field, a paired ionization chamber method is a standard for fast neutron dosimetry. In principle, the method requires compensation of gamma-ray dose, where the conversion factor used to derive the doses from the detector output causes an uncertainty of the fast neutron dose. Also, perturbation of the radiation field caused by the detectors must be taken into account.

In this study, a fast neutron dosimetry method using a solid-state nuclear track detector (SSNTD), which is not sensitive to gamma-rays and has less field perturbation than ionization chambers, is investigated as an alternative method. The detection characteristics for low-energy recoil protons, which account for most of the fast neutron dose impartation, are important to evaluate its applicability to BNCT irradiation field. A method for characteristic measurement of low-energy protons generated from $^{14}N(n, p)^{14}C$ reaction in the atmospheric air is introduced in this report.

MATERIALS AND METHODS: Consider the situation where the SSNTD is placed in a uniform field of thermal neutron formed in the atmospheric air. Protons are produced by the reaction with an initial kinetic energy of 584 keV, slowed down by collisions with molecules in the atmosphere, and then incident on the SSNTD with a reduced energy corresponding to the distance from the position where the reaction occurred. It is known that a diameter of a pit formed in the SSNTD by chemical etching depends on LET of incident particles [1]. Based on an energy spectrum of the incident protons, relationship between LET and pit diameter can be experimentally evaluated for low-energy protons. To confirm the usefulness of this technique, we performed an experiment using a low-energy neutron beam from the E-3 neutron guide tube at KUR [2]. A commercially available SSNTD (Baryotrack, Nagase Landauer, Ltd.) was located downstream of the beam collimated to 5 mm in diameter. After irradiation for 1 hour at 1 MW operation, etching with 6M NaOH solution was performed for 2 hours at 70°C, and the pits formed were observed with an optical microscope. In addition, the energy spectrum of protons produced in the atmosphere and incident on the SSNTD was estimated by simulation calculation using PHITS [3].

RESULTS: The formation of pits was observed on the SSNTD with a variety of its size, where a maximum diameter is a few micrometers. The characteristic analysis of these pits is now in progress. The calculated energy spectrum of the incident protons is shown in Fig. 1. Based on these initial results, methods for the irradiation experiments and their analysis are being investigated to establish a more appropriate evaluation method.

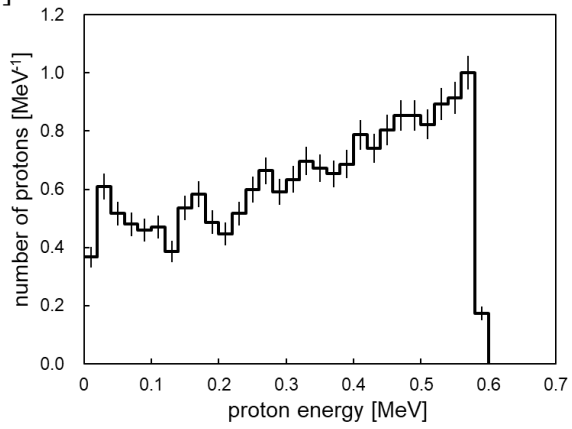

Fig. 1. Calculated energy spectrum of incident protons on SSNTD.

REFERENCES:

[1] M. Caresana *et al.,* Nucl. Instrum. Methods Phys. Res. Sect. A, **638** (2012) 8-15.

[2] T. Kobayashi and K. Kanda, Nucl. Instrum. Methods, **204** (1983) 525-531.

[3] T. Sato *et al.,* J. Nucl. Sci. Technol., **55** (2018) 684-690.

Fiber-reading Radiation Monitoring System with an Optical Fiber and Red-emitting Scintillator at the ^{60}Co Radiation Facility and KUR

S. Kurosawa[1,2,3], D. Matsukura[2,4], C. Fujiwara[2,4], A. Yamaji[1,2], T. Takata[5], H. Tanaka[5]

[1]*New Industry Creation Hatchery Center, Tohoku University*
[2] *Institute for Materials Research Tohoku University*
[3] *Institute of Laser Engineering, Osaka University*
[4] *Department of Materials Science, Graduate School of Engineering, Tohoku University*
[5] *Institute for Integrated Radiation and Nuclear Science, Kyoto University*

INTRODUCTION: Decommissioning reactors at nuclear power plant safety is an important is-sue, and a real-time dose-rate monitor in extremely high radiation dose conditions is required. We have proposed a dose-rate monitor system consisting of a scintillator, optical fiber and Charge Cou-pled Device (CCD) spectrometer, and scintillation photons through the fiber are read under the lower dose condition with the CCD. As we mentioned in the previous reports [1-2], the scintillator is required to have a long-emission wave-length (550 – 1,000 nm) and (ii) high light output (over 40,000 photons/ thermal neutron). Cs_2HfI_6 (CHI) has a high light output (over 60,000 pho-tons/MeV) and red and infrared emission (600 – 800 nm) [1][3].

On the other hand, we need evaluate some noises to understand the sensitivity for such detectors, and such noises can be generated as Cherenkov photons or/and scintillation photons originating from some emission centers like defects or OH part in the optical fiber itself. Moreover, such back-ground noises are expected to have some dose and position information, so that we evaluated the noises in this time.

EXPERIMENTS: Evaluation of the noises was operated using a ^{60}Co gamma-ray source (approximately 60 TBq) at Institute for Integrated Radiation and Nuclear Science, Kyoto University. The system consisted of CCD spectrometer (Preconfigured QE Pro Series Spectrometer, Ocean Insight) and 20 m-long optical fiber (S.600/660, Fujikura) with a core-diameter of 600 μm and minimum bending radius of 132 nm. In this time, we did not set the scintillator, and the exposure time was 3 seconds for 1 measurement with the CCD.

RESULTS: We succeeded in obtained wavelength spectra for the background noises, and the noise was observed to be dominant under 500 nm. Moreover, some absorption bands originating from OH absorption was also observed in the emission bands. In this time, some points through the fiber were irradiated with gamma rays from the ^{60}Co source, and using this data, the distance from CCD spectrometer to radiation hot spots was found to be estimated. The details of this results and discussion were reported in ref [4]. Using this background noises and signal intensities, we evalu-ated the dose-rate dynamic range, and this result of the range was estimated to be 0.1 mGy/h to a few kGy/h, which is suitable range for the application in Fukushima Daiichi Nuclear power plant and other decommissioning reactors. Here, the details of the signal intensities and this dynamic range are planned to describe in a new regular paper.

REFERENCES:
[1] S. Kurosawa *et al.*, KURNS PROGRESS REPORT 2020 (2021) 79.
[2] S. Kurosawa *et al.*, KURNS PROGRESS REPORT 2021 (2022) 248.
[3]. S. Kodama *et al*., Radiat. Meas., **124** (2019) 54-58.
[4] D. Matsukura *et al*., Instrumentation, **19** (2024) C02053.

Improvement To Increase Accuracy of Absolute Fast Neutron Flux Intensity Monitor for BNCT

I. Murata, K. Sagara, R. Kawahata, S. Tamaki, S. Kusaka, H. Tanaka[1], Y. Sakurai[1], T. Takada[1]

Graduate School of Engineering, Osaka University
[1]Institute for Integrated Radiation and Nuclear Science, Kyoto University

INTRODUCTION: BNCT is a promising cancer therapy which kills only tumor cells selectively. The neutron field of neutron sources for BNCT includes not only thermal and epi-thermal neutrons but also fast neutrons that are harmful to the human body. Therefore, we have to measure the absolute integral flux intensity of fast neutrons (10 keV ~ 1 MeV) to evaluate their exposure dose. Now we are developing a monitor to precisely measure it and repeatedly improving the monitor [1]. In the previous research, the experimental value was found to overestimate by about 226 % compared to the calculated value [2]. We discussed this discrepancy was caused by scattered neutrons generated in the irradiation laboratory of the KUR, Kyoto University Reactor. Therefore, the objective of this work is to modify the monitor to shield scattered neutrons.

EXPERIMENTS: For the fast neutron monitor, two detectors are used. One of them has a cubic PE and a small piece of B_4C in the cubic PE and GaN foil covered with a Cd sheet at the center of the cubic PE (PE type). The other one consists of a cubic PE surrounded by a B_4C sheet and a GaN foil covered with a Cd sheet is placed at the center of the cubic PE (B_4C type). In addition to the above, we placed a $^{10}B_4C$ plate in front of the monitor, and B_4C cover to shield scattered neutrons. Fig.1. shows the overview of the modified monitor. In this study, the performance of the modified monitor was verified experimentally at KUR. Irradiations were carried out for 20 min in 5 MW operation for each detector.

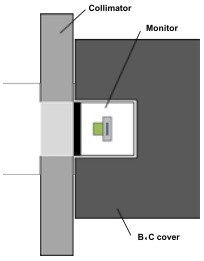

Fig. 1. Overview of the monitor surrounded with a $^{10}B_4C$ cover.

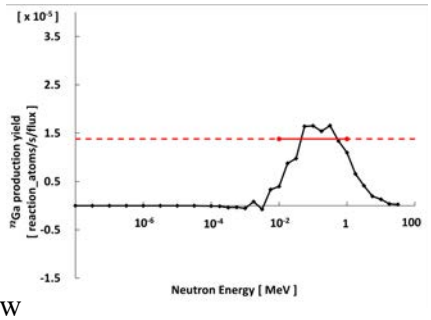

Fig. 2. Sensitivity of the fast neutron monitor.

RESULTS: After the irradiation at KUR, the absolute fast neutron flux was deduced from the ^{72}Ga activities and the sensitivity shown in Fig. 2. From Table 1, the experimental value is overestimated by about 196 % relative to the calculated value and improved by about 30 % compared with the previous research. However, the experimental result is still much larger than the calculated value. This could be due to the fact that sensitivity in high-energy region is not constant. When evaluating the experimental values, it was assumed that the sensitivity was constant. However, since the actual sensitivity is not constant, the discrepancy is considered to have occurred. Therefore, it is necessary to optimize the design of the monitor to make it as constant as possible in the future.

Table 1 Absolute fast neutron flux intensity obtained by the improved monitor.

	Experimental value (E)	Calculated value (C)	E/C
^{72}Ga activity*1 [Bq]	162.4±3.2	–	–
^{72}Ga activity*2 [Bq]	171.1±3.0	–	–
ϕ_{fast} [n/cm^2/sec]	15.3x10^7	5.17x10^7	2.96

*1 For the PE type detector.
*2 For the B_4C type detector.

REFERENCES:

[1] K. Aoki, “Development of absolute epi-thermal and fast neutron flux intensity detector for BNCT”, Thesis, University of Osaka, 2021.
[2] K. Sagara, “Improvement of absolute fast neutron flux intensity monitor for BNCT”, Thesis, University of Osaka, 2023.

PR9-13

Study on Hybrid Radiation Detector for BNCT

N. Matsubayashi, T. Takata, S. Sakurai, H. Tanaka

Institute for Integrated Radiation and Nuclear Science, Kyoto University

INTRODUCTION: The BNCT system requires the measurement of gamma-ray dose and thermal neutron flux in water phantoms for quality control/quality assurance (QA/QC). Thermofluorescence dosimeters and gold activation methods have been used to measure gamma-ray doses and thermal neutron flux, respectively. Recently, medical institutions have started insured treatment using the accelerator BNCT system, and it is desired to establish a rapid and simple method for measuring gamma-ray doses and thermal neutron fluxes in QA/QC that can replace the conventional methods. Therefore, the purpose of this study is to develop a hybrid radiation detector that can discriminate and measure gamma-rays and thermal neutrons by combining an ionization chamber and a scintil-lator for thermal neutron measurement.

A system combining a Eu:$LiCaAlF_6$ (LiCAF) scintillator and a quartz fiber will be adapted for measuring thermal neutron flux. Since air is present in the sensitive volume of the ionization cham-ber, the charge from charged particles produced by the $^{14}N(n,p)^{14}C$ reaction will be mixed. The gamma-ray dose can be discriminated and measured by subtracting the charge due to the $^{14}N(n,p)^{14}C$ reaction from the thermal neutron flux. In this year, we tested the characteristics of the LiCAF scintillator.

EXPERIMENTS: A LiCAF scintillator with 0.6 mm long side mounted on the tip of quartz fiber to reduce gamma-ray sensitivity was used[1]. The scintillator light entered the fiber and reached a photomultiplier tube (PMT). The signal from the PMT was then processed by a multi-channel analyzer (MCA). The pulse height distribution obtained by the MCA with the peak corresponding to neutron events was fitted via a gaussian distribution, and the counts were summarized from the mean to +2σ as neutron events[2]. To use the LiCAF scintillator as the thermal neutron monitor, it is necessary to determine the relationship between the counts and the thermal neutron flux. The counts obtained by the LiCAF scintillator were calibrated by an irradiation test using a water phantom at the Heavy Water Neutron irradiation facility (HWNIF) in Kyoto University. When the LiCAF scintillator was placed in the phantom at a depth of 10cm, the count rates were measured. The thermal neutron flux was evaluated via a gold activation method using a gold wire placed in the same position as the LiCAF scintillator.

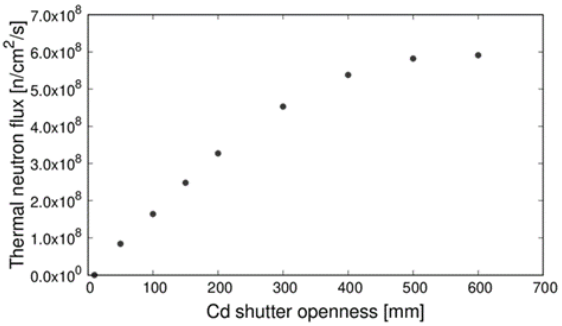

Fig. 1. Relationship of the thermal neutron flux and the Cd shutter openness.

The irradiation tests in free air were performed at the HWNIF. A Cd shutter of 1mm thickness was installed to change the thermal neutron flux with each openness. To investigate the thermal neutron flux per the openness, the irradiation tests were carried out by changing the Cd shutter openness to 0, 50, 100, 150, 200, 300, 400, 500, 600mm. The calibrated LiCAF scintillator was set at the center of a collimator, and the count rates were measured.

RESULTS: Fig. 2 shows the thermal neutron flux by changing the Cd shutter openness. The thermal neutron flux of HWNIF was found to be from 1.1×10^7 to 5.9×10^8 cm^{-2} s^{-1} depending on the Cd shutter openness. It was found that the range of thermal neutron flux was over an order of magnitude at HWNIF, and the intensity can be monitored in real-time by using the LiCAF scintillator.

REFERENCES:

[1] H. Tanaka *et al.,* Review of Scientific Instruments, **88(5)** (2017) 056101.
[2] N. Matsubayashi *et al.,* Radiation Measurements, **140** (2021) 106489.

Measurement of Thermal Neutron-Induced Soft Error Rates in Semiconductor Memories

H. Tanaka, [1]R. Nakamura, and [1]T. Kato

Institute for Integrated Radiation and Nuclear Science, Kyoto University
[1]Reliability and Engineering Department, Socionext Inc.

INTRODUCTION: Soft errors are radiation-induced errors in semiconductor devices. With aggressive scaling down of the devices, the soft error susceptibility is increasing. Therefore, to assess the reliability of electronic systems, it is necessary to investigate the characteristics of the soft errors. It has been reported that in recent semiconductor devices the thermal neutron-induced soft errors appear due to the contamination of ^{10}B atoms during manufacturing processes [1]. In previous ex-periments, the authors have demonstrated that the detailed characteristics of the thermal neu-tron-induced soft errors in static random access memories (SRAMs) [2]. This study investigates the thermal neutron-induced soft errors in SRAMs with different technologies and circuit designs. Soft error rates (SERs), which are the occurrence rates of soft errors, are measured by neutron irradiation testing at KUR.

EXPERIMENTS: Neutron irradiation tests were performed using Heavy Water Neutron Irradiation Facility (HWNIF) of KUR. The irradiation modes used were "OO–0000F" and "CO–0000F." The thermal neutron sensitivity was examined by comparing SERs between "OO–0000F" and "CO–0000F" irradiations.

The test samples were SRAM chips manufactured in two process technologies, which were labeled as Tech. A and Tech. B. For Tech. B, three designs of SRAMs (Type I, II, and III) were measured. During the irradiation, the SRAM chips were remotely operated, and the error events were recorded. The SERs were then statistically calculated according to the JEDEC standard. Thermal neutron fluxes at the locations of the samples were measured by the gold activation method.

RESULTS: Fig. 1 presents the measured SERs for Tech. A and Tech. B. Fig. 1(a) shows the comparison of "OO–0000F" and "CO–0000F." Fig. 1(b) shows the comparison of SRAM designs for Tech. B. For both technologies, the SER of "CO–0000F" was significantly lower than that of "OO–0000F," as seen in Fig. 1(a). This clearly demonstrates that thermal neutrons induce soft errors, indicating the containing of ^{10}B atoms. The results also showed that the thermal neutron sensitivity is higher for Tech. B than for Tech. A. For Tech. B, the different SRAM types showed different thermal neutron sensitivity. It is found from Fig. 1(b) that the SER of Type III is higher than that of Type I. This result suggests that the thermal neutron sensitivity is determined not only by manufacturing processes but also by SRAM designs. In summary, we demonstrated that the thermal neutron sensitivity depends on both the manufacturing process and the SRAM design. This result indicates the importance of thermal neutron irradiation testing for assessing soft error reliability.

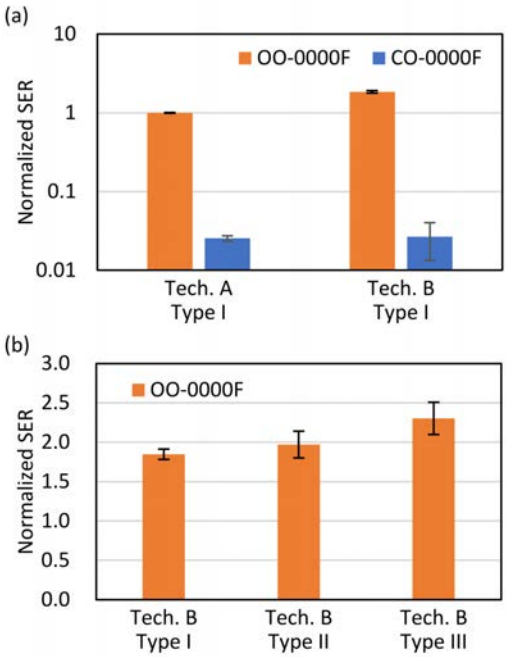

Fig. 1. Measured SERs: (a) Technology comparison and (b) SRAM design comparison.

REFERENCES:

[1] Y. Fang *et al.,* IEEE Trans. Device Mater. Rel., **14** (2014) 583.
[2] T. Kato *et al.,* IEEE Trans. Nucl. Sci., **68** (2021) 1436.

I-2. COLLABORATION RESEARCHES

1. Neutron Scattering
2. Nuclear Physics and Nuclear Data
4. Material Science and Radiation Effects
5. Geochemistry and Environmental Science
6. Life Science and Medical Science
7. Neutron Capture Therapy
8. Neutron Radiography and Radiation Application
9. TRU and Nuclear Chemistry
10. Health Physics and Waste Management
12. Others

CO1-1

Trial of mass production of *m=6* neutron focusing supermirrors

M. Hino, T. Hosobata[1], M. Takeda[1], Y. Yamagata[1], T. Oda[2], H. Endo[3]

Institute for Integrated Radiation and Nuclear Science, Kyoto University
[1]RIKEN Center for Advanced Photonics
[2]Institute for Solid State Physics, the University of Tokyo
[3]Institute of Materials Structure Science, KEK

INTRODUCTION: Recently new construction project for research reactor is progressing at "Monju" site at Tsuruga city in Fukui prefecture. Major utilization of the research reactor is for thermal and cold neutron beam utilization for wider utilization [1]. Actual use of the focusing mirror is one of very important to be on par with top level institute. We have established fabrication method for aspherical focusing supermirror with metal substrate [2-3]. The metallic substrate is robust and ductile, to which able to fabricate steeply curved surface with high form accuracy. It is also applicable to use under high radiation irradiation and high temperature filed, even at a place close to the neutron target and moderator. We have realized smooth surface for high-*m* supermirror coating. Here *m* is the maximum critical angle of the mirror in units of critical angle of natural nickel. In this study, we report a status of mass production for high-m neutron focusing supermirrors.

EXPERIMENTS: We fabricated ellipsoidal metallic substrates with electroless nickel-phosphorus plating, based on the technology using ultrahigh precision cutting with correction processing, followed by mechanical precision polishing. The first precise manufacturing was conducted at a CNC machine for development of neutron optical devices at workshop of the KURNS. The ultra-precise manufacturing, polishing and cleaning of the metallic substrate were conducted at RIKEN. The supermirror coating was con-ducted with ion beam sputtering machine at the KURNS (KUR-IBS) [3]. Figure 1(a) shows typical photograph of ellipsoidal supermirror deposited on one LOT and silicon substrates. The semi-major and semi-minor axes of the ellipsoidal supermirror were 1250 mm and 65.4 mm, respectively. Eventually, we have fabricated m=6 NiC/Ti(C) supermirrors in which effective number of layers was 9750, where the half of the layers were very thin carbon interlayers. The neutron experiments were conducted at C3-1-2(MINE) port of JRR-3.

RESULTS: By adding very thin carbon interlayer between NiC and Ti layers, we have realized m=6 supermirror with high reflectivity. There was a bit difference each LOT because some condition was difference as following: Because cleaning condition was a bit difference between LOT21 and LOT22, and the deposition rate of Ti target of LOT18 was smaller than those of LOT21 and LOT22.

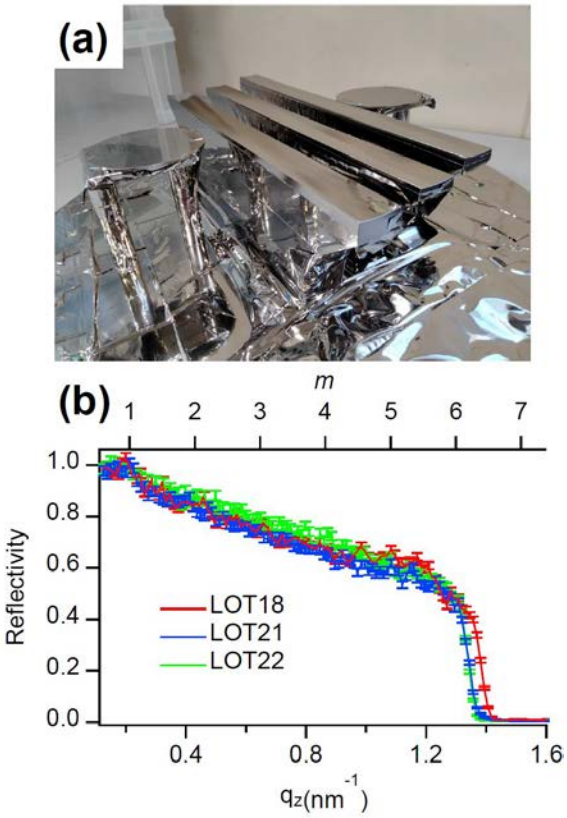

Fig. 1. (a) The photograph of m=6 supermirror deposited on one LOT (three ellipsoidal metal substrates) and two Si wafers (b) Neutron reflectivities of the supermirrors on Si wafers of which LOT number are 18, 21 and 22.

REFERENCES:

[1] https://www.jaea.go.jp/04/nrr/jp/ (in Japanese)
[2] T. Hosobata, *et al.*, Optics Express, **25** (2017) 20012, Optics Express, **27** (2019)26807.
[3] M. Hino, *et al.*, Nucl. Instr. and Meth., **797**(2015) 265.

CO1-2

Structural Analysis of Viscosity Index Improver Molecules Using Small-Angle X-ray Scattering

T. Hirayama, N. Yamashita, N. Sato[1] and M. Sugiyama[1]

Department of Mechanical Engineering and Science, Graduate School of Engineering, Kyoto University
[1]Institute for Integrated Radiation and Nuclear Science, Kyoto University

INTRODUCTION: Lubricating oils are necessary for friction reduction and high wear durability of sliding surfaces in machine components, and the development of the best oils is highly demanded by the industry. Viscosity index improver (VII) is a type of additive used to mitigate the decrease in viscosity of lubricating oil due to temperature rise. Classical textbooks say that VII molecules work by changing their equivalent radius in the base oil according to the oil temperature. However, there are few papers investigating the equivalent radius of VII molecules by small-angle X-ray scattering (SAXS) and/or small-angle neutron scattering (SANS)[1], and there is still room for discussion about the behaviour and working mechanism of VII molecules in oil. This study attempted to investigate the radius of gyration of several types of VII polymers in base oil at different temperatures by SAXS, and the behaviour of the VII polymers was investigated and discussed.

EXPERIMENTS: To investigate the structure of VII polymer in lubricant, we used a SAXS instrument (NANOPIX, Rigaku) with a Cu-Kα X-ray source (MicroMAX-007, Rugaku) and a semiconductor 2D detector (HyPix-6000, Rugaku). The 1.2 mm-thick aluminium cell with optical windows made of 20 μm heat resistant engineering plastic film (Superio-UT, Mitsubishi Chemical) was used for the measurement. The cell temperature was successively increased to 25, 40, 60, 80 and 100ºC, and the final measurement was carried out again at 25ºC after cooling to check the degeneration of the VII molecule. Comb-shaped poly(methyl acrylate) (PMA) type VII was prepared as a typical one used in engine oil in the study. Squalane was used as a model base oil and the concentrations of PMA in squalane were 0.5 and 2.0 mass%.

RESULTS: The SAXS profiles from squalane with 0.5 and 2.0 mass% Comb-PMA type VII at each temperature were shown in Fig. 1. The profiles were obtained by subtracting the SAXS profiles from pure squalane at each temperature. The figure shows that the profiles obtained at low temperature appear to be formed by the addition of two profiles derived from the different structural forms of Comb-PMA on the low-q and high-q ranges, but as the temperature increases, the profiles on the low-q side become relatively smaller. This indicates that comb-PMA type VII undergoes a significant structural change in response to temperature rise, which is linked to its high thickening effect as VII. In order to quantitatively analyze what this morphology looks like, fitting is currently being carried out on the macromolecular model proposed by Pedersen[2].

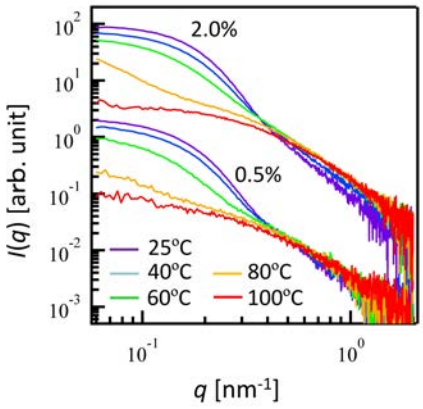

Fig. 1. SAXS profiles from comb-PMA molecules in squalane.

REFERENCES:

[1] M. J. Covitch and K. J. Trickett, Adv. Chem. Eng. Sci., **5** (2015) 134-151.
[2] J. S. Pedersen, Small-Angle Scattering from Surfactants and Block Copolymer Micelles. In: Borsali, R., Pecora, R. (eds), Soft Matter Characterization (Springer, Dordrecht, 2008).

CO1-3

Improvement of multilayer mirrors for neutron interferometer

M. Kitaguchi, T. Fujiie[1], T. Nambu[1], and M. Hino[2]

KMI, Nagoya University
[1]*Graduate School of Science, Nagoya University*
[2]*Institute for Integrated Radiation and Nuclear Science, Kyoto University*

INTRODUCTION: Neutron interferometry is a powerful technique for studying fundamental physics. Numerous interesting experiments [1] have been performed since the first successful test of a single-crystal neutron interferometer [2]. However, the single-crystal interferometer is inherently not able to deal with a neutron that has a wavelength longer than twice its lattice constant. In order to investigate problems of fundamental physics, including tests of quantum measurement theories and searches for non-Newtonian effects of gravitation, the interferometry of cold neutrons is extremely important, since the sensitivity of interferometer for small interaction increases with the neutron wavelength. A large scale of interferometer also has the advantage to increase the sensitivity to small interactions. One of the solutions is an interferometer using neutron multilayer mirrors [3,4]. We can easily control parameters such as Bragg angle, reflectivity, and Bragg peak width by selecting the deposited material and tuning the bilayer thickness and the number of layers.

EXPERIMENTS AND RESULTS: We demonstrated a multilayer interferometer for pulsed cold neutrons at the beamline 05 NOP in J-PARC MLF [5]. Figure 1 shows the interference fringes with etalons according to time-of-flight. The phase of interferogram depends on the wavelength of neutrons. We also demonstrated the measurements of neutron coherence scattering length of some nuclei. The better stability of the measurements was demonstrated.

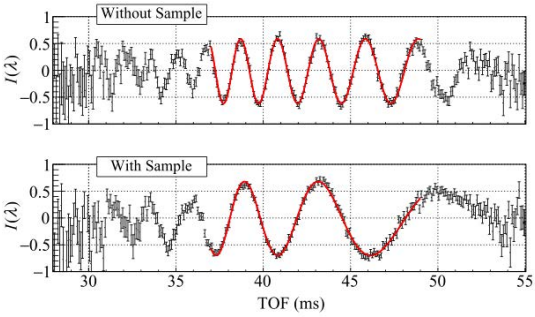

Fig. 1. Interference fringes without and with sample. The phase was changed due to the refraction index of the material.

In order to enlarge the number of neutrons, neutron supermirrors which can reflect wide bandwidth of wavelength were developed for interferometer by using Ion Beam Sputtering facility in KURNS. Figure 2 shows the reflectivity of the half mirrors with wide bandwidth. We tried to utilize the mirrors into the interferometer. The geometrical arrangement of the interferometer was confirmed, however, the interferogram was not observed. It is considered that this was due to deformation of the mirror substrates and non-uniformity of the mirror thickness. The results suggested that uniformity of better than a few percent is required. We are continuing to research and develop the neutron mirrors for the interferometer.

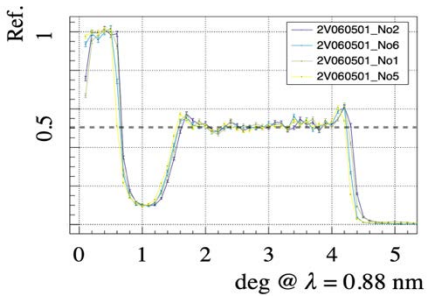

Fig. 2. Reflectivity of the half mirror with wide band of neutron wavelength measured at MINE2 in JRR3.

REFERENCES:

[1] H. Rauch and S. Werner, Neutron Interferometry Ox-ford University Press, Oxford, 2000.
[2] H. Rauch, W. Treimer, and U. Bonse, Phys. Lett., **47A** (1974) 369.
[3] M. Kitaguchi, *et.al.,* Phys. Rev., A **67** (2003) 033609.
[4] Y. Seki, *et. al.,* J. Phys. Soc. Jpn., **79** (2010) 124201.
[5] T. Fujiie, *et. al.,* Phys. Rev. Lett., **132** (2024) 23402.

CO1-4

Development of efficient spin filters for ultracold neutrons

T. Higuchi[1], M. Hino[1], S. Kawasaki[2], M. Kitaguchi[3]

[1]*Institute for Integrated Radiation and Nuclear Science, Kyoto University*
[2]*Institute of Particle and Nuclear Studies, KEK*
[3]*Kobayashi-Maskawa Institute for the Origin of Particles and the Universe, Nagoya University*

INTRODUCTION: A finite electric dipole moment (EDM) of the neutron implies violation of time-reversal symmetry, and has been searched since 1950s. Searches for a non-zero neutron EDM in high sensitivity constitute stringent tests of theories beyond the Standard Model of particle physics and shed light in the mystery of baryon asymmetry of the universe. In the state-of-the-art neutron EDM experiment, spin-precession frequencies of ultracold neutrons (UCNs), neutrons with kinetic energies on the order of 300 neV or less, are compared under different electromagnetic configurations. One of the key components required for neutron EDM experiments is spin analyzer of UCNs, whose efficiency directly impacts the precision of the spin-precession frequency measurement, thus the sensitivity of the neutron EDM search. Because of extremely low energies of UCNs, magnetized Fe thin films with small coercivities can be used as effective UCN spin analyzers, functioning as filters that selectively transmit the high-field seeking state of UCNs. In this project at the Institute for Integrated Radiation and Nuclear Science, Kyoto University, we have developed sputtered thin Fe films produced with KUR-IBS [1], whose performance have been tested with a cold neutron beam at JRR-3/MINE2, and with pulsed UCNs at J-PARC/MLF.
****

EXPERIMENTS: During the FY2023, we have applied a new method of Fe sputtering and succeeded in producing Fe film that has significantly small magnetic coercivities than what has been previously developed by ourselves. The coercivity H_c as measured by vibrating sample magnetometry has been reduced from about 20 Oe to 9 Oe, this enables us to design a UCN spin analyzer with small stray magnetic fields, which has numbers of practical merits for building the system including magnetically sensitive components. The new films have been tested with cold and ultracold neutrons during the FY2023. For the test at MINE2, we newly constructed a polarized neutron reflectometry setup with a dedicated θ-2θ stage.
****

RESULTS: The results of polarized neutron reflectometry measurements of the new Fe film as compared to the previously developed film is shown in the figure. The new film is demonstrated to function as a neutron spin filter at a smaller magnetic field than the previously developed one.
****

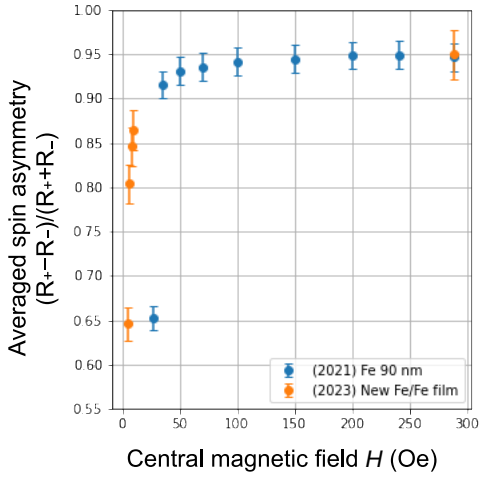

Fig. 1. Results of polarized cold neutron reflectometry at MINE2. Averaged spin asymmetry derived from neutron reflectivity of different neutron spins. The new film developed in 2023 functions as a high performance spin analyzer at a smaller applied magnetic field than the previously developed Fe film. The absolute spin asymmetry is limited by the beam polarization.

REFERENCES:

[1] M. Hino *et al.*, Nucl. Instr. and Meth. A, **797** (2015) 265.

CO1-5

Development of Cold/ultracold Neutron Detector Using Nuclear Emulsion

N. Naganawa, H. Ekawa[1], M. Hino[2], N. Muto and M. Nakagawa[1]

Institute of Materials and Systems for Sustainability, Nagoya University
[1]High Energy Nuclear Physics Laboratory, Cluster for Pioneering Research, RIKEN
[2]Institute for Integrated Radiation and Nuclear Science, Kyoto University

INTRODUCTION: We have been developing a cold/ultracold neutron detector using nuclear emulsion for measuring spatial distributions of ultracold neutrons in the Earth's gravitational field [1, 2]. It was fabricated by sputtering a thin layer of $^{10}B_4C$-NiC-C on a silicon substrate and coating it with a fine-grained nuclear emulsion [3]. It is also possible to be used for neutron imaging [4, 5]. For high-spatial-resolution imaging, capability of accumulating tracks with high density is im-portant. In the study in ref. [5], saturation of degree of blackening was observed when track density was more than 3×10^4 tracks/(100 μm)^2. In this study, we attempted to avoid the saturation by re-ducing the thickness of the emulsion layer of the detector and shortening tracks.

EXPERIMENTS:

Detectors were fabricated by sputtering thin layers of $^{10}B_4C$(1 μm)-NiC-C on 0.4 mm-thick silicon plates and coating the substrate with the emulsion. The sputtering was done at KURRI by an ion beam sputterer (KUR-IBS) [6]. The coating was done at Nagoya University with two different thickness of usual 10 μm and very small 0.3 μm. Four samples for each were produced. They were exposed to neutrons with wavelength of 0.2 nm at 20 cm downstream of the neutron guide tube in CN-3 beam line. Detection efficiency of the detectors were 1% from the thickness of $^{10}B_4C$ layers and the wavelength. Exposures were conducted with four different times and track density as shown in Table 1. Neutron flux of the beam was 7.6×10^5 n/cm^2/s when thermal power of the reactor was 1 MW.

Table 1. Sample IDs, thickness of emulsion layer, exposure time and accumulated density of tracks.

sample IDs and emulsion thickness		exposure time and thermal power	track density [/(100 μm)^2]
10 μm	0.3 μm		
A-1	B-1	0.37 h (1 MW)	1×10^3
A-2	B-2	3.7 h (1 MW)	1×10^4
A-3	B-3	7.0 h (1 MW) + 6.0 h (5 MW)	1×10^5
A-4	B-4	42 h (1 MW) + 6.0 h (5 MW)	2×10^5

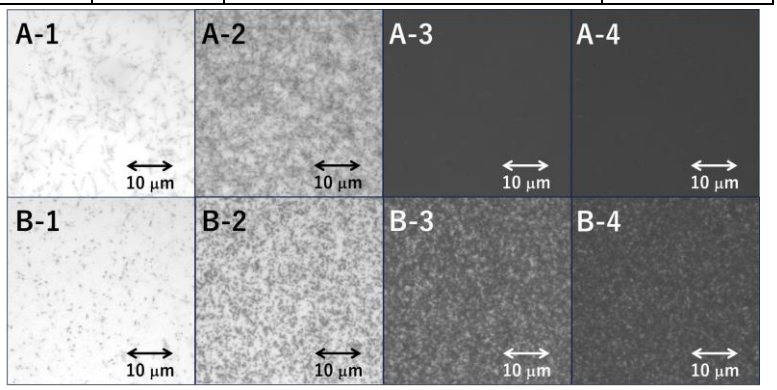

Fig. 1. Micrographs of emulsion samples. Views of A-3 and A-4 were filled with tracks, and degree of blackening saturated, which was not the case in B-3 and B-4.

RESULTS: After the exposure, samples were developed at Nagoya University. Their micrographs (Fig. 1) were taken under a manual optical microscope with an epi-illumination system. All of them were taken with the same illumination condition. From comparison between A-1 and B-1, it was seen that tracks were successfully shortened by thinning the emulsion layer. Furthermore, the saturation was not seen in B-3 with exposure density higher than 3×10^4 tracks/(100 μm)^2.

REFERENCES:

[1] N. Naganawa., Eur. Phys. J. C., **78** (2018) 959.
[2] N. Muto *et al.,* JINST, **17** (2022) P07014 .
[3] T. Asada *et al.,* Prog. Theor. Exp. Phys., **2017(6)** (2017) 063H01.
[4] K. Hirota *et al.,* J. Imaging, **7(1)** (2021) 4.
[5] A. Muneem *et al.,* J. Appl. Phys., **133** (2023) 054902.
[6] M. Hino *et al.,* Nucl. Instrum. Methods Phys. Res. A, **797** (2015) 265–270.

CO1-6

High-temperature test for BGaN semiconductor neutron detectors

S. Okita, T. Sakurai[1], R. Kudo[1], K. Takagi[2], T. Nakano[1] and M. Hino[3]

HTGR project management office, JAEA
[1]*Electronics and Materials Science Department, Shizuoka University*
[2]*Research Institute of Electronics, Shizuoka University*
[3]*Institute for Integrated Radiation and Nuclear Science, Kyoto University*

INTRODUCTION: The BGaN semiconductor neutron detectors are currently under development at Shizuoka University as promising compact and high-temperature resistant neutron detectors [1]. In this study, we conduct a preliminary experiment to confirm the operability of the BGaN semiconductor neutron detectors in high-temperature environments. Furthermore, through this experiment, technical issues are identified for future development.

EXPERIMENTS: In this experiment, we observe the pulsed detection signals for thermal neutron beams irradiated to the BGaN semiconductor neutron detectors installed on a high-temperature hot plate. A picture of the experimental set-up is shown in Fig. 1. The BGaN semiconductor detectors are connected to preamplifier devices (CSP02, ANSeeN Inc.) through high-temperature resistant MI cables, and then, the pulsed signals processed in the preamplifier devices are discriminated at each wave height and rise time in a multi-channel analyzer (ZMCAN-CH04, ANSeeN Inc.). Voltage is applied to the detectors with DC stabilized power supply devices (PA250-0.25A, KENWOOD Co., and PA600-0.1B, TEXIO Technology Co.) In parallel, the waveform of the electrical signals is monitored with an oscilloscope (MSO5074, RIGOL Technologies Inc.). This experiment is performed in the cold neutron beam line (CN-3) [2] in KUR, which has relatively low background noise and can irradiate low-energy neutrons for sensitive detection. Two BGaN semiconductor neutron detectors are irradiated at the same time, and hot plate temperature is set to 300°C. For convenience, they are referred to as Detector 1 and Detector 2 in order from the upstream of the beamline, respectively. Measurement condition is summarized in Table 1.

Fig. 1 A picture of the experimental set-up.

Table 1 Measurement condition

Items	Detector 1	Detector 2
Type	p-up	p-up
BGaN layer thickness	5 μm	3.5 μm
Diameter of electrodes	500 μmφ	500 μmφ
Voltage	75 V	20 V
Reactor power	5 MW	

RESULTS: As shown in Fig. 2, clear pulsed detection signals were successfully found several times per hour for both detectors. The rise time of the pulse is set to the origin (0μs). This pulsed signal is presumably attributed to neutron-induced reaction in the BGaN layer because the signal is sufficiently large compared to the surrounding electrical noise, and the rising time of the pulse is sharp. These results suggest that the BGaN semiconductor neutron detectors demonstrate the operability at around 300°C at least.

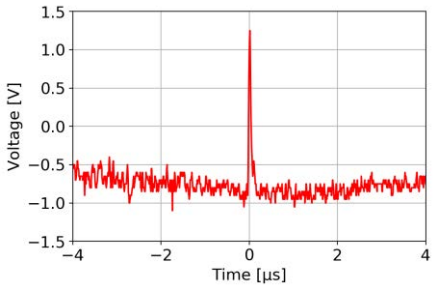

Fig. 2 Voltage time variation around a pulsed detection signal of the BGaN semiconductor neutron detectors.

ACKNOWLEDGEMENT: This study was supported by MEXT Innovative Nuclear Research and Development Program (JPMXD0221459236).

REFERENCES:

[1] T. Nakano *et al.*, J. Appl. Phys., **130** (2021) 1245-1 .
[2] K. Kawabata *et al.*, Physica B, **311** (2002) 106-111.

CO2-1

Neutron resonance analysis technique in neutron time-of-flight for shielded nuclear materials

F. Rossi[1], J. Lee[1], Y. Kodama[1], Y. Yoshimi[1], K. Hironaka[1], M. Koizumi[1], J. Hori[2], T. Sano[3] and Y. Matsuo[3]

[1]*Integrated Support Center for Nuclear Nonproliferation and Nuclear Security, Japan Atomic Energy Agency*
[2]*Institute for Integrated Radiation and Nuclear Science, Kyoto University*
[3]*Atomic Energy Research Institute, Kindai University*

INTRODUCTION: The Japan Atomic Energy Agency is developing various active neutron interrogation techniques [1] to supplement safeguard verifications. Neutron resonance analysis aims to combine the neutron resonance transmission analysis [2,3], together with the neutron resonance capture analysis [3,4] and the newly proposed neutron resonance fission neutron analysis (NRFNA) [5]. In a NRFNA method, using a pulsed neutron beam with the neutron time-of-flight (TOF) technique, prompt capture gamma rays and fast fission neutrons from fissile nuclides are measured at the sample location. The use of plastic scintillators with good n/γ pulse shape discrimination (PSD) is necessary to distinguish fission neutron events from gamma ray events. In this paper, we report a demonstration experiment for shielded nuclear materials performed at KURNS-LINAC.

EXPERIMENTS: The KURNS-LINAC was operated with an acceleration energy of ~30 MeV, and an average current of ~42 μA. Pulsed neutrons were produced with a repetition rate of 50 Hz and a pulse width of 2 μs. Natural uranium samples of 1.5, 3.0, and 6.0 mm thickness were placed in lead (Pb), polyethylene (PE), and borated polyethylene (B-PE) boxes. Each box has external dimensions of 7x7x7 cm^3 with a wall thickness of 2 cm. Six hexagonal PSD plastic scintillation detectors (Eljen, EJ-276) surrounded by lead shielding were used for NRFNA. The setup used is shown in Fig. 1, for the case of the Pb shielding box. The output signals of the detectors were sent to the CAEN digitizer V1730D (14bit, 500MSample/s); the data were recorded in list mode with 1h autosave.

RESULTS: Obtained data are being analyzed by the PSD technique [5]. Fig. 2 shows the TOF spectra of a 3.0 mm natural uranium sample inside the Pb box. In the gamma-ray spectrum, resonance peaks from ^{238}U(n,γ) reaction are clearly visible at 6.67, 20.87 and 30.68 eV; in the neutron spectrum, the characteristics peaks from ^{235}U(n,f) reaction are observed at all energies from 1 to 35 eV. Similar results can also be achieved with smaller sample. This shows a possibility to identify fissile nuclides in heavy material shielding container. Further analyses are ongoing to quantify the fissile content.

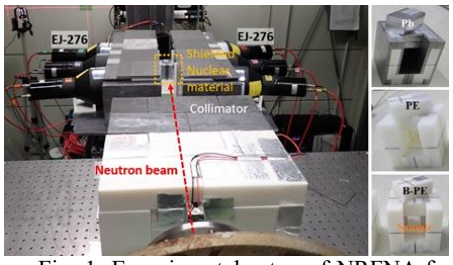

Fig. 1. Experimental setup of NRFNA for shielded materials (Pb, PE, and B-PE).

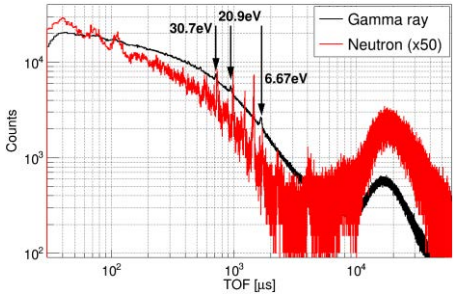

Fig. 2. TOF spectra of 3 mm natural uranium in Pb shielding.

ACKNOWLEDGEMENTS: This research was implemented under the subsidy for "promotion of strengthening nuclear security and the like" of the MEXT (the Ministry of Education, Culture, Sports, Science, and Technology of the Japanese government).

REFERENCES:

[1] M. Koizumi *et al.*, INMM&ESARDA (2021) 201.
[2] P. Schillebeeckx *et al.*, Nuclear Data Sheets (2012) 113.
[3] H. Postma *et al.*, Neutron Resonance Capture and Transmis-sion Analysis (2009).
[4] H. Postma *et al.*, J. Radioanal. Nucl. Chem., (2006)
[5] K. Hironaka *et al.*, NIM-A, **1054** (2023) 168467.

CO2-2

Neutron Activation Analysis for High-Purity Niobium Compound and Metal

H. Fujioka, S. Oikawa, K. Takamiya[1]

Department of Physics, Tokyo Institute of Technology
[1]Institute for Integrated Radiation and Nuclear Science, Kyoto University

INTRODUCTION: Unlike typical atomic nuclei composed of both protons and neutrons, multi-neutron systems, especially tetraneutron, have attracted much attention [1]. We have been searching for tetraneutrons (^{4}n), which might be emitted in thermal fission of uranium, by means of the activation method. When we insert a sample containing a nuclide, ^{A}Z, into a reactor, tetraneutrons may interact with a nucleus and produce an isotope, $^{A+3}$Z, by the ^{A}Z(^{4}n,n) reaction. If the isotope $^{A+3}$Z is unstable and emits γ-rays after β decay, the amount of $^{A+3}$Z after the irradiation can be evaluated by γ-ray spectroscopy. This method resembles the neutron activation analysis, except for the reaction.

In the first irradiation experiment, we used ^{88}Sr-enriched strontium carbonate, and determined an upper limit of the emission rate of tetraneutrons in uranium fission [2]. We learned that a silica tube which was used to confine powder of strontium carbonate was a large source of background in the obtained γ-ray spectrum. To avoid using a sample in powder form, we have decided to focus on a different element. The target nucleus ^{A}Z should be chosen carefully, based on the neutron capture cross section and the half-life of $^{A+1}$Z, both of which directly affect the radioactivity of the sample after irradiation, and the half live of $^{A+3}$Z, as well as the chemical properties and the purity of the sample. A mononuclidic element is suited in view of the availability of a high-purity sample, and niobium will be one of the promising elements meeting the aforementioned criteria.

EXPERIMENTS: We prepared three kinds of niobium samples: (1) niobium pentoxide (Nb_2O_5), (2) and (3) niobium metals from different companies. In general, niobium metal contains tantalum, whose chemical properties are similar to those of niobium. On the other hand, niobium pentoxide does not contain tantalum. However, As niobium pentoxide was in powder form, we made a pellet by using a press machine so as to avoid using a silica tube. We irradiated samples at the pneumatic tube Pn-2 and the hydraulic conveyer Hyd in order to investigate the γ-rays emitted from the activated sample, which are mainly due to impurities in the samples. This measurement is important in determining a detailed plan of the next search experiment of tetraneutrons with a longer irradiation time.

PRELIMINARY RESULTS: Figure 1 shows the γ-ray spectra for the three samples. As expected, photopeaks from tantalum are seen for samples (2) and (3). Moreover, the background level is comparable between them, while that of sample (1) is sizably larger. A detailed analysis is in progress.

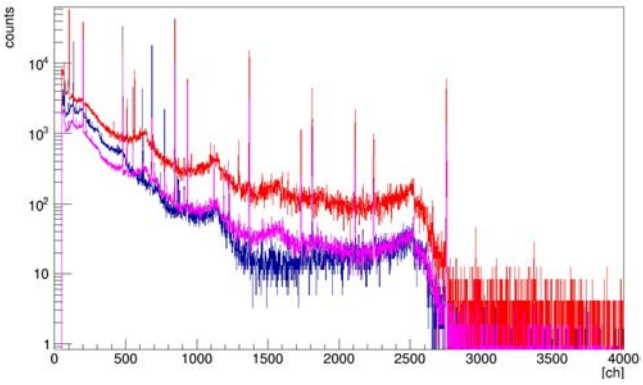

Fig. 1 γ-ray spectra for the three samples [(1): red, (2): blue (3): magenta]. The spectra are normalized for 1 gram of niobium.

REFERENCES:

[1] F. Miguel *et al.,* Eur. Phys. J. A, **57** (2021) 105.
[2] H. Fujioka *et al.,* Phys. Rev. C, **108** (2023) 054004.

CO2-3

Development of thimble-type ionization chamber for an intense epi-thermal neutron beam

T. Matsumoto[1], A. Masuda[1], S. Manabe[1], H. Harano[1], K. Terada[2] and J. Hori[2]

[1]*National Metrology Institute of Japan, National Institute of Advanced Industrial Science and Technology*
[2]*Institute for Integrated Radiation and Nuclear Science, Kyoto University*

INTRODUCTION: The need to ensure traceability to neutron standards at AIST for hospitals performing boron neutron capture therapy (BNCT) has been discussed. For this purpose, we are developing a real-time detector that can measure high-intensity neutrons used in BNCT. It is required that the detector can measure neutrons in appropriate measurement time at standard neutron fields whose fluxes are 4 to 5 orders of magnitude lower than those at BNCT as well.

EXPERIMENTS: A thimble type ionization chamber was developed as a neutron detector for high intensity neutrons. The ionization chamber is made of aluminum and has a dome shape with a diameter of 13 mm and a length of 15 mm. An aluminum needle-shaped electrode with a diameter of 1 mm is set in the center. The chamber was filled with a mixture of ^{3}He gas (0.5 atm) and Ar gas (1.4 atm). Characterization of the ionization chamber was performed using a pulsed white neutron source produced using an electron linac at the Institute for Integrated Radiation and Nuclear Science of the Kyoto University. The ionization chamber measured neutrons by two-dimensional measurements of neutron time-of-flight (TOF) and pulse height. In addition, in the current output mode, the measurement was performed by varying the applied voltage for the neutrons.

RESULTS: Figure 1 shows a TOF spectrum obtained from the ionization chamber in the pulse mode. Neutron components were successfully observed using the ionization chamber. Figure 2 shows the relation between the applied voltage and output current from the center electrode in the current mode. This figure indicate that the ion saturation region and proportional region are successfully obtained. However, signal to noise ratio was insufficient. In the future, we will evaluate the detection efficiency and stability. In addition, it is necessary to accumulate data for various gas mixing patterns to improve S/N.

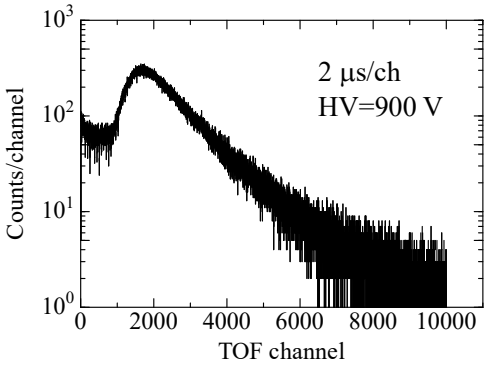

Fig. 1. TOF spectrum for the pulsed neutron source obtained from the electron linac. The thermal bump was clearly observed.

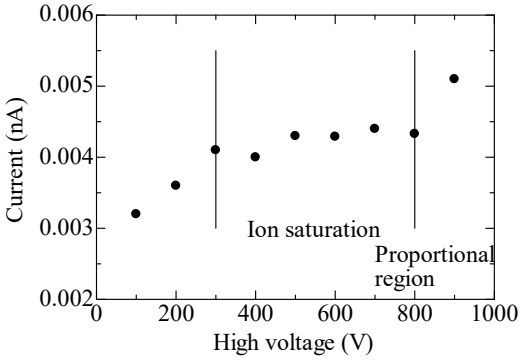

Fig. 2. Relation between applied voltage and output current.

REFERENCES:

[1] K. Kobayashi *et al.,* Annu. Rep. Res. Reactorinst. Kyoto Univ. **22** (1989) 142.

This work was supported by JSPS KAKENHI (21H03755 and 19K12638).

CO2-4

Identification of β-delayed γ and x-rays of ^{157}Nd using an Isotope Separator On-Line KUR-ISOL

M. Shibata, S. Sakakibara[1], T. Kuga[1], K. Abe[2] and A. Taniguchi[3]

Radioisotope Research Center, Nagoya University
[1]Graduate School of Engineering, Nagoya University
[2]School of Engineering, Nagoya University
[3]Institute for Integrated Radiation and Nuclear Science, Kyoto University

INTRODUCTION: The decay data of the fission products are important for nuclear engineering and nuclear physics. We have focused on the decay studies of A~150 region because of few decay information due to their short half-lives and low fission yields. Continuing from last year, we conducted study on the decay of ^{157}Nd to identify β-delayed γ-rays and KX-rays. The half-life of ^{157}Nd with β-counting and the level scheme of ^{157}Pm had been proposed in ref.[1,2], respectively. In August last year, the β-delayed γ-rays and a decay scheme using an on-line mass separator for ^{252}Cf spontaneous fission [3] have been proposed for the first time ahead of us. In this experiment, the β-delayed KX-ray was identified although there was less information on γ-rays than ref.[3].

EXPERIMENTS The amount of 72mg of 93% enriched $^{235}UF_4$ target was installed in the through-hole facility in Kyoto University Reactor. The nuclei of interest were produced by thermal neutron-induced fission and mass-separated with KUR-ISOL. They were collected on a computer-controlled thin Mylar tape and transported to the measurement position periodically. The clover detector, which has four large Ge crystals (80 mmø×90 mmL) and a through hole 15 mmø, and two semi-cylindrical β-particle detectors made of plastic scintillator set in the through-hole were used for β-γ coincidence measurements. The detectors were shielded with 10 cm thick lead and boron-doped polyethylene bricks to reduce the background radiation. Data were recorded on APV data acquisition systems (Techno AP Co.) with list mode including time information. The time interval of collection-measurement was set at 3 s-3 s, respectively.

ANALYSIS and RESULTS: To determine the half-lives, the measured data were reconstructed to each 0.5 s spectra to analyze with spectrum multi-scaling (SMS). Fig.1 shows the typical decay curves of the 66 keV γ-rays. The half-life was determined 1.2(5) s, approximately. The half-lives of the 255 and 1703 keV γ-rays also agree the value of ref.[3] with in the uncertainty. In KX-ray region, Sm KX-ray of the daughter nuclide were intensively observed than Pm KX-ray. Then the decay curves were analyzed with the time differential spectra of each 1 s. As shown in Fig.2, the Pm KX-ray was certainly observed in the first differential spectrum and almost disappeared in the next differential spectrum. The Pm KX-ray is considered to decay with about 1 s associated with the β-decay of ^{157}Nd. In these analyses, the three γ-rays and Pm KX-ray were identified as the β-delayed γ-rays and KX-ray with the half-life of about 1 s.

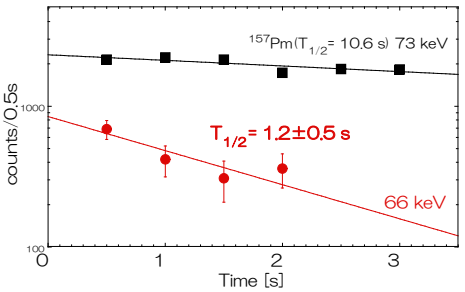

Fig. 1. Decay curve of the 66 keV γ-ray.

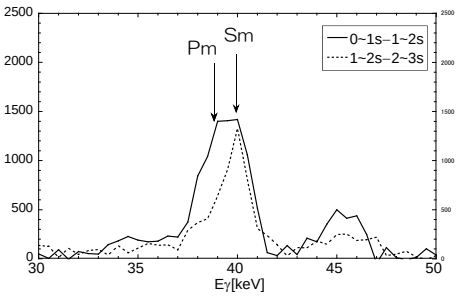

Fig. 2. The X-ray region of the time differential spectra.

REFERENCES:

[1] J. Wu *et al.*, Phys. Rev. Lett., **118** (2017) 072701.
[2] S. Bhattacharyya *et al.*, Phys. Rev., **C98** (2018) 04316.
[3] D. J. Hartley *et al.*, Phys. Rev. C, **108** (2023) 024307.

CO2-5

Experimental study on photo-neutron reaction of uranium by bremsstrahlung photons

H. Sagara[1], K. Tanabe[1], K. Krittanai[1], J. Hori[2], Y. Takahashi[3], K. Terada[2],

[1] *Tokyo Institute of Technology*
[2] *Kyoto University*

INTRODUCTION: Due to the social demands to enhance the nuclear security, non-destructive assay technology has been developed for detect the unauthorized transfer of nuclear material especially highly enriched uranium(HEU) by utilizing the photo-fission signals induced by bremsstrahlung photons [1]. Based on the numerical analysis, it was suggested the feasibility of HEU detection by different energy of bremsstrahlung photons with 7 MeV and 13.5 MeV injected electrons to the Ta target[1]. For the validation of the proposed principle, the experimental study has been started to detect the photo-neutrons signals from uranium target by using the bremsstrahlung photons produced by LINAC accelerator. In the fiscal year 2023, the preliminary experiments were performed for detector characterization and background noise reductions to clarify the experimental set-up requirement for uranium photo-neutrons signals.
****

EXPERIMENTS: The LINAC electron beam energy was set as 13, 18, and 30MeV, and multiple target materials were examined such as natural uranium, lead, Iron and void. To detect the photo-neutron signals, liquid scintillator for gamma-neutron co-counting, He-3 tube detectors with poly-carbonate neutron moderator and Cd filter were installed. For the background noise reduction by the photo-neutron reaction by structure materials or others, the Cd and Poly-Block with B were introduced in the beam duct between the LINAC electron target room to the measurement room. As for the reference data, Cf-252 standard source was measured by the set-up detectors. The measurements were performed
****

RESULTS: As preliminary results, the detector response of liquid scintillator and He-3 tube were well examined and found their detectability under the bremsstrahlung photon beam irradiation to the target materials(*Fig*. 1). The comparison between the target materials of uranium, lead and irons suggested the different the neutron detection responses. More data analysis and parametric studies will be needed to examine the photo-neutron reactions especially for uranium targets. As for the background noise reduction, the installation of neutron absorbers of Cd filter or Poly-Block with B in the beam duct have not shown the significant background neutron reduction, more analysis is needed including the effect of other structure materials. As a summary, we could achieve the fundamental data for planning the next experiments.
****

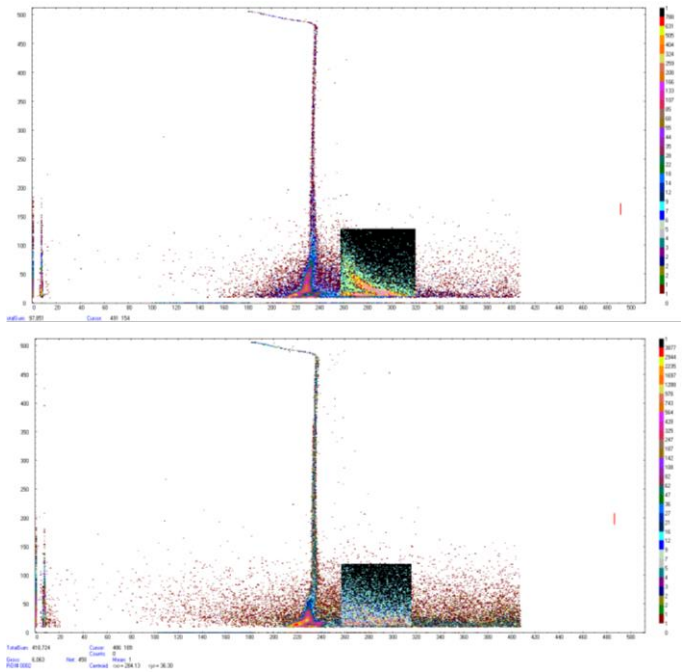

Fig. 1 Liquid Scintillator Response (Up: Cf-252 Neutron Source, Down: Bremsstrahlung photon irradiation to NU, Black area: ROI for neutrons)

REFERENCES:

[1] K.W.Chin *et al.,* Annals of Nuclear Energy, **158** (2021) 108295.

CO2-6

Validation Experiment of Thermal Neutron Scattering Law Data for Innovative Reactor

J. Hori, K. Terada, T. Takahashi, H. Yashima and T.Sano[1]
Institute for Integrated Radiation and Nuclear Science, Kyoto University
[1]*Atomic Energy Research Institute, Kindai University*

INTRODUCTION: Small modular reactors (SMRs) with a solid hydride moderator have been studied [1]. Improvement of accuracy of thermal neutron scattering law (TSL) data of candidate solid moderators such as Zirconium-hydride (ZrH_2) and Calcium-hydride (CaH_2) is required for developing innovative reactor system. Therefore, the project entitled as "Development of Nuclear Data Evaluation Framework for Innovative Reactor" has been carried out. In the project, we preformed the integral experiments to validate TSL data of JENDL-5 using a pulsed neutron source.

EXPERIMENTS: The experiment was performed at the Institute for Integrated Radiation and Nuclear Science, Kyoto University (KURNS-LINAC). Pulsed fast neutrons from the photo neutron source were produced without neutron moderator. A beam width and a frequency were 5 μs and 50 Hz, respectively. The flight path used in the experiment is in the direction of 135 degrees to the electron beam. The pulsed neutron beam was collimated to 30 mm in diameter.

Each sample assembly was placed at about 10 m from the neutron source. The cylindrical containers made of aluminum 60 mm in diameter and 55 mm in height and were filled with powders of ZrH_2 or CaH_2. The weights of ZrH_2 and CaH_2 were 476 g and 150 g, respectively. The neutron spectrum by slowing-down in the sample was measured by a ^{6}Li-glass detector with a TOF method. The distance between the center of the container and the surface of the detector was 30 cm. The net thermal neutron spectrum was obtained from the difference between TOF spectra with and without Cd sheet of 0.5 mm thickness around the cylindrical container.

RESULTS: The comparison of the net experimental thermal neutron spectrum with the calculated ones using JENDL-5 [2] for ZrH_2 sample is shown in Fig. 1. The calculations were performed by the Monte Carlo simulation code MCNP-6.3 considered with and without the S(α,β) effect. The thermal bump was observed in about 65 μs of the calculation results with the S(α,β). The experimental values almost supported the calculation with the S(α,β) of JENDL-5.

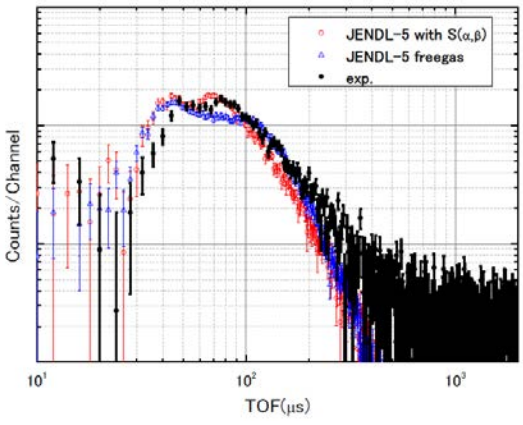

Fig. 1 Comparison of the experimental thermal neutron TOF spectrum with the calculated ones for ZrH_2 sample.

The present study includes the result of "Development of Nuclear Data Evaluation Framework for Innovative Reactor" founded by the Ministry of Education, Culture, Sports, Science and Technology of Japan.

REFERENCES:

[1] R. Kimura *et al.,* Proc. ICAPP2019, Juan-les-pine, France, May 12-15, (2019) 083.
[2] O. Iwamoto *et al.,* J. Nucl. Sci. Technol., **60(1)** (2023) 1-60 .

CO2-7

Neutron cross-section measurement of molybdenum

Y. Takahashi, J. Hori, K. Terada

Institute for Integrated Radiation and Nuclear Science, Kyoto University

INTRODUCTION: Kyoto University Critical Assembly (KUCA) is currently preparing to use a new reactor fuel using uranium-molybdenum (UMo). This is the first reactor in the world to use this fuel, and it is expected to be used as a research reactor fuel worldwide in the future. In the core analysis of a reactor using UMo fuel, the reliability of nuclear data has been sufficiently confirmed for conventional uranium-aluminum alloy fuel, but core analysis using UMo fuel, especially molybdenum, is not sufficient, and it is necessary to improve the nuclear data of molybdenum.

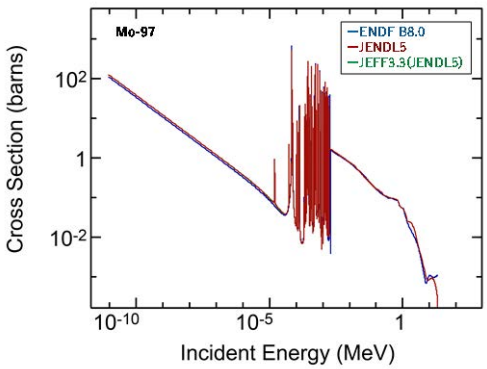

Fig. 1. Cross-section of Mo-97

In fact, when Mo-97 in JENDL5 and ENDF/BVIII are compared shown in Fig.1, there are some different points are observed. Therefore, this study aims to contribute to the improvement of nuclear data of molybdenum by measuring cross sections using a KURNS-Linac for some molybdenum nuclides with a view to upgrading the core analysis of KUCA.

EXPERIMENTS: In this experiment, natural Mo plate of different thickness were used as samples for the preliminary test. The thickness of Mo plate were 0.5 mm, 1.0 mm and 3.0 mm, and size were 18 x 18 mm. The samples for TOF method were set at the 90 degree and 10 m distance from the target. The target was surrounded by pack-man type water moderator. A BGO scintillator (2 inch diam. and 2 inch long) was used for measuring total energy absorption gamma-rays and set at 122 mm from the sample. Only LiF plate was set in front of the detector for neutron shield and no other shield was set. The conditions of the accelerator were as follows: short mode, average beam current was 16.7 μA, frequency was 50 Hz and pulse width was 100 ns. The size of beam is 50 mm diameter.

RESULTS: Fig. 2 shows the TOF measurement results for three different sample thicknesses. Each measurement result is normalized by the measurement time. One channel in this figure corresponds to 100 ns. As an example of the experimental results, there was no large difference in the resonance peak value of 44 eV with increasing thickness. This indicates that $n\sigma_{tot}$ is large enough to saturate the resonance capture due to the neutron self-shielding effect in the sample.

In the future, we plan to conduct cross-section measurement experiments using thinner samples by selecting appropriate sample thicknesses by preliminary calculations.

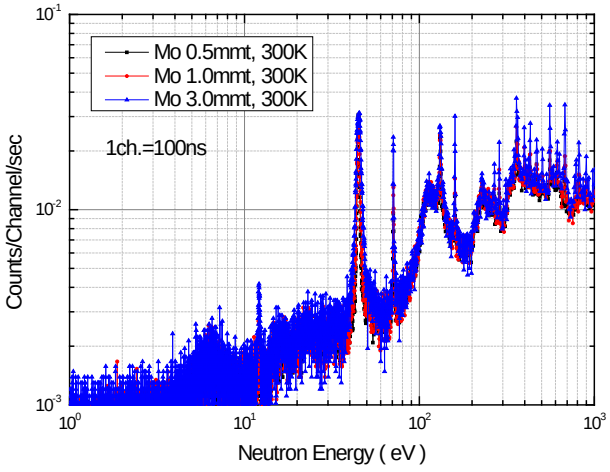

Fig. 2 Result of TOF

CO2-8

Measurement Neutron Reaction Rate Ratio using the TOF method in the KURNS-LINAC

T. Sano, Y. Matuo, Y. Takahashi[1], K. Terada[1], H. Yashima[1], J. Hori[1] and H. Unesaki[1]

Atomic Energy Research Institute, Kindai University
[1]Institute for Integrated Radiation and Nuclear Science, Kyoto University

INTRODUCTION: In thorium fuel loaded nuclear reactor systems, it is important to have reliable evaluated nuclear data on the neutron capture reaction of the parent material Th-232 and the fission reaction of U-233. The authors have previously carried out differential experiments using the electron linear accelerator at the Institute for Integrated Radiation and Nuclear Science, Kyoto University (KURNS-LINAC) to measure the fission cross section of U-233 and the neutron capture cross section of Th-232. As a result, the followings have been observed from these measurements: 1) the U-233 fission cross section measurement, the experimental values are generally in good agreement with the JENDL-4.0 [1]. 2) the Th-232 neutron capture cross section measurements showed differences in the neutron widths of the 69 eV, 121 eV and 170 eV resonances compared to JENDL-4.0 [2]. On the other hand, these resonance parameters have not been revised in the latest JENDL-5 [3], released in December 2021. Therefore, in the present study, the Th-232 neutron capture cross section was remeasured.

EXPERIMENTS: The experiment was performed on the 12 m neutron flight path shown in Figure 1. The samples were Th-232 and B-10 for neutron flux measurement. Th-232 and its daughter nuclides emitted γ rays as background. To reduce the background γ rays, a 10-mm-thick piece of lead was placed between the Th-232 sample and the BGO detector. In the measurement of B-10 for neutron measurement, a single γ ray of 478 keV emitted by the (n,α) reaction between the B-10 sample and neutrons was measured, and the TOF information was observed with the Ta target in-cident of accelerated electrons as the start signal and the prompt gamma ray emitted by the reaction be-tween the sample and neutrons as the stop signal.

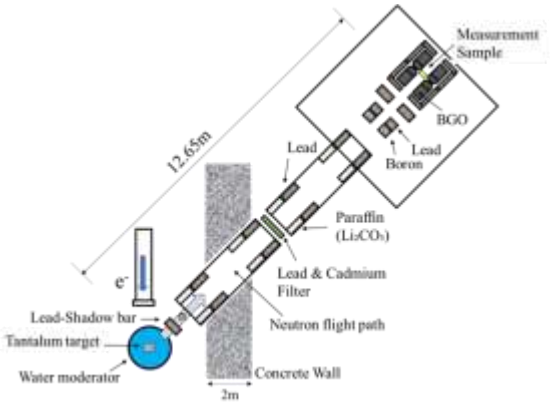

Fig.1 Experimental geometry

RESULTS: Figure 2 shows the observed TOF spectra (Th-232 sample and blank run). The TOF spectra in this figure have been processed for background and so on. The TOF spectra in this figure show that resonance is observed in the region above about 500ch (below 1 keV). In the next step, neutron capture cross section and resonance parameters will be to determine from the measured data.

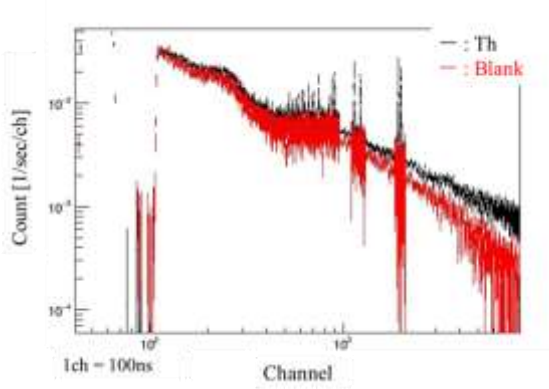

Fig.2 Obtained TOF spectrum

REFERENCES:

[1] K. Shibata *et al.,* J. Nucl. Sci. Technol., **48** (2011) 1.
[2] J. Lee *et al.,* Energy Procedia, **13** (2017) 106-311.
[3] O. Iwamoto *et al.,* J. Nucl. Sci. Technol., **60** (2023) 1.

CO2-9

Measurement of Neutrino Helicity using ^{152m1}Eu

K. Fujiki, Y. Hori, N. Nakamura, R. Shinoda, K. Kataoka[1], M. Kawaue[1], S. Kitao[2], Y. Kobayashi[2], J. Suzuki[1], O. Tajima[1], M. Tanigaki[2], A. Taniguchi[2],

Faculty of Science, Kyoto University
[1]Graduate School of Science, Kyoto University
[2]Institute for Integrated Radiation and Nuclear Science, Kyoto University

INTRODUCTION: Parity violation in the weak interaction was discovered in the beta decay process. Left-handed property (i.e., negative helicity) of neutrino is the origin of the parity violation. Another unique property of the neutrino is very small mass. We can interpret it as mass-less fermion in the most of decay processes, and we expect the helicity of -1 for the neutrino. Using a radio isotope irradiated in KUR, we measured the neutrino helicity to confirm this expectation.

EXPERIMENTS: This study was performed to measure the neutrino helicity by using neutrino emission process, $^{152m1}\mathrm{Eu} + e^- \rightarrow {}^{152}\mathrm{Sm}^* + \nu_e$. $^{152}\mathrm{Sm}^*$ promptly goes to the ground state with gamma-ray emission. Because $^{152}\mathrm{Sm}^*$ has non-zero momentum, the gamma ray energy to "forward" (or "backward") direction has approximately 1% higher (or lower) energy than the rest frame as illustrated in Fig. 1. We selected "forward" process using the similar setup as previous study [1]. The gamma ray loses its energy via the Compton scattering. In Sm_2O_3 scatterer, resonant interaction occurs when the gamma energy is equal to the excitation energy of ^{152}Sm, i.e., 963 keV. We measured the resonant gamma rays (841 keV or 963 keV) by using a scintillation counter. By changing the direction of magnetic field, we modulate the cross section of the Compton scattering with respect to the helicity.

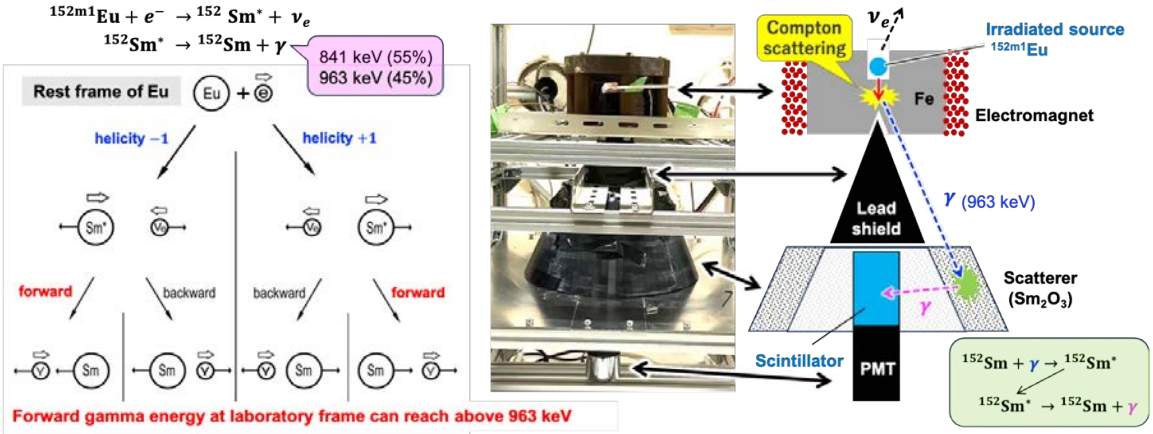

Fig. 1. Experimental principle and setup to measure the neutrino helicity.

RESULTS: Figure 2 shows measured asymmetry of the energy spectrum based on the modulation. This result favors negative helicity. The obtained helicity is –1.5 ± 0.9 which is statistically consistent with the previous study, –1.0 ± 0.3 [1].

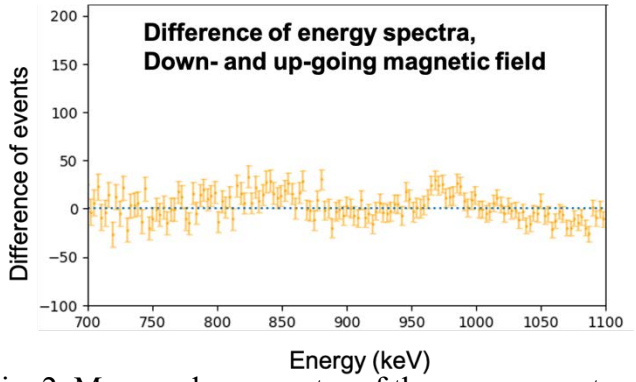

Fig. 2. Measured asymmetry of the energy spectrum.

REFERENCES:

[1] M. Goldhaber, L. Grodzins, and A. W. Sunyar, Phys. Rev., **109** (1958) 1015.

CO4-1

Effect of Soft X-rays on the Vacancy-type Defects in Highly Hydrogenated DLC Films

K. Kanda, T. Mishima, D. Niwa, F. Hori[1], A. Yabuuchi[2] and A. Kinomura[2]

Laboratory of Advanced Science and Technology for Industry, University of Hyogo
[1] *Department of Materials Science, Osaka Metropolitan University*
[2] *Institute for Integrated Radiation and Nuclear Science, Kyoto University*

INTRODUCTION: Diamond-like carbon (DLC) films are generally known to be highly resistant to X-ray irradiation. However, our group has reported that highly hydrogenated DLC (H-DLC) films with a hydrogen content greater than 40 at.% are modified by the irradiation. By the irradiation of soft X-rays to H-DLC film, the film volume and hydrogen content decrease and film hardness and $sp^2/(sp^2 + sp^3)$ ratio of carbon atoms increase [1]. However, it is not known how the free volume in DLC films is changed by soft X-ray irradiation. In this study, we prepared samples with different doses of white soft X-ray irradiation and performed positron annihilation spectroscopy (PAS) measurements using the slow positron beam apparatus. We measured how vacancy-type defects in H-DLC films are changed by soft X-ray irradiation and discussed the hydrogen desorption process of H-DLC films by soft X-rays in terms of vacancy-type defects.

EXPERIMENTS: H-DLC film used in this work was deposited on Si wafers using an amplitude-modulated radio-frequency plasma-enhanced chemical vapor deposition method (Nippon ITF Co.). The irradiation of the H-DLC film by SR was carried out at BL06 of the NewSUBARU synchrotron facility. The SR at the BL06 sample stage had a continuous spectrum from infrared to soft X-rays, below 1 keV. In this work, four samples were prepared at SR dose, 500 mA·h, 1000 mA·h, 4000 mA·h, and before irradiation. PAS measurements were performed using a slow positron beam system installed at the B-1 hole of the KUR. In the present study, we performed two kinds of PAS measurements, Doppler broadening and the positron annihilation lifetime spectroscopy.

RESULTS: The dependence of S-parameters and positron annihilation lifetimes (PAL) on soft X-ray dose is shown in Fig. 1. The positron lifetime increases with the soft X-ray dose. This means that the increase in density of H-DLC film due to soft X-ray irradiation is not due to a decrease in vacancy-type defect, but to a decrease in the composition ratio of hydrogen in the film.

On the other hand, the S-parameter was decreased by soft X-ray irradiation. In H-DLC films, the vacancy-type defect is considered to be almost entirely surrounded by hydrogen, which has only valence electron. Soft X-ray irradiation causes hydrogen around the vacancy-type defect to desorb, resulting in an increase in the size of the vacancy-type defect and an increase in PAL. On the other hand, desorption of hydrogen changes the atoms surrounding the vacancy-type defect to carbon. Since carbon has inner-shell electrons, the fraction of inner-shell electrons that annihilate with positrons is expected to increase, resulting in a decrease in the S-parameter.

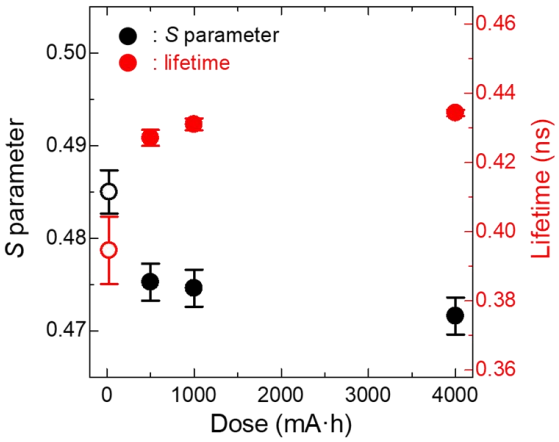

Fig. 1. The soft X-ray dose-dependence of S-parameter and PAL.

REFERENCES:

[1] K. Kanda *et al.,* Sen. Mater., **29** (2017) 817-826.

CO4-2

Hydrogen trapping behavior at vacancy in Fe-Al alloy with electron irradiation

F.Hori, S.Hirayama, J.Tian, K.Miyazumi, K.Ohsawa[1], Q.Xu[2], A.Kinomura[2], A.Yabuuchi[2], N.Abe[2] and K.Yasunaga[3]

Osaka Metropolitan University
[1]*Res. Inst. of Appl. Mech., Kyushu University*
[2]*Res. Reactor Inst., Kyoto University*
[3]*Wakasa-wan Energy Research Center*

INTRODUCTION: B2 ordered Fe-Al alloy is used as high strength at high temperature material because of its good properties such as specific strength to weight ratio, oxidation resistance. However, it is known that Fe-Al alloy with B2 ordered structure is easy to form vacancy and anti-site atom defects. These defects strongly affect the physical and mechanical properties. So far, we have investigated the nature of defect structures in B2 type Fe-Al alloy. On the other hand, the vacancy type defects in this alloy first principles calculation result indicate that not only one hydrogen atom but also several hydrogen atoms can be trapped in a single vacancy in B2 ordered Fe-Al alloy. However, the interaction between vacancies and hydrogen atoms in this type of Fe-Al alloy is not cleared yet. In this study, we have performed slow positron beam measurements for electron irradiated and hydrogen introduced $Fe_{50}Al_{50}$ alloys to estimate the hydrogen trapping state at a vacancy.

EXPERIMENTS: B2 ordered Fe-Al alloys with stoichiometric composition were prepared by arc melting method in argon gas atmosphere. Sliced samples with the thickness of 0.5 mm were annealed at 1273 K for 20 h and cool down to 973 K slowly and then quenched into water. These specimens were irradiated with 8 MeV electron up to the fluence of 4×10^{18} /cm^2 at KURRI, Kyoto University. Irradiation was carried out at about 330 K with temperature controlling water cooling system. After irradiation, hydrogen was injected by electrochemical method for 8, 16, 80 and 160 hours. These samples were examined by X-ray diffraction and positron annihilation Doppler broadening measurements by using slow positron beam at KURRI facility.

RESULTS: Fig. 1 shows the X-ray diffraction peak change of (211) plane after electron irradiation and hydrogen charging. The trends of peak shift due to vacancy generation and hydrogen absorption are opposite. This means that the strain introduced by the formation of vacancies due to electron irradiation was relaxed by the trapping of hydrogen within the vacancies. In addition, as the hydrogen charging time increases, the peak moves to a lower angle compared to that for before irradiation. This is thought to be due to trapping of multiple hydrogen atoms within the vacancy. Fig. 2 shows the depth profile of positron Doppler S parameter for each hydrogen charging time. As the charging time becomes longer, the S value decreases at a deeper position and the amount of decrease became larger. This result is consistent with the XRD results and suggests that multiple hydrogen atoms may be trapped within one vacancy.

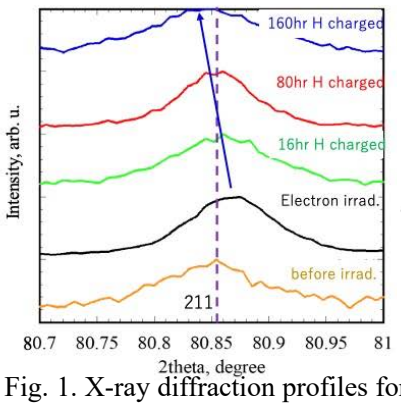

Fig. 1. X-ray diffraction profiles for electron irradiated and hydrogen absorbed Fe-50%Al.

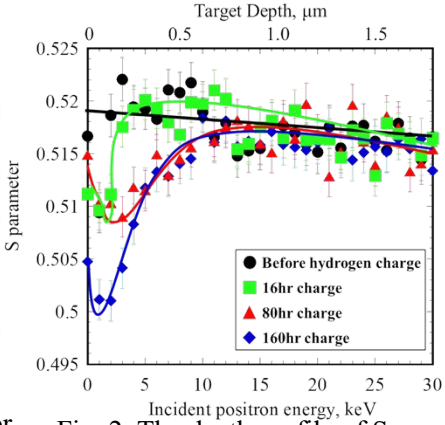

Fig. 2. The depth profile of S parameter for electron irradiation and hydrogen absorbed samples.

CO4-3

Structural Changes of Amorphous Germanium Oxide at Shock Compression

H. Araga, Y. Seto[1], Y. Umeda[2] and T. Okuchi[2]

Graduate School of Engineering, Kyoto University
[1]Graduate School of Science, Osaka Metropolitan University
[2]Institute for Integrated Radiation and Nuclear Science, Kyoto University

INTRODUCTION: The germanium oxide system has been widely studied at high-pressure conditions. This system is an ideal analog of silicate mineral systems, which are major components of terrestrial planets. Silicon and germanium are similar in their valence electron configuration, whereas the larger ionic radius of Ge^{4+} relative to Si^{4+} facilitates structural changes of the germanium oxides to increase their coordination numbers at lower pressures than the silicates. Understanding the structural changes of germanium oxides are thus important for understanding and predicting the high-pressure behavior of silicates within the planets.

The structure of amorphous GeO_2 consists of interconnected tetrahedra centered by Ge^{4+} with oxygen coordination number of 4 at ambient pressure. The coordination number gradually increases to 6 in the pressure range up to about 23 GPa under static compression [1]. Under shock compression, both amorphous and crystalline GeO_2 were also expected to have structural changes to increase their coordination number from 4 to 6. However, there have been few structural observations of recovered samples of GeO_2 after shock compression. In this study, therefore, we investigated the structure of shock-compacted amorphous GeO_2.

EXPERIMENTS: The starting sample was prepared by melting GeO_2 crystal powder of 99.999% purity at 1400 °C for 14 hours and at 1450 °C for 6 hours. The recovered sample was crushed and ground with a mortar and pestle made of tungsten carbide, and then pelletized and sealed into a sample container made of SUS304. Shock recovery experiments using these samples and containers were conducted using a single-stage explosive gun at the National Institute for Materials Science [2]. Two experiments were undertaken separately at peak pressures of 17 GPa and 19 GPa. After the sample containers were shock-compressed and recovered, they were cut using a metal blade. Then, one side of the sample was homogenized and analyzed using a powder X-ray diffractometer (Ultima IV). The other side of the sample was analyzed using a focused X-ray diffractometer (SmartLab 9kW) to resolve structures of several points of ~100 μm diameters that emerged on the cross-section surface.

RESULTS AND DISCUSSION: Fig. 1 shows the powder X-ray diffraction patterns before and after the compression. These samples consisted of 4-coordinated α-quartz-type and 6-coordinated rutile-type GeO_2 in addition to amorphous matrix. The peak intensity of the α-quartz type became stronger at 19 GPa; the growth of the α-quartz type was strongly affected by the peak pressure. The growth of the rutile type was much less sensitive to it. Such a difference suggested that the transformation pathways to the α-quartz type and the rutile type were independent and coexisted. Whereas the α-quartz type may be grown in a 4-coordinated amorphous structure in the remaining heat after the pressure release, the rutile type should only be grown in a 6-coordinated amorphous structure during the compression.

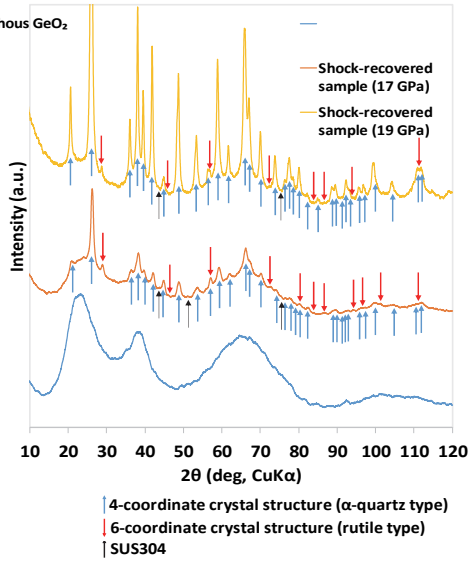

Fig. 1. X-ray diffraction patterns of samples after shock compression at 17 and 19 GPa and that before the compression.

REFERENCES:

[1] Y. Kono *et al*., PNAS, **113** (2015) 3436–3441.
[2] Y. Umeda *et al*. J. Mineral. Petrol. Sci., **119** (2024) 230706.

Characterization of Precipitates in Cu-Ni-Si alloy using Small-Angle X-ray Scattering

Y. Oba, H. Sasaki[1], H. Muramatsu, M. Ito

Department of Mechanical Engineering, Toyohashi University of Technology
[1]Furukawa Electric Co., Ltd.

INTRODUCTION: Cu-Ni-Si alloy is one of general precipitation-strengthened Cu alloys and is widely used as electrodes in electronic devices. In this alloy, while nano-sized Ni-Si precipitates are dispersed in Cu matrix and improve the mechanical strength, solute Ni and Si reduce the electric conductivity. Therefore, the precise control of precipitation by aging heat treatment is an important issue. Small-angle X-ray scattering (SAXS) can quantitatively characterize the shape and size of the precipitates in alloys and provide useful knowledge for precipitation mechanism [1-3]. In this study, we performed the SAXS measurements of the Ni-Si precipitates in Cu-Ni-Si alloy with various aging conditions.

EXPERIMENTS: The sample was Cu-Ni-Si alloy. The ingot of the alloy was solution-treated and then aged at the temperature between 623 and 773 K. SAXS measurements were performed using the SAXS instrument (NANO-Viewer, Rigaku) with Mo $K\alpha$ radiation. Scattering patterns were measured using a photon-counting-type two-dimensional detector (PILATUS 100k, Dectris) using a Si converter with the thickness of 1000 μm. The X-ray path from the X-ray entrance slit to the window just before the detector was evacuated to reduce the background scattering from air. The SAXS measurements were performed using two sample-to-detector distances of 0.4 and 1.7 m to cover the q range from 0.1 to 9 nm^{-1}, where q is the magnitude of the scattering vector. The scattering patterns were reduced using our original program written in Igor Pro (WaveMetrics).

RESULTS: Fig. 1 shows the SAXS profiles of the solution-treated and aged Cu-Ni-Si alloys. The profile of the solution-treated sample monotonically decreases and has a plateau in the high q region. These are typical characteristics of the solution-treated sample and reflect the scattering of coarse structures other than precipitates. In contrast, the profile of the aged sample shows a shoulder, which indicates the formation of the nano-sized precipitates with aging. The higher scattering intensity in the solution-treated sample than in the aged sample is due to the larger thickness. We also observed the shift of the shoulder toward lower q with increasing aging time. This means that the size of the precipitates becomes larger with aging. Further analysis is in progress. The size and number density of the precipitates will be compared with the mechanical and electric properties.

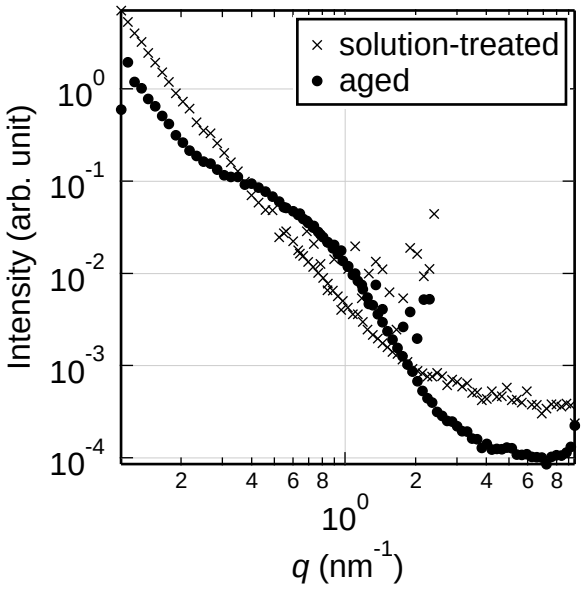

Fig. 1. SAXS profiles of Cu-Ni-Si alloys. Crosses and circles denote the solution-treated and aged samples, respectively.

REFERENCES:
[1] H. Sasaki *et al.*, Mater. Trans., **63** (2022) 1384-1389.
[2] T. Saito, J. Alloys Compd., **983** (2024) 173852.
[3] T. Kumada, J. Nucl. Mater., **528** (2020) 151890.

CO4-5

Positron Annihilation Spectroscopy in Neutron-irradiated Fe-Cr Alloys 2

K. Sato, Y. Noshita, R. Kasada[1], Q. Xu[2], A. Yabuuchi[2], A. Kinomura[2]

Graduate School of Science and Engineering, Kagoshima University
[1]Institure for Materials Research, Tohoku University
[2]Institute for Integrated Radiation and Nuclear Science, Kyoto University

INTRODUCTION: Ferritic stainless and heat resistant steels used as nuclear reactor peripheral materials have high Cr content [1]. In these materials, ductility and toughness remarkably decrease, and hardness and tensile strength increase by aging from 593 to 813 K. This phenomenon is caused by the formation of Fe-rich and Cr-rich phase, and is called 475˚C embrittlement [2]. These changes in mechanical properties are an important issue in terms of evaluation of aged deterioration when it was used as a reactor structural material. Positron annihilation spectroscopy (PAS) is very powerful tool to obtain the information of vacancy-type defects (even single vacancies) and precipitates. In Fe-Cr alloys used in this study, positron affinity of Fe is lower than that of Cr [3]. Therefore, we can detect the formation of Fe-rich phase in phase separation of Fe-Cr alloys using PAS. The purpose of this study is to detect the progress of phase separation using PAS, and to obtain the correlation between the hardness and phase separation in Fe-Cr binary alloys irradiated with neutrons at 473K and 573 K.

EXPERIMENTS: Fe-x wt.%Cr (x = 0, 9, 15, 30, 45, 50, 70, 85, 91, and 100) binary alloys were used in this study. The weight of high purity Fe (99.99%) and Cr (99.99%) were measured, and samples were melted by the arc melting. For neutron irradiation, samples with diameters of 3 mm and thickness of 0.25 mm were cut using the wire electric discharge machine. Fe-xCr (x = 30, 45, 50, 70, 85, 91, and 100) were annealed at 1273K for 1h, and Fe-xCr (x = 0, 9, 15) were annealed at 1073K for 1h in a vacuum ($< 4 \times 10^{-4}$ Pa), and then water-quenching was performed for the suppression of phase separation. The neutron irradiation was carried out at the Material Controlled Irradiation Facility (SSS) of Kyoto University Reactor (KUR) [4]. The irradiation doses were 0.44×10^{-3} , 0.5×10^{-3} and 2.1×10^{-3} dpa. The irradiation temperature was 473K (0.5×10^{-3} dpa) and 573K (0.44×10^{-3} and 2.1×10^{-3} dpa). Measurements of coincidence Doppler broadening (CDB) were performed at room temperature. The region of S parameter of CDB spectra was defined as $|p_L| < 4 \times 10^{-3}\ m_0c$, and the region of W parameter was defined as $12 \times 10^{-3}\ m_0c < |p_L| < 28 \times 10^{-3}\ m_0c$ (m_0: rest mass of electrons, c: velocity of light).

RESULTS: CDB ratio curves in the region of W-parameter heightened after irradiation in Fe-xCr (x = 70, 85, and 91) irradiated at 473 K and in all Fe-Cr alloys irradiated at 573 K. This result indicates that Fe-rich phase grows, and the amount of positrons, which are annihilated with core electrons of Fe atoms, increases. Form PAL measurements, vacancy clusters were not detected in Fe-xCr (x = 70, 85, and 91). These results indicate that almost all positrons are annihilated in Fe-rich phase, and vacancy clusters are not formed in Fe-rich phase. In Fe-xCr (x = 9, 15, 30, 45 and 50) irradiated at 473 K, the decrease in the W-parameter region is caused by the increase in the S-parameter region. After progress of phase separation by neutron irradiation, we cannot obtain the information of defects in Cr-rich phase using positron annihilation spectroscopy.

REFERENCES:

[1] R.L. Klueh *et al.,* J. Nucl. Mater., **191** (1992) 116.
[2] R.O. Williams, Trans. AIME, **212** (1958) 497.
[3] M.J. Puska *et al.,* J. Phy. Condes. Matter, **1** (1989) 6086.
[4] T. Yoshiie *et al.,* Nucl. Instr. Meth. Phys. Res. A, **498** (2003) 522.

Radiation Properties of Wide-bandgap Semiconductor Sensors for High-Energy Physics Experiments

T. Kishishita, H. Yashima[1], Y. Sakurai[1], R. Kosugi[2], T. Nakano[3,4], R. Kudo[4], T. Sakurai[4], Y. Hashimoto[4]

High Energy Accelerator Research Organization, KEK
[1] *Institute for Integrated Radiation and Nuclear Science, Kyoto University*
[2] *National Institute of Advanced Industrial Science and Technology*
[3] *Department of Electronics and Materials Science, Shizuoka University*
[4] *Research Institute of Electronics, Shizuoka University*

INTRODUCTION: Wide-bandgap semiconductor sensors have been considered as a potential alternative to Si for the manufacture of dosimeters, spectrometers, and charge particle detectors in high energy physics experiments, by virtue of its operation capability in strong radiation and/or high-temperature environments. To take advantage of such properties for future radiation detectors with a comparable size of silicon, we investigated two different semiconductor materials, SiC and BGaN this year. This study focuses on the influence of the SiC's bulk defects on the radiation sensor characteristics under the reverse-bias condition and neutron-detectability with BGaN sensors, by irradiating neutrons at Institute for Integrated Radiation and Nuclear Science, Kyoto University.

EXPERIMENTS: The reverse blocking characteristics and leakage current characteristic are primary concerns of the radiation effects on SiC. On the other hand, BGaN, a mixed semiconductor of GaN and BN, is expected to be a novel neutron detection material because it contains boron (B), a neutron-capturing element, as a semiconductor constituent. Therefore, we conducted different measurements with each sensor. As for the SiC sensor, we irradiated fast neutrons to SiC pn-diodes under the bias condition of 1 kV [1]. Fig. 1 shows the photograph of the measurement setup. We installed two SiC sensors at the front of the rail-instrument. After the 1MW operation, we carried out measurements of the leakage current and compared with those of the pre-irradiation samples. As for the BGaN, the sensor signals have been taken during the irradiation by external DAQ system and signal amplitudes and rise times were evaluated in off-line. The irradiation tests were both conducted at KUR.

RESULTS: The typical I-V characteristics of SiC sensors before and after irradiation showed similar characteristics, and we did not observe any degradation in leakage currents. The reverse blocking property was also retained up to 1 kV, which is required for full depletion of the SiC devices. As for the BGaN sensors, neutron-detectability was confirmed with sufficient event rates. Figure 2 is the time vs. neutron's event rate. For irradiations of less than 300 minutes, the counting rate decreased with irradiation time. The counting rate recovered and stabilized after more than 300 minutes of irradiation. This result suggests that neutron irradiation formed damage that affected device properties, but that further irradiation may have recovered the damage. Detailed evaluation of reproducibility and crystallinity dependence is needed to elucidate the mechanism in the future.

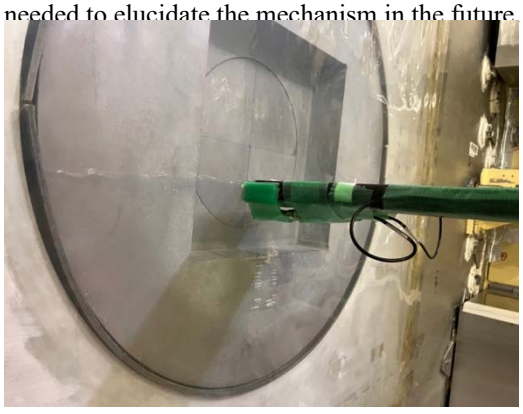

Fig. 1. Photograph of the measurement setup.

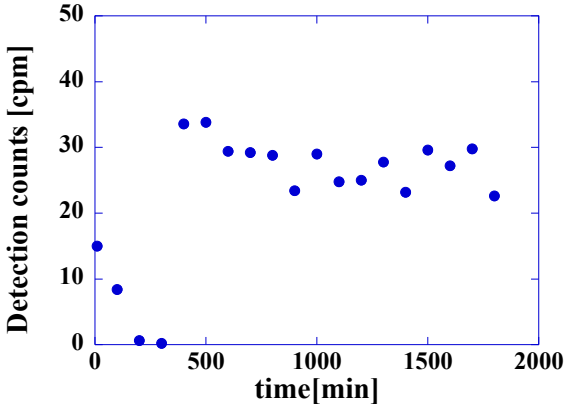

Fig. 2. Irradiation time dependence of neutron detection counting rate with BGaN detector.

REFERENCES:

[1] T. Kishishita *et al.*, IEEE Trans. Nucl. Sci., **68** (2020) 2787-2793.
[2] K. K. Lee *et al.,* Nucl. Instrum. Methods Phys. Res. B, **210** (2003) 489-494.

CO4-7

Effect of gamma radiation on ultra-micro structure of hardwood cell-wall

K. Murata, Y. Imataki, T. and T. Saito[1]

Graduate School of Science, Kyoto University
[1]Institute for Integrated Radiation and Nuclear Science, Kyoto University

INTRODUCTION: Space-wood project (LignoStella project) is performed by Kyoto University collaborating with Sumitomo forestry Co Ltd in order to challenge to use wood-material in out-er space. Firstly, possibility to use wood material in outer space has to be confirmed because a small wooden artificial satellite is going to launch until 2024. Space exposure test of wood specimen started on ExBAS at ISS in March 4, 2022. The wood specimen was exposed for about 1 year and came back to Earth in March, 2023. They were affected by atomic oxygen and cosmic ray. In this study, effect of gamma-ray irradiation on cell-wall of wood material was studied on the ground in parallel with the exposure tests in outer space.

EXPERIMENTS: The honoki specimens (*Magnolia obovate*) were conditioned in 20°C and 60%RH (dry wood) or 20°C and 97%RH (wet wood) for a few weeks before the irradiation test. To prevent moisture content changes during irradiation, they were wrapped in polyethylene film. The specimens were then irradiated for 24 hours, with three different doses applied: 100 kGy, 14 kGy, and 1 kGy. The fracture properties of the irradiated specimens were measured using a single-edge notched bend (SENB) test conducted on a material testing machine (AG-I/100kN, Shimadzu, Kyoto, Japan). This test measured the load and displacement at the center point.

RESULTS: The relationship between fracture energy and fracture toughness values and absorbed dose is shown in Fig. 1. Note that 0 kGy is expressed as 0.01 kGy. Fracture energy in fracture mechanics tests is related to the formation of the fracture progression zone (FPZ), which may reflect the viscosity of the wood. Fig. 1 shows that the fracture energy decreased by 70% at 100 kGy. This suggests that a change in plastic deformation may have occurred at 100 kGy. Murata et al. [1] reported that pyrolysis of wood affects fracture energy. Thermal treatment affects fracture energy of wood, as the fracture energy of spruce wood after heat treatment decreased linearly from heat treatment above 150°C. The reduction in fracture energy observed in this study aligns with their findings.

Fig. 1 shows that the fracture toughness values exhibited a decreasing trend at 1 kGy and decreased to approximately 80% compared to the control at 100 kGy. Murata et al. [1] reported that the maximum load on heat-treated spruce wood began to decrease with heat treatment above 130°C and remained unchanged beyond 150°C. The fracture toughness values obtained in this study align with the findings of previous research.

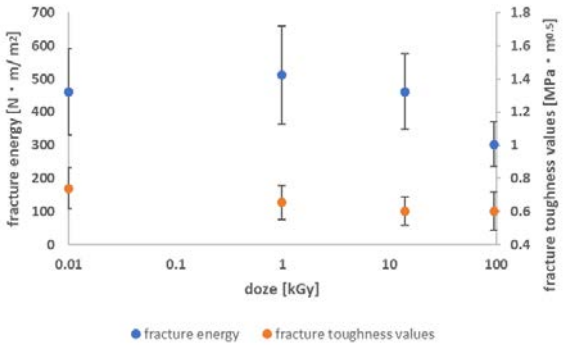

Fig. 1. The relationship between fracture energy and fracture toughness values and absorbed dose.

REFERENCES:

[1] T. Aoki *et al.*, bulletin of the Wood Research Institute Kyoto Univ., **62** (1977) 19-28.
[2] K. Murata *et al.*, Materials., **6** (2013) 4186-4197.

CO4-8

The effect of ion irradiation on $YBa_2Cu_3O_y$ and $FeSe_{0.5}Te_{0.5}$ superconducting films using a slow positron beam

T. Ozaki, H. Sakane[1] and A. Yabuuchi[2]

School of Engineering, Kwansei Gakuin University
[1] *SHI-ATEX Co., Ltd.*
[2] *Institute for Integrated Radiation and Nuclear Science, Kyoto University*

INTRODUCTION: Cuprate and iron-based superconducting films are being developed for use in high magnetic field applications such as generators for wind turbine, magnetically-levitated trains and electric aircraft. For these applications, increasing critical current, which is a maximum value of zero-resistivity current, property in magnetic fields is very important. Critical current properties in magnetic fields are improved by introduction of lattice defects with nano-meter size using ion-irradiation techniques. Positrons are useful for characterizing irradiation-induced defects. Last year, we have probed two kinds of pristine superconducting films, cuprate superconductor $YBa_2Cu_3O_y$ (YBCO) and iron-based superconductor $FeSe_{0.5}Te_{0.5}$ (FST), using a slow positron beam. In this study, we evaluated the irradiation defect in these films using the positron annihilation measurement.

EXPERIMENTS: The YBCO(~500 nm) films and the FST(~100 nm) films were irradiated with 10 MeV Au^{4+} (9.5×10^{12} cm^{-2}) and 2 MeV Au^{2+} (4.6×10^{12} cm^{-2}) ions, respectively. These films were probed by the KUR slow positron beam and the Doppler broadening of annihilation radiation (DBAR) spectra were acquired with incident positron energies E_+ = 9 keV. The sharpness of the DBAR spectra is evaluated by a value called the *S*-parameter, which becomes generally lower when positrons annihilate in a perfect lattice, and higher when positrons are trapped into vacancies [1].

RESULTS: Figure 1 shows the *S*-parameters as functions of the incident positron energy for (a) YBCO and (b) FST thin films before and after irradiation. The *S*-parameters for both irradiated samples did not show a clear change, compared with corresponding those for the unirradiated samples. This could be indicative of the presence of vacancy-type defects in high concentration (vacancy concentration: $C > 10^{19}$ /cm^3) in both unirradiated samples, so that most of the positrons are trapped at those vacancy-type defects.

We will identify the type of vacancy in these unirradiated films by comparing the momentum distribution of annihilated electrons with the result of the first-principles calculation.

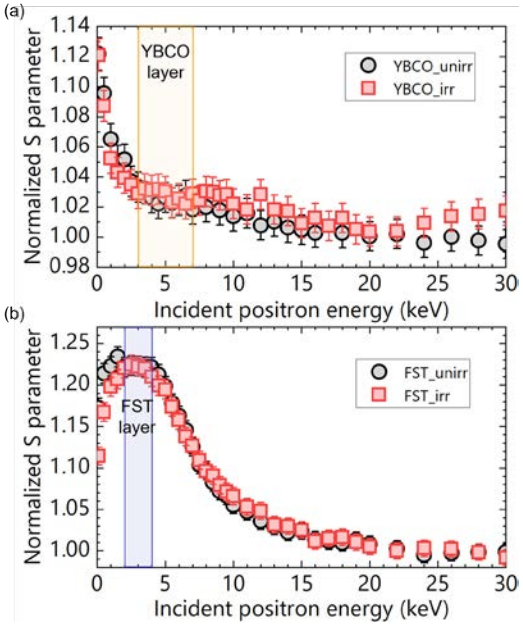

Fig. 1 *S*-parameters as functions of the incident positron energy for (a) 10 MeV Au^{4+} irradiated YBCO films and (b) 2 MeV Au^{2+} irradiated FST films, respectively.

REFERENCES:

[1] R. W. Siegel, Ann. Rev Mater. Sci., **10** (1980) 393−425.

CO4-9

Measurements of hyperfine fields in $Cd_xFe_{3-x}O_4$

W. Sato, M. Fujii[1], M. Konaka[2], T. Ito[1], H. Hirahara[2], S. Komatsuda[3], A. Taniguchi[4], and Y. Ohkubo[4]

Institute of Science and Engineering, Kanazawa University

[1]*Graduate School of Natural Science and Technology, Kanazawa University*
[2]*School of Chemistry, Kanazawa University*
[3]*Institute of Human and Social Sciences, Kanazawa University*
[4]*Institute for Integrated Radiation and Nuclear Science, Kyoto University*

INTRODUCTION: Spinel ferrites have a characteristic structure comprised of two different sublattices with cubic closest packed oxygen atoms with a crystallographic formula of $(M^{2+}_{1-\delta}Fe^{3+}_{\delta})_A[M^{2+}_{\delta}Fe^{3+}_{2-\delta}]_BO^{2-}_4$. Because the main constituent cations are Fe ions, their magnetic property has attracted attention from the view point of application to functional materials. Among a number of candidates of the introduced cations M, we directed our interest to Cd, and investigated Cd-content dependence of hyperfine fields in $Cd_xFe_{3-x}O_4$.

EXPERIMENTS: Powder $Cd_xFe_{3-x}O_4$ of each x was individually synthesized by a conventional solid-state reaction, and characterized the synthesized samples by powder X-ray diffraction patterns [1]. Time-differential perturbed angular correlation (TDPAC) spectroscopy with the $^{111}Cd(\leftarrow{}^{111}In)$ probe was applied to the samples to measure the hyperfine fields at the Cd nucleus in the A site. (In our previous work, we found Cd ions specifically occupy the A site by means of the spectroscopy with the $^{111}Cd(\leftarrow{}^{111m}Cd)$ probe generated in KUR [2].)

RESULTS: The room-temperature TDPAC spectra obtained for the samples of x = 0.1, 0.25, and 0.46 are shown in Fig. 1. The damping structure becomes marked as x increases, indicating the effect of Cd doping on the distribution of the hyperfine field at the probe. We also investigated the temperature dependences of the Larmor frequency of the precession of the $^{111}Cd(\leftarrow{}^{111}In)$ probe, ω_L, induced by the magnetic hyperfine fields supertransferred to the probes. We observed diminishing trend in the frequencies with increasing temperature, showing activated thermal fluctuation of ordered spins in surrounding Fe ions at higher temperature. The temperature dependences of ω_L were able to be reproduced well by the following power law:

$$\omega_L(T) = \omega_L(0)\left(1 - \frac{T}{T_C}\right)^{\beta} \qquad (1)$$

Here, T_C is the the Curie temperature. The fits for $Cd_xFe_{3-x}O_4$ of x = 0.1, 0.25, and 0.46 gave the T_C values of 806(1) K, 733(3) K, and 658(1) K, respectively. This observation demonstrates that T_C decreases as the Cd-content x increases, suggesting that the effect of thermal fluctuation of Fe spins is enhanced with increasing Cd content.

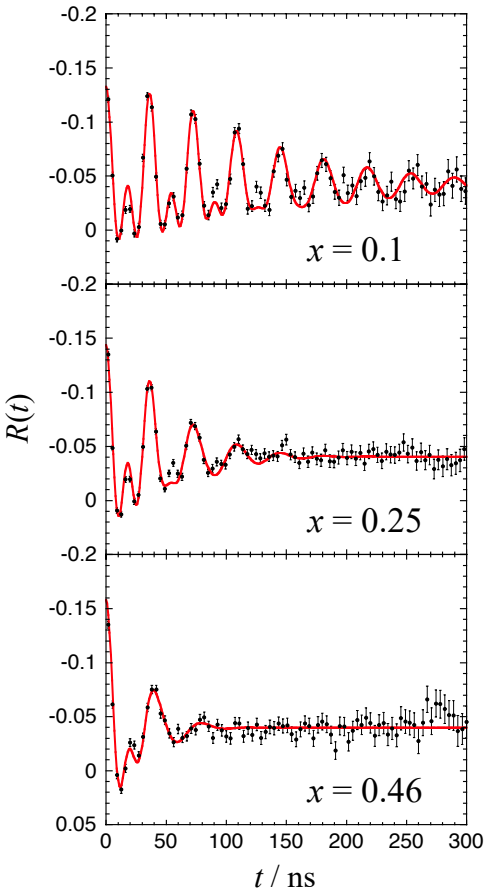

Fig. 1. TDPAC spectra of $Cd_xFe_{3-x}O_4$ (x = 0.1, 0.25, and 0.46) obtained at room temperature.

REFERENCES:

[1] W. Sato *et al.*, Appl. Radiat. Isotopes, in press.
[2] W. Sato *et al.*, J. Appl. Phys, **120** (2016) 145104 (1-7).

CO4-10

Slow Positron Beam Analysis of Polymer Composite Materials

Z. Chen, Y. Kobayashi[1], A. Yabuuchi[2] and A. Kinomura[2]

Department of Materials Science and Technology, Wuhan Institute of Technology, People's Republic of China
[1]Waseda Research Institute for Science and Engineering, Waseda University
[2]Institute for Integrated Radiation and Nuclear Science, Kyoto University

INTRODUCTION: Membrane treatment technology has the characteristics of low cost, low energy consumption and high efficiency [1]. Polyamide/Polysulfone membrane is one of the popular membranes which have been widely applied in water treatment due to its high salt rejection and excellent water flux. And this membrane has also been applied to treat the low-dose rate radioactive waste water. Considering the irradiation could accelerate the polymer degradation, the radioactive waste water may lead to the faster deterioration of membrane performance. In order to achieve better performance of the separation membrane, it is necessary to study the irradiation effect on the microstructure of the separation membrane. In this study, the polyamide/polysulfone membrane irradiated by an electron beam has been investigated via positron annihilation techniques coupled with a positron beam.

EXPERIMENTS: The membranes were prepared via an interfacial polymerization method in the laboratory. And the membranes were irradiated by an electron beam at different doses. Positron measurements were performed with the positron beam system at the Institute for Integrated Radiation and Nuclear Science, Kyoto University. The positron annihilation Doppler broadening was expressed by the *S* parameter, which is defined as the ratio of annihilation photon counts in a predetermined window centered at 511 keV to the total counts in the annihilation peak.

RESULTS: As shown in Fig. 1, the layer structure of the four membranes can be distinguished from the *S*-*E* curves. Here *E* denotes the incident positron energy; the higher the *E*, the deeper the positrons are injected. It can be seen from Fig. 1 that, the *S*-*E* curves can be divided into two stages, a surface polyamide layer (0~3 keV) and a polysulfone underlayer (3~20 keV). The *S*-*E* shape is similar to the positron results of polyamide/polysulfone membranes in the previous study [2]. Besides, one can find that the *S* parameters decrease when the membrane irradiated at higher dose. The decrease of the *S* parameters might be attributed to the formation of polar groups formed during the irradiation process.

REFERENCES:
[1] J. Yin and B. Deng, J. Membrane Sci., **479** (2015) 256-275.
[2] Z. Chen *et. al.*, J. Phys. Chem. C, **115** (2011) 18055-18060.

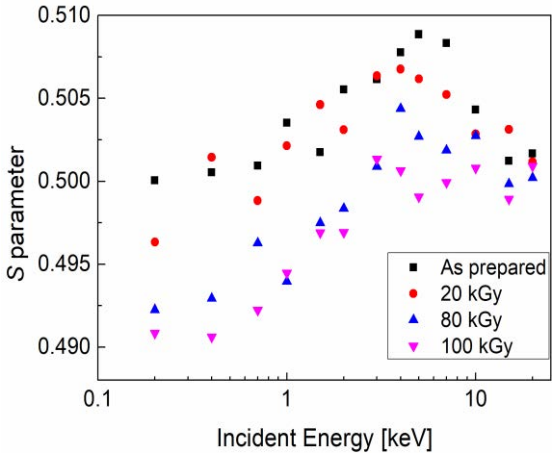

Fig. 1. The *S*-*E* plots for the composite membranes.

CO4-11

Effects of lead addition on tritium recovery for Li_2TiO_3-Li_4SiO_4 mixed breeder material

Y. Oya[1], A. Sanfukuji[1], Q. Zhou[2], M. Kobayashi[3]

[1]*Graduate School of Integrated Science and Technology, Shizuoka University*
[2]*School of Materials Science and Engineering, Wuhan University of Technology*
[3]*National Institute for Fusion Science*

INTRODUCTION

Tritium will be produced by (n, α) reaction with lithium (Li) in the fusion reactor because the amount of tritium in nature is small. Tritium breeder needs good chemical stability and easy to recover tritium. Lithium silicate (Li_4SiO_4) and lithium titanate (Li_2TiO_3) have different characteristics. For example, lithium silicate has a high lithium density, while lithium titanate is good chemical stability and has a good crushing load. Advanced tritium breeder materials should have both of higher tritium production rate and recovery efficiency. LTO-LSO mixed ceramic materials are expected to have both advantages. Lead (Pb) is a neutron multiplier that contributes to the improvement of the tritium breeding ratio and has a lower affinity with tritium. The addition of Pb into Li ceramics is expected to have a potential advantage for efficient tritium recovery.

EXPERIMENTS

LTO-LSO-5wt.%Pb, a powder sample of lithium titanate and lithium silicate mixture with 5wt.%Pb addition, was prepared at Wuhan University of Technology. Those samples were irradiated by neutron at Kyoto University Research Reactor (KUR) with the neutron fluence of 8.0×10^{15} n cm^{-2} and 8.0×10^{16} n cm^{-2}. After the neutron irradiation, tritium release behavior was evaluated by Tritium-thermal desorption spectroscopy (T-TDS) system by heating the samples separately from R.T. to 1113 K with the heating rates of 10, 20, and 30 K min^{-1}. Liquid scintillation counter (LSC) was used to measure the total T amount trapped by the water bubbler at Shizuoka University.

RESULTS AND DISCUSSION

Fig. 1 shows the T-TDS spectra for LTO-LSO-5wt.%Pb with two different neutron fluences. The amount of tritium released was increased as the fluence was increased. The sample with the low neutron fluence of 8.0×10^{15} n·cm^{-2} showed a large desorption stage located at a lower temperature side of 400 K, whose activation energy was 0.15-0.33 eV, ascribing to the desorption of tritium adsorbed on the surface. As the fluence increases, the desorption of tritium from the bulk was the major tritium desorption stage. Fig. 2 shows the T-TDS spectra for mixed sample without Pb with neutron fluence of 8.0×10^{16} n·cm^{-2} at 20 K min^{-1}. Compared to the mixed sample without Pb in the pebble sample and the mixed sample including Pb in the powder sample, the major desorption stage was shifted to the lower temperature side. This is due to more efficient tritium recovery with the addition of Pb. In this experiment, it was found that the amount of irradiation defects caused by neutron irradiation decreased with the addition of Pb. It can be said that the number of trap sites for tritium desorption in the bulk decreased. Therefore, it is considered that the addition of Pb reduces the number of trapping and de-trapping processes, and thus tritium recovery can be achieved at low temperatures. The TDS spectrum did not change significantly, suggesting that the process of tritium desorption should be the same.

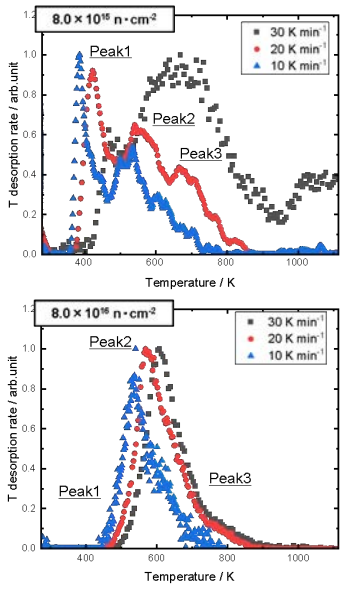

Fig. 1 TDS spectra of LTO-LSO-5wt%.Pb with the neutron fluence of 8.0×10^{15} and 8.0×10^{16} n・cm^{-2}.

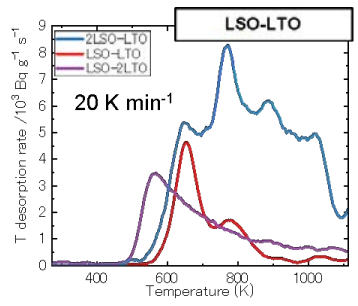

Fig. 2 TDS spectra of 2LSO-LTO, LSO-LTO and LSO-2LTO with the neutron fluence of 8.0×10^{16} n・cm^{-2} at 20 K min^{-1} [1].

REFERENCES

[11] S. Hirata *et al.*, J. Nucl. Mater. (2022) 1538383.

CO4-12

Effect of rhenium doping on vacancy formation in electron-irradiated tungsten studied with positron annihilation spectroscopy

T. Toyama, Z. Zhang, A. Kinomura[1], Q. Xu[1], A. Yabuuchi[1], K. Inoue and Y. Nagai

Institute for Materials Research, Tohoku University
[1]Institute for Integrated Radiation and Nuclear Science, Kyoto University

INTRODUCTION: Tungsten (W) is promising as a plasma-facing material for fusion reactors, and material development is ongoing both domestically and internationally. Although W has the lowest hydrogen solubility limit among metal elements, the retention and accumulation of hydrogen isotopes can become a problem under irradiation. However, it has been reported that adding rhenium (Re) significantly reduces the accumulation of hydrogen isotopes [1]. This is thought to be due to the suppression of the formation of irradiation-induced defects, which serve as hydrogen trapping sites, by the addition of Re. Indeed, we reported that the formation of vacancy-type defects is significantly suppressed in W-5Re compared to pure W using neutron-irradiated or electron-irradiated W alloys. This study aims to further investigate the effect of Re addition on the formation of vacancies by introducing only simple Frenkel pairs through electron irradiation in W-Re dilute alloys and examining vacancy-type defects using positron annihilation spectroscopy.

EXPERIMENTS: The test materials are pure W and W-*x*Re alloys (x = 0.1, 0.3, 1.0, 5.0 at.%). After annealing at 1800°C for one hour (1600°C for one hour for x = 5.0), electron irradiation (8 MeV, <100°C, approximately 3.5×10^{23} e^-/m^2) was carried out at the Kyoto University Linac. After irradiation, vacancy-type defects were examined using positron lifetime measurements.

RESULTS: Figure 1(a) shows the Re composition dependence of the average positron lifetime (τ_{ave}). In the unirradiated samples, τ_{ave} ranged from 110 to 117 ps. Since these values are close to those of bulk W, it is believed that there were almost no vacancy-type defects serving as positron trapping sites before irradiation. After irradiation, τ_{ave} increased for all samples compared to before irradiation, indicating positron trapping in irradiation-induced vacancy-type defects. For all samples, the positron lifetime spectra exhibited little to no long-lived component, suggesting minimal positron trapping in vacancy clusters. Figure 1(b) shows the increase in τ_{ave} ($\Delta\tau_{ave}$) due to irradiation. Compared to pure W, $\Delta\tau_{ave}$ increased with Re composition up to about 1%, indicating an increase in positron trapping in vacancy-type defects. However, at 5% Re composition, $\Delta\tau_{ave}$ was smaller than in pure W, consistent with the previous report on W-5Re. In that previous study, the mechanism proposed was that Re strongly binds to W interstitial atoms, reducing their mobility and increasing the frequency of interstitial-vacancy recombination, thereby suppressing the formation of vacancy-type defects [2]. However, the results of this study suggest the need to consider other mechanisms. For example, Re has a positive (attractive) binding energy of 0.22 eV with vacancies in W [3], suggesting the possibility that it stabilizes vacancies.

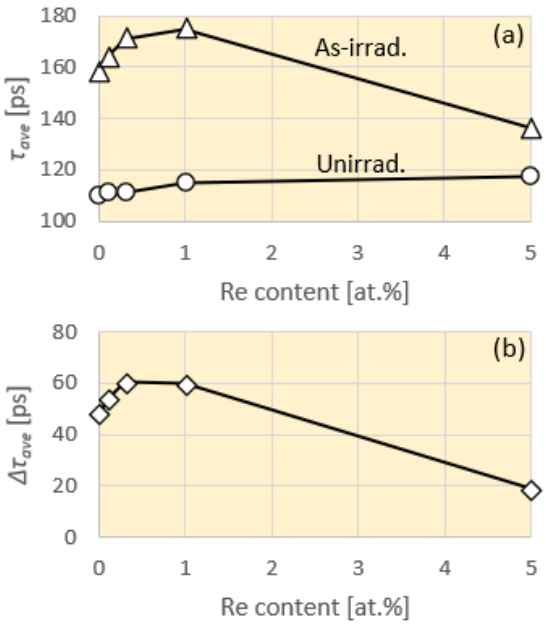

Fig 1. (a)Average positron lifetime in pure W and W-Re alloys before/after electron irradiation. (b) Increase of the average positron lifetime in pure W and W-Re alloys.

REFERENCES:

[1] J. Wang *et al.*, J. Nucl. Mater., **559** (2022) 153449.
[2] T. Suzudo *et al.*, Sci. Rep., **6** (2016) 36738.

CO4-13

Dependence of In Concentration on the Local Structure of In Doped in $SrTiO_3$

S. Komatsuda, M. Kawakami[1], W. Sato[2], A. Taniguchi[3], M. Tanigaki[3], and Y. Ohkubo[3]

Institute of Human and Social Sciences, Kanazawa University
[1]*Graduate School of Professional Development in Teacher Education, Kanazawa University*
[2]*Institute of Science and Engineering, Kanazawa University*
[3]*Institute for Integrated Radiation and Nuclear Science, Kyoto University*

INTRODUCTION: $SrTiO_3$ is one of the most promising candidates for photocatalytic materials. It is known that trivalent cation doping at the Ti^{4+} site is one of the effective methods to improve photocatalytic activity. According to previous research, it is known that doping trivalent cations such as In^{3+} into Ti^{4+} suppresses the formation of Ti^{3+} recombination centers and improves the photocatalytic activity of $SrTiO_3$. On the other hand, if a secondary phase of indium oxide is formed due to excessive doping, it is thought that the secondary phase becomes a recombination center and the photocatalytic activity decreases. For the precise control of photocatalytic properties of In-doped $SrTiO_3$, therefore, it is necessary to examine the local surroundings of In^{3+} dopant of various In concentrations. For the microscopic study of the local fields at In sites, TDPAC measurements were performed for $^{111}Cd(\leftarrow{}^{111}In)$ in undoped and In-doped $SrTiO_3$.

EXPERIMENTS: $SrTiO_3$ powders doped with 0.1, and 1 at.% In were synthesized by the conventional solid-state reaction as described in the references[2]. Commercially available ^{111}In HCl solution was added in droplets onto the disks of undoped $SrTiO_3$ and each In-doped $SrTiO_3$ sample. After the disks were dried up by heat, they were heated in air at 1473 K for 24 h for the diffusion of the probe. Each disk was then ground into powder and sealed in a pyrex tube. TDPAC measurements were performed at room temperature by the detection of the 171–245-keV cascade γ rays with the intermediate spin $I = 5/2$ having a half-life of 85.0 ns

RESULTS: Figure 1 shows the TDPAC spectra of the $^{111}Cd(\leftarrow{}^{111}In)$ probe embedded in undoped, 0.1 at.%, and 1 at.% In-doped $SrTiO_3$ measured at room temperatures. From the fitting parameters of the TDPAC spectrum in Fig. 1(a), it is suggested that the $^{111}Cd(\leftarrow{}^{111}In)$ probe is uniformly doped into $SrTiO_3$ and occupies three types of sites. Considering the previous study, In^{3+} ions occupy the *B* sites in $SrTiO_3$[1]. Therefore, there would be three types of local structures in the vicinity of the $^{111}Cd(\leftarrow{}^{111}In)$ probes at the substitutional Ti^{4+} site. For Fig.1(b), the parameters of quadrupole frequencies between the two results of Fig.1(a) and (b) were the same within the fitting error range. Therefore, it is suggested that 0.1% of In^{3+} is uniformly doped into $SrTiO_3$. However, in the TDPAC spectrum shown in Fig. 1(c), components derived from the secondary phase of In_2O_3 were observed, which suggests that In^{3+} partially forms In_2O_3 in 1 at.% In-doped $SrTiO_3$. These results suggest that in the case of In-doped $SrTiO_3$ synthesized by the conventional solid-state reaction, the solubility limit of In^{3+} is between 0.1 and 1 at.%.

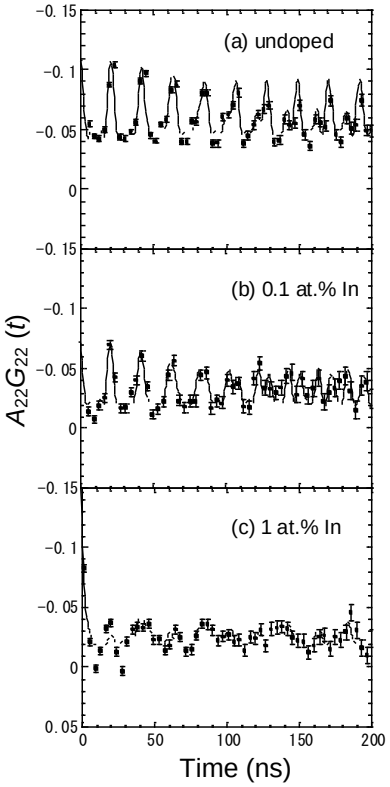

Fig. 1. TDPAC spectra of $^{111}Cd(\leftarrow{}^{111}In)$ in undoped and In-doped $SrTiO_3$ samples.

REFERENCES:

[1] H. Sudrajat *et al.*, Phys. Chem. Chem. Phys., **22** (2020) 19178-19187.
[2] S. Komatsuda *et al.*, Interactions, **245** (2024) 37.

Sample Preparation for Study on HPLC Elution Behavior of Heavy Lanthanide Metallofullerene Using Chlorobenzene Eluent

K. Akiyama, D. Nakamura, T. Kuroda, K. Takamiya[1], and S. Kubuki

Department of Chemistry, Tokyo Metropolitan University
[1]Institute for Integrated Radiation and Nuclear Science, Kyoto University

INTRODUCTION: Lanthanide (Ln) metallofullerene (EMF): Ln@C_{82} is a clathrate compound encapsulating metal atom in fullerene C_{82} and known that two or three electrons are transferred to C_{82} cage from the encapsulated Ln atom [1]. In the previous work, we succeeded to obtain the high performance liquid chromatography (HPLC) elution behavior on a pyrenyl stationary phase for Ln@C_{82} of La, Ce, Pr, Nd, Gd, Tb, Dy, Ho, and Er with a toluene as an eluent by the thermal neutron activation method [2]. In order to obtain further knowledge about the HPLC elution behavior of Ln@C_{82}, we used chlorobenzene (CB), which has a similar structure to toluene, as an eluent in this study. In general, the neutron activation of compounds containing Cl is required some precaution. In particular, since Dy which has a short half-life (^{165}Dy: $T_{1/2}$ = 2.3 h) is expected to be affected very much, we investigated the influence of ^{38}Cl on the measurement prior to this study.

EXPERIMENTS: Ln@C_{82}s of Dy, Ho, and Er were prepared by previously reported [2]. These purified samples were injected into a Buckyprep column using CB as an eluent. The eluate from the column was fractionated every 2 minutes at room Temperature (RT) and every 30 seconds at 50 ºC. These fractionated eluates were evaporated to dryness and re-dissolved to carbon disulfide and then dropped onto paper filters with 12 mm diameters and dried for 2 or 3 days in the evacuated desiccator. After sufficient drying, these samples were measured XRF spectra to confirm the amount of Cl on the filters and sealed into polyethylene bags and irradiated in ethylene vial. These sealed samples were activated by a thermal neutron in the KUR of the Institute for Integrated Radiation and Nuclear Science, Kyoto university. After the irradiation, the γ rays emitted from the samples were measured by a Ge detector.

RESULTS: As the results of XRF, characteristic X ray derived from Cl on the filters was not observed with the significant intensity for almost all samples. The averaged count rate of the observed γ-ray from ^{38}Cl at 1643KeV for each activated sample was 15.6±2.6 cps for all samples and was found that it had almost no effect on the γ-ray measurement of activated Ln@C_{82}. Figure 1 shows the HPLC chart of heavy Ln@C_{82} (Ln: Dy, Ho, and Er) with CB as eluent at RT (top) and 50 ºC (bottom). In both chromatograms, the HPLC elution behavior of Dy, which had a short half-life and was expected to be most affected by ^{38}Cl, was confirmed with sufficient intensity. Therefore, it was found that it is possible to use as an eluent containing chlorine by sufficient drying.

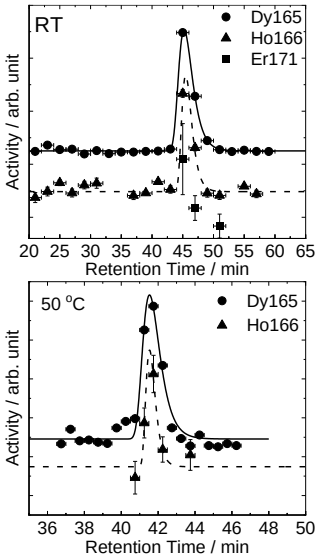

Fig. 1. HPLC chart of heavy Ln@C_{82} (Ln: Dy, Ho, and Er) with CB as eluent at RT (top) and 50 ºC (bottom).

REFERENCES:

[1] H. Shinohara, Rep. Prog. Phys., **63** (2000) 843-892.
[2] K. Akiyama *et al.,* KURNS Prog. Rep., 2022 CO4-1.

Valuation of Surface Damage on Si induced by the Plasma Treatment using the Positron Annihilation Method

J. Yanagisawa, R. Shigesada, Q. Xu[1], A. Yabuuchi[1], K. Takamiya[1], and A. Kinomura[1]

School of Engineering, The University of Shiga Prefecture
[1]Institute for Integrated Radiation and Nuclear Science, Kyoto University

INTRODUCTION: We have been studying the effect of the surface damages, which are induced during the plasma treatment on Si substrates, using the positron annihilation method. In the present study, the effect of the plasma species with the different plasma condition of our previous study [1] and the ion-irradiation damage on Si surfaces during the SF_6-plasma processing were investigated.

EXPERIMENTS: The Si substrates with the size of 18 mm x 18 mm were prepared by cleavage of a Si (100) wafer. To study the effect of the plasma species, each Si substrate was exposed to SF_6, Ar or CHF_3 plasma (gas pressure: 10 Pa, RF power: 40 W, exposed time: 30 min.). To study the effect of the ion irradiations during the plasma processes, SF_6 plasma (30 Pa, 100 W, 30 min.) were exposed to two Si substrates, the one (SF_6-1) was positioned on the sample stage, which is connected to blocking condenser and negatively charged during the plasma exposure, and the other (SF_6-2) was positioned on the cover of the chamber, which is connected to ground. After the plasma treatment, the S-parameters obtained from the Doppler broadening for the energy of the γ-ray by the positron-electron annihilation were measured for all samples.

RESULTS: Figure 1 shows the S-parameters for samples with different plasma species as a function of positron energy. The result is almost the same tendency with our previous results [1] (30 Pa, 5 W) except for the result of CHF_3 plasma, which was also observed for BF^{2+} ion implanted Si [2]. This might be because of the sputtering effect of the C-related material, which is deposited on the surface by the dissociation of CHF_3, by ions due to larger RF power in this study. From Fig. 2, it is found that the S-parameters of SF_6-1 was larger than those of SF_6-2, indicating that the ion irradiation induces the damages, such as vacancies, near the surface region during the plasma treatment.

REFERENCES:

[1] J. Yanagisawa *et al*., KURNS Progress Report 2022 (Kyoto University) 112 (CO4-21).
[2] A. Uedono *et al*., Jpn. J. Appl. Phys. **36** (1997) 969.

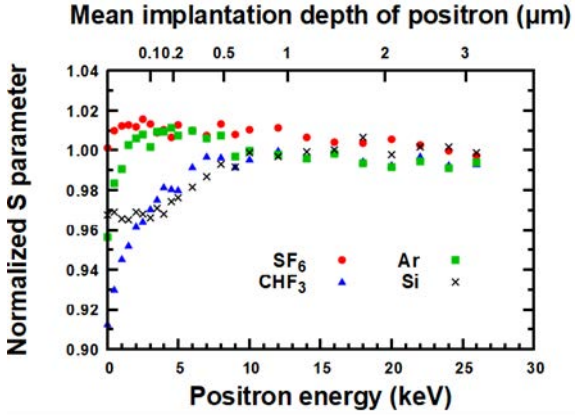

Fig. 1. S-parameters of Si exposed to plasma using various kind of gas species at gas pressure of 10 Pa and RF power of 40 W for 30 min.

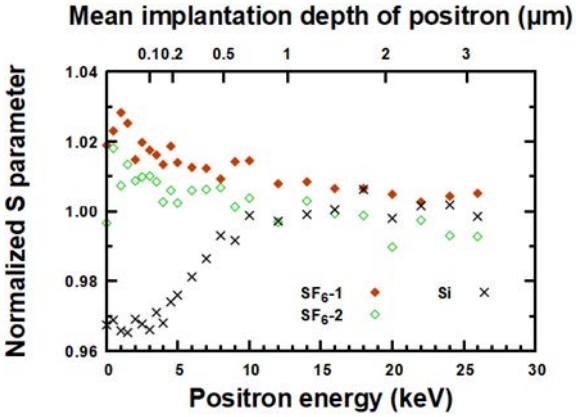

Fig. 2. S-parameters of SF_6 plasma (gas pressure: 30 Pa, RF power: 100 W, 30 min.) exposed Si substrate positioned on the sample stage (SF_6-1) and the cover of the chamber (SF_6-2).

CO4-16

Study on ^{99m}Tc separation/concentration technolog from ^{99}Mo by (n, γ) method (2)

Y. Fujita, X. Hu[1], Y. Yang[1], T. Kitagawa[1], Y. Fujihara[2], H. Yoshinaga[2], J. Hori[2], T. M. D. Do[1], T. Suzuki[1], H. Suematsu[1] and H. Ide

Department of JMTR, Japan Atomic Energy Agency
1Graduate School of Engineering, Nagaoka University of Technology
2Institute for Integrated Radiation and Nuclear Science, Kyoto University

INTRODUCTION: The research and development have been carried out to produce ^{99}Mo by the (n, *γ*) method in terms of nuclear security. To apply the (n, *γ*) method to a ^{99}Mo/^{99m}Tc generator, it is necessary to improve the adsorption properties of alumina (Al_2O_3) used as a Mo adsorbent. In this work, several types of alumina were synthesized based on two references that mentioned alumina with excellent adsorption properties and their applicability to the generator was evaluated.

EXPERIMENTS: MoO_3 pellet pieces were irradiated with Pn-2 and dissolved with 6M-NaOHaq. The solution was adjusted to a Mo concentration of 10 g/L and pH4. Three types of alumina were prepared: the alumina ($Al_2O_{3\ 4:1}$, $Al_2O_{3\ 6:1}$) calcined at 300 °C with raw material ratios of 4:1 and 6:1 based on reference [1], and the alumina ($Al_2O_{3\ HMMA}$) based on reference [2]. The Mo solution was added to approximately 0.3 - 0.5 g of the alumina and left for 3 hours, then the alumina was washed with water and transferred to a column. Saline was run through the alumina-filled column to remove ^{99}Tc. For milking, 10 mL of saline was flowed through the columns every 24 hours for 2 days. The radioactivity of the obtained solutions was measured using a *γ*-ray spectrometer.

RESULTS: Figure 1 shows SEM images of each alumina. For $Al_2O_{3\ 4:1}$ and $Al_2O_{3\ 6:1}$, an agglomerated surface of fine particles was observed. On the other hand, $Al_2O_{3\ HMMA}$ had uniform pores on the surface. Table 1 shows the Mo adsorption capacities and ^{99m}Tc elution rates, ^{99}Mo/^{99m}Tc ratios for each alumina. In the literature, the Mo adsorption capacity of $Al_2O_{3\ HMMA}$ was reported to exceed 200 mg-Mo/g, but the highest Mo adsorption capacity in the test results was 98.3 mg-Mo/g for $Al_2O_{3\ 6:1}$. The elution rates of ^{99m}Tc were almost the same for all alumina. ^{99}Mo/^{99m}Tc, which is an indicator of ^{99}Mo desorption rate from the column, deviated from the standard value (≤ 0.015%). The ^{99}Mo desorption rate from $Al_2O_{3\ HMMA}$ was particularly high. Therefore, under this experiment conditions, the surface condition of the alumina may have little effect on Mo adsorption and large effect on the ability to retain Mo. In the future, we will evaluate its applicability to the generator under more practical conditions, where Mo is adsorbed with the column packed with alumina.

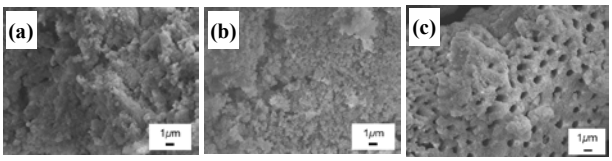

Fig. 1. The SEM images of each alumina.
(a) $Al_2O_{3\ 4:1}$, (b) $Al_2O_{3\ 6:1}$, (c) $Al_2O_{3\ HMMA}$

Table 1. ^{99}Mo adsorption capacities of the Alumina, ^{99m}Tc elution rates and ^{99}Mo/^{99m}Tc rates at milking

Sample	^{99}Mo adsorption capacity (mg-Mo/g)	Day	^{99m}Tc elution rate (%)	^{99}Mo/^{99m}Tc (%)
$Al_2O_{3\ 4:1}$	90.7	1	76.8	1.545
		2	69.0	1.132
$Al_2O_{3\ 6:1}$	98.3	1	79.4	1.889
		2	69.8	1.361
$Al_2O_{3\ HMMA}$	91.6	1	77.7	8.008
		2	72.1	2.961

REFERENCES:
[1] X. Hu *et al.*, Mater. Res. Bull., **47** (2012) 4271–4277.
[2] J. Wang *et al.*, Appl. Radiat. Isot., **178** (2021) 109986.

CO4-17

Observing the effect of deuterium charge in the modeled metal bilayers of hydrogen embrittlement-resistant alloys

M. Yamada[1], T. Nakayama[2], M. Hino[3], K. Ikeda[4], K. Mori[1]

[1]*Institute of Materials Structure Science, KEK*
[2]*Formerly: Kobe Steel, Ltd.*
[3]*Institute for Integrated Radiation and Nuclear Science, Kyoto University*
[4]*Comprehensive Research Organization for Science and Society (CROSS) Neutron Science and Technology Center*

INTRODUCTION:

As the technology for lightweighting structural metal materials and hydrogen infrastructure are being developed for the purpose of global environmental protection, measures to prevent hydrogen embrittlement of high-strength structural materials are an urgent issue. Elucidation of the mechanism of hydrogen embrittlement is essential for the development of high-performance steels with high strength and resistance to hydrogen embrittlement.

One kind of hydrogen embrittlement-resistant alloys has a system in which nano-precipitates (such as TiN and TiC) are dispersed in steel matrix [1,2]. In this study, we aim to elucidate the behavior of hydrogen trapping by using a metallic multilayer film that models the interface between the nanoprecipitates and the matrix.

EXPERIMENTS:

The metal-multilayer sample was deposited by using ion beam sputtering at KURNS [3]. The sample consisted of 20 repetitions of the bilayer of Fe (0.5 nm) and Ti (0.5 nm) on glass substrate. Because the multilayers of Fe and TiN did not show any significant changes by hydrogen/deuterium charge in the preceding study, we modified the material of TiN layer to Ti because one of hydrogen storage materials is FeTi(H). The Ti-layers were sputtered under hydrogen atmosphere. The sample area was 40x50 mm^2.

Deuterium(D) was charged to the multilayers by cathodic electrolysis at a current density of 2 mA/cm^2 for 30 minutes using a deuterium aqueous solution of 3mass% NaCl + 0.01mol/l KSCN.

Prior to the neutron reflectivity measurement (NR) at the MINE beamline, the thicknesses of multilayers were determined by X-ray reflectivity (XR) measurement. The results showed that the total thickness of the pair of Fe and Ti(H) changed from 1.18 nm to 1.23 nm after the D charge, which corresponds to 4% increase of total thickness.

Finally, we conducted NR measurement at C3-1-2 (MINE), JRR-3 to test its sensitivity to the change by D charge by observing the critical angle that define the Scattering Length Density (SLDs) of layers.

RESULTS:

NR measurement on the multilayer sample showed the significant increase in the critical angle between before and after the D charge. Those results from XR and NR confirmed that significant amount of D was charged in [Fe/Ti(H)]x20 multilayers and XR and NR are suitable tools. The next step is to measure the difference of SLD between D and hydrogen (H) by NR. We will continue further study for optimizing the ideal model multilayers to identify the location and status of charged D or H.

REFERENCES:

[1] Takenori Nakayama *et al.,* Materia, **41(3)** (2002) 230.
[2] Japanese Patent No.2932943, etc.
[3] M. Hino, *et al.*, Nucl. Instr. and Meth., **797**(2015) 265.

CO4-18

Complex Structure of Ions Coordinated with Hydrophilic Polymer 24. - Obstruction of Iodine Doping by Solute.

A. Kawaguchi and Y. Morimoto

IIRNS, Kyoto University (KURNS)

INTRODUCTION: We have been investigating dynamical and interacted structures between iodine and polymers. Present "iodine" is "polyiodide ions" (I_n^{m-}, *m, n*: integer, $n > 1$: "Poly-Iod.(s)" mentioned below), which are defined as charged molecules constructed with more than one iodine atom. And, "Poly-Iod.(s)", mono iodide ion (I^-) and iodine (I_2) can actively interact with each other as molecular (re)structuring between (or among) them. While such (re)structuring can be observed in coordination within organic crystals, it is more emphasized through interaction with macromolecular matrices.[1] We had observed diffusion, coordination and (re)structuring of "Poly-Iod.(s)" in some hydrophilic polymers, such as polyamide-6 (PA6); there are observed both rapid diffusion of "Poly-Iod.(s)" into polymers and restructuring as coordinated materials while diameter of iodine atom (or "Poly-Iod.(s)") is relatively large, c.a. 0.4nm.[2,3] Through past researches of characteristic behaviors in coordination of iodine in polymers, we are clarifying unexpected discovery behind simple operation and generality in popular experiments, such as "iodine-starch reaction".

EXPERIMENTS: Keeping proportion between I^- (potassium iodide, KI) and I_2 as 3:1, solutes of "Poly-Iod.(s)" were prepared as "0.2N": i.e., 0.1 mol/L for I_2 and 0.3mol/L for KI. On the other hand, composition of solutes for 3:1 "iodine (1st) doping" were prepared with H_2O and ethanol (EtOH) as H_2O : EtOH = 4:0 ("Et:0") / 3:1 ("Et:25") / 1:1 ("Et:50") / 1:3 ("Et:75"). As "iodine (1st) doping" process, dried PA6 films ("Rayfan" in 0.1mm thickness, TORAY) were immersed in the "Poly-Iod.(s)" solutes for more than 3 weeks at R.T. After "iodine (1st) doping" as termination, iodine-doped samples were rinsed with mixture solutes of H_2O and EtOH without iodine as similar proportion ("Et:0" / "Et:25" / "Et:50" / "Et:75") as doping solutes,

RESULTS AND DISCUSSION: As consequence, mass increasing with iodine doping (Δm) are lowered with proportion of ethanol of solutes: i.e., Δm(Et:0) > Δm(Et:25) > Δm(Et:50) > Δm(Et:75); composition of ethanol prevents "iodine (1st) doping". And, past research with modifying concentration of KI also shows that, even with constant [I_2], increasing [I^-] prevents "iodine (1st) doping".[4] If only solved concentration of iodide ion (I^-) and iodine (I_2) could control diffusion of "Poly-Iod.(s)" and structures after "iodine (1st) doping", neither composition of solutes (ethanol ratio) nor additional [I^-] would influence results; effects by "Et:xx" and [I^-] actually indicate that complicated mechanism behaves as interaction between "Poly-Iod(s)" or with polymers.

Strictly speaking on definition, "Poly-Iod(s)" should include neither (mono) iodide ion, I^-, which has been charged but is constructed by one iodine atom, nor simple iodine, I_2, which does not have charge. Nevertheless, "Poly-Iod(s)" interact with both I^- and I_2 actively. Furthermore, there can be dynamical structures constructed and modified among them; anisotropic structuring among "Poly-Iod(s)" is achieved through characteristic coordination between iodine atoms. Such interaction or structuring is called "iodine bonds" and is attributed to anisotropic linking between "Poly-Iod(s)" or "σ-hole" which is most conspicuous positive charge deviation in arrays comparing with other halogen atoms. "Modified orientation" reported previously should also be explained by such dynamism.

REFERENCES:

[1] T.J. Marks & D.W. Kalina, "Extended Linear Chain Compounds" vol.1 ch.6., ed. J.S. Miller (Plenum Press, 1982).
[2] A. Kawaguchi, Polymer, **35** (1994) 3797-3798.
[3] A. Kawaguchi *et.al.,* SPring-8 User Exp. Rep. **5** (2000) 354-354.
[4] A. Kawaguchi, Polymer, **37** (1996) 4877-4880.

CO4-19

Gamma-ray induced light emission from imprity doped GaP single crystal

T. Nakamura[1], T. Nishimura[1], K. Kuriyama[1], Atsushi Kinomura[2]

[1]*Research Center of Ion Beam Technology, Hosei Uni-versity, Koganei, Tokyo 184-8584, Japan*
[2]*Institute for Integrated Radiation and Nuclear Science, Kyoto University, Kumatori, Osaka 590-0494, Japan*

INTRODUCTION: Gallium phosphide (GaP) is usually employed in the manufacture of low-cost red, orange, and green light-emitting diodes (LEDs). We recently succeeded in detection of the gamma-ray induced photo emission from GaN [1] and ZnO [2] single crystal wafers. It is interesting topic that the light-emission by the excita-tion of gamma-ray at room temperature in GaP as similar to GaN and ZnO. This is because it can be used as an application as a gamma-ray detector. In the present study, we investigate the emission properties in the gamma-ray excitation to two GaP crystal samples, which is impurity doped and undoped crystal to reveal the role of the impurities for the light emission.

EXPERIMENTS: GaP single crystal wafers with a size of several cm square and a thickness of several 100 μm meters were used for the present study. The crystals were irradiated at room temperature with gam-ma-rays of 1.17 and 1.33 MeV from a cobalt-60 source of Institute for Integrated Radiation and Nuclear Science, Kyoto University. The gamma-ray irradiation induced photo emission measurements were performed by using a charge coupled device (CCD) equipped spectrometer (QE Pro, Ocean Insight Co. Ltd.).

RESULTS: Fig. 1 shows the gamma-ray induced photo emissions for un-doped and impurity doped GaP single crystal samples. These emissions were measured at room temperature with an absorbed dose rate of about 0.8 kGy/h us-ing GaP single crystal wafer with 200 μm in thickness. The gamma-ray induced photo emission from impurity doped GaP was observed from 750 nm to 1000 nm, with a peak at around 850 nm and a half width of 250 nm. The greater width of the spectra with the greater width observed in GaP has been attributed to donor-acceptor pair transitions. These spectra are usually broad because of strong phonon-assisted transitions arising from the tight binding of the O donor. The donor – acceptor pair transition energy $h\nu$ is rep-resented by,

$$h\nu = E_g - (E_D + E_A) + e^2/4\pi\varepsilon_o\varepsilon_r r,$$

where E_g is the energy band gap (2.26 eV at 300 K [3]), E_D and E_A the isolated donor and acceptor binding energies, ε_o the static dielectric constant (11.1), r the distance between the isolated donor and acceptor. Using 0.893 eV as E_D for O in P site [4], 0.204 eV as EA for Si in P site [5], and r = 3.853 Å as the nearest neighbor distance of P site, $h\nu$ is calculated to be 1.4998 eV (826 nm). This calculated wavelength is close to the observed peak. Therefore, the gamma-ray induced photo emission observed in GaP would be attributed to the O donor – Si acceptor pair transition. On the other hand, the gamma-ray induced photo emission was not observed in un-doped GaP wafers, suggesting that the existence of impurity is important for the photo emission.

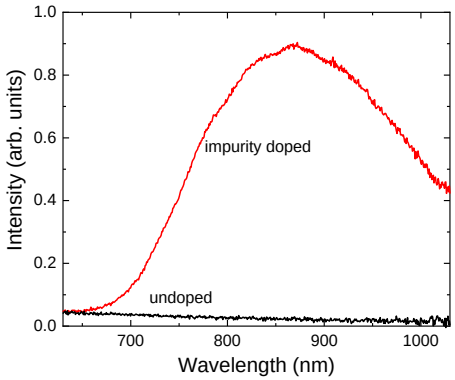

Fig. 1. Gamma-ray-induced photoemission spectra of impurity doped, and un-doped GaP single crystal wafers.

REFERENCES:

[1] T. Nakamura *et al.,* Appl. Phys. Lett., **118** (2021) 032106.
[2] T. Nakamura *et al.,* Solid State Commun., **336** (2021) 114413.
[3] M. R. Lorenz *et al.,* Phys. Rev., **171** (1968) 876.
[4] P. J. Dean *et al.,* Phys. Rev., **168** (1968) 812.
[5] P. J. Dean *et al.,* J. Appl. Phys., **39** (1968) 5631.

CO4-20

A study on destruction of cesium aluminosilicate compounds by gamma irradiation (5)

H. Ohashi, R. Tawatari, T. Saito[1]

Faculty of Symbiotic Systems Science, Fukushima University
[1]Research Reactor Institute, Kyoto University

INTRODUCTION: Pollucite which is one of cesium aluminosilicate compounds have attracted attention as a final storage material of ^{134}Cs and ^{137}Cs. Pollucite is easily synthesized by hydrothermal method in low temperature below 300°C [1]. Pollucite has various properties that favor the immobilization of Cs ions. However, the damage to the aluminosilicate framework by radiation decay is concerned because it contains ^{134}Cs and ^{137}Cs. It has been reported that the effect of β-ray emission and nuclide conversion by β-decay of ^{137}Cs on aluminosilicate framework is minor [2, 3]. On the other hand, there are few reports of effects by gamma rays on pollucite framework. Therefore, we examined the effect of gamma radiation on the aluminosilicate framework of Pollucite. In this report, we have studied on cesium leakage from pollucite with varying irradiation doses.

EXPERIMENTS: Sodium aluminate, sodium metasilicate and cesium chloride were dissolved in sodium hydroxide solution. The solution was placed in a Teflon inner cylinder pressure container. Pollucite was synthesized by hydrothermal method, holding the container at 180°C. The resulting precipitate was washed by distilled water or/and hot water. Thereafter, each solid was collected by filtration and dried at 110°C for 12 hours or more. Hydrothermal syntheses were also performed by replacing the sodium salts of the above reagents with potassium salts.

The powder samples were characterized by XRD, and gamma-irradiated with varying doses by ^{60}Co source. The leaching test by PCT-A method [4] was carried out to evaluate the change of Cs retention performance by framework damage. Concentration of cesium in solution leached was estimated by atomic absorption spectrophotometry.

RESULTS: Figure 1 shows the results of leaching tests performed with various conditions. As a result of the Fig.1, we found that the leakage of cesium from pollucite depends largely on the cleaning procedure but not on the irradiation dose.

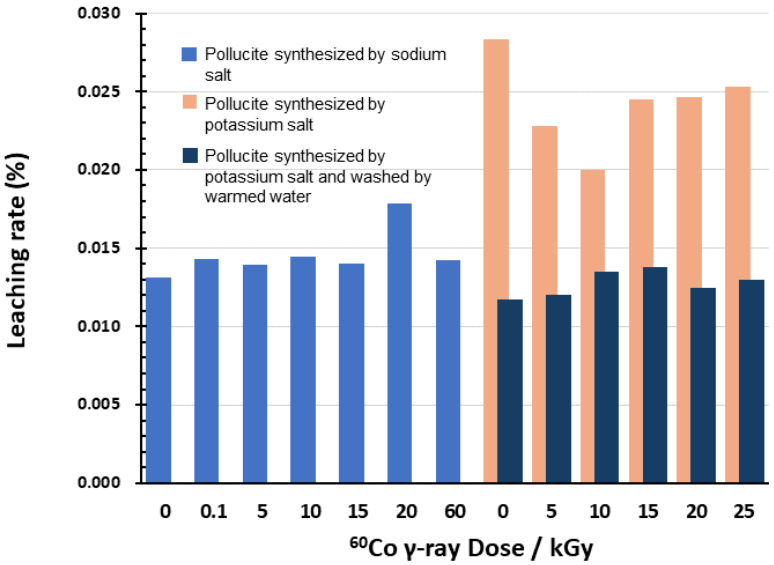

Fig. 1. Results for leaching tests of cesium from pollucite with varying doses by ^{60}Co source.

REFERENCES:

[1] Y. Yokomori *et al.*, *Sci. Rep.*, **4** (2014) 4195.
[2] J. Fortner *et al.*, Argonne National Laboratory, Argonne, Illinois 60439 (2001).
[3] N. J. Hess *et al.*, *J. Nucl. Mater.*, **281** (2000) 22-33.
[4] ASTM C 1285-02 (2008).

CO4-21

Study on the porosity of DLC coatings with different microstructures by positron annihilation spectroscopy

J. Choi[1], S.M. Bae[1], and A. Kinomura[2]

[1] *Department of Mechanical Engineering, Tokyo City University*
[2] *Institute for Integrated Radiation and Nuclear Science, Kyoto University*

INTRODUCTION: The increasing need to enhance the operational efficiency of mechanical systems has brought an increased focus on low-friction coatings. In response, diamond-like carbon coatings (DLCs) have garnered significant attention due to their exceptional mechanical and tribological properties [1]. Specifically, the microstructure of DLC coatings can be modified to meet various industrial demands; their possible structures can extend to graphite-like carbon (GLC) and polymer-like carbon (PLC) by altering deposition conditions and fabrication methods [2]. These structural characteristics are determined by factors such as hydrogen content and the ratio of carbonaceous bonds (sp^2 and sp^3). However, studies have indicated that defects also play a role in influencing the characteristics of coatings [3]. Positron annihilation spectroscopy (PAS) is a useful method for elucidating the defect behavior of materials. This study aims to investigate the porpsity of the DLC coatings with different microstructures using PAS.

EXPERIMENTS: The hydrogenated (H-) and fluorinated (F-) DLC coatings were fabricated by a plasma-based ion implantation (PBII) technique. The coatings were prepared onto Si (100) wafers. Different negative bias voltages, ranging from -1 to -10 kV, were directly applied to a target as a deposition parameter to vary their microstructure. The deposition period was adjusted to have a thickness of approximately 1 μm. The behavior of defect within the coating's microstructure was explained by the S-parameter and positron lifetime, obtained at a positron energy of 5 keV.

RESULTS: Figure 1 illustrates the variations in the S-parameter and the corresponding positron lifetime of the two types of coatings, (a) H-DLC and (b) F-DLC, deposited at different bias voltages. For H-DLC coatings, the S-parameter and positron lifetime increased to ~0.492 and ~0.373, respectively, with increasing the negative voltage up to -5kV. However, the S-parameter decreased with a further increase in the negative bias voltage. This suggests that initially, the size of voids increased at -5 kV, and subsequently the number of π electrons increased. In the case of F-DLC coatings, the S parameter and the positron lifetime tended to increase simultaneously, but the change in the S parameter at -10 kV was not significant. This indicates that the size of voids monotonically increased with no significant difference in the number of π electrons at -10 kV.

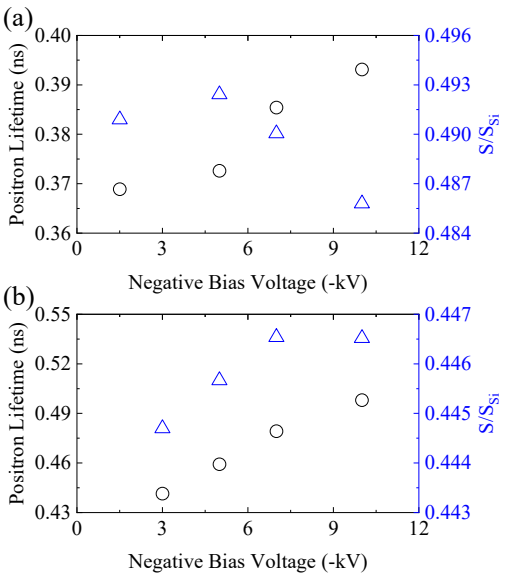

Fig. 1. The changes in S-parameter and positron lifetime for (a) H-DLC and (b) F-DLC coatings as the negative bias voltage increases.

REFERENCES:

[1] A. Erdemir *et al.*, J. Phys. D Appl. Phys., **39** (2006) R311.
[2] J. Choi *et al.*, Diam. Relat. Mater., **20** (2011) 845-848.
[3] S. Nakao *et al.*, Vacuum, **215** (2023) 112255.

CO4-22

Influence of Hydrogen Isotopes on Growth of Vacancy Clusters in Tungsten-Based Materials

Y. Hatano, A. Matsumoto[1], M. Nishimura[1], K. Fukuda[1], E. Taguchi[2], T. Takahashi[3], N. Abe[3] and A. Kinomura[3]

Hydrogen Isotope Research Center, University of Toyama
[1]Guraduate School of Science and Engineering, University of Toyama
[2]Department of Chemistry, Faculty of Science, University of Toyama
[3]Institute for Integrated Radiation and Nuclear Science, Kyoto University

INTRODUCTION: As a plasma-facing material of a fusion reactor, tungsten (W) will be exposed to fuel particles, deuterium (D) and tritium (T), and products of fusion reactions, helium and 14 MeV neutrons. Vacancies and vacancy clusters formed by neutron irradiation act as strong traps against hydrogen isotopes and increase T inventory in W [1]. Understanding of vacancy formation and clustering is necessary for accurate evaluation of T inventory in a vacuum vessel of a fusion reactor. Displacements by neutrons occur under exposure to hydrogen isotope plasma, and hence hydrogen isotopes may affect on growth and decomposition of vacancy clusters.

The objective of this study is to investigate the influence of hydrogen isotopes on behaviors of vacancy and vacancy clusters to construct a kinetic model of clustering and annihilation. To reach this goal, W samples with monovacancies and vacancy clusters are prepared by electron beam irradiation. Then, the irradiated samples are heated with and without hydrogen isotopes, and the difference in size distributions of vacancy clusters is examined using positron annihilation spectroscopy.

EXPERIMENTS: Disk samples of W were wrapped with aluminum foils and immersed in a flowing water. Then the samples were irradiated with 8 MeV electrons using KURNS-LINAC to 10^{-3} displacement per atom (dpa). A part of irradiated samples was exposed to D atoms at 200 ℃ to introduce D atoms and then heated under D_2 gas atmosphere at 0.1 MPa and 400 ℃ for 20 h. The other part of samples without D atoms were heated in vacuum at 400 ℃ for 20 h. Positron lifetime was measured by using ^{22}Na source at Institute for Materials Research, Tohoku University [1].

RESULTS AND DISCUSSION: The results of positron lifetime measurements are summarized in Table 1. The positron lifetime increased from 143 ps to 233 ps by irradiation of 8 MeV electrons. This means vacancy and vacancy clusters were generated by irradiation [2]. The exposure to D atoms resulted in reduction in positron lifetime to 204 ps because each trapped D atom brought 1 electron into a vacancy or vacancy cluster. Subsequent annealing at 400 ℃ under D_2 gas atmosphere led to increased positron lifetime of 226 ps because of growth of vacancy clusters. In contrast, annealing of the sample without D loading in vacuum at 400 ℃ resulted in reduction of lifetime to 212 ps due to decomposition of vacancy clusters. This clear difference indicated that vacancy clusters were stabilized and decomposition was hindered under the presence of D atoms.

Table 1 Positron lifetime (ps)

Sample	As-received	e-beam irradiated	D atom exposed	Annealed under D_2 gas at 400 ℃	Annealed in vacuum at 400 ℃
with D atoms	143	233	204	226	–
w/o D atoms	143	233	–	–	212

REFERENCES:

[1] T. Toyama *et al.,* J. Nucl. Mater., **499** (2018) 464-470.
[2] T. Troev *et al.,* Nucl, Instr. And Meth. B, **267** (2009) 535-541.

CO4-23

Impurity doping effect on vacancy-type defects in γ-CuI studied using a slow positron beam

M. Kitaura, K. Michishio[1], S. Watanabe[2], M. Ishizaki, A. Kinomura[3]

Faculty of Science, Yamagata University
[1]Research Institute for Measurement and Analytical Instrumentation, AIST
[2]Innovative Technology Laboratories, AGS Inc.
[3]Institute for Integrated Radiation and Nuclear Science, Kyoto University

INTRODUCTION: Copper iodide of γ-type (γ-CuI) is known as a promising candidate of the p-type semiconductor for thin-film transistors and hole transport layers in organic light emitting diodes (OLEDs). The effect of impurity doping on electronic properties of this material has been studied experimentally and theoretically [1]. It was recently reported that the hole concentration is controllable in the range of 10^{14}-10^{18} cm^{-3} by zinc-doping [2]. This is based on the result that zinc doping reduces the hole concentration. The physical model for the reduction of hole concentration due to zinc doping has been proposed. One is that zinc atoms substituting copper atoms (Zn_{Cu}) play as an electron donor. The other is that the zinc atoms introduce copper vacancyies (V_{Cu}), leading to the formation of a Zn_{Cu}-V_{Cu} pair. To demonstrate which is more suitable model to explain the effect of zinc doping on electronic properties in zinc-doped γ-CuI, it is important to visualize the existence of Cu vacancies by positron annihilation spectroscopy (PAS). We performed positron annihilation lifetime spectroscopy (PALS) experiment of γ-CuI by using a slow positron beam from Kyoto University research reactor (KUR).

EXPERIMENTS: Samples were undoped and Zn and I-doped γ-CuI polycrystalline pellets. A Kapton film was used to evaluate the background of PALS spectra. PALS spectra of samples were measured at 300 K using a slow positron beam with the energy of 25 keV. The positron annihilation lifetimes (PALs) were analyzed using the software POSITRONFIT.

RESULTS: Figure 1 shows PALS spectra of undoped, Zn- and I-doped γ-CuI. The spectra are reproduced by a single exponential decay component. The intensities reached over 95 %. The PALs were determined to be 314±1 ps, 338±1 ps and 315±1 ps for undoped, Zn- and I-doped γ-CuI, respectively. These values were almost agreement with the calculated PAL for the V_{Cu} defect (=320 ps). It is apparent that the V_{Cu} defect is dominant in our samples. This fact is reasonable, because the theoretical calculation of defect formation energies revealed that the V_{Cu} defect is the most stable among vacancy-type defects in γ-CuI [2,3]. It was reported that Zn doping reduces the hole concentration. Actually, the reduction in hole concentration by Zn-doping was confirmed. However, it could not be clarified whether Zn-doping changes the concentration of V_{Cu} defect. Further investigations are needed to clarify the effect of Zn-doping on the formation of V_{Cu} defects in γ-CuI.

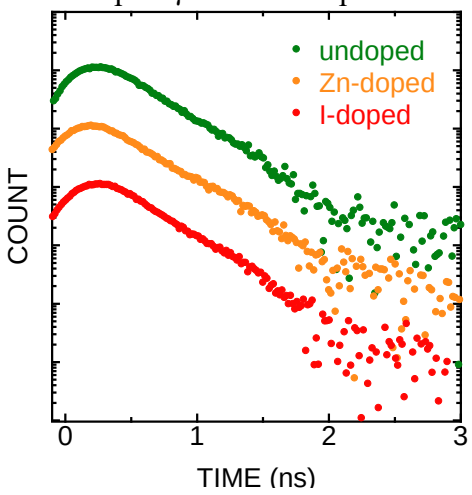

Fig. 1. PALS spectra of undoped, Zn- and I-doped γ-CuI, measured at 300K using a slow positron beam from KUR.

REFERENCES:

[1] M. Grundmann *et al.*, Phys. Status Solidi A, **210** (2013) 1671-1703.
[2] M. Tsuji *et al.*, ACS Appl. Mater. Interfaces, **14** (2022) 33462-33471.
[3] K. Matsuzaki *et al.*, J. Am. Chem. Soc., **144** (2022) 16572-16578.

CO4-24

TDPAC Measurement of ^{111}Cd(←^{111}In) in Ultrafine Bubble Water

M. Tanigaki, K. Takeshita[1], A. Taniguchi, Y. Ueda[2], Y. Tokuda [3], and Y. Ohkubo

Institute for Integrated Radiation and Nuclear Science, Kyoto University
[1]Graduate School of Science, Kyoto University
[2]Research Institute for Sustainable Humanosphere, Kyoto University
[3]Depertment of Education, Shiga University

INTRODUCTION: Ultrafine bubbles, the gaseous cavities with diameters less than 1 μm, have recently attracted much attention because of their multi-functionalities [1]. Fundamental studies on such multi-functionalities of ultrafine bubbles are not well extended because they are smaller than the wavelength of radiant rays. The time differential perturbed angular correlation (TDPAC) of ^{111}Cd(¬ ^{111}In) in the aqueous solution with ultrafine bubbles is performed for the study of the interface of ultrafine bubbles, which should be one of the essential origins of its multi-functionality.

EXPERIMENTS: Typical four-counter TDPAC measurements were performed for the 171-245 keV cascade in ^{111}Cd(¬ ^{111}In) in Oxygen water and water with Oxygen-ultrafine bubbles. The average diameter and the density of the ultrafine bubbles were 188 nm and 6.1 ×10^5/mL, respectively. The aqueous solution of ^{111}InCl$_3$ at pH ~ 2 from Nihon Medi-Physics was added to each sample and adjusted to pH = 4.0 by just dilution with the respective solvent instead of adding NaOH or HCl in the previous studies [2][3]. The angular correlation term $A_{22}G_{22}(t)$ is given by the following equation,

$$A_{22}G_{22}(t) = \frac{2\big(N(180°,t) - N(90°,t)\big)}{N(180°,t) + 2N(90°,t)}$$

where $N(90°, t)$ and $N(180°, t)$ are the counting numbers of the 171-245 keV γ-γ cascade at 90 and 180 degrees, respectively. The time-dependent term $G_{22}(t)$ for each sample was obtained by normalizing $A_{22}G_{22}(t)$ by the asymmetry parameter of 171-245 keV cascade in ^{111}Cd, A_{22} = –0.18.

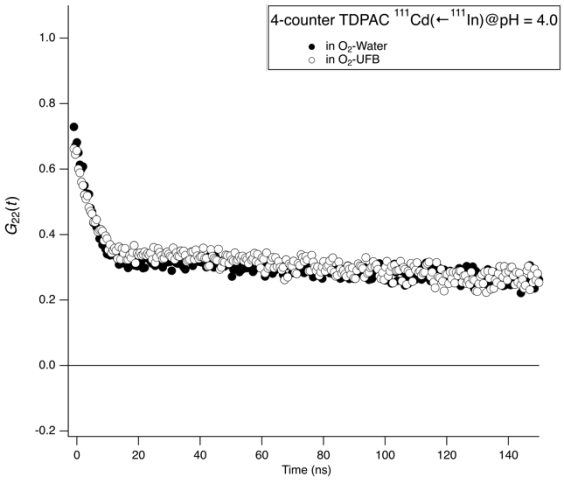

Fig. 2 TDPAC spectra of ^{111}Cd(¬ ^{111}In) in ultrafine bubble water and Oxygen water at pH = 4.0.

RESULTS: Fig. 1 shows the observed $G_{22}(t)$ for ^{111}Cd(¬ ^{111}In) in Oxygen water and water with Oxygen-ultrafine bubbles. These were similar to the cases of $G_{22}(t)$ in water at pH = 3.7 reported by Demille [3], but a slight difference was observed up to 60 ns between these spectra. This difference may be caused by the influence of the ultrafine bubbles on the formation of hydrated ions of In. More studies, such as the detailed pH dependence, are underway.

The present work is supported by JSPS KAKENHI Grant Numbers 18K03948 and 21K03854.

REFERENCES:

[1] E. G. Denis, The fine bubble breakthrough. https://www.iso.org/news/2014/05/Ref1844.html
[2] M. Tanigaki *et al.,* KURNS Progress Report 2021, p.124.
[3] M. Tanigaki *et al.,* KURNS Progress Report 2022, p.123
[4] G. R. Demille *et al.,* Chemical Physics Letters, **44** (1976) 164‑168.

CO4-25

Dynamics Analysis of Helical Polymers Using Small Angle X-ray Scattering/Dynamic Light Scattering/Molecular Dynamics Simulation

Y. Nagata[1], M. Suginome[2], M. Sugiyama[3], R. Inoue[3], N. Sato[3], and K. Morishima[3]

[1] *Institute for Chemical Reaction Design and Discovery, Hokkaido University*
[2] *Graduate School of Engendering, Kyoto University*
[3] *Institute for Integrated Radiation and Nuclear Science, Kyoto University*

INTRODUCTION: Due to their potential applications in asymmetric catalysts, chiral stationary phases, and chiroptical materials, the structural control of helical polymers has received much attention. Recently, we have reported that helical poly(quinoxaline-2,3-diyl) (PQX) with chiral side chains display solvent-dependent helix inversions,[1-3] which can serve as effective frameworks for chirality-switching materials.[4-7] For elucidating the mechanism of helix induction and helix inversion of PQXs, we have studied the detailed structures of a PQX (100mer) with right- or left-handed structures into tetrahydrofuran-d_8 (THF-d_8) or a mixed solvent of 1,1,2-trichloroethane-d_3 (1,1,2-TCE-d_3) and THF-d_8 (4/1, v/v) using small-angle neutron scattering (SANS) experiments in conjunction with theoretical calculations.[8] Our recent interest has been focused on the effect of the dynamics of the side chains on the induction of the helix sense. Previously, we performed quasi-elastic neutron scattering (QENS) measurements to elucidate the influence of molecular dynamics on the solvent-dependent helix inversion of PQX. In this study, we performed molecular dynamics (MD) simulations to analyze the results of the QENS measurements in detail.

EXPERIMENTS: The initial geometries of the *P*- and *M*-helical PQX were estimated by SANS measurements in our previous study.[8] The MD simulations were performed using the Forcite module of Materials Studio 2020 with the COMPASS II force field (version 1.2) at ultra-fine quality. Here, we have treated the difference in viscosity between the two solvents as a difference in temperature. MD simulations of the PQX were performed in a vacuum using a constant-volume/constant-temperature (NVT) canonical ensemble with a simulation time of 1000 ps at different temperatures (73.15 to 473.15 K).

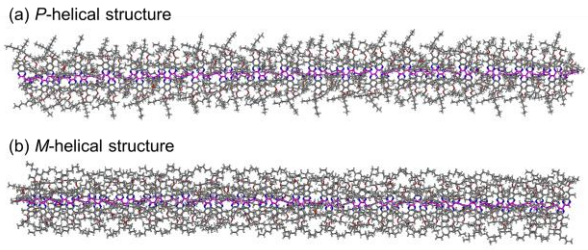

Fig. 1 The initial structures of the PQX

RESULTS: We have compared the QENS simulations using the MD trajectories at varying temperatures and measured values. We found good agreement with the MD simulations at 313.15 K for the *P*-helical structure at 73.15 K for the *M*-helical structure. To elucidate the mechanism of helix inversion, we will analyze the obtained MD trajectories in the future.

REFERENCES:

(1) T. Yamada *et al.,* Chem. Commun., **46** (2010) 4914-4916.
(2) Y. Nagata *et al.,* J. Am. Chem. Soc., **135** (2013) 10104-10113.
(3) Y. Nagata *et al.,* J. Am. Chem. Soc., **137** (2015) 4070-4073.
(4) Y. Nagata *et al., Chem. Commun.*, **48** (2012) 11193-11195.
(5) Y. Nagata *et al.,* M. J. Am. Chem. Soc., **136** (2014) 9858-9861.
(6) Y. Nagata *et al.,* Angew. Chem. Int. Ed., ***55*** (2016) 7126-7130.
(7) T. Nishikawa *et al.,* ACS Macro Lett., **6** (2017) 431-435.
(8) Y. Nagata *et al.,* J. Am. Chem. Soc., **140** (2018) 2722-2726.

CO4-26

Resonant frequency change with irradiation dose of piezoelectric PZT element

M. Kobayashi, T. Miyachi, S. Takechi[1], Shoki Maeda[1], Shuhei Tominaga[1], A. Takahashi1, R. Takahashi[1], S. Katayama[1]

Planetary Exploration Research Center, Chiba Institute of Technology
[1]Graduate School of Engineering, Osaka City University

INTRODUCTION: This study aims to establish an inexpensive method for dosimetry in high-dose environments. We consider changes in piezoelectric (PE) properties of PE elements due to irradiation for dosimetry in high-dose environments. For this purpose, the mechanism of radiation-induced change of PE properties has been investigated.
In a previous experiment conducted at NIRS/HIMAC, PZT PE elements were irradiated with 400 MeV/n Xe particles, and the decrease in the electromechanical coupling coefficient k was investigated [1][2]. As a result, it was found that k_r of the irradiated PZT element was -0.35%/kJ, which is a phenomenon concerning the irradiation dose [3]. To investigate what happens to PE elements due to irradiation, electron beam irradiation experiments have been conducted at KURNS-LINAC. The effect of temperature, which was negligible in the Xe particle experiments, has been investigated and controlled in the experiments at KURNS-LINAC [4].
EXPERIMENTS IN THE FISCAL YEAR 2023: In this study, to re-examine the effect of temperature rise on the piezoelectricity of PZT, PZT PE elements were irradiated with electron beams under sufficiently controlled beam intensity conditions to investigate the radiation-induced change in k. Furthermore, the retentivity of the change in k was verified by irradiating the device multiple times over a period of days [5]. The electron beam irradiation experiments were carried out twice, in June and December 2023. The irradiated samples were disc-shaped PZT (soft material, Honda Electronics) with a radius of 9 mm and thickness of 1 mm, and the irradiation experiments were carried out in the same way as before. The beam conditions were the same as before, with an energy of 20 MeV and a beam current (beam intensity) of 1.1 μA, which was sufficiently low compared to the current value of 4.8 μA in the previous experiment. The temperature of the controlled irradiated samples was constantly monitored during irradiation and air-cooling was used to ensure that the temperature did not rise above 60-70 °C. The temperature of the samples was monitored by thermocouples attached to the sample surface. The irradiation time per day was limited to about 2 hours, and irradiation was carried out over a period of 3-4 days. This was to determine the effect of the recovery of the k, which had changed while the irradiation was stopped.
RESULTS: The results of the two experiments were similar, except for the effects of poor measurements, which may have been due to inadequacies in the experimental set-up. The results can be summarized as follows. A change of more than one order of magnitude was obtained compared to the change in k due to temperature rise. This is the net k change due to electron beam irradiation. The result shows that the rate of change of k with respect to the absorbed dose (absorbed energy) applied to the PZT PE element, a value of -0.24 ± 0.015 [%/kJ] was obtained. [5]

REFERENCES:
[1] M. Kobayashi *et al*., Jpn. J. Appl. Phys., **52** (2013) 126604.
[2] M. Kobayashi *et al.*, Jpn. J. Appl. Phys., **53** (2014) 066602.
[3] S. Takechi *et al.*, Jpn. J. Appl. Phys., **60** (2021) 038003.
[4] S. Takechi *et al*., Jpn. J. Appl. Phys., **61** (2022) 128001.
[5] M. Maeda, Master Thesis, Graduate School of Engineering, Osaka Metropolitan University (2024).

CO4-27

Tritium release behavior from neutron irradiated $LiAlO_2$

K. Katayama, H. Isogawa[1], S. Kobayashi[2], H. Matsuura[3], K. Akashi[2], T. Takeishi[2], Y. Iinuma[4]

Faculty of Engineering Science, Kyushu University
[1]Interdisciplinary Graduate School of Engineering Sciences, Kyushu University
[2]School of Engineering, Kyushu University
[3]Faculty of Engineering, Kyushu University
[4]Institute for Integrated Radiation and Nuclear Science, Kyoto University

INTRODUCTION: To launch a deuterium – tritium fusion reactor, it is required to produce enough among of tritium in advance. A high temperature gas-cooled reactor is proposed as a tritium production device [1]. One critical issue is tritium confinement at high temperature conditions. One idea is to combine alumina (Al_2O_3), which has a low hydrogen isotope permeability, with zirconium (Zr), which has a high hydrogen isotope solubility [2]. Tritium is generated in a lithium (Li) compound by a nuclear reaction with neutrons, and the tritium released from the Li compound is confined by the Al_2O_3 wall. Zr packed within the Al_2O_3 wall reduces tritium partial pressure and suppresses tritium permeation through Al_2O_3 wall. $LiAlO_2$ is expected to be a promising Li compound due to its chemical stability. However, the tritium release characteristics from $LiAlO_2$ are not completely understood. In this study, Al_2O_3 powder was irradiated by neutrons in Kyoto University Research Reactor and tritium release behavior by heating was observed.

****

EXPERIMENTS: Commercial powder of $LiAlO_2$ was packed in a quartz tube with vacuum sealing and was irradiated by neutrons with 5.5×10^{12} 1/(cm^2·s) in flux and 3 minutes in irradiation period. The weight of powder was 0.25 g. After neutron irradiation, the samples were transported to Kyushu University for tritium release experiments. The schematic diagram of the experimental apparatus is shown in Fig.1. The irradiated $LiAlO_2$ powder was packed in a quartz reaction tube. The sample was heated by an electric furnace to 900 °C in Ar gas flow. The released gaseous tritium (HT) and tritiated water vapor (HTO) were separately collected in water bubblers.

****

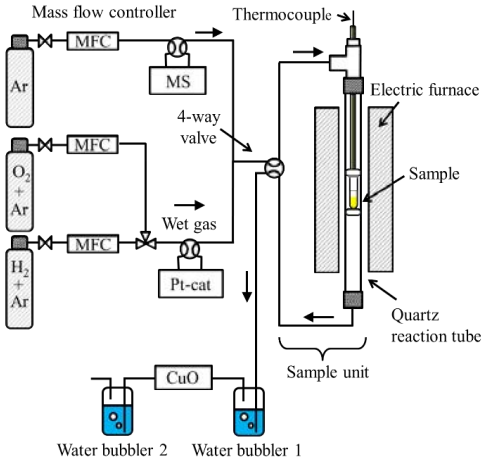

Fig. 1. Experimental apparatus.

RESULTS: Fig.2 shows the release behavior of tritium from neutron irradiated $LiAlO_2$ powder. The chemical form of the released tritium was mostly tritiated HTO. HTO was released over a wide range of temperatures from 100 °C to 900 °C, with large peaks observed at around 250, 550, and 700 °C. The total amount of tritium released was 1.0×10^5 Bq, and the ratio of HTO was 97 %, and the ratio of HT was 3 %. It was found that the tritium absorption performance of Zr from HTO and the permeation property of tritium from HTO through $LiAlO_2$ wall are important.

****

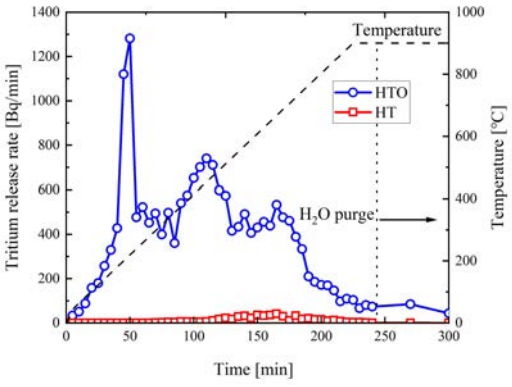

Fig. 2. Tritium release behavior from neutron irradiated $LiAlO_2$ powder.

REFERENCES:

[1]H. Matsuura, *et al*., Nucl. Eng. Des., **243** (2012) 95–101.
[2]H. Nakaya, *et al*., Nucl. Eng. Des., **292** (2015) 277–282.

CO4-28

Vacancy Migration Energy in VNbMoTaW High-Entropy Alloy

H. Araki, M. Mizuno, A. Yabuuchi[1] and A. Kinomura[1]

Graduate School of Engineering, Osaka University
[1]Institute for Integrated Radiation and Nuclear Science, Kyoto University

INTRODUCTION: Tsai *et al*. [1] originally proposed the concept of sluggish diffusion in the high-entropy alloy(HEA). However, the reason for the sluggishness of diffusion is not quite clear. VNbMoTaW is known to form a quinary single-phased body-centered cubic structured solid solution. In the VNbMoTaW HEA at high temperatures, atomic diffusion is expected to proceed via a vacancy mechanism because they are substitutional solid solutions. Therefore, vacancy formation and migration energies in the VNbMoTaW HEA and its subsystems are important indexes for understanding the sluggish diffusion. In this work we have evaluated the vacancy migration energy in VNbMoTaW HEA by observing the vacancy migration and annihilation behavior during an annealing process after electron irradiation, with the use of the positron lifetime spectroscopy.

EXPERIMENTS: An ingot of VNbMoTaW HEA was cut into 10 mm × 10 mm × 1 mm plates, and carried out with solid solution heat treatment at 1423K for 24 h under argon atmosphere. The X-ray diffraction analysis shows that all the samples are composed of single phase with a bcc structure. Then, the samples were irradiated in water with 8 MeV electrons at a fluence of approximately, 1.78×10^{19} e^{-} m^{-2} below 373 K using the electron linear accelerator at the Institute for Integrated Radiation and Nuclear Science, Kyoto University. The irradiated samples were isochronally annealed in a temperature range from 373 to 1023 K. The temperature step during the isochronal annealing was 50 K and the duration of exposure to each temperature was 1 h. The positron lifetime measurements were made at 297–299 K.

RESULTS: Before the electron irradiation the positron lifetime spectrum for the solution-treated alloys was represented by only one component of 125 ps, which indicates that positrons annihilate in the bulk. After electron irradiation, the mean positron lifetime was increased to 155 ps. The analysis of positron lifetime spectra for the as-irradiated sample shows that many positrons are trapped and annihilate in the monovacancies introduced by electron irradiation, because the lifetime component, τ_2 , of trapped positrons was 176.7 ps. Fig.1 shows the relative change in the vacancy concentration during the isochronal annealing of the irradiated sample, which was evaluated on the basis of the two- or three-component analyses for the positron lifetime spectra. As shown in Fig.1, the theoretical curve of Dryzek *et al*.'s model [2] assuming that vacancy migration energy is 1.32 eV is in good agreement with the experimental data. The melting point of VNbMoTaW is reported to be 2946K. Taking into account the high melting point, the results of this work do not fully support the sluggish diffusion mechanism that has been proposed for HEAs.

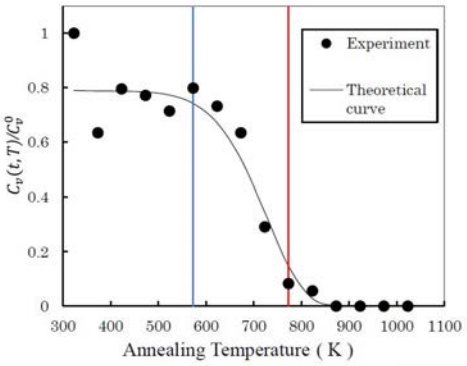

Fig. 1. The relative change in vacancy concentration during the isochronal annealing of irradiated sample.

REFERENCES:

[1] K. Y. Tsai, M. H. Tsai and J. W. Yeh, Acta Mater., **61** (2013) 4887.
[2] J. Dryzek, C. Wesseling, E. Dryzek and B. Cleff, Mater. Lett., **21** (1994) 209.

Operando Measurement of a Lithium-Ion Battery Using an Internal Positron Source Technique

A. Yabuuchi, N. Oshima[1], T. Fujiwara[1], K. Michishio[1], and M. Hino

Institute for Integrated Radiation and Nuclear Science, Kyoto University
[1]National Institute of Advanced Industrial Science and Technology

INTRODUCTION: Positron annihilation spectroscopy enables nondestructive detection of changes in electronic states of materials. However, in general, it is necessary to inject positrons from outside of the sample, making it difficult to investigate the interior of thick samples. For example, positrons emitted from the commonly used ^{22}Na positron source are injected only to a depth of less than 100 μm below the iron surface. Another technique is to inject a high-energy gamma-ray beam into the sample to pair-produce positrons inside the sample [1], but in this case it is not possible to investigate a specific region inside the sample. In this study, a lithium-ion battery (LIB) sample was exposed to thermal neutrons at KUR CN-3 to produce positron-emitting nuclide ^{64}Cu in the copper foil, which is the anode current collector. Then, the Doppler broadening of the annihilation radiation (DBAR) was measured while discharging the LIB sample.

EXPERIMENTS: Positrons emitted from the copper foil are injected into the graphite coated on the copper foil as an anode material. DBAR spectra were measured while discharging the LIB sample from a charged state over 25 hours using a fixed resistor circuit. The shape change of each spectrum was evaluated by the S-parameter [2].

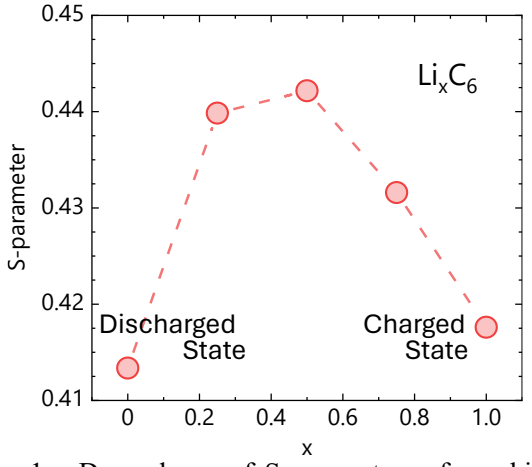

Fig. 1. Dependence of S-parameters of graphite anode on Li concentration (Li_xC_6).

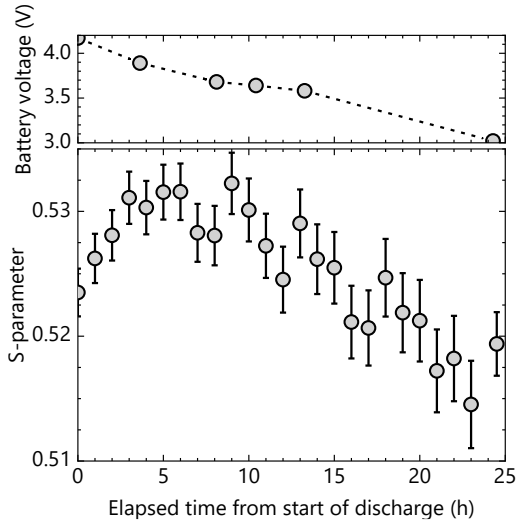

Fig. 2. S-parameter change while discharging.

RESULTS: Figure 1 shows the change in S-parameter caused by intercalation of lithium atoms into the graphite anode, obtained from first-principles calculations. Li_1C_6 and Li_0C_6 correspond to the charged and discharged states, respectively. During the discharge process of the LIB, the calculated S-parameters of graphite once increase and then begin to decrease. Figure 2 shows the change in the S-parameter measured while discharging the LIB sample. Although it should be noted that the discharge current was not constant (i.e., the Li de-intercalation rate was not constant), a trend like the change expected from the first-principles calculations is observed. The reason why the absolute values of the S-parameters differ between the calculated and experimental values is mainly due to the use of different S-parameter definition formulas. We successfully probed the change of Li intercalation state in the anode of the LIB using positrons.

REFERENCES:

[1] Y. Taira *et al.*, Rev. Sci. Instrum., **93** (2022) 113304.
[2] F. A. Selim, Mater. Charact., **174** (2021) 110952.

CO4-30

Vacancies in P-Doped β-$FeSi_2$ Film Probed By a Slow Positron Beam

A. Yabuuchi

Institute for Integrated Radiation and Nuclear Science, Kyoto University

INTRODUCTION: As an environmentally friendly infrared luminescent material, β-$FeSi_2$ is expected. For practical use, however, a further increase in luminescence intensity is desired. Atomic vacancies have a significant impact on the luminescence characteristics in semiconductors. Using the KUR slow positron beam, vacancies in β-$FeSi_2$ films doped with Mn or Al, which are acceptor impurities that substitute the Fe and Si sites, respectively, have been investigated. As a result, Al doping, which has been reported to enhance luminescence intensity, was found to promote the formation of Fe vacancies. In this study, vacancies in β-$FeSi_2$ films doped with Co or P, which are donor impurities that substitute the Fe and Si sites, respectively [1,2], were studied.

EXPERIMENTS: The ion beam synthesis method was used to prepare undoped, Co-doped, and P-doped β-$FeSi_2$ films. These films were probed by a slow positron beam at the Kyoto University Research Reactor [3]. The Doppler broadening of annihilation radiation (DBAR) spectra were acquired. The shape of the obtained DBAR spectra was characterized by the S parameter [4], which depends on the fraction of positron annihilation with low-momentum electrons. Positrons trapped in vacancies increase the probability of annihilation of low-momentum valence electrons, resulting in an increase in the S parameter.

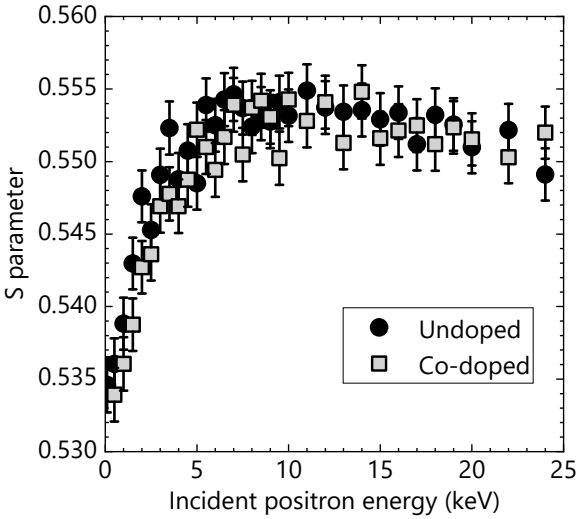

Fig. 1. S parameters of undoped and Co-doped films as a function of incident positron energy.

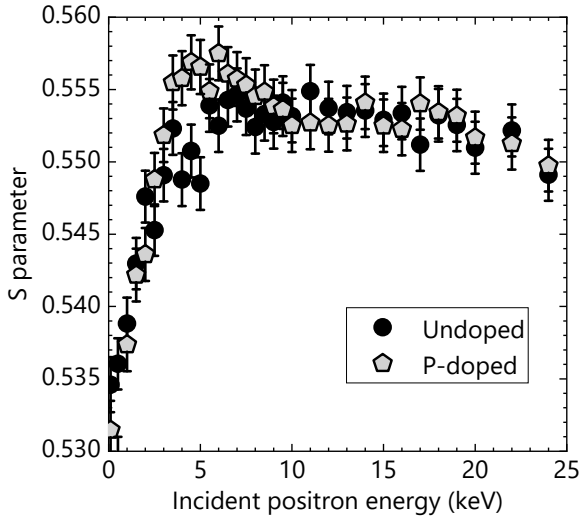

Fig. 2. S parameters of undoped and P-doped films as a function of incident positron energy.

RESULTS: Figs. 1 and 2 show the S parameters of each film as a function of incident positron energy. The incident positron energy of around 3−5 keV corresponds to the annihilation gamma-ray signal from the β-$FeSi_2$ film formed on the Si substrate surface. Focusing on that energy range, the S parameter is slightly lower in the Co-doped film, which substitutes Fe sites, than in the undoped film. In contrast, the S parameter of P-doped film, which substitutes Si sites, increases compared to the undoped film. This indicates that P-doping promotes vacancy formation. In the future, coincidence DBAR spectra will be measured to reveal whether the vacancies formed by the P-doping are Fe vacancies or Si vacancies.

REFERENCES:

[1] J. Tani and H. Kido, J. Solid State Chem., **163** (2002) 248.
[2] Y. Wanjun *et al.*, J. Semicond., **34** (2013) 103003.
[3] A. Yabuuchi, Nucl. Instrum. Method Phys. Res., Sect. B, **513** (2022) 44.
[4] F. Tuomisto and I. Makkonen, Rev. Mod. Phys., **85** (2013) 1583.

CO4-31

Radiation Induced Demagnetization of Neodymium Magnets

Y. Fuwa, Y. Kuriyama[1], Y. Iwashita[1], K. Takamiya[1], T. Takayanagi

J-PARC Center, Japan Atomic Energy Agency
[1]Institute for Integrated Radiation and Nuclear Science, Kyoto University

INTRODUCTION: Permanent magnets are essential devices in the transport and control of charged particle and neutron beams due to their lower power consumption, compactness, and the fact that they do not require ancillary equipment [1-3]. On the other hand, demagnetization due to radiation is one of the concerns when using permanent magnets, but quantitative evaluation of its effects is insufficient. Therefore, we have systematically evaluated the effects of radiation-induced demagnetization using the irradiation facility at KUR over the last few years [4]. Magnet manufacturers add several additives to improve coercivity. Naturally, the additives are trade secrets and undisclosed. Previous studies have shown that even the same neodymium magnets show significant differences in the rate of demagnetization caused by radiation, and one of the reasons for this is thought to be the dysprosium content. However, other substances are also expected to have a significant influence on resistance to radiation. As additives other than the main magnet component have not been published, an attempt has been made to measure the correlation between additives and the effect of demagnetization.

EXPERIMENTS: In this study, differences in radiation demagnetization effects for neodymium magnets were evaluated. The irradiated sample were five types of neodymium magnets; N38H, N38EH, N39SH, N39UH, N48H made by SHIMONISHI SEISAKUSHO Co,. Ltd. The shape of the sample was cylindrical with a thickness of 1 mm and a diameter of 5 mm. The irradiation experiments were performed at KUR Pn-2 port and Tc-Pn. Irradiation was also carried out for elemental identification using activation analysis methods.

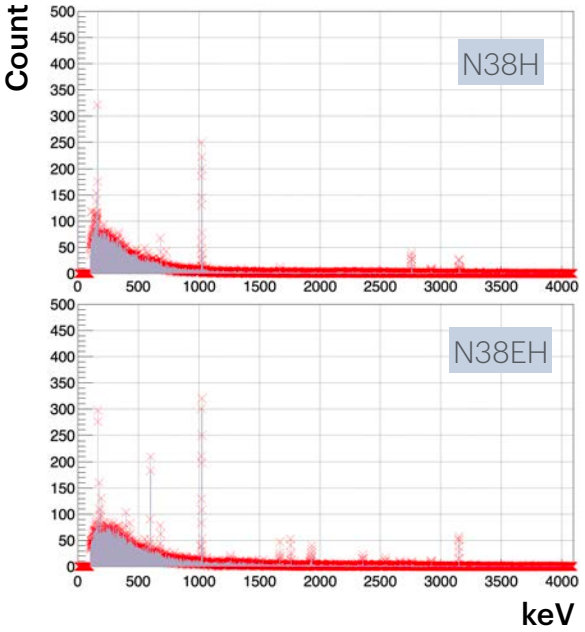

Fig. 1. Gamma-ray energy spectrum taken with a Ge detector at about 3.5 hours after irradiation of 3 seconds using Pn-2. Upper is N38H, lower is N38EH, respectively.

RESULTS: The evaluation of demagnetization is ongoing, as we need to wait for the radiation levels of the samples to decrease. Fig. 1 shows the typical gamma-ray spectrum taken with a Ge detector at about 3.5 hours after irradiation of 3 seconds using Pn-2. As shown in Fig. 1, it is expected that there are differences in the substances contained in N38H and N38EH as well. Measurements with a Ge detector have been made at several times after irradiation. The nuclides will be identified and their correlation with radiation demagnetization will be investigated in detail.

REFERENCES:

[1] Y. Fuwa *et al.*, Prog. Theor. Exp. Phys., **2017(2)** (2017) 023G01.
[2] Y. Kuriyama *et al.*, IEEE Trans. Appl. Supercond., **34(5)** (2024) 4004005.
[3] M. Yamada *et.al.*, Prog. Theor. Exp. Phys., **2015(4)** (2015) 043G01.
[4] Y. Fuwa *et al.*, MT-27 Int. Conf. on Magnet Technology, (2021) TUE-P01-115-05 .

CO4-32

Performance of Field Emitter Based Photo-detection Device under Gamma-ray Irradiation

Y. Gotoh, Y. Neo[1], N. Sato[2], M. Nagao[3], and T. Okamoto[4]

Graduate School of Engineering, Kyoto University
[1]Research Institute of Electronics, Shizuoka University
[2]Institute for Integrated Radiation and Nuclear Science, Kyoto University
[3]National Institute of Advanced Industrial Science and Technology (AIST)
[4]National Institute of Technology, Kisarazu College

INTRODUCTION: One of the most important issues for nuclear decommissioning of Fukushima Daiichi nuclear power plant is to develop image sensor reliable even in the radiation circumstance. The authors have been developing an image sensor based on the field emitter arrays, exhibiting the high durability against γ-ray irradiation [1]. We have already shown the fundamental characteristics of the photo-detection device based on field emitter array (FEA) under a normal circumstances [2]. In this study, the operational performance of the photo-detection device under γ-ray irradiation and in normal circumstances were investigated.

EXPERIMENTS: The photo-detection device was consisted of an FEA, mesh electrode, and photoconductor. The FEA which was used in the previous study [2] was again used. γ-ray irradiation was performed at the Co-60 gamma-ray irradiation facility, Research Institute for Integrated Radiation and Nuclear Science, Kyoto University. The emitter was grounded and the gate was biased to 60 V to extract electrons. The mesh was given a potential of 200 V. The anode characteristics was acquired with varying the anode voltage from 0 V to 50 V. The dose rate of irradiation was approximately 50 – 60 Gy h^{-1}.

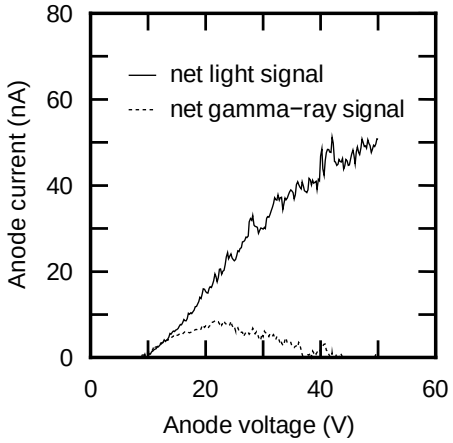

Figure 1. Anode characteristics under visible light and γ-ray irradiation.

RESULTS: The signals of visible light and γ-ray are shown in Fig. 1 [3]. The dotted line shows the net γ-ray signal which was obtained by subtracting the dark current from the anode current under γ-ray irradiation. The solid line shows the net visible light which was obtained by subtracting the dark current from the anode current under visible light irradiation. The power of the light was 10 μW. It is clearly seen that the anode current flows only a little under the γ-ray irradiation, as compared to the current with visible light incident. It is clearly seen that the present device has higher sensitivity for visible light than for γ-ray. From this result, the device could be used as a in the primary containment vessel in which the dose rate is approximately 100 Gy h^{-1}.

ACKNOWLEDGMENTS: The present work was partly supported by Japan Society for the Promotion of Science, through a Grant-in-Aid for Scientific Research B, JP21H01860.

REFERENCES:
[1] Y. Gotoh *et al.*, IEEE Trans. On ED **67** (2020) 1660-1667.
[2] Y. Gotoh *et al.*, KURNS Progress Report 2022 (2023) 114.
[3] Y. Gotoh *et al.*, The 58th Meeting of KURNS 2024, P15.

CO4-33

Fundamental study of damage on tungsten by heat and particle loading

K. Tokunaga, M. Matsuyama[1], Y. Hatano[1], M. Hasegawa, K. Nakamura and Q. Xu[2]

Research Institute for Applied Mechanics, Kyushu University
[1]Hydrogen Isotope Research Center, University of Toyama
[2]Institute for Integrated Radiation and Nuclear Science, Kyoto University

INTRODUCTION: It is of a great importance to clarify phenomena of implantation, retention, diffusion and permeation of tritium (T) on surface of the armor materials of the first wall/blanket and the divertor on the fusion devices from a viewpoint of precise control of fuel particles, reduction of tritium inventory and safe waste management of materials contaminated with tritium. In the present works, T exposure experiments have been carried out on W samples which were irradiated by high energy electrons to investigate effects of high energy electrons irradiation on microstructure and tritium retention of W. In this fiscal year, pure W and recrystallized W were irradiated by high energy electron beam. Before and after that, positron annihilation experiment was carried out to identify the radiation defect. In this fiscal year, tritium exposure experiments at 350 °C using a tritium (T) exposure device is reported.

EXPERIMENTS: W samples used were ITER specification W (ALMT-grade) (SR-W) and its recrystallized W (RC-W). The SR-W was fabricated via a powder metallurgical route including cold isostatic pressing, sintering, hot rolling, and heat treating to relieve the residual stresses. Some of the machined SR specimens were subjected to a full recrystallization treatment at 2000 ºC for 1 hr in vacuum. High energy electrons irradiation has been carried out using LINAC in Institute for Integrated Radiation and Nuclear Science, Kyoto University. An peak energy of electron irradiated was 8 MeV and DPA was 5.8 x 10^{-3}. Temperature during the irradiation was measured by thermocouples which was contacted with a backside of the W samples. Before and after that, positron annihilation experiment was carried out to identify the radiation defect. In addition, a high energy ion irradiation experiment has been carried out. The sample surface was irradiated by 2.5 MeV Fe ions with a flence of 5 x 10^{18} ions/m^2 at RT. T exposure experiments have been carried out using a T exposure device in University of Toyama. Pressure of the T gas was 1.3 kPa and T exposure was kept for 4 h at 350 ºC. T concentration in the gas was about 5 %. After the exposure to T gas, T amount retained in surface layers of the sample was evaluated by imaging plate (IP) measurements and β-ray-induced X-ray spectrometry (BIXS).

RESULTS: Figure 1 shows X-ray spectra observed by BIXS. Signal of Ar(Kα) is from T near the sample surface. On the other hand, W(Mα) shows amount of T near a depth of a few μm from the surface. The results indicate that depth distributions of T are different between e-irradiated and Fe irradiated samples because the ratios of W(W(Mα))/Ar(Kα) are different. These results are considered to be related with T retention by radiation damage near the sample surface.

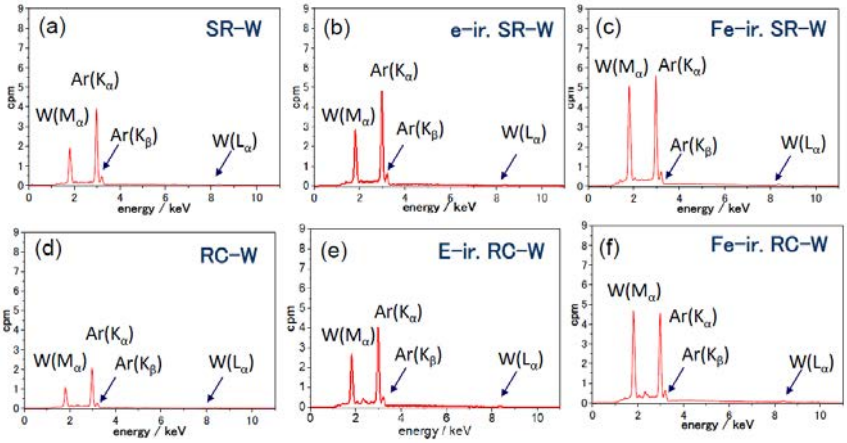

Fig. 1. Results of BIXS measurement. T exposure temperature is 350 °C. (a): SR-W, (b): electron irradiated SR-W, (c): Fe irradiated SR-W, (d): RC-W, (e): Fe irradiated RC-W, (f): Fe irradiated RC-W.

CO4-34

Correlation between irradiation defect density and hydrogen isotope retention in tungsten

M.I. Kobayashi[1,2], N. Abe[3] and T. Takahashi[3]

[1]*National Institute for Fusion Science, National Institutes of Natural Sciences*
[2]*The Graduate University for Advanced Studies, SOKENDAI*
[3]*Institute for Integrated Radiation and Nuclear Science, Kyoto University*

INTRODUCTION: Tungsten (W) will be used in the deuterium-tritium (D-T) fusion reactor to face to energetic particles such as fast neutrons. W atoms at lattice points in the crystal structure are recoiled by fast neutrons, forming irradiation defects. About two orders of magnitude larger D retention in neutron irradiated W has been reported [1]. This result should suggest that irradiation defects strongly trap hydrogen isotopes, leading to a drastic change of hydrogen isotope transport behaviors in W. In this study, we tried to evaluate the quantitative correlation between irradiation defect density and hydrogen isotope retention in W.

EXPERIMENTS: The W sample was purchased from A.L.M.T co. The thickness of the sample was 500 μm. A sample was pre-annealed at 1173 K for 0.5 hours under high vacuum. Then, samples were shipped to KURNS-LINAC for electron irradiation. The electron acceleration voltage was 8 MV. The dose was evaluated as 4.3×10^{-3} dpa according to an atomic displacement cross-section of 70.4 barns and a displacement threshold energy of 84 eV [2]. The irradiation temperature was less than 353 K due to the water coolant.
For evaluating the irradiation defects formed in the sample, positron lifetime measurements were conducted at Kagoshima Univ. The sample was faced to ^{22}Na deposited on the plastic substrate. ^{22}Na emits a positron and a 1.27 MeV gamma-ray. The scintillators surrounding the sample detected 1.27 MeV gamma-ray, then the elapsed time to detect the positron-electron annihilation gamma-rays was measured as the positron lifetime.

RESULTS: The results of the positron lifetime measurements are shown in Fig. 1. The results of annealed W and electron irradiated W were similar, although a slight difference can be found in the decay behaviors. From the decay behaviors the positron lifetimes of annealed W and electron irradiated W were evaluated to be 151 ps and 186 ps, respectively. The components with longer positron lifetime were not detected. This indicates that small size defects such as mono-vacancies and dislocation loops were formed by electron irradiation.

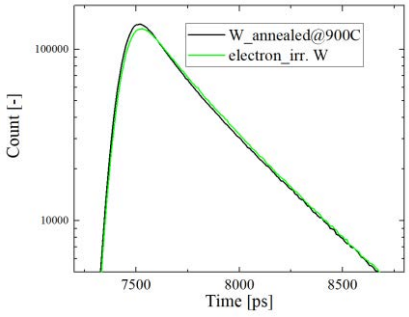

Fig. 1 The results of positron lifetime measurements.

To measure the trapping behavior of hydrogen isotopes in defects produced by electron irradiation, tritium ion irradiation was carried out using the tritium ion irradiation apparatus shown in Fig. 2 placed in Hydrogen Isotope Research Center, University of Toyama. The depth profile of tritium concentration will be measured by the combination of electrolytic polishing and the liquid scintillation counter. For these measurements, the polishing rates of W materials are estimating by the weight loss method, and the tritium concentration measurement in electron irradiated W will be done in FY2024.

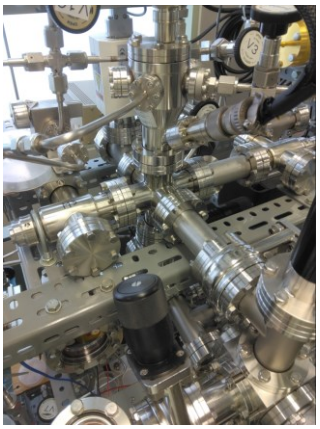
Fig. 2 Tritium ion irradiation apparatus

REFERENCES:
[1] Y. Hatano *et al.,* Nucl. Fusion, **53** (2013) 073006.
[2] K. Sato *et al.,* Nucl. Mater. Ene., **9** (2016) 554.

CO4-35

Neutron Irradiation Tests for Components of ITER Diagnostics System

T. Ushiki, E. Yatsuka, K. Nojiri. T. Yokozuka, H. Murakami, T, Kikuchi, T. Maruyama, M. Ishikawa, and Y. Nunoya

National Institutes for Quantum Science and Technology

INTRODUCTION: ITER [1] is the world's largest fusion experiment reactor and is under construction in southern France. Components of diagnostic systems installed in the ITER tokamak are exposed to high neutron radiations. Therefore, it is important to investigate the effect of neutron irradiation on these components. In this study, neutron irradiation tests on many kinds of components of diagnostic systems of ITER have been conducted. This report presents the result of the neutron irradiation test on the ultrasonic motor of Infrared Thermography system (IRTh) [2] and the pressure gauge of the Edge Thomson Scattering system (ETS) [3] and Divertor Impurity Monitor system (DIM) [4].

****

(1) Irradiation test for the ultrasonic motor for IRTh

IRTh plans to use a steering mirror driven by an ultrasonic motor for optical axis adjustment in the ITER. In this study, neutron irradiation tests on the ultrasonic motor were conducted.

EXPERIMENTS: The ultrasonic motor was irradiated at neutron fluence up to 1.0 x 10^{16} (n/cm2), equivalent to neutron fluences during 20 years of ITER operations. The characteristics of rotational speed relative to torque for the motor were compared before and after the irradiation under three conditions: when the torque was zero (no load) at rotational speeds of 80, 120, and 150 rpm.

RESULTS: Figure 1 shows the irradiation test result of the ultrasonic motor. As shown in Fig. 1, a slight degradation in torque was observed due to the neutron irradiation up. However, since the torque required for driving the steering mirror is approximately 0.2 Nm, focusing around 0.2 Nm revealed no significant performance degradation was observed.

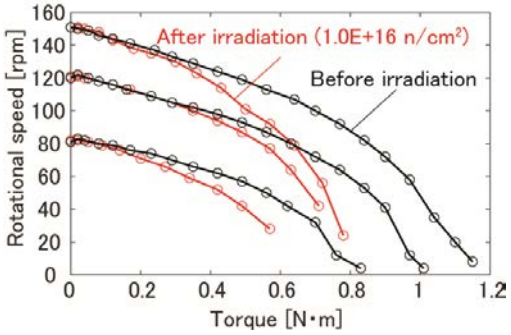

Fig. 1: Rotational speed relative to torque for the ultrasonic motor before and after neutron irradiation

****

(2) Irradiation Tests of the pressure gauge of DIM, ETS and IRTh

DIM, ETS and IRTh plan to use pressure gauges in the port cell area of ITER. In order to estimate how much neutron shielding is needed to use the pressure gauge without replacement during 20 year's ITER operation, the neutron irradiation tests on the pressure gauge were conducted.

EXPERIMENTS: For the irradiation test of the pressure gauge, the Slant exposure tube was used. The pressure gauge was irradiated at multiple neutron fluences up to 2.0 x 10^{12} n/cm^2. The performance of the pressure gauge was compared before and after the neutron irradiation.

RESULTS: No change in the performance of the pressure gauge was observed before and after the irradiation up to 2.0 x 10^{12} n/cm^2. The neutron irradiation test will be continued at neutron fluence up to 1.0 x 10^{13} n/cm^2 which is equivalent to 20 years of ITER operation to investigate the effects of neutrons.

REFERENCES:

[1] B. Bigot, Fusion Eng. Des., **146** (2019) 124.
[2] T. Ushiki *et. al.,* Fusion. Eng. Des., **168** (2021) 112665.
[3] E. Yatsuka *et. al.,* Fusion. Eng. Des., **136** (2018) 1068.
[4] H. Ogawa *et. al.,* Kasai, Fusion Eng. Des., **83** (2008) 1405.

CO4-36

Electron Microscopy of Pure Aluminium Deformed at Static High Pressures

T. Sano, N. Tomioka[1] and T. Okuchi[2]

Graduate School of Engineering, Osaka University
[1]Kochi Institute for Core Sample Research, Japan Agency for Marine-Earth Science and Technology
[2]Institute for Integrated Radiation and Nuclear Science, Kyoto University

INTRODUCTION: Metals are often processed to experience severe plastic deformation to modify their physical properties. A fine-grained microstructure with grain sizes of several hundreds of nanometers or less often forms after such processing. It has been known that, after extensive deformation processing, metals without alloying elements, such as pure aluminum, can significantly increase their physical strength. This is considered to be primarily because of their grain size reduction. In addition to the grain sizes, dislocation density, and lattice-preferred orientation are considered to be important features that physically affect the strength of metals. Therefore, it is important to transform such microtextural features of pure metal and analyze them using nano-scale analytical methods.

EXPERIMENTS: We have been trying to transform and analyze microstructures of pure aluminum experiencing extensive deformation at controlled static high-pressures using a diamond anvil cell apparatus, which is capable of generating pressures of the order of 10 GPa ~ 10^5 atmospheres [1,2]. Aluminum powder with a grain size of 75 μm and purity of 99.99% was annealed at 250°C for 24 hours to prepare initial specimens. This annealing procedure effectively removed dislocations. The specimens were then packed and compressed in a sample chamber of a diamond anvil cell ap-paratus of 600 μm culet size with a metal plate gasket and without a pressure medium to induce a high-strain environment at high sealing pressure. The pressure was determined by the ruby fluores-cence method. The recovered specimens were cut and thinned by focused ion beam apparatus, and the thin sections were observed by transmission electron microscopy to analyze inter-grain orienta-tion differences, dislocation densities, and grain size trends [1,2].

RESULTS: A typical result of transmission electron microscopy is shown in Fig. 1, which was taken using a bright-field method. The average grain sizes were determined by image analysis of these results. Orientations of the observed crystals grins were determined using the limited-field electron diffraction method, and the orientation angle differences between the grains were measured. It was found that the average orientation difference between grains increased with increasing pressure [1]. As this finding, the microstructures of aluminum obtained after extensive compression and deformation at static high pressures showed some systematic characteristics [2], which will be summarized and reported separately.

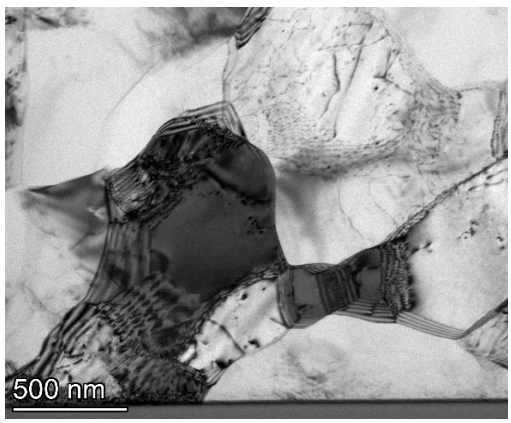

Fig. 1. Aluminum after compression at 1.5 GPa

REFERENCES:

[1] Y. Tanaka *et al.,* Special Issue of the Re-view of High Pressure Science and Technology, **31** (2021) p.104 (1P04).
[2] T. Okuchi *et al.,* S 2023 Annual Meeting of Japan Associaton of Mineralogical Sciences Abstract Volume, R3-13.

CO4-37

Study to improve transport and measurement performance of a slow positron beamline

A. Kinomura, N. Oshima[1], A. Uedono[2] and A. Yabuuchi

Institute for Integrated Radiation and Nuclear Science, Kyoto University
[1]National Institute of Advanced Industrial Science and Technology (AIST)
[2]University of Tsukuba

INTRODUCTION: Positron annihilation spectroscopy is an important analytical method to detect vacancy-type defects and vacant spaces of materials. Energy-variable mono-energetic positron beams (slow positron beams) are essential to perform depth-dependent positron annihilation spectroscopy of surface layers such as ion-implanted layers or thin films formed on substrates. As moderation efficiencies to obtain slow positron beams are not very high, intense positron sources are required for practical use. In general, positron sources based on pair creation can provide higher intensity than radioisotope-based positron sources. A positron source using pair-creation by gamma-rays from a nuclear reactor have been developed by using Kyoto University research Reactor (KUR) to obtain a slow positron beam for materials analysis. In the KUR slow positron beamline, a lifetime measurement system based on a pulsing system using a radiofrequency-driven buncher was developed for the KUR slow positron beamline. In this report, standard samples for positron annihilation lifetime spectroscopy using a slow positron beam were prepared to obtain better performance of the positron lifetime system.

EXPERIMENTS: Standard samples for the lifetime of Si divacancies were prepared by 200 keV Si ion irradiation at room temperature to FZ-grown Si samples of 1.5×1.5 cm. The amorphization threshold dose for 200 keV ion irradiation to Si was estimated to be around 2×10^{14} cm^{-2} [1]. Thus, several irradiation doses in the range of 2×10^{12} – 2×10^{14} cm^{-2} were examined with respect to this threshold dose. Positron annihilation lifetimes of the irradiated samples were measured by the KUR slow positron beamline at an incident energy of 6 keV.

RESULTS: Fig. 1 shows the positron annihilation lifetime spectra of Si samples irradiation to dose of 2×10^{12} and 2×10^{13} cm^{-2} compared with a Kapton spectrum. The obtained lifetime spectra of the Si-irradiated samples were analyzed by the PALSfit code. The 2×10^{13} sample gave one lifetime component of τ=0.3037±0.007 ns. The measured value is in agreement with the reported Si-divacancy lifetime [2]. The 2×10^{12} sample gave two lifetime components of τ_1=0.0271±0.0137 ns τ_2=0.3011±0.0011 ns, where the annihilation in bulk was detected. Considering about the easiness of the sample preparation and lifetime measurement, the 2×10^{13} sample is better as a standard sample. In particular, unirradiated Si cannot be used as a standard for positron energies below 20 keV owing to the positron diffusion to the surface. The standard samples prepared in this study is useful.

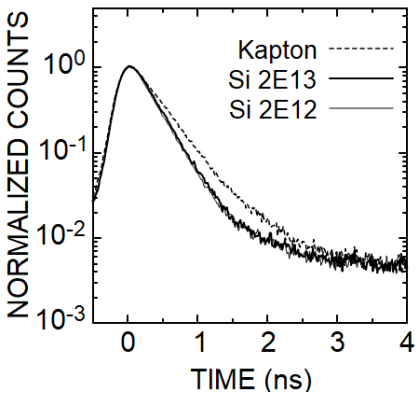

Fig. 1. Positron lifetime spectra for Si-irradiated Si and Kapton samples.

REFERENCES:

[1] A. Kinomura *et al.,* Appl. Phys. Lett., **88** (2006) 241921.
[2] G. Amarendra *et al.,* Phys. Rev. B, **63** (2001) 22411.

CO4-38

Development of a slow positron source using a electron linear accelerator

A. Kinomura, Y. Kawakami, K. Irie, Q. Xu, T. Takahashi and N. Abe

Institute for Integrated Radiation and Nuclear Science, Kyoto University

INTRODUCTION: Slow positron beams (energy-variable monoenergetic positron beams) have been widely used to investigate vacancy-type defects in thin films or near-surface layers of various functional materials. Intense slow positron beams can be generated exclusively from large-scale experimental facilities such as nuclear reactors and accelerators, while radioisotope-based positron sources are used for medium intensity facilities. In terms of accelerator-based positron sources, so far, radiofrequency-driven electron linear accelerators (LINAC) have been used. In principle, LINAC-generated positron beams are not continuous (i.e., pulse beams), while reactor-based positron beams are continuous. The pulse beams can be potentially applied for unique applications such as pump-probe type measurements [1].

EXPERIMENTS: The KURNS-LINAC was used to generate slow positrons in this study. The KURNS-LINAC with two acceleration tubes driven by L-band (1.3 GHz) radiofrequency can generate 30 MeV electron beams with a repetition rate around 100 Hz and a pulse width up to 5 μs. Fig. 1 shows the plan view image of the beamline configuration. It should be noted that preliminary experiments using the KURNS-LINAC reported slow-positron beam generation with intensities of $>10^7$ e^+/s [2].

RESULTS: By using the SIMION code for charged-particle trajectory simulation, the performance of the conventional beamline components such as mesh-shaped moderators, magnetically guided beam ducts and a linear storage section, have been evaluated for effective beam generation and transport. As result of the SIMION simulation, cylindrical electrodes were used for a linear storage section to obtain higher positron intensity. The calculation using the PHITS code was used optimize the converter to generate positrons through pair creation reactions. Consequently, a tungsten converter with a thickness of 4 mm was used. Mesh-type moderator electrodes with annealed Pt foils with thickness of 50 μm was installed. The calculation indicated that the slow positron intensity close to 6×10^6 e^+/s can be expected for the current setup assuming a moderator efficiency of 4.5×10^{-5} [3]. Beamline components designed based on the conceptual design were made and installed in the target and measurement rooms of the KURNS-LINAC buiding as shown in Fig. 1.

Preliminary experiments to generate slow positron beams were performed using a 30 MeV electron beam. As the beamline construction was not completed, the generated slow positron beam was detected at the end of the linear storage section by a scintillation detector. Signals attributed to the slow positron beam were clearly detected. The storage section successfully trapped positron beams in the range close to 1 ms. Currently, the beamline was fully connected and extended to a sample chamber.

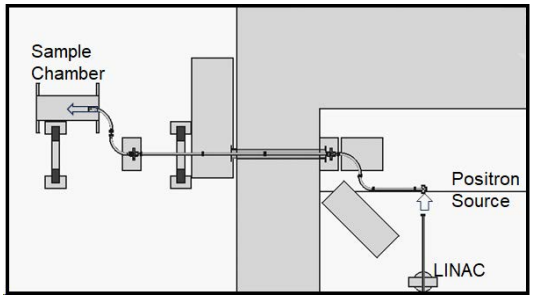

Fig. 1 Plan-view image of the slow positron beamline using the KURNS-LINAC.

REFERENCES:

[1] A. Kinomura *et al.,* Rev. Sci. Instrum., **85** (2014) 123110.
[2] H. Tanaka *et al.,* Jpn. J. Appl. Phys., **31** (1992) 4029.
[3] B.E. O'Rourke *et al.,* Rev. Sci. Instrum., **82** (2011) 063302.

CO4-39

Effects of Pulse Irradiation by Charged Particles on Damage Structures in Metals

T. Yoshiie, K. Irie[1], A. Kinomura[1], F. Hori, T. Nishimura[2]

Department of Quantum Beam Science, Osaka Metropolitan University
[1]Institute for Integrated Radiation and Nuclear Science, Kyoto University
[2]Research Center of Ion Beam Technology, Hosei University

INTRODUCTION: For the development of nuclear materials, irradiation experiments are important. High energy charged particles such as ions and electrons, which are produced in accelera-tors are frequently employed for these experiments. Ion and electron beams from accelerators driv-en by radiofrequency or accelerators with beam scanners possess time structures (periodic/discontinuous intensities). Examples of pulse trains are shown in Fig. 1. The pulse frequency is $1/T$ and H is the beam intensity, but we consider H to be the damage rate (dpa/s) in a pulse duration τ. It's uncertain if the irradiation effects of these pulse beam operations change depending on the pulse frequencies.

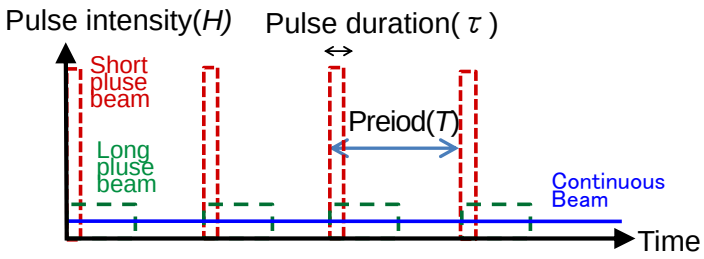

Fig. 1 Examples of time trains.

EXPERIMENTS: For the study of pulse frequency effect on damage structures, the electron irradiation experiments with two irradiation frequences, 10 Hz and 100 Hz, were performed by the KURNS-LINAC with an acceleration energy of 8 MeV and a pulse width of 5 μs at 363 K to a dose of 2.8×10^{-4} dpa. The positron annihilation lifetime spectroscopy (PALS) of the specimens was measured at room temperature using Na-22 and a conventional fast–fast spectrometer. The lifetime spectra were analyzed using the PALSfit program [1].

RESULTS: Table 1 shows the results of PALS in Ni and Fe. The long lifetimes 220 ps (100 Hz) and 240 ps (10 Hz) in Ni indicate the existence of micro-voids of 3 and 4 vacancies in average, respectively. In Fe, there exist micro-voids of 5 vacancies (100Hz) and 9 vacancies (10 Hz) [2]. These results clearly indicate the existence of irradiation frequency effects. For the understanding of the effects, the reaction kinetics analysis is in progress.

Table 1. PALS of Ni and Fe irradiated at 363 K to 2.8×10^{-4} dpa.

	Short lifetime	Intensity of short lifetime	Long lifetime	Intensity of long lifetime	Averale lifetime
Ni-100Hz	0.1094 (±0.0018)	86.6 (±2.74)	0.2212 (±0.0146)	13.4 (±2.72)	0.1244 (±0.0011)
Ni-10Hz	0.1064 (±0.0013)	86.8 (±1.67)	0.2412 (±0.0115)	13.2 (±1.66)	0.1243 (±0.0011)
Fe-100Hz	0.1047 (±0.0014)	79.2 (±1.61)	0.2476 (±0.0081)	20.8 (±1.58)	0.1344 (±0.0052)
Fe-10Hz	0.1007 (±0.0010)	80.4 (±0.877)	0.2802 (±0.0061)	19.6 (±0.858)	0.1359 (±0.0032)

REFERENCES:

[1] P. Kirkegaard *et al.*, Roskilde: Technical University of Denmark; 2009.
[2] H. Ohkubo *al.*, Mater. Sci. Eng. A, **350** (2003) 95-101.

CO4-40

Research on freezing of materials under high pressure by Bessel-beam driven micro-explosions in transparent materials

H. Nakamura, Y. Ota, K. Taketoshi, Y. Nakanishi, N. Yamagata, T. Pikuz, T. Okuchi[1], Y. Umeda[1], L. Rapp[2], A. Rode[2], T. Shobu[3], A. Tominaga[3], Y. Seto[4], R. Kodama, N. Ozaki

Graduate School of Engineering, Osaka University
[1]*Institute for Integrated Radiation and Nuclear Science, Kyoto University*
[2]*Australian National University*
[3]*Japan Atomic Energy Agency*
[4]*Graduate School & School of Science, Osaka Metropolitan University*

INTRODUCTION: It is possible to create extreme pressure and temperature conditions in the tab-letop laboratory experiments with 100-fs ultra-short laser pulses focused inside a transparent material, with intensity in the focal spot significantly above the threshold for optical breakdown [1]. Tight focusing of a -laser pulse with a few micro-Joule energy deep inside a crystal can deposit an energy density up to several MJ/cm^3 in a sub-micron volume. Pressure created by the plasma expansion is high enough to generate new material phases, which is referred to as micro-explosion [2 ,3]. Here we report an experiment relative to a micro-explosion. Targets were transparent oxide materials (MgO). Hence, we demonstrated X-ray diffraction (XRD) analysis of the material under high pressure and high temperature phase.

EXPERIMENTS:

(1) Micro-explosions experiment with femtosecond laser

The beam of a 250 fs amplified Ti:Sapphire laser with a central wavelength of 800 nm was focused inside MgO crystal with depth of 30 μm from the surface. The energy and spot size were 200 nJ and 1.2 μm, respectively.After laser processing, the structures of void inside MgO were observed with Scanning Electron Microscope (SEM).

(2) XRD analysis with by Rigaku Ultima IV at KURNS

XRD analysis was demonstrated with the material with void formed inside by micro-explosions to observe high pressure phase of Mg. X-ray energy was 8.04 keV (Cu-Kα).

RESULTS:

Results of observation of void structure with SEM shows the length and diameter were 30 μm and 350 nm, respectively. The volume of the void is ~2 femtolitres.

Figure 1 shows the results of XRD. Signal of 2θ diffraction with angles of 44.5 and 64.45 degrees. These observations indicate the signals derived from Mg high pressure phase (Mg-bcc) [4]. Further analyses are underway to better understand the data

REFERENCES:

[1] S. Juodkazis *et al.,* Phys. Rev. Lett., **96** (2006) 166101.
[2] A. Vailionis *et al.,* Nat. Com-mun. **2** (2011) 445.
[3] L. Rapp *et al.,* Sci. Rep., **6** (2016) 34286.
[4] C. W. Greeff and John A. Mo-riarty, Phys. Rev. B, **59** (1999) 3427.

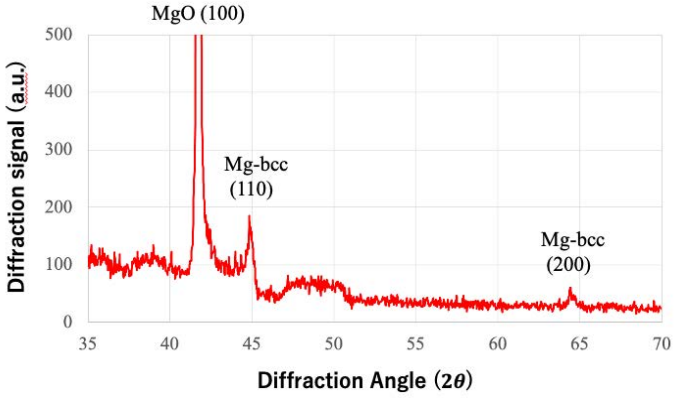

Fig. 1. The results of XRD analysis.

CO4-41

Irradiation Damage Study of New Materials and Industry Materials Under Irradiation and after Irradiation

E. Wakai, A. Yabuuchi[1], T Yoshiie[2], K. Sato[3], Y. Kobayashi[1], T. Takahashi[1], T. Ishida[4], Y. Iwamoto[5], H. Noto[6], T. Wakui, K. Saruta

J-PARC Center, Japan Atomic Energy Agency
[1]Institute for Integrated Radiation and Nuclear Science, Kyoto University
[2]Department of Physics, Osaka Metropolitan University
[3]Research Field of Engineering, Kagoshima University
[4]J-PARC Center, High-Energy Accelerator Research Organization (KEK)
[5]Nuclear Science and Engineering Center, Japan Atomic Energy Agency
[6]Department of Research, National Institute for Fusion Science

INTRODUCTION: Materials and instruments used in a radiation environment must have irradiation resistant properties. Therefore, it is important to promote research and development not only of existing applied and industrially developed materials, but also of innovative materials such as high entropy alloys [1,2] with even better properties. One of the objectives of this study is to understand the basic process of irradiation damage of high-entropy alloys as innovative materials. The electron-beam irradiation method, which can produce the simplest lattice defect, the Frenkel pair (energy must be adjusted), is an important experimental technique. Our efforts in this study have another objective. This is to detect the appearance of elastic waves produced by the stresses to which the material is subjected by the pulsed beam, and to measure and evaluate them using the four-terminal electrical resistance method as a nondestructive testing technique.

EXPERIMENTS: The electron irradiation experiments were performed using the electron linear accelerator at Kyoto University. In order to investigate the threshold energy of the atomic displacement process in Fe- and Ti-based high-entropy alloys (Fe-Mn-Cr-V-Al-C and Ti-V-Cr-Zn-Ta) caused by collisions with energetic incident particles, the temperature of the samples was kept at temperature about 4.0 K in a vacuum and the acceleration voltage of the electron beam was varied from 0.3 MV to 2.0 MV, and the electrical resistance of the sample was measured at each acceleration voltage by the four-terminal electrical resistance method [3]. Elastic waves excited in the solid by pulsed electron beam waves (10, 20, and 30 Hz) around room temperature were also measured by the same 4-terminal electrical resistivity method in air at an energy of 8.0 MeV.

RESULTS: While the electrical resistance of Fe-based HEA began to change at about 0.25 MeV to 0.3 MeV, that of Ti-based HEA was found to change for the first time at about 1.8 MeV, which is considered higher than the generally assumed threshold energy of Ti alloys. On the other hand, the results of the measurement by the 4-terminal electrical resistance method for elastic waves (stress waves) in solids induced by pulsed electron beams in the temperature region above room temperature were as follows. In 316L steel, the change in electrical resistance increased with increasing frequency (10-30 Hz); in Fe-based HEA, the change was significantly larger than that in annealed 316L steel, which was assumed to be due to the interaction between the elastic waves and the unique internal strain of the HEA alloy. The results of this research and a detailed investigation of these material properties will be submitted to journals in the near future [4,5].

REFERENCES:

[1] E. Wakai *et al.*, Mater. Char., **211** (2024)113881.
[2] E. Wakai *et al.*, Sci. Talks, **8** (2023)100278.
[3] Y. Iwamoto *et al.*, J. Nucl. Mater., **458** (2015) 369-375.
[4] E. Wakai *et al.*, Nature (or Nature Mater. or Nature Com.) to be submitted in 2024.
[5] E. Wakai *et al.*, Journal to be submitted in 2024.

CO4-42

Attempt at neutron activation analysis of wood using the k_0-method

K. Murata, Y. Mimoto, M. Inagaki[1], K. Takamiya[1]

Graduate School of Agriculture, Kyoto University
[1]Institute for Integrated Radiation and Nuclear Science, Kyoto University

INTRODUCTION: The Space-wood project (LignoStella Project), which is conducted by Kyoto University in collaboration with Sumitomo Forestry Co. Ltd., aims to explore the use of wood materials in outer space. The project is currently underway and plans to launch a small wooden satellite in 2024. Researchers are particularly interested in understanding the effects of cosmic radiation on wood. Secondary cosmic rays, specifically neutrons, are generated when protons from cosmic radiation collide with the International Space Station (ISS) vehicle. There has been few studies of the effects of neutron collision on wood chemical components [1]. Iin this study, we attempt to analyze the neutron activation of wood using the k_0-method [2].

EXPERIMENTS: Three types of specimens were cut from a honoki board (*Magnolia obovata*): sapwood, intermediate wood, and heartwood. Each specimen had dimensions of 75 mm (length) × 10 mm (radial) × 10 mm (tangential). After measuring the dimensions and weight, the specimens were stored in an air-dry state at room temperature. The test specimen was irradiated with neutrons using KUR's pneumatic transport tube (pn-3) for 60 seconds (1 MW). Following neutron irradiation, the test specimen underwent gamma ray spectrometry using a Ge semiconductor detector immediately, 1 hour later, and 24 hours later. By analyzing the measured γ-ray energy spectrum, the k0 method was employed on a computer to identify and quantify the elements.

RESULTS: As shown in Fig. 1, K, Mg, Cl, Na, Ar, Mn, Al, and Sr were confirmed as trace elements that become γ-ray producing nuclides upon activation in Honoki. Concentration changes in the trunk differed depending on the element, with some concentrations being higher in the sapwood (K, Cl), some in the heartwood (Ar, Al), and some with less clear change trends (Na, Mn). In addition, Mg increased from sapwood to intermediate wood, but was not detected in heartwood in all individuals. It was found that the identification and quantification of trace elements within an individual is possible using the k_0 method.

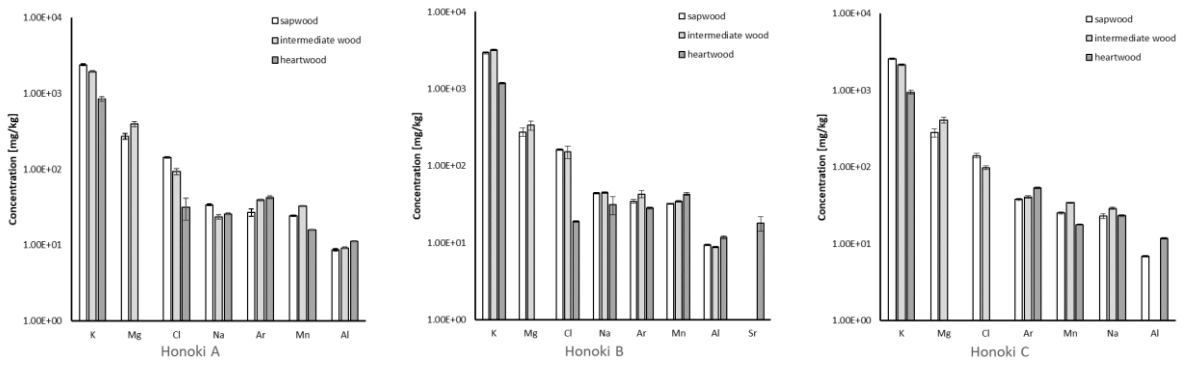

Fig. 1. Nuclides detected by K_0 method in honoki. A, B and C are sapwood, intermediate wood and heartwood, respectively.

REFERENCES:

[1] Y. Katayama *et al.,* Radioisotopes, **35(11)** (1986) 577-582.
[2] Moens L. *et al.,* Journal of Radioanalytical and Nuclear Chemistry, **82(2)** (1984) 385-452.

CO5-1

Examination of anomolous fading for foraminifera luminescence dating

N. Hasebe, G.Shuukhaaz[1], E.Ueyama[1], K. Oohashi[2], Y. Iinuma[3], and K. Takamiya[3]
Institute of Nature and Environmental Technology, Kan-azawa University
[1]*Graduate School of Natural Science and Technology, Kanazawa University*
[2]*Graduate School of Science and Technology for Innova-tion, Yamaguchi University*
[3] *Institute for Integrated Radiation and Nuclear Science, Kyoto University*

INTRODUCTION: Luminescence dating observes the natural accumulated radiation damage caused by radioisotopes such as U and Th as a form of glow after stimulation by heating or lighting. Typically, quartz and feldspar are target minerals for thermoluminescence (TL) dating; however, carbonate minerals, although less frequently studied, have also been investigated in TL dating. Foraminifera, some species of which have carbonate shells, are found in marine sediments and are age index fossils [1]. Foraminifera fossils have often been dated by the ^{14}C dating method. Given that TL dating has a potential, in principle, to measure older samples than the ^{14}C method, we tested the feasibility of TL dating applied to foraminifera by examining the stability of luminescence sites formed by different radiation sources.

EXPERIMENTS: The carbonate rich ooze, whose main component is foraminifera, collected from the western tropical Pacific during IODP Expedition 363 was treated with hydrogen peroxide, rinsed with distilled water, and dried at 60°C. X-ray diffraction (XRD: Rigaku Ultima IV) identified the mineral type as calcite. This study exposed foraminifera rich samples to α (Am^{241}), β (Sr^{90}), and γ (Co^{60}) sources, and thermoluminescence was measured immediately or after storage in darkness for a period of time to study the luminescence fading behavior. The γ -ray exposure was carried out at the Institute for Integrated Radiation and Nuclear Science, Kyoto University, and 4000 Gy was given to the sample. For α and β exposures, a single disc was repeatedly irradiated and measured, whereas for γ-ray exposures, multiple discs were used and each disc was measured only once. TL was measured in Kanazawa University for a temperature range of 100-450°C after a preheating at 80°C for 10 seconds. IRC-65L and R-60 filters were used. An X-rays unit (Varian, VF-50JW) is installed in the luminescence reader and characteristics of luminescence by X-ray are also investigated.

RESULTS: The luminescence signal measured in this experiment was limited to a few dozen to several hundred counts. There was no significant signal decay after α, β, and γ irradiation over several weeks (Fig. 1), while X-ray irradiated sample showed notable signal reduction within about a week. Therefore, foraminifera calcite has the potential to store luminescence from natural radiation. However, the luminescence signal intensity is weak, and only a long irradiated sample (old sample) would be dated.

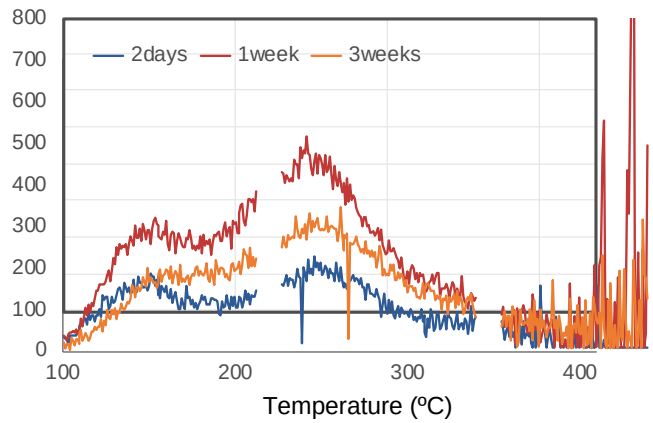

Fig. 1 Results of TL measurement after gamma-ray irradiation of 4000 Gy.

REFERENCES:

[1] T. Toyofuku and Y. Nagai, J. Jap. Assoc. Crystal Growth., **46(3)** (2019) 1-10.

CO5-2

High-pressure transformations of olivine under high differential stress

N. Tomioka[1], T. Okuchi[2], M. Miyahara[3]

[1]*Kochi Institute for Core Sample Research, Japan Agency for Marine-Earth Science and Technology*
[2]*Institute for Integrated Radiation and Nuclear Science, Kyoto University*
[3]*Graduate School of Advanced Science and Engineering, Hiroshima University*

INTRODUCTION: Phase equilibria studies have demonstrated that $(Mg, Fe)_2SiO_4$ olivine transforms into a spinelloid structure (wadsleyite) and then into a spinel structure (ringwoodite) with increasing pressure. Based on the characterization of planar defects in wadsleyite and ringwoodite found in meteorites, shear-promoted mechanisms were proposed for the high-pressure transformations between the olivine polymorphs [1]. The transformation models also predicted the possible occurrence of an intermediate phase with a new spinelloid structure. This phase has recently been discovered as a new mineral poirierite in shocked meteorites [2]. In this study, we have performed high-pressure transformation experiments on olivine to constrain the formation conditions of poirierite.

EXPERIMENTS: A natural $(Mg_{0.91}, Fe_{0.09})_2SiO_4$ olivine crystal was crushed into a powder with a heterogeneous grain size of less than 100 μm to generate non-hydrostatic stress among the olivine grains in high-pressure experiments. The powder was kept at 12–16 GPa and 900 °C for 120 minutes by using a Kawai-type high-pressure apparatus. The product phases in the recovered samples were first characterized using a micro-area X-ray diffractometer (XRD) at KURNS. The portions at the reaction boundaries were extracted and processed into ultrathin sections by using a focused ion beam apparatus, and then examined using a transmission electron microscope (TEM).

RESULTS AND DISCUSSION: The olivine grains partially transformed at their grain boundaries in all the experiments. XRD patterns show that the product phases are wadsleyite, wadsleyite+ringwoodite, and ringwoodite at 12, 14, and 16 GPa, respectively (Table 1). These phases occur as euhedral and subhedral crystals with grain sizes of 0.5–1.5 μm under TEM (Fig. 2). Most of the ringwoodite grains exhibit stacking faults on {110}. Their electron diffraction (ED) patterns show weak extra ED spots other than ringwoodite, corresponding to the poirierite structure (Fig. 2). The ED patterns also show that both phases have a topotaxial relationship: $(001)_{Poi}//\{001\}_{Rw}$ and $(100)_{Poi}//\{110\}_{Rw}$. Some of the wadsleyite grains exhibit stacking faults on the (010) plane, but no extra electron diffraction spots. The relict olivine grains have high dislocation densities of 1.4–2.1 x 10^9 /cm^2, corresponding to a differential stress of 0.5–0.6 GPa according to an olivine piezometer [3]. These microstructural and crystallographic results suggest that nanoscale poirierite lamellae are only metastably formed from ringwoodite grains above 14 GPa, when high differential stresses are applied at relatively low temperatures.

Table 1. μXRD and TEM results

Run No.	P (GPa)	T (°C)	Duration (min.)	Major products	Superlattice reflections (Rw/Wad)	Dislocation density (relict olivine) (1/cm^2)
OE-02	16	900	120	Rw	Common	$1.4x10^9$
OE-03	14	900	120	Rw>Wad	Rare	$2.1x10^9$
OE-04	12	900	120	Wad	No	$1.6x10^9$

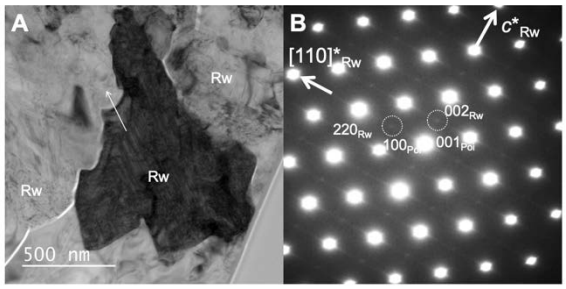

Fig. 1. Transmission electron micrograph (A) and electron diffraction pattern (B) of a ringwoodite (Rw) grain with intergrown poirierite (Poi) in the olivine sample kept at 14 GPa. The arrow in (A) indicates the direction of the stacking faults.

REFERENCES:

[1] M. Madon and J. P. Poirier, Phys. Earth Planet Inter., **33** (1983) 31–44 .
[2] N. Tomioka *et al.*, Commun. Earth Environ., **2** (2021)16.
[3] Kohlstedt *et al.*, in Physics and Chemistry of Minerals and Rocks, (1976) 35–49.

CO5-3

NAA and Ar-Ar dating for small-sized extraterrestrial samples

R. Okazaki[1], M. Inagaki[2], J. Park[3], and S. Sekimoto[2]

[1]*Department of Earth and Planetary Sciences, Kyushu University*
[2]*Research Reactor Institute, Kyoto University*
[3]*Kingsborough Community College, the City University of New York*

INTRODUCTION: Minor element abundances and Ar-Ar ages of extraterrestrial materials are one of the important information to elucidate the origin and evolution history of the solar system materials. We have developed and applied the combination analytical method that enables us to carry out gamma-ray measurements and Ar-Ar dating for the same individual samples of sub-milligram mass (e.g., Projects #R3007, R3038, and R3127).

EXPERIMENTS: In this project, we have conducted irradiation experiments under two different conditions in Oct 2023 and Jan 2024. The first one is a short-duration irradiation (1MW × 24 hours) for young (~300 Ma) samples with smaller amounts of radiogenic ^{40}Ar. We irradiated terrestrial minerals as analytical standards; Madagascar orthoclase [1] and Japanese wollastonite were used for the K and Ca corrections, respectively. The Allende CV chondrite (provided by Smithsonian museum [2]), the Murchison CM chondrite, and the Tagish Lake ungrouped-carbonaceous chondrite powdered samples were used as our laboratory standards. Plagioclase mineral separates from eucrites (Agoult, HaH262, Y-792510, Y-792769, Y980319, Y980433, and Y983366) were also irradiated. The second irradiation was conducted under our nominal condition (1MW × 47 hours + 5MW × 6 hours). In the 2nd experiment, the Asuka 12325 shergottite (a bulk sample and a shock-vein separate) and the Holbrook L/LL chondrite (a bulk and plagioclase separate) samples were irradiated in addition to the standard mineral and meteorite samples as used in the 1st one.
Each of the samples was placed in a conical dimple (φ1, depth ~ 0.5 mm) of a sapphire disk (φ5.5, 1.5 mm thick), and covered with a sapphire disk (φ5.5, 0.3 mm thick). Each of the sapphire container was wrapped with pure aluminum foil. These Al-wrapped containers were stacked and sealed in the capsules for the Hydro irradiation.
The 1st-irradiated samples were recovered from the irradiation Al capsule in Dec 2023, and a portion of the samples were transported to Kyushu University for noble gas analyses. The noble gas analyses were carried out in Jan-Feb 2024. The 2nd-irradiated samples were recovered and transported in Feb 2024. The gamma-ray measurement was done for the meteorite standards and the Holbrook samples. Noble gas analyses will be conducted in Apr 2024.

RESULTS: We have obtained noble gas data from the eucrite plagioclase separates irradiated in the 1st experiment. The ^{39}Ar/^{40}Ar ratios for the samples give Ar-Ar ages consistent with our previous measurements and previous reports (e.g., [3]). The analytical uncertainties on the Ar isotopic ratios of the 1st experiment samples are reasonably small. Therefore, we can choose an appropriate irradiation condition for extraterrestrial samples with various ages ranging from 300 Ma (e.g., shergottites) to 4.6 Ga (e.g., eucrites and chondrites). We are currently calculating precise Ar-Ar ages and preparing a paper in conjunction with the data we have obtained in the series of our experiments at KUR. The NAA data and Ar-Ar age for the Holbrook chondrite will also be obtained and compiled for another publication, along with the data obtained by Dr. Sekimoto.

REFERENCES:
[1] S. Weiss, Mineralien Magasin Lapis., **16** (1991) 13–14.
[2] E. Jarosewich *et al.*, Smithsonian Contributions to the Earth Sciences, **27** (1987) 1–49.
[3] T. Iizuka *et al.,* Geochimica et Cosmo-chimica Acta, **267** (2019) 275–299.

CO5-4

Gallium concentration of GSJ rock samples

C. Kato, S. Fukutani[1], and T. Fujii

Graduate School of Engineering, Osaka University
1 Institute for Integrated Radiation and Nuclear Science, Kyoto University

INTRODUCTION: Geological reference materials are used as a terrestrial standard in various studies. The Geological Society of Japan issues rock reference materials, which are mainly composed of igneous and sedimentary rocks that were collected throughout Japan. Although these are standard reference materials, not all elemental concentrations have been certified within them. Gallium (Ga) is one element that has not been certified in all reference materials. Although Ga is a metal, it exists in the crust at high concentrations at 18 ppm [1]. Since the advent of Multi Collector-Inductively Coupled Plasma-Mass Spectrometer (MC-ICP-MS) and the development of high precision isotope measurements for low concentrated elements, Ga has been recently studied extensively, in terrestrial [2, 3], lunar [4] and meteorites [5]. Currently, there are 14 rock standards that do not have a certified value. In this study, we measured the Ga concentration in GSJ rock reference samples that do not have a certified Ga concentration value as well as those that do have for confirmation.

EXPERIMENTS: Samples used in this study were JA-1a (Andesite), JB-2a (Basalt), JB-3a (Basalt), JB-1b (Basalt), JF-1(Feldspar), JG-1(Granodiorite), JGb-1(Gabbro), JSy-1(Syenite). 0.1 g of rock samples were measured and dissolved in a HNO_3 and HF solution and heated at 100°C for 1 week. The samples were then dried down and redissolved in HCl. The Ga concentration was measured by Inductively Coupled Plasma-Quadrupole Mass Spectrometry (ICP-QMS) at Kyoto University.

RESULTS: Out of the samples measured for their Ga concentration in this study, JB-1b, JB-2a and JB-3a do not have certified values. Their Ga concentrations were JB-1b: 20.3 ppm (n = 2), JB-2a: 20.3 ppm (n = 2) and JB-3a: 22.9 ppm (n = 2). For samples that have a known value, their values were JA-1a: 27 ppm (n = 1), JF-1: 31 ppm (n = 1), JG-1: 31 ppm (n = 1), JGb-1: 24.2 ppm (n = 2), JSy-1: 37ppm (n = 1). These values were all up to 1.7 times enriched compared to literature values [6] suggesting that further measurement of multiple batches of the samples is needed.

REFERENCES:

[1] H. Palme and H. St. C. O'Neill, in Treatise on Geochemistry, edited by A. M. Davis (Elsevier Press, New York, 2003), Vol 2
[2] C. Kato *et al.,* Chem. Geol., **448** (2017) 164-172.
[3] Y. Zhang *et al.,* Geosci. Front., **12** (2021) 101137.
[4] C. Kato and F. Moynier, Sci, Adv., **3** (2017) e1700571.
[5] C. Kato and F. Moynier, Earth Planet. Sci. Lett., **479** (2017) 330-339.
[6] N. Imai *et al.,* Geostand. newsl., **19** (1995) 135-213.

CO5-5

Volcanic and Tectonic History of Philippine Sea Plate (South of Japan) Revealed by $^{40}Ar/^{39}Ar$ Dating Technique

O. Ishizuka, Y. Yoshino[1], H. Yoshinaga[1],Y. Iinuma[1],R. Okumura[1], T. Fujii[2]

Geological Survey of Japan, AIST
Graduate School of Science, Kyoto University
[1]Institute for Integrated Radiation and Nuclear Science, Kyoto University
[2] Graduate School of Engineering, Osaka University

INTRODUCTION: Robust tectonic reconstruction of the evolving Philippine Sea Plate for the period immediately before and after subduction initiation at ~52 Ma to form the Izu-Bonin-Mariana arc is prerequisite to understand cause of subduction initiation. Understanding of nature and origin of overriding and subducting plates is especially important because plate density is a key parameter controlling subduction initiation based on numerical modelling. There is increasing evidence that multiple geological events related to changing stress fields took place in and around Philippine Sea plate about the time of subduction initiation at ~52 Ma [1,2]. To understand tectonics during the period of subduction initiation, it is important to understand the pattern and tempo of these geological events, particularly the duration and extent of seafloor spreading in the Mesozoic arc terrane (Daito Ridge Group). This year we focused on the intersection of the WPB spreading center and the Kyushu-Palau Ridge, which is a remnant of ancient Izu-Bonin-Mariana arc, to understand tectonic relationship between the West Philippine Basin (WPB) and the Izu-Bonin-Mariana arc. This remains one of the key issues to reconstruct tectonics at subduction initiation of the Philippine Sea Plate.

EXPERIMENTS: Ages of the igneous rocks were determined using the $^{40}Ar/^{39}Ar$ dating facility at the Geological Survey of Japan/AIST. 10-15 mg of phenocryst-free groundmass, crushed and sieved to 180 – 250 μm in size, was analyzed using a stepwise heating procedure. The samples were treated in 6N HCl for 30 minutes at 95˚C with stirring to remove any alteration products (clays and carbonates) present in interstitial spaces. After this treatment, samples were examined under a microscope. Sample irradiation was done either at the Kyoto University Reactor (KUR). The neutron irradiation was performed for 10 h at the hydro-irradiation port under 1 MW operation, where thermal and fast neutron fluxes are 1.6×10^{13} and 7.8×10^{12} n/ cm^2 s, respectively, or for 2 h under 5 MW operation, where thermal and fast neutron fluxes are 8.15×10^{13} and 3.93×10^{13} n/cm^2 s respectively. Argon isotopes were measured in a peak-jumping mode on an IsotopX NGX noble gas mass spectrometer fitted with a Hamamatsu Photonics R4146 secondary electron multiplier.

RESULTS: 5 samples from the western escarpment of the Kyushu-Palau Ridge have been dated by the laser-heating $^{40}Ar/^{39}Ar$ dating technique. These basaltic samples show age range between 32.0 and 33.0 Ma. The strike of the escarpment is at high angle to the remnant spreading center of the WPB, probably formed as fault along the boundary between the KPR and the WPB in association with spreading of the WPB. Ages of basaltic lava blocks from this escarpment provide constraint on the age of formation of this escarpment, i.e., the escarpment must have formed after these volcanics. This means that the escarpment probably formed after32 Ma, which implies that the intersection between the spreading center and the Kyushu-Palau Ridge occurred after this age.

REFERENCES:
[1] O. Ishizuka *et al.*, Earth and Planet. Sci. Lett., **306** (2011) 229-240.
[2] O. Ishizuka *et al.*, Geochem. Gepphys. Geosyst., **23** (2022) e2021GC010242D.

CO5-6

Experimental evaluation of shock-induced reactions of carbonate minerals: Implications for understanding environmental change by planetary impacts

Y. Umeda[1, 2], N. Tomioka[3], T. Sekine[4], M. Miyakawa[5], T. Kobayashi[5], H. Yusa[5], and T. Okuchi[1,2]

[1]*Institute for Integrated Radiation and Nuclear Science, Kyoto University*
[2]*Graduate School of Engineering, Kyoto University*
[3]*Kochi Institute for Core Sample Research, X–star, Japan Agency for Marine–Earth Science and Technology*
[4]*Center for High Pressure Science and Technology Advanced Research*
[5]*Research Center for Materials Nanoarchitectonics, National Institute for Materials Science*

INTRODUCTION:

Planetary impacts by asteroids and comets can dramatically alter the state of the planetary surface due to their high energy density. Carbonate minerals are the main reservoirs of carbon species (e.g., CO_2 and C) on the Earth's surface, and have significant effects on the carbon cycle and atmospheric circulation in the Earth. To model planetary impacts and evaluate impact-induced environmental changes, we need to understand the shock behavior of carbonate minerals under extreme conditions induced by the impact process. In this study, shock-compression recovery experiments were performed on several carbonate minerals to experimentally simulate planetary impacts. After shock compression, the recovered samples were investigated by X-ray diffraction (XRD) measurement for crystal phase identification and by transmission electron microscopy (TEM) for microstructural observation in order to evaluate the shock metamorphism and shock-induced reactions of carbonate minerals.

EXPERIMENTS:

Shock recovery experiments were performed using a single–stage propellant gun at the National Institute for Materials Science, Japan [1]. The peak shock pressure was estimated by the impedance mismatch method [2]. After the experiments, shocked sample were subjected to XRD analysis for the phase identification, using a Rigaku Ultima IV diffractometer with CuKα radiation driven at 40 mA and 40 kV, which is installed at the Institute for Integrated Radiation and Nuclear Science, Kyoto University (KURNS). In addition, the shocked sample was subjected to TEM and scanning transmission electron microscopy (STEM) analyses. Several 150 nm thick sections for TEM and STEM analysis were prepared using focused ion beam (FIB) instruments FEI Quanta3D200i installed at KURNS, and HITACHI SMI4050 installed at the Japan Agency for Marine Earth Science and Technology (JAMSTEC). TEM and STEM observations of the ultrathin sections were performed using a transmission electron microscope (JEOL JEM– ARM200F) at JAMSTEC, operating at an accelerating voltage of 200 kV.

RESULTS:

We have successfully performed shock recovery experiments on three types of carbonate minerals: calcite $CaCO_3$, dolomite $CaMg(CO_3)_2$, and siderite $FeCO_3$. Each sample was subjected to the shock pressure of 35, 40, and 45 GPa, respectively. The result of XRD measurements showed the presence of MgO, FeO and Fe_3O_4 as decomposition products of dolomite and siderite in shock induced reactions. The decomposition reaction of dolomite and siderite occurs at shock pressures above ~40 GPa due to the high temperature and high pressure caused by shock compression. Based on these results, we first focused on dolomite and tried to observe the shock deformation microstructure by TEM. The TEM observation revealed a bubbled microstructure as a trace of the decomposition reaction of dolomite: $CaMg(CO_3)_2 \rightarrow MgO + CaCO_3 + CO_2$ (Figure 1). Selected area electron diffraction (SAED) results of this structure showed the presence of MgO (inset in Figure 1). In future work, we will try to clarify the dominant shock response of other carbonates at each shock pressure. Our goal is to establish the shock metamorphic indicator of carbonate minerals through the study of other recovered samples.

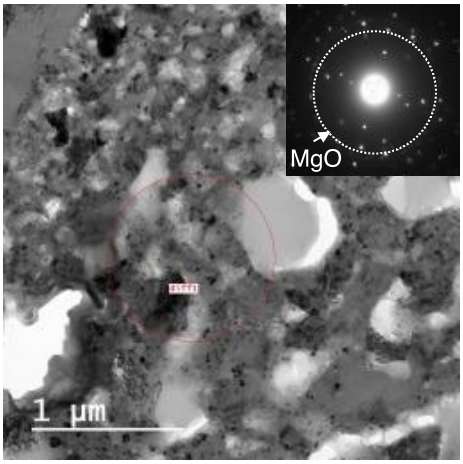

Fig. 1. TEM image of recovereddolomite shocked at 40 GPa. Inset: SAED pattern obtained from the area diff 1.

REFERENCES:

[1] Y. Umeda *et al.*, J. Mineral. Petrol. Sci., **119** (2024).
[2] T. Sekine, Eur. J. Solid State Inorg. Chem., **34** (1997).

CO5-7

Determination of Abundance of Rare Metal Elements in Seafloor Hydrothermal Ore Deposits by INAA Techniques-10: Determination of Barium in Sulfide-sulfate Ore

J. Ishibashi, T. Naritomi[1], S. Juhri[1], K. Yonezu[1], H. Yoshinaga[2], Y. Iinuma[3], R. Okumura[3] and K. Takamiya[3]

Ocean-bottom Exploration Center, Kobe University
[1]Department of Earth Resources Engineering, Faculty of Engineering, Kyushu University
[3]Institute for Integrated Radiation and Nuclear Science, Kyoto University

INTRODUCTION: Instrumental neutron activation analysis (INAA) has several advantages for geochemical tools to provide useful information for mineral exploration. For example, INAA enables highly sensitive multi element analysis without geochemical pretreatment. We have conducted studies using mineralized samples collected from seafloor hydrothermal deposits, with a view to extend the range of application of this technique. Barite ($BaSO_4$ as chemical formula) is one of gangue minerals of seafloor hydrothermal ore deposits and Ba content in sulfide-sulfate ore widely varies from a few hundred ppm to more than 50 wt%. Since barite is useful for chronological studies, we focus on determination of Ba content in this report.
****

EXPERIMENTS: INAA analysis was conducted by two runs. For short life nuclides, powdered samples of 10-20 mg were irradiated at Pn-3 (thermal neutron flux = 4.68×10^{12} n/cm^2/sec) for 30 seconds, and the gamma ray activity was measured for 3 minutes after adequate cooling time (3~10 minutes). Barium content was determined using the peak at 165.85 keV of Ba-139 ($t_{1/2}$=1.38 hours). For long life nuclides, powdered samples of 10-20 mg were irradiated at Pn-2 (thermal neutron flux = 5.50×10^{12} n/cm^2/sec) for 20 minutes, and the gamma ray activity was measured for 15 minutes after adequate cooling time (~30 hours). Barium content was determined using the peak at 496.26 keV of Ba-131 ($t_{1/2}$=11.8 days).
****

RESULTS: In the case that Ba content is less than 1000 ppm (=0.1 wt%), determination by Ba-139 was inaccurate because of high background level. Determination by Ba-131 is applicable for sulfide-sulfate ore with Ba content around a hundred ppm. Figure 1 shows the result of comparison between Ba content determined by Ba-131 and that determined by Ba-139. The latter content was systematically lower than the former content, although scatter of data is not so significant. Further study based on a cross check with other analytical techniques is necessary.

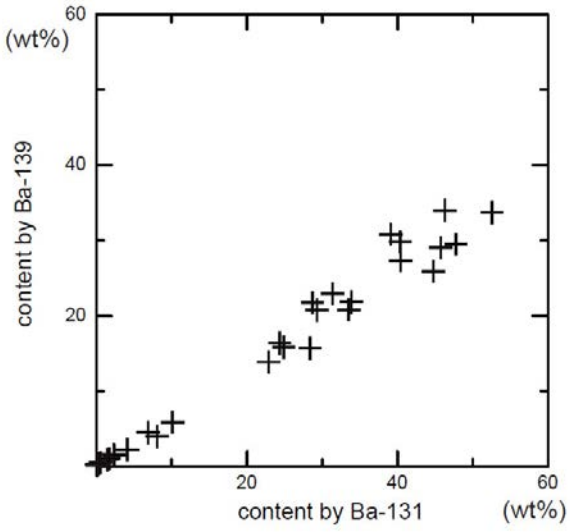

Fig. 1. Comparison between Ba content determined by Ba-131 and Ba content determined by Ba-139

CO5-8

Yearly Change in Concentration of Soil Particles in the Atmospheric Aerosols at Sakai

N. Ito, A. Mizohata, Y. Iimura[1], H. Yoshinaga[1]

Radiation Research Center, Osaka Metropolitan University
[1] Institute for Integrated Radiation and Nuclear Science, Kyoto University

The soil particles in the atmospheric aerosols which are main constituents in the atmospheric coarse particles have made a yearly decreasing change in the concentration of the coarse particles observed at Sakai (Fig.1). The decrease trend in the soil particles have been estimated from the result of concentration change in Al,Ca, which are the main elements in the soil particles. We found the difference of the increase (decrease) trend in the Al,Ca concentration by the coarse particle size rages (>11μm, 7.0-11μm, 4.7-7.0 μm, 3.3-4.7μm, 2.1-3.3μm). The most largest particle size rage (>11μm,) has the biggest decrease rate, meaning the contribution from local soil effect has decrease trend. By the way, in the smallest particle size range(3.3-4.7μm, 2.1-3.3μm), Ca has bigger decrease trend than other particle size rage (7.0-11μm, 4.7-7.0 μm,) contrast to Al decrease trend that does not show explicit difference between the ranges(7.0-11μm, 4.7-7.0 μm, 3.3-4.7μm, 2.1-3.3μm). This result shows the characteristic change in element on the China land particle(,Kosa Particle) which effect the smaller soil particle(3.3-4.7μm, 2.1-3.3μm)[1] because of its easy transportation in the long distance. This characteristic change in the constituents elements in which Al and Ca are main constituents , might make the decrease trend of ratio of Ca to Al (Ca/Al)(Fig.2).

METHODS: Aerosol samples have been collected by the Andersen sampler which can collect the atmospheric aerosols by 9 particle size ranges (>11μm, 7.0-11μm, 4.7-7.0 μm, 3.3-4.7μm, 2.1-3.3μm, 1.1-2.1μm, 0.65-1.1μm, 0.43-0.65μm, <0.43μm) at Sakai,Osaka since 1994. The atmospheric aerosols are collected on polyethylene sheet(80 mmφ) attached to the dishes in the each particle size. The elements in the particles of some samples were analyzed by the neutron activation analysis using Kyoto Nuclear Reactor.

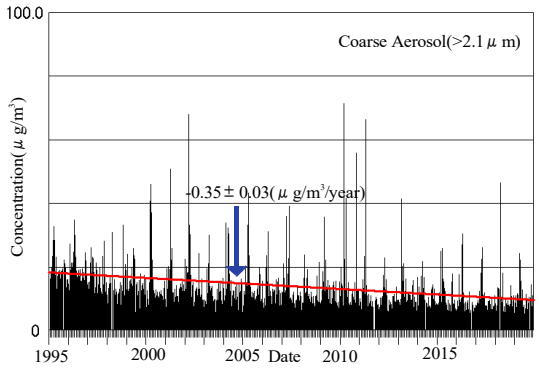

Fig.1 Yearly change in coarse particle concentration at Sakai since 1994

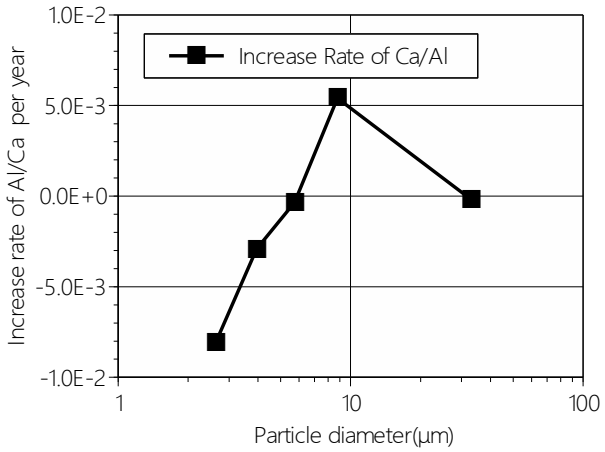

Fig.2 Increase rate of Ca/Al by the particle size range in the coarse atmospheric aerosols

REFERENCES:
[1] M. NISHIKAWA *et al.,* AEROSOL KENKYU, **6** (1991) 157-164.

CO5-9

Absorption of alkali metal ions by white radish sprouts (V)

M. Yanaga, T. Nakamura[1], H. Shimoda[2], H. Mitta[2], H. Yoshinaga[3], R. Okumura[3] and Y. Iinuma[3]

Center for Radioscience Education and Research, Faculty of Science, Shizuoka University
[1]Department of Science, Graduate School of Integrated Science and Technology, Shizuoka University
[2]Department of Chemistry, Faculty of Science, Shizuoka University
[3]Institute for Integrated Radiation and Nuclear Science, Kyoto University

INTRODUCTION: According to a consumer awareness survey on agricultural, forestry, and fisheries products produced in the disaster area conducted by the Consumer Affairs Agency in January 2024; Of those who answered that they "care" or "somewhat care" about the country of food production when shopping, 9.3% said "I want to buy food that does not contain radioactive materials." even though it has been about 13 years since the Fukushima Daiichi Power Plant accident occurred [1]. Therefore, in order to prevent damage by rumors it is necessary separating radioactive cesium from the soil.

Our previous reports have shown that adding the stable cesium to contaminated soil and growing plants can remove radioactive cesium from the soil [2, 3]. However, addition of excess amount of stable cesium caused an obstacle to growth of plant [4]. Therefore, in the present work, effects of alkali metal ions on plant growth were investigated using white radish sprouts.

EXPERIMENTS: Hydroponic cultivation of white radish sprouts was carried out by adding various concentrations of cesium or the congener element rubidium ion. Cultivation was also caried out in soil (andosol and vermiculite) that had been simulated decontaminated using cesium or rubidium, and determination of trace elements in leaves and stems was performed by INAA. Soil washed with water after simulated decontamination was also studied. The samples in polyethylene capsules were irradiated in Pn-3 for 90 seconds and in Pn-2 for 4 hours, for short and long irradiation, respectively.

RESULTS: The results of soil cultivation experiments are described here. In the cultivation experiment after simulated decontamination, andosol or vermiculite was immersed in 0.01 mol/L $CsNO_3$ or $RbNO_3$ and then either left unwashed or washed once or three times with water. No growth disorder was observed in the white radish sprouts grown in each soil. As a result of our separate experiments, 0.014 or 0.14 mol/L of Rb^+ and Cs^+ showed a decontamination rate of about 40% for andosol, and that of 10 to 15% for vermiculite. The Cs^+ and Rb^+ contained in leaves and stems of radish sprouts grown in andosol were 2 to 10 times higher than those grown in vermiculite. Concentration of both ions decreased as the number of washings increased. Generally, Cs ions are easily adsorbed by vermiculite. However, no difference in the uptake rate between Cs^+ and Rb^+ was observed because Cs^+ was washed before being adsorbed to the adsorption sites of vermiculite. A tendency for K^+ concentration in the stems of radish sprouts grown in the andosol used for simulated decontamination with Cs to decrease was observed, suggesting that absorption of K^+ was inhibited. However, no effect was observed on the appearance of growth. No significant changes were also observed in the concentrations of other trace elements.

REFERENCES:

[1] Consumer Affairs Agency, Survey of consumer awareness regarding reputational damage (17th), https://www.caa.go.jp/notice/entry/036516/ [in Japanese].
[2] M. Yanaga *et al.,* NMCC ANNUAL REPORT, **22** (2015) 185-190.
[3] M. Yanaga *et al.,* NMCC ANNUAL REPORT, **23** (2016) 172-179.
[4] M. Yanaga *et al.,* KURNS Progress Report 2018 (2019) CO5-10.

CO5-10

Basic Research on Trace Elemental Analysis of Airborne Particulate Matters in an Environment by INAA & IBA

N. Hagura[1,2,3], I. Sato[1,2,3], T. Uchiyama[2], H. Matsuura[1,2,3]

[1] *Nuclear Safety Engineering, Science and Engineering, Tokyo City University*
[2] *Atomic Energy Research Laboratory, Science and Engineering, Tokyo City University*
[3] *Cooperative Major in Nuclear Energy, Integrative Science and Engineering, Tokyo City University*

INTRODUCTION: To discuss the elemental distribution of airborne particulate matter (APM) in environments with large variability, it is necessary to accumulate a large amount of measurement data. This requires sufficient time and a large number of samples. In order to efficiently perform a large number of measurements and analyses, we believe it is important to use both ion beam and reactor-based analytical methods in parallel. Tokyo City University Atomic Energy Research Laboratory (TCU-AERL) operated the Musashi reactor until 1989 and conducted research using neutrons, including instrumental neutron activation analysis (INAA). Although currently in the decommissioning phase, the facility is still in operation for RI-based experiments. In 2018, a 1.7 MV Pelletron Tandem Accelerator (TCU-Tandem) was installed and began research using IBA [1], including particle-induced X-ray emission (PIXE) [2] and ion beam induced ion luminescence (IBIL) analysis [3-4]. In this study, APM samples were analyzed for trace elements by instrumental neutron activation analysis and ion beam analysis using a tandem accelerator.

EXPERIMENTS: A high-capacity air sampler (Shibata Scientific Technology LTD: AD-VAN-TEC, QR-100 (collection efficiency: 99.99% for 0.3 μm particles)) was used, with an intake flow rate of 700 L min^{-1}. The radioactivity of the collected filters was measured with a high-purity germanium (HP-Ge) semiconductor detector, and some of the filters were stored for INAA. Irradiation was performed at the research reactor KUR at the Institute for Integrated Radiation and Nuclear Science, Kyoto University, and four machine times were conducted from October to February in FY2023. Irradiation conditions are shown in Table 1.

RESULTS: Several samples of stocked airborne dust were measured. In addition, PIXE and IBIL analysis is being conducted at TCU-Tandem. Figure 1 shows an example of a typical IBIL spectrum. It shows IBIL measurements of compounds containing various forms of Eu, where luminescence is easily observed. Different chemical bonding states have different energy levels, and light originating from transitions between different energy levels was identified.

Table 1. Irradiation conditions

Irradiation			Operating power	Thermal neutron flux
date	time	position		
2023/10/11	60 min	Pn-2	1 MW	5.5 x 10^{12} n/cm^2/sec
2023/12/6	60 min	Pn-2		5.5 x 10^{12} n/cm^2/sec
2024/2/7	60 min	Pn-2		5.5 x 10^{12} n/cm^2/sec
2024/2/14	30 sec	Pn-3		4.7 x 10^{12} n/cm^2/sec

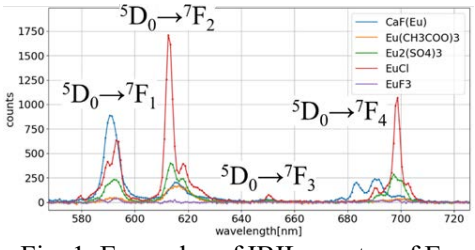

Fig. 1. Examples of IBIL spectra of Eu

REFERENCES:

[1] N. Hagura *et al.,* Trans. of the AESJ, **17 (3-4)** (2018) 111-117.
[2] R. Kamata, N. Hagura *et al.,* Int'l J. PIXE (in print).
[3] Y. Chikamatsu, *et al.,* 2022 IEEE NSS MIC RTSD, NSS-20-156 (2022).
[4] R. Maejima *et al.,* the 33rd Annual Meeting of MRS-J, (Nov. 14-16, 2023) P-14-001.

CO5-11

Model Improvement for the Transport of Cs in Soil on Forest Slopes

H. Matsumoto, Y. Motoie[1], M. Yoneda[1], Y. Shimada[1], S. Fukutani[2], M. Ikegami[2]

Faculty of Engineering, Kyoto University
[1]Graduate School of Engineering, Kyoto University
[2]Institute for Integrated Radiation and Nuclear Science, Kyoto University

INTRODUCTION: In this study, the estimation model for the transport of radioactive Cs in the forest slope, which was developed in the previous study [1] to evaluate the distribution of radioactive Cs concentrations in soil and changes over time in air doses in forests resulting from the Fukushima Daiichi Nuclear Power Plant accident, is first improved to be more realistic by examining the physical meanings of the parameter values used in the model. Furthermore, we will measure the distribution of radioactive Cs in forest soil in the slope direction in Kawauchi-village, Fukushima Prefecture, to examine the validity of the simulation results using the improved model by comparing them with the measured values, which was not done in the previous study.

MODEL IMPROVEMENT: As an improvement of the model, the previous study assumed that the flow rate in the forest soil becomes constant after a certain distance from the top of the slope. In this study, the maximum value of the flow rate was determined from the saturated hydraulic conductivity and the hydraulic head gradient, and the flow rate was improved to be constant after reaching that value. The values of the saturated hydraulic conductivity and the depth of the slope through which water flows were adjusted so that the simulation results were close to the measured concentration of radioactive Cs in the soil of a wooded area in Mariyama district of Kawauchi Village, Fukushima Prefecture as shown in Fig. 1. The estimated saturated hydraulic conductivity value of 5×10^{-3} cm/sec and the soil depth of 5 cm on the slope through which water flows are considered to be reasonable values for a forest in this area.

MODEL VALIDATION: The improved model was validated using measured data in 2018 and 2023 in Modo Area, Kawauchi Village, Fukushima Prefecture, and estimated values for the concentration of radioactive Cs in rice fields, which is estimated from the cumulative amount of radioactive Cs discharged after the Fukushima Daiichi Nuclear Power Plant accident, were close to the measured values in both years. In the measured data, there were cases where the concentration increased or decreased between 2018 and 2023, even at the same lower end, depending on the slope, and it was difficult to match the simulation results of the secular change of concentration to the measured values for all slopes.

RESULTS: In the improvement of the model for estimating the amount of radioactive Cs in forests in the direction of slope, the slope inclination and saturated hydraulic conductivity of soil were assumed to be constant over the entire area of the slope in this study. However, in order to reproduce the actual measured values of soil radioactive Cs concentrations on the slopes in the Modo area in the simulation, it was considered necessary to consider the case where these values vary from place to place.

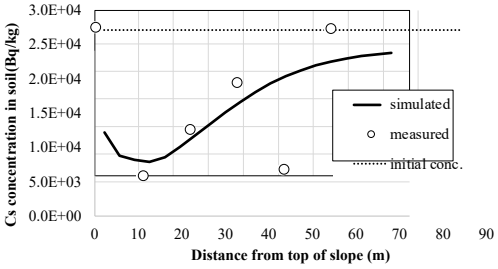

Fig. 1. Fitting of parameters by comparison with measured data.

REFERENCES:

[1] Y. Motoie *et al.*, The 12th Environmental Radiation Decontamination Research Conference S4-4, Fukushima City Japan (2023).

CO5-12

^{40}Ar-^{39}Ar Dating of Extraterrestrial Materials in KURNS

N. Iwata, Y. N. Miura[1], M. Inagaki[2]

Faculty of Science, Yamagata University
[1]Earthquake Research Institute, University of Tokyo
[2]Institute for Integrated Radiation and Nuclear Science, Kyoto University

INTRODUCTION: Radiometric dating is a valuable tool for unveiling the formation and evolution process of planetary material. The K-Ar and ^{40}Ar-^{39}Ar methods are invaluable in determining the timing of heating events on planetesimals and asteroids (e.g. Swindle et al. (2014) [1]). The ^{40}Ar-^{39}Ar dating method with laser heating technique is suitable for tiny samples (e.g. Kelley, 1995[2] and Hyodo, 2008 [3]). To obtain ^{40}Ar-^{39}Ar dates of the extraterrestrial material using the facility in KURNS, we have continued developing a ^{40}Ar-^{39}Ar dating system, which includes laser-heating gas extraction and gas purification lines. The system was initially designed by Dr. R. Okazaki (Kyushu University) and has been developed for several years. Previous progress reports have de-scribed details and the schematic diagram of the system (Nos. 31126, R2079, R3121, R4068).

EXPERIMENTS: In FY2023, we continued assembling the gas extraction and purification system (Fig. 1). We baked out the gas extraction and gas purification lines to attain ultra-high vacuum conditions. We also degassed the SORB-AC pump. Separately, we commissioned the Nd-YAG laser.

RESULTS: After the bakeout of gas extraction and gas purification lines, vacuum pressure in the vacuum plumbing lines reached 1×10^{-6} Pa at a vacuum gage on the top of the turbomolecular pump and 4×10^{-4} Pa at a vacuum gage in the purification line under pumping. The vacuum quality is insufficient for ^{40}Ar-^{39}Ar dating in KURNS, so we need more bakeout treatments. We tried to test-run the Nd-YAG laser, but we couldn't confirm the presence of laser output. It is necessary to reexamine the condition of Nd-YAG laser equipment and its usage procedure.

The next step in this development is to install a charcoal trap on a gas purification line, install a quadrupole mass spectrometer, and make an electrical connection for a noble pump.

REFERENCES:

[1] T. D. Swindle *et al.,* in Advances in ^{40}Ar/^{39}Ar Dating: from Archaeology to Planetary Sciences, edited by Jourdan, Mark, Verati (Geol. Soc., London, Spec. Pub. 378, (2014) 333-347.

[2] S. P. Kelley, in Microprobe techniques in the earth sciences, edited by Potts, Bowles, Reed, Cave (Chapman & Hall, London, (1995) 327-358.

[3] H. Hyodo., Gondwana Res., **14** (2008) 609-616.

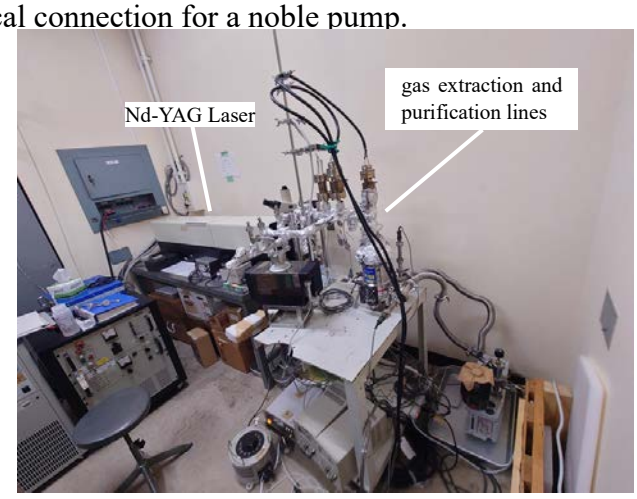

Fig. 1. Overview of the ^{40}Ar-^{39}Ar dating system. The layout of the equipment was changed in FY2023.

CO5-13

An Evaluation of Three Halogens (Cl, Br, and I) Data from a GSJ Geochemical Reference Materials by RNAA

N. Shirai, M. Ebihara[1] and H. Yoshinaga[2]

Faculty of Science, Kanagawa University
[1]Department of Chemistry, Tokyo Metropolitan University
[2]Research Reactor Institute, Kyoto University

INTRODUCTION: Among the five halogens, F, Cl, Br, and I are present in the environment as stable elements. Halogens are highly mobile, volatile, and incompatible elements in a range of geochemical processes. Due to their chemical characteristics, these elements have been widely used to trace the water cycle in subduction zones, understand the mechanism of magma degassing, and evaluate the recycling of solid earth materials in the crust and mantle. Despite the importance of halogens in geochemical processes, the determination of halogens in geological samples is scarce. The reason for this is the difficulty in determining these elements due to their volatility and low concentrations in geological samples. In this study, a total of 12 GSJ geochemical reference materials (JA-1, JB-2a, JB-3a, JF-2, JG-3, JGb-1, JH-1, JP-1, JR-3, JCp-1, JCt-1, and JSO-1) were analyzed by using RNAA. This will contribute to establishing certified or recommended values of these halogens for these materials and to expanding the utility of these materials for the determination of halogens.

EXPERIMENTS: The analytical procedure of RNAA is described in Sekimoto and Ebihara [1]. GSJ reference materials were weighed into plastic vials and an appropriate amount of each halogen standard solution dropped on a filter paper was sealed in polyethylene as halogen reference samples. Both of these were irradiated for 10 min at the Kyoto University Research Reactor Institute. Know amounts of three halogens and Mn carriers were added into a Ni crucible with the irradiated reference materials and then were fused in NaOH. The fuse cake was digested in water, and a hydroxide precipitate was removed from the supernatant, which contained the halogens. After acidification of the supernatant, iodine was precipitated as PdI_2, and Cl and Br were precipitated as a mixture of AgCl and AgBr precipitates. These precipitates were subjected to the measurement of ^{128}I, ^{38}Cl, and ^{82}Br. The chemical yields of the three halogens during radiochemical separation were determined using the reactivation method.

RESULTS: The mean values for the chemical yields were 72% for Cl, 58% for Br, and 67% for I in this study. Our three halogen contents were compared with the literature values obtained using NAA, IC, ID-MS, ICP-MS, and NI-NGMS. Our RNAA data for the three halogens are in agreement with literature values using NAA, ID-MS, and IC. Almost all of our RNAA data are higher than the NI-NGMS [2] and ICP-MS [3] data. In NI-NGMS, the sample is irradiated with a high dose of neutrons, and the noble gas nuclides produced through beta-decay of the neutron capture halogen nuclides are extracted by stepwise heating, it is likely that the lower values produced by NI-NGMS can be explained by the loss of noble gasses during the procedure. In the ICP-MS procedure with pyrohydrolysis, a sample mixed with V_2O_5 is placed into a quartz tube and heated. The evaporated Br and I are collected in a trap solution containing tetramethylammonium hydroxide. As mentioned by Sekimoto and Ebihara [1], the quantitative collection of Br and I cannot always be achieved by the pyrohydrolysis for some solid samples. Thus, our higher Br and I values can be explained by the fact that the quantitative collection of Br and I cannot achieved in the ICP-MS procedure combined with pyrohydrolysis.

REFERENCES:

[1] S. Sekimoto and M. Ebihara, Anal. Chem., **85** (2013) 6336-6341.
[2] M. Kobayashi *et al.*, Chem. Geol., **582** (2021) 120420.
[3] J. Y. Chai and Y. Muramatsu, Geostand. Geoanal. Res., **31** (2007) 143-150.

CO5-14

Halogen and noble gas characteristics of Archean ultramafic rocks from the Isua Supracrustal Belt in southwestern Greenland

H. Sumino, N. Fukushima, Y. Hibiya, Y. Iinuma[1], R. Okumura[1] and H. Yoshinaga[1]

Research Center for Advanced Science and Technology, University of Tokyo
[1]Institute for Integrated Radiation and Nuclear Science, Kyoto University

INTRODUCTION: Since some of the halogens (fluorine, chlorine, bromine, and iodine) are converted to corresponding noble gas isotopes by neutron irradiation and detection limits for noble gas isotopes by mass spectrometry are low (down to ten thousand atoms), they can be analyzed with high sensitivity by using neutron irradiation and noble gas mass spectrometry [1]. We investigated the halogen and noble gas geochemistry of ultramafic rocks from the Isua Supracrustal Belt (ISB) in southwestern Greenland. Water plays a crucial role in recycling volatiles on Earth through the subduction of oceanic/crustal plates, but the composition of mantle volatiles and their modification processes remain largely unknown. In this study, noble gas and halogen analyses were performed on Archean ultramafic rocks from ISB to constrain the volatile element evolution of the mantle. The ISB is an arch-like supracrustal package about 30 km long and 4 km wide, subdivided into two terranes, southern (3.8 Ga, where Ga = billion years ago) and northern (3.7 Ga). The 3.7 Ga terrane contains ultramafic bodies, including dunite (olivine-dominated peridotite) lenses A and B [2]. Both have different and complex metamorphic histories, such as hydration and dehydration (e.g., [3]). The origin of the dunite has been proposed as either residual peridotite of mantle melting [2] or as olivine cumulate formed from basaltic melt intruding the crust [4]. The Lens A dunite samples are likely composed of primary olivines, except for grain boundaries. Valuable information from this period may be preserved within the fluid/melt inclusions in the olivines.

EXPERIMENTS: The samples of 5-50 mg each and standards for neutron fluence were wrapped with aluminum foil and put in aluminum capsules of ϕ10 mm x 30 mm. The capsules were irradiated with neutrons in KUR. After the irradiation, the samples were sent to the University of Tokyo. The samples were loaded into an ultra-high-vacuum, noble gas extraction, purification, and separation line. Noble gases were extracted from the samples by heating up to 1800°C, purified with hot Ti-Zr getters, separated into each noble gas with temperature-controlled cold traps, and then determined their isotope compositions with a noble gas mass spectrometer [1]. The thermal and fast neutron flux was estimated from the production of ^{39}Ar and ^{38}Ar from ^{39}K and ^{37}Cl in the Hb3gr hornblende standard, in which K and Cl contents have been determined.

RESULTS: The noble gas composition of fluid/melt Inclusions In the peridotites reflects the contribution of noble gases from a radiogenic (crust-like) component. Two models can be proposed to explain the crustal noble gas signatures: (1) slab-derived fluid/melt penetrated and was trapped in the dunite, and (2) crustal fluid was trapped in the dunites during the metamorphism of the ISB. If (1) is correct, it suggests the possibility that the mantle experienced substantial contributions from radiogenic components in fluids/melt derived from partial melting of the slab.

Halogen compositions of the Lens A dunites are consistent with (1) since the halogen composition cannot be explained without the contribution of a slab-derived subduction component. The results of this study suggest the possibility that the recycling of volatile components into the mantle beneath ancient subduction zones was more active than it is today, indicating an essential process for modifying volatile components in the mantle during this period [5].

REFERENCES:

[1] M. Kobayashi, *et al.*, Chem. Geol., **582** (2021) 120420. [2] C.R.L. Friend *et al.*, Geology, **39** (2011) 663-666. [3] J.M. Guotana *et al.*, Geosci. Front., **13** (2022) 101298. [4] P.Waterton *et al.*, Earth Planet. Sci. Lett., **579** (2022) 117348. [5] N. Fukushima, Ph.D Thesis, Univ. Tokyo (2024).

CO5-15

Improvement of Determination Method of Uranium-Containing Particles as Close-In Fallout from A-Bomb Using Fission-Track Analysis

K. Takamiya, N. Toe, M. Inagaki, Y. Oki and Y. Igarashi

Institute for Integrated Radiation and Nuclear Science, Kyoto University

INTRODUCTION: The fission track analysis technique combined with heavy-liquid separation developed in the previous work demonstrated to be effective in detecting particles containing a high concentration of uranium in soil samples [1]. This method can detect the presence of uranium particles by detecting a cluster of fission tracks. The soil particle sample in which many clusters were detected in the previous work was observed using SEM/EDX, and particles containing several percent uranium were found. Since the concentrations of uranium of particles derived from the atomic bomb would be much higher, these particles are thought to be natural soil particles containing high concentrations of uranium. It is necessary to distinguish between natural and atomic bomb-derived uranium particles to extract the latter particles in a soil sample. Uranium particles derived from the atomic bomb have a higher ^{235}U content than natural soil particles, so particles of the same size generate more than thousand times tracks in the fission track analysis. Therefore, it might be possible to distinguish between natural particles and atomic bomb-derived uranium particles by reducing neutron irradiation fluence in the fission track analysis.

EXPERIMENTS: A part of soil sample collected in Hiroshima was mixed with sodium polytungstate (SPT) solution adjusted to 3.0 g/cm^3 and centrifuged at 3000 rpm for 10 minutes to separate particles of higher relative density particles. The separated particles were collected on a PTFE filter and attached to a track detector. Particles and the detector were irradiated by about 3×10^{13} n/cm^2 of thermal neutrons using the pneumatic irradiation facility (TC-Pn) at Kyoto University Research Reactor. After the irradiation, the track detectors were etched and observed by optical microscope.

RESULTS: The number of tracks generated by one particle under the above irradiation conditions is estimated to be about ten thousand by assuming that the uranium particles derived from the atomic bomb have a diameter of 2.5 μm, uranium concentration of 100% (^{235}U isotope ratio of 80%), and a specific gravity of 19 g/cm^3. On the other hand, even if natural uranium-rich soil particles are assumed to have a diameter of 10 μm, a concentration of natural uranium of 10%, and a specific gravity of 3 g/cm^2, the number of generated tracks is expected to be less than one. Those mean only the uranium particles derived from the atomic bomb will be detected as clusters of tracks.

An example of the detected cluster is shown in figure 1. The cluster has several thousand tracks, and the particle generating this cluster is thought to be originated from the atomic bomb. However, no particles containing high concentrations of uranium could be found using SEM. Since the particle size estimated by the number of tracks is few μm which is less than position resolution of the SEM system applied in this work, it is considered difficult to detect.

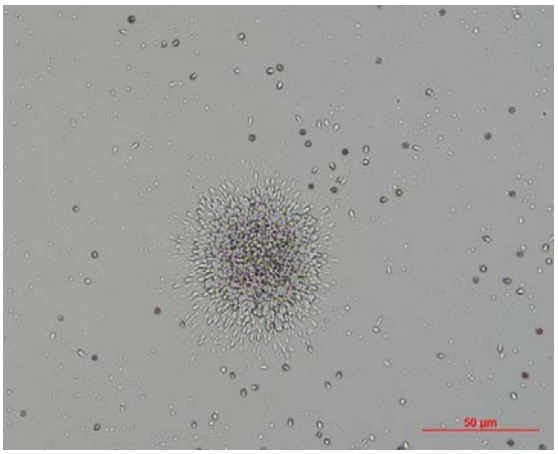

Fig. 1 The cluster of fission track generated by neutron irradiation using TC-Pn of KUR.

REFERENCES:

[1] K. Takamiya *et al.,* KURNS Progress Report 2022 (2023) 134.

CO5-16

Concentration of ^{137}Cs in litter in *Quercus serrata* and *Cryptomeria japonica* forests

T. Ohta, Y. Mahara[1], S. Fukutani[2] and T. Kubota[3]

Department of Nuclear Technology, Nagaoka University of Technology
[1]Kyoto University
[2] Institute for Integrated Radiation and Nuclear Science, Kyoto University
[3]Agency for Health, Safety and environment, Kyoto University

INTRODUCTION: Vast forest was markedly contaminated by radioactive plums containing radiocesium in the wide range of the eastern part of Japan in 2011 [1–7]. As forests have an important role in preventing landslides and maintaining the ecological and hydrological system, the destructive forest should be avoided and an appropriately managed tree-felling should be conducted. In our previous field study [1], most of the radiocesium in the tree rings was directly absorbed by the atmospheric direct uptake via the bark and leaves rather than by roots. We directly measured root distribution of *Cryptomeria japonica* [3], indicating that mature it is not effective to absorb radiocesium by the root uptake due to the distribution of the fine root [3, 5]. The radiocesium is higher in Konara than in *Cryptomeria japonica* [1]. *Quercus serrata* with shallow roots and lateral distribution *is* more likely to absorb radiocesium than *Cryptomeria japonica.*
Focusing on litter, from which radiocesium is more easily leached than mineral soil, the distribution of radiocesium in litter in *Quercus serrata and Cryptomeria japonica* forest in a 1m x 1m area was investigated. We measured the concentration of radioactive cesium in litter layer, and then we reconsidered most severe absorption concentration of it.

EXPERIMENTS: Litters were collected at the Koriyama, Fukushima. The sampling sites were forest in *Quercus serrata* and *Cryptomeria japonica*. The collected the samples in the field were transported to the laboratory and stored it in the dark for 12 years. The ^{137}Cs in the litter was deter-mined by gamma-ray spectrometry (HPGe). The concentration of ^{137}Cs was corrected on March 12, 2011.

RESULTS: ^{137}Cs in litter were from 1.3×10^4 Bq/kg to 1.7×10^4 Bq/kg (av: $(1.6 \pm 0.1) \times 10^4$ Bq/kg, n=10) in *Quercus serrata* area and from 1.6×10^4 Bq/kg to 3.2×10^4 Bq/kg (av: $(2.2 \pm 0.5) \times 10^4$ Bq/kg, n=10) in *Cryptomeria japonica* area. The average transfer factors of stable Cs estimated for the sapwood region ($(9.59 \pm 2.56) \times 10^{-3}$ for *Quercus serrata* and $(8.34 \pm 2.55) \times 10^{-4}$ for *Cryptomeria japonica* [1]). Therefore, even under the condition that all fine roots are in the litter layer, utmost ^{137}Cs in the xylem for *Quercus serrata* and *Cryptomeria japonica* would be 150Bq/kg and 18 Bq/kg, *respectively.* However, such concentration of it in the xylem for *Quercus serrata* are not found in the area. Currently, it is considered as follows: 1) the leaching rate of radioactive cesium in litter is not so high, and 2) the fine roots of *Quercus serrata* are also located deeper in the soil and are not easily leached into the soil water. Therefore, even if we take the most conservative conditions into account, the amount of ^{137}Cs in xylem will not increase.

REFERENCES:

[1] Y. Mahara *et al.*, Sci. Rep., **4** (2014) 7121.
[2] T. Ohta *et al*., J. Radioanal. Nucl. Chem., **310** (2016) 109-115.
[3] Y. Mahara *et al.*, Sci. Rep., **11** (2021) 8404.
[4] T. Ohta *et al*., Radiological Issues for Fukushima's Revitalized Future, Ed Takahasi (Springer)(2016) 13-24.
[5] T. Ohta *et al*., KURNS Progress Report 2021 (2022) 151.
[6] T. Ohta *et al*., Ana. Sci., **29** (2014) 941-947.
[7] T. Ohta *et al*., J. Environ. Radioact., **111** (2012) 38-41.

CO5-17

Identification of Products in Traces of "Black Rain"on the Gold Folding Screen (made of Western gold leaf)

T. Mukai[1,2], N. Toe[1], Y. Shibahara[1], M. Ikegami[1], H. Yashima[1], S. Fukutani[1], K. Takamiya[1], J. Inoue[2], T. Adachi[3], and Y. Igarashi[1]

[1]Institute for Integrated Radiation and Nuclear Science, Kyoto University, [2]Osaka Metropolitan University [3]ATOX Co., Ltd

INTRODUCTION: In 2022, the gold folding screen (Western gold leaf: copper alloy foil containing zinc) with traces of the "Black Rain" was discovered in a private house in Hiroshima City. As a result of analyzing the traces with an optical microscope and an electron microscope, it was found that Cu, the main component of the gold leaf, was dissolved by S and N, which are elements thought to constitute the "Black Rain". Consequently, we aimed to identify the products containing Cu, S, and N by X-ray diffractometry (XRD). Furthermore, we attempted to verify the products obtained from the corrosion simulation experiment of a model gold screen using sulfuric acid containing S and nitric acid containing N.

EXPERIMENTS: Three gold folding screen pieces with black traces (Sample ID: No.3, No.6, No.8), a control piece (No.2), and products obtained from corrosion simulation experiments were analyzed using a fully automated X-ray diffractometer (Rigaku SmartLab Cu Kα source, tube voltage 40 kV, tube current 200 mA, micro-incident optics, scan speed 0.5°/min). In simulated experiments, aqueous solution at pH 1 is dropped onto a model gold screen "RSY-001" (Western gold leaf) and exposed indoors for several days to months.

RESULTS: Analysis of the black traces of No. 3 shown in Fig. 1 revealed copper sulfate pentahydrate (presumed) as indicated by the arrow in Fig. 2, but no copper nitrate compounds were detected. No copper nitrate compounds were not detected in No.6 and No.8. This is presumably due to the amount of traces and the presence or absence of crystallinity. That is, copper sulfate hydrate is detected due to its crystalline nature, but copper nitrate compounds are not detected due to their tidal nature[1]. The experimental results showed that the copper sulphate hydrate was a crystalline product and the copper nitrate compound (presumed) was a liquid product. The ageing products have not been analyzed. In conclusion, no copper nitrate compounds were detected in the “Black Rain” traces on the gold screen, but copper sulfate hydrates were estimated to be mixed in the traces. This suggests the possibility that sulfuric acid was mixed in the “Black Rain”.

REFERENCES:[1] H. Suzuki., Encyclopedia of Nitrogen Oxides, Maruzen, Tokyo (2008).

ACKNOWLEDGMENTS: We are grateful to the staff of the Hiroshima Peace Memorial Museum, especially the curatorial staff and the donor for permission to cut the gold folding screen. We thank Rekiseisha Co., Ltd. for a model gold screen and Prof. Takuo Okuchi of our institute for his guidance in XRD analysis.

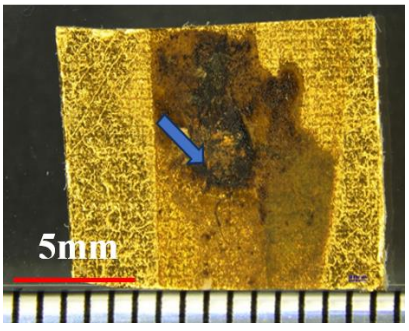

Fig.1 "Black Rain" trace of No.3 cut from the gold folding screen.

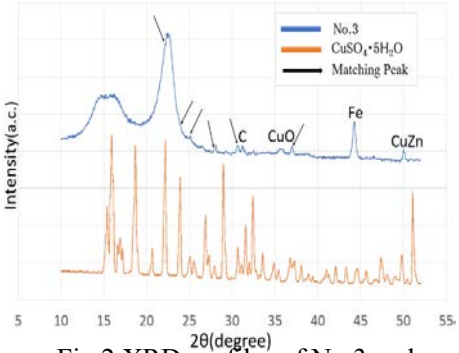

Fig.2 XRD profiles of No.3 and $CuSO_4 \cdot 5H_2O$.

CO6-1

Radiolabeling of composite natural material chicken eggshell membrane via neutron irradiation 6Li(n,α) 3H reaction

M. Shimizu[1], E. Ohto-Fujita[1], N. Nogawa[2], H. Yoshinaga[3], K. Takamiya[3], A. Enomoto[4], K. Tanoi[5], T. Yamashita[6], and Y. Atomi[1]

[1]*Teikyo University, Advanced Comprehensive Research Organization, Division of Open Innovation*
[2]*Isotope Science Center, The University of Tokyo*
[3]*Institute for Integrated Radiation and Nuclear Science, Kyoto University*
[4]*Isotope Facility, Graduate School of Medicine, The University of Tokyo*
[5]*Isotope Facility for Agricultural Education and Research. Graduate school of Agricultual and Life Sciences, University of Tokyo.*
[6]*Department of dermatology, Graduate School of Medicine, The University of Tokyo*

INTRODUCTION: Chicken eggshell membrane (ESM) has been listed as an excellent wound-healing agent in Chinese pharmacopoeia book entries for 400 years. It is a non-woven fabric composed of fibrous biopolymers that are mainly protein-based and contain a large amount of extracellular matrix such as collagen and proteoglycans, as well as antibacterial proteins, cross-linked by lysyl-oxidase [1]. Recently, proteomic analysis has revealed that it contains more than 400 different proteins. We previously found that hydrolyzed ESM provide young extracellular environment to dermal fibroblast [2] and improved skin elasticity and reduced facial wrinkles when topically applied as cosmetics [3]. Ingestion of this non-woven fabric has been reported to improve pain in knee joints and prevent liver fibrosis and ulcerative colitis in animal experiments. In our previous studies, we have found that eggshell membrane supplements improved skin elasticity, respiratory function, and locomotion (especially balance function) in healthy adults within 8 weeks of taking the supplements [4]. ESMs are secreted by cells in the narrow oviduct of the parent bird and serve as a biomineralization scaffold for eggshell formation and to protect chick embryo from drying and infection. We applied the tritium labeling of organic compounds via the 6Li(n,α)3H reaction, which has been used for radiolabeling of natural products that are difficult to synthesize and for tissue distribution in individuals, to ESM and conducted pilot experiments to determine whether ingested ESM are indeed digested and absorbed and distributed to various tissues. The labeled eggshell membrane was orally administered to mice and was digested and absorbed. The radioactivity derived from the labeled ESM was detected in blood 2 hours after administration, peaking 6 hours later, and was also detected in almost all tissues [5]. However, in the previous irradiation experiment with JRR-4 (3.5 MW, 20 min), many parts of the sample were scorched, and the optimization of the eggshell membrane to lithium carbonate ratio and irradiation conditions remained an issue. The Kyoto University furnace is beneficial for irradiating protein samples because its low power output does not raise the sample temperature during irradiation.

****

EXPERIMENTS: ESM (nano-sized extra-fine form, Almado Inc.) + Li_2CO_3 (65:35 by weight) and lysozyme or ovotransferrin (one of the major proteins of ESM) + Li_2CO_3 (65:35 by weight) sealed in quartz glass were irradiated under milder conditions (Pn-2, 1 MW, 70 min). After irradiation, samples were transferred to The University of Tokyo for biochemical and in vivo study.

****

RESULTS:【R4193 tritium-labeled ESM (2022) (research update)】Mice were orally fed once with tritium-labeled ESM for detailed verification of the pharmacokinetics and cellular uptake. The tritium-labeled eggshell membrane was mixed with medical jelly and given to B6 mice as a single oral dose as a supplement and kept individually in metabolic cages. Then, 0.5, 2, 5, 24, 48, and 72 hours later, blood was drawn from an abdominal vein under anesthesia, and PBS was perfused through the

heart to drain blood from the tissues. Approximately 30 different organs were isolated (n=4 each time). A tritium count study in serum revealed a peak at about 5 hours, like the results of the previous pilot experiment [4]. Continuous study is ongoing to quantify the distributed radioactivity to more than 20 tissues using a liquid scintillation counter. One of the tissue (liver) specimens was prepared for histochemical analysis using a cryostat, and the ^{3}H distribution was analyzed using an imaging analyzer. A preliminary experiment showed that the detection of radioactivity was not successful after 7 months of exposure to the image plate. Thus, multiple administrations of rebelled eggshell membranes are necessary for this purpose.

【R5010 tritium-labeled ESM and lysozyme (2023) study (to be performed)】The chemical integrity of the protein after Pn-2 irradiation and the peptide size after digestion and absorption into the serum and mouse tissues will be determined using SDS-PAGE and peptide gel. Using cell line, uptake of labeled protein and secretion of ECM (decorin, type III collagen, MMP2) will determine the biological activity of the irradiated protein sample.

****

REFERENCES:

[1] M. Shimizu *et al.*, The journal of Japan Mibyou Association, **30** (2024) 23-26.
[2] E. Ohto-Fujita *et al.*, Cell Tissue Res., **345** (2011) 177-190.
[3] E. Ohto-Fujita *et al.*, Cell Tissue Res., **376** (2019)123-135.
[4] E. Ohto-Fujita *et al.*, Journal of Fiber Science and Technology, **77** (2021) 258-265 (2021) 115-120.
[5] E. Ohto-Fujita *et al.*, Journal of Fiber Science and Technology, **77** (2021) 182-187.

CO6-2

Interaction between Mint3 and FIH-1 involved in hypoxia stress responses

R. Maeda, S. Nagatoishi[1], K. Tsumoto[1], K. Morishima[2], R. Inoue[2], M. Sugiyama[2] and M. Hoshino
Graduate School of Pharmaceutical Sciences, Kyoto University
[1]*Institute of Medical Science, the University of Tokyo*
[2]*Institute for Integrated Radiation and Nuclear Science, Kyoto University*

INTRODUCTION: Oxygen is essential for many organisms to produce ATP efficiently from nutrients in food. Temporal or local drop of oxygen level induces cells to change the metabolic pathway. This is called stress responses, which are mainly triggered by hypoxia inducible transcriptional factors (HIFs). Under the normal oxygen conditions, transcriptional activities of HIFs in the cells are inhibited by the factor inhibiting HIF-1 (FIH-1). Munc-18 interacting protein 3 (Mint3) is recently found to activate the hypoxia responses by binding and inhibiting the activity of FIH-1 in these cells under the normal oxygen conditions [1]. Although the N-terminal 214 residues (Mint3NT) are found to be necessary for the interaction with FIH-1 to inhibit its activity, little is known about inhibitory mechanisms. We investigated the interaction between Mint3NT and FIH-1 by small-angle X-ray scattering, analytical ultracentrifugation, and solution-state NMR.

EXPERIMENTS: The N-terminal fragment proteins of Mint3 (Mint3NT) and full-length FIH-1 were expressed by *E. coli* BL21 strains. The proteins were expressed in bacteria grown in LB-broth and ^{15}N-enriched M9 minimal medium to produce unlabeled and ^{15}N-labeled proteins, respectively. NMR experiments were performed on a Bruker Avance 600 spectrometer equipped with a triple-resonance probe. A typical ^{1}H-^{15}N HSQC experiments were performed at protein concentration of 50 μM dissolved in 20 mM sodium phosphate (pH 7.3) and 10% D_2O.

RESULTS: We measured the ^{1}H-^{15}N HSQC spectrum of Mint3NT, and found that the dispersion of resonance peaks was very poor particularly along the ^{1}H-axis, suggesting the absence of strong hydrogen-bonding interactions. We prepared several fragment proteins of 214-residue protein Mint3NT. The superposition of the spectra separately recorded with the fragment proteins were found to be essentially the same as that of the whole protein, suggesting that the absence of significant interaction between the N- and C-terminal regions of Mint3NT. With these fragment proteins of Mint3NT, we unambiguously assigned more than 95% peaks by analyzing several triple-resonance spectra. The titration experiment of ^{15}N-labled Mint3NT by unlabeled FIH-1 revealed that the peak intensities for many residues were remarkably decreased in a concentration dependent manner. By mapping the change in the peak intensity along the primary structure of the protein, we found that a broad range of residues were significantly affected by the addition of unlabeled FIH-1, suggesting the involvement of these residues in the interaction between Mint3NT and FIH-1.

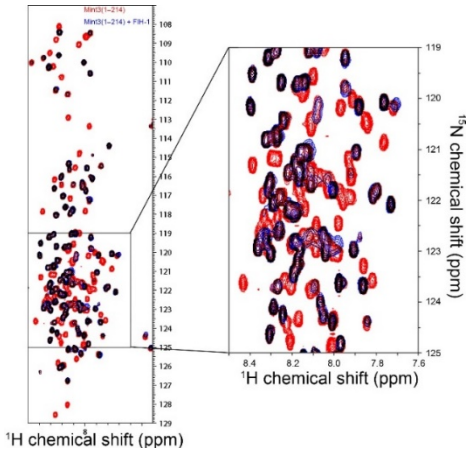

Fig. 1. ^{1}H,^{15}N-HSQC spectra of ^{15}N-Mint3NT in the absence (red) and presence (blue) of equimolar amount of unlabeled FIH-1. Peaks significantly decreased in intensity are shown in red.

REFERENCES:
[1] Sakamoto *et al.,* Mol. Cell Biol., **34** (2014) 30-42.
[2] Ten *et al.,* J. Biol. Chem. **297** (2021) 101304.

CO6-3

Integrated structural analysis of clock protein complex using analyatical ultracentrifugation and small-angle X-ray scattering

K. Morishima, M. Shimizu, A. Okuda, N. Sato, R. Inoue, and M. Sugiyama

Institute for Integrated Radiation and Nuclear Science, Kyoto University

INTRODUCTION:

Cyanobacteria has one of the simplest circadian clocks which consists of only three clock proteins (KaiA, KaiB, and KaiC) and adenosine triphosphate (ATP). The three clock proteins undergo an association-dissociation cycle correlated with phosphorylation-dephosphorylation oscillation of KaiC with 24 h-period. In the circadian cycle, the three types of complexes appear; KaiA-KaiC (AC), KaiB-KaiC (BC), and KaiA-KaiB-KaiC (ABC) complexes. Among them, AC complex has a significant function for the circadian cycle, that is, the promotion of phosphorylation of KaiC. To understand the molecular mechanism of the phosphorylation, it is necessary to reveal the three-dimensional structure of AC complex. However, there are obstacles on the structural analysis of AC complex.

EXPERIMENTS:

In this study, we utilized the small-angle X-ray and neutron scattering (SAXS and SANS; collectively called SAS) to analyze its solution structure. The SAS profile purely from AC complex is essential for building its structural model. Nevertheless, AC complex cannot be predominantly purified with a general separation method such as size exclusion chromatography due to the fast association-dissociation equilibrium, KaiA + KaiC ↔ AC complex. To overcome this problematic situation, we applied to the integrated approach with analytical ultracentrifugation (AUC) and SAS, namely AUC-SAS [1,2].

RESULTS: AUC offered the concentration distribution of KaiA, KaiC, AC complex, and their aggregates in the mix solution of KaiA and KaiC. The experimental SAXS profile of the mix solution (open circles in Fig.1) was given as the ensemble-average of these components. Therefore, we derived the SAXS profile of AC complex from the experimental profile with AUC-SAS as shown in Fig.1. (Here, the SAXS profiles of KaiA and KaiC were obtained by the individual measurements.) Finally, we obtained the candidate structural model of AC complex through the combination of the SAXS profile and coarse-grained molecular dynamics simulation.

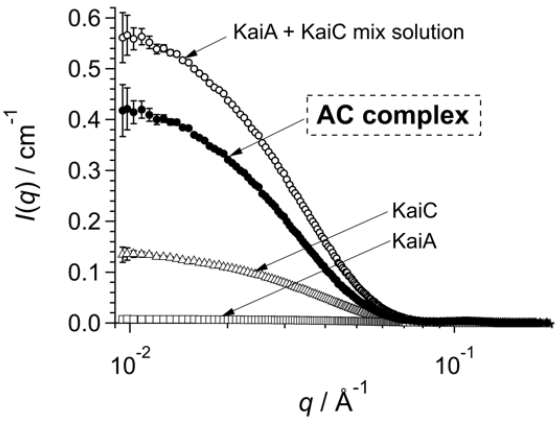

Fig. 1. Open circles, squares, triangles represent the experimental SAXS profiles of the KaiA + KaiC mix solution, KaiA, and KaiC, respectively. Closed circles show the SAXS profiles of AC complex derived with AUC-SAXS-treatment.

REFERENCES:

[1] K. Morishima *et al.,* Commun. Biol., **3** (2020) 294.

[2] K. Morishima *et al.,* J. Appl. Crystallogr., **56** (2023) 624.

CO6-4

Elucidation of the effects of dose rate of radiation on normal and tumor tissues

T. Watanabe[1], Y. Sanada[2], T. Takata[3], G. E.Sato[4], M. Yoshimura[4], Y. Sakurai[3], H. Tanaka[3], M. Suzuki[1], T. Mizowaki[4]

Institute for Integrated Radiation and Nuclear Science, Kyoto University
[1]Particle Radiation Oncology, Particle Radiation Oncology Research Center
[2]Particle Radiation Medical Physics, Particle Radiation Oncology Research Center
[3]Division of Radiation Life Science
[4]Radiation Oncology and Image-Applied Therapy, Faculty of Medicine, Kyoto University

INTRODUCTION: Radiation with different dose rates is known to have different effects on normal tissues [1]. On the other hand, the effect of dose rate on the antitumor effect is minor, and a higher dose rate may improve the therapeutic efficacy ratio of radiation [2]. The purpose of this study is to ascertain whether the dose rate alters the effects of various normal tissues. In addition, experiments were conducted to see if the antitumor effect of radiation could be differentiated by differences in dose rate, which had previously been equivalent, by using drugs that affect the anti-tumor effect of radiation in combination.

****

EXPERIMENTS: A mouse subcutaneous transplantation model of mouse-derived squamous cell carcinoma cells (SCC7) was used for experiments in C3H mice under the lower limb skin. The differences in the effects of irradiation with electron beams with high dose rates and X-rays with low dose rates on normal and tumor tissues were investigated. The irradiation area was limited to the lower extremities, the remaining area was shielded, and the tumor tissue was irradiated with a single 14 Gy dose. Changes in the skin after irradiation were observed over time in the X-irradiated group and the high-dose-rate electron irradiated group. SCR, which is the inhibitor of non-homologous end joining mechanism in DNA reapair, was used as agents affecting the DNA-repair mechanism after irradiation [3]. SCR was each administered 1 hour before irradiation, and tumor tissue was irradiated to confirm tumor size over time.

****

RESULTS: The skin in the irradiated also showed obvious alopecia, wet desquamation and dermatitis in the X-ray group, whereas the skin in the high-dose-rate electron beam group showed only slight alopecia, no wet desquamation, and no dermatitis. Compared to the X-ray group, the high-dose rate electron beam group showed the same tumor control under the same irradiation dose. When X-rays were irradiated after preadministration of SCR to subcutaneous tumors in mice, the anti-tumor effect of X-rays was sensitized. However, contrary to our expectation, the sensitization effect of SCR was not enhanced in the high-dose rate electron beam irradiation compared to the X-ray group. When SCR was preadministered to subcutaneous tumors of mice and then irradiated with high-dose-rate electron beams, the effect to the normal tissue including the surrounding skin was also similar to that in X-ray group.

****

REFERENCES:

[1] B. Lin *et al.,* Front Oncol., **11** (2021) 644400.
[2] E. Konradsson *et al.,* Advances in Ra-diation Oncology., **7** (2022) 101011.
[3] M. Srivastava *et al.,* Cell., **151** (2012) 1474-87.

CO6-5

Design, Synthesis, and BNCT Effect of Macrocyclic Polyamine-type Boron Carriers for BNCT

S. Aoki[1,2], H. Ueda[3], W. Yoshida[1], M. Suzuki[3], Tanaka, T.[1,4] S Masunaga[3], N. Kondo[3], and Y. Sakurai[3]

[1]*Faculty of Pharmaceutical Sciences, Tokyo University of Science*
[2]*Research Institute for Science and Technology, Tokyo University of Science*
[3]*Research Reactor Institute, Kyoto University*
[4]*Faculty of Pharmaceutical Sciences, Okayama University*

INTRODUCTION: Neutron capture therapy using boron-10 (^{10}B) (BNCT) is one of powerful therapies for local tumor control in the treatment of brain tumor, melanoma, and related diseases. We previously designed and synthesized phenylboronic acid-pendant 9-, 12-, and 15-membered macrocyclic amines such as **^{10}B-1a~3a** and their corresponding Zn^{2+} complexes **^{10}B-1b~3b** (Fig. 1) [2], based on high intracellular uptake pendant-cyclen (cyclen = 1,4,7,10-tetraazacyclododecane) in cancer cells. It was reported that the metal-free **^{10}B-1a~3a** are introduced into cancer cells (A549 and HeLa S3 cells) more efficiently than their Zn^{2+} complexes **^{10}B-1b~3b** with considerably high cancer/normal cells selectivity. Besides, it was found that 12- and 15-membered derivatives **^{10}B-2a~3a** exhibit a higher BNCT effect than **^{10}B-1a**, possibly because **^{10}B-2a~3a** form the corresponding Zn^{2+} complexes **^{10}B-2b** & **3b**, which strongly interact with DNA in living cells, resulting in the efficient breakdown of DNA double-strand upon the neutron irradiation.

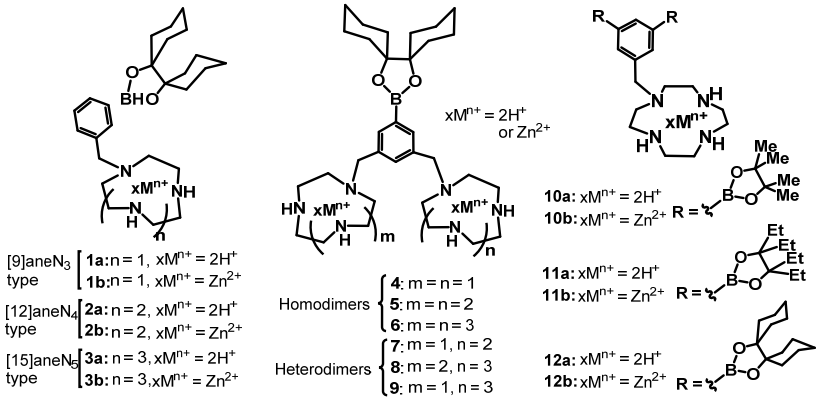

Figure 1. Chemical Structures of Borono Compounds **1**～**12**

Next, we conducted the design and synthesis of dimeric macrocyclic polyamines connected via one phenylboronic acid unit such as **4~6** (homodimers) and **7~9** (heterodimers) and their corresponding Zn^{2+} complexes (Fig. 1), because it was well established that polymeric Zn^{2+} complexes would form more stable complexes with DNA double strand than monomeric Zn^{2+} complexes [3]. However, the intracellular uptake of **4~9** and their Zn^{2+} complexes were lower than monomeric compounds **1~3**, possibly due to their lower hydrophobicity than that of **1~3.**

EXPERIMENTS and RESULTS:

The aforementioned results have prompted us to synthesize monomeric polyamines equipped with two boronic ester units for higher intracellular uptake and BNCT effect and for the observation of these ^{11}B-containing compounds (naturally occurring abundant content) for non-invasive magnetic resonance imaging (MRI) of BNCT agents in living systems. In 2023, **10a~12a** and their corresponding Zn^{2+} complexes **10b~12b** were synthesized and the evaluation of their intracellular uptake and toxicity against cancer cells is now in progress.

REFERENCES:

[1] H. Ueda *et al.,* J. Med. Chem., **64** (2021) 8523-8544.
[2] S. Aoki, E. Kimura, Chem. Rev., **104** (2004) 769-788.
[3] H. Ueda *et al.,* Eur. J. Inorg. Chem., **2022** (2022) e202100949 (24 pages).
[4] S. Aoki *et al.,* In "*Characteristics and Applications of Boron*" 2022, pp 83-105, Charchawal Wongchoosuk, Ed., IntechOpen, Croatia

CO6-6

Small-angle X-ray scattering analysis of nucleosomes containing parasite histones

S. Sato[1], K. Morishima[2], R. Inoue[2], N. Sato[2], M. Dacher[1], N. Horikoshi[1], M. Sugiyama[2], H. Kurumizaka[1]

[1]*Institute for Quantitative Biosciences, The University of Tokyo*
[2]*Institute for Integrated Radiation and Nuclear Science, Kyoto University*

INTRODUCTION: In eukaryotic cells, genomic DNA is organized into chromatin, which plays an essential role not only in tightly packaging DNA into the cell nucleus, but also in dynamically regulating biological events such as gene transcription, DNA repair, and replication. The nucleosome is the structural unit of chromatin, in which 145-147 base-pairs of DNA are wrapped around a histone octamer, containing two molecules each of histone proteins H2A, H2B, H3, and H4. The dynamics of nucleosomes impacts those of chromatin, which is fundamentally composed of the nucleosome array. A large number of unicellular eukaryotes are infectious human parasites, with low sequence identity to human histones. The characteristics of parasite chromatin remained unknown until now. Here, we investigated the structures of the nucleosomes in solution, containing histones from *Plasmodium falciparum*, the parasite responsible for human malaria.

EXPERIMENTS: The nucleosomes were prepared by *in vitro* reconstitution [1]. Recombinant human or parasite histones were mixed with a 145 base-pair DNA fragment containing a strong nucleosome positioning sequence under high salt conditions, followed by a gradual decrease in salt concentration to promote nucleosome formation, and then purification using a method based on polyacrylamide gel electrophoresis [1]. The nucleosomes thus obtained were analyzed by small-angle X-ray scattering (SAXS) under conditions of 50 or 150 mM NaCl concentration, as ionic strength is known to affect nucleosome conformation. SAXS intensity of the buffer solution was measured for background subtraction, using the same conditions and procedure as for the nucleosome samples. SAXS data were collected using a laboratory-based instrument equipped with a high-brilliance point-focused generator of a Cu Ka source. To assess aggregation and dissociation of nucleosome samples, sedimentation velocities were measured by analytical ultracentrifugation [2]. Scattering profiles (one-dimensional intensity data $I(q)$ as a function of magnitude of scattering vector q) of nucleosomes were calculated as aggregated components were removed [2]. Radius of gyrations (R_g) were estimated from the fitting curves of the $I(q)$ data using Guinier plot, as previously described [3].

RESULTS: The R_g of the parasite nucleosome is similar to that of the human nucleosome under conditions of 50 and 150 mM NaCl. DNA detachment from the histone surface of the nucleosome leads to an increase of R_g [3]. Our data suggest that the intact nucleosome containing parasite histones retains a canonical structure under physiological condition of ionic strength, even though the amino acid sequences diverge from those of human histones.

REFERENCES:

[1] T. Kujirai *et al.*, Methods Mol. Biol., **1832** (2018) 3-20.
[2] K. Morishima *et al.*, J. Appl. Crystallogr., **56** (2023) 624-632.
[3] Y. Arimura *et al.*, Sci. Rep., **3** (2013) 3510.

CO6-7

Elucidation of the oligomeric structure and activation mechanism of the small heat shock protein HspB7

K. Iino, M. Ogawa, K. Morishima[1], R. Inoue[1], M. Sugiyama[1] and M. Yohda

Department of Biotechnology and Life Science, Tokyo University of Agriculture and Technology
[1]Institute for Integrated Radiation and Nuclear Science, Kyoto University

INTRODUCTION: Small Heat Shock Proteins (sHSPs) are known to exhibit chaperone function by changing its oligomeric structure [1]. A mammalian sHsp, HspB7, possesses a strong chaperone function to prevent the aggregation of polyQ. We tried to create functional HspB7 and analyze its structure and functional mechanism. However, as the acquisition of functional HspB7 was unsuccessful, we proceeded with a change in the objective. Analysis of the oligomer dissociation mechanism and the structure of the dissociated active state of sHSP has not progressed due to the difficulty of conducting experiments at high temperatures. *Methanococcoides burtonii* is a psychrophilic archaeon with an optimal growth temperature of 21°C [2]. The genome of *M. burtonii* encodes two sHSPs (MbHsp19.8 and MbHsp17.3). In this study, we aimed to elucidate the temperature-dependent oligomeric dissociation mechanism of sHSP by performing structural and functional analyses of sHSP oligomers under heat stress using MbHsp17.3.

EXPERIMENTS: The synthetic DNA of MbHsp17.3 was cloned into pCold IV vector. Using the plasmid, MbHsp17.3 was expressed in *E. coli* BL21(DE3), then purified using anion exchange chromatography, hydrophobic chromatography, and gel filtration chromatography. Structural analysis was conducted using analytical ultracentrifugation (AUC) and small-angle X-ray scattering (SAXS). To assess the temperature and concentration dependence of oligomer dissociation, analytical ultracentrifugation measurements were performed at various temperatures and concentrations. Chaperone functional was analyzed by the aggregation inhibition effect on citrate synthase (CS).

RESULTS: The oligomers of MbHsp17.3 were confirmed to dissociate temperature- and concentration-dependently from the results of AUC (Fig 1). interestingly, at 40°C, the oligomers nearly completely dissociated, with various smaller structures detected, albeit with a decreased amount simultaneously detected. This suggests the formation of aggregates not detectable by AUC at high temperatures. At 4°C, there were oligomeric structures of 20 subunits or more, but measurements at 25°C showed the main peak at 16 subunits, which was confirmed to be a structure close to 16 subunits by SAXS analysis. MbHsp17.3 was suggested to form similar 24 subunit oligomers to other archaeal sHsps at low temperatures and exhibit activity at 16 subunits. Weak aggregation inhibition activity was confirmed by CS aggregation suppression assay.

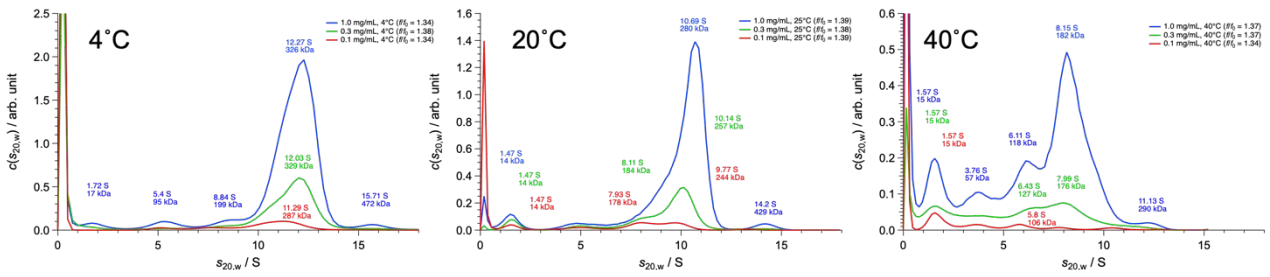

Fig. 1. AUC results of MbHsp17.3 at 4 °C, 25 °C, and 40 °C

REFERENCES:

[1] N. Kurokawa *et al.*, Int J Mol Sci., **22** (2021) 10797.
[2] P. D. Franzmann *et al.*, Syst. Appl. Microbiol., **15** (1992) 573–581 115-120.

CO6-8

Visualization of intrinsically disordered structure of F_1-ATPase ε subunit through integration of AUC-SAXS measurement and MD simulation

T. Oroguchi[1], K. Morishima[2], R. Inoue [2], M. Sugiyama[2], Y. Yamada[3]

[1] *Department of Physics, Faculty of Science and Technology, Keio University*
[2] *Institute for Integrated Radiation and Nuclear Science, Kyoto University*
[3] *Department of Life Science, College of Science, Rikkyo University*

INTRODUCTION: The ε subunit of F_oF_1-ATPase synthase plays as an intrinsic regulator of ATPase activity of F_1-ATPase depending on ATP concentration. The C domain of this subunit is an intrinsically disordered region, and the specific binding to ATP induces the structural formation of this domain and switches the inhibitory state off [1,2]. Furthermore, it has been recently reported that the disordered structure of the ε subunit is also involved in regulating the rotational coupling between F_o and F_1-ATPase [3]. Therefore, to elucidate the regulatory mechanism by the ε subunit, it is necessary to visualize its disordered structure. However, such visualization is difficult for the existing structural analyses methods such as X-ray crystal structure analyses, cryo-electron microscopy, etc. In this study, we challenge to visualize the disordered structure of the ε subunit through the technique integrating SAXS experiments and MD simulation [4]. Due to its tendency to aggregate, the ε subunit was measured using AUC-SAXS [5], which allows to confirm oligomeric states during measurement. **********

EXPERIMENTS: We condensed the purified isolated ε subunit to a concentration of 4 mg/ml, where SAXS intensity could adequately obtained, and conducted AUC-SAXS measurements. The measurements were conducted for both the ATP-unbound and the ATP-bound states. The ionic strength of the measurement buffer was adjusted to 150 mM to minimize aggregation.
****

RESULTS: Through the present measurements, we were able to observe the structural change of the ε subunit due to ATP binding (Fig. 1A), consistent with the previous biochemical data [1,2]. The SAXS data revealed that the adopted condensation protocol and measurement conditions allowed us to obtain the non-aggregated ε subunit. However, the AUC also showed that at the used concentration, the ε subunit exists in a monomer-dimer equilibrium for both ATP-unbound and ATP-bound states (Fig. 1B). We additionally conducted the AUC measurements for the lower concentration, and the results revealed that the equilibrium shifted to the monomeric state. From all these results, we established the sample preparation protocol and measurement condition, which allow us to obtain the data for the isolated ε subunit at the next measurement.
****

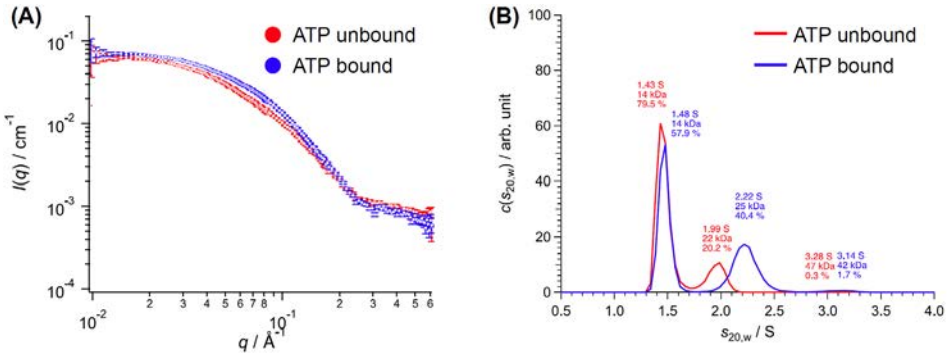

Fig. 1 (A) SAXS data, (B) AUC data of the ε subunit.

REFERENCES:

[1] Y. Kato-Yamada & M. Yoshida, J. Biol. Chem., **278** (2003) 36013-36016.
[2] S. Kato, M. Yoshida & Y. Kato-Yamada, J. Biol. Chem., **282** (2007) 37618-37623.
[3] F. Kadoya, S. Kato, K. Watanabe & Y. Kato-Yamada, Biochem. J., **437** (2011) 135-140.
[4] T. Oroguchi *et al.*, Biophys. J., **96** (2009) 2808-2822 .
[5] K. Morishima *et al.*, Comm. Biol., **3** (2020) 294.

CO6-9

Change of Microglia/ Macrophage after immuno- and/or radiation therapy

N. Kondo[1], Y. Shimizu[2], and Y. Sakurai[1]

[1] *Particle Radiation Oncology Research Center, Institute for Integrated Radiation and Nuclear Science, Kyoto University (KURNS)*

[2]*Dept. of Diagnostic Imaging and Nuclear Medicine, Graduate School of Medicine, Kyoto University.*

INTRODUCTION: Radiotherapy such as X-rays and γ-rays is used as a standard treatment as a safe and effective cancer treatment. After radiation therapy, vascular permeability increases in the irradiated tissue, and infiltrating immune cells increase then causing inflammation. There are many unknown points, such as the interaction between infiltrated immune cells and residual tumors in the microenvironment, the effects of immune cells on organs and tumors outside the irradiated area. In addition, immune checkpoint inhibitors have come into use, and interactions mediated by immune cells have been emphasized. Also, abscopal effect is boosted with immunotherapy [1]. In this study, we investigated how immune cells (macrophages, regulatory T cells, cytotoxic T cells, etc.) infiltrate and interact with irradiated tissues and organs throughout the body (outside the field of irradiation), including the brain, after irradiation. We will also investigate the changes that occur when immune checkpoint inhibitors are used in combination with radiation therapy.

EXPERIMENTS:

Cells:

We used Lewis Lung Cell Carcinoma cell line (LLC). They were cultured in RPMI 1640 medium with 10% heat-inactivated fetal bovine serum in 5 % CO_2 incubator.

Innoculation of tumor and drug treatment to animals

We used C57BL/6 mice. $5E^5$ LLC cells were inoculated subcutaneously in a thigh of the mice. We created four groups (non-treatment, immunotherapy alone, radiation therapy alone, and immunotherapy and radiation therapy combined) and each group contained 9 animals. After the inoculation, we administrated anti-mouse PD-1 antibody on the day 6 and 12 (250 μg/body).

Irradiation:

We used the Cobalt 60 gamma-ray irradiation device in KURNS. On the day 13, we irradiated the tumor on the thigh of mice at the dose of 20 Gy shielding the body and head with lead.

Measurement of tumor size and sampling of tumors and brains

After the irradiation, we measured the major and minor axes of the tumors until mice were sacrificed. We sacrificed three mice in each group on 2, 7, 14 days after irradiation. The brain and tumor were removed and fixed in 10 % buffered formalin for pathological samples.

Immunohistochemistry:

We prepared paraffin sections, and stained microglia or macrophages using a monoclonal Iba-1 antibody for 1st antibody. DAB staining was used for second antibody. We analyzed the numbers of Iba-1 positive cells in the hippocampus and cortex of the brain or in the tumor.

RESULTS:

Tumor size: Only in the combination group, tumor size was significantly reduced compared with the control at 14 days after irradiation.

Pathology: The number of microglia in hippocampus tended to increase in immunotherapy alone group at 2 days after irradiation. We still continue counting.

REFERENCES:

[1] Ngwa W. *et.al.,* Nat Rev Cancer.; **18(5)** (2018) 313-322. (doi)10.1038/nrc.2018.6.

CO6-10

Growth of transthyretin amyloid protofibrils monitored by AUC and SAXS

N. Yamamoto[1], K. Morishima[2], R. Inoue[2], E. Chatani[3], M. Sugiyama[2]

[1]*Schoole of Medicine, Jichi Medical University*
[2]*Institute for Integrated Radiation and Nuclear Science, Kyoto University*
[3]*Graduate School of Science, Kobe University*

INTRODUCTION: Transthyretin (TTR) is a blood protein required for transporting thyroxine and retinol to liver. TTR is composed of 127 amino-acid residues forming a homo tetramer in a physiological condition. TTR is known to form amyloid fibrils which are abnormal protein aggregates composed of β-sheet stacked structure along with the fibril axis. TTR amyloid fibrils accumulate in various kinds of organs such as heart. As a result, their functions are lost, which finally leads death of patients. Therefore, understanding the mechanism of the amyloid fibril formation of TTR is required to find ways for preventing the accumulation of the fibrils. Recently, we found that protofibrils appear prior to the emergence of the TTR amyloid fibrils in vitro, which finally convert to the amyloid fibril (unpublished data). In this study, we tracked the growth of the protofibrils using small-angle X-ray scattering (SAXS) and analytical ultra centrifuge (AUC).

EXPERIMENTS: Wild type TTR at the concentration of 100 μM in 10 mM HCl was incubated at 75 °C. AUC was performed at a few time points at 25 °C using XL-I (Beckman Coulter, Indiana). SAXS profiles were obtained using a SAXS equipment, NANOPIX (Rigaku, Japan) at the same time points as AUC at 25 °C.

RESULTS: Figure 1 shows the result of AUC. At 1 h, only one peak is observed at around 9.4 S. However, at 16 h another peak appeared around 28 S. This peak shifted larger as a function of time, which finally became around 50 S at 48 h. These results are consistent with our previous observation that the protofibrils become longer as a function of time.

The SAXS profiles are shown in Figure 2. Overall intensities decrease as a function of time. Whereas the intensity starts to get flat as q decreases at 1 h at the low-q region, the intensity continues to increase as q decreases at 24 h or 48 h. These results indicate that the decrease in the overall intensities as a function of time is due to the low-q shift of the SAXS profiles due to the formation of larger components. The interpretation is consistent with the results observed in AUC.

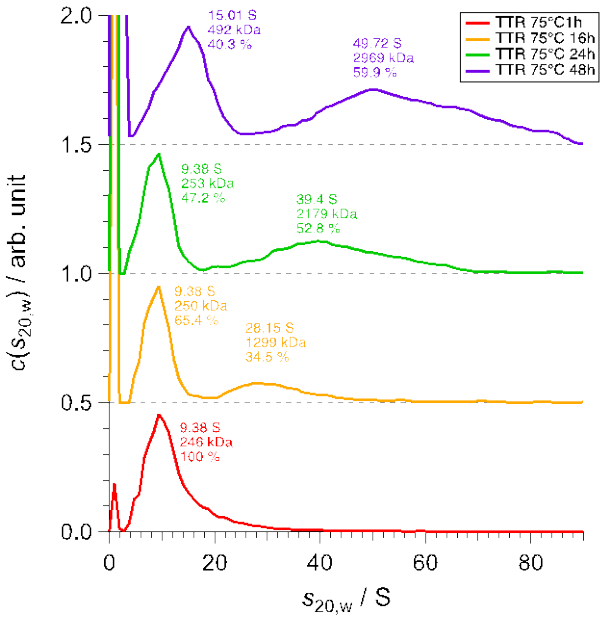

Figure 1 and 2. The AUC profiles (Figure 1; left) and SAXS profiles (Figure 2; bottom), respectively.

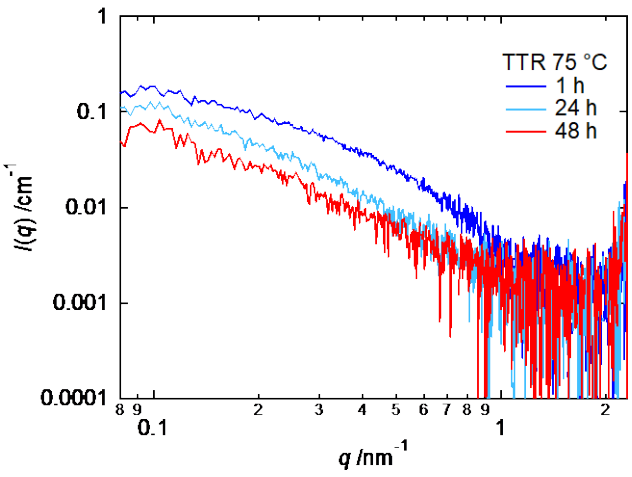

CO6-11

Evaluation of radiation resistance of lens constituent proteins involved in age-related cataract

T. Takata and K. Lampi[1]

Institute for Integrated Radiation and Nuclear Science, Kyoto University
[1] Oregon Health & Science University

INTRODUCTION: The transparency of the lens is maintained by the stable long-lived protein interactions, comprising three kinds of crystallin families. Those proteins are very stable, but are decreased their stability with age. A kind of intrinsic damages of lens tissues, such as heat damage, or extrinsic damages such as UV damage are increased with life time. Several researches suggested the amount of heat/UV damage on lens crystallins could be well described by the amount of modifications of amino acid residues [1]. When the crystallin species or partially model peptides are subjected to high intensity oxidative stress, site-specific oxidative modifications of amino acids accumulated [2]. This is analogous to the disease manifestations of sunlight-induced age-related cataracts. Due to the technical troubles, we lost the model peptides of lens crystallin after γ-rays irradiation before LC-MS analysis. Therefore, in order to observe irradiation effect for lens components, we performed γ-ray irradiation (50–5000 Gy) to recombinantly human βB2-crystallin oxidation mimic proteins (βB2 mimics) again, and evaluated solubilities for each protein.

EXPERIMENTS: Each of five tryptophan residue (Trp) in βB2-crystallin was replaced by phenylalanine residue (Phe) respectively by site-directed mutagenesis to make βB2 mimics (W59F, W82F, W85F, W151F and W196F). Each sample were prepared to 1 mg/mL in 50 mM phosphate buffer (pH 7.0) in 1.5 mL polypropylene tubes, and were irradiated with 0 (control), 50, 500, and 5000 Gy of γ-rays using a $_{60}$Co γ-ray source installed at the Institute for Integrated Radiation and Nuclear Science, Kyoto University. After γ-ray irradiation, each tube was centrifuged at 15,000 x g for 10 minutes at 4°C, and the protein concentration in the soluble fraction was measured using Bio-Rad's protein assay kit. The % of βB2 mimic is obtained from the formula on the right.

$$\text{[Protein] in soluble fraction [\%]} = \frac{\text{[Protein] after irradiation}}{\text{[Protein] at 0 Gy}} \times 100$$

RESULTS: A dose-dependent decreasing of the amount of βB2 mimics was observed in the γ-ray -irradiated βB2 mimics compared to the non-irradiated recombinantly human βB2-crystallin (Fig. 1). All samples showed a decreasing trend in the amount of crystallin in the soluble fraction as a function of irradiation dose. A slight decreasing the amount of soluble fraction after γ-irradiation was observed, however no significant difference could be obtained. Since some proteins were adhered to the inner wall of each tube on high dose experiments as white layer, we considered that those may cause huge error at each of dose and uncertain similarities at high dose. The irradiation may induce abnormal sticky protein state in solution.

Fig. 1. Aggregation tendency of βB2 mimics due to reduced oxidative stress tolerance

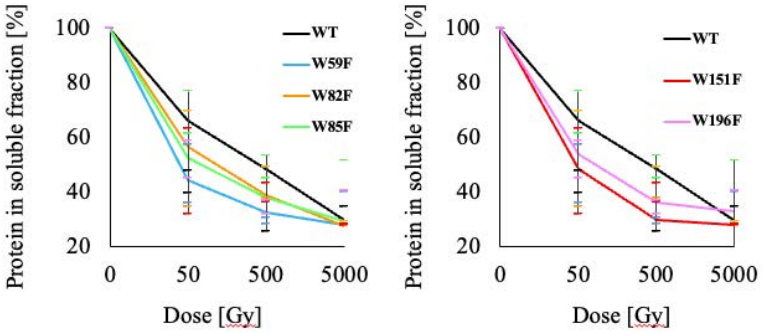

REFERENCES:

[1] B. Searle *et al.*, J Proteome Res., **4** (2005) 546-554.
[2] I. Kim *et al.*, Biochem Biophys Res Commun., **466** (2015) 622–628.

CO6-12

Solution strcuture of protein under high pressure as studied by small-angle scattering and molecular dynamics simulation

R. Inoue, N. Aizawa, M. Shimizu, K. Morishima and M. Sugiyama

Institute for Integrated Radiation and Nuclear Science, Kyoto University

INTRODUCTION: The free-energy landscape of protein is strongly perturbated by the application of high pressure, promoting the denaturation of protein. In fact, pressure denaturation has been experimentally reported for proteins with small molecular weight. However, it is also reported that special proteins from high-pressure environments (e.g., the deep sea) maintain their folded conformation even under high pressure and express their biological functions. Therefore, analysis of solution structure and dynamics of these proteins under high pressure is strongly expected to elucidate the structural stability mechanism of proteins under high pressure. Here, we especially focused on GSJ, an α-glucosidase derived from a deep-sea microorganism (Geobacillus sp. HTA-462). As shown in Fig.1, the crystal structure of GSJ has already been reported, however the solution structure of GSJ under high pressure has not yet been clarified. Therefore, we determined to elucidate the solution structure of GSJ under high pressure through the combination of small-angle scattering experiments and all-atom molecular dynamics (MD) simulations.

Fig. 1 Schematic view of structure of GSJ.

EXPERIMENTS: High pressure small-angle neutron scattering measurement was performed with SANS-U of the Institute for Solid State Physics, University of Tokyo, installed at JRR-3 (Tokai, Japan). Utilizing high pressure cell, solution structures of GSJ solution at 0.1 MPa and 100 MPa were studied. All-atom MD simulation under high pressure was performed by inserting water molecules inside the protein.

RESULTS: Figure 2 shows the scattering profiles of GSJ solution at 0.1 MPa and 100 MPa. It is clearly seen that the SANS profile at high pressure is significantly different from that at ambient pressure. To exhibit the structural perturbation by high pressure, we analyzed the radius of gyration (R_g) at two pressure conditions. At ambient pressure, it was calculated that R_g value was 25.3±2.8 Å. On the other hand, R_g value at 100 MPa was increased to 53.6±13.1 Å, meaning an experimental detection of denaturation at high pressure. In the case of living organism at deep sea, the concentration of osmolyte such as trimethyl amino-oxide is high compared to those at ambient pressure. Hence, the absence of osmolyte in GSJ solution is mainly concerned for the observation of denaturation at 100 MPa from the present SANS measurements. Figure 3 shows time dependence of R_g value calculated from all-atom MD simulation under high pressure. It was revealed that R_g value from the MD simulation reached to the R_g value from SANS measurements, supporting the possibility of reproduction of high pressure induced denaturation of protein from present MD simulation. Further calculation is still on progress to validate the present results from MD simulation.

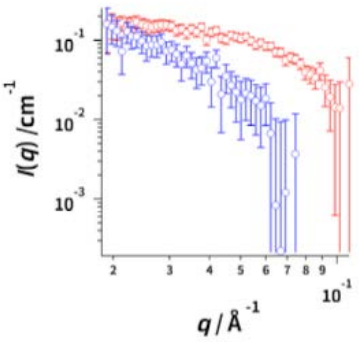

Fig. 2 SANS profiles of GSJ solution at 0.1 MPa (red circle) and 100 MPa (blue circle).

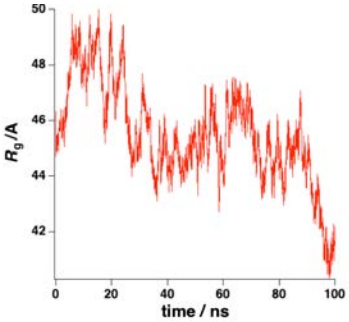

Fig. 3 Time course of from all-atom MD simulation.

CO6-13

Solution structure of proteasome α7 double ring

K. Kato[1,2,3], M. Yagi-Utsumi[1,2,3], S. Yanaka[1,2,3], H. Yagi[1,2], T. Satoh[1], Y. Yunoki[4], K. Morishima[4], R. Inoue[4] and M. Sugiyama[4]

[1]*Graduate School of Pharmaceutical Sciences, Nagoya City University*
[2]*Exploratory Research Center on Life and Living Systems (ExCELLS), National Institutes of Natural Sciences*
[3]*Institute for Molecular Science, National Institutes of Natural Sciences*
[4]*Institute for Integrated Radiation and Nuclear Science, Kyoto University*

INTRODUCTION:

Proteasomes are large protein complexes involved in cellular proteolysis and are widely distributed across the three domains of life. The 20S proteasome is the core complex of the eukaryotic proteasome composed of layered α and β heptameric rings. The α and β heptameric rings are composed of seven different homologous subunits each, α1–α7 and β1–β7. Interestingly, the α7 subunit forms a homotetradecamer consisting of two layers of α7 heptameric rings (α7 double ring) [1,2]. The structure of the α7 double ring in solution has not been fully revealed. In this study, we investigated its solution structure with small-angle X-ray scattering (SAXS).

EXPERIMENTS:

The human proteasome α7 subunit was expressed and purified as described previously [1, 2]. The sample was dissolved in a buffer containing 20 mM Tris-HCl (pH 8.0) and 150 mM NaCl. SAXS measurement was carried out with NANOPIX (Rigaku) installed in KURNS at 25 ºC. The *q*-range (magnitude of the scattering vector) covered was from 0.010 Å-1 to 0.70 Å-1, using two sample-to-detector distances (SDD) of 1333 and 295 mm. To remove the effect of non-specific aggregates on the SAXS profile, we applied the integrated reduction method utilizing analytical ultracentrifugation (AUC) and SAXS, namely AUC-SAXS [3,4]. AUC measurement was conducted with ProteomeLab XL-I (Beckman Coulter) at the rotation speed of 60,000 rpm at 25 ºC.

RESULTS:

Figure 1 displays the SAXS profile of the proteasome α7 double ring. The candidate structure obtained from Cryo-EM (model 1) did not completely match the experimental SAXS profile. Thus, we performed the normal mode analysis (NMA) using model 1 as the initial structure to search appropriate structural model in solution. As a result, we found that a structure in which the α7 ring (model 2) was significantly deformed compared to model 1 reproduced the SAXS profile.

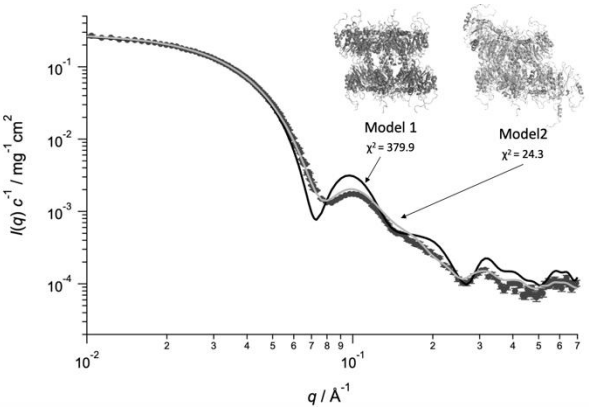

Fig. 1. Black circles represent SAXS profile of the proteasome α7 double ring. Solid black and gray lines show the scattering curves calculated from model 1 and 2, respectively.

REFERENCES:

[1] M. Sugiyama *et al.*, Biophys. J., **101** (2011) 2037-2042.
[2] C. Song *et al*., Int. J. Mol. Sci., **22** (2021) 4519.
[3] K. Morishima *et al.,* Commun. Biol., **3** (2020) 294.
[4] K. Morishima *et al.,* J. Appl. Crystallogr., **56** (2023) 624.

CO6-14

SAXS study on the interaction manner between the α-crystallin domain of αB-crystallin and insulin B-chain protofibrils

Y. Kokuo, K. Yuzu, N. Yamamoto[1], K. Morishima[2], A. Okuda[2], R. Inoue[2], M. Sugiyama[2], J. Hayashi[3], J. A. Carver[3], E. Chatani

Graduate School of Science, Kobe University
1Graduate School of Medicine, Jichi Medical University
2Institute for Integrated Radiation and Nuclear Science, Kyoto University
3Research School of Chemistry, The Australian National University

INTRODUCTION: Amyloid fibrils are protein aggregates involved in amyloidoses and neurodegenerative diseases. A cellular strategy for preventing the formation of amyloid fibrils is the expression of small heat shock proteins (sHsps), of which αB-crystallin (αB-C) is a representative member in mammals. Our previous measurements have shown that the α-crystallin domain (ACD) of αB-C inhibits the growth of insulin B-chain protofibrils strongly [1]. In this study, to gain insights into the binding manner of the ACD with B-chain protofibrils, a small-angle X-ray scattering (SAXS) measurement was performed in combination with analytical ultracentrifugation (AUC).

EXPERIMENTS: Insulin B-chain was dissolved at a final concentration of 400 μM in 50 mM Tris-HCl buffer (pH8.7) and incubated at 25 °C to form protofibrils. After the ACD was mixed with the protofibrils in a molar ratio of B-chain:ACD = 1:0.1, the samples were then subjected to SAXS measurements to investigate changes in size and shape of protofibrils in the presence of the ACD. A SAXS profile was collected at 25 °C and 30-minute exposure with a NANOPIX equipped with a HyPix-6000 (Rigaku Corpo-ration, Japan). A Cu K-α line (MicroMAX-007HFMR) was used as a beam source, which was further focused and collimated with a confocal multilayer mirror (OptiSAXS). The camera length was set to 1.33 nm.

RESULTS: As shown in Fig. 1A, the slope of the log-log plot was close to −1, suggesting that protofibrils keep a rod-like morphology even after the ACD binding. When a cross-section plot was constructed, the slope of this plot did not show any significant change as shown in Fig. 1B. This is contrastive to the result of full-length αB-C, in which the complex become thicker after the binding to protofibrils [2]. Although the length was difficult to be estimated from the SAXS profile because of limited *q* range, it has been suggested that the αB-C ACD tends to bind to the protofibril edges rather than the side, preventing further protofibril growth. It is likely that the remaining domains, i.e., the N- and C-terminal domains, mediate lateral binding to the protofibril, and which may not be important for inhibition of protofibril growth.

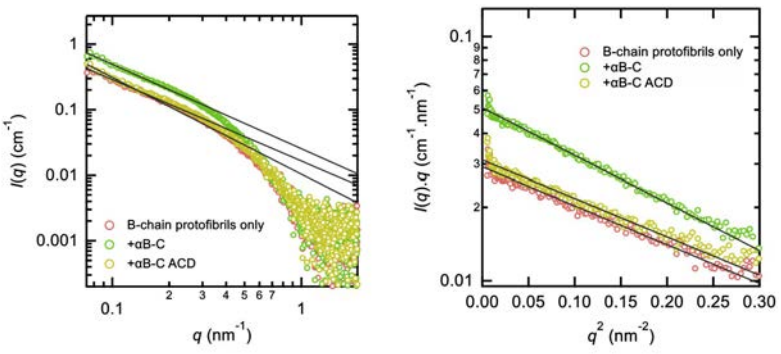

Fig. 1. (A) SAXS profiles and (B) their cross-section plots of the insulin B-chain-αB-C ACD complex. The profiles of B-chain alone and B-chain-αB-C complex are also shown for references. The fraction of unreacted αB-C ACD or αB-C estimated from the AUC analysis was subtracted from the SAXS profile to obtain the profiles of the complex selectively.

REFERENCES:

[1] Y. Kokuo, Master Thesis, Kobe Univ. (2023).
[2] Y. Kokuo, KURNS Progress Report 2022, (2023) CO6-9.

CO6-15

Development of Boron Cluster-Loaded Nanoparticles for BNCT

A.B. Fithroni[1], M. Ishimoto[2], K. Watanabe, H[1]. Inoue, S[1]. Zhou, T.F.N. Hakim[1], M. Suzuki[3], T. Ohtsuki[1], and E. Matsuura[1]

[1]*Department of Interdisciplinary Science and Engineering in Health Systems, Okayama University*
[2]*J-BEAM, Inc.*
[3]*Institute for Integrated Radiation and Nuclear Science, Kyoto University*

INTRODUCTION: Boron neutron capture therapy (BNCT) is a non-invasive nuclear therapeutic modality that induces apoptosis in cancer cells, without any harmful effects in neighboring normal cells. To overcome the issues of limited application in clinically approved boron compounds, such as BPA and BSH, we developed self-forming nanoparticles consisting biodegradable polymer, namely, "Lactosome micelles" with a hydrophobic boron cluster [1]. In the previous study, we were able to develop a stable Lactosome micelles highly loaded with a hydrophobic boron cluster that may be applicable for BNCT [2]. Currently, we evaluated the efficacy of *in vitro* and *in vivo* neutron irradiation to the AsPC-1 cells (human pancreatic cancer cells) or those derived tumors in xeno-grafts which were treated with a boron cluster-loaded Lactosome micelles.

EXPERIMENTS: For *in vitro* study, we irradiated AsPC-1 cells were subjected with reactor power of 1 MW for 40 min after incubation with a boron cluster-loaded Lactosome micelles for 2 h. After the neutron irradiation, colony formation assay was performed by culturing in 12-well plates and incubated under 5% CO_2 at 37 °C for 14 days. For *in vivo* study, the AsPC-1 cells-bearing ice were intravenously (*i.v.*) injected with a boron-cluster loaded Lactosome micelles, and then, the neutron irradiation was performed with nuclear power of 5 MW for 40 min. Data were represented as mean ± S.E.M. Significant differences were represented by $^{**}p < 0.01$ and $^{*}p < 0.05$.

RESULTS: In *in vitro* irradiation study, the results obviously indicated that boron cluster-loaded Lactosome micelles showed significant inhibitory effect in the colony formation of the AsPC-1 cells (Table 1). *In vivo* irradiation study also showed that a group *i.v.* injected with boron cluster-loaded Lactosome micelles by irradiating with neutron significantly suppressed the tumor growth on day 24 after irradiation, as compared to cold control and hot control (Table 2). Overall, *in vitro* and *in vivo* neutron irradiation study showed that our novel development of boron cluster-loaded Lactosome micelles are promising candidates (drug) for BNCT.

Table 1. *In vitro* inhibitory effect by neutron irradiation on AsPC-1 cells' growth under the treatment with boron cluster-loaded Lactosome micelles.

Group	Colony formation rate	
	0 min	40 min
Control (DPBS)	1	0.73 ± 0.41
Lactosome micelles	1	0.53 ± 0.16
-loaded with boron cluster A	1	0.03 ± 0.01**
-loaded with boron cluster B	1	0.05 ± 0.00**

Table 2. *In vivo* inhibitory effect by neutron irradiation on AsPC-1 cell-derived tumors' growth under the treatment with boron cluster-loaded Lactosome micelles.

Group	Percent of tumor growth on days 24
Control (cold)	315.7 ± 89.4
Control (hot)	195.0 ± 39.3
Lactosome micelles	
- loaded with boron cluster A	62.9 ± 17.6**
- loaded with boron cluster B	12.0 ± 19.7**

RFERENCES:

[1] E. Hara *et al.*, Biochim Biophys Acta., **1830** (2013) 4046–4052.
[2] Fithroni, A.B. *et al.,* Cells, **11** (2022), 3307.

CO6-16

Asp racemization/isomerization in shedding products of cell adhesion molecule 1 is potentially involved in the neurodegeneration induced by elevated pressure

A. Yoneshige[1], A. Ito[1] and T. Takata[2]

[1]*Department of Pathology, Kindai University*
[2]*Institute for Integrated Radiation and Nuclear Science, Kyoto University*

INTRODUCTION: The elevation of internal pressure is often involved in neurodegeneration; intraocular and intraventricular pressure elevations over 20–30 cmH2O cause glaucoma and hydrocephalus, respectively. Previously, to investigate the mechanisms by which elevation of intraluminal pressure causes cell or tissue de-generation, we devised a novel two-chamber culture system that enabled us to subject cultured cells to low levels of water pressure (2-50 cmH2O pressure load) [1,2]. We found that mouse primary neurons degenerated when the water pressure was above 30 cmH2O, and that ectodomain shedding of synaptic cell adhesion molecule 1 (CADM1) increased in a water pressure-dependent manner [1]. We also discovered that the increase of intracellular product of CADM1 shedding (C-terminal fragment, CADM1-CTF) resulted in decreased neurite density with punctate localization of CADM1 suggesting its aggregation in neurites [1]. CADM1-CTF is rich in Asp residues neighbored by Ala residues, and the conversion of these amino acids to poly-Gly diminished its aggregation state. Since the racemization and isomerization of Asp residues contributes to aggregation of various proteins and it likely occurred when the neighboring residues are small [3,4], these in-sights led us to hypothesize an involvement of Asp racemization/isomerization in the neurodegeneration induced by internal pressure elevation.
EXPERIMENTS: (1) Synthetic peptide of internal sequence of CADM1-CTF (GADDAADADTAIINAEGGQNNSEEK) was incubated at 50℃ for 0-15 days and applied to LC-MS to identify Asp isomer-containing peptides. (2) Mouse neuroblastoma cell line Neuro-2a cells with exogenously expressed CADM1-CTF were cultured un-der 50 cmH2O and were prepared for LC-MS analysis. (3) To mimic oxidative stress induced by internal pressure elevation, Neuro-2a cells expressing CADM1-CTF were treated with hydrogen peroxide and the cells were subjected to the isolation of CADM1-CTF by immuno-precipitation (IP). The amounts and purity of CADM1-CTF-IP were quantified using immunoblotting and silver staining.
RESULTS: (1) In LC-MS analysis of CADM1-CTF synthetic pep-tide, multiple peaks were detected after 1 day at pH 6.0 or pH 7.0 indicating that Asp racemization/isomerization could occurred under neutral pH. (2) CADM1-CTF proteins in Neuro-2a cells were solubilized with water, Triton X-100 containing buffer, or SDS containing buffer after 3 days culture under 50 cmH2O, and CADM1 immunoblot was carried out. CADM1-CTF protein yields (CADM1-CTF / total proteins) were in the order Triton X-100 > SDS > water, however, the peptide peak was not identified using with LC-MS. (3) Previously, we found that CADM1 shedding was increased by oxidative stress as a cause of pulmonary emphysema in cigarette smoke exposure [5]. We furthermore showed that Lipocalin-2, an iron binding protein was upregulated in the retinae under 50 cmH2O pressure [6]. Since iron dysregulation induces oxidative stress, we decided to explore the linkage between oxidative stress and Asp racemization/isomerization of CADM1-CTF. We successfully obtained a huge amount of partial purified CADM1-CTF from large-scale Neuro-2a cell culture, coupled with IP purification. Future experiments are planned for identification of Asp isomer by LC-MS.
REFERENCES: [1] A. Yoneshige *et al.,* Mol. Neurobiol., **54** (2017) 6378-6390. [2] M. Hagiyama *et al.,* Front. Physiol., **8** (2017) 997. [3] N. Fujii *et al.,* J. Biochem., **116** (1994) 663-669. [4] T. Takata *et al.,* Protein Sci., **29** (2020) 955-965. [5] A. Ri *et al.,* Front. Cell Dev. Biol., **6** (2018) 52. [6] A. Yoneshige *et al.,* Front. Cell Dev. Biol., **9** (2021) 664327.

CO6-17

The regulation of the cyanobacterial circadian rhythm by KaiC hexamers capable of assuming diverse phosphorylation states

Y. Yunoki[1], K. Morishima[2], N. Sato[2], R. Inoue[2], A. Okuda[2], R. Urade[2], M. Sugiyama[2]
[1]*Center for iPS Cell Research and Application, Kyoto University*
[2]*Institute for Integrated Radiation and Nuclear Science, Kyoto University*

INTRODUCTION: The circadian rhythm is controlled by clock proteins. In cyanobacteria, the clock operates through interactions among KaiA, KaiB, and KaiC, resulting in a cyclic oscillation of KaiC phosphorylation facilitated by ATP. KaiC forms a homohexamer and exhibits ATPase activity during autophosphorylation and dephosphorylation processes. Despite the potential for up to 700 phosphorylation states within the KaiC hexamer due to the presence of two phosphorylation sites per subunit, previous studies have only showed the average phosphorylation state of the KaiC hexamer. To address the oscillation mechanism, we have developed native mass spectrometry to simultaneously analyze the phosphorylation states within the KaiC hexamer and the interactions between Kai proteins, such as the KaiB-KaiC interaction.
****

EXPERIMENTS: nMS measurements were conducted using a microTOF II ESI mass spectrometer (Bruker) at room temperature, employing the microTOF II software. KaiB and KaiC proteins derived from thermophilic cyanobacteria, T. elongatus BP-1, were produced in Escherichia coli and purified through anion-exchange chromatography and size-exclusion chromatography. To manipulate the phosphorylation state within the KaiC hexamer, two KaiC mutants, $KaiC_{AA}$ and $KaiC_{DD}$ (where Ser431 and Thr432 were substituted with aspartate and alanine residues, respectively), were employed to mimic the dephosphorylated and phosphorylated states of KaiC, respectively. To create a heterogeneous phosphorylation state group within the KaiC hexamers, prior to ATP addition, we combined unlabeled $KaiC_{AA}$ mutant and ^{13}C-labeled $KaiC_{DD}$ subunit. This strategy enabled the generation of seven different types of KaiC hexamers with distinct phosphorylation states.
****

RESULTS: We successfully generated a heterogeneous phosphorylation state group within the KaiC hexamer (Fig. 1). Then, we decided to elucidate the KaiB-KaiC interaction.
Our findings, shown in Fig. 1, demonstrate that the KaiB-KaiC interaction is determined by the proportion of KaiCDD subunits within the KaiC hexamer. The KaiB-KaiC complex facilitates the dephosphorylation of KaiC. Based on our observations, it is hypothesized that KaiC promotes its own dephosphorylation by binding to KaiB when it becomes hyperphosphorylated.
We propose that KaiC modulates the KaiB-KaiC interaction through alterations in the phosphorylation state of the KaiC hexamer. We anticipate that these findings will enhance our understanding of the oscillation mechanism involving the dissociation and assembly of Kai proteins.

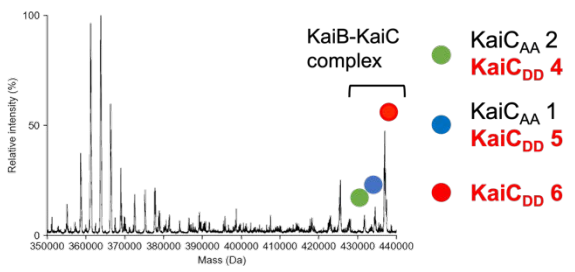

Fig. 1. KaiB-KaiC interaction is regulated by the KaiC hexamer phosphorylation state.

The native mass spectra depict a heterogeneous phosphorylation state within the KaiC hexamer in the presence of KaiB. The circles represent the KaiB-KaiC complex, with green, black, and red circles indicating KaiC hexamers comprised of different ratios of $KaiC_{AA}$ and $KaiC_{DD}$ subunits, specifically 2:4, 1:5, and 0:6, respectively.

****

CO6-18

Analysis of flexible structure of flexible multi-domain protein

T. Oda, R. Inoue[1], K. Morishima[1], A. Okuda[1], M. Sugiyama[1]

J-PARC Center, Japan Atomic Energy Agency.
[1]Institute for Integrated Radiation and Nuclear Science, Kyoto University.

INTRODUCTION: Proteins that are composed of multiple domains and intrinsically disordered regions (IDRs) are flexible and perform various biological functions. Their flexible nature makes it difficult to analyze their structures by crystallography or cryo-electron microscopy. In this study, we focused on a DNA repair protein Hef from hyperthermophilic archaeon as a flexible muti-domain protein and attempt to determine the flexible structure as an ensemble using SAXS and SANS. Hef consists of an N-terminal helicase domain, a C-terminal nuclease domain, and an IDR connecting the two domains [1,2]. From SAXS analysis using only the IDR, we found that IDR becomes more compact at high temperatures (323K ~ 363K) than at room temperature. Considering the physiological temperature of hyperthermophilic archaeon, we speculate that this compaction is related to the function of Hef. Therefore, we attempted to analyze structure of full-length Hef at high temperature (353K). Since the entire molecule contributes to scattering in SAXS, it is difficult to determine the ensemble structure of a multi-domain protein based solely on the SAXS profile. Therefore, to obtain another experimental constraint, we prepared a full-length Hef protein with 75% deuteration in only the helicase or the nuclease domain (segmentally deuterated samples, Fig.1(a)) and measured SANS. Note, in 100% D_2O, the 75% deuterated domain is matched out, and only scattering of the non-deuterated region can be observed. Therefore, it is expected that the ensemble structure can be determined correctly by combining it with the SAXS profile.

EXPERIMENTS: The segmentally deuterated samples were prepared by ligation the 75% deuterated domain and the non-deuterated region using a protein ligation enzyme. Since Hef tends to aggregate, we performed size exclusion chromatography to remove aggregates and performed SANS measurements using a dilute sample (0.6 mg/ml). The SANS measurements were performed with SANS-U installed at JRR-3. To check for the presence of aggregates, the sample solution after SANS measurement were analyzed by analytical ultracentrifugation (AUC).

RESULTS: The SANS profiles of the segmentally deuterated samples at 353K are shown in Fig. 1(b). The SANS profiles did not show any sharp rise at the low angle. Thus, at first glance it appears that there are no aggregates in the samples. However, the AUC analysis of the sample after SANS measurement, indicated the presence of aggregates and degradant (Fig. 1(c)). In this experiment, we performed long exposure time (totally 16 and 24 hours for each sample) to obtain data with sufficient statistical accuracy from extremely dilute samples. Therefore, it is possible that aggregates and degradant were generated during long-time experiments. It will be necessary to consider experimental conditions that prevent aggregation and degradation.

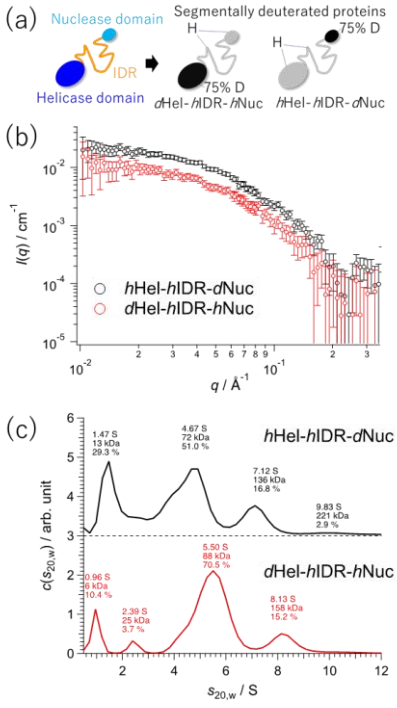

Fig 1. Schematic view of segmentally deuterated proteins (a) and its profiles of SANS (b) and AUC (c).

REFERENCES: [1] R. Fujikane *et al.,* Genes Genet. Syst., 85 (2010) 243.
[2] S. Ishino *et al.,* J. Biol. Chem., 289 (2014) 21627.

CO6-19

Character of DNA damage induced by nuclear plant neutron beams

H. Terato, T. Hanafusa[1], M. Isobe, Y. Sakurai[2], H. Tanaka[2], and T. Saito[2]

Advanced Science Research Center, Okayama University
[1]Neutron Therapy Research Center, Okayama University
[2]Institute for Integrated Radiation and Nuclear Science, Kyoto University

INTRODUCTION: The results of many previous radiation studies suggest that DNA is the primary target of radiobiological effects and that DNA damage is a major contributor to them. We have studied radiation-induced DNA damage. We have dealt not only with gamma- and X-rays, but also with heavy ion beams such as carbon ions, and have investigated whether DNA damage shows a specificity for the kind of radiation [1, 2]. In this research project, we have studied the characteristics of DNA damage caused by neutron radiation (see last year's report). This has been observed for DNA damage directly caused by neutrons, and from this year the characteristics of DNA damage species in BNCT (Boron Neutron Capture Therapy) will also be examined, because BNCT has had a predominant clinical application and much remains unknown about the molecular mechanisms of their cell death, i.e. the DNA damage modality. We here analyze the DNA damage caused by BNCT in cultured cells, in line with previous research methods.

EXPERIMENTS: Cultured cells of Chinese hamster ovary (CHO) strains with various DNA repair backgrounds were irradiated with neutron beams in the Kyoto University Reactor (KUR). The cells were cultivated with the conventional method. The logarithmic growing cells were recovered by trypsinization and the cells were mixed in BPA (L-4-Boronophenylalanine, Interpharma Praha, a. s, Czech) or BSH (Sodium mercaptododecaborate, Katchem spol. s. r. o., Czech) solution. The concentration of these chemicals was 25 μg mL^{-1} [3]. The mixture were set into polypropylene tubes for irradiation. The estimated dose rate of the neutron was 1 Gy h^{-1}. The irradiation periods were 0, 30, 60, 90, 120, 150 min. The irradiated cells were divided into two groups, one for viability and the other for DNA damage analysis by the same methods reported previously [4].

RESULTS: In this study, a slight decrease in survival and a slight increase in DNA damage were observed in the BPA- and BSH-treated groups compared to the untreated (control) group. DNA damage is viewed here as DNA double-strand breaks. This reduction in survival was not as dramatic as observed with usual BNCT treatment. This suggests that the BNCT drug treatment was inadequate in this study. The concentrations administered to the cells were each based on those previously reported [3], but the treatment time may have been too short. In the future study, we elongate the treatment time with BNCT drugs to increase the intracellular concentration by treating the cells from the time of cell culture.

REFERENCES:

[1] H. Terato *et al*., J. Radiat. Res., **49** (2008) 133-146.
[2] Y. Tokuyama *et al*., J. Radiat. Res., **56** (2015) 446-455.
[3] Y. Kinashi *et al*., Radiat. Oncol., **6** (2011) 106.
[4] H. Terato *et al*., KURNS Progress report 2022, (2023) 158.

CO6-20

Solution scattering study of of biomacromolecules depending on external environment

M. Shimizu, K. Morishima, R. Inoue, M. Sugiyama

Institute for Integrated Radiation and Nuclear Science, Kyoto University

INTRODUCTION: Most protein have unique tertiary structure depending on their amino-acid sequence. The tertiary structures are realized by various kinds of intra-molecule interactions, such as hydrogen bonding, salt bridge, etc. In addition, interaction between protein and surrounding water molecules are another important determinant of protein structures. Therefore, measuring dynamics of water molecules and other small molecules in the vicinity of protein surface is important for understanding protein structures. However, while computational modeling was reported [1], experimental methods to study the surrounding small molecules have not yet been established. We thought that a comparison of protein solution series with different osmolyte concentration would realize experimental analysis of the solvation environment, since osmolytes would change solvation state rather than tertiary structure of proteins.

EXPERIMENTS: We prepared three bovine serum albumin (BSA) solutions, which contain 0.1 M, 0.5 M, or 1.0 M betaine (FUJIFILM Wako Chemicals), respectively. The samples were prepared by dialyzing BSA standard (Thermo Fisher Scientific Inc.). Small-angle X-ray scattering was conducted for the aqueous solution of the BSA protein with the various concentration of betaine, using a NANOPIX (RIGAKU, Tokyo, Japan). Then radius of gyration was calculated from Guinier plot of the profiles. Analytical ultracentrifugation was also performed for the BSA samples by a ProteomeLab XL-I analytical-ultracentrifuge (Beckman Coulter). SAngler and SEDFIT were used for analysis [2, 3].

RESULTS: Guinier plots of the BSA solution are shown in Fig. 1. The radius of gyration for BSA solution with 0.1 M betaine, 0.5 M betaine, and 1.0 M betaine were, 28.8±0.2 Å, 28.9±0.2 Å, and 29.3±0.2 Å, respectively. Basically, the scattering profiles were similar each other. Nevertheless, a slight difference was observed between the radius of gyration of BSA solution with 0.1M betaine and that with 1.0M betaine. To examine whether the difference is assigned to difference in solvation state, oligomerization status of the BSA was investigated by analytical ultracentrifugation. As a result, the fraction of monomeric BSA was 98.9%, 96.7%, and 94.7% for the solution containing 0.1 M betaine, 0.5 M betaine, and 1.0 M betaine, respectively. The results suggest that the difference in the radius of gyration is mainly caused by difference in contents of oligomeric BSA. In conclusion, these experiments demonstrate that it is difficult to solvation state of biomolecules only from small-angle X-ray scattering because a series sample that differs only in the solvation cannot be prepared.

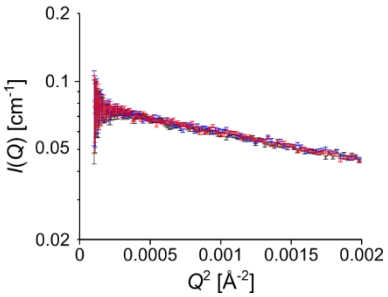

Figure 1. Guinier plots of BSA proteins for various betaine concentrations. The profile at 0.1 M betaine is shown by black open circle, that at 0.5 M betaine is shown by blue open square, and that at 1.0 M betaine is shown by red open triangle, respectively. The error bars show standard deviations.

REFERENCES:

[1] D. Nerukh, *et al.,* J. Phys. Chem. Lett. **3** (2012) 3663–3664.
[2] N. Shimizu, *et al.*, AIP conf. Proc., **1741** (2016).
[3] P. Schuck, Biophys. J., **78** (2000)1606-1619.

CO6-21

Neutron activation of gold nanoparticles for future theranostics

A. Toyoshima, N. Koshikawa[1], Y. Kadonaga, Y. Kikuchi[1], K. Tokoi[2], H. Kato, K. S. Tanaka[1], and J. Kataoka[1]

Institute for Radiation Sciences, Osaka University
[1]Graduate School of Advanced Science and Engineering, Waseda University
[2]Graduate School of Science, Osaka University

INTRODUCTION: Gold nanoparticles (AuNPs) are promising drug carriers, and its visualization is essential because various factors, such as their size and shape, can change its biodistribution. However, methods to visualize AuNP directly and with high sensitivity has not yet been established. Therefore, we propose activation imaging of AuNP[1]. When gold nanoparticles are irradiated with neutrons, stable ^{197}Au becomes radioactive ^{198}Au (half-life: 2.7 days), which predominantly emits 412-keV gamma rays that allows imaging. In this study, neutron-activated AuNP, [^{198}Au]AuNP, was synthesized, injected to the tumor-bearing mice, and visualized by wide-band X-rays/gamma-ray imager, hybrid Compton camera (HCC)[2]. Moreover, we labeled the alpha-emitting therapeutic drug, ^{211}At, on the [^{198}Au]AuNP and demonstrated in-vivo imaging.

EXPERIMENTS: We first synthesized [^{198}Au]AuNP with [^{198}Au]$HAuCl_4$ and $NaBH_4$ as a reductant. After purification of [^{198}Au]$HAuCl_4$ by ultrafiltration, surface-modification of [^{198}Au]$HAuCl_4$ was performed with mPEG(5k)-SH. Synthesized [^{198}Au]AuNP-S-mPEG(5k) was finally purified by ultrafiltration. We injected 0.3 MBq of [^{198}Au]AuNP to the mice intratumorally and visualized with HCC. Moreover, [^{198}Au]AuNP-S-mPEG(5k) was quantitatively astatinated. We injected [^{211}At/^{198}Au]AuNP-S-mPEG(5k), which is 0.2 MBq as ^{198}Au and 0.7 MBq as ^{211}At, intravenously to the mice. Subsequently, imaging was performed with HCC.

RESULTS: As shown in Fig. 1, [^{198}Au]AuNP in the tumor of the mouse was clearly visualized 9 minutes and 4 days after the injection. Spread of the accumulation observed in the image obtained 4 days after the injection may indicate the migration of the AuNP from the tumor to other organs. Fig. 2 shows the images of the mice injected with [^{211}At/^{198}Au]AuNP. (a-1) and (a-2) are the distribution of ^{211}At obtained using 79-keV X-rays 9 minutes and 2 days after the injection, and (b-1) and (b-2) are the distribution of ^{198}Au obtained using 412-keV gamma rays 9 minutes and 2 days after the injection. Simultaneous imaging of ^{211}At and ^{198}Au was demonstrated by the images (a-1) and (a-2). Moreover, 2.7-days half-life of ^{198}Au allowed the long-term visualization of drugs even after visualization of ^{211}At became impossible 2 days after the injection because of its short half-life (7.2 hours).

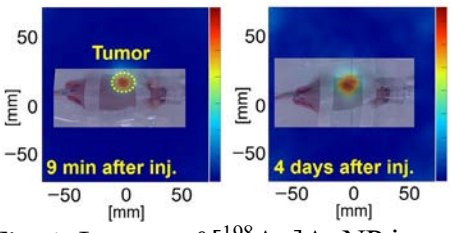

Fig. 1. Images of [^{198}Au]AuNP intratumorally injected to the mouse.

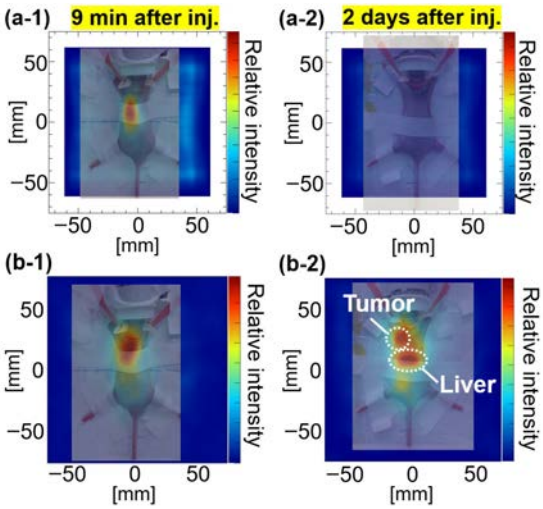

Fig. 2. Images of [^{211}At/^{198}Au]AuNP intravenously injected to the mouse. ^{211}At (a-1) and ^{198}Au (b-1) 9 min after injection, ^{211}At (a-2) and ^{198}Au (b-2) 2 days after injection.

REFERENCES:

[1] N. Koshikawa *et al.*, Nucl. Instr. and Meth., A, **1045** (2023) 167599.
[2] A. Omata *et al.*, Sci. Reports, **10** (2020) 14604.

CO6-22

Structural study of water-soluble vitamin K_2 from *Bacillus subtilis natto*

T. Chatake, A. Okoda, K. Morishima, R. Inoue, M. Sugiyama, T. Takata, Y. Yanagisawa[1]

Institute for Integrated Radiation and Nuclear Science, Kyoto University
[1]Faculty of Pharmacy, Chiba Institute of Sciences

INTRODUCTION: Natto is one of the popular traditional Japanese foods made from soybeans fermented by *Bacillus subtilis natto* (BSN). BSN produce several kinds of bioactive substances, vitamin K_2 [1], nattokinase [2], dipicolinic acid, and so on. Interestingly, BSN produce a water-soluble complex of menquinone-7, which is a kind of vitamin K_2, and peptides [3]. In our previous studies, the water-soluble complex (hereafter called *natto*-MK-7) was highly purified from the liquid medium of BSN, and its size was estimated by dynamic light scattering [4]. In addition, peptides in *natto*-MK-7, called K-binding factor (KBF), were investigated by MALDI-TOF mass spectrometry (MALDI-TOF MS) and amino acid analysis [5]. Recently, KBF was extracted and purified by HPLC. The latest results are presented here.

EXPERIMENTS: *Natto*-MK-7 was extracted from the liquid culture medium of BSN and purified by fast protein liquid chromatography [4]. KBF was isolated from *natto*-MK-7 by *reversed-phase high performance liquid chromatography* (RP-HPLC). This liquid chromatography was performed by isocratic elution with 0.1% TFA in acetonitrile using a C18 column. Two peaks were collected, and the molar mass of peak containing each peptide was confirmed by MALDI-TOF MS.

RESULTS: Two peaks were observed at 41.8 and 43.2 min in RP-HPLC of *natto*-MK-7, as shown in Fig. 1. The two peaks correspond to KBF in *natto*-MK-7. Fig. 2 shows the MALDI-TOF MS spectrum of *natto*-MK-7 before RP-HPLC, and 41.8 min and 43.2 min fractions of RP-HPLC. They show significant peaks between m/z = 1,020 ~ 1,100, indicating the molecular weight of KBF. MALDI-TOF MS and amino acid analysis of *natto*-MK-7 suggested that KBF were the various combinations of nine amino acids, including Asx, Glx, Val, Leu, and Met (Asx: Asp or Asn, Glx: Glu or Gln). The 41.8 min and 43.2 min fractions had the different combinations of peaks at m/z = (1030.4, 1062.6, 1066.4, 1076.4 and 1080.4) and (1044.4, 1058.5, 1062.6 and 1076.4), respectively. In conclusion, the present RP-HPLC could isolate and separate the KBF into two groups.

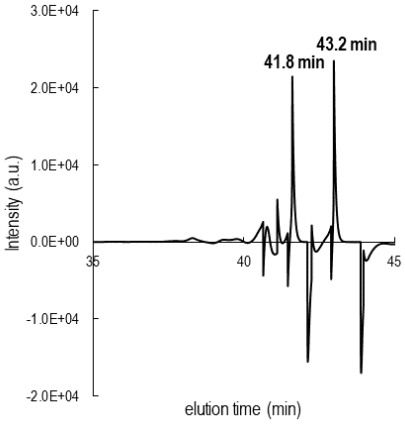

Fig. 1. The chromatography charts of RP-HPLC of *natto*-MK-7.

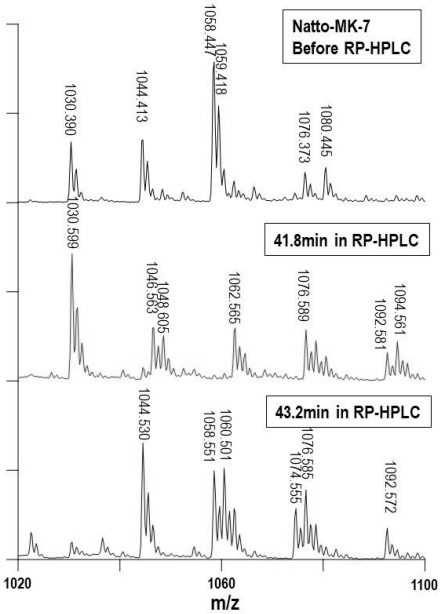

Fig. 2. The MALDI-TOF MS spectrum of *natto*-MK-7, KBFs (41.8 and 43.2 min).

REFERENCES:

[1] L. Wen *et al.*, Mol. Med. Rep., **18**, (1999) 3-15.
[2] (a) H. Sumi *et al.*, Experientia, **43** (1987) 1110-1111. (b) Y Yanagisawa *et al.*, J. Synchrotron Rad., **20** (2013) 875–879.
[3] H. Ikeda, Y. Doi, Eur. J. Biochem., **192**, (1990) 219-224.
[4] T. Chatake *et al.*, J. Food Biochem., (2018) e12630.
[5] T. Chatake *et al.*, J. Biochem., **174** (2023) 383-389.

CO6-23

Distribution analysis of the chemical modification of the amino acid residues in mice lens structural proteins during age-related cataract

S. Matsushita[1], A. Nakamura[1], Y. Suzuki[1] and T. Takata[2]

[1] *Dept of Materials and Applied Chemistry, Nihon University*
[2] *Institute for Integrated Radiation and Nuclear Science, Kyoto University*

INTRODUCTION: Age-related cataracts are the leading causes of blindness in world. Several risk factors, contributing to the development of cataracts, have been reported. Above all, abnormal lens protein aggregation and insolubilization has been believed as the main process. Alteration of lens protein structure, caused by covalently post-translational modifications, are thought to be critical for maintaining lens protein homeostasis [1]. We have shown that covalent modifications of amino acid residues as a scale for a lens aging. To do this, mass spectrometry is an efficient tool to quantitative analysis, however the distributions of modifications were very obscured. Therefore, we are to address revealing the distribution of modifications (isomerization of Asp) in the lens section using by Imaging Mass Spectrometry (IMS) [2]. This technique requires the preparation of high-quality sections, but we could not have prepared the samples available for IMS so far. Since it has been very difficult to attach water-rich lens tissues to analytical glass plate, we tried to spray lens model peptide for the sample plate for analysis.

EXPERIMENTS: We constructed a system to make uniformed spraying sample plate for IMS, which was coated by a chemically synthesized peptide (Fig. 1). Then, we synthesized model peptide containing a site where isomerize Asp has been detected in crystallin, which serves as a lens model. The modification was confirmed using by LC-MS systems in Institute for Integrated Radiation and Nuclear Science, Kyoto University (data not shown). Next, we tried to purify the enzyme to cleave D-Asp in peptide/protein. This is because of that to obtain subtracted MS images before digestion and after digestion. In order to get pure enzyme, we used his-tag systems and then cleaved his-tag after purification.

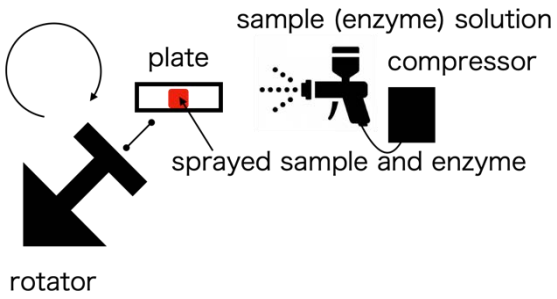

Fig. 1. The schematic drawings for uniformed spraying samples/enzyme into glass plate.

RESULTS: The uniformed spraying system for samples/enzyme was constructed (Fig. 1). This system would help to optimize sample preparation for obtaining ideal images for IMS. We also obtained protease for D-Asp containing peptide/protein. The purity of enzyme was confirmed by SDS-PAGE (Fig. 2). Since the size of enzyme was smaller than those from amino acid sequence data, some degradation/truncation would be occurred under current situation. To the end, we success to obtain the optimized system, samples and specific enzyme for this study. After check the activity of this enzyme, we will use all for IMS systems.

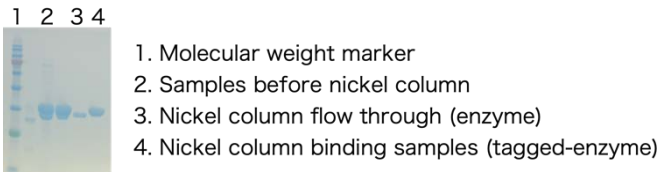

Fig. 2. The purification of enzyme that specific digestion of D-Asp containing peptide/protein.

REFERENCES:

[1] N. Fujii *et al.*, Biochim. Biophys. Acta, **1860** (2016) 183-191.
[2] J. McMahon *et al.*, J. Am. Soc. Mass. Spectrrom., **11** (1995) 1047-1058.

CO6-24

Molecular dynamics analysis of oxidative folding enzyme ER-60 with solution scattering measurement

A. Okuda, M. Shimizu, K. Morishima, R. Inoue, R. Urade and M. Sugiyama

Institute for Integrated Radiation and Nuclear Science, Kyoto University

INTRODUCTION: ER-60, an oxidative protein folding enzyme, is a multi-domain protein. ER-60 has **a** and **a'** domains with catalytically active cysteine pairs and **b** and **b'** domains in the order **a-b-b-b'-a'**. In the process of oxidative protein folding, ER-60 might have the appropriate domain conformations to function, and it is estimated that the structure fluctuates and changes according to the redox state of active cysteine pairs in the solution [1]. Neutron scattering measurement takes advantage of the large difference in neutron scattering length between hydrogen and deuterium, is useful for observing the dynamics and structures of such multi-domain proteins, ER-60 in solution. When 75% deuterated and hydrogenated proteins are in 100% deuterated solvent, the deuterated proteins are scatteringly invisible, and only the hydrogenated proteins could be observed. Applying this method to multi-domain proteins, the domain of the hydrogenated domains could be selectively observed. To reveal the structure-function correlations of ER-60, we aim to analyze selective domain dynamics by quasi-elastic neutron scattering (QENS). The segmental deuterated proteins for this experiment were prepared by connecting the domains with the ligation enzyme *Oa*AEP [2].

EXPERIMENTS: The 75% deuterated (*d*) and hydrogenated (*h*) domains were expressed in *E. coli* cultured in M9 medium containing 75% deuterium and LB medium without deuterium, respectively [3]. The purified domains were mixed in buffer containing 200 mM Tris-HCl (pH 7.4) / 150 mM NaCl. Then, 0.2 μM of the ligation enzyme *Oa*AEP was added to the mixture, and the protein ligation reaction was performed at 20°C for 64 hours. The results of ligation reactions were confirmed by SDS-PAGE. SAXS measurements were performed at 25 °C with 4 hours of exposure-time using a NANOPIX (Rigaku, Tokyo, Japan). The sample-to-detector distance was set to 1330 mm and 300 mm. The q range was from 0.01 to 0.80 Å $^{-1}$.

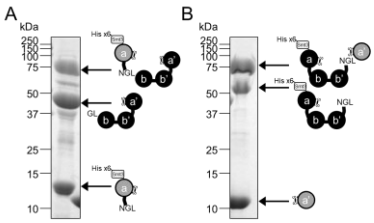

Fig. 1. The ligation products from (A) (*h*)**a** and (*d*)**bb'a'** domains and (B) (*d*)**abb'** and (*h*)**a'** domains of ER-60 by *Oa*AEP.

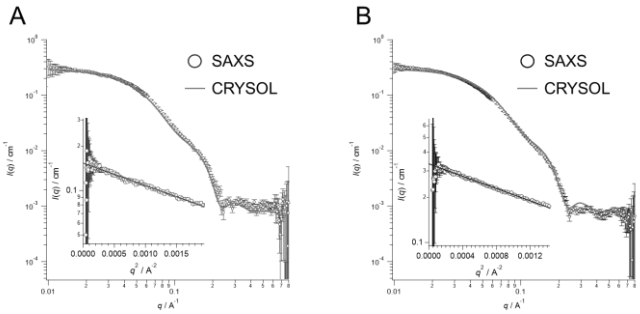

Fig. 2. The SAXS profiles of (A) (*h*)**a**-(*d*)**bb'a'** and (B) (*d*)**abb'**-(*h*)**a'** of ER-60. the radius of gyration (R_g) of these are 32.2 ± 0.3 Å and 37.3 ± 0.2 Å, respectively. Inset panels are guinier plots of them.

RESULTS: The band of ligation product, (*h*)**a**-(*d*)**bb'a'** and (*d*)**abb'**-(*h*)**a'**, connecting the deuterated and hydrogenated domains were observed, indicating the progress of the protein ligation reaction (Fig. 1). In the SAXS profiles of (*h*)**a**-(*d*)**bb'a'** and (*d*)**abb'**-(*h*)**a'** (Fig. 2), there were no significant differences from the profiles predicted by CRYSOL [4] from the crystal structure, and no structural disruption occurred. However, R_g of **abb'**-(*h*)**a'** was larger than predicted, suggesting the possibility of aggregations. Currently, we are examining the conditions for obtaining the stable samples.

REFERENCES:

[1] A. Okuda *et al.*, Sci Rep., **11** (2021) 5655.
[2] A. Okuda *et al.*, Angew Chem Int Ed Engl., **62** (2023) e202214412.
[3] A. Okuda *et al.*, Biophys Physicobiol., **18** (2021) 16-27.
[4] D. Franke *et al.*, J. Appl. Cryst., **50** (2017) 1212-1225.

CO6-25

Synthesis and evaluation of BPA-Nitroimidazole conjugates as smart drug for treatment of hypoxic cells

K. Tanabe,[1] T. Nishihara,[1] T. Ozasa[1] and M. Suzuki[2]

[1]*Department of Chemistry and Biological Science, College of Science and Engineering, Aoyama Gakuin University*
[2]*Institute for Integrated Radiation and Nuclear Science, Kyoto University*

INTRODUCTION: The fast and accurate treatment of hypoxic regions in living tissue is critical for medical treatment of solid tumor, because it has been associated closely with the malignant phenotype of cancer cells, resistant to cancer therapies and the high mortality rate of cancer patients.[1] For treatment of tumor hypoxia, a considerable number of studies have been conducted over the past few decades on the development of radiosensitizers and prodrugs for treatment of tumor hypoxia. However, estimation of treatment method for this pathological tissue remains inadequate, and there are increasing demands for a convenient protocol for its treatment.

These research contexts prompted us to prepare a novel drug that could be used to treat hypoxic cells and tumor hypoxia by BNCT. We conjugated drug for BNCT, BPA, with 2-nitroimidazole derivatives (NIs) to form new hypoxia-treating drug (BPA-NI, Fig 1). NIs are known as an exogeneous marker for hypoxia because of its characteristic reactions in hypoxic cells. NIs are selectively reduced by nitroreductase under hypoxic conditions to form reactive products that can irreversibly bind to cellular nucleophiles. Ultimately, the binding of NIs to cellular macromolecules leads to their accumulation in hypoxic cells and regions. In this study, we prepared the BPA-NI and characterized its cytotoxic effects upon thermal neutron irradiation.

EXPERIMENTS:

Cellular experiments using BPA-NI. The BPA-NI (0 or 250 μM) was administered to the SAS cells and then the cells were incubated for 3 h. After incubation and wash, the cells were irradiated (neutron, 1 MW) for 45 min at KUR. After incubation, WST 8 was added to the cells, and the cell viability assay was performed using Microplate Reader.

RESULTS: The Huisgen reaction was utilized to introduce the NI group into BPA: a benzyl azide group was introduced into the amino group of BPA, which was then condensed with the acetylene group of the NI group in the presence of a copper catalyst. The resulting BPA-NI was identified using NMR and MS spectra.

Next, the cytotoxic effect of neutron irradiation with BPA-NI was evaluated. BPA-NI was administered to human squamous cell carcinoma cells SAS and cultured under hypoxic or aerobic conditions. Subsequent irradiation with thermal neutron beams showed a high cell-killing effect in hypoxic cells, while the effect was limited in aerobic cells. These results strongly indicate that BPA-NI selectively accumulated in hypoxic cells due to the effect of NI substituent and showed toxicity under irradiation conditions. Thus, we successfully developed novel drug for hypoxic cells. The in vivo experiments for evaluation of cytotoxic effects of BPA-NI is in progress.

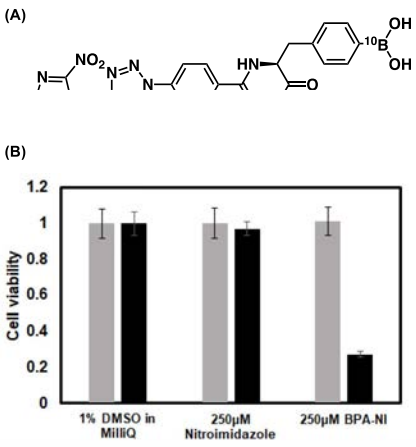

Fig. 1. (A) Chemical structure of BPA-NI. ((B) Cytotoxic effect of BPA-NI and control compound 2-nitroimidazole with (black) or without (gray) thermal neutron irradiation.

REFERENCES:

[1] Harris, A. L., Nat. Rev. Cancer, **2** (2002) 38.

CO6-26

Evaluation of fluorodeoxyuridine derivative bearing azide-methyl substituent as prodrug for FLASH-RT

K. Tanabe,[1] T. Nishihara,[1] T. Ozasa[1] and M. Suzuki[2]

[1]*Department of Chemistry and Biological Science, College of Science and Engineering, Aoyama Gakuin University*
[2]*Institute for Integrated Radiation and Nuclear Science, Kyoto University*

INTRODUCTION: Radiation therapy (RT) is known as a major treatment modality in cancer therapy and is widely used. However, its application in the treatment of tumors that exhibit radioresistance remains limited by dose-limiting normal tissue complications. Under these circumstances, FLASH-RT has been attracting attention. FLASH-RT is an ultrafast RT with dose rates that are generally thousands of times higher than those currently used in routine clinical practice. A major advantage of FLASH-RT is that when irradiated to living tissue, normal tissue is protected compared to conventional RT. These research contexts prompted us to design smart drugs which are applicable to FLASH-RT.
Here we discuss an application of radiation-activated prodrug of antitumor agent, 5-FdUrd, with an azidomethyl group (N3-FdUrd),[1] a known substituent that can be desorbed under X-irradiation conditions. We expected that N3-FdUrd would be activated by reducing species generated by radiolysis (Figure 1), which would remove azide methyl unit to give 5-FdUrd. We prepared the N3-FdUrd and assessed the radiation-dependent cytotoxicity of N3-FdUrd using living cells.

EXPERIMENTS:
Cellular experiments using N3-FdUrd. The N3-FdUrd (0 or 10 μM) was administered to the A549 cells and then the cells were incubated for 24 h. After incubation and wash, the cells were irradiated (0 or 20 Gy) under normoxic conditions using KURNS-LINAC. After incubation, WST 8 was added to the cells, and the cell viability assay was performed using Microplate Reader.

RESULTS: N3-FdUrd was prepared according to the previous report.[1] Next, we attempted to test the cytotoxic effects of N3-FdUrd by irradiating A549 cells under normoxic conditions in the presence or absence of N3-FdUrd to characterize the radiation-dependent cytotoxic effects of N3-FdUrd. As shown in Figure 1B, the cells were viable even in the presence of 10 μM N3-FdUrd without irradiation. On the other hand, radiation in the presence of N3-FdUrd significantly enhanced the radiation sensitivity of the A549 cells, resulting in low cell viability. When the concentration of N3-FdUrd was changed, higher concentrations of N3-FdUrd showed higher cell-killing effects, suggesting that prodrug activation is involved in the enhancement of cell-killing effects by irradiation. These results strongly indicate that N3-FdUrd released toxic 5-FdUrd by radiolytic reduction in hypoxic cells, which led to enhanced cytotoxicity.

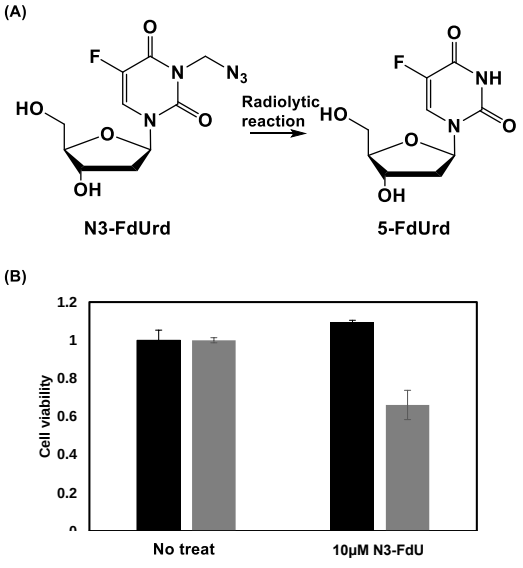

Fig. 1. (A) Radiolytic reaction of N3-FdUrd to form 5-FdUrd. ((B) Cytotoxic effect of N3-FdUrd with or without irradiation (0 Gy: black, 20 Gy: gray).

REFERENCES:
[1] Tanabe, K.; Ishizaki, J.; Ando, Y.; Ito, T.; Nishimoto, S., Bioorg. Med. Chem. Lett., **22** (2012) 1682.

CO6-27

N-Acetylneuraminic Acid Functioned as the Scavenger for Reacive Oxygen Species

N. Fujii and T. Takata[1]

Radioisotope Research Center, Teikyo University
[1] Institute for Integrated Radiation and Nuclear Science, Kyoto University

INTRODUCTION: *N*-Acetylneuraminic acid (Neu5Ac) is a sialic acid in mammals, certain mollusks and some microorganisms. The Neu5Ac was found with a capping sugar in the oligosaccharide chains of glycoproteins and glycolipids [1]. Most studies on glycanic Neu5Ac have focused primarily on cell protection, fertilization, immunology, inflammation and tumors [2-4]. Free Neu5Ac molecules is well oxidized by H_2O_2, then produce its decaroxy product, 4-(acetylamino)-2,4-dideoxy-D-glycero-D-galacto-octonic acid (ADOA) [5]. As a result, monomeric Neu5Ac is the potent defense molecule against oxidative damage. In this study, we used ionizing radiation for decomposing water to generate various reactive oxygen species (ROS), then the scavenged ROS by Neu5Ac was screened.

EXPERIMENTS: Nu5Ac, Ascorbic acid (Asc), Glutathione (GSH), Catalase and Superoxide dismutase (SOD) were dissolved in water, and the pH of the solution was adjusted to about 7.0 with sodium hydroxide. Gamma-irradiation was carried out at the Co-60 Gamma-ray Irradiation Facility of the Kyoto University Institute for Integrated Radiation and Nuclear Science. Sample aqueous solutions were irradiated with gamma ray at a dose of 1 kGy. The quantitative analysis of ADOA was used by LC-MS/MS. The high-performance liquid chromatography was used a U3000HPLC system (Thermo Fisher scientific). The mass spectrometer was used Q Exactive (Thermo Fisher scientific). ADOA was measured by parallel reaction monitoring (PRM) in the positive ion mode, using transitions m/z 282.11 → m/z 186.07.

RESULTS: To quantitatively investigate the amount of ADOA, PRM method was set the optimal for commercial standard. Fig. 1 show the production of ADOA from Neu5Ac aqueous solution with the addition of various scavengers for samples. The 1 kGy gamma-ray irradiation for 10 mM Neu5Ac solution increased the ADOA amount to about 140 μM (Fig. 1: control). Asc and GSH partially suppressed some amounts of ADOA, indicated the presence of the hydroxyl radical (·OH). Catalase suppressed the formation of ADOA completely at 10 U, but SOD did not at the same concentration. Those data implied the presence of hydroxyl radical and hydrogen peroxide, but major source of ADOA would be the hydrogen peroxide in sample after irradiation by gamma-ray.

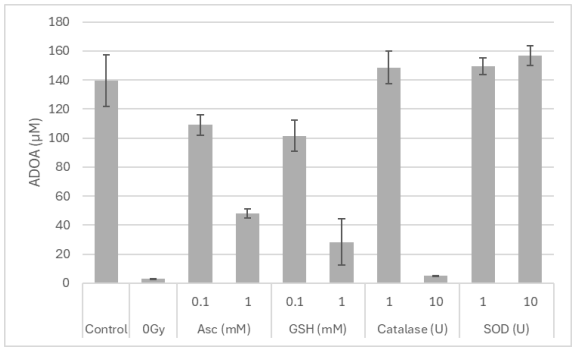

Fig. 1. The amount of ADOA in the presence of various scavengers**.**

REFERENCES:

[1] R. Schauer R., Zoology, **107** (2004) 49-64.
[2] T. Angata *et al.*, Chem. Rev., **102** (2002) 439-469.
[3] R. P. Crocker, Curr. Opin. Struct. Biol., **12** (2002) 609-615.
[4] K. Takayama *et al.*, Proc. Natl. Acad. Sci. USA **93** (1996) 10662-10667.
[5] R. Iijima *et al.*, FEBS Lett., **561** (2004) 163-166.

CO6-28

^{11}C Medical-isotope Production via ^{12}C(γ,n)^{11}C Reaction with Single-walled Carbon Nanotubes

N. Takahashi[1,2], M. Kurosawa[1], M. Tamura[1], M. Fujiwara[1,2], T. Kubota[3], N. Abe[4], and T. Takahashi[4]

[1]*Research Center for Nuclear Physics, Osaka University*
[2]*Kyoto Medical Technology*
[3]*Agency for Health, Safety and Environment, Kyoto University*
[4]*Institute for Integrated Radiation and Nuclear Science, Kyoto University*

INTRODUCTION: L-[^{11}C]-Methionine is used as a positron emission tomography (PET) reagent for medical diagnosis of brain tumors [1]. The medical ^{11}C radioisotopes are mostly produced in a cyclotron via the ^{14}N(p,α)^{11}C reaction by bombarding enriched nitrogen gas with a proton beam [2]. Instead of producing ^{11}C with the cyclotron, we developed a novel method of producing ^{11}C using the bremsstrahlung γ-rays with a single-walled carbon nanotubes (SWCNT) to get a reasonable number of the ^{11}C activity.

EXPERIMENTS: Figure 1 shows the experimental scheme for the ^{11}C production via the ^{12}C(γ,n)^{11}C reaction. Bremsstrahlung γ-rays were produced by impinging a 40 MeV electron beam on platinum converter at the electron LINAC facility. The γ-rays were irradiated to SWCNT sealed in aluminum vessel with non-woven masks as gas inlet/outlet filter. The produced ^{11}C inside the vessel were oxidized to ^{11}CO or ^{11}CO$_2$ in O$_2$ gas, which was continuously flown during the irradiation. The ^{11}C gas (^{11}CO and ^{11}CO$_2$) were trapped in two 13X molecular sieve columns and 511-keV γ-rays from positron-electron annihilation were detected with CdZnTe detectors. The SWCNT with a diameter of 2-3 nm were used as target.

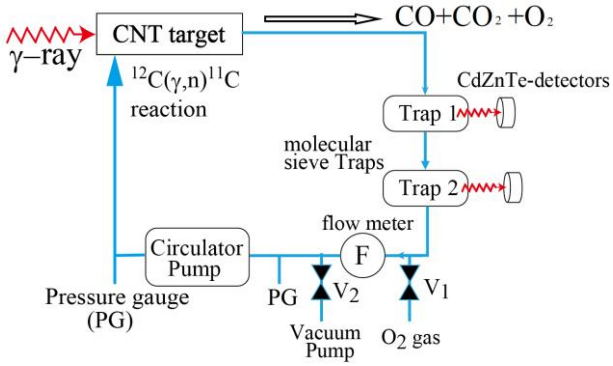

Fig. 1 Experimental scheme to produce ^{11}C and measure the extraction rate of ^{11}C gas.

RESULTS: Table 1 shows the normalized activity of ^{11}C gas for SWCNT which have different bulk density. The normalized activity slightly increases as bulk density increased. All the values shown in Table 1 are higher than 8.71 kBq/μA/g/min for SWCNT with a diameter of 1-1.4 nm used in the previous experiments.

Based on the experimental production rate of ^{11}C gas, we estimate that we can obtain the ^{11}C activity of 58 GBq when we use a SWCNT target under the conditions with 1) a length of 50 cm, 2) weight of 1.13 kg for 0.155 g/cm^3, 3) a 40 MeV electron beam intensity of 100 μA for 40 minutes bombardment.

Table 1 Normalized activity of ^{11}C gas for each bulk density

Bulk density of SWCNT (mg/cm^3)	Normalized activity of ^{11}C gas (kBq/μA/g/min)
3.27	13.30±0.07
6.53	13.94±0.07
9.80	14.41±0.06
13.06	14.92±0.05

REFERENCES:

[1] Kobayashi K. *et al.*, Eur. J. Nucl. Med. Mol. Imaging, **42** (2015) 1071-1080.
[2] David R. Christman *et al.*, Int. J. appl. radiat. isot., **26** (1975) 435-442.

CO6-29

Fundamental study for the production of radionuclide endohedral fullerenes using an infrared fiber laser

M. Inagaki, H. Nakada[1], S. Sekimoto and T. Ohtsuki

Institute for Integrated Radiation and Nuclear Science, Kyoto University
[1]Graduate School of Engineering, Kyoto University

INTRODUCTION: Radioactive isotopes (RI) are widely used in medical diagnosis and treatment. To utilize RI for diagnosis and treatment, techniques for transporting RI in the body and accumulating it at the affected site, known as drug delivery systems (DDS), are required. Fullerene, due to its cage-like structure capable of encapsulating metal atoms, etc. [1], can serve as a molecule for DDS if it is chemically modified to possess functionality to accumulate at the affected site. Therefore, this study aimed to develop a simple method for generating fullerene encapsulating RI.

EXPERIMENTS: (1) Graphite was placed in a quartz vessel, and the vessel was purged with argon gas at 50 kPa. Laser irradiation was applied to the sample from the outside of the vessel. The laser used was a continuous-wave fiber laser with a wavelength of 1080 nm and a power of 300 W. After irradiation, o-dichlorobenzene (*o*-DCB) was added to the sample, and the soluble components were extracted and analyzed by HPLC.
(2) Graphite (70 mg) and radioactive CeO_2 (8 mg) were placed in a quartz vessel, and laser irradiation was conducted under the same conditions. The radioactive CeO_2 was produced using the electron linear accelerator of the Institute for Integrated Radiation and Nuclear Science, Kyoto University. After irradiation, *o*-DCB was added to the sample, the soluble components were extracted, filtered through a membrane filter, and then gamma-ray measurements were performed using a Ge semiconductor detector. Subsequently, similar extractions were performed using aniline and pyridine, followed by gamma-ray measurements.

RESULTS and DISCUSSION: The results of HPLC are shown in Figure 1. From the HPLC results, it was found that fullerenes of C_{60}, C_{70}, and higher fullerenes such as C_{84} were successfully generated by this method. Gamma-ray measurement results of *o*-DCB, aniline, and pyridine solutions obtained from the RI-encapsulating fullerene generation experiment are presented in Table 1. Gamma rays originating from ^{139}Ce and ^{141}Ce were observed more strongly in the aniline and pyridine solutions than in the *o*-DCB solution. Since CeO_2 is insoluble in *o*-DCB, aniline, and pyridine and does not pass through the membrane filter, this result indicates that a component containing ^{139}Ce and ^{141}Ce, insoluble in *o*-DCB but soluble in aniline and pyridine, was formed. Further work will be done to identify this component.

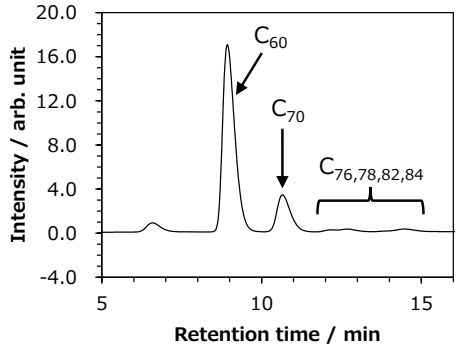

Fig. 1. Chromatogram obtained by HPLC.

Table 1. Gamma-ray measurement results.

solvent	Gamma ray intensity / cps	
	^{139}Ce	^{141}Ce
o-DCB	0.26	0.08
Aniline	0.96	0.30
Pyridine	1.74	0.55

REFERENCES:
[1] Y. Chai *et al.*, J. Phys. Chem., **95** (1991) 7564–7568.

CO6-30

Screening for substances that inhibit abnormal protein aggregation

H. Yagi[1] Y. Kagasawa[2] and T. Takata[2]

[1] *Faculty of Engineering, Tottori University*
[2] *Institute for Integrated Radiation and Nuclear Science, Kyoto University*

INTRODUCTION: Cataract, Alzheimer's disease, Parkinson's disease, and prion disease are diseases that share a common basis in abnormal protein aggregation and typical fibrosis. However, the cause of protein aggregation/fibrosis has been very obscured, and the pathogenesis of these diseases has not yet been elucidated. *In vivo*, accumulation of large amounts of protein aggregates has been observed at disease-causing sites. Therefore, one way to control disease would suppress the formation of abnormal protein aggregates. To do that, the important factor for successful screening of inhibitors is the establishment of monitoring system with a simple and reproducible mechanism of protein aggregation. In past years, we have used γ-ray irradiation to artificially create abnormal protein folding products [1]. We produce recombinant human βB2-crystallin, one of the human lens component proteins by *E. coli*. This protein can be completely denatured with various stresses or chemicals, but then refolded by rapid dilution under appropriate conditions. In this study, we irradiated βB2-crystallin to induce abnormal chemical modification of amino acid residues in it, then monitored refolding process using their intrinsic native tryptophan fluorescence. The purpose of this study is to develop monitoring systems for screening small molecules affecting folding/misfolding pathway of proteins.

EXPERIMENTS: Material Recombinantly expressed human lens βB2-crystallin was prepared and purified as described previously [2]. 1.0 mg/mL aliquots of βB2-crystallin in phosphate buffered saline solution were flash frozen in liquid nitrogen and stored at −80 °C until use. Irradiation was carried out at the $_{60}$Co Gamma-ray Irradiation Facility of the Kyoto University Institute for Integrated Radiation and Nuclear Science [1]. Irradiated samples were centrifuged then collected supernatant. The concentration of βB2-crystallin was measurements by BCA assay kit (ThermoFisher). Unfolding of βB2-crystallin was performed by using 6 M Urea. Refolding was initiated by rapid dilution in ten times of the same buffer in the absence of urea [3].

RESULTS: The amount of βB2-crystallin was decreased in the water-soluble fraction as a function of irradiation dose (Fig. 1). The amount of unfolding/refolding of βB2-crystallin was observed in native fluorescence with some decreasing peak intensity even after low dose (~5 Gy) irradiated (Fig. 2). In independent experiment, we identified that irradiation induces oxidization of five tryptophan residues in βB2-crystallin. This would impact the current folding/misfolding monitoring system. Further improvements of current monitoring systems are required, based on the reduction in fluorescence intensity due to modification.

Fig.1. Aggregates of βB2-crystallin after irradiation.

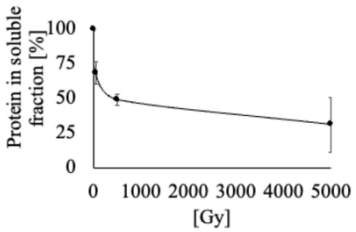

Fig.2. Monitoring of refolding process of low dose (~5 Gy) irradiated βB2-crystallin.

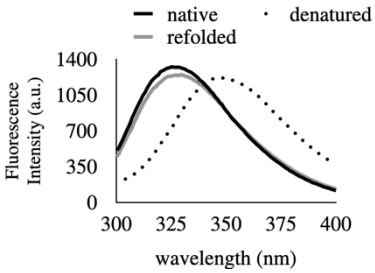

REFERENCES:

[1] I. Kim *et al.*, Amino Acids., **48** (2016) 2855-2866.
[2] T. Takata *et al.*, Mol Vis., **15** (2009) 241-249.
[3] T. Takata *et al.*, FEBS J., **285** (2018) 2263-2277.

CO6-31

Elucidating the Molecular Basis for the Increased Risk of Nuclear Cataract Development with Global Warming

N. Yamamoto[1] and T. Takata[2]

[1] *Fujita Health University*
[2] *Institute for Integrated Radiation and Nuclear Science, Kyoto University*

INTRODUCTION: The transparency of the lens is important for focusing target onto retina. Lens cells contain rich stable long-lived structural proteins, which is called as crystallin. Recently, the worldwide epidemiological survey confirmed that the risk of nuclear cataract (NUC) is significantly higher in residents living in areas where the annual number of days with temperatures of 30°C or higher is higher. Furthermore, in an *in silico* simulation study, the applicant group showed that the incidence of NUC differs within a range of internal temperature differences (35.0-37.5°C) [1]. Based on these results, this study aims to clarify the relationship between the formation of NUC and temperature. There were also significant changes in cell proliferation and expression of crystallins during the process, indicating that temperature-dependent changes occur during protein biosynthesis inside the cell. After reviewing these results, we came to the hypothesis that there is a temperature dependence in the crystallin folding pathways inside the cell, and decided to conduct the following study to demonstrate temperature dependent different folding pathway *in vitro*.

EXPERIMENTS: Recombinantly expressed human βB2-crystallin was unfolded, then refolded by dilution in the presence of each concentration of urea. The ratio of fluorescence intensities between folded (320 nm) and unfolded (360 nm) states were used for the folding index under various urea concentration. This refolding experiment was performed under at two different temperature environment (35.0 vs 37.5°C). On the other hand, a mutant (Trp59Cys) was also prepared as a model for hereditary NUC development, but it was difficult to express under 37 °C because of that aggregated at the expression stage as previously reported [2].

RESULTS: The recombinantly expressed human βB2-crystallin refolding pathway was investigated in two different temperatures, but no significant differences were found (Fig. 1). Thus, it was suggested that there is no significant effect between 35 °C and 37.5 °C with respect to temperature effects on βB2-crystallin folding *in vivo*. This would be caused by the heat stability of βB2-crystallin itself. Since the mimicking congenital cataracts were not expressed in the soluble fraction at 37.5C, suggesting a possible temperature effect on such mimic.

Fig. 1. The βB2-crystallin folding pathway was observed in the presence of each concentration of urea in different temperature.

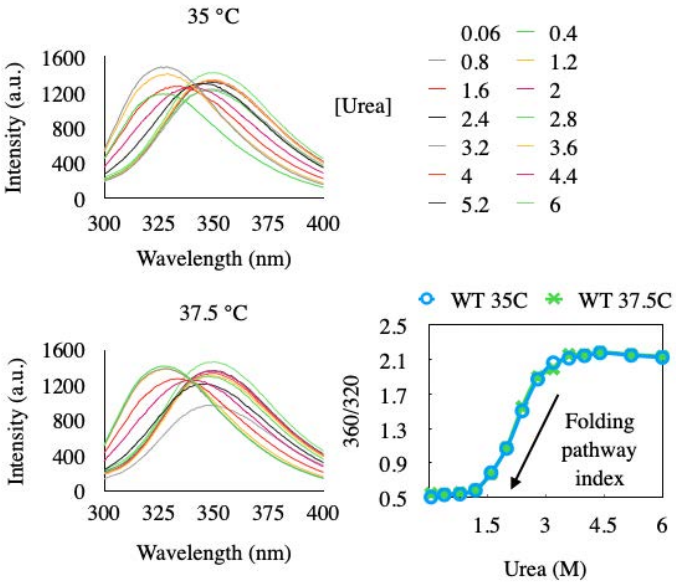

REFERENCES:

[1] N. Yamamoto *et al.*, Cells., **12** (2020) 2670.
[2] W. Zhao *et al.*, J Biol Macromol., **103** (2017) 764–770.

CO6-32

Survey on Radioactive Cesium Migration between Environment and Body of Wild Boar (*Sus scrofa*) Living in Fukushima Prefecture

M. Fukushima[1], Y. Tsuji[1], Y. Iinuma[2], H. Komatsu[3], H. Sugawara[4], S. Mochizuki[4], K. Murakami[3], K. Kanda[3]

[1]*Faculty of Science and Engineering, Ishinomaki Senshu University*
[2]*Research Reactor Institute, Kyoto University*
[3]*Fukushima Prefectual Centre for Environmental Creation*
[4]*Faculty of Food and Agriculture Sciences, Fukushima University*

INTRODUCTION: To study the migration of radioactive cesium caused by Fukushima-Daiichi Reactor accident between environment and several species of wild animals, stable cesium levels in muscles, blood, and livers of wild boars living in Fukushima Pref. were analyzed.

EXPERIMENTS: Wild boars were trapped in Namie, Futaba, Ohkuma, and Katsurao, (inside of Difficult-to-return Zone, n = 25 in total) from May to September 2023, and Nihonmatsu (outside of Difficult-to-return Zone, n = 21) from December 2021 to February 2023 under the permission of Fukushima Pref.. After euthanasia by neck shot, musclus quadriceps, contents of the stomach, blood, and the liver were removed from body, freeze-dried, pulverized, and gamma-ray counting was done for Cs-134 and Cs-137 radioactivity. Also, before freeze-drying, some amount of stomach content was kept in 70% ethanol soln. and separated each materials unter optical microscope for estimating wild boar diet; n = 166 and 40 for wild boars from inside and outside of Difficult-to-return Zone, respectivily. One portion of dried power was supplied for short irradiation in KUR. Eight elements of Ca, Cl, Cu, K, Mg, Mn, Na, and V of wild boar diet were analyzed by the condition of TcPn irradiation, also eight elements of Co, Cr, Cs, Fe, Rb, Sc, Se, and Zn of muscles, blood, and livers were analyzed by irradiation for 1 hour.

RESULTS: **<Radioactive Cs levels in diet, muscles, blood, and livers>** Cesium-137 levels in diet collected from Namie and Nihonmatsu, muscles, blood and livers from inside and outside of Difficullt-to-return Zone are shown in Fig.1. In all samples except diet samples, Cs-137 levels of the samples from inside of Difficult-to-return Zone were 1-2 order higher than those from outside.

<Correation between Cs-137 and stable Cs> Strong correation between Cs-137 and stable Cs in muscles, blood, and livers were found for all three organs, especially organs from Difficult-to return Zone. Correation between Cs-137 and stable Cs is shown in Fig. 2 for livers from Difficult-to-return Zone. This may be thought that Cs-137 in the wild boar diet moves in a same metabolism as stable Cs in the body of wild boars.

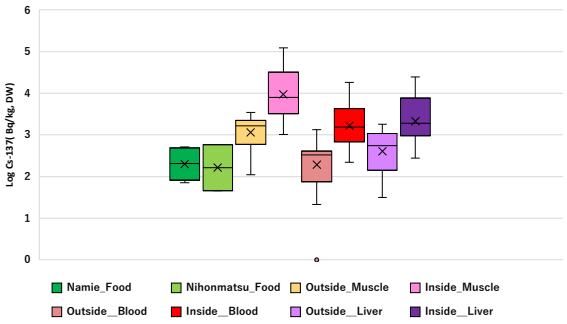

Fig.1 Cs-137 levels in diet, muscles, blood, and livers from inside and outside of Difficult-to return Zone.

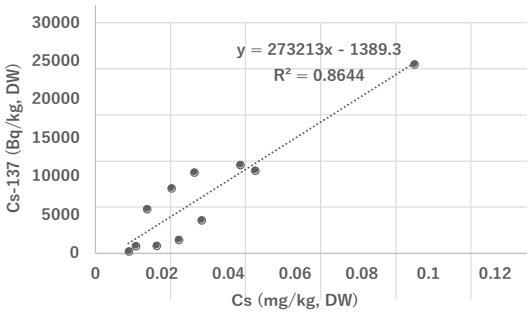

Fig.2 Correation between Cs-137 and stable Cs in livers from Difficult-to return Zone.

CO7-1

Development of Albumin Nano Particles Loaded with Gd(III)-Thiacalixarene Complex for Gd-NCT

N. Iki[1], K. Ohama, M. Komiya[1], T. Nagasaki[2], and M. Suzuki[3]

[1]*Graduate School of Environmental Studies, Tohoku University*
[2] *Graduate School of Engineering, Osaka Metropolitan University*
[3]*Research Reactor Institute, Kyoto University*

INTRODUCTION: Owing to a large thermal neutron capture cross section, gadolinium attracts growing attention as an alternative to boron in NCT [1]. Because free gadolinium ($Gd(OH_2)_9^{3+}$) has toxicity, a safe carrier of Gd to tumor not to release free Gd is required. We recently found that thiacalix[4]arene-*p*-tetrasulfonate (TCAS) self-assembled three Gd ions to form a sandwich-type complex, Gd_3TCAS_2 (Fig. 1) [2], the characteristic features of which is high kinetic stability and ^1H relaxation arising from the Gd center [3]. Nano-sized particles are frequently used as a drug carrier toward tumor by enhanced permeability and retention effect. We have so far studied nano-carriers for Gd_3TCAS_2 such as silica nano-particle (NP) [4] and albumin NP (ANP) [5–7] aiming at Gd-NCT. This FY, we compared the ability of three types of ANP installed with Gd_3TCAS_2 at the surface (shell type), inside (core type), and both at the surface and core of ANP (core-shell type) to deliver Gd into cell and NCT effect.

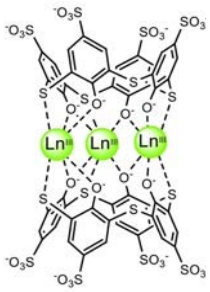

Fig. 1 Ln_3TCAS_2 complex.

EXPERIMENTS: *Preparation of ANPs.* We followed the procedure of previous reports [5–7]. *Cell experiment.* MCF-7 cells were seeded in a 6-well plate at a cell concentration of 1.0×10^5 cells/mL and incubated for 24 h. After supernatant was removed, RPMI medium and solution containing Gd in a form of shell, core, and core-shell ANPs, free Gd_3TCAS_2, 4) Gd-DTPA, 5) PBS (as control) were added to each well and incubated for 24 hr. The concentration of Gd in the medium to incubate MCF-7 was set to be 50 μM. After washing with PBS, the cells were detached from the well and transferred to tubes to be irradiated with thermal neutron for 20 min. The cell viability was assessed by the colony assay [7].

RESULTS: The largest amount of Gd delivered to MCF-7 cells was found with core-shell ANP (1.33 ± 0.06 nmol/10^6 cells), owing to the loading capacity of Gd_3TCAS_2 on ANP (8.13%) larger than that of shell (1.10%) and core (1.44%). The cytotoxicity of core-shell ANP was not observed up to 100 μM. Cell viability after neutron irradiation suggests that the largest NCT effect was obtained with free Gd_3TCAS_2 (Fig. 2). Among ANPs, core-shell type showed meaningful NCT effect, indicating that it can be a promising candidate for Gd agent in NCT.

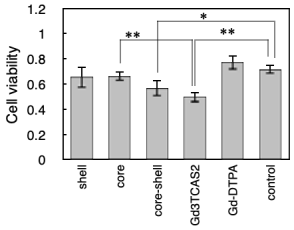

Fig. 2 Cell viability of MCF-7 cells incubated in the presence of Gd agents followed by washing out of free Gd agents and irradiation with thermal neutron. Incubation: 50 μM Gd for 24 h. Neutron fluence: 1.1×10^{12} thermal neutrons cm^{-2}, 1.9×10^{11} epithermal neutrons cm^{-2}.

REFERENCES:

[1] M. Takagaki *et al*., Future Application of Boron and Gadolinium Neutron Capture Thrapy, in Boron Science, Ed N. S. Hosmane (CRC Press) (2012) 243.
[2] N. Iki *et al.*, Eur. J. Inorg. Chem., **2016** (2016) 5020-5027.
[3] N. Iki *et al.*, Inorg. Chem., **55** (2016) 4000-4005.
[4] T. Yamatoya *et al.*, KURNS Progress Report 2019 (2020) 31P11-8.
[5] N. Iki *et al*., KURNS Progress Report 2020 (2021) R2P5-2.
[6] N. Iki *et al*., KURNS Progress Report 2021(2022) R3P2-2.
[7] N. Iki *et al*., KURNS Progress Report 2022 (2023) R4044.

CO7-2

Development of Theranostic Agents for Neutron Capture Therapy (NCT) and Its Companion Diagnostics

K. Ogawa[1], S. Imai, and M. Suzuki[2]

Graduate School of Medical Sciences, Kanazawa University
[1]Institute for Frontier Science Initiative, Kanazawa University
[2]Institute for Integrated Radiation and Nuclear Science, Kyoto University

INTRODUCTION: Boron neutron capture therapy (BNCT) using ^{10}B-labeled agents with companion diagnostics is promising for cancer theranostics. If BNCT and companion positron emission tomography (PET) imaging can be performed with compounds with the same structure, it will be possible to predict the therapeutic and side effects of the compound for BNCT with higher accuracy. Recently, our research group developed a probe, *closo*-dodecaborate-(Ga-DOTA)- c(RGDfK) (**1**) (Fig. 1), containing *closo*-dodecaborate ($[B_{12}H_{12}]^{2-}$) as a boron cluster, [$^{67/68}$Ga]Ga-DOTA as a stable $^{67/68}$Ga complex for single photon emission computed tomography (SPECT) or PET imaging, and an arginine–glycine–aspartic acid (RGD) peptide targeting $\alpha_v\beta_3$ integrin expressed on the cancer cell membrane [1].

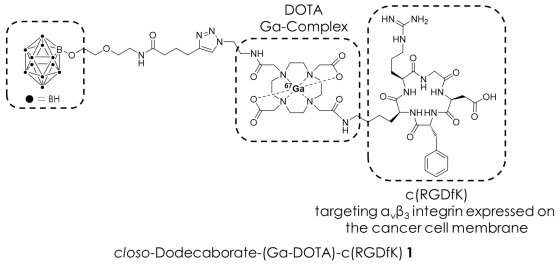

Fig 1. Chemical structure of *closo*-dodecaborate-[^{67}Ga](Ga-DOTA)-c(RGDfK) ([^{67}Ga]**1**).

[^{67}Ga]**1** showed high accumulation in tumors and low accumulation in non-target tissues. However, the synthetic method of **1** resulted in low yields and the radiolabeling time exceeding 6 h. Consequently, its application to ^{68}Ga ($T_{1/2}$: 68 min) was not feasible.
In this study, [^{10}B]**2** with a slightly modified synthetic method and structure was synthesized. Moreover, the precursor for **2** could also coordinate with gadolinium, which is expected to be useful as an element for neutron capture therapy, to from a heptacoordinate complex. Therefore, [^{10}B]**3** with two beneficial isotopes, ^{10}B and Gd, for NCT was also synthesized and evaluated.

EXPERIMENTS: [^{10}B]BPA (192 μM), [^{10}B]**3** (16 μM), and a mixture of [^{10}B]BPA (192 μM) and **3** (16 μM) were dissolved in FBS-free EMEM medium. In a microtube, U-87MG cells were suspended in the prepared medium and shaken for 3 h. After removing drug-containing medium, the amount of boron was measured using ICP-MS. [^{10}B]BPA (192 μM), [^{10}B]**2** (16 μM) and [^{10}B]**3** (16 μM) were dissolved in FBS-free EMEM medium. In a microtube, U-87MG cells were suspended in the prepared medium and shaken for 3 h. Neutron irradiation (1 MW) was performed for 30 min. The irradiated cells were incubated for 24 h. After adding WST-8 and incubating for 90 min, the absorbance at 450 nm was measured using a plate reader.

RESULTS: By combining a *closo*-dodecaborate derivative with an NHS ester structure and DOTA-Lys-RGD with an amino group, a precursor was obtained that is capable of metal coordination in the final step. Compound **2** was obtained with a yield of 6.6% (6 steps). Compound **3** was obtained with a yield of 4.8% (6 steps). In the cell uptake study, the amount of uptake of a mixture of [^{10}B]BPA and **3** was almost the same as the sum of uptake of [^{10}B]BPA and [^{10}B]**3**. In the neutron irradiation experiment in vitro, [^{10}B]BPA, [^{10}B]**2**, and [^{10}B]**3** showed significantly lower cell viability than the control group. These results suggest that [^{10}B]**2** and [^{10}B]**3** would be useful as theranostic drugs for NCT.

REFERENCE: [1] K. Mishiro *et al.*, J. Med. Chem., **65(24)** (2022) 16741-16753.

CO7-3

Optimization of polymer-BPA conjugates for non-clinical studies

T. Nomoto, K. Konarita[1,2], D. Tokura[1,2], M. Suzuki[3], N. Nishiyama[1,2]

Graduate School of Arts and Sciences, the University of Tokyo
[1]Institute of Innovative Research, Tokyo Institute of Technology
[2]School of Life Science and Technology, Tokyo Institute of Technology
[3]Institute for Integrated Radiation and Nuclear Science, Kyoto University

INTRODUCTION: Boronophenylalanine (BPA) has been the most powerful drug in boron neutron capture therapy (BNCT). BPA can selectively accumulate within tumors through LAT1 [1]. Meanwhile, BPA is sometimes exchanged with extracellular amino acids including tyrosine due to the antiport mechanism of LAT1 and shows short-term retention in a target tumor, compromising therapeutic effect [2]. In this regard, we found that poly(vinyl alcohol) (PVA) can form complexes with BPA through boronate esters in aqueous solution and that the PVA-BPA complex can be internalized within tumor cells via LAT1-mediated endocytosis, prolonging the retention time of BPA [3].

In this study, we prepared various compositions of PVA-BPA and evaluated their BNCT effects.

EXPERIMENTS: PVA-BPA complexes with various compositions were intravenously administered to the mice bearing subcutaneous BxPC-3 tumors. When intratumoral boron concentrations reached their highest values, the tumor was irradiated with epi-/thermal neutrons at 1 MW for 50 min using the Kyoto University Research Reactor (KUR).

RESULTS: While all the samples exhibited the strong antitumor effects, PVA-BPA with a specific composition showed considerably high response rate 42 days after irradiation (Fig. 1). This result is consistent with boron concentration indicated in biodistribution study (data not shown).

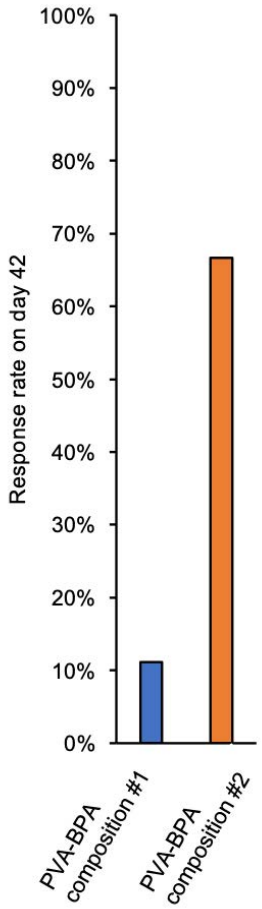

Fig. 1. BNCT effects of PVA-BPA.

REFERENCES:
[1] P. Wongthai *et al*., Cancer Science, **106** (2015) 279-286.
[2] A. Wittig *et al*., Radiat. Res., **153** (2000) 173-180.
[3] T. Nomoto *et al*., Sci. Adv., **6** (2020) eaaz1722.

CO7-4

Development of novel boron delivery systems improving accumulation contrast

D.Tokura[1,2,3], K. Konarita[1,2,3], M. Suzuki [4], N. Nishiyama[2,3], T. Nomoto[1,2]

[1]*Graduate School of Arts and Sciences, the University of Tokyo*
[2]*School of Life Science and Technology, Tokyo Institute of Technology*
[3]*Institute of Innovative Research, Tokyo Institute of Technology*
[4]*Institute for Integrated Radiation and Nuclear Science, Kyoto University.*

INTRODUCTION: Boron neutron capture therapy (BNCT) is a treatment that kills cancer cells by nuclear reaction between thermal neutrons and boron atoms (^{10}B). In a clinical condition, the boron concentration in the tumor must be 25 ppm or higher, and the boron concentration ratio between the tumor and blood (T/B ratio) and the surrounding normal organs (T/N ratio) must be 2.5 or higher to obtain an efficient therapeutic effect while keeping radiation exposure to normal tissue low. Although many studies have developed drug delivery systems (DDSs) such as polymeric micelles [1] and lip-osomes [2], these conventional DDSs should show appreciably prolonged retention in the blood-stream to increase the chance of leakage from tumor vessels into tumor tissue and the eventual tumor accumulation. Thus, simply converting conventional DDSs to BNCT does not necessarily result in a high T/B ratio, and even if high tumor accumulation is achieved, the dose of thermal neutron irradia-tion is limited and does not lead to improved therapeutic effects. Here, we developed a DDS that can actively increase the T/B ratio in a light-responsive manner.

EXPERIMENTS: The DDS was synthesized by conjugating low-molecular-weight boron drugs, which are immediately excreted by the kidney as a single agent, with the side chains of a derivative of the biocompatible poly(2-hydroxypropyl methacrylate) (PHPMA) via a photolabile linker. The accumulation of the boron drug in a tumor and various organs was investigated in a murine subcutaneous tumor model after intravenous injection. The similar experiment was conducted with photoirradiation and the result was compared with that without photoirradiation. Based on the results of the revealed pharmacokinetics, the conditions for neutron capture therapy were determined, and the BNCT effects were investigated.

RESULTS: The DDS could increase the T/B ratio in a light dose-dependent manner, thereby accomplishing significantly enhanced BNCT effects under the condition mimicking a practical situation (Fig. 1).

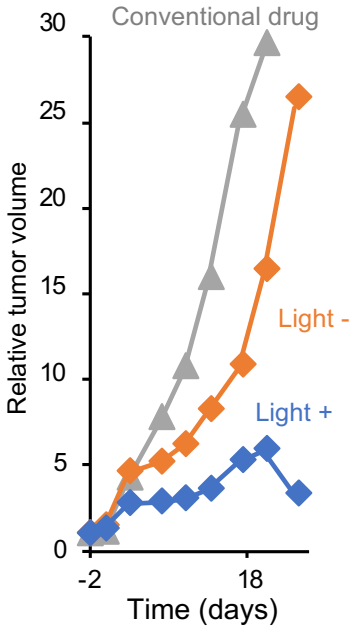

Fig. 1. BNCT effects.

REFERENCES:
[1] H. Cabral *et al.,* Chem. Rev., **118 (14)** (2018) 6844-6892.
[2] Theresa M Allen and Pieter R Cullis, Adv Drug Deliv Rev., **65** (2013) 36-48.

CO7-5

Elucidating the effects of boron neutron capture therapy on host immunity in mice tumor models

T. Watanabe[1], Y. Sanada[2], T.Takata[3], G. Edward Sato[4], M. Yoshimura[4], Y. Sakurai[3], T. Mizowaki[4], H. Tanaka[3], M. Suzuki[1]

Institute for Integrated Radiation and Nuclear Science, Kyoto University

[1]Particle Radiation Oncology, Particle Radiation Oncology Research Center
[2]Particle Radiation Medical Physics, Particle Radiation Oncology Research Center
[3]Division of Radiation Life Science
[4]Radiation Oncology and Image-Applied Therapy, Faculty of Medicine, Kyoto University

INTRODUCTION: Boron neutron capture therapy (BNCT) is a type of radiation therapy that utilizes a reaction in which boron atoms (^{10}B) capture neutrons and cause them to fission into alpha particles and lithium nuclei [1]. By selectively delivering boron atoms in the form of drugs to tumor cells, subsequent neutron irradiation can selectively induce nuclear reactions in the delivered cancer cells, resulting in the death of the cancer cells. In particular, immune cells are known to be more radiosensitive than normal cells and can be killed even by small doses of radiation [2]. On the other hand, it has also been shown that irradiation of tumor tissue releases the immune escape mechanism, which is designed to prevent tumor tissue from being attacked by the immune system, and that irradiation of tumors makes it easier for immune cells to attack tumor cells [3]. BNCT is also a type of radiation and may have some effect on the number and function of host immune cells after BNCT, but there have been only a few reports on the immune response after BNCT in detail [4]. The purpose of this study is to elucidate the effects of BNCT on host immune cells.
****

EXPERIMENTS: A tumor model was created in which mouse-derived malignant melanoma cells B16 and mouse-derived squamous cell carcinoma SCCVII were transplanted subcutaneously into the lower leg skin of C57BL/6 and C3H mice, respectively. Mouse-derived malignant melanoma cells B16 and mouse-derived squamous cell carcinoma SCCVII were transplanted subcutaneously into the lower leg skin of C57BL/6 and C3H mice, respectively. Subcutaneous tumor size was assessed after treatment between BNCT or BNCT plus immunotherapy (anti-PD-1 antibody) group. Tumor tissue was removed after BNCT and BNCT + immunotherapy combination treatment, and the tumor tissue was enzymatically treated and separated into single cells. Then, flow cytometry was used to examine the percentage of T cells infiltrating the tumor and memory function.
****

RESULTS: We found that the combination group of immunotherapy and BNCT showed better long-term tumor growth inhibition in the tumor curve. The BNCT group showed significantly increased expression of chemokines. Since the combination of BNCT and immunotherapy showed a long-term inhibition of tumor growth compared to the control group and the BNCT alone group, we focused on the memory function of lymphocytes, which is involved in immune memory and shows a long-term inhibition of tumor growth, and examined the percentage of CD3+ T cells with a memory function among the lymphocytes infiltrating the tumor. However, contrary to the hypothesis, no significant differences were found between the treatment groups or in comparison with the control group. Flow cytometric results showed that although lymphocytes in both the X-ray and BNCT groups decreased temporarily after irradiation, they recovered more quickly in the BNCT group than in the X-ray-irradiated control group.
****

REFERENCES:

[1] R. F Barth *et al.,* Radiat Oncol., **7** (2012) 146.
[2] Guillaume Vogin and Nicolas Foray., Int J Radiat Biol., **89** (2013) 2-8.
[3] Tsubasa Watanabe *et al.,* Int J Clin Oncol., **28** (2023) 201-208.
[4] A. A. Khan *et al.,* PLoS One., **14** (2019) e0222022.

CO7-6

Basic research to expand the indication of boron neutron capture therapy to non-neoplastic diseases

T. Watanabe[1], Y. Hattori[2], T.Takata[3], G. E. Sato[4], M. Yoshimura[4], Y. Sakurai[3], T. Mizowaki[4], H. Tanaka[3], M. Kirihata[2], M. Suzuki[1]

[1]Institute for Integrated Radiation and Nuclear Science, Kyoto University, Particle Radiation Oncology, Particle Radiation Oncology Research Center

[2]Osaka Metropolitan University

[3]Institute for Integrated Radiation and Nuclear Science, Kyoto University, Particle Radiation Medical Physics, Particle Radiation Oncology Research Center

[4]Radiation Oncology and Image-Applied Therapy, Faculty of Medicine, Kyoto University

INTRODUCTION: The purpose of this study is to explore the possibility of applying BNCT, which has been developed as a cancer therapy [1], to intractable diseases other than cancer (intractable non-tumor diseases) using mouse models, in order to further develop BNCT as a medical field and to discover potential indications of BNCT for diseases other than cancer [2]. Intraperitoneal administration of β-glucan to mice (Balb/c-derived offsprings) induces an immune response and symptoms similar to collagen disease in some mice models [3]. We aim to develop boron agents targeting the cause of inflammation based on boronated-antibodies.

****

EXPERIMENTS: When 30 mg of laminarin, a β-glucan, was administered intraperitoneally to mice, swelling of bilateral wrist joints was observed from 7 days after administration, and 10-14 days after administration, redness of the wrist joints was observed, suggesting clear inflammation. No obvious diarrhea was observed in this mouse model or at the β-glucan dose.

In order to make specific boron compounds targeting the cause of inflammation, we attached boron compounds to the stationary portion (Fc portion) of a commercially available IgG antibody. The number of boron atoms was quantified by binding the FITC-bound boronated module to the isotype antibody and measuring the fluorescence intensity per antibody molecule.

A new boron drug targeting the IL17 receptor was prepared by the above method, and its therapeutic effect was examined by comparing it with that of the neutron alone irradiation group, the L-BPA administration group, and the boron drug targeting the immune response group.

****

RESULTS: After binding a boronated module to a commercially available anti-mouse IL17 receptor and administering 200 μg to a mouse model of arthritis created by intraperitoneal administration of β-glucan, the therapeutic effect on arthritis was observed by irradiating bilateral wrist joints with neutrons. Mice with arthritis were prepared under the same conditions, and the same neutron irradiation was performed on the following two control groups; control group 1: Neutron irradiated without boronated antibody, control group 2: Neutron irradiated with boronated derivatives of amino acids, which are commonly used as boron drugs for BNCT. No obvious improvement in arthritis was observed when evaluated by scoring over time after neutron irradiation.

****

REFERENCES:

[1] R. F Barth *et al.,* Radiat Oncol., **7** (2012) 146.
[2] T. D Malouff *et al.,* Front Oncol., **11** (2021) 601820.
[3] S. Sakaguchi *et al., F*EBS Letters, **585** (2011) 3633-3639.

CO7-7

Development of Fluorescent Dodecaborate Conjugated anti-EGFR Antibody as Theranostic Type Boron Carrier for BNCT

Y. Hattori, M. Ishimura, I. Nakase[1], M. Kirihata

Research Center of Boron Neutron Capture Therapy, Osaka Metropolitan University
[1] Graduate School of Science, Osaka Metropolitan University

INTRODUCTION: Boron neutron capture therapy (BNCT) has been recognized as an essential treatment for refractory cancers such as glioma, head and neck cancer, and melanoma in recent years. Although many types of boron compounds, including amino acids, peptides, nucleic acids, anticancer drugs, and liposomes have been reported as boron delivery agents for BNCT, only two compounds, *p*-borono-L-phenylalanine (L-BPA, Boropharan-10B) and mercaptododecaborate (BSH), are clinically used in the treatment of cancer with BNCT. In light of these factors, novel useful boron-pharmaceuticals for BNCT are in high demand. BSH, a class of water-soluble anionic boron cluster compounds with low toxicity, is clinically used as boron carrier for the treatment of brain tumors. However, tumor selectivity and cell membrane permeability of BSH is slightly low. In the course of our developing studies on new boron carrier for BNCT, we have designed and synthesized thiododecaborate ($[B_{12}H_{11}S]^{2-}$) unit-containing tumor seeking compounds such as amino acids, peptides and antibodies [1-3]. In BNCT, development of theranostic type boron carrier is highly noted, because visualization of the boron distribution and determination of tumor/normal ratio by non or minimally invasive examination are very important for the planning of BNCT. To develop the theranostic type boron carrier for BNCT, we have been developed bifunctional boron cluster containing compounds which linked Near-infrared (NIR) fluorescent dye (Cy5.5) and alkyl linker (Cy-BSH-OSu) to conjugate with tumor seeking compounds. In this paper, we report the conjugation of novel NIR fluorescent boron cluster with antibody, and the biological evaluation of boronated antibody as boron carrier for BNCT.

RESULTS and Discussion: In this study, anti-EGFR Mab Cetuximab was chosen as tumor target moiety. The synthetic route of bifunctional boron cluster containing compounds was illustrated in Fig. 1. The S-alkylation of cyanoethyl BSH (**1**) with 6-bromohexanoic acid was achieved by previously reported method in good yield. After deprotection of S-cyanoethyl group, the brominated Cy5.5 was treated to give Cy-BSH-OH followed by treatment with an ion-exchange resin. The succineimide ester type compound (Cy-BSH-OSu) was prepared by the reaction of Cy-BSH-OH with di(N-succinimidyl)carbonate (DSC). The conjugation of Cy-BSH-OSu boron compounds with Cetuximab were proceeded in 0.1 M Na_2HPO_4 to give Cy-BSH-Cetuximab (The number of Cy-BSH per antibody was about 3). In the next step, we evaluated the Cy-BSH-Cetuximab as boron carrier using EGFR high expressed tumor cell (A431 human carcinoma). Cy-BSH-Cetuximab was delivered boron atom to A431 cell, and cotreatment with EGF induce macropinocytosis enhanced the cellular uptake of Cy5.5-DB-Cetuximab. Further evaluation of boronated compounds as boron carrier for BNCT and is now under investigation.

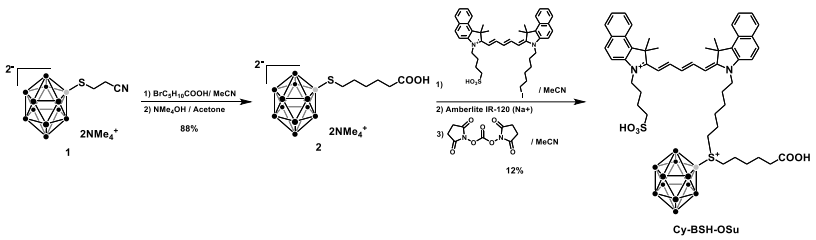

Fig 1. Synthesis of Cy-BSH-OSu.

REFERENCES:

References:

[1] Y. Hattori *et al.,* J. Med. Chem., **55** (2012) 6980-6984.
[2] I. Nakase *et al.,* Chemm. Commun., **55** (2019) 13955-13958.
[3] I. Nakase *et al.,* ACS Omega, **5** (2020) 22731-22738.

CO7-8

HER-2 targeted boron delivery system using the complex of β-1,3-glucan-boron nitride nanotube complex

Riku Kawasaki,[1] Keita Yamana,[1] Kosuke Kondo,[1] Yu Sanada,[2] Kaori Bando,[3] Takushi Takata,[2] Yoshinori Sakurai,[2] Hiroki Tanaka,[2] Tomoki Kodama,[4] Seiji Kawamoto,[4] Takeshi Nagasaki,[3] Atsushi Ikeda[1]

[1]*Program of Applied Chemistry, Graduate School of Advanced Science and Engineering, Hiroshima University*
[2]*Institute for Integrated Radiation and Nuclear Science, Kyoto University*
[3]*Department of Applied Chemistry and Bioengineering, Graduate School of Engineering, Osaka Metropolitan University*
[4]*Program of Bioengineering, Graduate School of Integrated Science for Life, Hiroshima University*

INTRODUCTION: With minimal invasiveness, boron neutron capture therapy has been considered as one of the promising modalities to treat cancer.[1] As cell destruction can be attained in cells uptaking boron agents actively, the deliverability of boron to tumor tissue is the key to enhance therapeutic benefits of BNCT. For these points of views, various types of delivery platforms have been studied such as liposomes and nanogels. Here, boron nitride nanotubes (BNNT) have been expected as a promising candidate as a boron agent for BNCT due to their large contents in each material and their one-dimensional morphology. Despite of their fascinating properties of BNNT, the biomedical application of BNNT was limited because of their poor dispersibility in aqueous media. In this work, we demonstrate the applicability of HER-2 targeting antibody conjugated β-1,3-glucanBNNT (HER-2-GL/BNNT) complex as a boron agent for BNCT.
EXPERIMENTS: Protein A mimicking moiety (PAM) was introduced to GL as antibody conjugate unit. The substitution degree of PAM was quantified by ^{1}H-NMR. Complexation of BNNT with PAM-GL was conducted high-speed vibration milling (HSVM) and the complex was extracted by water. The basic characterization of the complex was addressed by dynamic light scattering (DLS), transmission electron microscopy (TEM), and inductively coupled plasma-atomic emission spectroscopy (ICP-AES). Conjugation of anti-HER-2 antibody with PAM-GL/BNNT was examined by fluorescence resonance energy transfer (FRET) using fluorescently labeled GL and antibody. BNCT activity *in vitro* was evaluated toward human ovarian cancer cells overexpressing HER-2 (SK-OV-3). Finally, tumor targeting delivery using HER-2-GL/BNNT in tumor xenograft model mice by *in vivo* imaging system and ICP-AES.
RESULTS: Synthesized PAM-GL could disperse BNNT at 540 ppm via HSVM and the hydrodynamic diameter of the complex was determined to be 80 nm (PDI, 0.16). TEM observation without staining revealed rod like structure. After complexation with antibody, FRET was observed, indicating the antibody was successfully conjugated with PAM-GL/BNNT complex. In addition, conjugation with antibody did not significantly change the hydrodynamic diameter of the complex and morphology. BNCT activity of HER-2-GL/BNNT complex toward SK-OV-3 was 29 times higher than that of L-BPA/fructose complex. To address these differences in BNCT activity, we compared cellular uptake amount of HER-2-GL/BNNT with L-BPA/fructose complex in SK-OV-3. After exposure to boron agents, we quantified the accumulated boron atom within cells using ICP-AES. As a result, HER-2-GL/BNNT enhanced cellular uptake of boron atom to SK-OV-3 cells by 12-fold. Finally, we demonstrated deliverability of the system using tumor xenograft model mice, which was established by transplantation of SK-OV-3 to nude mice, by *in vivo* imaging system. After administration of HER-2-GL/BNNT via intravenously, the complex was gradually accumulated in tumor tissue with time and the accumulation reached peaks at 6 h-post injection. Moreover, the HER-2-GL/BNNT could enhance the accumulated amount of BNNT in tumor tissue compared with GL/BNNT complex, indicating our system work as HER-2 targeting system.

REFERENCES: [1] K. Yamana *et al.,* Nanoscale Adv., **5** (2023) 3857.

CO7-9

Evaluatiomnof in vitro tumor-killing effects of surface-modified gadolinium-loaded chitosan nanoparticles for gadolinium neutron capture therapy

T. Andoh[1], T. Fujimoto[2], M. Suzuki[3], T. Takata[4], Y. Sakurai[4] and H. Ichikawa[1].

[1]Faculty of Pharmaceutical Sciences, Kobe Gakuin University, Japan.
[2]Department of Orthopaedic Surgery, Hyogo Cancer Center, Japan.
[3]Particle Radiation Oncology Research Center, Institute for Integrated Radiation and Nuclear Science, Kyoto University, Japan.
[4]Division of Radiation Life Science, Institute for Integrated Radiation and Nuclear Science, Kyoto University, Japan

INTRODUCTION: Gadolinium neutron-capture therapy (Gd-NCT) is a cancer therapy that utilizes γ-rays and electrons emitted due to ^{157}Gd (n, γ) ^{158}Gd reactions. We have been developing gadolinium-loaded chitosan nanoparticles (Gd-nanoCPs) to control Gd delivery in Gd-NCT. Accumulation of Gd in Gd-nanoCP treated tumors is based primarily on the bioadhesive (cationic), biocompatible (nontoxic), and biodegradable (bioerodible) properties of chitosan nanoparticles. Our previous studies demonstrated that neutron-capture reactions after intratumoral (i.t.) injection of Gd-nanoCPs in tumor-bearing mice could significantly suppress tumor growth; however, the inhomogeneous distribution of Gd-nanoCPs in tumor masses prevents complete cure. One can expect that increased dispersion stability of Gd-nanoCPs will improve the heterogeneous distribution of Gd in tumor tissues and increase the tumor-killing effect of electrons by shortening the adhesion length between Gd-nanoCPs and tumor cells. Thus, we aimed to investigate the impact of PEG modifica-tion on the *in vitro* tumor-killing effect of Gd-nanoCPs in Gd-NCT

EXPERIMENTS: Gd-nanoCP was prepared using chitosan and Gd-DTPA through the previous-ly developed w/o emulsion-droplet coalescence technique. The condensation reaction of the amino group present in intact Gd-nanoCP and NHS-activated ester-PEG prepared direct PEG-modified Gd-nanoCP (PEG-Gd-nanoCP). Mean particle size and zeta potential of the resultant Gd-nanoCPs were measured by Zetasizer® (Malvern). Gd concentration of tumor tissue was determined by in-ductively coupled plasma atomic emission spectrometry (ICP-AES, SPS3100) followed by incin-eration of each sample. Tumor-killing effect was evaluated by a cellular viability assay with SCC VII cells after thermal neutron irradiation.

RESULTS: Mean particle diameter and zeta potential of the Gd-nanoCP, and PEG-Gd-nanoCP, were 171 and 168 nm, 15 and 20 mV, respectively. No difference was observed in the average parti-cle size. Still, there was a difference in the settling tendency when left to stand, suggesting that PEG-Gd-nanoCP has higher dispersion stability. The tumor-killing effect of Gd-nanoCPs and PEG-Gd-nanoCP was increased in a concentration-dependent manner. Most notably, PEG-Gd-nanoCP exhibited a stronger tumor-killing effect than Gd-nanoCP at the same Gd dose. This tumor-killing effect could be ascribed to the higher association between Gd-nanoCPs and tu-mor cells, improved distribution of Gd in cells exposed to PEG-Gd-nanoCP, and increased influ-ences due to Auger and Coster-Kronig electrons, which have shorter path lengths and more vital tumor-killing ability than do γ-rays. Therefore, improving the dispersion stability of Gd prepara-tions within the tumor cells is crucial for achieving uniform Gd distribution. The improvement in dispersion stability with surface modification possibly led to the homogenization of Gd distribution because the particle sizes of the two Gd formulations did not differ significantly.

CO7-10

The effect of boron neutron capture therapy (BNCT) to gastrointestinal stromal tumor(GIST)

S. Hagihara[1], J. Arima [1], K. Taniguchi[1,2], Y. Inomata[1], A. Miyamoto[1], M. Suzuki[3], and Sang-Woong Lee [1]

[1] *Department of General and Gastroenterological Surgery, Osaka Medical and Pharmaceutical College, Osaka, Japan*
[2] *Translational Research Program, Osaka Medical and Pharmaceutical College, Osaka, Japan*
[3] *Department of Particle Radiation Oncology, Research Reactor Institute, Kyoto University, Kumatori, Osaka, Japan.*

INTRODUCTION: Gastrointestinal stromal tumors (GIST) are the most frequent soft-tissue sarcomas substantially arising from the gastrointestinal tract. Surgery is the first choice of treatment for primary GISTs. However, local recurrence or metastasis still occurs in 10% to 50% of patients after curative resection. Imatinib mesylate (imatinib) classified in a tyrosine kinase inhibitors is the primary agent of choice used to treat GISTs. On the other hand, drug resistance to imatinib poses a major obstacle to treatment efficacy.
In this study, we investigated the effectiveness of
boron neutron capture therapy (BNCT) to GIST-T1 and imatinib-resistant GIST-T1(GIST-T1/IM-R) using the mouse model.
****

EXPERIMENTS: We used Boronophenylalanine (BPA) as a boron compound. In vitro study, Cytotoxicity by BNCT with BPA was evaluated by colony forming assay. GIST-T1 and GIST-T1/IM-R cells were incubated with 20 μg B/mL BPA and boron-free medium for 1h at 37 ◦C in 5% atmospheric CO2. In vivo study, GIST-T1 cells were concentrated to 2.0×10^7/100μL in 0.1ml of PBS and injected into the right leg of each mouse. Animals were divided into three groups (5-7 animals per group); the cold control (no treatment, no neutron irradiation), hot control (neutron irradiation only), and BNCT (intraperitoneal BPA administration and neutron irradiation) groups.
****

RESULTS: In vitro study, **Fig.1** showed the results of the neutron irradiation for GIST-T1 and GIST-T1/IM-R cells. The Survival Fractions of GIST-T1 and GIST-T1 (GIST-T1/IM-R) cells decreased as the neutron fluence increased. In vivo study, **Fig.2** showed that tumor volume (mm^3) significantly reduced in the BNCT group compared with the cold and hot control groups. All mice did not have symptoms such as diarrhea and survived until the endpoint. Remarkable weight loss was not observed in three groups at the endpoint. (**Fig.3)**
****

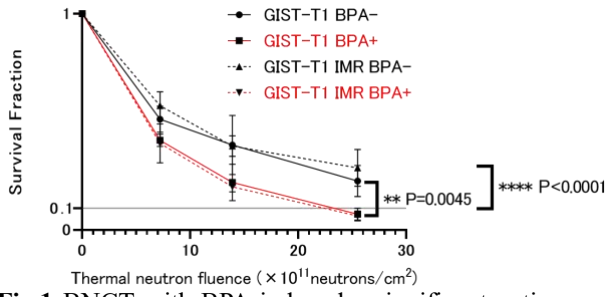

Fig.1 BNCT with BPA induced a significant anti-cancer effect in both GIST-T1 and GIST-T1 IMR compared to control.(****P<0.0001, **P=0.0045)

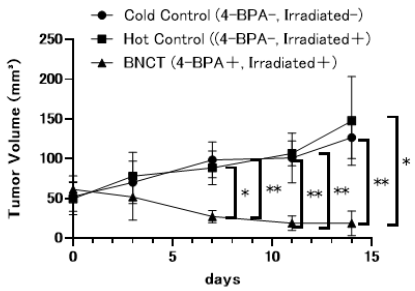

Fig.2 BNCT with BPA induced a significant anti-cancer effect compared to Cold and Hot control in GIST bearing mice. (*P<0.05, **P<0.01)

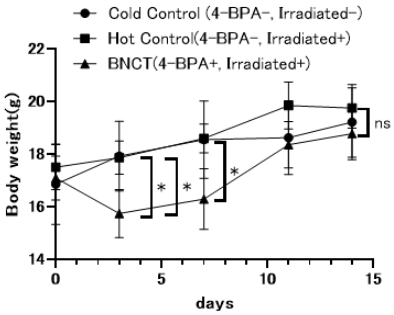

Fig.3 Body weight loss were observed a week after irradiation in BNCT group. There were not a significant difference in body weight two weeks after irradiation. (*P<0.05)

Ongoing study: We are making a mouse model of GIST-T1/IM-R, planning to investigate effect of BNCT. Also, we intend to clarify the mechanism of the antitumor effect using HE and TUNEL staining.
We will continue this study and the results will be published in the future.

REFERENCES:
[1] M. Sasaki *et al.,* PLOS ONE, Apri 7, 2021
(doi) 10.1371/journal.pone.0249650

CO7-11

Evaluating the Efficacy and Safety of Boron Neutron Capture Therapy in Treating Metastatic Spinal Tumors

Y. Fujikawa, S. Kawabata, K. Tsujino, H. Yamada, T. Takata[1], H. Tanaka[1], M. Suzuki[1], N. Hu[2], S-I. Miyatake[2], T. Takami, and M. Wanibuchi

Department of Neurosurgery, Osaka Medical and Pharmaceutical University
[1]Institute for Integrated Radiation and Nuclear Science, Kyoto University
[2]Kansai BNCT Medical Center, Osaka Medical and Pharmaceutical University

INTRODUCTION: Metastatic spinal tumors have been treated with multidisciplinary interventions such as surgical resection, fixation, and radiation therapy. Despite the advancements in radiation therapy techniques, it remains challenging to achieve better quality of life and activity of daily living. This study aims to evaluate the efficacy and safety of boron neutron capture therapy (BNCT) for the treatment of metastatic spinal tumor using a mouse model. Through this investigation, we aim to contribute to the evolving landscape of therapeutic strategies, potentially offering an innovative alternative that could enhance clinical outcomes for patients afflicted with this condition.
****

EXPERIMENTS: ***In vitro:*** A549 human lung adenocarcinoma cells were exposed to neutron irradiation at 1 MW reactor power for 0-30 minutes and photon irradiation at doses of 0-8 Gy, aiming to assess their biological impact on the cell lines. For neutron irradiation, cells were exposed to 4-borono-L-phenylalanine (Boronophenylalanine; BPA) at a concentration of 10 μg Boron/mL for 24 hours before irradiation. The biological effects were evaluated using colony-forming assay to confirm the effect on cellular viability and proliferative capacity. ***In vivo:*** For the in vivo assessment, a mouse model was developed using metastatic spinal tumors derived from A549 cells. The mice bearing these tumors were randomly assigned into three groups: a control group receiving no treatment (untreated; n = 10), a group subjected to neutron irradiation alone (neutron only; n = 9), and a BNCT group (BNCT; n = 10. The BNCT group received an intravenous injection of BPA at a dose of 250mg/kg, followed by neutron irradiation 2.5 h later. Overall survival and neurological function of the hindlimb, and any adverse events were assessed post-irradiation.
****

RESULTS: ***In vitro:*** Neutron irradiation, particular with BPA, revealed a markedly enhanced cell-killing effect in comparison to photon irradiation. ***In vivo:*** In the in vivo assessment involving a metastatic spinal tumor mouse model, the BNCT group demonstrated significantly prolonged survival in comparison to both the untreated group, ($p < 0.01$) and the neutron only group ($p < 0.05$) as determined by the log-rank test. Furthermore, preservation of hindlimb neurological function was significantly more pronounced in the BNCT group relative to the untreated ($p = 0.0004$) and neutron only groups ($p = 0.0051$), based on multivariate analysis of variance. Notably, an assessment of adverse events across the three study groups showed no significant occurrences, indicating a favorable safety profile of BNCT treatment in this experimental setting.
****

These findings emphasize the potential of BNCT not only to prolong survival but also to preserve quality of life by preserving neurological function without inducing adverse effects. These results therefore advocate further exploration and development of BNCT as a feasible and promising treatment option for patients with metastatic spinal tumors.

CO7-12

ASCT2-Targeted Boron Agent Enhances BNCT Efficacy in Glioma Treatment

K. Tsujino, S. Kawabata, Y. Fujikawa, H. Kashiwagi, R. Hiramatsu, H. Tanaka[1], M. Suzuki[1], S-I. Miyatake, T. Akaki[2], T. Morita[2], H. Nakamura[2], and M. Wanibuchi

Department of Neurosurgery, Osaka Medical and Pharmaceutical University
[1] Institute for Integrated Radiation and Nuclear Science, Kyoto University
[2] Laboratory for Chemistry and Life Science, Institute of Innovative Research, Tokyo Institute of Technology

INTRODUCTION: Boron Neutron Capture Therapy (BNCT) is a cutting-edge particle irradiation technique that utilizes the nuclear reaction triggered by the irradiation of non-radioactive boron-10 with thermal neutrons, selectively annihilating tumor cells that have incorporated boron. Although BNCT has demonstrated efficacy in the treatment of malignant gliomas, the reliance on Boronophenylalanine (BPA) for boron delivery has exposed certain limitations, including resistance observed in specific cell types, tissues, and varieties of cancer. This resistance highlights the necessity for innovative strategies to enhance BNCT's clinical efficacy and applicability. This study pivots towards the Alanine-serine-cysteine transporter 2 (ASCT2) - a transporter distinct from LAT1-investigating its potential as a gateway for the development of innovative boron carriers, with the aim of expanding the clinical applicability and effectiveness of BNCT.
****

EXPERIMENTS: This research embarked on in vitro investigations to evaluate boron accumulation in F98 and C6 rat glioma cells, and 9L rat gliosarcoma cells, following 24 hours of exposure to BPA and ASCT2-targetting new compound (GluB-2), each at a concentration of 10 μg B/mL. Complementary in vivo studies involved the intravenous administration of these compounds to an F98 rat brain tumor model, with the subsequent measurement of boron distribution within the tissues at intervals of 2.5, 6, and 24 hours post-administration. The therapeutic efficacy of these treatments was then evaluated through neutron irradiation experiments. The outcomes of these interventions were measured in terms of the survival periods of the treated subjects, offering valuable data on the viability and effectiveness of the investigated boron carriers in extending the life span of animals afflicted with glioma.
****

RESULTS: In vitro experiments revealed that GluB-2 achieved a significantly higher cellular boron concentration in F98 cells compared to BPA ($p=0.02$). In vivo, the peak of boron distribution in tumors occurred at 2.5 hours post-BPA treatment and at 6 hours post-GluB-2 treatment, with GluB-2 showing a superior maximum intratumor boron concentration. Survival analysis revealed mean survival periods of 28.0±2.5 days for the neutron-only group, 37.7±5.0 days for the BPA IV + BNCT group at 2.5 hours, 55.1±19.9 days for the GluB-2 IV + BNCT group at 6 hours, and 25.3±1.4 days for the untreated group. Remarkably, the GluB-2 IV + BNCT group demonstrated significantly prolonged survival compared to the BPA IV + BNCT group ($p<0.001$, log-rank test). These findings highlight the potential of GluB-2 as an effective boron carrier for enhancing BNCT efficacy in glioma treatment.
****

These results suggest that GluB-2 holds promise as a superior boron carrier for enhancing the efficacy of BNCT in treating glioma.

CO7-13

Basic research on new BNCT strategies for melanoma

H. Michiue[1], T. Fujimoto[1,2], N. Kanehira[1,2], K. Igawa[1], M. Shirawaka[1] Y. Sakurai[3], N. Kondo[4], T. Takata[3], and M. Suzuki[3]

[1]Neutron Therapy Research Center, Okayama University; 2-5-1, Shikata-cho, Kita-ku, Okayama City, Okayama, Japan.
[2]Department of Gastroenterological Surgery, Okayama University; 2-5-1, Shikata-cho, Kita-ku, Okayama City, Okayama, Japan.

[3]Institute for Integrated Radiation and Nuclear Science, Kyoto University, 2-1010, Asashiro-Nishi, Kumatori-cho, Sennan-gun, Osaka, Japan.

INTRODUCTION: The starting point for melanin synthesis in vivo is aromatic amino acids such as phenylalanine and tyrosine, and melanin synthesis is enhanced in cutaneous malignancies such as malignant melanoma. Boron-phenylalanine (BPA), a boron atom bonded to these amino acids, was created as a melanoma-targeted boron drug, and the success of BPA-BNCT was demonstrated in the 1989 Lancet article by Dr Mishima et al: "Treatment of malignant melanoma by single Malignant melanoma by single thermal neutron capture therapy with melanoma-seeking 10B-compound", published by Dr Mishima et al in the Lancet in 1989 [1]. This clinical study paved the way for the effectiveness of BNCT with boron drugs with cell-specific uptake and neutron irradiation of the cancer tissue area.

Melanoma is a cutaneous malignancy with an incidence of 1-2 per 100 000 people and is considered a rare cancer. In Australia, it is a disease with regional and racial variation, with an incidence of around 35 per 100 000 people. Surgery is the standard treatment of first choice for localized melanoma, and the prognosis is very good for Stage I melanomas, which have a low likelihood of spreading to the regional lymph nodes. The prognosis, mainly surgery, for localized melanoma is very good with a 5-year survival rate of 95-100% and the disease is reported to be curable by surgery. The usefulness of BNCT for localized melanoma is that there is no pain or functional impairment associated with surgery, which makes BNCT highly useful for melanoma patients, many of whom are elderly.

Clinical trials with BPA-BNCT for cutaneous malignancies (melanoma, angiosarcoma) are currently underway at the National Cancer Centre, and the results of the efficacy in these trials are expected.

While the efficacy of mainly surgical therapies in localized melanoma has been established, the development of treatments in inoperable advanced-stage melanoma is setting a new direction for malignancies as a whole. In particular, the discovery of immune checkpoint inhibitors targeting PD-1 by Professor Honjo Tusk and colleagues, who were awarded the 2018 Nobel Prize in Physiology or Medicine, has led to new breakthroughs in cancer treatment. Immune cells in our bodies are quick to attack foreign invaders such as viruses. On the other hand, they are unable to attack cancer cells that originate from our own cells because they are our own cells, even if they multiply in the body. Dr Honjo and colleagues have shown that the reason for the immune cells' inability to recognize antigens on cancer cells is due to the binding of an immune checkpoint molecule called PD-1 on the surface of cytotoxic T cells.

****

EXPERIMENTS: We purchased the B16-F10 mouse melanoma cell line to create a melanoma model, B16-F10 has high melanin synthesis capacity and has a large amount of black mel-anin pigment even in cultured cells. We used melanoma model mice transplanted with B16-F10 into C57BL/6 mice and Balb/c nu/nu mice. Animal experiments were performed after strict approval by the ethics committees for animal experiments at Okayama University and Kyoto University.

Experiments were conducted targeting CD8-positive T cells to verify the immune effects of cytotoxic T cells.**********

RESULTS: We used BPA as an effective boron agent for melanoma and confirmed the anti-tumor effect of neutron irradiation. The results suggest that anti-tumor immunity is influenced by the function of CD8-positive T cells. The results were favorable, and are useful for the development of BPA-BNCT for melanoma in the future. We would like to express our deepest gratitude to the many collaborators who assisted in this project.

****

REFERENCES: [1] Y. Mishima *et al.,* Lancet, **334** (1989) 388–389.

CO7-14

New boron drug development research targeting pancreatic cancer

H. Michiue[1], T. Fujimoto[1,2], N. Kanehira[1,2], K. Igawa[1], Y. Sakurai[3], N. Kondo[4], T. Takata[3], and M. Suzuki[3]

[1]Neutron Therapy Research Center, Okayama University; 2-5-1, Shikata-cho, Kita-ku, Okayama City, Okayama, Japan.
[2]Department of Gastroenterological Surgery, Okayama University; 2-5-1, Shikata-cho, Kita-ku, Okayama City, Okayama, Japan.
[3]Institute for Integrated Radiation and Nuclear Science, Kyoto University, 2-1010, Asashiro-Nishi, Kumatori-cho, Sennan-gun, Osaka, Japan.

INTRODUCTION: Pancreatic cancer refers to malignant tumors arising from the pancreas, but generally refers to pancreatic ductal carcinoma. Ductal carcinoma originates from the pancreatic duct epithelium and accounts for 80-90% of all neoplastic lesions in the pancreas. According to national statistics, it was the fifth leading cause of death after lung cancer, stomach cancer, colorectal cancer, and liver cancer. Pancreatic cancer in our country has been on the rise in recent years, with more than 30,000 people dying from pancreatic cancer each year.

The number of pancreatic cancer deaths has increased more than eightfold in the past 30 years, and the disease is more common in people in their 60s and slightly more common in men. It has been associated with smoking, family history of pancreatic cancer, diabetes, and chronic pancreatitis. Ultrasonography, CT, MRI, endoscopic pancreatography, and angiography are used to diagnose pancreatic cancer. If pancreatic cancer is suspected, the pancreas cannot be seen from the surface of the body, so an ultrasound or CT scan is first performed to check for the presence of a mass in the pancreas. CT scan can also be used to check for metastasis of pancreatic cancer to other organs such as the lungs and liver. One of the characteristic imaging findings of pancreatic cancer is that the normal pancreas is contrasted without contrasting the pancreatic cancerous area when contrast enhanced CT scan is performed. Usually, malignant tumors have more pronounced tumor vascular growth than normal tissues due to the rapid development of tumor blood vessels to nourish the tumor. In addition, these tumor vessels maintain a very leaky structure to provide a high degree of oxygen and nutrition to the tumor and are easily detectable using contrast media. However, pancreatic cancer, despite being a malignant tumor, is characterized by the fact that tumor blood vessels are somewhat scarce compared to normal, and the stroma between tumor cells is hyperplastic, making it difficult to receive the contrast effect of contrast media.

DDS (Drug Delivery System) is a research field that delivers drugs such as anticancer agents to such malignant tumors. It has been reported that when a liposomal formulation containing a drug is administered to a tumor-bearing model, such a macromolecular drug accumulates specifically in the tumor by leaking from the tumor blood vessels. This effect is called the EPR effect (Enhanced Permeability and Retention effect) and has been proposed as a theory that minimizes drug damage to normal tissue and maximizes the effect on tumor tissue. For pancreatic cancer that does not undergo contrast effect, we believe that it is difficult to use polymeric DDS formulations, which mainly have EPR effect, for future clinical applications. Therefore, we focused on PET (Positron Emission Tomography) using 18F-FDG, which is used in the diagnosis of pancreatic cancer. FDG is a test reagent of a glucose derivative called fluorodeoxyglucose F18. Glucose is labeled with 18F, a radionuclide, and is used as a test reagent for various types of cancer. In this study, we focused on glucose metabolism in cancer, and decided to develop a glucose-based boron drug [1].

****

EXPERIMENTS: In the present study, we planned to develop a boron drug for pancreatic cancer, a small molecule compound that does not utilize the EPR effect and targets glucose transporters. We focused on the tumor marker carbohydrate antigen CA19-9, called carbohydrate antigen 19-9, in the classification of pancreatic cancer. It has a high positive predictive value for cancer and is known to be elevated in uterine, ovarian and lung cancers, etc. Pancreatic cancers with high CA19-9 levels are known to have a poor prognosis and a CA19-9 high human pancreatic cancer cell line and CA19-9 low pancreatic cancer cells were used in the present experiment. Experiments were conducted with three different boron agents: glucose boron, BPA and BSH.

****

RESULTS: The glucose boron drug was found to be efficiently introduced into cells via glucose transporters (GLUTs), which are highly expressed in pancreatic cancer. The anti-tumor effect of a novel drug agent in a mouse model of pancreatic cancer was confirmed in vitro and in vivo by neutron irradiation in a nuclear reactor, CA19-9, at the Institute for Complex Nuclear Science, Kyoto University, where a high therapeutic effect was obtained in a pre-experiment. The results are further developed and reported as a novel boron drug for targeting pancreatic cancer with high CA19-9 levels.

****

REFERENCE: [1] Leone RD. *et al.,* Science, **366(6468)** (2019) 1013-1021.

CO7-15

Evaluation of A Retinoid X Receptor-binding BSH Derivative for Inhibition of Cell Proliferation under Neutron Irradiation

Hiroki Kakuta[1], Ryuya Otani[1], Atsushi Mashimo[1], Yuta Takamura[1], Natsuko Kondo[2], Yoshinori Sakurai[2]

[1]*Division of Pharmaceutical Sciences, Okayama University Graduate School of Medicine, Dentistry and Pharmaceutical Sciences.*

[2]*Institute for Integrated Radiation and Nuclear Science, Kyoto University.*

INTRODUCTION: While boron compounds that target nuclear receptors have been reported, there is no information regarding the use of these compounds for neutron irradiation. The substances identified as these molecules contain carboranes, which are boron clusters (Ref. 1). The authors chose to create more hydrophilic boron compounds because they believed that although carboranes' high lipid solubility enhances intracellular storage, it may also cause cytotoxicity and reduce water solubility. Through synthesizing several compounds that bind to the retinoid X receptor (RXR), the authors discovered that CBTF-EE-BODIP (**1a**), in combination with the fluorescent cluster BODIPY that contains boron, had RXR-binding characteristics (Ref. 2). Thus, compound **1b** was made by substituting BSH for the BODIPY moiety of **1a**. Its intracellular concentration was then determined, and colony experiments using neutron irradiation and medication therapy were carried out on the RXR-expressing human breast cancer cell line MCF-7.

EXPERIMENTS: Chemical compounds were synthesized by the authors. MCF-7 cell line was obtained from RIKEN BioResource. A maximum exposure concentration of **1b** was set at 100 μM and a 24-hour exposure period. Following chemical exposure, cells were harvested, trypsin-EDTA treated, and washed with PBS. All of the resultant cells were lysed using RIPA buffer, and ICP-MS (Agilent 7900/MassHunter) was used to measure the content of ^{10}B in the resulting samples. For neutron irradiation experiment, the cells treated were then centrifuged in a 15 mL centrifuge tube, aspirated off, and 2 mL of media was added to count the number of cells. After transferring one milliliter of the cell suspension into 1.5 mL Eppendorf tubes, the samples were exposed to 1.2×10^{12} cm^{-2} (5 MW, 2 min) of thermal neutron fluence. After that, cells were sown at a density of 1×10^3 cells/well in 12-well plates and cultivated for 7 days at 37°C with 5% CO_2. Following the medium removal, cells were stained with crystal violet, fixed in 80% EtOH, and the number of colonies was counted. To calculate the colony formation rate, the total number of colonies was divided by the total number of implanted cells. Also, WST-8 experiment was performed according to supplier's protocol, after adding 10 μL of WST-8 reagent to each well, cells were incubated at 37°C for 2 hours and absorbance at 450 nm was measured with a plate reader.

RESULTS: **1b** gave an intracellular boron content of *ca* 1 fmol/cell. This is equivalent to the macrocyclic polyamine compounds reported by Ueda et al. (Ref. 3), albeit being less than borofaran. It was therefore anticipated that this would prohibit cell proliferation when exposed to neutron radiation. WST-8 and colony assays were conducted on cells that had been exposed to compound **1b** for 24 hours at a final concentration of 100 μM. The cells were then exposed to neutron irradiation. The outcomes demonstrated that compound **1b** clearly inhibited cell proliferation. These results shed light on the potential utility of boron compounds that bind to nuclear receptors as boron delivery carriers for BNCT and indicate that **1b** may be employed as an intracellular 10B carrier.

REFERENCES:

[1] a) Chem. Pharm. Bull., (Tokyo), **47** (1999) 398-404. b) Bioorg. Med. Chem Lett., **14** (2004) 5913- 5918. c) Chem Pharm. Bull., (Tokyo). **48** (2000) 312-314. d) J. Am. Chem. Soc., 2011, **133** (2011) 20933-20941. [2] ACS Med. Chem. Lett., **12**(2021) 1024-1029. [3] J. Med. Chem., **64** (2021) 8523-8544.

CO7-16

Intracellular Uptake of BSH in Combination with An Existing Drug and Effects of Neutron Irradiation

Hiroki Kakuta[1], Atsushi Mashimo[1], Natsuko Kondo[2], Yoshinori Sakurai[2]

[1]Division of Pharmaceutical Sciences, Okayama University Graduate School of Medicine, Dentistry and Pharmaceutical Sciences.
[2]Institute for Integrated Radiation and Nuclear Science, Kyoto University.

INTRODUCTION: A cancer treatment called boron neutron capture therapy (BNCT) uses the nuclear reaction that occurs between neutrons and boron-10 (^{10}B). The amount of boron present in the cancer tissue is crucial since the treatment's efficacy is dependent on the collision of neutrons and ^{10}B. Two of the substances that have undergone clinical testing are BSH, a boron cluster, and borofaran, a phenylalanine derivative. Borofaran is authorized for use in medicine, and its absorption into cancer cells is facilitated by the amino acid transporter LAT-1. Tissues with low LAT-1 expression induce low borofaran delivery. BSH, on the other hand, is an anionic substance with incredibly limited cell membrane permeability. Thus, the goal of this study was to provide a novel approach.

BSH is an anionic material with extremely low cell membrane permeability. Michiue et al. reported employing the surfactant peptide A6K to deliver BSH intracellularly as a remedy (Ref. 1). The purpose of this study was to see whether any other medications, aside than A6K, might be utilized to enhance BSH's intracellular delivery. For intellectual property purposes, this study's result, which is an existing medication that increases BSH's intracellular delivery capacity, shall be referred to as drug A.

EXPERIMENTS: Using mouse B16BL6 cells, the intracellular delivery of BSH was investigated: After cultivating B16BL6 cells in six-well plates, the cells were exposed to the test compound-containing media for six hours. Following this, PBS rinsed, and cell lysates were made. The procedure used to identify CR-39 cells using BNCR was as follows: In 6 well plates (2 cm square), cells were cultivated, immersed in CR-39 medium, and then exposed to the test compound-containing medium for two hours. Following a PBS wash, the cells were processed to create cell lysates. Neutrons were used to irradiate the CR-39 cells. At KUR, a 20-minute exposure to 1 MW of neutron radiation resulted in a thermal neutron fluence of 2.22×10^{12} cm^{-2}. Samples were divided into four categories: BSH (500 μM) alone, BSH (500 μM) + drug A (0.002 mg/mL), BSH (500 μM) + drug A (0.02 mg/mL), and BSH (500 μM) + drug A (0.2 mg/mL).After neutron irradiation, the materials were treated with alkali according to Ref 1 and photographed using an optical microscope and processed in accordance with Ref. 2. Image J performed an analysis on the photographs.

RESULTS: Examining the intracellular translocation of BSH alone and in combination with already-approved medication A, it was shown that the latter significantly increased intracellular boron concentration as compared to a 2-hour exposure to 500 μM BSH alone. BSH alone or in conjunction with drug A was administered to B16BL6 cells seeded on CR-39 that had measurable BNCR, and the cells were exposed to neutron radiation. After irradiation, etch pits on CR-39 were measured. The findings showed that treatment with drug A raised the BNCR and, in a concentration-dependent manner, the intracellular absorption of BSH.

REFERENCES:

[1] H. Michiue *et al.,* J. Control Release., **330** (2021) 788–796.
[2] T. Kusumoto *et. al.,* Radiat. Res., **191** (2019) 460-465.

CO7-17

Evaluation of Retinoid X Receptor Degradation by a RXR-Binding BSH Derivative under Neutron Irradiation

Hiroki Kakuta[1], Yukina Tanaka[1], YutaTakamura[1], Natsuko Kondo[2], Yoshinori Sakurai[2]

[1]*Division of Pharmaceutical Sciences, Okayama University Graduate School of Medicine, Dentistry and Pharmaceutical Sciences.*
[2]*Institute for Integrated Radiation and Nuclear Science, Kyoto University.*

INTRODUCTION: In order to achieve intracellular boron concentrations necessary to generate boron neutron capture reactions (BNCR), we have concentrated on developing boron agents that specifically target intracellular receptors. Among the several retinoid X receptor (RXR) binding compounds that we have so far produced, CBTF-EE-BODIP (**1a**, Fig. 1) with a fluorescent group that contains bo-ron, BODIPY, demonstrated RXR binding (Ref. 2). This time, we made **1b** (Fig. 1) by substituting BSH for the fluorescent group BODIPY moiety of **1a**, and we discovered that it inhibits cell proliferation when exposed to neutrons (R5047). Our goal in this work was to verify whether neutron irradiation cleaves RXR itself when it is attached to **1b**.

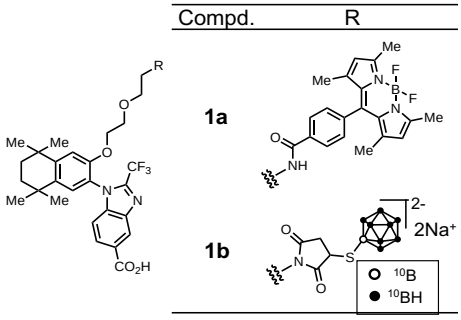

Figure 1. Chemical structures of **1a** and **1b**.

EXPERIMENTS: Chemical compounds were synthesized by us, and HPLC verified that they were at least 95% pure. RXR ligand binding domain (RXRα-LBD) was kindly provided by Prof. Nakano at the University of Shizuoka. Reporter gene tests toward RXR were conducted following Refs. 1 and 2. The radiation level of the neutron beams was 2.9×10^{13} cm^{-2}. RXRα-LBD (10 μM), **1b** (200, 100, 50 μM, converted to ^{10}B concentrations of 24, 12, 6 ppm), bexarotene (20 μM or no addition), and buffer (10 mM HEPES, 150 mM NaCl, 2 mM $MgCl_2$, 5 mM DTT, 5% DMSO) were the preparation methods for irradiated samples (100 μL). The aforesaid buffer was used to dilute the irradiated samples ten times, then they were combined with a 4:1 composition of BPB-containing buffer and electrophoresed for 70 minutes at 250 V and 20 mA. CBB staining was used to assess the RXRα-LBD concentration.

RESULTS: The binding affinity of **1b** to RXRα-LBD measured using the fluorescent RXR ligand, **1a**, was *K*i = 3 μM. When **1b** was present at the concentration ratios, neutron irradiation did not produce band splitting that would have indicated RXR cleavage; instead, a 24-hour incubation with 100 μM **1b** produced a concentration of 1 fmol/cell, and additional neutron irradiation at 1.2×10^{12} cm^{-2} inhibited cell growth. It has been discovered that there is inhibition of cell proliferation (R5047). The results of this experiment indicate that there is no cleavage of RXR in these circumstances, which may indicate that boron compounds that target nuclear receptors are effective boron delivery vehicles for BNCT.

REFERENCES:

[1] M. Watanabe *et. al.,* J. Med. Chem., **64** (2021) 430-439.
[2] M. Takioku *et al.,* ACS Med. Chem. Lett., **12** (2021) 1024-1029.

CO7-18

Mechanism of Glioma Resistance After BNCT via Small Extracellular Vesicles

Natsuko Kondo[1], Tadatoshi Kinouchi[2], Manabu Natsumeda[3], Eishu Hirata[4], Yoshinori Sakurai[1], and Minoru Suzuki[1]

Graduate School of Science, Kyoto University

[1] Particle Radiation Oncology Research Center, and [2]Division of Radiation Biochemistry, Institute for Integrated Radiation and Nuclear Science, Kyoto University

[3]Department of Neurosurgery, Brain Research Institute, Niigata University,
[4] Division of Tumor Cell Biology and Bioimaging, Cancer Research Institute of Kanazawa University

INTRODUCTION: Boron Neutron Capture Therapy (BNCT) have been applied to recurrent malignant glioma and even after standard therapy (surgery, chemo-radiation therapy) because of the selective damage to the tumor. Especially, glioblastoma (GBM) is the most miserable cancer, whose patient survival is 14.6 months and remarkably resistant to chemo-radiation and immuno-therapy. With BNCT, we achieved better local control and survival benefit in malignant glioma using thermal neutrons produced by the reactor in Kyoto University. However, the recurrence locally or distantly is inevitable after BNCT. And distant recurrences, named cerebrospinal fluid (CSF) space dissemination, more frequently occur after BNCT compared with the cases after standard radiation-chemotherapy. Reasons for recurrence after BNCT have not been fully elucidated. Small extracellular vesicles (sEVs) are small membrane vesicles with sizes ranging from 50 to 150 nm. They serve as functional mediators and promote intercellular communication during physiological and pathological processes. including migration, treatment resistance, and metastasis in cancer. miRNAs are encapsulated in lipid membranes such as extracellular vesicles in blood and body fluids, exist stably, are taken up by the cells they reach, and act negatively on target genes, performing post-translational modification. In this study, we investigate miRNAs in sEVs secreted from glioblastoma cells after BNCT using microarray, which may explain the possible mechanism of local recurrence or CSF dissemination after BNCT.

EXPERIMENTS:

BPA Treatment and Neutron irradiation

Glioblastoma U87 MG cells were treated with 25 ppm of BPA in the culture media for 2 hours and irradiated with thermal neutrons in plastic tubes for 70 min.

After irradiation, they were plated into dishes and cultured for 3 days in the 5 % CO2 incubator. Then, sEVs released into the medium were collected by column chromatography, and miRNAs in sEVs were comprehensively investigated using microarrays.

RESULTS: An increase in 21 individual miRNAs (ratio>2) and a decrease in 2 individual miRNAs (ratio<0.5) were detected in BNCT cells compared to non-irradiated cells. Up-regulated miRNAs included miR-650, a prognostic marker in malignant glioma, miR-3147, which may serve an oncogenic role in vulvar squamous cell cancer, miR-4725-3p, which is known to be involved in xanthohumol, a prenylated flavonoid extracted from the hop plant Humulus lupulus L., inhibition of glioma invasion, and miR-4270, that is reported to modulate radiation sensitivity in nasopharyngeal squamous carcinoma.

CO7-19

Rational Design, Multistep Synthesis and in Vitro Evaluation of Poly (glycerol) Functionalized Nanodiamond Conjugated with Boron-10 Cluster and Active Targeting Moiety for Boron Neutron Capture Therapy

Masahiro Nishikawa,[1,2] Jie Yu,[1] Heon Gyu Kang,[1] Minoru Suzuki,[3] and Naoki Komatsu [1]

[1] *Graduate School of Human and Environmental Studies, Kyoto University*
[2] *Innovation and Business Development Headquarters, Daicel Corporation*
[3] *Institute for Integrated Radiation and Nuclear Science, Kyoto University*

Boron neutron capture therapy (BNCT), advanced cancer treatment utilizing nuclear fission of ^{10}B atom in cancer cells, is attracting increasing attention. As ^{10}B delivery agent, sodium borocaptate (^{10}BSH, $^{10}B_{12}H_{11}SH{\cdot}2Na$), has been used in clinical studies along with L-boronophenylalanine (BPA). Recently, this boron cluster has been conjugated with lipids, polymers or nanoparticles to increase selectivity to and retentivity in tumor. In this work, we designed the anticancer nanoformulations for BNCT consisting of poly(glycerol) functionalized detonation nanodiamonds (DND-PG) as a hydrophilic nanocarrier [1], the boron cluster moiety ($^{10}B_{12}H_{11}^{2-}$) as a dense boron-10 source, and phenylboronic acid or RGD peptide as an active targeting moiety (Fig. 1) [2]. Some hydroxy groups in PG were oxidized to carboxy groups (DND-PG-COOH) to conjugate the active targeting moiety [3]. Some hydroxy groups in DND-PG-COOH were then transformed to azide to conjugate $^{10}B_{12}H_{11}^{2-}$ through click chemistry [4]. The nanodrugs were evaluated *in vitro* using B16 murine melanoma cells in terms of cell viability, BNCT efficacy and cellular uptake. As a result, $^{10}B_{12}H_{11}^{2-}$ moiety is found to facilitate cellular uptake probably due to its negative charge. Upon thermal neutron irradiation, the nanodrugs with $^{10}B_{12}H_{11}^{2-}$ moiety exhibited good anticancer efficacies with slight differences with and without targeting moiety [5].

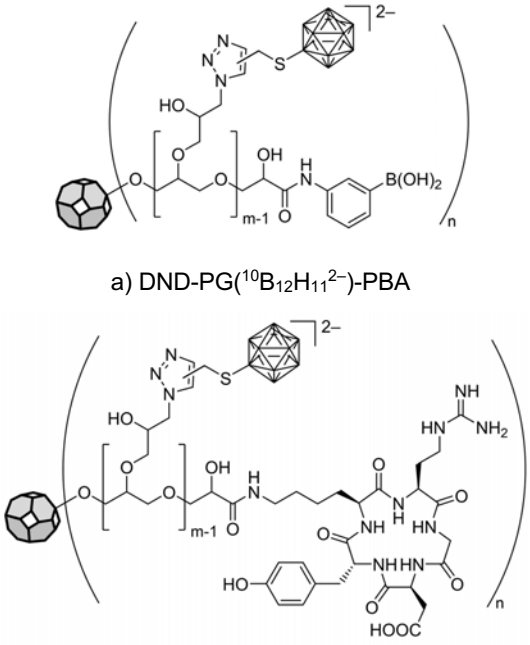

a) DND-PG($^{10}B_{12}H_{11}^{2-}$)-PBA

b) DND-PG($^{10}B_{12}H_{11}^{2-}$)-c(RGDyK)

Fig. 1. Chemical structures of DND-PG conjugated with ^{10}B cluster ($^{10}B_{12}H_{11}^{2-}$) and phenylboronic acid (PBA) (a) or cyclic peptide (L-Arg-Gly-L-Asp-D-Tyr-L-Lys) (b).

REFERENCES:

[1] L. Zhao *et al.,* Angew. Chem. Int. Ed., **50(6)** (2011) 1388-1392. [highlighted at back cover].
[2] M. Nishikawa *et al.,* Bull. Chem. Soc. Jpn., **94(9)** (2021) 2302-2312. [selected paper, highlighted at the inside cover].
[3] M. Nishikawa *et al.,* ChemNanoMat, **9(9)** (2023) e20230020. [highlighted at the front cover, open access].
[4] L. Zhao *et al.,* Adv. Funct. Mater., **24 (34)** (2014) 5348-535. [highlighted at the inside front cover].
[5] M. Nishikawa *et al.,* Chem. Eur. J., **29(63)** (2023) e202302073. (11 pages)[highlighted at the cover, hot paper].

CO7-20

Development of Novel Small-molecule Boron Neutron Capture Therapy Drugs Targeting Tumor-specific Enzymatic Activity

J. Tsunetomi[1], M. Suzuki[2], Y. Urano[1,3]

[1] *Graduate School of Pharmaceutical Sciences, The University of Tokyo*
[2] *Institute for Integrated Radiation and Nuclear Science, Kyoto University*
[3] *Graduate School of Medicine, The University of Tokyo*

INTRODUCTION: In boron neutron capture therapy (BNCT), p-boronophenylalanine (BPA), the only approved BNCT agent, is selectively taken up by tumor cells through LAT1, which is a biomarker-transporter over-expressed in tumor cells. However, BPA faces the following challenges: 1) BPA accumulation is insufficient in some types of cancer because of poor LAT1 expression, and 2) BPA gradually leaks out of cells over time. Therefore, the development of new BNCT drugs that target another cancer biomarker and have a mechanism for prolonged intracellular retention is necessary to expand the indications for BNCT and improve therapeutic effect.
In this project, we focused on aminopeptidase activities which were proved to be higher in cancer cells than peripheral normal cells, and by utilizing these enzymatic activities we designed and synthesized EP-4OCB-FMA, a novel small-molecule carborane-containing drug candidate targeting DPP-4 activity which is known to be upregulated in esophageal cancers in human patients [1]. This drug is designed to stay inside cells for a long time by generating aza-quinone methide species by being hydrolyzed by DPP-4, which is enough nucleophilic to form a covalent bond with intracellular nucleophiles such as proteins and glutathione. Last year, we conducted BNCT experiments with tumor bearing mice by injecting EP-4OCB-FMA intratumorally, and found that tumor growth was suppressed in a drug-, enzyme-, and neutron-irradiation-dependent manner. These results indicate that EP-4OCB-FMA is a useful BNCT drug that targets tumor cell-selective enzymatic activity with an intracellular retention ability. So this year, we started to inject EP-4OCB-FMA systemically, and examined the blood half-life and accumulated boron atoms in tumors and surrounding normal tissues by LC-MS and E3.

EXPERIMENTS: EP-4OCB-FMA was then administered intravenously to obtain the blood half-life and various kinetic parameters. Specifically, EP-4OCB-FMA was injected intravenously into mice at a dose of 40 mg/kg intravenously by tail, and after intraperitoneal administration of a triad of anesthetics at a predetermined time, blood was collected from the heart. Then, protein was removed from the collected whole blood and the concentration of EP-4OCB-FMA was analyzed by LC-MS. For comparison, EP-FMA without carborane skeleton was also evaluated.

RESULTS: The blood half-life of EP-4OCB-FMA was estimated to be 0.40 h. Given that the concentration of EP-FMA without carborane was so low that the blood half-life could not be calculated, it is suggested that the blood half-life is considerably prolonged by the carborane structure. This may be due to the interaction of EP-4OCB-FMA with blood albumin via the carborane backbone, as described above. On the other hand, however, the blood half-life of 0.40 h was not sufficient, suggesting that it was lost from the blood very quickly. The poor blood retention is likely due to excretion of the drug from the liver and kidneys, and indeed high boron concentrations have been detected in urine. From these results, we started to re-design the probe molecule targeting another peptidases whose structure is based on the Protide chemistry, and completed its synthesis. Evaluation of the accumulated boron atoms with living cells are now on going, and BNCT experiments will be conducted next year.

REFERENCES: [1] H. Onoyama *et al.,* Sci Rep., **6** (2016) 26399.

CO7-21

Synthesis of PEPT1-targeted boron containing dipeptides for pancreatic cancer therapy

F. Tamanoi[1], K. Matsumoto[1], A. Komatsu[1], Y. Higashi[1] and M. Suzuki[2]

[1]*Institute for Advanced Study, Institute for Integrated Cell-Materials Sciences, Kyoto University*
[2]*Institute for Integrated Radiation and Nuclear Science, Kyoto University*

INTRODUCTION: Peptide transporter 1 (PEPT1) is of interest because it is expressed in various types of cancer cells. It has been reported that PEPT1 is highly expressed in pancreatic cancer cells. Earlier studies showed that boron containing dipepetides are taken up by PEPT1 transporter. However, BNCT efficacy of these dipeptides has not been investigated. We have synthesized ^{10}B containing dipeptides that have higher solubility and longer retention time in the tumor than BPA. We investigated whether these ^{10}B-dipeptides have better BNCT efficacy than BPA using KUR.

EXPERIMENTS: We synthesized three types of dipeptides. They were intravenously injected to CT26-tansplanted BALB/c mice or FaDu-transplanted nude mice. Boron contents in the tumor were investigated by ICP. We then investigated whether these reagents exhibit improved BNCT efficacy compared with BPA by neutron irradiation at KUR. They were intravenously injected into mice 2 hours before neutron irradiation (12 minutes at 5MW). After neutron irradiation, tumor volume and body weight were measured for 6 weeks (up to 42 days after irradiation).

RESULTS: The dipeptides synthesized showed higher solubility than BPA; they can be dissolved in solvents that include water. When injected into tumor-bearing mice, a significantly higher concentration of boron was detected in tumor samples compared to BPA. We also observed a longer retention time (>4 hours) in the tumor.
We then investigated BNCT efficacy of these boron compounds. They were intravenously injected into CT26-transplanted mice 2 hours before neutron irradiation. These mice were held to 12 mouse holder and placed in front of KUR, and neutron irradiation was carried out. Tumor was almost disappeared with dipeptides-injected mice and tumor regrowth was not observed up to 27 days after the irradiation. In contrast, tumor regrowth was observed in BPA-injected mice. Similar results were obtained using FaDu-transplanted mice. FaDu tumor was almost eliminated with these boron reagents. These results show that newly synthesized dipeptides provide a promising reagent for BNCT. We are in the process of preparing a paper to be submitted for publication.

CO7-22

Construction of novel boron-containing silica nanoparticles and BNCT experiments

F. Tamanoi[1], K. Matsumoto[1], A. Komatsu[1], Y. Higashi[1] and M. Suzuki[2]

[1]*Institute for Advanced Study, Institute for Integrated Cell-Materials Sciences, Kyoto University*
[2]*Institute for Integrated Radiation and Nuclear Science, Kyoto University*

INTRODUCTION: We continue to develop novel boron containing nanoparticles for BNCT. We have previously developed BPA-BPMO and BSH-BPMO and have used tumor spheroids and mouse models to demonstrate their BNCT efficacy. However, it is necessary to improve their tumor accumulation capability. Tumor accumulation is influenced by various features of nanoparticles. To do this, we are systematically changing features of the nanoparticles including size and surface charge. We are also including PEG surface modification. To examine tumor accumulation, we are using mouse model systems and ICP measurements.

EXPERIMENTS: Various nanoparticles were examined for their tumor accumulation in mouse models. We are particularly interested in small size nanoparticles that have weakly positive surface charge as well as PEG. These nanoparticles will be injected intravenously into mice and tumor accumulation of the nanoparticles will be investigated by Rhodamine-B fluorescence as well as by ICP measurement of boron and silicon. CT26 as well as FaDu transplanted mouse models will be used. In addition, we will use the CAM model prior to the mouse experiments to gain insight into the tumor accumulation of the nanoparticles. For the mouse experiments, different routes of nanoparticle administration including iv, ip and sc will be tested. To achieve successful tumor accumulation by the EPR mechanism, it is necessary for the nanoparticles to have prolonged circulation time. We will test 3, 12, 24 and 36 hours after injection to test tumor accumulation. Nanoparticles will be intravenously injected to mice at 5 mg/mouse or 2 mg/mouse. We will dissect tumor as well as various organs which include liver, lung, spleen, intestine and kidney. Nanoparticle fluorescence will be detected with an inverted fluorescence microscope. Moreover, tumor and organs will be ashed with the mixture that includes perchrolic acid and hydrogen peroxide and then silica and boron contents in tumor and each organs will be examined by ICP analysis.

RESULTS: We tested nanoparticles that have less than 50 nm of diameter. SEM and TEM microscopy were used to analyze the nanoparticles. We found that these nanoparticlea are homogeneous and well dispersed.
As a preliminary test, we used the CAM model, a simple and convenient model that uses fertilized eggs. After incubation for eight days, a window was made on the egg shell and human cancer cells are placed on the CAM membrane. Tumor growth was observed in four to five days. At four days, the nanoparticles were injected intravenously and tumor accumulation of the nanoparticles was confirmed.
We then tested tumor accumulation of the nanoparticles in the CT26 transplanted mouse models. Examination of the tumor and various organs including liver, lung and kidney by fluorescent microscope showed excellent tumor accumulation. Fluorescence in the liver was observed but this was less than that found with the tumor. Maximum tumor accumulation was observed 24 hours after the injection.

CO7-23

Antitumor effect of boron neurton capture therapy in cervical cancer mouse model

A Toji[1], S Terada[1], S Tsunetoh[1], T Tanaka[1], M Ohmichi[1], J Arima[2], K Taniguchi[2], M Su-zuki[3]
1Department of Obstetrics and Gynecology, Osaka Medical and Pharmaceutical University, Takatsuki, Japan
2Department of general and gastroenterological sur-gery, Osaka Medical and Pharmaceutical University, Ta-katsuki, Japan
3Institute for Integrated Radiation and Nuclear Sci-ence, Kyoto University, Asasiro-Nishi, Kumatori-cho, Japan

INTRODUCTION: In Japan, approximately 10,000 women develop cer-vical cancer and 2,900 women die from the disease annually. The incidence and mortality rates of cervical cancer in Japan are on the rise. Squamous cell carci-noma (SCC) is the most common histological type at 80%, and adenocarcinoma (Adeno) accounts for about 20%. Main treatment options for cervical cancer are surgery or radiation therapy. However, sometimes se-rious adverse events occur, the new treatment modali-ties for cervical cancer are needed. In the present study, we investigated the efficacy and safety of boron neutron capture therapy (BNCT) for cervical cancer in a mouse model.

EXPERIMENTS: BPA (L-isomer) was supplied by Stella pharma (Osaka, Japan) and converted to fructose complex. 4-6 week-old female nude mice (BALB/c Slc-nu/nu) were purchased from SLC, Japan. Patient-derived xenograft (PDX) was created using cervical cancer tissue (SCC/Adeno). PDX is a procedure in which a patient's tumor tissue is transplanted into immunocompromised mice, and the response to treatment has been reported to be highly consistent with the effect on the pa-tients themselves. [1] Treatment was initiated 4-6 weeks af-ter cell injection. Mice were divided into cold control (no treatment), hot control (neutron irradiation only) and BNCT (peritoneal BPA fol-lowed by neutron irra-diation) groups. 2.5 hours before neutron irradiation, BPA (250 mg/kg) was injected intraperitoneally into mice in the BNCT group. After irradiation, tumor size and mouse weight were measured, and tumor volume was calculated as follows.
V=ab2/2

RESULTS: Fig.1 shows the tumor volume of squamous cell car-cinoma PDX in the cold control, hot control and BNCT groups. The tumor was suppressed in the BNCT group than in the hot control group ($P<0.05$). The body weight was no remarkable change in the both groups. Fig.2 shows the tumor volume of adenocarcinoma PDX in the hot control and BNCT groups. The tumor volume did not differ between the both groups.

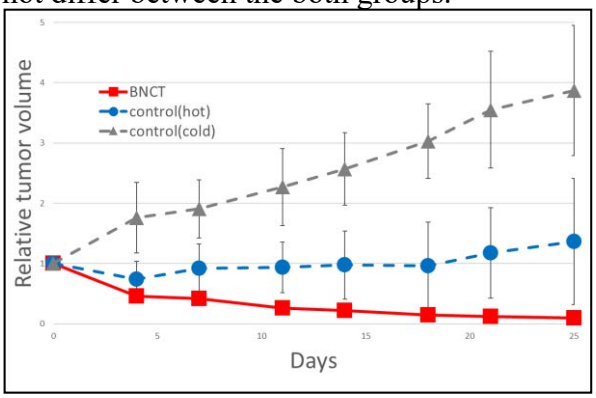

Fig.1 Antitumor effect on subcutaneous PDX (squamous cell carcinoma) tumor model.
Tumor grows curves in the cold control (no treat-ment) and the hot control (irradiation only) and BNCT (irradiation after BPA administration) groups (n=12).

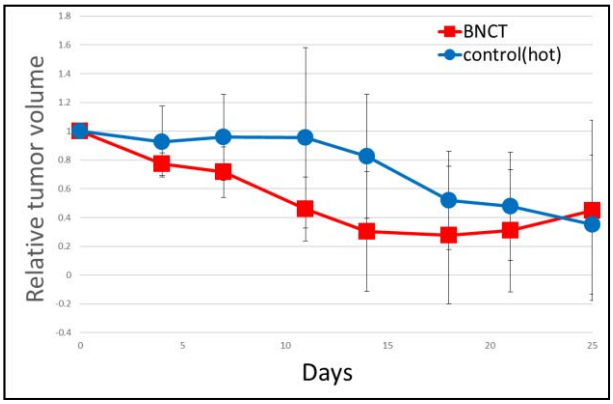

Fig.2 Antitumor effect on subcutaneous PDX (adeno carcinoma) tumor model.
Tumor grows curves in the hot control (irradiation only) and BNCT (irradiation after BPA administra-tion) groups (n=9). (n=12).

REFERENCES:

[1] Shahrokh Abdolahi *et al.,* J Transl Med., **20(1)** (2022) 206.

CO7-24

Quantitative Analysis of Elements Causing Activation in Radiation Shielding Concrete Using Internal Standards

T. Takata, K. Kimura[1], Y. Sakurai, H. Tanaka and K. Takamiya

Institute for Integrated Radiation and Nuclear Science, Kyoto University
[1]Fujita Corporation

INTRODUCTION: Concrete is widely used as radiation shield in nuclear reactors and accelerator facilities because of its flexibility, sufficient supply and low cost. On the other hand, in the cases of the reactors or high energy accelerators, once these facilities start operating, the shielding concrete becomes radioactive by nuclear reaction with neutrons generated. Under these circumstances, low-activation concrete is one of the ways to mitigate the problems such as human exposure and decontamination of the facilities. The application of low-activation concrete is particularly effective in accelerator facilities for BNCT, which uses high intensity neutrons. To estimate the level of activation, we have performed neutron activation analyses (NAA) on more than several hundred samples of shielding concrete and raw materials using KUR facilities [1]. In this report, we describe the internal standards utilized to reduce the uncertainties regarding to the experimental procedure of NAA, such as fluctuation of neutron flux and detection efficiency of a gamma-ray detector.

EXPERIMENTS: Three nuclides produced by reactions of ^{151}Eu(n,γ)^{152}Eu, ^{59}Co(n,γ)^{60}Co and ^{133}Cs(n,γ)^{134}Cs in concrete and raw materials were subject to quantitative NAA. An in-house reference powder samples (std_0) and commercially available rock reference materials (std_1) with known concentrations of Eu, Co and Cs were prepared as the internal standards. These standards and the samples subjected were encapsuled and irradiated simultaneously for 1 hour at Pn-2 under 1 MW operation of KUR. In addition to the capsules with the regular samples, the capsule with 12 standard samples (std_0) was prepared. The gamma-ray spectrum of each sample was measured one by one with an HP-Ge detector with automatic measurement system, where the photo-electric peaks at 1408 keV for ^{152}Eu, 1333 keV for ^{60}Co, and 795 keV for ^{134}Cs were analyzed.

RESULTS: Fig. 1(a) shows the inter-capsule variation of peak count rates with decay correction between 8 capsules. A similar trend was observed for all nuclides by the capsules, reflecting the flux fluctuation. Fig. 1(b) shows the intra-capsule variation of the count rates of 12 standards. A similar trend was observed for all nuclides by the samples, suggesting the influence of flux distribution in the capsule as well as insufficient uniformity of the elements between the standard samples.

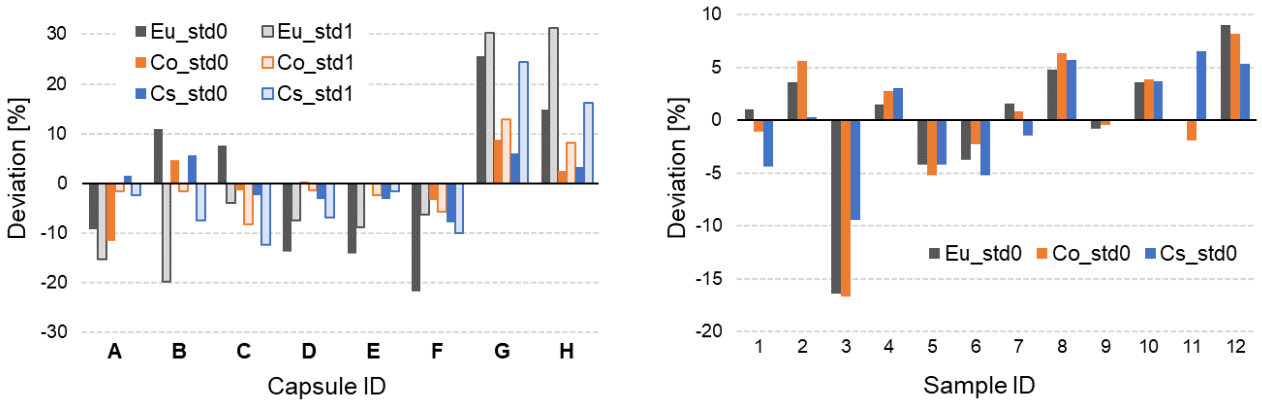

Fig. 1 (a) Inter- and (b) intra-capsule variation of peak count rates of the standard samples.

REFERENCES:

[1] K. Kimura *et al.,* KURNS Progress Report 2018–2022.

CO7-25

Examination of improvement of BNCT treatment efficiency by L-phenylalanine deficiency in mice tumor models

Y. Tamari[1, 2], R. Saba[1], T. Takata[2], M. Suzuki[2], H. Yamazaki[1], K. Yamada[1]

[1]*Department of Radiology, Kyoto Prefectural University of Medicine*
[2]*Institute for Integrated Radiation and Nuclear Science, Kyoto University*

INTRODUCTION: L-Boronophenylalanine (L-BPA), a boronated isotope of L-phenylalanine (Phe), is used as a boron drug and is taken up by the tumor through its enhanced metabolism of amino acids. LAT1 is an exchange transporter, releasing one amino acid molecule into the extracellular space for the uptake of one amino acid molecule into the cell [1]. However, L-BPA is also taken up by normal cells via LAT2 and other pathways [2], and the improvement of the boron concentration ratio (T/N ratio) between tumor and normal tissues has become an issue. In this study, we attempted to improve the therapeutic effect of BNCT by restricting Phe and improving L-BPA uptake.

EXPERIMENTS: 5.0 x 10^5 human tongue carcinoma-derived cell lines SAS were transplanted into the thighs of 6-week-old female nude mice. Two weeks after transplantation, the carcinoma-bearing mice were fed Phe-free feed, and 500 mg/kg of L-BPA was administered after 24 hours. At 0.5, 1, 2, and 3 hours after administration, each organ (blood, brain, lung, liver, tongue, intestine, muscle, skin, and kidney) containing tumor was sampled and boron concentration was measured by ICP-AES. Carcinoma-bearing mice were fed Phe-free feed for 24 hours, and 2 hours after administration of 500 mg/kg L-BPA, they were neutron irradiated. Neutron-irradiated carcinoma-bearing mice were kept until approximately one month after irradiation, during which time their body weight and tumor size were regularly measured.

RESULTS: Although Phe restriction did not significantly increase L-BPA uptake in non-tumor organs, Phe restriction significantly increased L-BPA uptake in tumor tissue.
Furthermore, the change in tumor size after neutron irradiation was strongly suppressed in the L-BPA neutron-irradiated group compared to the control and neutron-irradiated-only groups. In particular, tumor size in the Phe-restricted L-BPA and neutron irradiated group was significantly reduced compared to the L-BPA and neutron irradiated group without Phe restriction. There was no change in body weight in all groups after neutron irradiation.

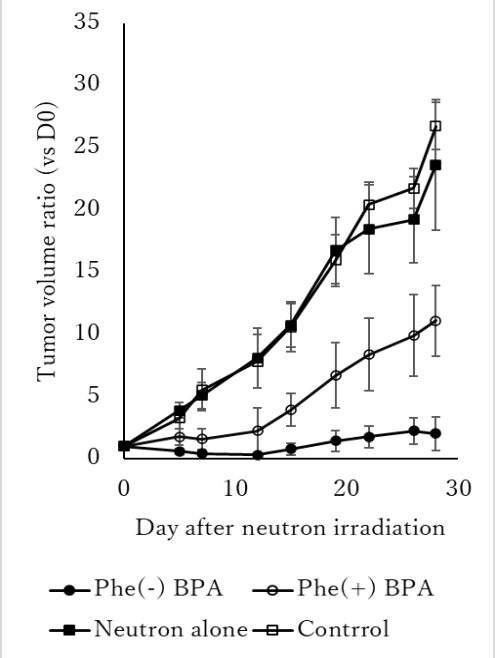

Fig. 1. Change over time in tumor size ratio after Phe-restricted BNCT.

REFERENCES:
[1] A. Wittig *et al*., Radiat Res., **153** (2000) 173-180.
[2] P. Wongthai *et al.*, Cancer Sci., **106** (2015) 279-286.

CO7-26

Establishment of BNCT equivalence evaluation methods with different neutron sources (iBNCT accelerator and KUR reactor)

Y. Matsumoto[1,2], Y. Sugawara[1,2], K. Nakai[1,2], H. Kumada[1,2], M. Suzuki[3], H. Tanaka[3], K. Nishimura[4], H. Nakamura[4], K. Tsujino[5], S. Kawabata[5] and H. Sakurai[1,2]

[1]*Institute of Medicine, University of Tsukuba*
[2]*Proton Medical Research Center, University of Tsukuba Hospital*
[3]*Institute for Integrated Radiation and Nuclear Science, Kyoto University*
[4]*Laboratory for Chemistry and Life Science, Institute of Innovative Research, Tokyo Institute of Technology*
[5]*Department of Neurosurgery, Osaka Medical and Pharmaceutical University*

INTRODUCTION: In recent years, clinical trials and regulatory approvals using accelerator based BNCT devices have been underway in Japan. However, currently, one device is being applied for approval for one case, and bioequivalence evaluation between the devices is essential to make effective use of the few valuable accelerator-based neutron sources and to further expand the range of indications. Recently, papers on optimal methods for BNCT experiments have been reported [1,2], but there are no reports specifically evaluating equivalence among multiple facilities. The purpose of this study was to evaluate the bioequivalence between an accelerator-based neutron source (iBNCT001) developed by the University of Tsukuba and a reactor-based neutron source (KUR) at the Institute for Integrated Radiation and Nuclear Science, Kyoto University which has long been used for BNCT research, using cells and mice.

EXPERIMENTS: For *in vitro* experiments, cells were treated with p-boronophenylalanine (L-BPA) for 1 h in prepared medium at ^{10}B concentrations of 0, 10, 25, and 40 ppm, and neutron irradiation was performed by iBNCT001 and KUR. For *in vivo* experiments, 1x10^6 cells/10 μL were transplanted into the right lower limb thigh of 7–8-week-old nude mice and irradiated with neutrons when the tumor grew to 8-10 mm in diameter after 2 weeks. Irradiation of cells and mice was performed using the same system in iBNCT001 and KUR. The dose corresponding to the proton charge (mC) or irradiation time (min) was calculated by Monte Carlo calculations using the PHITS code.

RESULTS: The cell survival curves were plotted on the horizontal axis of the biological isoeffective dose (GyEq) calculated from the BPA treatment and neutron fluence at each boron concentration. The difference between the two facilities (iBNCT and KUR) was ±3~7% when comparing the isoeffective dose, D_{10} (the dose required to achieve 10% survival) (Table 1). In the analysis of anti-tumor effects in the carcinoma-bearing mice, tumor growth curves were obtained by measuring tumor size at least once a week after exposure to isoeffective doses (4.02 and 4.04 GyEq or 8.04 and 8.08 GyEq) in the iBNCT and KUR. Although the trend of enhanced antitumor effect with increasing dose was similar at both centers, a 25-45% difference between iBNCT and KUR was observed when the effect ratios were compared at 7, 14, 21, and 28 days after irradiation, respectively. The reason for the large differences in the in vivo experiments could be due to differences in feeding facilities, food, temperature and humidity during the experiment, and the person who measured tumor size.

^{10}B conc. (ppm)	0		10		25		40	
Facility	iBNCT	KUR	iBNCT	KUR	iBNCT	KUR	iBNCT	KUR
D_{10}	8.99	9.71	2.43	2.31	2.92	2.84	2.91	2.77
iBNCT/KUR	0.93		1.05		1.03		1.05	

Table 1. Isoeffective doses at iBNCT and KUR and differences between the two facilities.

REFERENCES:

[1] Y. Hattori *et al.*, J. Radiat. Res., **64** (2023) 859-869.
[2] N. Kondo *et al.,* Cancer Biother. Radiopharm., **38** (2022) 173-183.

CO7-27

Development of Boron Agents for MRI-Guided BNCT

S. Okada, K. Nishimura[1], Q. Ainaya[1], K. Miura, T. Takada[2], M. Suzuki[2], H. Nakamura

Laboratory for Chemistry and Life Science, Institute of Innovative Research, Tokyo Institute of Technology
[1]School of Life Science and Technology, Tokyo Institute of Technology
[2]Institute for Integrated Radiation and Nuclear Science, Kyoto University
[3]Institute for Integrated Radiation and Nuclear Science, Kyoto University

INTRODUCTION: Boron Neutron Capture Therapy (BNCT) is a promising treatment for tough and inoperable malignant tumors. To achieve the highest BNCT effect, thermal neutrons should be irradiated at the point when the boron concentration in tumors reaches its peak. Magnetic Resonance Imaging (MRI) is a widely-used, non-invasive diagnostic method. Consequently, gadolinium (Gd) contrast agents with boron sources have been developed for MRI-guided BNCT. Furthermore, the ^{157}Gd isotope possesses the highest thermal neutron capture cross-section. Therefore, synthesizing compounds containing both boron and gadolinium can not only help estimate the biodistribution of boron drugs under MRI guidance but also aid in the development of efficient neutron capture cancer therapy [1]. We have developed maleimide-functionalized *closo*-dodecaborate (MID) albumin conjugates that demonstrate high and selective accumulation in tumor tissue with no toxicity in the absence of thermal neutrons, thus representing a promising boron delivery system [2]. In this study, we synthesized Gd complexes to functionalize MID albumin conjugates for MRI-guided BNCT.

EXPERIMENTS: Bovine serum albumin (BSA) was conjugated with Gd-DO3A-Mal and then purified using an ultrafiltration filter. The resulting Gd-BSA conjugate was functionalized with MID and purified by ultrafiltration to obtain Gd-MID-BSA. We monitored the accumulation of Gd-MID-BSA in tumors using a 9.4 T MR scanner. T1-weighted images of the tumor were taken at predose and 3, 6, 12, and 24 h postdose. Subsequently, the therapeutic effect was examined by irradiating thermal neutrons on tumor mouse models injected with Gd-MID-BSA. Gd-MID-BSA and MID-BSA were intravenously injected into CT26 tumor-bearing mice at a dose of 5 mg[^{10}B]/kg, followed by thermal neutron irradiation of the tumor with 3.1–3.4 × 10^{12} neutrons/cm^2 at 24 h after injection.

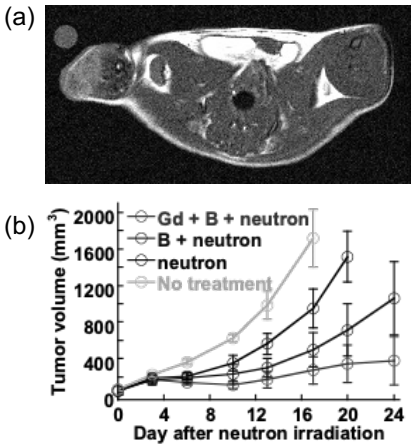

Fig. 1. (a) Representative T_1-weighted images of the tumor at 3h postdose. (b) Tumor growth curves after irradiation of the thermal neutron.

RESULTS: As shown in Fig. 1a, MRI signals in the tumors significantly increased at 3 h after injection and plateaued by 24 h, indicating prolonged blood retention and efficient accumulation of Gd-MID-BSA in the tumor. Tumor growth curves after thermal neutron irradiation are plotted in Fig. 1b. Tumor growth in the group injected with Gd-MID-BSA was significantly suppressed compared to the other groups, including MID-BSA, demonstrating that the neutron capture reaction of ^{157}Gd assisted in the BNCT effect. These results contribute to the advancement of MRI-guided neutron capture therapy as a potential treatment for malignant tumors [3].

REFERENCES:

[1] H. Nakamura *et al.*, Chem. Pharm. Bull., **48** (2000) 1034−1038.
[2] K. Kawai *et al.*, Mol. Pharmaceutics, **17** (2020) 3740-3747.
[3] S. Okada *et al.*, Mol. Pharmaceutics, **20** (2023) 6311-6318.

CO7-28

Effects of overexpression of LAT1 in cancer stem cell-like cells on suppression of tumor growth by boron neutron capture therapy

K. Ohnishi[1], T. Tani[2], M. Suzuki[3], Y. Sugawara[1], Y. Matsumoto[1, 4] and H. Sakurai[1, 4]

[1]*Proton Medical Research Center, University of Tsukuba Hospital*
[2]*National Institutes for Quantum Science and Technology*
[3]*Institute for Integrated Radiation and Nuclear Science, Kyoto University*
[4]*Institute of Medicine, University of Tsukuba*

INTRODUCTION: L-type amino-acid transporter 1 (LAT1) [1], through which boronophenylalanine (BPA) is transported into cells, is expressed in various types of tumor cells including glioblastoma but not in normal cells [2]. We transfected pCMV/LAT1-GFP plasmids into a glioblastoma cell line, T98G, and selected several clones overexpressing LAT1. The sensitivity of clones to neutron and γ-ray fluences was well correlated with the expression level of LAT1 and the level of BPA uptake in the clones [3]. These results showed that overexpression of LAT1 in cancer cells results in enhanced anticancer effects of BNCT and BNCT combined with gene therapy is beneficial for tumors with low LAT1 expression. In our later study [4], we transfected pCD133-TRE/LAT1-tdTomato/IRES/tTA plasmids into T98G cells. The plasmids were designed to overexpress LAT1 tagged with tdTomato on cytoplasmic membranes of CD133 positive cancer cells (cancer stem cell-like cells) selectively. We established several clones which stably overexpress LAT1 in hypoxic microenvironment of spheroids including CD133 positive cells and showed that overexpression of LAT1 in CD133 positive cells results in enhanced sensitivity of spheroids to neutron and γ-ray fluences. In KUR experiments performed in 2022, we obtained preliminary data indicating that tumor regrowth after BNCT is relatively delayed in mice with tumors formed with the pCD133-TRE/LAT1-tdTomato/IRES/tTA plasmid-transfected cells compared with mice with control cells. The aim of this study is to confirm the preliminary experiment.

EXPERIMENTS: We transplanted tumors formed with a clone (T98G/K10, pCD133-TRE/LAT1-tdTomato/IRES/tTA-transfected, LAT1-overexpressed cells in CD133 positive cell selectively), or a clone (T98G/KC2, control plasmid-transfected, LAT1-nonoverexpressed cells) into femoral region of nude mice. Accumulated amounts of ^{10}BPA in blood and tumor were measured using prompt gamma-ray assay (PGA) on 1 h after ^{10}BPA s.c. injection (100 mg/kg, 1 h before irradiation). The thermal and epithermal neutron fluence for 60 min irradiation was 5.1×10^{12} cm^{-2}. The total dose was 1.40 Gy for neutrons (1.077 Gy) and γ-rays (0.323 Gy), and the estimated boron dose was 0.325 Gy/ppm.

RESULTS: Tumor growth in ^{10}BPA-treated T98G/K10 and T98G/KC2 mice was strongly suppressed for approximately 40 days after neutron irradiation. However, such suppression was not observed in PBS-treated T98G/K10 and T98G/KC2 mice. We are now continuously measuring tumor size after BNCT in ^{10}BPA-treated T98G/K10 and T98G/KC2 mice. Significant differences in the tumor regrowth between two groups are not observed at present stage (data not shown). We plan to do additional experiments to confirm the effect of BNCT on tumor regrowth using CD133 expressing cell-selective LAT1 overexpression cells and control cells.

REFERENCES:

[1] Y. Kanai *et al.,* J. Biol. Chem., **273** (1998) 23629-23632.
[2] K. Kaira *et al.,* Br. J. Cancer, **107** (2012) 632-638.
[3] K. Ohnishi *et al.,* Radiat. Res., **196** (2021) 17-22.
[4] T. Tani *et al.,* Radiat. Res., **200** (2023) 21-31.

CO7-29

Enhancement of Tumour Growth Suppression by Electroporation with Intra-Tumoural Injection of ^{10}Boron-Polyplex for Boron Neutron Capture Therapy to Pancreatic Cancer Model *in vivo*

Hironobu Yanagie[1,2,3], Masashi Yanagawa[4], Yoshiteru Yanagie[5], Minoru Suzuki[6], Yoshinori Sakurai[6], Hiroki Tanaka[6], Masayuki Nashimoto[3], Haruo Yamauchi[2,7], Minoru Ono[2,7], Takumichi Sugihara[3], and Hiroyuki Takahashi[1,2,8]

[1]*Institute of Engineering Innovation, School of Engineering, The University of Tokyo*
[2]*Cooperative Unit of Medicine & Engineering, The University of Tokyo Hospital*
[7]*Dept. of Cardiac Surgery, The University of Tokyo Hospital*
[8]*Dept of Bioengineering, School of Engineering, The University of Tokyo*
[3]*Niigata Univ of Pharmacy & Applied Life Sciences*
[4]*ER Hachioji Ad-vanced Animal Medical and Clinical Care Center*
[5]*Faculty of Medicine, Teikyo University*
[6]*Kyoto Univ Institute for Integrated Radiation & Nuclear Science*

INTRODUCTION: It is necessary to accumulate high concentration of Boron atoms into the tumor tissues selectively for effective Boron neutron capture therapy(BNCT) [1, 2]. Electroporation is an method for selec-tive delivery of compound into the cells by open the membrane poles electorically in the field of gene therapy and chemotherapy [3, 4]. In this study, we evaluated the electroporation with intra-tumoral injection of ^{10}Boron-Polyplex; ^{10}Boro-plex (^{10}Boron / hyaluronic acid / protamine-mixed with cationic liposome) by in vivo experiment on AsPC-1 human pancreatic tumor bearing mice.

EXPERIMENTS: ^{10}Boro-plex were prepared mixed with 1.5mL of ^{10}BSH(^{10}B:23809 ppm) or ^{10}BPA(^{10}B:1290 ppm), 0.3mL of a solution of 10mg/mL hyaluronic acid sodium, and 0.15mL of 20mg/mL of protamine incubating at room temperature for 30min, then, these mixing solutions were poured into cationic Liposome; Lipofectamine 3000(0.15mL+reaction solution 0.15mL). We prepared human pancreatic cancer AsPC-1($5x10^5$) model by transplanting to right lower leg. Electroporation was performed after intra-tumoral injection of 0.2mL of ^{10}Boro-plex, then, we performed thermal neutron irradiation at Institute for Integrated Radiation and Nuclear Science, Kyoto University (average neutron fluence of 3.0×10^{12} n/cm2). The change in tumor growth and survival rate of the mice reflected the anti-tumor effect of ^{10}Boro-plex.

RESULTS: Tumor growth suppression was achieved in the ^{10}Boro-plex+EP group in NCT groups compared with non-irradiated group. The experimental results showed that 10Boro-plex+EP group was revealed the tu-mor growth suppression, and no significant weight loss were observed after treatment suggesting low systemic toxicity of this system.

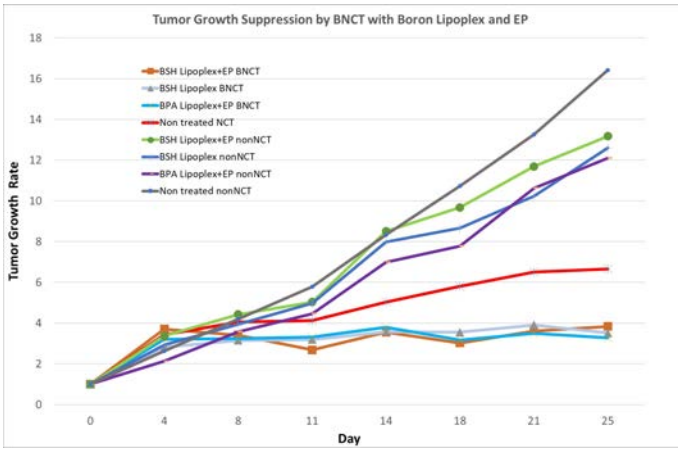

Figure1. Tumor growth suppression in ^{10}Boro-plex+EP group by NCT was superior compared with non-irradiated group.

REFERENCES:

[1] H. Yanagie *et al.*, In Vivo, **35(6) (**2021) 3125-3135.
[2] B. Trotovšek *et al.*,World J Gastroenterol, **27(48)** (2021) 8216-8226.

R5089

CO7-30

Tumor Growth Suppression of Gadolinium Neutron Capture Therapy with Gd_2O_3 polymeric nanocarries

Hironobu Yanagie[1,2,3], Masashi Yanagawa[4], Shang Wei Li[5], Horacio Cabral[5], Minoru Suzuki[6], Yoshinori Sakurai[6], Hiroki Tanaka[6], Masayuki Nashimoto[3], Haruo Yamauchi[2,7], Minoru Ono[2,7], Takumichi Sugihara[3], and Hiroyuki Takahashi[1,2,5]

[1]*Institute of Engineering Innovation, School of Engineering, The University of Tokyo*
[2]*Cooperative Unit of Medicine & Engineering, The University of Tokyo Hospital*
[3]*Niigata Univ of Pharmacy & Applied Life Sciences*
[4]*ER Hachioji Ad-vanced Animal Medical and Clinical Care Center*
[5]*Dept of Bioengineering, School of Engineering, The University of Tokyo*
[6]*Kyoto Univ Institute for Integrated Radiation & Nuclear Science*
[7]*Dept. of Cardiac Surgery, The University of Tokyo Hospital*

INTRODUCTION: On the basis of Gadolinium-neutron capture therapy(GdNCT), Gadolinium atoms react thermal neutron and offers cytotoxic effect by 1μm-range high LET Auger electron, and long-range gamma rays [1, 2, 3]. Recently, nanoscale drug becomes more and more popular because it can promote the accumulation of Gd agents in tumor through the enhanced effect of per-meability and retention (EPR). In this study, we built a series of Gd entrappednanomicelle(Gd_2O_3) to improve the accumulation in tumor and evaluated its antitumor effect through the comparison of tumor size.

EXPERIMENTS: Preparation of polymeric nanocarriers; A hydrophobic part, Poly-γ-Benzyl-L-Glutamate (PBLG) was combined to hydrophilic polymer. PEG was used for modify molecular weight and water solubility, and P(Asp) was used for combining to gadolinium chelator. Gd3+ was oxi-dated to Gd_2O_3 for stability improvement. Due to the certain size, this nanomicelle tends to accumulate near tumor tissue and keep a long retention time. After 24h injection into colon 26 tumor-bearing mice with Gd_2O_3 nanomicelle, the tumor-bearing mice received thermal neutron irradiation at Nuclear Reactor Facility of Kyoto Univ Institute for Integrated Radiation & Nuclear Science (3.0×10^{12} n/cm^2).

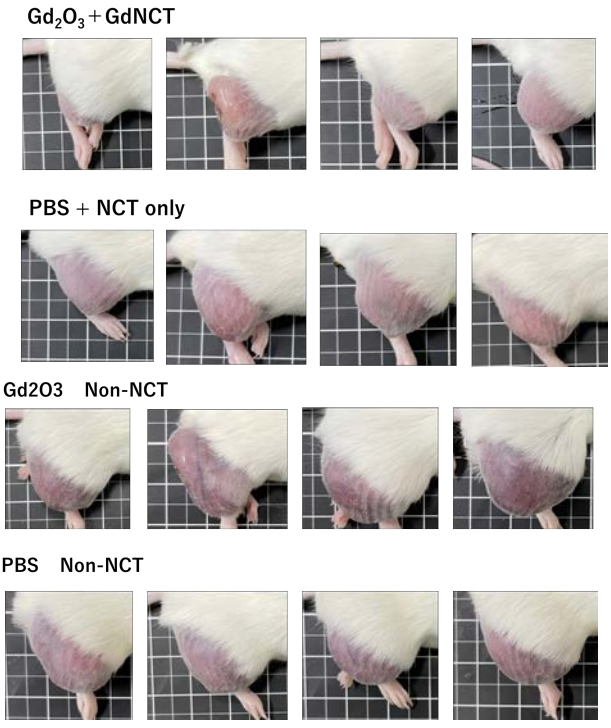

Figure 1. Tumor growth suppression by GdNCT using Gd_2O_3 nanomicelle.

RESULTS: Tumor growth was suppressed with the injection of Gd_2O_3 nanomicelle and according to the comparison in the control group, the suppression worked not only through the irradiation, but the influence of Gd_2O_3 nanocarriers. We hope to increase the concentrations of Gd atoms entrapped into the nanomicelle, and more selective targeting to cancer cells using ligands.

REFERENCES:

[1] N. Dewi *et al.,* J Can.Res.Clin.Oncol., **142(4)** (2016) 767-75.
[2] P. Mi *et al.*, J Cont. Release, **174** (2014) 63-71.
[3] C. Qin *et al.,* ChemNanoMat., **6** (2020) 412-419.

CO7-31

Research and Development of New Technology for Boron Neutron Capture Therapy

M. Xu[1], T. Watanabe[3], X. Zhou[1], C. Jin[1], R. Ohgaki[1,2], H. Okanishi[1], H. Tanaka[3], M. Suzuki[3], and Y. Kanai[1,2]

[1]*Department of Bio-system Pharmacology, Graduate School of Medicine, Osaka University*
[2]*Integrated Frontier Research for Medical Science Division, Institute for Open and Transdisciplinary Research Initiatives (OTRI), Osaka University*

[3]*Institute for Integrated Radiation and Nuclear Science, Kyoto University*

INTRODUCTION: Boron Neutron Capture Therapy (BNCT) relies on accumulating boron-containing compounds within cancer cells, followed by irradiation with a neutron beam. Ensuring a high accumulation of boron-containing compounds within the cells is crucial to optimize the nuclear reaction between ^{10}B and neutrons in cancer cells. One of the most widely used boron carriers for BNCT is L-*p*-boronophenylalanine (L-BPA), which is taken up by cancer cells due to their elevated amino acid transport mechanisms [1]. However, a challenge in using L-BPA for BNCT is the rapid decrease in intracellular L-BPA levels caused by the efflux of L-BPA from cancer cells through specific transporters. This study aims to experimentally validate an approach to enhance the effects of neutron irradiation on cancer cells by inhibiting the transporters responsible for L-BPA efflux. Employing cultured cells and tumor-bearing mice as model systems, we investigated the potential of this approach to improve the efficacy of BNCT using L-BPA.

EXPERIMENTS: For the cell irradiation experiment, the mouse-derived tumor cell line 4T1 was treated with L-BPA by adding it to the culture medium. After a washing step, the cells were incubated for 60 min in a medium either with or without inhibitors that target the transporters responsible for L-BPA release. The cells were then harvested using Hanks' Balanced Salt Solution (HBSS) and transferred to 1.5 mL tubes to serve as samples for neutron irradiation. A control sample was also prepared by irradiating cells that had not been loaded with L-BPA. After neutron irradiation, cell numbers were adjusted, and the cells were seeded into 10 cm dishes. Viable cells were evaluated for colony formation to assess cell survival.

For the in vivo mouse irradiation experiment, human-derived tumor cell line MCF7 and mouse-derived 4T1 were subcutaneously implanted into nude mice and Balb/c mice, respectively, to establish tumor models. Mice were administered 125 mg/kg and 400 mg/kg of L-BPA for MCF7 and 4T1, respectively, via tail vein injection. This was followed by administering a transporter inhibitor (25mg/kg as active stereoisomer), responsible for preventing L-BPA release, at 1 h and 1.5 h post-L-BPA injection. As a control, mice were prepared for neutron irradiation without L-BPA loading but received the inhibitor treatment alone. Neutron irradiation was conducted at 5 MW for 20 and 30 min for MCF7 and 4T1, respectively. The therapeutic effects on tumor regression were subsequently compared between the experimental and control groups after neutron irradiation.

RESULTS: In cell irradiation experiments, 4T1 cells were treated with L-BPA and washed. The cells were then divided into two groups: Group 1 was incubated for 60 min in RPMI 1640 cell culture medium containing an inhibitor of the transporter responsible for L-BPA release. Group 2 was incubated for 60 min in a culture medium without the inhibitor. Group 3 was prepared as an additional control, consisting of cells not treated with L-BPA. All groups were then subjected to neutron irradiation. After irradiation, cell viability was assessed by measuring colony formation in low-density cultures. The results indicated no significant difference in cell survival between Group 2 and Group 3 (non-BNCT), suggesting that the intracellular L-BPA content had decreased to levels less effective for BNCT within 60 min after L-BPA treatment. In contrast, the survival rate in Group 1 was significantly lower than in Group 2, demonstrating an enhancement of BNCT efficacy by inhibiting the transporter responsible for L-BPA release.

In in vivo mouse irradiation experiments, MCF7 cells and 4T1 cells were implanted into the hind limbs of mice to form tumors. Mice were then administered L-BPA intravenously and divided into two groups. Group 1 received an intravenous injection of a transporter inhibitor responsible for L-BPA release at 1 h and 1.5 h after L-BPA administration. Group 2 did not receive inhibitor treatment following L-BPA administration. Additionally, Group 3 was prepared by administering saline instead of L-BPA, followed by injections of the transporter inhibitor at 1 h and 1.5 h post-saline administration. For each group, mice were anesthetized 2.5 h after administering L-BPA or saline and subjected to neutron irradiation. Tumors were excised two weeks after irradiation, and their sizes were measured. The results indicated that, for both MCF7 and 4T1 tumors, tumor sizes in Group 1 were significantly smaller than in Group 2, demonstrating that inhibiting the transporter responsible for L-BPA release significantly enhanced BNCT efficacy.

The results of this study have confirmed the proposed concept for optimizing L-BPA-based BNCT.

REFERENCES: [1] P. Wongthai *et al.*, Cancer Sci., **106** (2015) 279-286.

CO7-32

Early responses of tumor cells to BNCT

Y. Tong[1], Gao Zhongming[1], B. Saraswat[1], A. Vadi Velu[1], Y. Sasaki[1], M. Ishiai[2,3], S. Imamichi[1,2,3], T. Nozaki[1,5], M. Suzuki[4], Y. Sanada[4], and M. Masutani[1,2,3]

1 Dept. of Molecular and Genomic Biomedicine, Center for Bioinformatics and Molecular Medicine, Nagasaki University Graduate School of Biomedical Sciences
2 Division of Boron Neutron Capture Therapy, EPOC, National Cancer Center
3 Central Radioisotope Division, National Cancer Center Research Institute
4 Institute for Integrated Radiation and Nuclear Science, Kyoto University
5 Dept. Pharmacology, Osaka Dental Univ.

INTRODUCTION: Boron neutron capture therapy (BNCT) is a cutting-edge cancer treatment approach that employs high-energy alpha particles and lithium nuclei generated by nuclear reactions. This method offers precision, brevity, and minimal side effects. To enhance the effectiveness of BNCT, it is essential to conduct comprehensive analysis of its response to cancer cells and therapeutic efficacy. We conducted extensive research on the consequences of BNCT on tumor cells, such as cell death and various biological responses. Using cancer cell lines and xenograft mouse models can significantly bolster this endeavor.

EXPERIMENTS: Neutron irradiation experiments at the KUR reactor were conducted at a constant power level of 1 MW in all cases. Gold foil activation analysis and thermoluminescence dosimeters (TLDs) were employed. The irradiation mode used at KUR was OO-0000F, with a Dr ratio of approximately 9.4. The total physical dose was calculated using the flux-to-dose conversion factor [1]. The relevant data is presented in Tables 1-3.

The human squamous cell line SAS and malignant melanoma A375 cells were incubated with ^{10}B-boronophenylalanine fructose complex (BPA) (Catchem) for 2.0 hrs in suspension. The cell survival was analyzed by colony formation assay and culture supernatants were harvested at 6 and 24 hrs for RNA and proteins isolation and molecular analysis.

Mouse melanoma cell lines B16F10 and the variant were grafted to the hind legs and were locally irradiated using ^{6}LiF containing thermal neutron shield. Mice were injected with BPA at 500 mg/kg bodyweight approximately 30 min before irradiation. Mice were euthanized on days 7 and 13 after irradiation, and blood, tumors, and other organs were analyzed.

RESULTS: The measurement of thermal neutron fluence and doses for mice (Table 1) and cells were shown in Table 1 & 3. A potential role of HMGB1 as an early biomarker was indicated by cellular and *in vivo* responses to BNCT and proteome analysis of exosomes derived from SAS cells showed basic data for identifying biomarkers for the response to BNCT [2, 3].

Table 1. Irradiated doses for local irradiation of mice on Dec. 5, 2023 (Cart, irradiation room).

Irradiation time	Irradiation (min)	Position	Fluence (/cm²)		(Gy)					
			Thermal neutron (/cm²)	Epi-thermal neutron	Thermal neutron (GY)	Epi-thermal neutron (GY)	Fast neutron (GY)	Gamma ray (GY)	Physical dose (GY)	B-10* (1 ppm)
12:27-13:27	60	Center	4.10E+12	7.30E+11	5.40E-01	5.80E-02	4.00E-01	3.10E-01	1.30E+00	3.00E-01
13:38-14:38	60	Center	4.20E+12	7.60E+11	5.70E-01	6.00E-02	4.20E-01	2.30E-01	1.30E+00	3.20E-01

Table 2. Irradiated doses at cells on Dec.12, 2023 (Single layer, E-4 rail port)

Irradiation time	Irradiation (min)	Position	Fluence (/cm²)		(Gy)					
			Thermal neutron (/cm²)	Epi-thermal neutron	Thermal neutron (GY)	Epi-thermal neutron (GY)	Fast neutron (GY)	Gamma ray (GY)	Physical dose (GY)	B-10* (1 ppm)
10:41-10:51	10	Center	1.10E+12	1.90E+11	1.40E-01	1.50E-02	1.10E-01	7.80E-02	3.40E-01	8.00E-02
11:02-12:02	60	Center	6.10E+12	1.10E+12	8.10E-01	8.70E-02	6.00E-01	4.30E-01	1.90E+00	4.50E-01
12:21-12:29	8	Center	8.90E+11	1.60E+11	1.20E-01	1.30E-02	8.80E-02	7.40E-02	2.90E-01	6.60E-02
12:30-12:36	6	Center	7.00E+11	1.20E+11	9.30E-02	9.90E-03	6.90E-02	4.80E-02	2.20E-01	5.20E-02
12:38-12:42	4	Center	4.50E+11	8.10E+10	6.10E-02	6.50E-03	4.50E-02	3.80E-02	1.50E-01	3.40E-02
12:44-12:46	2	Center	2.40E+11	4.20E+10	3.20E-02	3.40E-03	2.30E-02	1.90E-02	7.70E-02	1.80E-02

Table 3. Irradiated doses at cells on January 17, 2024 (Single layer, E-4 rail port)

Irradiation time	Irradiation (min)	Position	Fluence (/cm²)		(Gy)					
			Thermal neutron (/cm²)	Epi-thermal neutron	Thermal neutron (GY)	Epi-thermal neutron (GY)	Fast neutron (GY)	Gamma ray (GY)	Physical dose (GY)	B-10* (1 ppm)
8:32-8:34	2	Center	2.50E+11	4.40E+10	3.30E-02	3.50E-03	2.40E-02	1.20E-02	7.20E-02	1.80E-02
8:37-8:41	4	Center	5.10E+11	9.00E+10	6.80E-02	7.20E-03	5.00E-02	2.80E-02	1.50E-01	3.80E-02
8:43-8:49	6	Center	7.80E+11	1.40E+11	1.00E-01	1.10E-02	7.70E-02	1.40E-02	2.10E-01	5.80E-02
8:51-8:59	8	Center	9.90E+11	1.80E+11	1.30E-01	1.40E-02	9.80E-02	1.20E-02	2.60E-01	7.40E-02
9:08-9:10	2	Center	2.50E+11	4.40E+10	3.30E-02	3.50E-03	2.50E-02	9.90E-03	7.10E-02	1.90E-02
9:12-9:16	4	Center	4.40E+11	7.90E+10	5.90E-02	6.30E-03	4.40E-02	2.10E-02	1.30E-01	3.30E-02
9:18-9:24	6	Center	6.60E+11	1.20E+11	8.70E-02	9.30E-03	6.50E-02	4.60E-02	2.10E-01	4.90E-02
9:25-9:33	8	Center	9.60E+11	1.70E+11	1.30E-01	1.40E-02	9.40E-02	3.40E-02	2.70E-01	7.10E-02
9:36-10:36	60	Center	6.90E+12	1.20E+12	9.20E-01	9.80E-02	6.80E-01	4.60E-01	2.20E+00	5.10E-01

REFERENCES:

[1] S. Nakamura *et al.,* Proc Jpn Acad Ser B Phys Biol Sci., **93** (2017) 821-831.
[2] S. Imamichi *et al.,* Biology, **11**(2022) 420.
[3] D. Perico *et al.,* Cells. **12(12)** (2023) 1562.

CO7-33

Development of boron carriers based on the characteristics of energy metabolism of cancer

A. Niitsu[1], R. Yamamoto[1], T. Watanabe[2], Y. Sanada[2], M. Tsuji[1], T. Hirayama[1], S. Masunaga[3] and H. Nagasawa[1]

[1] *Laboratory of Medicinal & Pharmaceutical Chemistry, Gifu Pharmaceutical University*
[2] *Institute for Integrated Radiation and Nuclear Science, Kyoto University*
[3] *Hanwha Daini Senboku Hospital*

INTRODUCTION: Glutamine functions as a carbon and nitrogen source for biosynthesis, energy metabolism, and redox homeostasis in cancer cells. Dysregulated glutamine metabolism is a prominent metabolic hallmark of cancer cells. Thus, the glutamine metabolic pathway is a breakpoint in cancer therapy, as many cancer cells exhibit a marked dependence on glutamine, also known as glutamine addiction. Glutamine is transported into cells through ASCT2, and the imported glutamine can be used or exchanged through the L-type amino acid transporter (LAT1 or SLC7A5) for hydrophobic or aromatic amino acids such as isoleucine, valine, methionine, tryptophan, and phenylalanine. It is known that these transporters are over-expressed in a variety of tumor cells. Therefore, we are developing boron carriers that efficiently accumulate 10B atoms in tumors by exploiting amino acid transporters that are highly expressed in cancers. We have synthesized various amino acid derivatives containing boron clusters as hydrophobic pharmacophores and screened them by boron uptake into cells, resulting in several promising candidate compounds.

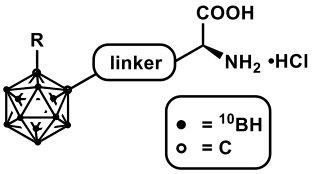

In this study, we synthesized a new derivative, BCY2, and compared its cellular uptake and the tumor cell-killing effect under neutron irradiation with BC2.

EXPERIMENTS: Boron compounds are synthesized by a microwave reaction in which the corresponding alkyne reacts with decaborane in the presence of a Lewis base to construct car-borane. T98G was treated with 10 ε gB/mL boron carrier for 30 minutes or 1 hour, washed with cold PBS, dis-solved in nitric acid directly, and intracellular boron up-take was measured by ICP-AES. To evaluate the enhancement of neutron irradiation by the compound, T98G cells were treated with 10 or 20 ε g ^{10}B/mL boron carrier for 2 hours, then the cells were washed with PBS, suspended in serum-containing medium, dispensed into Teflon tubes, and irradiated. The cells were irradiated with a neutron beam at a power of 1 MW at the Heavy Water Facility of the Kyoto University Research Reactor (KUR). Survival of irradiated cells was measured using a conventional colony assay; D10 of BNCT was calculated from the survival curve shown in Fig. 2.

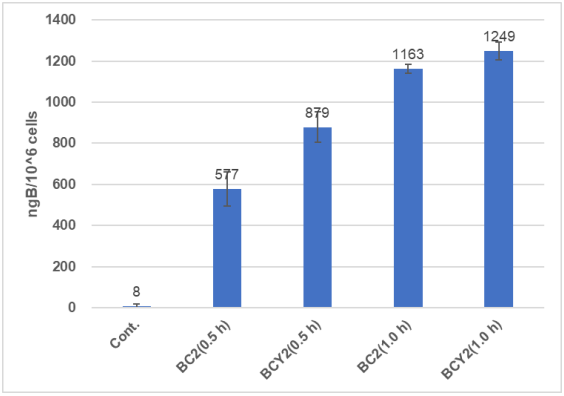

Fig. 1. Incorporation of boron carriers into T98G.

RESULTS: As previously reported, BC2, which showed the highest cellular uptake, increased intracellular boron content up to 2 hours treatment time and remained the same with further treatment time. Therefore, we compared the treatment times up to 1 hour and found that BCY2 tended to be taken up more than BC2, as shown in Fig. 1. When cells suspended in fresh medium after drug treatment were irradiated with neutrons, BCY2 also significantly enhanced the cell-killing effect of neutron beams to the same degree as BC2. This result suggests that these car-borane-containing amino acids remain in the cell without being excreted by the cell.

From the above, it was predicted that these compounds are taken up by cells by a different mechanism than BPA, which is currently under investigation. Due to the low water solubility of these compounds, structural modifications are being performed for pharmacokinetic analysis in a tumor-bearing mouse model.

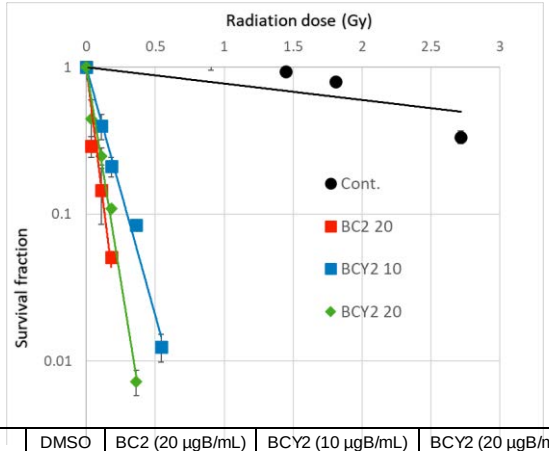

	DMSO	BC2 (20 μgB/mL)	BCY2 (10 μgB/mL)	BCY2 (20 μgB/mL)
D10 (Gy)	8.959	0.133	0.296	0.172
ER	1.0	67.2	30.2	52.0

Fig. 2. Survival fraction of T98G cells treated with BC2 and BCY2 with mixed-neutron irradiation.

ACKNOWLEDGEMENTS: This research was supported by JSPS KAKENHI (JP19H03352 and JP26670059).

CO7-34

Detection of Boron-10 Compound in a Plant Seed Using a Neutron Capture Reaction

T. Kinouchi

Institute for Integrated Radiation and Nuclear Science, Kyoto University

INTRODUCTION: One of the optimal solutions to ensure a sustainable food supply is to increase and stabilize crop yields through plant breeding. However, because of the extremely low rate of naturally occurring mutant varieties, breeding methods that efficiently produce new plant varieties by artificially inducing mutations have been sought. Therefore, breeding using radiation or chemicals as mutagens continues to be practiced around the world. Fast neutrons can efficiently introduce random mutations into the target genomes, but they also have the disadvantage of causing cell death because of their high energy. Against this background, we have developed a boron neutron capture reaction breeding method (BNC breeding method), which can maintain a high survival rate while introducing random mutations. The BNC breeding method uses the nuclear reaction of $^{10}B(n,\alpha)^{7}Li$. The basic principle of this method is that thermal neutrons are irradiated toward the seeds of plants that have absorbed a ^{10}B compound, and the α-rays generated thereafter introduce mutations. The thermal neutrons irradiated are very low energy, equal to one to four millionth of fast neutrons, and are used merely as a trigger for this reaction. Therefore, the side reactions are expected to be much lower than those in the conventional method using fast neutrons. The objective of this study was to visualize the distribution of ^{10}B compounds absorbed in the tissues of rice seeds for the practical application of the BNC breeding method.

EXPERIMENTS: Materials> Rice seeds (*Oryza sativa* L. cv. Nipponbare) were kindly gifted from Dr. Segami, Research Institute of Environment, Agriculture and Fisheries, Osaka Prefecture. ^{10}B-boric acid aqueous solution was kindly gifted from Dr. Hattori, Research Center for BNCT, Osaka Metropolitan University.

In situ visualization of ^{10}B compounds in seeds> rice seeds were immersed in ^{10}B-boric acid sol. (10 mM) for 24 hrs. Slices (10-μm thickness) of the seeds were mounted onto a solid-state nuclear tracking detector, CR-39 (20 mm×30 mm) and irradiated with epithermal neutrons for 20 min by applying them to the pneumatic tube in the graphite thermal column (Tc-Pn) of Kyoto University Research Reactor (KUR). The irradiated CR-39 plate was etched in 6 M NaOH solution for 60 min at 70°C, and the resulting etch-pits were observed under an optical microscope.

RESULTS: Both Fig. 1(A) and 1(B) show close-up images of cross-sections prepared from the same rice seed, which was immersed in ^{10}B-boric acid sol. (10 mM). Fig. 1(A) is a bright-field image. Fig. 1(B) is an α-tracking autoradiograph, which was generated by the BNC reaction, and reveals the distribution of ^{10}B compounds in the cross-section. The areas enclosed by the circle indicate the embryo. A large number of etch-pits derived from ^{10}B were imaged throughout the section as small black spots. It was observed that a large amount of ^{10}B accumulated in the embryo compared to the area not circled (endosperm).

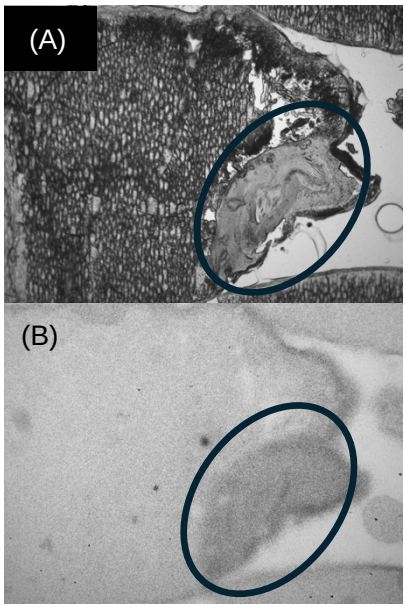

Fig. 1. Detection of ^{10}B compounds absorbed into the rice seed.

Tumor eradication by GdNCT-immunotherapy with gadolinium-containing nanoparticles

L. Zhao[1], W. Huang[2], X.Han[2], M. Suzuki[3] and N. Komatsu[2]

[1] *School for Radiological and Interdisciplinary Sciences (RAD-X) and Collaborative Innovation Center of Radiation Medicine of Jiangsu Higher Education Institutions, Soochow University, China*

[2] *Graduate School of Human and Environmental Studies, Kyoto University, Japan*
[3] *Institute for Integrated Radiation and Nuclear Science, Kyoto University, Japan*

Neutron capture therapy (NCT) as a promising radiotherapy of cancer has attracted great attention in recent years. The NCT using boron- and gadolinium-based sensitizers are called BNCT and GdNCT, respectively. GdNCT is capable of killing cancer cells with Auger electrons of high linear energy transfer (LET) as well as low-LET γ photons, which are generated by the capture reaction of Gd and thermal neutrons. ^{157}Gd with a natural abundance of 15.7% has the largest thermal neutron cross section of all the stable isotopes at 254,000 barns, which is much higher than that of ^{10}B (3,840 barns).[1] Despite its potential, GdNCT research is limited compared to BNCT, partly due to the scarcity of effective Gd-based sensitizers that can accumulate selectively in tumors.

Immune checkpoint blockade (ICB) is a groundbreaking immunotherapy that involves the use of immune checkpoint inhibitors to combat various types of cancer. These inhibitors work by blocking checkpoint proteins from binding with their partner proteins, essentially preventing the immune system from being suppressed and allowing it to attack cancer cells. This approach helps enhance the body's immune response against cancer. Recent findings suggest that combining GdNCT with ICB immunotherapy not only substantially inhibits primary tumor growth but also induces shrinkage in distant tumors receiving no GdNCT treatment.[2]

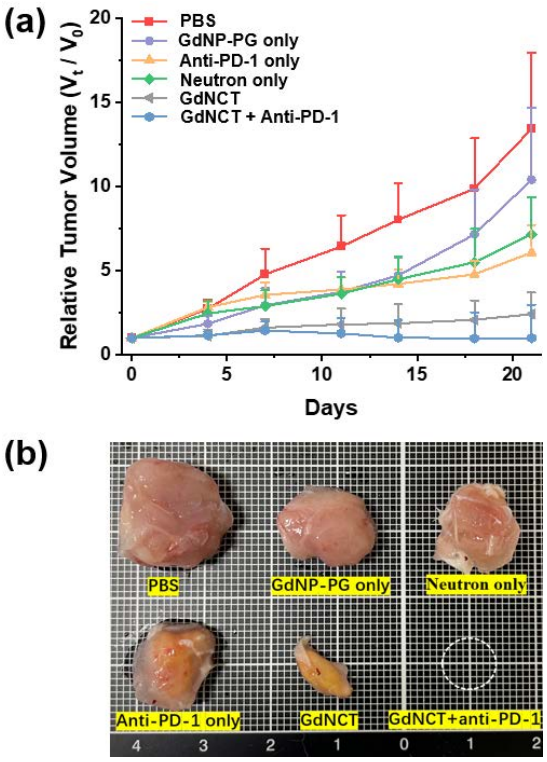

Figure 1. GdNCT-immunotherapy mediated with GdNP-PG nanoparticles. (a) Tumor growth curve (n=4); (b) Representative photographs of the CT26 tumors in different groups after treatment for 21 days.

We have recently developed GdNP-PG nanoparticles as an efficient sensitizer for GdNCT. In this work, we evaluated the efficacy of GdNCT-immunotherapy mediated with GdNP-PG nanoparticles. The mice bearing CT26 tumor were intravenously injected with the PBS dispersion of GdNP-PG. After the injection for 24 h, the mice were irradiated with thermal neutrons at a reactor power of 5 MW for 12 min. Subsequently, anti-PD-1, an inhibitor of immune checkpoint, was administrated through intraperitoneal injection on days 0, 4, 7, and 11. The preliminary results show that GdNCT significantly suppressed the growth of CT26 tumor as compared to control groups. More importantly, three out of four mice in GdNCT + anti-PD-1 group exhibited nearly complete tumor regression, and tumor recurrence was not observed after the treatment for more than 2 months. Further study to elucidate the mechanism of GdNCT-immunotherapy is in progess.

Reference:

[1] S. L. Ho *et al.,* *ACS Omega*, **7(3)** (2022) 2533-2553.
[2] D. Duan *et al.,* *CCS Chemistry*, **5** (2023) 2589-2602.

CO7-36

MnO_2 modified albumin nanoboron drug for MRI image-guided BNCT

Z. Zhang[1,2], Q. Dai [1,2], Y. Qin [2], X. Sun [2], Q. Yang[1], L. Liu[1], M. Suzuki [3], M. Han[2], Q. Wei[1]

[1] Department of Radiation Oncology, Key Laboratory of Cancer Prevention and Intervention, The Second Affiliated Hospital, College of Medicine, Zhejiang University
[2] College of Pharmaceutical Sciences,Zhejiang University
[3] Division of Particle Radiation Oncology, Particle Radiation Oncology Research Center, Institute for Integrated Radiation and Nuclear Science, Kyoto University

INTRODUCTION: Boron neutron capture therapy (BNCT) has shown significant efficacy for malignant glioma[1]. We constructed BPA-F&DOTA-Gd@LIPO using boron phenylalanine-fructose (BPA-F) complex as the boron capture agent and DOTA-Gd as the part that provides the MRI image, which were co-loaded in lipid nanoparticles using microfluidic method. The therapeutic effect of BPA-F&DOTA-Gd@LIPO after neutron irradiation was evaluated in this experiment.

EXPERIMENTS: The glioma cell line U87MG was seeded onto a 6-well plate, and after 24 hours of incubation, PBS, BPA-fructose, BSA-BPA, and BSA-BPA-MnO_2 (with ^{10}B concentrations equiv-alent to 25 μg/ml) were added, respectively. The effect of boron neutron irradiation with these new compounds were investigated with colony formation assay.

Using U87MG tumor-bearing nude mice, two *in vivo* experiments were performed. In first experiment, BPA-fructose solution, BSA-BPA-MnO_2 at boron concentration of 2.5mg/kg and PBS as control and mice injected with each preparation were subdivided into neutron-irradiated and non-irradiated groups. In second experiment, BPA-F&DOTA-Gd solution, BPA-F&DOTA-Gd@LIPO at boron concentration of 2.5mg/kg and PBS as control were used and the mice injected these compoundswere subdivided into neutron-irradiated and non-irradiated groups. Mice in the neutron irradiation group were irradiated with KUR. After that, body weight and tumor volume of mice in six groups were measured every four days. The body weight curve and tumor volume curve were recorded.

RESULTS: U87MG cells were incubated with each preparation at a concentration of 25 μg/mL ^{10}B for 4 hours and then irradiated with thermal neutrons for different times (0, 15, 30, 45 min). According to the colony formation results, it can be seen that the boron drug BSA-BPA and BSA-BPA-MnO_2 can effectively kill tumor cells at the cellular level, and the effect is slightly stronger than BPA-fruc-tose.

Compared with the control group injected with PBS only, mice in the BSA-BPA-MnO_2 + neutron irradiation group showed significant inhibition of tumor growth within 30 days. Meanwhile, the trend of body weight change was basically the same in all groups, illustrating that experimental BNCT treatment did not bring obvious body damage to the animals.

It was observed that in the short term, the tumor growth of the neutron irradiation groups had a significant tendency to be suppressed. Then, we performed the experiment again using the same method and the results are shown in Figure 4. Compared with the control group injected with PBS only, mice in the BPA-F&DOTA-Gd@LIPO + neutron irradiation group showed significant inhibition of tumor growth within 30 days. Meanwhile, the trend of body weight change was basically the same in all groups, illustrating that experimental BNCT treatment did not bring obvious body damage to the animals.

REFERENCES:

[1] Yamamoto, T., K. Nakai, and A. Matsumura, Cancer Lett., **262** (2008) 143-152.

CO7-37

Analysis of boron compound micro-distribuion in BNCT

M. Suzuki, H. Ueda and Y. Sakurai,

Institute for Integrated Radiation and Nuclear Science, Kyoto University

INTRODUCTION:

In boron neutron capture therapy (BNCT), the adverse effects of normal tissues depend on micro-distribution of boron compound. For example, boronophenylalanine (BPA) accumulates mucosal epithelium, which lead to oral mucositis in BNCT for head and neck cancer. In this study, the micro-distribution of BPA in the esophagus was investigated.

EXPERIMENTS

Mice: Ten- to twelve-week-old female C3H/He mice were used. The mice were purchased from Japan SLC, Inc.

Analysis of BPA micro-distribution by autoradiography using CR-39: BPA was administered subcutaneously at the dose of 500 mg/kg. At one hour after the BPA administration, the esophagus was extracted and embedded in Optimal Cutting Temperature (O.C.T) Compound. The samples were sliced 10 μm thickness using cryostat. The detailed procedure for analysis of BPA micro-distribution was referred to the previous published paper from our laboratory [1]

RESELTS

Figure 1 shows the superimposed image of the dots on CR-39 and hematoxylin and eosin (HE) image. The dots on CR-39, to some extent, appears to overlay the basal cells in the esophageal mucosa.

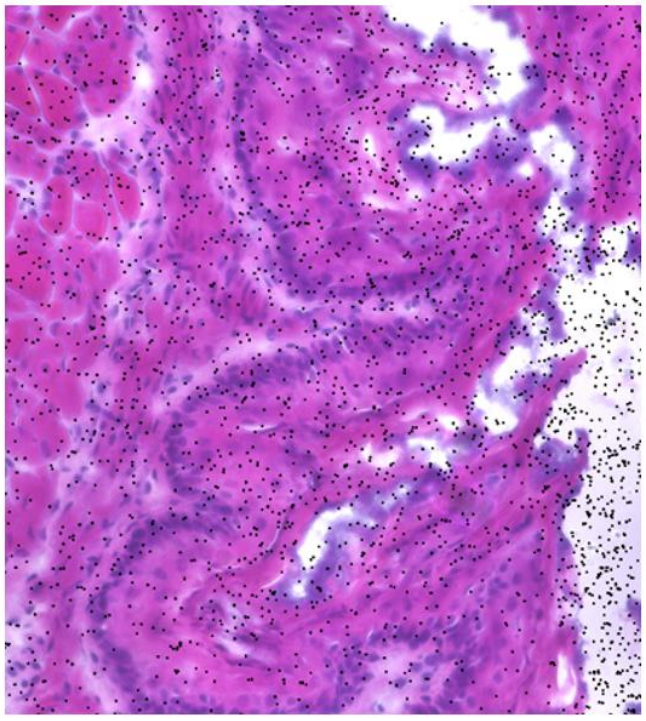

Fig.1. superimposed image of the dots on CR-39 and HE image.

REFERENCES:

[1] S. Takeno, Physica Medica, **82** (2021) 306-320.

CO7-38

Effects of neutron irradiation on immune cells

M. Shirakawa[1,2], A. Zaboronok[2], H. Michiue[1], K. Igawa[1], H. Kumada[2], T. Sakae[2], A. Matsumura[2], T. Takata[3], N. Kondo[3], Y. Sakurai[3], M. Suzuki[3]

[1] *Neutron Therapy Research Center, Okayama University*
[2] *Institute of Medicine, University of Tsukuba*
[3] *Institute for Integrated Radiation and Nuclear Science, Kyoto University*

INTRODUCTION:

Recent studies have shown that irradiation of normal tissue, such as skin, results in an accumulation of tumor-infiltrating regulatory T cells (Treg cells), which subsequently leads to tumor resistance to radiotherapy [1]. In light of these findings, we sought to determine whether similar effects are observed with neutron irradiation and will present some of the key results here.

EXPERIMENTS:

1. In vivo animal model

Female, 3-week-old C57BL/6J mice were purchased from CLEA Japan Inc., Tokyo, Japan. The mice were acclimatized for one week at the Kyoto University Institute for Integrated Radiation and Nuclear Science (KURNS). A radiation-affected model was established by exposing the mice to thermal neutron irradiation. Irradiation was performed with a flux of 1.0-1.2 × 10^9 neutrons/cm^2/s for durations of 4, 8, and 12 minutes.

2. Injection of tumor cell line.

The left flank skin and right lower limb of irradiated recipient mice were shaved. Subsequently, 5×10^5 B16-F10 cells were injected subcutaneously into the left flank, and 2×10^5 cells were injected intramuscularly into the right lower limb. Tumor size was measured over time with an electronic caliper until day 16 post-irradiation, and tumor volume was calculated using a previously applied formula [2]. On the final measurement day, two mice in each of the 8-minute and 12-minute irradiation groups died spontaneously. Therefore, significant differences in tumor sizes between groups were calculated on day 13 using one-way ANOVA with Tukey's multiple comparison tests.

RESULTS:

As shown in Figure 1, tumor growth was more rapid in the left flank compared to the right lower limb. However, by day 13, no significant differences were observed between the groups exposed to different irradiation times, suggesting that the impact of neutron irradiation on immune cells is very limited. Additionally, no significant weight loss was observed in any of the groups.

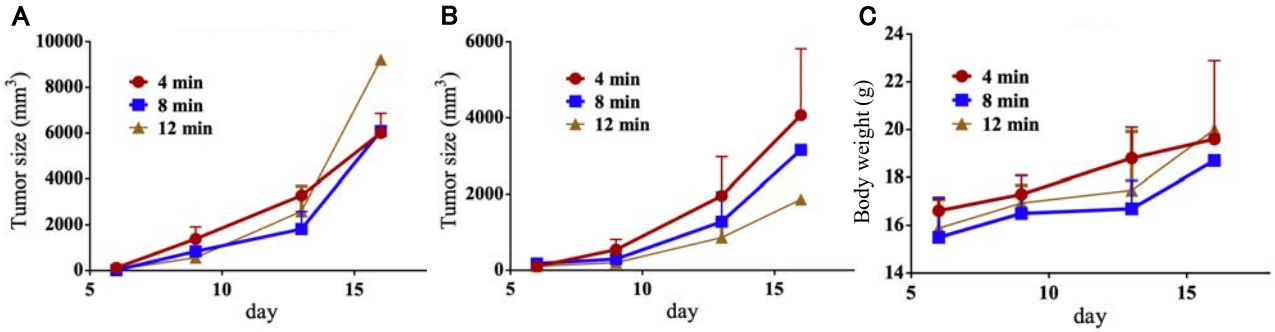

Fig.1) In vivo effect of neutron irradiation (n=3). (A) Tumor growth at the injected/non-irradiated sites. (B) Tumor growth at the injected/irradiated sites. (C) Body weight.

REFERENCES:

[1] Jeremy G Price *et al.*, Nature Immunology, **16** (2015) 1060-1068.
[2] M. Shirakawa *et. al.,* KURRI PROGRESS REPORT 2017 (2018) 69 .

CO7-39

Attempts to sensitize tumor cells by exploiting the tumor microenvironment

Y. Sanada, T. Takata, Y. Sakurai, H. Tanaka and T. Watanabe

Institute for Integrated Radiation and Nuclear Science, Kyoto University

INTRODUCTION: Boron neutron capture therapy (BNCT) is a radiotherapy that kills tumor cells via the $^{10}B(n, \alpha)^{7}Li$ reaction [1]. Especially for BNCT with BPA, SLC7A5 (LAT1) protein expression level is an important factor for the anti-tumor efficacy, since the LAT1 is a major transporter for intracellular uptake of BPA. Recent studies suggest that tumor microenvironment, such as hypoxia, may influence the expression profiles of SLC7A5 and hinder the intracellular uptake of BPA. However, it has not been fully understood how the disturbance of SLC7A5 expression affects the anti-tumor efficacy of BPA-BNCT. In the present study, we generated multiple tumor cell lines that lack the function of SLC7A5 and that overexpress SLC7A5 proteins, and compared the sensitivity of these cells to BPA-BNCT.

EXPERIMENTS: Like previously established SCCVII (mouse squamous cell carcinoma cell lines)-SLC7A5 deficient cells [2], A2058 (human melanoma cell lines)-SLC7A5 deficient cells were generated using CRISPR-Cas9 system. Since two SLC7A5 pseudogenes have been found in the human genomes, the exon 2 of human SLC7A5 locus were chosen as the CRISPR-Cas9 target-site in order to minimize the off-target effects. To generate SCCVII that overexpress SLC7A5 proteins, the SCC VII cells were transfected with the SLC7A5 expression vector generated by modifying pBApo-EF1α vector. To examine the sensitivity to BPA-BNCT, these cells were exposed to neutron beams (KUR Heavy Water Facility) and then clonogenic cell survival assays were performed.

RESULTS: We examined the sensitivity of SCC VII-ΔSLC7A5 (SLC7A5 deficient) cells and SCC VII cells overexpressing recombinant SLC7A5 proteins to BPA-BNCT. As shown Fig. 1, the result suggested that the expression level of SLC7A5 proteins is slightly, but not significantly, related to the cellular survival. We also measured the cellular survival of A2058-ΔSLC7A5 (SLC7A5 deficient) cells. A2058-ΔSLC7A5 was more resistant to BPA-BNCT than the parental A2058 cells. Although a further investigation is needed, changes in SLC7A5 expression levels likely affect the cellular survival after BPA-BNCT to an extent that depends on cell type.

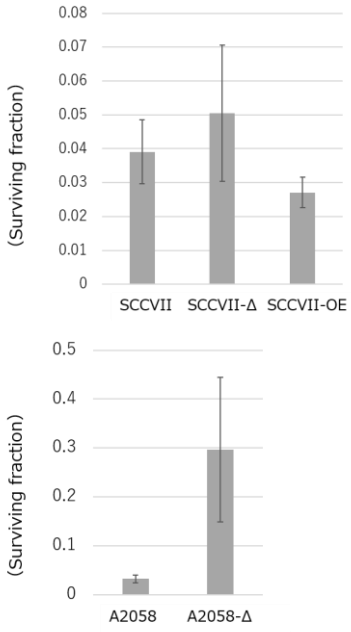

Fig.1 Survival fractions of neutron-irradiated cells. Cell suspensions prepared with BPA containing medium were exposed to neutrons for 20 min (thermal neutrons at a fluency of 2.1×10^{12} n/cm^2).

REFERENCES:
[1] S. Masunaga *et al.,* Int. J. Rad. Biol., **92** (2016) 187-194.
[2] Y. Sanada *et al.,* Int. J. Rad. Biol., **97** (2021) 1441-1449.

CO7-40

Sensitization of BPA-BNCT by Regulating the Polarity of Tumor-Associated Macrophage Using All-*Trans* Retinoic Acid

N. Yasukawa, N. Matsuda, K. Bando, R. Kawasaki[1], N. Kondo[2], Y. Sanada[2], Y. Sakurai[2], M. Suzuki[2] and T. Nagasaki

Graduate School of Engineering, Osaka Metropolitan University

[1] Graduate School of Advanced Science and Engineering, Hiroshima University
[2]Institute for Integrated Radiation and Nuclear Science, Kyoto University

INTRODUCTION: In the tumor microenvironment (TME), various stromal cells such as immune cells, fibroblasts, and vascular endothelial cells interact with cancer cells and are involved in the proliferation and progression of cancer cells. Tumor-associated macrophages (TAM) are attracting attention as major players in the TME. TAMs are broadly divided into tumor-suppressive type M1 and tumor-promoting type M2, and TAMs mainly exist as an M2-like phenotype in the TME [1]. M2-like macrophages are involved in promoting angiogenesis and suppressing antitumor immunity. Therefore, if the phenotype of tumor-infiltrating macrophages can be induced from M2 to M1, it will lead to the novel method for cancer prevention and treatment. Since the predominance of STAT3 activation results in M2 macrophage polarization, STAT 3 inhibitors are promising as TAM polarity regulators. Although all-*trans* retinoic acid (ATRA) shifts the polarity of macrophages from M2 type to M1 type by suppressing the STAT3 signal transduction pathway [2], it has a problem of poor water solubility as a drug. Therefore, we attempted to create a TAM-targeted nanogel formulation by including β-1,3-glucan, which functions as a ligand for Dectin-1, a membrane protein of macrophages, as a solubilizer. Furthermore, we confirmed the combination effects of ATRA/β-1,3-glucan nanogel on BPA-BNCT toward SCCVII tumor cells-bearing C3H mice.

****

EXPERIMENTS: A subcutaneous inoculation of 6 x 10^5 SCCVII cells in female C3H mice was established for 14 days. Thermal neutron beam irradiation (1MW, 70 min) was started from the time point of 120 min after the s.c. injection of BPA (250 mg/kg)-fructose. BNCT effects were evaluated on the basis of the changes in tumor volume. In order to estimate a combination effect on ATRA, the complex of ATRA/ β-1,3-glucan ([ATRA]=100 μM, 200 μL) was administered via the tail vein at the time points of 1, 5, 7 days after irradiation. Treated mice were sacrificed 8 days after thermal neutron beam irradiation, tumor tissues were removed, and frozen sections were prepared. The samples were observed using a microscope BZ-X800 (KEYENCE), and the percentage of positive cells within the tumor was analyzed using a BZ-X Analyzer.

****

RESULTS: In the combination experiment of BPA-BNCT with ATRA treatment, the combination treatment group effectively suppressed tumor volume increase compared to BPA alone. Additionally, tumor recurrence was observed in both groups from around day 20, however, the combined treatment group maintained a relatively low increase in tumor volume. As shown in Fig. 1, On day 8, the rate of iNOS-positive cells, which are M1 phenotype macrophages, were 4.93% and 0.58% in the ATRA/β-GC nanogel and BPA-BNCT combination treatment group and the BPA-BNCT alone treatment group, respectively.

These results suggest that the presence of a TAM polarity regulator during BNCT treatment affects the TME, increases M1-type TAMs, and sensitized the BPA-BNCT effect.

****

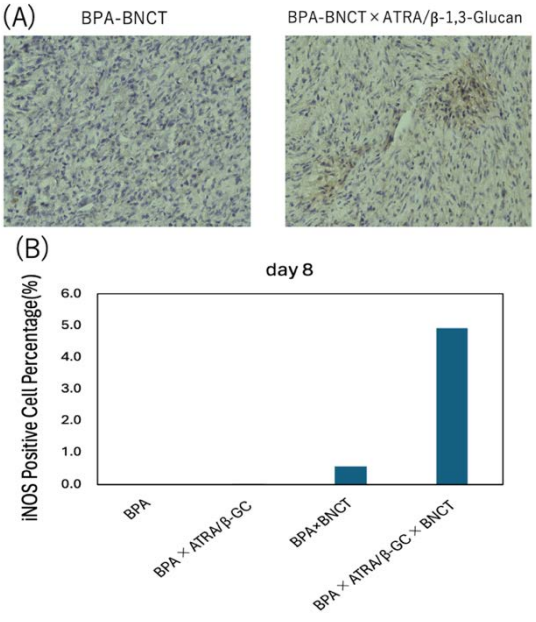

Fig. 1. Examples of immunostains used to identify M1 macrophages (A). Percentage of iNOS-positive cells that are M1 phenotype macrophages on day 8 (B).

REFERENCES:

[1] A. Sica *et al.*, J. Clin. Invest., **117** (2007) 1155.
[2] A. Alatshan *et al*., Cells, **9** (2020) 1591.

CO7-41

Synthesis and evaluation of a novel boron neutron capture therapy agent

H. Kimura[1], M. Suzuki[2]

[1]*Research Center for Experimental Modeling of Human Disease, Kanazawa University*
[2]*Institute for Integrated Radiation and Nuclear Science, Kyoto University*

INTRODUCTION: Neuroendocrine Tumor (NET) is known to be characterized by high expression of somatostatin receptors (SSTRs) on the tumor cell membrane. Somatostatin is a cyclic peptide discovered as a hypothalamic factor that potently inhibits growth hormone secretion from the pituitary gland. There are five subtypes of somatostatin receptors (SSTR1-5), and SSTR2 is highly expressed in NETs. Therefore, somatostatin analogs with high binding to SSTR2 are used for treatment[1) - 2)]. Furthermore, Peptide Receptor-mediated Radionuclide Therapy (PRRT), which uses somatostatin analogs as nuclear medicine drugs for NET patients, has recently been implemented in Europe, and LUTATHERA® was approved for manufacturing and marketing in Japan for the first time on June 23, 2021 as a drug for PRRT in Japan. However, there is a need for the development of new therapies with greater therapeutic efficacy. Therefore, in this study, we conducted a basic study on the potential of BNCT for NETs. In addition, we developed BNCT agents targeting EphA2, which is expressed in cancer. Erythropoietin-producing hepatocellular receptor A2 (EphA2) is overexpressed in cancer cells and causes abnormal cell proliferation[3)].

EXPERIMENTS: This year, since I was unable to conduct animal experiments due to transfer to another university, I focused on *in vitro* evaluations.
SSTR: BSH-conjugated somatostatin derivatives were synthesized. Binding of BSH-conjugated somatostatin derivatives to SSTR was evaluated using AR42J cells.
EphA2: BSH reacted with EphA2-230-1 antibody. BSH-conjugated EphA2-230-1 antibody was used to evaluate the proliferative potential of U87MG cells (human brain glioblastoma cells). After adding the drug to the cells, the cells were irradiated with neutrons at 5 MW for 3 minutes of 1 MW for 15 minutes.

RESULTS: *SSTR:* Binding of BSH-conjugated somatostatin derivatives to SSTR was evaluated using AR42J cells, and it was found that 30% of the amount of drug added was bound to the cells. Next year, we would like to evaluate cell killing by neutron irradiation.
EphA2: The number of BSH bound to the EphA2-230-1 antibody was evaluated using MALDI-TOF MS. As a result, 10 molecules of BSH were introduced into one molecule of EphA2-230-1antibody. Binding of BSH-conjugated EphA2-230-1 antibody to EphA2 was confirmed. The proliferative capacity of cancer cells was evaluated by colony formation assay. Although we have not completed all the analysis, we think that the irradiation conditions need to be optimized. In addition, we think that the cellular internalization rate of BSH-bound EphA2-230-1 antibodies should also be determined.

REFERENCES:
[1] Ozge Keskin, Suayib Yalcin., Onco Targets Ther., **6** (2013) 471-483.
[2] Thomas Gunther *et al*., Phar-macological Reviews, **70** (2018) 763-835.
[3] Pasquale E. B., Nat. Rev. Cancer, **10** (2010)165–180.

CO7-42

Estimation of Macro Leathal Distribution Around Tumor Mass in GdNCT

M. Takagaki[1], N. Kondo[2], Y. Sakurai[2], and M. Suzuki[2]

[1]*RCNP*
[2]*Institute for Integrated Radiation and Nuclear Science, Kyoto University*

INTRODUCTION: Gadolinium neutron capture therapy is not necessarily unrealistic. For Gd neutron capture therapy (Gd-NCT) to be successful, sufficient amounts of Gd must be delivered and maintained within the tumor. In recent years, it has become possible to deliver and maintain in tumor high concentrations of Gd using nano micelles［1］.
Therefore, considering the distribution of the lethal effect of GdNCT is an important step for practical application, and is also of great radiobiological interest.
The peritumoral dose distribution of GdNCT is very complex depending on the tumor shape and the Gd concentration within the tumor［2］. In this experiment, we investigated the practicality of GdNCT using a simple model to investigate the distribution of lethal effects depending on dose near the tumor.

EXPERIMENTS and RESULTS:

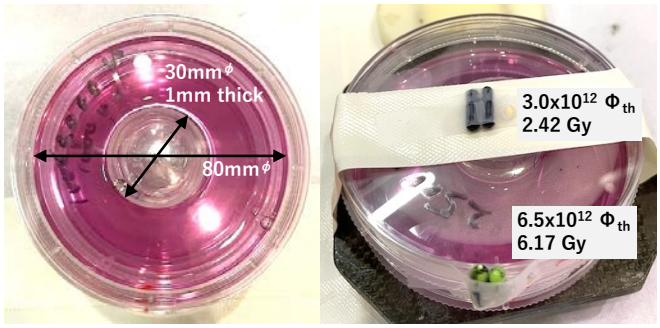

Fig.1 A model for estimating the lethal effect of tumor margins for GdNCT; Concentrical double structured petri dish.

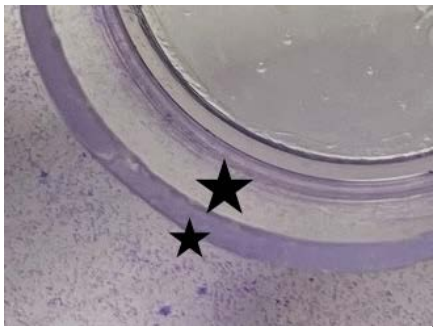

Fig.2 Paucity of surviving cells was observed at 2-3 mm rim (★) around the petri dish.

A gas-sterilized double-walled petri dish was created as shown in Fig.1(*left*). A 3 cm diameter Petri dish was fixed concentrically in the center of an 8 cm Petri dish. After filling the periphery with 1x10E5 cell suspension of U87 and allowing the periphery with 1x10E5 cell suspension of U87 and allowing the cells to adhere to the Petri dish in a usual incubator, a small Petri dish in the center was filled with a maximum concentration of 500 mmol/L of GdDTPA (approximately 12,285 ppm ^{157}Gd) and thermal neutrons were horizontally irradiated Thermal neutron fluence and Gy dose are shown to the *right*.
A high degree of cell death was observed within 2-3 mm rim of the Petri dish, and significant cell death was observed in the fur peripheral area in accordance with Gd concentration, which will lead to a safety indication of GdNCT. For detailed analysis, we will improve and conduct further experiments this year to confirm reproducibility and reevaluate.

REFERENCES:
［1］RR. Zairov *et al.,* KURNS Progres Report 2022 (2023) C07-12.

［2］N. Hosmane *et al.,* Boron and Gadolinium Neutron Capture Therapy for Cancer Treatment. World Scientific, 2012.

CO7-43

Establishment of innovative BNCT treatment method for intractable bladder cancer

P. Huang[1], K. Igawa[1], T. Kasai[1], Y. Sakurai[2], H. Michiue[1] and M. Suzuki[2]

[1]*Neutron Therapy Research Center, Okayama University*
[2]*Particle Radiation Oncology Research Center, Institute for Integrated Radiation and Nuclear Science, Kyoto University*

INTRODUCTION: Bladder cancer generally has a high survival rate, but it has a poor prognosis and tends to repeat recurrence, which accounts for 70% of cases. In order to verify this new boron neutron capture therapy for refractory bladder cancer, we will use cell lines and the mouse bladder orthotopic cancer model for the neutron irra-diation necessary for BNCT at Kyoto University's Institute for Integrated Radiation and Nuclear Science. The results obtained in this experiment are expected to expand the indications of BNCT and contribute to improving the results of bladder cancer treatment.

****

EXPERIMENTS: We used human bladder cancer T24 cells, BCG-resistant T24 cells, and the human bladder transitional epithelial cell line hBMSC, and perform neutron irradiation after adding boron chemicals.
After irradiation, analyze cell viability using XTT.
Boron addition concentration is (0, 5, 25, 50, 100, 500)
Cells were cultured at 96W and analyzed for XTT for 72 hours after irradiation
(each concentration N>20)

****

RESULTS: As shown in Fig. 1, The effects of BNCT on bladder cancer T24 cells and BCG-resistant T24 cells were dose- and time-dependent.
No effect in human bladder transitional epithelial cell line hBMSC at boron concentrations of less than 50ug/ml.

****

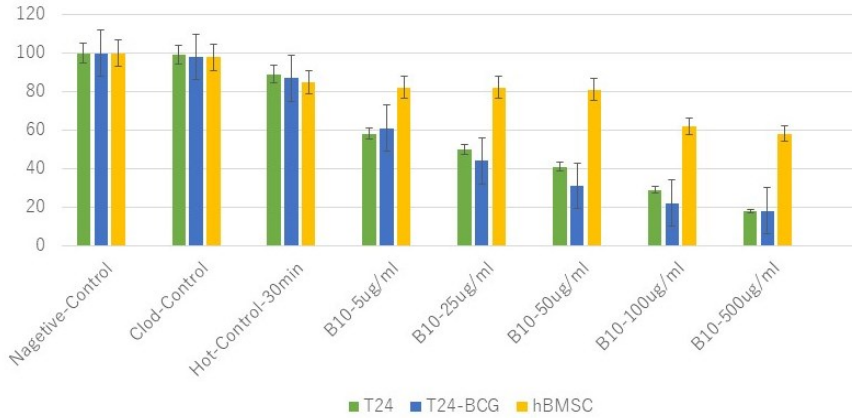

Fig. 1. The cell viability assay of 72 hours after Neutron irradiation.

Neutron irradiation for 30 minutes after Boron added for 3 hours; Boron addition concentration is (0, 5, 25, 50, 100, 500ug/ml) **(N>20)**

REFERENCES:

[1] Y. Zhang *et al.,* Adv Mater., **35** (2023) e2301479.

[2] J. Arima *et al.,* Biomed Pharmacother., **154** (2022) 113632.

[3] R. Kayama *et al.,* Sci Rep., **14** (2024) 8265.

CO7-44

Analysis of the Structural Change of Boronophenylalanine by Boron Neutron Capture Reaction

M. Suzuki, Y. Sakurai, T. Takata, H. Ueda

Institute for Integrated Radiation and Nuclear Science, Kyoto University

INTRODUCTION:

Boron neutron capture therapy (BNCT) is one of the potent radiotherapies based on the combination of boron-containing molecules and epi-/thermal neutron irradiation. In this therapy, high linear energy (LET) particles, alpha (^{4}He) and lithium (^{7}Li) nucleus, are generated from boron-10 (^{10}B) atom due to the nuclear reaction between ^{10}B and neutrons. In 2020, L-4-boronophenylalanine (BPA) is approved as a BNCT agent for the treatment of recurrent head and neck cancer in Japan [1]. Although BPA have been used in BNCT research for decades, the effect of boron neutron capture reaction on the molecular structure of BPA is unclear. In this work, we attempted the initial studies to identify the structural change of BPA in aqueous solution after epi-/thermal neutron irradiation.

EXPERIMENTS and RESULTS

The aqueous solution of BPA was prepared by using ^{10}B-enriched BPA purchased from Inter-Pharma (Prague, Czech Republic). The boron concentration was determined by Prompt Gamma-ray Analysis (PGA) and/or Inductively Coupled Plasma Atomic Emission Spectrometry (ICP-AES) using the same standard solutions (1, 2, 5, 10, 20, 50 ppm ^{10}B). Teflon tubes containing boron solution were irradiated with epi-/thermal neutrons using the Heavy Water Neutron Irradiation Facility of the Kyoto University Research Reactor (KUR) operated at 1 MW and/or 5 MW for several times. The activation rate of samples was confirmed by the measurement of gamma-ray from the irradiated samples, and the change of BPA was analyzed by some methods. In this study, a preliminary investigation of structural change analysis was carried out. However, the change of boron concentrations was not observed possibly due to deficiency of neutron irradiation. We need further studies and optimization of conditions such as sample preparation, irradiation time, and evaluation methods.

****

REFERENCES:

[1] M. Suzuki, Int. J. Clin. Oncol., **155** (2021) 182-187.
[2] D.D. Pierro *et al.*, Anal. Biochem., **284** (2000) 301-306.
[3] S. Caquani *et al.*, Int. J. Radiat. Oncol. Bioll. Phys., **72** (2008) 562-567.
[4] L. Dick *et al.*, J. Pharm. Biomed. Anal., **56** (2011) 633-636.
[5] G. Halbert *et al.*, Eur. J. Pharm., **48** (2013) 735-739.

CO8-1

Demonstration experiment of detecting the HEU sample covered with lead using a neutron rotation machine and water Cherenkov neutron detector

M. Komeda[1], K. Tanabe[2], Y. Toh[1], Y. Kitamura[3] and T. Misawa[3]

[1]*Nuclear Science and Engineering Center, Japan Atomic Energy Agency*
[2]*National Research Institute of Police Science*
[3]*Institute for Integrated Radiation and Nuclear Science, Kyoto University*

INTRODUCTION: A compact (transportable) and low-cost non-destructive inspection system to detect hidden nuclear material is required in the fields of nuclear security. We developed a new nuclear material detection method, called the active rotation method, using a neutron rotation machine that rotates a neutron source like Californium-252 at a speed of thousands of rpm. In addition to the rotation machine, we developed a water Cherenkov neutron detector (WCND) as a low-cost neutron detector. The system for detecting nuclear materials can be composed with the neutron rotation machine and WCND, leading to a compact and low-cost. In previous studies, we accomplished to detect a few grams of high enriched uranium (HEU) using the system. Incidentally, gamma ray measurements are common for detecting nuclear materials due to its ease of measurement. However, it is easy to shield gamma rays from HEU with thin lead plates since those gamma rays are low energy. The purpose of this year is to detect the HEU covered with lead plates that cannot be detected by a gamma ray detector.

EXPERIMENTS: The HEU is surrounded by lead plates, and covered polyethylene blocks around it. The experimental setup is shown in Fig.1. Note that the lead plates inside the polyethylene blocks are visible, but in the experiment, they are covered with the entire blocks and inside is not visible. The dimensions of the neutron rotation machine are approximately 60cm in width, depth, and height. The rotation machine can rotate the disk (diameter 32cm), where a neutron source is installed at its outer periphery, at a rotation speed between 0 and 4000 rpm. A neutron source of Californium-252 is set in the disk, the radioactivity was 2.2 MBq. In this experiment, we used approximately 4 g of HEU. The WCND basically consists of an aquarium (30x25x30cm), four PMTs (Photomultiplier tube) and boron rubber. The PMT diameter is 2 inches. The boron rubber is attached on the surface of the aquarium to prevent thermal neutrons from entering. The neutron time distributions were measured by a multi-channel scaler (MCS) that was synchronized with the disc rotation signal from the servomotor.

RESULTS: It was confirmed that low-energy gamma rays generated from HEU were effectively blocked by lead plates by measurements using a Ge detector. We successfully detected its HEU shielded with lead plates using a neutron rotation machine and WCND. Then, we estimated whether the object included the nuclear material by a comparison between the time-distribution spectra at 4000 rpm and 300 rpm. The measurement time for each speed was 10 minutes. Figure 2 shows an example of measurement result (time-distribution spectrum) at the rotation speed of 4000 rpm. As a next step for our study, we are going to work on detecting unevenly distributed nuclear materials inside the container.

Fig. 1 The rotation machine (left), the water Cherenkov detector (right), and measurement object (middle). The center part of the object is HEU covered with lead plates.

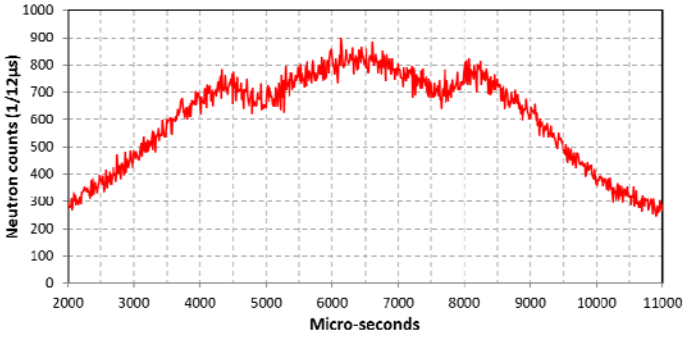

Fig. 2 Neutron events distribution in the case of HEU covered with lead plates. The measurement time was 10 minutes with the rotation speed of 4000 rpm.

CO8-2

Establishment of a novel mutation breeding using Boron Neutron Capture Reaction (BNCR)

M. Kirihata, S. Segami[1], Y. Hattori, T. Kinouchi[2], Y. Kinashi[2]

Research Center of BNCT, Osaka Prefecture University
[1]Research Institute of Environment, Agriculture and Fisheries, Osaka Prefecture
[2]Research Reactor Institute, Kyoto University

INTRODUCTION: Boron Neutron Capture Reaction (BNCR) is based on the nuclear reaction of ^{10}B atom with thermal/epithermal neutron already applied to cancer treatment (BNCT). As a new utilization method of BNCR, this study aims to establish a novel mutation breeding using BNCR. The method attempts mutagenesis by immersing plant seeds in a ^{10}B-enriched boron compound, re-drying, and then irradiating the seeds with thermal neutrons to induce BNCR. Its mutagenic effect depends on chemical and physical factors such as ^{10}B concentration, thermal neutron intensity, and irradiation time. Previously, we tested ^{10}B-enriched boric acid ($H_3{}^{10}BO_3$), ^{10}B-enriched *p*-boronophenylalanine (BPA), and mercaptododecaborate (BSH) as boron compounds for treating rice seeds. In this report, two new experiments were performed. The first was the experiment using C12-BSH. This compound introduced an alkyl chain on the thiol group of BSH to enhance the hydrophobicity, which has a higher internalization amount than BSH into cells in animal cells. The second evaluated the effects of $H_3{}^{10}BO_3$ treatments at low concentrations below 10 mM.

EXPERIMENTS: The experimental material used *Oryza sativa* L. cv. Nipponbare. The dry seeds were immersed into different boron concentrations (0, 10, 100, 1000, 2000 ppm) of ^{10}B-enriched C12-BSH and 0, 0.5, 1, 2.5, 5, 7.5, 10 mM $H_3{}^{10}BO_3$ for 24 h. The solvents were distilled water and PBS buffer for C12-BSH and $H_3{}^{10}BO_3$, respectively. The samples were washed with water and re-dried. The seeds in 6-mL tubes were irradiated with thermal neutron for 90 minutes. After the irradiation treatment, the seeds were cultured in Petri dishes with continual moistening of filter paper at 25℃ under a photoperiod of 16 h light and 8 h dark. The germination rate was examined 7 days after sowing (DAS) and growth 14 DAS. As a control experiment, seeds only treated with $H_3{}^{10}BO_3$ soaking and not irradiated with thermal neutrons were sown using the same method, and germination rates were investigated.

Fig.1 Comparison of growth 14DAS
Left：Control (10 mM $H_3{}^{10}BO_3$ treatment and no irradiation)
Right：10 mM $H_3{}^{10}BO_3$ treatment and irradiation

RESULTS: The C12-BSH treatment did not decrease the germination rate and growth in any of the concentrations. This result is similar to the result of the BSH treatment, and it is not clear at this time whether it is not taken up by seeds, whether there is no difference in the internalization amount into cells in the plant cells, or whether the selective uptake has no effect on the germination rate. For the $H_3{}^{10}BO_3$ experiment, the germination rate at 7 DAS was not decreased in any concentrations. On the other hand, at 14 DAS, no effects were observed at 5mM or less on growth, but shoot length and root volume varied at 7.5 mM treatment, and shoot less than 1 cm and no rooting were observed in all individuals at 10 mM treatment, indicating a strong effect of BNCR (Fig.1). These effects and the decreased germination rate at higher concentrations were not seen without neutron irradiation at the same concentration of immersion treatment, suggesting that BNCR caused it. The germination rate was consistent with previous results over a wide range of treatments and did not decrease with treatments below 10 mM. However, this observation confirmed that treatments above 7.5 mM affected growth. For mutagenesis, 10 mM treatment, where severe effects on growth are observed, should be avoided, and 7.5 mM or less is considered preferred.

CO9-1

Interpretation of solubility based on solid-state of trivalent lanthanide hydroxides and oxides

T. Kobayashi, T. Sasaki, K. Takamiya[1]

Graduate School of Engineering, Kyoto University
[1] Institute for Integrated Radiation and Nuclear Science, Kyoto University

INTRODUCTION: Safety assessment of radioactive waste disposal requires a quantitative prediction of the migration behavior of radionuclides under the waste disposal conditions. Radionuclides in trivalent states such as Am(III) and Cm(III) undergo strong hydrolysis reactions, and poorly soluble hydroxide precipitates ($M(OH)_3(s)$) in the neutral to alkaline pH range in the absence of any complexing ligands. In order to predict the migration behavior of these nuclides, it is necessary to understand the solubility of $M(OH)_3(s)$ and their thermodynamic data, such as hydrolysis constants and solubility products [1]. For the solubility of tetravalent metal hydroxides ($M(OH)_4(s)$), their solubility products have been found to increase in inverse proportion to their particle size [2]. Therefore, it is interesting to explore the particle size effect for $M(OH)_3(s)$. In this study, the solubility samples for La(III) hydroxide solid phase ($La(OH)_3(s)$) were prepared and investigated together with the solid phase analysis such as crystal structure and particle size. An interpretation of solubility was discussed based on the solid phase structure.

EXPERIMENTS: Sample solutions containing La(III) solid phase were prepared using the oversaturation and unsaturation methods. In the oversaturation method, a 0.01 mol/L La(III) nitrate was prepared as a mother solution, and the pH was adjusted to pH 7 to 12 by the addition of NaOH to precipitate $La(OH)_3(s)$. In the unsaturated method, $La_2O_3(cr)$ was added as a solid phase to a sample solution whose pH was adjusted in advance to 7 to 12. Sample solutions were kept at 25°C or 90°C for one month. After the aging, the supernatant was ultrafiltered through a 3 kDa membrane filter. The La concentration contained in the filtrate was determined by ICP-MS. The solid phase contained in each sample solution was collected in a suspended state and filled into a Kapton membrane cell with a thickness of 1 mm. These samples were measured at the small-angle X-ray scattering (SAXS) beamline (BL8S3) at the Aichi Synchrotron Center. The X-ray wavelength used in the measurements was 0.92 Å, and the X-rays scattered by the sample were detected at three camera lengths (0.21 m, 1.23 m, and 3.97 m) using a large-area pixel detector (PILATUS 2M detector).

RESULTS: Regarding the SAXS intensity ($I(q)$) of the solid phase prepared by the oversaturation method, in the range of scattering vector q ($q = 4\pi\sin\theta/\lambda$, θ is the scattering angle) > 10 (nm^{-1}), a diffraction peak appeared, identified as $La(OH)_3(cr)$ based on the peak position. Since it has been found that $La_2O_3(cr)$ changed to $La(OH)_3(cr)$ in the unsaturated method [3], and the oversaturation and undersaturation methods obtained the same crystal structure. In the region of $0.06 < q < 4$ (nm^{-1}), an inflection point was observed around q = 0.8 and 0.25 (nm-1) for the sample solutions kept at 25°C and 90°C, respectively. This suggests that both solid phases have the same crystal structure, but the respective primary particle sizes are different. The solubility of $La(OH)_3(cr)$ kept at 90°C was about two orders of magnitude lower than those kept at 25°C, indicating the particle size effect for the solubility $La(OH)_3(cr)$.

REFERENCES:

[1] I. Grenthe *et al.,* Chemical Thermodynamics, Vol. **14**, OECD-NEA (2020).
[2] M. Rand *et al.,* Chemical Thermodynamics, Vol. **11**, OECD-NEA (2009).
[3] Md. Moniruzzaman *et al.,* J. Nucl. Radiochem. Sci., **20** (2020) 32-42.

CO9-2

Redox potential of U in NaCl-$CaCl_2$ melt at 799 - 848 K

T. Murakami, Y. Sakamura and K. Takamiya[1]

Central Research Institute of Electric Power Industry
[1]Institute for Integrated Radiation and Nuclear Science, Kyoto University

INTRODUCTION: A NaCl-$CaCl_2$ mixture melt is proposed as a candidate of a base salt for molten chloride salt fast reactor. There are very limited reports on electrochemical properties such as redox potential of actinides in the melt, which are basic data to construct a reprocessing process of the spent molten chloride fuel salt. In this study, electrochemical measurements were carried out to obtain the redox potential of U in eutectic NaCl-$CaCl_2$ melt at a temperature range between 799 and 848 K.

EXPERIMENTS: All electrochemical measurements were performed in eutectic NaCl-$CaCl_2$ salt (50:50 mol%) containing UCl_3 which was melted in the electric furnace placed in the glove box filled with a purified Ar gas. W wire (1 mmφ) and glassy carbon rod (3 mmφ) were used as the working and counter electrodes, respectively. The Ag/AgCl reference electrode was used, of which potential was calibrated to be -1.257 V, -1.267 V and -1.273 V (vs. Cl_2/Cl^-) at 799 K, 837 K and 848 K, respectively.

RESULTS: Fig. 1 shows a cyclic voltammogram using W wire electrode in the melt at 799 K. A couple of cathodic and anodic currents was observed at around -2.5 V (vs. Cl_2/Cl^-), which was ascribed to U metal deposition (reaction 1) and its dissolution (reverse reaction of reaction 1), respectively,

$$U^{3+} + 3e^- \rightarrow U \quad (1)$$

Based on the results of the cyclic voltammetry, galvanostatic electrolysis at -18 mA cm^{-2} was performed for 5 seconds to deposit U metal on the W wire electrode. Then, the redox potential of the U metal deposited on the W (E_U) was measured in the melt by changing the applied current to 0 mA. The same procedure was carried out to obtain E_U at different temperatures, 837 K and 848 K. The obtained values were plotted against temperature as seen in Fig. 2, showing a linear relationship between E_U and temperature. The similar tendency was reported for the formal standard redox potential of U in LiCl-KCl melt at 673-823 K [1].

The concentration of UCl_3 in the melt (C_{UCl3}) will be measured in near future to convert the obtained E_U to the formal standard redox potential of U ($E_U^{0'}$) according to the following Nernst equation,

$$E_U = E_U^{0'} + \frac{RT}{3F}\ln C_{UCl3} \quad (2)$$

where R is gas constant, T is temperature in Kelvin, F is faraday constant.

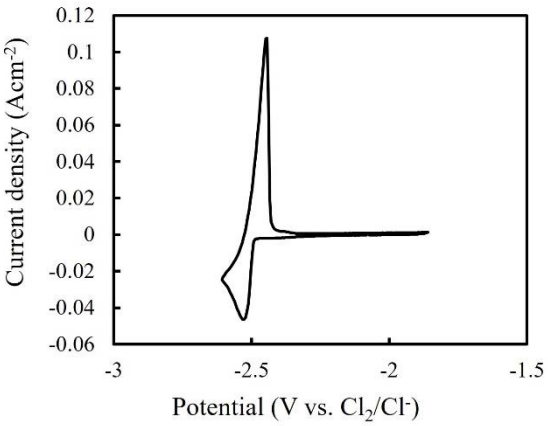

Fig. 1. Cyclic voltammogram using W wire electrode in NaCl-$CaCl_2$-UCl_3 melt at 799 K. Scan rate was 50 mV s^{-1}.

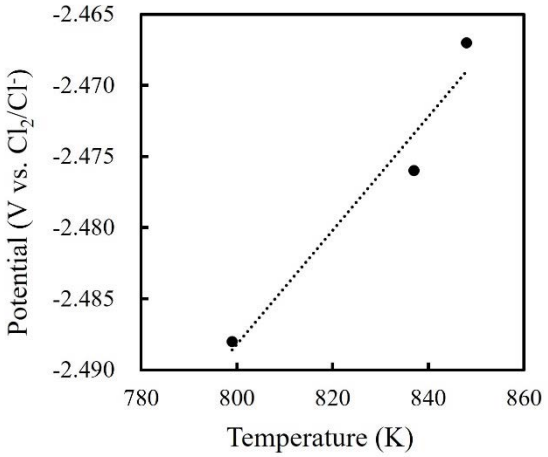

Fig. 2. Measured redox potentials of U in NaCl-$CaCl_2$-UCl_3 melt at 799 K, 837 K and 848 K.

REFERENCES:

[1] P. Masset *et al.*, J. Electrochem. Soc., **152** (2005) A1109-A1115.

Effect of Cyclic Structures of Water-soluble Cyclic Monoamide Compounds on Stability against γ-Ray Irradiation

D. Saegusa, M. Nogami, and N. Sato[1]

Faculty of Science and Engineering, Kindai University
[1]*Institute for Integrated Radiation and Nuclear Science, Kyoto University*

INTRODUCTION: It is of great importance to develop compounds with selectivity for uranium(VI) species in nitric acid media. Under such a background, we have investigated stability against γ-ray irradiation for a lot of monoamide compounds as candidates for resins[1-3]. This year, 2-piperidone (PP) and 2-pyrrolidone (PR) which are both water-soluble and compose the functional group of monoamide resins, VBPP[2] and VBPR[3], respectively, were taken. As seen in Fig. 1, both compounds are categorized into "cyclic monoamides". The former and the latter have a 6- and 5-membered ring, respectively, and the other parts are identical from the viewpoint of chemical structure. Previously, the difference in the stability between 6- and 5-membered rings of cyclic monoamides was investigated by using compounds where hydrocarbon atoms are bound with the nitrogen atom in cyclic monoamides, but clear tendency was not observed. In this study, γ-ray irradiation to both compounds was performed in nitric acid and hydrochloric acid solutions.

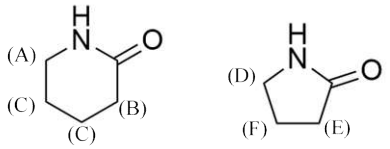

Fig. 1. Chemical structures of PP (left) and PR (right)

EXPERIMENTS: 6 mol/dm^3 (= M) HNO_3 solutions containing 0.5 M PP and PR, respectively, were prepared in Pyrex tubes for the samples for γ-ray irradiation. 6 M HCl solutions containing 0.5 M PP and PR, respectively, were also similarly prepared[1]. Irradiation was carried out by the ^{60}Co source up to 0.34 and 0.43 MGy for PP and PR, respectively, at room temperature under ambient atmosphere. Irradiated samples were analyzed by ^{1}H NMR. D_2O containing a known weight of formic acid which is a standard material was used as the NMR solvent. The residual ratios of PP and PR were calculated by the area ratio of each signal with that of formic acid.

RESULTS: In ^{1}H NMR spectra, neat PP and PR show several signals attributed to the position of hydrogen in the structure of both compounds. Those for PP and PR are shown as (A) through (C), and (D) through (F), respectively, in Fig. 1. The results on the stability are shown in Fig. 2. For both compounds, the residual ratios are found higher for HCl than for HNO_3. In addition, PP would be more stable than PR. The tendency is clearer in HCl media. One of the reasons for higher stability in the 6-membered ring might be larger number of possible steric structures leading to dispersion of given energy.

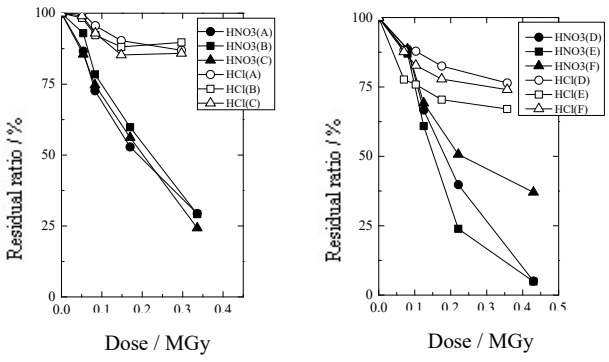

Fig. 2. Dependence of dose on residual ratio for PP (left) and PR (right).

REFERENCES:

[1] N. Miyata *et al.*, KURRI Progress Report 2010 (2011) CO9-1.
[2] M. Nogami *et al*., KURRI Progress Report 2017 (2018) CO9-8.
[3] Y. Yoshimura *et al.*, KURNS Progress Report 2019 (2020) CO9-6.

CO9-4

Solid-liquid extraction experiments of ^{47}Ca for the chemical study of nobelium

R. Wang,[1,2] Y. Kasamatsu,[1,2] Y. Itakura,[1,2] M. Konno,[1,2] K. Shibamoto,[1,2] E. Watanabe,[3] and K. Takamiya[4]

[1]*Graduate School of Science, Osaka University*
[2]*RIKEN Nishina Center for Accelerator-Based Science*
[3]*High Energy Accelerator Research Organization, KEK*
[4]*Institute for Integrated Radiation and Nuclear Science, Kyoto University*

INTRODUCTION: Element 102, nobelium (No), is the second element from the back of the actinide series. Unlike all other lanthanides and actinides, No was reported to exist as a divalent ion rather than trivalent in aqueous solutions and to have similar chemical properties to those of alkaline earth metals [1]. We focus on solid-liquid extraction using crown ether supporting resin (Sr resin), and have indeed performed extraction experiments with it. Sr resin is commercially available crown-ether supported resin and the crown ether has extraction selectivity for alkaline earth ions. This selectivity is sensitive to ligand ions in the aqueous solutions such as Cl^- and NO_3^- [2,3].

Our previous solid-liquid extraction experiment of ^{255}No in Sr resin/HNO_3 system has suggested that No exhibits similar behaviors to that of Pb, which is softer than alkaline earth metals [4]. For the systematic understanding of the chemical property of No, further investigation is needed.

This study performed extraction experiments using radioactive tracers of alkaline earth metals (^{47}Ca, ^{85}Sr, and ^{133}Ba) by Sr resin (tBuCH18O6 impregnated resin) in dithiophosphate which is softer than the nitrate ion to investigate the properties of No as a soft metal. In addition, the complex structure should be clear for calculation of the electron state of the complexes. We predicted complex structures of No and alkaline earth metals using the relativistic DFT calculation method to investigate the chemical properties of No.

EXPERIMENTS: ^{47}Ca was produced by thermal neutron irradiation to 280 mg of ^{nat}CaO for 1 h (5 MW) at Kyoto University research Reactor (KURNS). After irradiation, CaO was dissolved in conc. HCl solution and purified through an anion-exchange resin in conc. HCl system. In solid-liquid extraction, 0.5-1.0 mL of 60-320 mM sodium dithiophosphate solutions containing metal tracers (^{47}Ca, ^{85}Sr, and ^{133}Ba) was contacted with 50 mg of Sr resins for 1-30 min. After that, the resin and solution was separated through a filter unit.

After the extraction experiments, the samples were subjected to γ-ray measurement with a Ge semiconductor detector to measure the amount of ^{47}Ca, ^{85}Sr, and ^{133}Ba. The distribution coefficients, K_d, were calculated by the equation

$$K_d = (A_{STD} - A_s)V / A_s w,$$

where A_s and A_{STD} are radioactivities of the aqueous phase and the control (standard) sample which was obtained in the extraction without the resin. V is the volume of the aqueous phase (mL), and w is the mass of the dry resin (g).

RESULTS: The K_d values of all elements were almost constant for shaking time from 1 to 30 min. This result indicates that the chemical reactions involved in the present complexation and extraction are sufficiently fast for investigating the extraction behavior of ^{255}No whose half-life is about 3 min.

As depicted in Figure 1, the K_d values of Ca, Sr, and Ba depend on the concentration of dithiophosphate. In this system, the K_d values of Ca are extremely lower than those of Sr and Ba. It is presumed that the ionic size of calcium does not align with the size selectivity of the 18C6 ring. Being different from the values in the previous studies, the K_d values of Sr are lower than those of Ba, even though DFT calculations results show that the radius of Ba does not match the size of the crown ether ring. This phenomenon is considered to be attributed to strong bonding between soft acid and soft base: Ba and dithiophosphate. Owing to superior ion size selectivity, the No could exhibit higher K_d values compared to Ba, assuming that No possesses chemical properties of a soft acid.

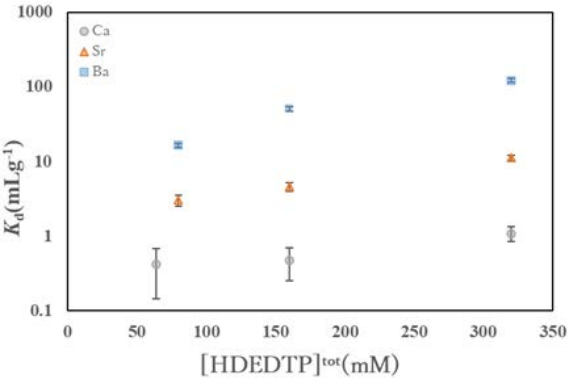

Figure 1 K_d dependence of Ca, Sr, and Ba on dithiophosphate concentration at pH 3.5

REFERENCES:

[1] R. Silva *et al.*, Inorg. Chem., **13** (1974) 2233.
[2] E. P. Horwitz *et al.,* Solvent. Extr. Ion Exch., **10** (1992) 313.
[3] D. V. Filosofov *et al.,* Solvent. Extr. Ion Exch., **33** (2015) 496.
[4] E. Watanabe, Doctor thesis, Osaka University (2023).

CO10-1

Effective Measures on Safety, Security, Hygiene and Disaster Prevention in Laboratories

T. Iimoto[1], S. Hashima[1], S. Mase[1], D. Kaminushi[1], K. Takamiya[2]
[1] *The University of Tokyo*
[2] *Integrated Radiation and Nuclear Science, Kyoto University*

INTRODUCTION: Important aspects of the study can be found in the following keywords, such as safety, security, hygiene and disaster prevention. Nuclear research reactor is one of representative target facilities of this study with these keywords under their operation. In addition, development of human resource and public literacy on nuclear science and technology is also within the scope of the re-search.

RESEARCH APPROACH: General research approach of this study is as follows. - It would not be a single year research, but maybe two to three years research for one theme. - Information source of facilities would not be only KUR, KUCA or the other facilities in Kyoto University, but also the Kindai university research nuclear reactor or the facility of National Institute of Fusion Science, etc. This research is an active joint-research with these relating facilities and positive researchers on safety management.Concrete discussion target in FY of 2023 was determined as 'developing a set of educational videos for radiation protection in English for International Nuclear Science and Technology Academy (INSTA)'.

WHAT IS INSTA?: INSTA was established in the Asia and the Pacific region with strong support from the International Atomic Energy Agency (IAEA) through the Technical Cooperation Project aimed at supporting nuclear science and technology (NST) education at tertiary levels. INSTA's vision is to foster empowered regional NST educators. The key objectives are: (1) Facilitating linkages among academic institutions and stakeholders to optimize resources and advance NST education, (2) Fostering educational programs and platforms to address current and emerging needs in NST education, and (3) Envisioning and organizing activities to engage and motivate NST educators and stakeholders.

CONCEPT AND CONTENTS OF RP-EDU-VIDEO: To support the INSTA activity, the authors developed an English educational video entitled as 'Radiation and Realism', whose contents of the video are; <Part I> Human perception -Defining perception -Factors that influence perception such as past historical benefit vs risk -their importance in many areas such as decision making etc., <Part II> Exploring what is Myth? -Sharing the common Myths related to radiation -Participants can share their own perception & discuss - some educators from non- NST background may also have similar perception. -May even share the stigma post Goiania incidents, can also include case studies of other incidents, <Part III> Radiation in reality -Elements and actual conditions of exposure in nature -Generals of Human Effects -Epidemiology of A-bomb and India -ICRP History and Principles of Radiation Protection -Justification, Optimization & Dose constraints -Radiation Application.

CO10-2

Application of KURAMA-II to Radiation Monitoring of Forests in Fukushima Prefecture

A. Maekawa, K. Kusakabe and M. Tanigaki[1]

Fukushima Prefectural Centre for Environmental Creation
[1]Institute for Integrated Radiation and Nuclear Science, Kyoto University

INTRODUCTION: KURAMA (Kyoto University RAdiation MApping system)-II is a radiation measurement system characterized by its compactness, autonomous operation, and acquisition of pulse-height spectrum data (Fig. 1) [1]. KURAMA-II measures ambient dose equivalent rate (hereafter called air dose rate) and GPS position and automatically transmits them to a dedicated cloud server. In this study, we evaluated the effectiveness of a backpack-style KURAMA-II (Fig. 2) for the radiation monitoring of forests in Fukushima prefecture by comparing it with a NaI(Tl) scintillation survey meter conventionally used in radiation monitoring.

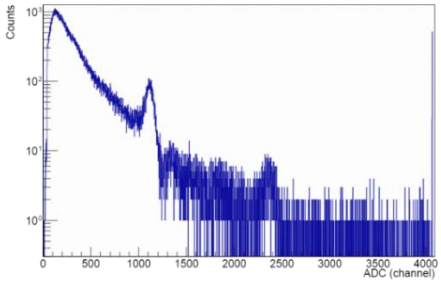

Fig. 1. A typical example of pulse-height spectrum obtained by KURAMA-II measurement.

Fig. 2. KURAMA-II in a backpack.

EXPERIMENTS: A 10 m interval grid (30 x 50 m) was established in five forests. The air dose rates were measured by a KURAMA-II in a backpack with a CsI (Tl) scintillation detector (C12137-01, Hamamatsu Photonics) walking along the grid line. The air dose rate and GPS position were measured every second. The air dose rate at 1 m above the center point of each grid was also measured by a NaI (Tl) scintillation survey meter (TCS-172B, Aloka). All measurement was carried out in Dec. 2023 - Jan. 2024.

RESULTS: Table 1 shows the air dose rate range at each forest site. All the measurement result of a survey meter were within the range of KURAMA-II. A typical radiation map by KURAMA-II and a survey meter is shown in Fig. 3 (site D). The spatial distribution of air dose rate measured by KURAMA-II was well consistent with that of a survey meter. In the present study, KURAMA-II showed promising performance in revealing a more detailed distribution of air dose rates.

Table 1. The air dose rate range at each forest site.

Site	Air dose rate by KURAMA-II (μSv/h)	Air dose rate by survey meter (μSv/h)
A	0.08-0.18	0.11-0.15
B	0.11-0.26	0.21-0.23
C	0.13-0.25	0.17-0.20
D	0.03-0.12	0.07-0.11
E	0.27-0.71	0.44-0.59

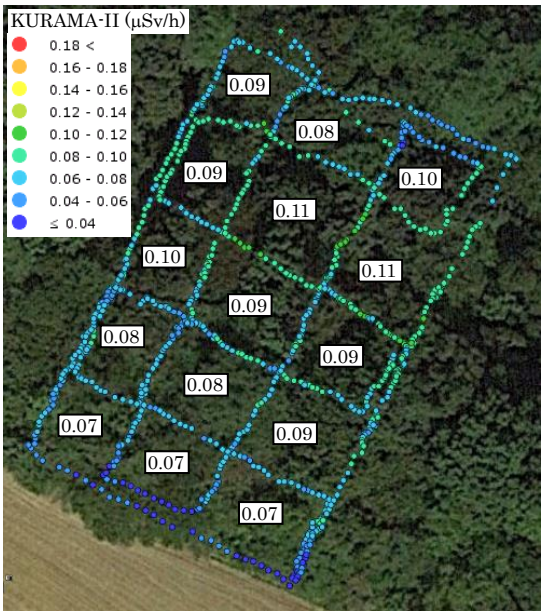

Fig. 3. The radiation map created by KURAMA-II (colored dots) and a survey meter (numerical data).

REFERENCES:

[1] M. Tanigaki *et al.,* Nucl. Instrum. Meth. Phys. Res., **781** (2015) 57-64.

CO10-3

Nationwaide Survey of Chlorine and Bromine Concentration in Dewatered Sewage Sludge Measured by Neutron Activation Analysis

T. Matsunaga[1], R. Homma[1], S. Fukutani[2], K. Oshita[1], and M. Takaoka[1]

[1]*Department of Environmental Engineering, Graduate School of Engineering, Kyoto University*
[2]*Research Reactor Institute, Kyoto University (KURRI)*

INTRODUCTION: In recent years, the use of sewage sludge as fertilizer has been promoted, but sewage sludge contains not only beneficial components but also harmful ones. In this study, neutron activation analysis (NAA) was performed on dewatered sewage sludges sampled from 34 wastewater treatment plants across Japan to analyze chlorine and bromine concentrations.

EXPERIMENTS: The dewatered sewage sludges were collected from 34 wastewater treatment plants in Japan in 2023, dried at 105°C, and then homogenized with a crusher. NAA was performed four times for each sample. Samples were irradiated for 1-5 min with a thermal neutron flux of 2.0-2.4$\times 10^{13}$ cm^{-2} $\cdot$ sec^{-1} at KURRI. ^{38}Cl ($t^{1/2}$ = 37.18 min, E_γ = 1642, 2168 keV) and ^{80}Br ($t^{1/2}$ = 17.68 min, E_γ = 616, 666 keV) were measured by using a Ge semiconductor detector for 300 sec.

RESULTS: Fig.1 shows histograms and cumulative relative frequency graphs of chlorine and bromine concentrations. For chlorine concentration, most of the sludge samples were in the low concentration range under 2,500 mg/kg-Dry-Solid(DS), while there were a few samples with extremely high concentrations. Also, half of the sludge samples had bromine concentrations in the relatively low range of 20-40 mg/kg-DS, while there were some samples with high concentrations. The treatment plant with the highest chlorine concentration had a large amount of industrial wastewater originating from chemical plants flowing into it, which could be affected by the industrial products contained in this wastewater.

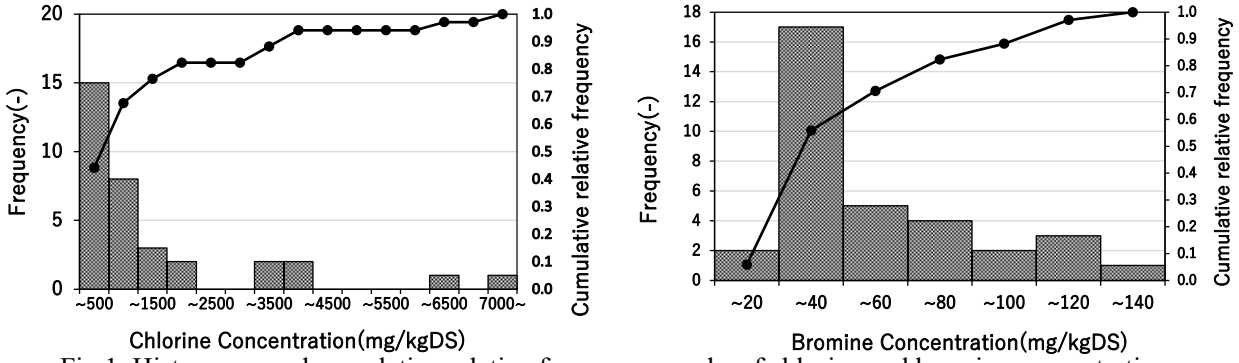

Fig.1. Histograms and cumulative relative frequency graphs of chlorine and bromine concentrations

The results were compared with those of chlorine and bromine concentrations from neutron activation analysis of dewatered sludge from 32 sewage treatment plants nationwide sampled between 2015 and 2016 by Chen *et al*. [1]. Statistical analysis of the Wilcoxon rank sum test showed that no significant difference existed between the results by Chen *et al*. for bromine concentration (p-value 0.7435), but a significant difference existed for chlorine concentration (p-value 0.0044). It is suggested that this is because the dewatered sludge sampled in this study included several samples that were thought to be inflow of industrial wastewater. Also, due to the difference in age between 2015 and 2023, the possibility exists that industrial development has increased the production of industrial products, resulting in an increase in chlorine emissions.

REFERENCES:

[1] M. Chen *et al*., Science of the Total Environment, **752** (2021) 141857.

CO10-4

Study for activity measurement of ^{41}Ar and ^{133}Xe using a plastic scintillator and an calibrated ionization chamber

Takahiro Yamada[1,2], Yuya Soeta[2], Seiya Ohtsuka[2], Ren Ichikawa[2], Rio Furukawa[3] and Hiroshi Yashima[4]

[1]*Atomic Energy Research Institute, Kindai University*
[2]*Graduate school of Science and Engineering, Kindai University*
[3]*National Metrology Institute of Japan*
[4]*Institute for Integrated Radiation and Nuclear Science, Kyoto University*

INTRODUCTION: To calibrate monitors used for measuring radioactive noble gases in nuclear facilities, use of activity reference measurement standard gases shall be required. The authors have been conducting absolute measurements of activity using a 4πβ-γ coincidence spectroscopy with plastic scintillator detectors, targeting ^{41}Ar and ^{133}Xe generated at KUR-SLY since FY2021, aiming to establish standards [1]. In this year, activity measurement using an inner-through-type ionization chamber, denoted later as IC, was conducted to compare with the result obtained by 4πβ-γ coincidence spectroscopy.

EXPERIMENTS: A 5 ml acrylic container was filled with pure argon gas to produce ^{41}Ar via ^{40}Ar(n, γ)^{41}Ar reaction. As for ^{133}Xe naturally occurring xenon gas consists of seven stable isotopes was filled into the 60 ml acryl container to produce ^{133}Xe via ^{132}Xe(n,γ)^{133}Xe reaction. Each gas container was irradiated for 60 s at the bottom of KUR-SLY operating at 1 MW thermal output.

An acrylic gas container was used as the β-detection part of the measurement system. The entire inner wall of the container was covered with a 1 mm thick plastic scintillator (PS), with a content volume of 80 ml. A photomultiplier tube (PMT) was connected to the top of the container and stored in a light-shielded case. The β-detector was placed onto the Ge detector, and the signal outputs from the β- and γ-detectors were fed to the signal inputs of a list-mode multi-channel analyzer (MCA). The 1.5L IC (Model I-409601, Ohkura Electric Co., Ltd.) was used to measure the activity of ^{41}Ar and ^{133}Xe. The calibration factor [pA per Bq cm^{-3}] required to convert the output current from the IC to the concentration of radioactive gases, was previously evaluated to be 0.288 pA Bq^{-1} cm^3 for ^{41}Ar [1]. For ^{133}Xe, since the calibration factor has not been evaluated, we attempted to identify the nuclide by observing the decrease of the currents comparing the half-life.

RESULTS: In the measurement of diluted ^{41}Ar using IC, activity concentration was determined as 21.8 Bq cm^{-3} at around 9 hours after irradiation. A half-life of 108.9 min was obtained from a set of IC measurements, shorter than the recommended half-life of 109.611±0.038 min[2]. The β-counting efficiency, determined as n_c/n_γ in the coincidence count measurement, was 0.920. Preliminary results of activity concentration determined from the 4πβ-γ coincidence spectroscopy was 22.7 Bq cm^{-3}. Fig. 1 shows changes in the output currents of the IC for Xe gas. The apparent half-lives of Xe gas were evaluated to be 3.5 d and 5.5 d from 48 to 84 hours and 96 to 126 hours after irradiation, respectively. The present difference could be due to the fact that the impurity nuclides, which have a shorter half-life than ^{133}Xe, decayed over time, resulting in a higher relatively higher activity of ^{133}Xe compared to that of the impurity nuclides. Further study should be required to determine activity of Xe gases.

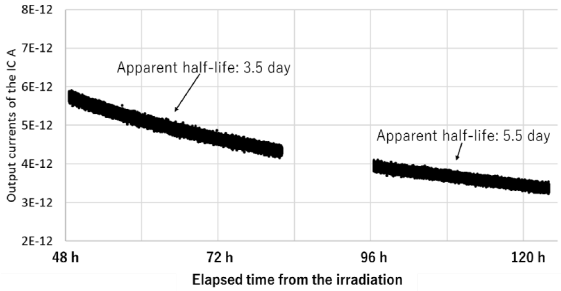

Fig. 1. The IC output currents in a series of Xe gas measurement.

REFERENCES:

[1] A. Yunoki *et al.,* Annl. Rep. of Coop. Res. at Kindai Univ. Reactor (2020) (in Japanese).
[2] Bé, M., 2011. Table of Radionuclides.

CO10-5

Determination of chlorine content in the cable jackets of power supplies in accelerator facilities

G. Yoshida, K. Nishikawa[1], E. Watanabe, K. Tsugane, K. Takahashi, T. Bui[2], and H. Yashima[3],

Radiation Science Center, KEK
[1]Department of Safety Management, QST
[2] Accelerator Science Program, SOKENDAI
[3]Institute for Integrated Radiation and Nuclear Science, Kyoto University

INTRODUCTION: A large-scale accelerator facility, such as the 12 GeV proton synchrotron facility of KEK (KEK-PS), produces various radionuclides. Some of these nuclides remain for long periods and become apparent as a radioactive waste when its decommissioning work. Although power cables are used in accelerator facilities in smaller quantities than concrete or metals (magnets and coils), the cable jacket is made from chlorine-containing plastic. It produces ^{36}Cl, which has a long half-life of 300,000 years for pure β-nucleus (difficult to measure), through the (n,γ) reaction of ^{35}Cl. We are developing the determination method for ^{36}Cl activity in cable jackets by Accelerator Mass-Spectrometry (AMS). Still, we are faced with the problem of the chlorine content in the jackets being unknown in many cases. Neutron activation analysis has been used to analyze chlorine in various samples and could be established to determine the chlorine contents of cable jackets.

EXPERIMENTS: The power cable jacket of the septum magnet of KEK-PS was collected, cut into 1-5 mm pieces, washed with water and ethanol, and weighed 100 mg to prepare irradiation samples. The chlorine-containing plastic standards (JSM_P713-1 series) distributed by the JFE Techno-Research Co. were employed as references and prepared in the same way. Samples were irradiated at Pn-3 with 1 MW for 10 s, and γ-ray spectrometry of ^{38}Cl was conducted with a Ge detector immediately after irradiation.

RESULTS: The γ-ray spectra of the representative sample and standard are shown in Fig. 1. The γ-ray peaks attributed to ^{38}Cl were observed in both standards and the cable jacket samples. From the measurement result of five different chlorine contents of standards, we found a good correlation between the 1634 keV γ-ray count rates and chlorine contents. Based on the calibration curve prepared from the standard samples, the chlorine content of the cable jacket was estimated to be approximately 17%.
In conclusion, it was found that chlorine content in power cable jackets can be determined accurately using Neutron activation analysis.

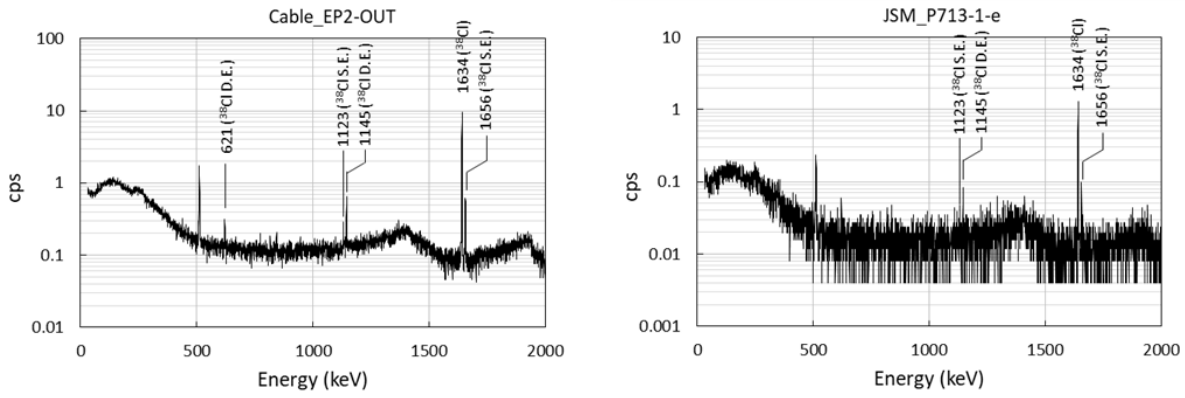

Fig. 1. γ-ray spectra of representative cable jacket sample (right) and standard (left)

CO10-6

Measurement of Number-Based and Radioactivity-Based Size Distributions of Aerosol Particles Generated in the Accelerator Room of an Electron LINAC Facility Using Screen-Type Diffusion Battery

Y. Oki, K. Takamiya and M. Inagaki

Institute for Integrated Radiation and Nuclear Science, Kyoto University

INTRODUCTION: With recent advances in high-intensity and high-energy accelerators, ensuring accelerator radiation safety has become increasingly important. We have previously reported on the use of a screen-type diffusion battery (SDB) technique to measure the particle size distribution of radioactive aerosols generated in accelerator rooms, which is useful for internal exposure assessment. This report describes the results of two methods of particle size measurement using SDB and the current problems.

EXPERIMENTS: When fine aerosol particles of about 100 nm or less pass through a stack of wire screens, some of the particles are deposited on the wire surface of the screen by diffusion, depending on the particle size. The percentage of particles that can pass through the screen (penetration ratio) is expressed as a function of particle size, roughness and number of screens, and particle flow rate. By measuring the penetration ratio by varying the number of screens or flow rate, the particle size can be calculated from the theoretical equation.

Radioactive aerosols produced by air irradiation using an irradiation chamber at the electron linac of our institute. The irradiated air containing the aerosols was introduced to the SDB consisting of multiple screens and a backup PTFE filter. This experiment was conducted in two ways. *Method 1:* Varying the flow rate: The irradiated air was simultaneously introduced to the SDB line and the compensation line. The SDB comprised two screens. The flow rate of air introduced into the SDB was varied from 0 to 15 L/min. At the same time, to keep the flow rate in the irradiation chamber constant, the flow rate into the compensation line was varied so that the total flow rate in the SDB line and the compensation line was constant. *Method 2:* Varying the number of screens: A maximum of 40 wire screens were used for the SDB. In addition, activity of the selected screens and the backup filter was simultaneously measured using a single large imaging plate [1]. The penetration ratio for the i-th screen was estimated from the intensity of photostimulated luminescence of the screens and the filter.

RESULTS: Since a stable lognormal-type particle size distribution was observed in the SMPS (scanning mobility particle sizer) measurement performed simultaneously with the SDB sampling, the geometric mean and geometric standard deviation of the particle diameter were calculated, assuming a lognormal particle size distribution, by fitting the penetration ratios obtained by each of the two methods to the theoretical equation [2]. Number-based particle diameter tended to increase with increasing beam current (20-100 μA) in the SDB measurements, ranging from 20 to 60 nm. At the same beam conditions, the size distributions obtained with Methods 1 and 2 were in good agreement, and the results were also in very good agreement with the SMPS measurements. In the radioactivity-based size measurement for ^{13}N-bearing aerosol particles, adsorptive gases such as $H^{13}NO_3$ adsorbed on the filters and screens sometimes may cause errors in the fitting results. An effective compensation technique was discussed to eliminate the influence.

REFERENCES:

[1] Y. Oki *et al.,* J. Radiat. Prot. Res., **41** (2016) 216-221.
[2] Y.S. Cheng and H.C. Yeh, J. Aerosol Sci., **11** (1980) 313-320.

CO10-7

Application of KURAMA-II to the analysis of air dose rate distribution around monitoring posts

M. Hosoda[1], M Watanabe[1], H Tanaka[1], M. Tanigaki[2]

[1]*Japan Chemical Analysis Center*
[2]*Institute for Integrated Radiation and Nuclear Science, Kyoto University*

INTRODUCTION: In the nationwide survey of environmental radioactivity levels commissioned by the Nuclear Regulation Authority, air dose rates are measured using portable monitoring posts at about 80 locations in Fukushima Prefecture. Air dose rates obtained by monitoring posts are representative values for each location, and we do not see the detailed distribution of the air dose rate due to the uneven distribution of the artificial radionuclide around the monitoring posts.

In this study, we measured air dose rates around the portable monitoring posts located in a difficult-to-return zone in Fukushima Prefecture by a car-borne survey system KURAMA (Kyoto University Radiation MApping system)-II as a walking survey. We analyzed the distribution of the air dose rate and the radioactive cesium using radiation mapping methods.

EXPERIMENTS: We walked with KURAMA-II around the monitoring post at the Ogaki Post Office in Namie Town, Fukushima Prefecture. The data were grouped by a 1 m mesh centered on the monitoring post, and an areal evaluation was performed by displaying the data on a map. From the measured air dose rate data and the pulse-height spectrum data of each mesh, the air dose rate from the natural radioisotopes and that given by the artificial radioisotopes, i.e., Cs-134 and Cs-137, were evaluated respectively using Equation (1) defined in ref. [1],

$$\begin{cases} \dot{D}_n = 0.062x \\ D_a = \dot{D}_t - \dot{D}_n, \end{cases} \quad (1)$$

where $\dot{D}_t$ is the measured air dose rate (μSv/h), x is the counting rates from 1400 to 2000 keV obtained by spectrum data, $\dot{D}_n$ is the air dose rate given by natural radioisotopes, and D_a is that given by the artificial radioisotopes.

RESULTS: Figure 1 shows the 1 m × 1 m mesh map of the air dose rate obtained by the present walking survey. The average air dose rate measured by the monitoring post was 2.12 μGy/h, whereas the average air dose rates per 1 m × 1 m mesh obtained by the walking survey ranged from 0.92 to 6.09 μGy/h. Figure 2 shows the spectrum data of the meshes (1), (2) and (3) in Figure 1, having different air dose rates. The counts below 1000 keV differed depending on the mesh, suggesting that the differences in the air dose rates are due to the uneven distribution of Cs-134 and Cs-137. Figure 3 shows the map display of the air dose rate given by natural radioisotopes for each mesh calculated by Equation (1). From these results, the differences in the air dose rates are not due to the uneven distribution of natural radioisotopes but the artificial radioisotopes, Cs-134 and Cs-137.

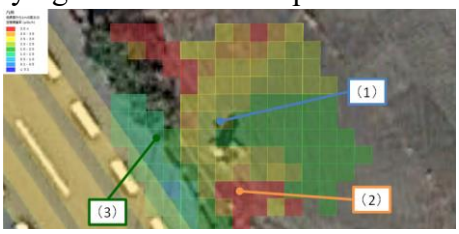

Figure 1. the 1 m × 1 m mesh map of the air dose rate(μGy/h) obtained by the present walking survey.

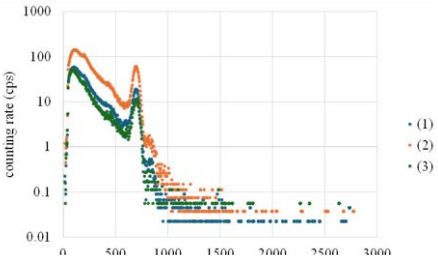

Figure 2. The spectrum data of mesh (1), (2), and (3) in Figure 1.

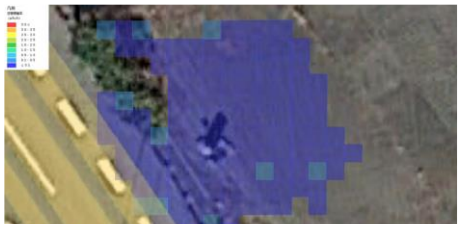

Figure 3. The map display of the air dose rate given by natural radioisotopes (μSv/h) for each mesh calculated by Equation (1).

REFERENCES:

[1] M. Ando *et al.,* T. J. At. Energy Soc. Jpn., **20(1)** (2021) 34-39. (In Japanese)

CO12-1

Instrumental neutron activation analysis of Ir in PtIr alloy

T. Miura[1], R. Okumura[2], Y. Iinuma[2] and H. Yoshinaga[2]

[1]*Advanced Industrial Science and Technology (AIST), National Metrology Institute of Japan*
[4]*Institute for Integrated Radiation and Nuclear Science, Kyoto University*

INTRODUCTION: Neutron activation analysis using comparator standard is recognized as a potential primary ratio method [1]. Despite the potential of neutron activation analysis as primary ratio method, the evaluation the measurement capability and the measurement uncertainty are required in any analysis. In general, there are three main components of uncertainty in neutron activation analysis, that is, sample preparation uncertainty, neutron flux homogeneity, and gamma ray measurement uncertainty. Usually, flux monitor is used to correct the neutron flux heterogeneity. However, although the flux monitor can correct the neutron flux variation using the count rate of the known amount of the monitor nuclide, it does not reflect the neutron flux of the actual sample. The most practical method to eliminate neutron flux heterogeneity to improve gamma ray measurement uncertainty is an internal standard method [2, 3]. In this study, we presented that capability of instrumental neutron activation analysis for determination of Ir in the PtIr alloy. Pt-Ir alloys are known to be stable and very difficult to completely decompose.

EXPERIMENTS: The PtIr (foil, 0.025 mm thick, 25 mm×25 mm, Alfa Aesar, 99.9 %, Lot No. I24T008) purchased from FUJIFILM Wako Pure Chemical Corporation. The composition ratio of the PtIr foil was indicated by the manufacture as Pt:Ir; 90:10. High purity Ir metal (Alfa Aesar, powder, 99.99 %, Lot No. M17E046) was used for calibration standard for Ir. The Au solution prepared from high purity metal was added in the irradiation samples for internal standard. The neutron irradiations for Ir in the PtIr alloy sample performed by KUR TcPn (thermal neutron flux: 8×10^{10} $cm^{-2}s^{-1}$) for 20 min. The irradiated samples were cooled appropriately. The gamma rays form irradiated samples were measured using ORTEC GEM 25185 Ge detector with Laboratory Equipment Corporation MCA 600. The measure radioactive isotopes were ^{192}Ir, ^{194}Ir and ^{198}Au.

RESULTS: Analytical results of Ir in the PtIr alloy were shown in Table 1. The measured values were in good agreement with manufacture indicated value. Analytical results demonstrate the effectiveness of instrumental neutron activation analysis.

Table 1. Analytical results of Ir in the PtIr alloy

Sample No.	Measured values, Ir g/g
1	0.0993±0.002
2	0.0992±0.004

REFERENCES:

[1] R. Greenberg *et al.*, Spectrochim. Acta B, **66** (2011) 193-241.
[2] T. Miura *et al*., Talanta, **82** (2010) 1143-1148.
[3] T. Miura *et al.*, J. Radioanal. Nucl. Chem., **303** (2015) 1417-1420.
[4] NuDat 2, National Nuclear Data Center in Brookhaven National Laboratory, https://www.nndc.bnl.gov/nudat2/index.jsp

Fundamental Study of Superposition of Coherent Transition Radiation Using a Ring-type Resonator

N. Sei and T. Takahashi[1]

Research Institute for Measurement and Analytical Instrumentation, National Institute of Advanced Industrial Science and Technology
[1]Institute for Integrated Radiation and Nuclear Science, Kyoto University

INTRODUCTION: Terahertz light sources based on linear accelerators are characterized by a high repetition frequency. In order to utilize this feature to develop a high-peak-power terahertz light, we have studied to confine coherent transition radiation (CTR) in an optical resonator to achieve pulse superposition, and to extract it from the resonator using Fresnel reflection [1]. By us-ing Tsurupika, which has low absorption in the terahertz region, as an output coupler, we success-fully observed that CTR pulses are superimposed in the optical resonator.

EXPERIMENTS: An electron beam with energy of 39 MeV was used for the pulse superposition experiments at the L-band linear accelerator of Kyoto University (KURNS-LINAC). The repetition and duration of the electron-beam macropulse were 15 Hz and 100 ns, respectively. The electron beam with a current of 1.0 μA passed through an aluminum collimator generated CTR by penetrat-ing two aluminum-deposited polyethylene films that composed a ring-type optical resonator. The generated CTR orbited the ring-type resonator with a circumference of 923 mm which correspond-ed to four times the CTR pulse interval. Therefore, the CTR pulses circulating around the resonator were superimposed on the CTR pulses generated after one rotation. A Tsurupica substrate with a thickness of 2 mm was inserted at 45° to the CTR beam in the part of the resonator that formed a parallel CTR beam. A portion of the superimposed CTR pulse was extracted from the resonator by Fresnel reflection on this substrate, and temporal structure and spectrum of the CTR pulses were measured in an experimental room.

RESULTS: Figure 1 shows CTR power measured by a Si bolometer while adjusting the circum-ference of the resonator. The CTR power in the figure is normalized to the power of a non-superimposed CTR pulse measured by inserting a millimeter-wave absorber into the resonator. The CTR power almost perfect synchronization condition of the resonator was nearly twice as high as that without superimposition. Moreover, the CTR power had minimums when a detuning length of the resonator was ±1 mm. Because the CTR spec-trum had a maximum around a wavenumber of 5 cm^{-1}, it was suggested that the second-lap CTR pulses superimposed with the first-lap CTR pulses, resulting in a decrease in CTR power. Therefore, it was confirmed that the electric field of the CTR pulses was superimposed by the resonator. At higher wavenumbers, the superposition of the CTR pulses becomes more effective because a diffraction loss in the resonator can be reduced. Our experimental results demonstrate that CTR pulses with high peak power can be generated by the pulse superposition.

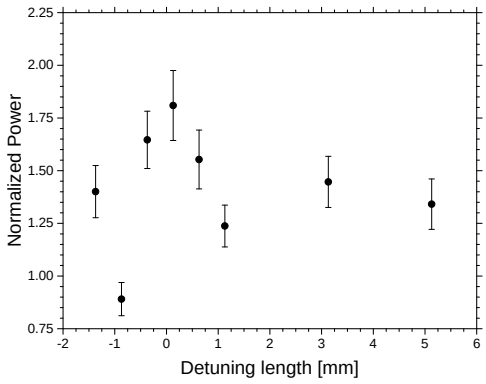

Fig. 1. CTR power vs. detuning length

REFERENCES:

[1] N. Sei and T. Takahashi, submitted to Appl. Opt.

SEM-EDS analysis of enlarged particles prepared by spraying $(U,Zr)O_2$ particle -immersed solution for decommissioning of Fukushima Daiichi Nuclear Power Plant

A. Toyoshima, K. Takamiya[1], and H. Furutani[2]

Institute for Radiation Sciences, Osaka University
[1]Institute for Integrated Radiation and Nuclear Science, Kyoto University
[2]Center for Scientific Instrument Renovation and Manufacturing Support, Osaka University

INTRODUCTION: First preliminary removal of the fuel debris remaining in the Units 1, 2, and 3 of Fukushima Daiichi Nuclear Power Plant is planned to be started soon. In the removal, fine particles containing alpha emitters of actinides such as ^{235}U and ^{239}Pu are concerned to be yielded in cutting the debris to put into a sealed container. We, therefore, aim to develop a novel real-time detection method for the dispersed particles using Aerosol Time-Of-Flight Mass Spectrometer (ATOFMS). At present, an improved type of ATOFMS is newly developed and an enlargement and condensation apparatus to increase the detection sensitivity of ATOFMS by enlarging its non-detectable tiny particles to detectable-sized ones before the ATOFMS measurement. In the present study, we performed SEM-EDS measurements for the enlarged ^{238}U particles using the apparatus.

EXPERIMENTS: Primary particles were produced from a $(U_{0.5}Zr_{0.5})O_2$ pellet by laser ablation in a closed chamber. The produced particles were swept out of the chamber by carrier gas of dried air and were continuously collected in water using PILS (Particle Into Liquid Sampler, Metrohm AG). Then, the water containing the primary particles were sprayed using a supersonic atomizer and sprayed droplets were dried by dried air at a flow rate of 0.1 L/min in a chamber. The droplets were also dried by passing a diffusion dryer filled with silica gel. The resulting dried particles were collected on a carbon tape attached in a small impactor. After transporting collected particle samples to KURNS, SEM-EDS measurement of the samples was carried out. Energy of bombarded electrons was 15 kV. SEM images and X-ray spectra of the samples were taken for lots of enlarged particles found on the carbon tapes.

RESULTS: In Fig. 1, a SEM image of the collected particles is shown. Many of the enlarged particles are observed. These have a diameter of around 1 μm, which is suitable to the particle detection using ATOFMS. Element composition was also obtained by the EDS analysis. Results showed U, Zr, O, Si, Fe, etc. were contained in the particles. This means that primary $(U_{0.5},Zr_{0.5})O_2$ particles were successfully enlarged, although other elements probably originated from the apparatus used are also contained in the particles.

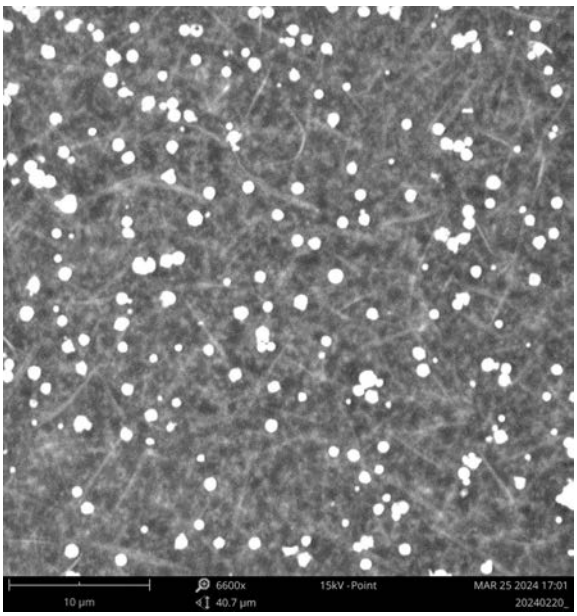

Fig. 1. SEM image of enlarged particles collected on a carbon tape.

CO12-4

Radiation degradation in ^{3}He-filled position sensitive neutron detector

H. Ohshita[1], H. Endo[1], T. Seya[1], S. Matoba[1] and M. Hino[2]

[1]*Institute of Materials Structure Science, KEK*
[2]*Institute for Integrated Radiation and Nuclear Science, Kyoto University*

INTRODUCTION: At the Materials and Life Science Experimental Facility (MLF) of J-PARC, over 5000 ^{3}He gas-filled position sensitive neutron detectors (^{3}He-PSNDs) have been installed to conduct neutron experiments. ^{3}He-PSNDs are cylindrical gas-proportional counters filled with a mixture of ^{3}He and CF_4 gases. ^{3}He gas serves as a neutron converter for detecting neutrons, and the charged particles emitted by the ^{3}He(n,p)^{3}H reaction are detected as neutron hits. CF_4 gas exhibits a high stopping power against charged particles, as well as a high electron drift velocity, and affords stable operation in large intense radiation environments owing to its enhanced rate characteristics. Recently, ^{3}He-PSNDs used in MLF have shown remarkable radiation degradation, and a decrease in the pulse height has been reported. This has been attributed to the accumulation of F_2 gas generated as a dissociation product of CF_4 gas. During the gas amplification process, chemically active neutral radicals, such as $\dot{F}$ (superscript letters indicate that they are neutral radicals), are produced. These neutral radicals react with the anode wire near the electron avalanche, rapidly producing metal fluorides. Concurrently, $\dot{F}$ accumulation in the form of F_2 occurs in the chamber gas, causing the gas amplification to decrease owing to electron attachment. Partially, recombination, which entails neutral radical consumption, occurs and leads to the regeneration of CF_4. Given the likely dependence of the amount of $\dot{F}$ produced on the magnitude of the gas amplification and the existence of further $\dot{F}$ consumption processes, the changes in the pulse height are expected to eventually stabilize. Based on this premise, we performed a neutron irradiation test on the ^{3}He-PSND at KUR CN-3.

EXPERIMENTAL RESULTS: The experimental setup was constructed downstream of the movable slit in KUR CN-3. The ^{3}He-PSND was covered by a shield made of B_4C resin with an aperture size of 1 cm × 4 cm. The ^{3}He-PSND has an outer diameter of 1/2 in and an active length of 150 mm. The filling pressures of ^{3}He and CF_4 were 6 atm and 0.56 atm, respectively. The width of the movable slit was set to 5 mm, and the neutron beam was irradiated for approximately 16 h. The beam power of KUR is 1 MW, and the expected neutron intensity is 7.6×10^5 neutrons/s·cm^2. The slit was periodically closed to measure the pulse-height distribution. The applied voltages were 1.8 kV and 1.3 kV for heavy irradiation with a 5 mm slit width and for measuring the pulse-height distribution, respectively. During heavy irradiation, the pulse-height distribution could not be measured owing to pile-up; therefore, the current of the high-voltage module was measured. Figure 1 shows the trend of ^{3}He-PSND currents during the neutron irradiation tests. A gradual decrease in the current and eventual saturation were observed immediately after the start of the experiment. The pulse-height distribution was measured in locations where the respective data were missing. Figure 2 shows a comparison of the pulse-height distributions immediately after and at the end of the experiment. At the end of the experiment, the distribution showed evident deformation, indicating the impact of radiation degradation. In the future, we plan to conduct another neutron irradiation test in the MLF to elucidate the radiation degradation mechanism and to select alternative gases.

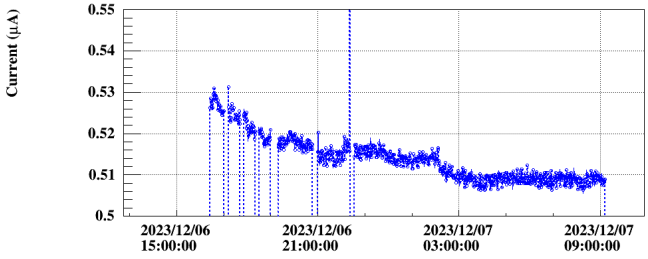

Figure 1. Trend of 3He-PSND currents during the neutron irradiation tests.

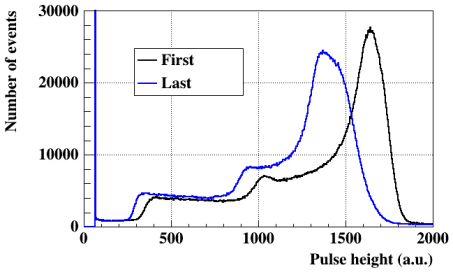

Figure 2. Comparison of pulse-height distributions.

CO12-5

Neutron Refectometry under High Shear in Narrow Gap for Tribology Study

T. Hirayama, N. Yamashita and M. Hino[1]

Department of Mechanical Engineering and Science, Graduate School of Engineering, Kyoto University
[1]Institute for Integrated Radiation and Nuclear Science, Kyoto University

INTRODUCTION: Many studies of mechanical sliding surfaces under lubricated conditions have been carried out in the field of tribology. The trend towards using low viscosity oil to reduce frictional losses has made lubricant additives particularly important in protecting surfaces. It is therefore essential to evaluate the properties of the adsorbed layer formed in a narrow gap by additives under lubricated conditions. In this study, neutron reflectometry was used to investigate the structure of adsorbed additive layers under high shear rates simulating liquid lubricated conditions. Neutron reflectometry is widely used in the field of tribology, but it is mainly used to evaluate the thickness and density of adsorbed additive layers in a static state. In contrast, few *operando* analyses have been carried out in a shear field and the change in the structure of the adsorbed layer formed by an additive on the sliding surfaces has not been clarified.

EXPERIMENTS: The purpose of this study was to establish an *operando* analysis method for evaluating the interfacial structure of an adsorbed layer formed by an additive on a metal surface under fluid lubrication conditions in which a non-contact condition was maintained with a few micrometers gap. To achieve this, we developed an analytical method that combines the use of a neutron reflectometer SOFIA (BL16, MLF) with that of a previously developed parallel-disk viscometer with a narrow gap kept by an aerostatic bearing system. The Si block with thin Cu layer sputtered on by KUR-IBS was used as a sample surface in the study.

RESULTS: Prior to the experiment, 40 μL of d-Sq containing PMA was added to the gap. First, the reflectivity profile was obtained without rotation to evaluate the structure of the polymer adsorbed layer formed on the surface of the Cu layer in the static condition. Then the upper sample was rotated and the reflectivity profile was obtained again. The rotation speed was 100 rpm, so the shear rate was 6.1×10^4 s^{-1}. The footprint was 2×10 mm and the reflectivity profile was obtained with an incident angle of only 0.6º. The reflectivity profiles obtained are shown in Fig. 1(a). This graph shows the results in air (top) and with lubricant under static (middle) and shear (bottom) conditions with fitting lines and offsets in the vertical axis direction for better visibility. The SLD profiles obtained from the fitting analysis are shown in Fig. 1(b). The surface structure of the Cu layer was first determined by fitting the reflectivity profile measured in air without lubricant. Then the structural changes in the adsorbed PMA layer without and with rotation of the top sample were evaluated using a model in which the state of the Cu layer determined by the measurement in air was assumed to remain unchanged and the adsorbed PMA layer was assumed to form on top of the Cu layer. The results show that both the thickness and density of the adsorbed PMA layer became lower under high shear than under static conditions, indicating that the polymer additive desorbed from the Cu surface, probably due to the high shear force. This finding will be useful in the design of lubricant additives that can function under a wide range of lubrication and high shear rate conditions.

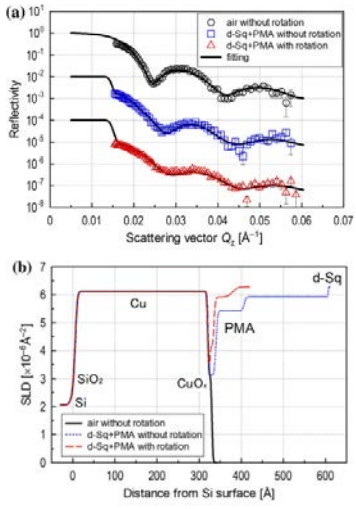

Fig. 1. Reflectivity profiles and estimated SLD profiles.

CO12-6

A trial to analyze the texture of the excavated medieval *Haji*-ware of different colour by INAA

M. Tomii, K. Takamiya[1], M. Inagaki[1], Y. Chiba[2], A. Ito[2], M. Kidachi[3], and H. Yoshii[2]

Faculty of Literature, Taisho University
[1]Institute for Integrated Radiation and Nuclear Science, Kyoto University
[2] Graduate School of Letters, Kyoto University
[3] College of Letters, Ritsumeikan University

INTRODUCTION: A collection of low-temperature-fired pottery (*Haji*-ware) of 14th century archaeologically excavated from a shallow deposition in the campus of Kyoto University [1]is analyzed. It is composed of the classic four types of the medieval Kyoto: white larger bowl, white tiny cup, reddish medium-sized plate, and reddish small plate. In Kyoto as the old capital, *Haji*-ware has long been used for ceremony/ritual even after introduction of higher-temperature-fired ceramics. Its marked difference in colour –white/red– has been widely recognized among archaeologists, and they also have known that such difference in colour corresponds with that in the manner to produce the shape of its base and rim. However, the reason for the colour difference remains to be explained; whether it resulted from the different group of potters, the different manner of making by the same potter group, or whatever. This study therefore tries to check in detail by using INAA whether the colour difference resulted from the different texture of pottery or not.

EXPERIMENTS: Conventional INAA was applied to determine the elemental composition of samples of the *Haji*-ware, each of whose main body had been drilled, or scraped, by the alumina drill into fine powder as a sample after removing off the very surface, and then had been enclosed in a polyethylene bag [2]. Every of above-mentioned four types of the *Haji*-ware has seven samples respectively from different pieces. Each of the 28 samples was neutron-irradiated at Pn-3 (1 MW for 90 seconds) for short-lived nuclides, and at Pn-2 (5 MW for 1 hours) for long-lived ones. The comparative standards were irradiated with the same condition. The gamma-ray spectrometry of the irradiated samples was performed after the irradiation. Along with the comparison method, the k_0-standardization method was also performed. For the latter method, three standard elements were prepared as a comparator: Au, Lu and Zr.

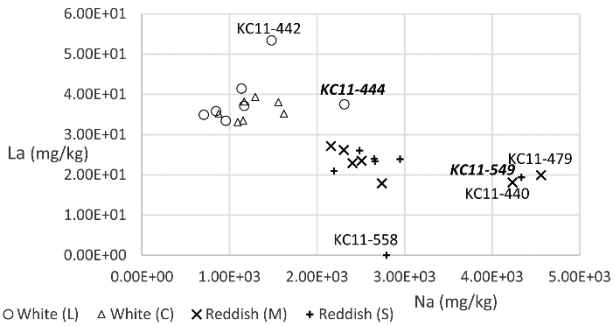

Fig 1 Distribution of 28 samples on the concentrations combination of Na with La.

RESULTS: By the k_0-standardization method, concentrations of two elements (K and Na) in every 28 sample were determined with irradiation by Pn-3, and La and Eu were also determined in most samples, though Mg, Ti, V, Mn, Ga and Sm were in around fifteen samples. The determination by comparison method for samples irradiated by Pn-3 and Pn-2, as well as the k_0-standardization method on ones by Pn-2, were not completed so far. However, it can be pointed out from the k_0-standardization method on short-lived nuclides that Na and La show clear difference in concentration to divide 28 samples into two groups, which correspond with the colour groups except for one sample: KC11-444 (Fig.1). As for the separately distributed samples, KC11-442, 440 and 479 represented slightly different colour in appearance, though KC11-549 did not. The result might suggest that the colour difference was brought by the texture difference, though KC11-444 might indicate another reason for the colour difference: the firing technique for instance.

REFERENCES:

[1] M. Tomii *et al.*, Annu. Rept. of Archaeological Researches in KU sites for 2013. (2015) 5-122.
[2] J. Sterba, J. Radio. Nucl. Chem., **316** (2018) 753-759

Neutron scattering imaging with Talbot-Lau interferometer at CN-3

Y. Seki, Y. Terakawa, M. Li[1], M. Hino[2]

Institute of Multidisciplinary Research for Advanced Materials, Tohoku University
[1]Department of Nuclear Engineering, Kyoto University
[2]Institute for Integrated Radiation and Nuclear Science, Kyoto University

INTRODUCTION: A neutron phase imaging system with a Talbot-Lau interferometer is installed at CN-3 port in the Kyoto University reactor [1]. The Talbot-Lau interferometer, a type of grating interferometer, can produce differential-phase and scattering images [2], in addition to conventional absorption images. For application research, scattering imaging is particularly attractive since it is sensitive to small-angle scattering intensity and can investigate microstructures in samples. The spatial scale that the visibility imaging can explore is characterized by an autocorrelation length ξ. This scale is related to the interferometer parameters as $\xi = \lambda z_s/d_2$, where λ is the neutron wavelength, d_2 is the period of an analyzer grating, and z_s is the distance between the sample and the analyzer grating. The autocorrelation length is usually changed by adjusting the sample position. The contrast of visibility imaging is described as $V_0/V_s(\xi) = \exp[-\Sigma(1 - G(\xi))]$, where V_0 is the visibility of interference fringes without samples, V_s is with samples, Σ is a macroscopic cross section of small-angle scattering which is proportional to λ^2, and G is an autocorrelation function of microstructures. Due to these wavelength dependences, the autocorrelation length is not obvious in the case of measurement with white beams. Therefore, we calibrate the autocorrelation lengths in visibility imaging with the current setup at CN-3 by measuring a sample whose visibility signal at a certain autocorrelation length is well known through the wavelength-resolved method.

EXPERIMENTS: The sample consisted of monodisperse silica spheres with a nominal diameter of 0.2 μm, randomly packed in a quartz cell. Visibility images of this sample have been observed using the time-of-flight method at BL22 RADEN in J-PARC MLF. At the CN-3, visibility imaging was performed through phase-stepping method with eight steps at seven sample positions. The exposure time was 3200 s per phase step at a reactor thermal power of 1 MW.

RESULTS: Figure 1 illustrates an example of visibility image of the sample. The visibility values were averaged within the sample region and plotted in Fig. 2. The effective wavelength that reproduced the results the RADEN was 2.95 Å, which was 9.3% larger than the design wavelength of the interferometer. The autocorrelation lengths were also evaluated using this effective wavelength with a pitch of 9.0 μm for the analyzer grating.

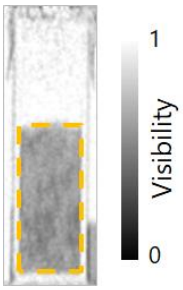

Fig. 1. Visibility image of the monodisperse silica spheres.

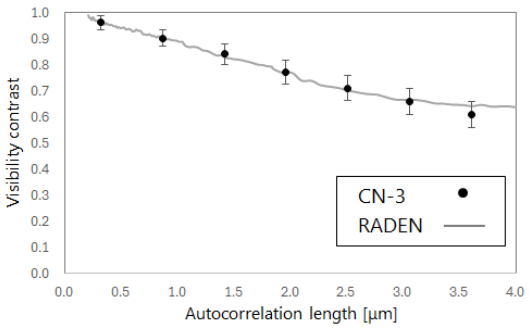

Fig. 2. Average visibility values versus calibrated autocorrelation lengths.

REFERENCES:

[1] Y. Seki *et al.*, Nucl. Instr. and Meth., **186** (1981)115-120.
[2] M. Strobl, Scientific Reports, **4** (2014) 7243.

A New Technique of the Micro bunch Interval Measurement in an Electron Linear Accelerator

T. Takahashi

Institute for Integrated Radiation and Nuclear Science, Kyoto University

INTRODUCTION: The coherent radiation from short bunches of electrons in an accelerator is useful of analysis of the specification of bunches. For example, it has been used in the high-resolution diagnosis of electron distribution in a bunch [1]. There are two kinds of detector in the millimeter wave region. One is a diode detector with narrow band and high-speed response. The other is a liquid-helium cooled bolometer with wide band and slow response. A bolometer is usually used with a spectrometer, for example a monochromator or an interferometer. In the experiment of FY2023 the time-domain measurement with a diode detector was used for the analysis of the micro bunch interval.

EXPERIMENTS: The experiment was performed with KURNS-LINAC. The energy of the electron beam was 39 MeV and the peak beam current measured by CT was 1.6 A. The repetition rate of the macro pulse was 60 pulses/s. Coherent transition radiation from a titanium window was guided to the coherent radiation beam line [2] in the experimental room and detected by a diode detector. This detector was a zero-biased W-band amplitude detector SFD-753114-103-10SF-N1 (SAGE Millimeter, Inc.), which detection speed was 10 ns. The output signal of the detector was measured by the mixed domain oscilloscope MDO3104 (Tektronix, inc.) with the bandwidth of 1 GHz and the sampling rate of 5 GS.

RESULTS: The observed waveform of coherent transition radiation in the case of 47-ns macro pulse is shown in Fig. 1. The number of micro bunches is 61 and the micro bunch interval is 770 ps calculated from the frequency of RF of 1.3 GHz. Fig. 2 shows the waveform in the case of 2-ns macro pulse. In both figures the sampling interval is 0.2 ns because of the sampling rate of the oscilloscope. The rise time of the signal is also slow. It is experimentally revealed that it is difficult to measure the micro bunch interval by a diode detector.

REFERENCES:

[1] Y. Shibata *et al.,* Phys. Rev. E, **50** (1994) 1479-1484.
[2] T. Takahashi *et al.,* Rev. Sci. Instrum., **69** (1998) 3770.

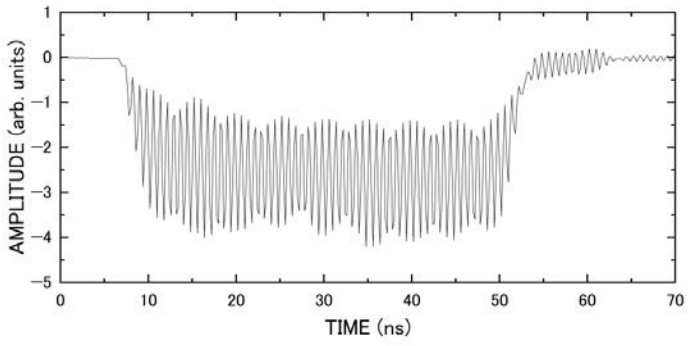

Fig. 1. The observed waveform of coherent transition radiation for 47-ns pulsed beam.

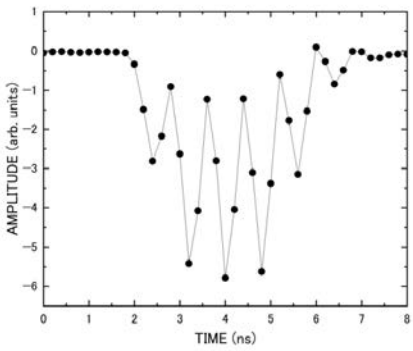

Fig. 2. The observed waveform of coherent transition radiation for 2-ns pulsed beam.

CO12-9

Study of Isotope Separation via Chemical Exchange Reaction

R. Hazama, P. Kumsut, T. Yoshimoto, A. Rittirong[1], C. Pitakchaianan, K. Kosinarkaranun, Y. Sakuma[2], T. Fujii[3], T. Fukutani[4], Y. Shibahara[4], and T. Kishimoto[1]

Graduate School of Human Environment, Osaka Sangyo University
[1]Research Center for Nuclear Physics, Osaka University
[2]Laboratory for Advanced Nuclear Energy, Tokyo Institute of Technology
[3]Graduate School of Engineering, Osaka University
[4]Institute for Integrated Radiation and Nuclear Science, Kyoto University

INTRODUCTION: Chemical isotope separation for calcium and lithium has been studied by liquid-liquid extraction (LLE) with DC18C6 crown-ether [1]. This report describes separation coefficient (ε) under the various temperature (1/T), ranging from -15℃ to 45℃, for the two phase (aqueous and organic) reaction of LLE.

EXPERIMENTS: Chemical Isotopic exchange occurs according to the following chemical exchange reaction: $^{6}Li^{+}_{(aq)} + {}^{7}LiL^{+}_{(org)} \rightarrow {}^{6}Li^{+}_{(aq)} + {}^{7}LiL^{+}_{(org)}$ (1)
, where L represents macrocyclic polyether (DC18-crown-6).

RESULTS: As shown in Fig. 1, the separation coefficient (ε) has the following temperature dependence with the second order polynomial, based on the Bigeleisen's new theory [2].

$$\varepsilon = \frac{a}{T^2} + \frac{b}{T} \quad , \quad \ln \alpha = a\left(\frac{\triangle M}{MM'}\right) + b\,\delta(r^2) + \ln K_{hf} \qquad (2)$$

, where a, and b are the scaling factor of nuclear mass effect and nuclear field effect, respectively. (T: Temperature(Kelvin), M and M': mass of heavier and lighter isotope, respectively, and △M is the difference of isotopes, and $\delta\langle r^2\rangle$ and $\ln K_{hf}$ are the change in mean square of the charge radii and the contribution of hyperfine splitting based on the nuclear spin, respectively.)

1/T (K)	℃	$\delta\langle r^2\rangle$ (fm^2)	ΔM/MM'	α(org)±σ	ε(α(org)−1)
0.003876	−15	−0.731	0.0238	0.990±0.005	0.010
0.003663	0			0.994±0.004	0.006
0.00339	22			0.991±0.003	0.009
0.003145	45			0.994±0.005	0.006

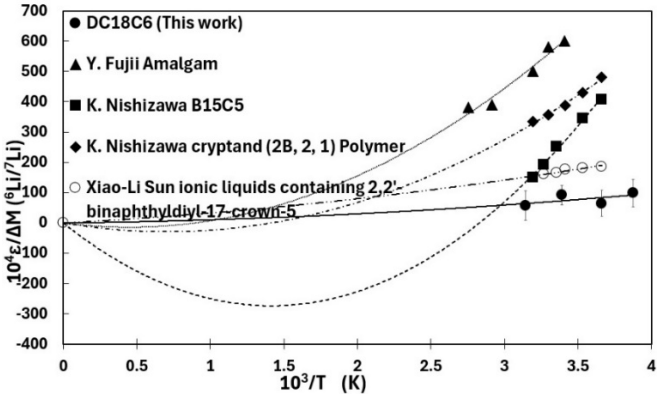

Fig. 1. Separation coefficient (ε) of litium based on the various extraction temperature ranging from –15℃ to 45℃, compared with the past research on amalgam, B15C5, cryptand, and ionic liquids [3,4,5,6].

The contribution ratio of nuclear field and nuclear spin to the nuclear mass effect are obtained as −0.039 and -1.6×10^{-7}, respectively (a and b are 4.6×10^{2} and 0.58, respectively.)

REFERENCES:

[1] A. Rittirong, Doctor Thesis, OSU (2022).
[2] J. Bigeleisen, J.Am.Chem.Soc., 118 (1996) 3676 .
R. Hazama *et al.,* arXiv0710.3840.
[3] Y. Fujii *et al.,* J. Nucl. Sci.Tec., 39 (2002) 413.
[4] K. Nishizawa *et al.,* J. Nucl. Sci. Tec., 21 (1984) 694.
[5] K. Nishizawa *et al.,* J. Nucl. Sci. Tec., 21 (1984) 133.
[6] X.Sun *et al.,* J. Nucl. Sci. Tec., 52 (2015) 332.

CO12-10

Development of Radiation Monitor for Space weather measuring Electrons (RMS-e) for the Himawari-10 satellite

K. Sakaguchi[1] and T. Namekawa[1]

[1]*National Institute of Information and Communications Technology*

INTRODUCTION: Monitoring of the radiation environment in geostationary orbit around the Earth are very important for space weather forecast. However, the instruments on board the currently operating Himawari 8 and 9 meteorological satellites have an insufficient energy range to fully monitor the space radiation environment. Therefore, we are developing Radiation Monitor for Space weather measuring Electrons (RMS-e) instrument installed on the next Himawari meteorological satellite. The RMS-e instrument is designed to measure the energy and flux of electrons between 50 keV and 6 MeV, which is an energy range sufficient to monitor the space radiation environment, using layered solid-state detectors (SSDs) made of silicon semiconductors. We conducted an evaluation of the measurement range for electron energy and energy resolution of > 2 MeV electrons by irradiating electrons emitted by Kyoto University, Institute for Integrated Radiation and Nuclear Science - Linear Accelerator (KURNS-LINAC) to the engineering model (EM) of RMS-e.

EXPERIMENTS: RMS-e EM was installed in the irradiation room and the monoenergetic electron beam generated by LINAC was injected perpendicular to the layered SSDs. The electron energies injected into RMS-e EM were 2.2, 2.6, 2.95, 3.3, 3.9, 4.5, 5.25, 6, and 7 MeV. The outer circumference of RMS-e EM was covered with lead blocks for radiation protection. Commands to control RMS-e EM were entered remotely from a PC installed in the control room.

RESULTS: Figure 1 shows the energy spectrum obtained using RMS-e EM for all incident electron beams (2.2, 2.6, 2.95, 3.3, 3.9, 4.5, 5.25, 6, and 7 MeV). For electron beams with energies below 6 MeV, a clear spectral peak is obtained. The shift of the peaks to lower energies and the tail of the peak extending to the low energy side are due to scattering of electrons by the Al shield to block low energy electrons. The energy resolution based on the full width half maximum of the peaks is about 10% for electrons below 5 MeV. The energy resolution for the 2.2 MeV electron beam can be affected by background γ-rays with energies of 1-1.5 MeV. The energy resolution also tends to be poor due to the small number of electrons detected, as RMS-e must be evaluated at very low beam flux. The result of this evaluation indicates that RMS-e can measure electrons between 2.2 MeV and 5 MeV with an energy resolution better than 10%, which is sufficient performance to measure the radiation environment in geostationary orbit around the Earth.

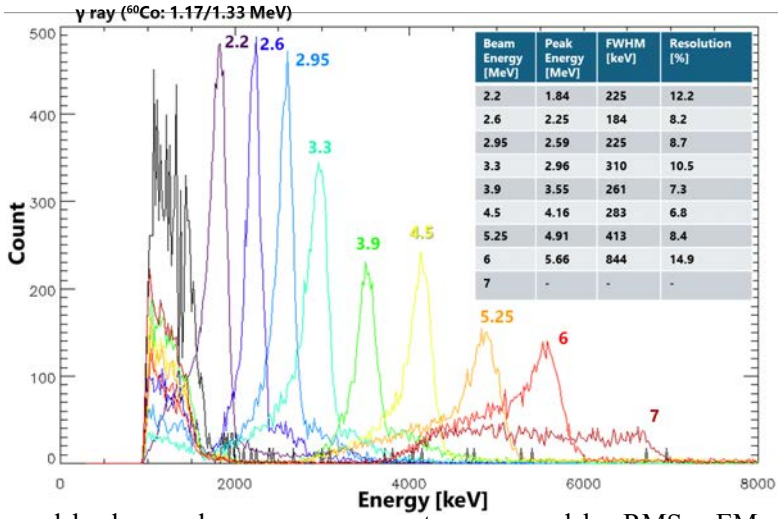

Beam Energy [MeV]	Peak Energy [MeV]	FWHM [keV]	Resolution [%]
2.2	1.84	225	12.2
2.6	2.25	184	8.2
2.95	2.59	225	8.7
3.3	2.96	310	10.5
3.9	3.55	261	7.3
4.5	4.16	283	6.8
5.25	4.91	413	8.4
6	5.66	844	14.9
7	-	-	-

Figure 1. The electron and background γ-ray energy spectra measured by RMS-e EM under the irradiation of monoenergetic electron beams (2.2, 2.6, 2.95, 3.3, 3.9, 4.5, 5.25, 6 and 7 MeV). The total number of electrons / γ-rays is the same for each energy spectrum.

II. PUBLICATION LIST
(APRIL 2023 – MARCH 2024)

1. Slow Neutron Physics and Neutron Scattering

Papers

Characterization of electroless nickel-phosphorus plating for ultracold-neutron storage
Akatsuka H., Andalib T., Bell B., Berean-Dutcher J., Bernier N., Bidinosti C.P., Cude-Woods C., Currie S.A., Davis C.A., Franke B., Gaur R., Giampa P., Hansen-Romu S., Hassan M.T., Hatanaka K., Higuchi T., Gibson C., Ichikawa G., Ide I., Imajo S., Ito T.M., Jamieson B., Kawasaki S., Kitaguchi M., Klassen W., Korkmaz E., Kuchler F., Lang M., Lavvaf M., Lindner T., Makela M., Mammei J., Mammei R., Martin J.W., Matsumiya R., Miller E., Mishima K., Momose T., Morawetz S., Morris C.L., Ong H.J., O'Shaughnessy C.M., Pereira-Wilson M., Picker R., Piermaier F., Pierre E., Schreyer W., Sidhu S., Stang D., Tiepo V., Vanbergen S., Wang R., Wong D., Yamamoto N.
Nuclear Instruments and Methods in Physics Research Section A: Accelerators, Spectrometers, Detectors and Associated Equipment 1049 (2023) 168106 (doi) 10.1016/j.nima.2023.168106

Ring compaction as a mechanism of densification in amorphous silica
Salmon Philip S., Zeidler Anita, Shiga Motoki, Onodera Yohei, Kohara Shinji
Physical Review B 107(14) (2023) 144203 (doi) 10.1103/PhysRevB.107.144203

Development of Neutron Interferometer Using Multilayer Mirrors and Measurements of Neutron-Nuclear Scattering Length with Pulsed Neutron Source
Fujiie Takuhiro, Hino Masahiro, Hosobata Takuya, Ichikawa Go, Kitaguchi Masaaki, Mishima Kenji, Seki Yoshichika, Shimizu Hirohiko M., Yamagata Yutaka
Physical Review Letters 132(2) (2024) 023402 (doi) 10.1103/PhysRevLett.132.023402

Study of the boundary friction of high-strength steel during the cold rolling
Shimura Masahiro, Yamashita Naoki, Hino Masahiro, Otsuka Takayuki, Hirayama Tomoko
Tribology - Materials, Surfaces & Interfaces (2024) (doi) 10.1177/17515831231216387

Proceedings

Confronting the Standard Model of particle physics by precision measurements of low-energy systems.
Takashi Higuchi
Proceedings of the 58th KURNS Scientific Meeting Kumatori, Japan/Online (Jan. 31- Feb. 1, 2024) 51-53 (In Japanese)

Photothermal 癌治療用増感剤 ICG-リポゾームの分光研究
Norio Miyoshi, Keita Iwasaki, Hidetoshi Sato, Kotaro Tsutsumi
第 21 回医用分光学研究会年会 Kansei Gakuin (Oct. 30-31, 2023) 34-36 (In Japanese)

2. Nuclear Physics and Nuclear Data

Papers

Gamma-Ray Spectrum Measurement from Capture Reactions of Uranium-238 for Thermal and Resonance Energy Neutrons
Nauchi Yasushi, Hori Jun-ichi, Terada Kazushi, Sano Tadafumi
EPJ Web of Conferences 284 (2023) 08010 (doi) 10.1051/epjconf/202328408010

Neutron Filtering System for Neutron Capture Cross Section Measurement at the ANNRI beamline of MLF/J-PARC
Gerard Rovira, Atsushi Kimura, Shoji Nakamura, Shunsuke Endo, Osamu Iwamoto, Nobuyuki Iwamoto, Tatsuya Katabuchi, Yu Kodama, Hideto Nakano, Jun-ichi Hori, Yuji Shibahara, Terada Kazushi
EPJ Web of Conferences 284 (2023) 06007 (doi) 10.1051/epjconf/202328406007

Measurements of the Neutron Capture Cross Section of Am-243 with the ANNRI beamline, MLF/J-PARC
Yu Kodama, Tatsuya Katabuchi, Gerard Rovira, Atsushi Kimura, Shoji Nakamura, Shunsuke Endo, Hideto Nakano, Yaoki Sato, Jun-ichi Hori, Yuji Shibahara, Kazushi Terada
EPJ Web of Conferences 284 (2023) 01024 (doi) 10.1051/epjconf/202328401024

Development of a non-destructive carbon quantification method in iron by negative muon lifetime measurement
Ninomiya Kazuhiko, Kubo Michael Kenya, Inagaki Makoto, Yoshida Go, Takeshita Soshi, Tampo Motonobu, Shimomura Koichiro, Kawamura Naritoshi, Strasser Patrick, Miyake Yasuhiro, Ito Takashi U., Higemoto Wataru, Saito Tsutomu
Journal of Radioanalytical and Nuclear Chemistry (2024) (doi) 10.1007/s10967-023-09289-2

Nuclear Resonance Vibrational Spectroscopy Definition of Peroxy Intermediates in Catechol Dioxygenases: Factors that Determine Extra- versus Intradiol Cleavage
Babicz Jeffrey T., Rogers Melanie S., DeWeese Dory E., Sutherlin Kyle D., Banerjee Rahul, Böttger Lars H., Yoda Yoshitaka, Nagasawa Nobumoto, Saito Makina, Kitao Shinji, Kurokuzu Masayuki, Kobayashi Yasuhiro, Tamasaku Kenji, Seto Makoto, Lipscomb John D., Solomon Edward I.
Journal of the American Chemical Society 145(28) (2023) 15230 (doi) 10.1021/jacs.3c02242

Helium gas cell with RF wire carpets for KEK Isotope Separation System
Hirayama Y., Mukai M., Schury P., Watanabe Y.X., Iimura S., Ishiyama H., Jeong S.C., Miyatake H., Niwase T., Rosenbusch M., Takamine A., Taniguchi A., Wada M.
Nuclear Instruments and Methods in Physics Research Section A: Accelerators, Spectrometers, Detectors and Associated Equipment 1058 (2024) 168838 (doi) 10.1016/j.nima.2023.168838

Activation cross sections of alpha-particle-induced reactions on natural tungsten for osmium and rhenium radionuclides
Ukon Naoyuki, Aikawa Masayuki, Saito Moemi, Hagiwara Masayuki, Yashima Hiroshi, Komori Yukiko, Haba Hiromitsu, Takács Sándor, Ditrói Ferenc, Szűcs Zoltán
Nuclear Instruments and Methods in Physics Research Section B: Beam Interactions with Materials and Atoms 539 (2023) 95-101 (doi) 10.1016/j.nimb.2023.03.032

Direct observations of spin fluctuations in hedgehog–anti-hedgehog spin lattice states in $MnSi_{1-x}Ge_x$ (x=0.6 and 0.8) at zero magnetic field
Aji Seno, Oda Tatsuro, Fujishiro Yukako, Kanazawa Naoya, Saito Hiraku, Endo Hitoshi, Hino Masahiro, Itoh Shinichi, Arima Taka-hisa, Tokura Yoshinori, Nakajima Taro
Physical Review B 108(5) (2023) 054445 (doi) 10.1103/PhysRevB.108.054445

Search for particle-stable tetraneutrons in thermal fission of U235
Fujioka Hiroyuki, Tomomatsu Ryutaro, Takamiya Koichi
Physical Review C 108(5) (2023) 054004 (doi) 10.1103/PhysRevC.108.054004

Monte Carlo perturbation method for optimum surface geometry due to sloshing motion
Yamamoto Toshihiro, Sakamoto Hiroki
Progress in Nuclear Energy 160 (2023) 104715 (doi) 10.1016/j.pnucene.2023.104715

Neutron phase imaging by a Talbot–Lau interferometer at Kyoto University Reactor
Seki Yoshichika, Shinohara Takenao, Hino Masahiro, Nakamura Riichiro, Samoto Tetsuo, Momose Atsushi
Review of Scientific Instruments 94(10) (2023) 103701 (doi) 10.1063/5.0157494

Proceedings

In-gas-cell laser ionization spectroscopy at KISS
Hirayama Yoshikazu, Mukai Momo, Watanabe Yutaka, Schury Peter, Niwase Toshitaka, Choi Hyunsuk, Hashimoto Takashi, Iimura Shun, Jeong SunChan, Miyatake Hiroari, Moon Jun Young, Nakada Hitoshi, Oyaizu Michihiro, Rosenbusch Marco, Takamine Aiko, Tajima Minori, Taniguchi Akihiro, Wada Michiharu
HYPERFINE 2023 Nara, Japan (Mar. 14-17, 2024) 1-13 (doi) 10.1007/s10751-024-01886-1

Experimental study on local interfacial parameters in gas-liquid two-phase flow within a plate-type fuel element
Vikrant Siddharudh Chalgeri, Xiuzhong Shen, Toshihiro Yamamoto
Proceedings of the 58th KURNS Scientific Meeting, Kumatori, Japan/Online (Jan. 31- Feb. 1, 2024) 33

Void fraction and interfacial area concentration of two-phase flow in a rod bundle fuel assembly
Jiaxu Zuo, Xiuzhong Shen, Vikrant Siddharudh Chalgeri, Toshihiro Yamamoto
Proceedings of the 58th KURNS Scientific Meeting, Kumatori, Japan/Online (Jan. 31- Feb. 1, 2024) 34

Design of a microwave spectrometer for high-precision Lamb shift spectroscopy of antihydrogen atoms
Tanaka T. A., Blumer P., Janka G., Ohayon B., Regenfus C., Asari M., Tsukida R., Higuchi T., Tanaka K. S., Crivelli P., Kuroda N.
The International Conference on Hyperfine Interactions and their Applications (HYPERFINE2023) Nara, Japan (Mar. 12, 2024) 30 (doi) 10.1007/s10751-024-01876-3.

In-beam Mössbauer Spectra of ^{57}Fe Obtained After ^{57}Mn Implantation into Ammonia Borane
S. Kimoto, M. Yoshida, M. Ito, Y. Kobayashi, Y. Watanabe, M. K. Kubo, M. Mihara, W. Sato, J. Miyazaki, T. Nagatomo, S. Sato, and A. Kitagawa
Proceedings of the Specialists' Meeting on "Nuclear Spectroscopy and Condensed Matter Physics Using Short-Lived Nuclei IX" Online (Jan. 11, 2023)13-16 (In Japanese)

Measurement of excitation level of nuclei generated by muon nuclear absorption reaction
K. Ninomiya, S. Asari, I. Chiu, T. Yoshimura, A. Sato, A. Amato, S. Biswas, L. Gerchow, C. Vigo, C. Wang, C. Mielke, D. Das, F. Hotz, T. Prokscha, T. Shiroka, Z. Salman, Z. Guguchia, H. Luetkens, K. Schoeler, M. Niikura, G. Janka and N. Ritjoho
Proceedings of the Specialists' Meeting on "Nuclear Spectroscopy and Condensed Matter Physics Using Short-Lived Nuclei IX" Online (Jan. 11, 2023) 31 (In Japanese)

Nuclear Excitation of Gd-155 Isotope with Synchrotron Radiation
S. Tsutsui, T. Kanetomo, R. Taniai, M. Enomoto, T. Ishida, M. Kadowaki, F. Iga, F. Honda, N. Nagasawa, Y. Yoda, Y. Kobayashi
Proceedings of the Specialists' Meeting on "Nuclear Spectroscopy and Condensed Matter Physics Using Short-Lived Nuclei IX" Online (Jan. 11, 2023) 26-30 (In Japanese)

Vacuum Ultraviolet Search from Thorium-229 Isomer in Crystal Toward Solid-State Nuclear Clock
Takatori S., Fukunaga Y., Guan M., Hiraki T., Masuda T., Ogake R., Okai K., Sasao N., Shimizu K., Uetake S., Yoshimi A., Yoshimura K., Yoshimura M., Tamasaku K., Kasamatsu Y., Yasuda Y., Beeks K., Schaden F., Schumm T., Kitao S., Seto M., Fujimoto H., Watanabe T., Konashi K., Watanabe M., Haba H., Shigekawa Y., Yamaguchi A., Nagasawa N., Yoda Y.
2023 Joint Conference of the European Frequency and Time Forum and IEEE International Frequency Control Symposium (EFTF/IFCS) Toyama, Japan (May 15-19, 2023) (doi) 10.1109/EFTF/IFCS57587.2023.10272086

Reviews

Trends in radiation standard Neutron standards - present and future -
Tetsuro Matsumoto, Hideki Harano, Akihiko Masuda, Seiya Manabe
Journal of the Atomic Energy Society of Japan 66(1) (2024) 37 (In Japanese)

3. Reactor Physics and Reactor Engineering

Papers

Calculation scheme for thermal neutron scattering cross-sections of hydrogenous molecules in liquid and solid phases by molecular dynamics
Abe Y., Funama F., Tasaki S., Hino M.
Annals of Nuclear Energy 194 (2023) 110101 (doi) 10.1016/j.anucene.2023.110101

Modeling noise experiments performed at AKR-2 and CROCUS zero-power reactors
Hursin M., Zoia A., Rouchon A., Brighenti A., Zmijarevic I., Santandrea S., Vinai P., Mylonakis A., Yi H., Demazière C., Lamirand V., Ambrozic K., Yamamoto T., Hübner S., Knospe A., Lange C., Yum S., Macian R., Vidal A., Ginestar D., Verdú G.
Annals of Nuclear Energy 194 (2023) 110066 (doi) 10.1016/j.anucene.2023.110066

Verification of Feynman-α formula including the effect of delayed neutrons
Yamamoto Toshihiro, Sakamoto Hiroki
Annals of Nuclear Energy 194 (2023) 110090 (doi) 10.1016/j.anucene.2023.110090

Measurement of ^{233}U-HU Substitution Reactivity Worth in KUCA for Integral Validation of ^{233}U Nuclear Data
Sano Tadafumi, Hori Jun-ichi, Takahashi Yoshiyuki, Terada Kazushi, Yashima Hiroshi, Kanda Takashi, Unesaki Hironobu
EPJ Web of Conferences 284 (2023) 08013 (doi) 10.1051/epjconf/202328408013

Development of capacitance sensor for void fraction measurement in a packed bed of spheres
Ito Daisuke, Odaira Naoya, Ito Kei, Saito Yasushi
Flow Measurement and Instrumentation 90 (2023) 102330 (doi) 10.1016/j.flowmeasinst.2023.102330

Multi-dimensional characteristics of upward bubbly flows in a vertical large-size square channel
Sun Haomin, Kunugi Tomoaki, Yokomine Takehiko, Shen Xiuzhong, Hibiki Takashi
International Journal of Heat and Mass Transfer 211 (2023) 124214 (doi) 10.1016/j.ijheatmasstransfer.2023.124214

A spurious-count effect observed in Rossi-α and Feynman-α analysis using fission counter for Kyoto University Reactor
Hohara Sin-Ya, Sano Tadafumi, Hori Jun-Ichi, Sakon Atsushi, Nakajima Kunihiro, Takahashi Yoshiyuki, Hashimoto Kengo
Journal of Nuclear Science and Technology 60(10) (2023) 1292-1300 (doi) 10.1080/00223131.2023.2177762

Relationship between neutron moderator and time-dependent background for neutron time-of-flight measurement
Lee Jaehong, Hironaka Kota, Ito Fumiaki, Koizumi Mitsuo, Hori Jun-Ichi, Sano Tadafumi
Journal of Nuclear Science and Technology (2023) 1-8 (doi) 10.1080/00223131.2023.2224330

Measurement of neutron spectra for various thicknesses of concrete and steel shielding at 24-GeV/c proton beam facility using Bonner sphere spectrometer
Matsumoto Tetsuro, Masuda Akihiko, Lee Eunji, Sanami Toshiya, Oyama Takahiro, Kajimoto Tsuyoshi, Nakao Noriaki, Yashima Hiroshi, Nagaguro Seiji, Uwamino Yoshitomo, Manabe Seiya, Shigyo Nobuhiro, Harano Hideki, Froeschl Robert, Iliopoulou Elpida, Infantino Angelo, Roesler Stefan, Brugger Markus
Journal of Nuclear Science and Technology 61(1) (2024) 98-110 (doi) 10.1080/00223131.2023.2274933

Measurement and simulations of high-energy neutrons through a various thickness of concrete and steel shields using activation detectors at CHARM and CSBF
Nakao Noriaki, Sanami Toshiya, Kajimoto Tsuyoshi, Yashima Hiroshi, Froeschl Robert, Bozzato Davide, Iliopoulou Elpida, Infantino Angelo, Lee Eunji, Oyama Takahiro, Hagiwara Masayuki, Nagaguro Seiji, Matsumoto Tetsuro, Masuda Akihiko, Uwamino Yoshitomo, Devienne Arnaud, Pozzi Fabio, Tisi Marco, Lorenzon Tommaso, Menaa Nabil, Vincke Heinz, Roesler Stefan, Brugger Markus
Journal of Nuclear Science and Technology (2023) 1-19 (doi) 10.1080/00223131.2023.2239243

Development of a critical heat flux correlation based on an annular film dryout mechanistic model under the annular flow conditions
Yodo Tadakatsu, Odaira Naoya, Ito Daisuke, Ito Kei, Saito Yasushi
Journal of Nuclear Science and Technology 60(10) (2023) 1182-1193 (doi) 10.1080/00223131.2023.2177761

Visualization of local two-phase flow structure in a packed bed of spheres
Ito D, Odaira N, Ito K, Saito Y
Journal of Physics: Conference Series 2605 (2023) 012032 (doi) 10.1088/1742-6596/2605/1/012032

Measurements of gas-liquid two-phase flow dynamics using high-speed neutron imaging
Ito D, Odaira N, Ito K, Saito Y, Kurita K, Iikura H
Journal of Physics: Conference Series 2605 (2023) 012024 (doi) 10.1088/1742-6596/2605/1/012024

Development of Tracer Particles for Thermal Hydraulic Experiment by Neutron Imaging
Saito Y, Ito D, Odaira N, Kurita K, Iikura H
Journal of Physics: Conference Series 2605 (2023) 012028 (doi) 10.1088/1742-6596/2605/1/012028

Monte Carlo simulations for gamma-ray spectroscopy using bismuth nanoparticle-containing plastic scintillators with spectral subtraction
Lim Taeseob, Song Siwon, Kim Seunghyeon, Park Jae Hyung, Kim Jinhong, Pyeon Cheol Ho, Lee Bongsoo
Nuclear Engineering and Technology 55(9) (2023) 3401-3408 (doi) 10.1016/j.net.2023.05.030

Feasibility study on fiber-optic inorganic scintillator array sensor system for multi-dimensional scanning of radioactive waste
Park Jae Hyung, Song Siwon, Kim Seunghyeon, Kim Jinhong, Cho Seunghyun, Pyeon Cheol Ho, Lee Bongsoo
Nuclear Engineering and Technology 55(9) (2023) 3206-3212 (doi) 10.1016/j.net.2023.06.002

Sensitivity of a control rod worth estimate to neutron detector position by time-dependent Monte Carlo simulations of the rod drop experiment
Park Jong Min, Pyeon Cheol Ho, Shim Hyung Jin
Nuclear Engineering and Technology 56(3) (2024) 916-921 (doi) 10.1016/j.net.2023.11.008

Neutron resonance fission neutron analysis for nondestructive fissile material assay
Hironaka K., Lee J., Koizumi M., Ito F., Hori J., Terada K., Sano T.
Nuclear Instruments and Methods in Physics Research Section A: Accelerators, Spectrometers, Detectors and Associated Equipment 1054 (2023) 168467 (doi) 10.1016/j.nima.2023.168467

Experimental Analyses of Capture Reaction Rates for Epithermal and Resonance Neutrons in Source-Driven Subcritical Cores
Aizawa Naoto, Pyeon Cheol Ho
Nuclear Science and Engineering 198(3) (2023) 658-672 (doi) 10.1080/00295639.2023.2212580

Void Reactivity in Lead and Bismuth Sample Reactivity Experiments at Kyoto University Critical Assembly
Pyeon Cheol Ho, Katano Ryota, Oizumi Akito, Fukushima Masahiro
Nuclear Science and Engineering 197(11) (2023) 2902-2919 (doi) 10.1080/00295639.2023.2172311

Optical and scintillation properties of Yb-doped $La_2Hf_2O_7$ crystal grown by core heating method for fiber reading remote-dosimetry system
Ishizawa Satoshi, Kurosawa Shunsuke, Kurashima Yutaro, Kodama Shohei, Morishita Yuki, Yamaji Akihiro, Ohno Maki, Ishikawa Shiori, Hayashi Masateru, Sasano Makoto, Makita Taisuke, Fujiwara Chihaya, Kochurikhin Vladimir, Yoshikawa Akira, Takata Takushi, Tanaka Hiroki
Optical Materials 142 (2023) 113941 (doi) 10.1016/j.optmat.2023.113941

High-pressure xenon gas time projection chamber with scalable design and its performance around the Q value of ^{136}Xe double-beta decay
Yoshida Masashi, Nakamura Kazuhiro, Akiyama Shinichi, Ban Sei, Hikida Junya, Hirose Masanori, Ichikawa Atsuko K, Iwashita Yoshihisa, Kashino Yukimasa, Kikawa Tatsuya, Minamino Akihiro, Miuchi Kentaro, Nakajima Yasuhiro, Nakamura Kiseki D, Nakaya Tsuyoshi, Obara Shuhei, Sakashita Ken, Sekiya Hiroyuki, Shinagawa Hibiki, Sugashima Bungo, Urano Soki
Progress of Theoretical and Experimental Physics 2024(1) (2024) 013H01 (doi) 10.1093/ptep/ptad146

Neutron reflectometry under high shear in narrow gap for tribology study
Yamashita Naoki, Hirayama Tomoko, Hino Masahiro, Yamada Norifumi L.
Scientific Reports 13 (2023) 18268 (doi) 10.1038/s41598-023-45161-9

High-performance thermoelectric properties of Cu_2Se fabricated via cold sintering process
Piyasin Piyawat, Palaporn Dulyawich, Kurosaki Ken,
Pinitsoontorn Supree Solid State Sciences 149 (2024) 107448 (doi) 10.1016/j.solidstatesciences.2024.107448

Proceedings

Capabilities of the converted KUCA cores for HALEU criticality studies
Hironobu Unesaki, Yoshiyuki Takahashi, Yasunori Kitamura, Tsuyoshi Misawa
2023 RERTR International Meeting (RERTR-2023) Denver, Colorado, USA (Nov. 5 - 8, 2023) 1

Estimation of ^{235}U enrichment by neutron induced gamma ray spectroscopy
Y. Nauchi, S. Sato, M. Suzuki, T. Sano, H. Unesaki
ICNC 2023 - The 12th International Conference on Nuclear Criticality Safety Sendai, Japan（Oct. 1 - 6, 2023）

Current status of new fabrication technique of absorption gratings for Talbot-Lau interfer-ometer
Mugeng Li, Masashiro Hino, Takuya Hosobata, Yoshichika Seki
Proceedings of the 58th KURNS Scientific Meeting Kumatori, Japan/Online (Jan. 31- Feb. 1, 2024) 22

Effect of fin arrangement on pressure drop characteristics of two-phase flow in a finned rectangular channel.
Shori Okunaka, Naoya Odaira, Daisuke Ito, Kei Ito, Yasushi Saito
Proceedings of the 58th KURNS Scientific Meeting Kumatori, Japan/Online (Jan. 31- Feb. 1, 2024) 46 (In Japanese)

Effect of interfacial drag term on pressure drop in gas-liquid two-phase flow within a packed bed of spheres.
Tomohiro Mizuno, Naoya Odaira, Daisuke Ito, Kei Ito, Yasushi Saito
Proceedings of the 58th KURNS Scientific Meeting Kumatori, Japan/Online (Jan. 31- Feb. 1, 2024) 40 (In Japanese)

Recent progress on neutron devices fabricated by KUR-IBS instrument
Masahiro Hino
Proceedings of the 58th KURNS Scientific Meeting Kumatori, Japan/Online (Jan. 31- Feb. 1, 2024) 37

Physics and engineering of unstable nuclei
Yoshichika Seki, Masahiro Hino, Mugeng Li
Proceedings of the 58th KURNS Scientific Meeting Kumatori, Japan/Online (Jan. 31- Feb. 1, 2024) 38 (In Japanese)

Towards neutron imaging for oscillating magnetic field by using neutron spin interferometry
Ryuto Fujitani, Takaya Suzuki, Seiji Tasaki, Masahiro Hino, Masaaki Kitaguchi, Tatsuro Oda, Riichiro Nakamura
Proceedings of the 58th KURNS Scientific Meeting Kumatori, Japan/Online (Jan. 31- Feb. 1, 2024) 24 (In Japanese)

Evaluation of burnable poison reactivity worth at The KUCA Graphite-Moderated System
Yamasaki Seiji, Moriya Soichiro, Simanullang Irwan L., Fujimoto Nozomu, Sakon Atsushi, Sano Tadafumi, Takahashi Yoshiyuki
The 30th International Conference on Nuclear Engineering (ICONE30) Kyoto, Japan（May 21- 26, 2023）1271 (doi) 10.1299/jsmeicone.2023.30.1271

First nuclear reactor physics experiment in subcritical pile using U-7Mo LEU fuel at KUCA
Yoshiyuki Takahashi, Koki Wakabayashi, Yasunori Kitamura, Hironobu Unesaki and Tsuyoshi Misawa
The European Research Reactor Conference (RRFM-2023) Antwerpen, Belgium (Apr. 16 - 20, 2023) 1-6

Measurement of internal conversion electron of ^{234m}Np using PIN diode at JAEA-ISOL
T. Miyazawa, M. Shibata, M. Asai, K. Tsukada, T. K. Sato, Y. Ito, and R. Aoki
Proceedings of the Specialists' Meeting on "Nuclear Spectroscopy and Condensed Matter Physics Using Short-Lived Nuclei IX" Online（Jan. 11, 2023）39-43 (In Japanese)

Reviews

Path forward for development of advanced reactor and nuclear fuel cycle technologies (1)
Ken Kurosaki
Journal of the Atomic Energy Society of Japan 66(1) (2024) 11-14 (In Japanese)

Recent Efforts and International Trends in Reduction of Uranium Enrichment for Research Reactors
Hironobu Unesaki
Journal of the Atomic Energy Society of Japan 65(10) (2023) 608-612（In Japanese）

4. Material Science and Radiation Effects

Papers

Mechanical Compatibility between $Mg_3(Sb,Bi)_2$ and MgAgSb in Thermoelectric Modules
Sun Yifan, Fu Jiahui, Ohishi Yuji, Toh Keita, Suekuni Koichiro, Kihou Kunihiro, Anazawa Ushin, Lee Chul-Ho, Kurosaki Ken
ACS Applied Materials & Interfaces 15(19) (2023) 23246-23254 (doi) 10.1021/acsami.3c02544

Effect of Sintering Temperature on the Thermoelectric Properties of Ag_2Se Fabricated by Spark Plasma Sintering with High Compression
Palaporn Dulyawich, Kurosaki Ken, Pinitsoontorn Supree
Advanced Energy and Sustainability Research 4(10) (2023) 2300082 (doi) 10.1002/aesr.202300082

Porous Ag_2Se Fabricated by a Modified Cold Sintering Process with the Average zT Around Unity Near Room Temperature
Palaporn Dulyawich, Pinitsoontorn Supree, Kurosaki Ken, Snyder G. Jeffrey
Advanced Materials Technologies 9(1) (2024) 2301242 (doi) 10.1002/admt.202301242

Single-crystal elasticity of (Al,Fe)-bearing bridgmanite up to 82 GPa
Fu Suyu, Zhang Yanyao, Okuchi Takuo, Lin Jung-Fu
American Mineralogist 108(4) (2023) 719-730 (doi) 10.2138/am-2022-8435

Low-Temperature Hydrogenation of CO_2 to Methanol in Water on ZnO-Supported CuAu Nanoalloys
Mosrati Jawaher, Ishida Tamao, Mac Hung, Al-Yusufi Mohammed, Honma Tetsuo, Parliniska-Wojtan Magdalena, Kobayashi Yasuhiro, Klyushin Alexander, Murayama Toru, Abdel-Mageed Ali M.
Angewandte Chemie International Edition 62(51) (2023) e202311340 (doi) 10.1002/anie.202311340

Quasi-elastic neutron scattering studies on fast dynamics of water molecules in tetra-n-butylammonium bromide semiclathrate hydrate
Shimada Jin, Tani Atsushi, Yamada Takeshi, Sugahara Takeshi, Hirai Takayuki, Okuchi Takuo
Applied Physics Letters 123(4) (2023) 44104 (doi) 10.1063/5.0157560

Development of an event-by-event based Li–ZnS(Ag) neutron imaging detector with selective neutron detection capability
Yamamoto Seiichi, Yoshino Masao, Nakanishi Kohei, Kamada Kei, Yoshikawa Akira, Tanaka Hiroki, Kataoka Jun
Applied Radiation and Isotopes 204 (2024) 111084 (doi) 10.1016/j.apradiso.2023.111084

Redox-controlled differential weathering of andesitic pumice: Possible catalytic effects of ferrous/ferric iron on rapid halloysite accumulation in a Holocene tephra layer
FUKUI Hirokazu, MATSUSHI Yuki, WATANABE Tetsuhiro, LYU Han, KITAO Shinji, KOBAYASHI Yasuhiro, SHINODA Keiji
CATENA 235 (2024) 107685 (doi) 10.1016/j.catena.2023.107685

Tritium and deuterium release behavior of Li_2TiO_3-0.5Li_4SiO_4–Pb ceramic
Zhou Qilai, Li Sicheng, Hirata Shiori, Sanfukuji Asahi, Tan Guangfan, Taguchi Akira, Oya Yasuhisa
Ceramics International 49(16) (2023) 26778-26785 (doi) 10.1016/j.ceramint.2023.05.214

Siliceous zeolite-derived topology of amorphous silica
Masai Hirokazu, Kohara Shinji, Wakihara Toru, Shibazaki Yuki, Onodera Yohei, Masuno Atsunobu, Sukenaga Sohei, Ohara Koji, Sakai Yuki, Haines Julien, Levelut Claire, Hébert Philippe, Isambert Aude, Keen David A., Azuma Masaki
Communications Chemistry 6(1) (2023) 269 (doi) 10.1038/s42004-023-01075-1

Ring-originated anisotropy of local structural ordering in amorphous and crystalline silicon dioxide
Shiga Motoki, Hirata Akihiko, Onodera Yohei, Masai Hirokazu
Communications Materials 4(1) (2023) 91 (doi) 10.1038/s43246-023-00416-w

Tritium release behavior from neutron-irradiated $Li_{z+x}TiO_{3+y}$ with 20wt% Li_2ZrO_3 pebbles under different atmospheres Ipponsugi
Akito, Katayama Kazunari, Hoshino Tsuyoshi
Fusion Engineering and Design 194 (2023) 113825 (doi) 10.1016/j.fusengdes.2023.113825

Tritium release behavior from neutron-irradiated FLiNaK mixed with Ti powder
Katayama Kazunari, Kubo Kaito, Ichikawa Toru, Oya Makoto, Fukada Satoshi, Iinuma Yuto
Fusion Engineering and Design 192 (2023) 113791 (doi) 10.1016/j.fusengdes.2023.113791

DynamicMC: An Open-source GUI Program Coupled with MCNP for Modeling Relative Dynamic Movement of Radioactive Source and ORNL Phantom in a 3-dimensional Radiation Field
Yu Kwan Ngok, Watabe Hiroshi, Zivkovic Milena, Krstic Dragana, Nikezic Dragoslav, Kim Kyeong Min, Yamaya Taiga, Kawachi Naoki, Tanaka Hiroki, Haque A.K.F., Shahmohammadi Beni Mehrdad
Health Physics 124(4) (2023) 301-309 (doi) 10.1097/HP.0000000000001670

Preparation of Mössbauer sources for ^{161}Dy, ^{166}Er, and ^{169}Tm
Kitao Shinji, Kobayashi Yasuhiro, Kurokuzu Masayuki, Kubota Takumi, Seto Makoto
Hyperfine Interactions 244 (2023) 10 (doi) 10.1007/s10751-023-01822-9

β-MoO_3 Whiskers in ^{99}Mo/^{99m}Tc Radioisotope Production and ^{99}Mo/^{99m}Tc Extraction Using Hot Atoms
Ngo Minh Chu, Fujita Yoshitaka, Suzuki Tatsuya, Dung Do Thi Mai, Seki Misaki, Nakayama Tadachika, Niihara Koichi, Suematsu Hisayuki
Inorganic Chemistry 62(32) (2023) 13140-13147 (doi) 10.1021/acs.inorgchem.3c02125

Experimental apparatus for detection of radiative decay of ^{229}Th isomer from Th-doped CaF_2
Hiraki Takahiro, Beeks Kjeld, Bartokos Michael, Fujimoto Hiroyuki, Fukunaga Yuta, Haba Hiromitsu, Kasamatsu Yoshitaka, Kitao Shinji, Leitner Adrian, Masuda Takahiko, Ming Guan, Nagasawa Nobumoto, Ogake Ryoichiro, Okai Koichi, Pimon Martin, Pressler Martin, Sasao Noboru, Schaden Fabian, Schumm Thorsten, Seto Makoto, Shigekawa Yudai, Shimizu Koutaro, Sikorsky Tomas, Tamasaku Kenji, Takatori Sayuri, Watanabe Tsukasa, Yamaguchi Atsushi, Yoda Yoshitaka, Yoshimi Akihiro, Yoshimura Koji
Interactions 245 (2024) 14 (doi) 10.1007/s10751-024-01844-x

Investigation of doping effect on the local structure and photocatalytic activity of $SrTiO_3$
Komatsuda Sayaka, Kawakami Miyuki, Sato Wataru, Taniguchi Akihiro, Tanigaki Minoru, Ohkubo Yoshitaka
Interactions 245 (2024) 37 (doi) 10.1007/s10751-024-01868-3

Design of a microwave spectrometer for high-precision Lamb shift spectroscopy of antihydrogen atoms
Tanaka T. A., Blumer P., Janka G., Ohayon B., Regenfus C., Asari M., Tsukida R., Higuchi T., Tanaka K. S., Crivelli P., Kuroda N.
Interactions 245(1) (2024) 30 (doi) 10.1007/s10751-024-01876-3

Measurement of the sub-nanometer vibration amplitudes using ^{57}Fe synchrotron Mössbauer source
Yamashita Hiroyuki, Kitao Shinji, Kobayashi Yasuhiro, Ota Hidetoshi, Masuda Ryo, Fujiwara Kosuke, Mitsui Takaya, Seto Makoto
Interactions 245 (2024) 15 (doi) 10.1007/s10751-024-01854-9

Recoilless fraction on ^{197}Au Mössbauer spectroscopy
kobayashi Yasuhiro, Ohashi Hironori, Kurokuzu Masayuki, Seto Makoto
Interactions 245 (2024) 42 (doi) 10.1007/s10751-024-01884-3

Hydrogen retention and affecting factors in rolled tungsten: Thermal desorption spectra and molecular dynamics simulations
Chen Hongyu, Wang Lin, Peng Feng, Xu Qiu, Xiong Yaoxu, Zhao Shijun, Tokunaga Kazutoshi, Wu Zhenggang, Ma Yi, Chen Pengqi, Luo Laima, Wu Yucheng
International Journal of Hydrogen Energy 48(78) (2023) 30522-30531 (doi) 10.1016/j.ijhydene.2023.03.151

Thermophysical Properties of Dense Molten Al_2O_3 Determined by Aerodynamic Levitation
Sun Yifan, Takatani Tomoya, Muta Hiroaki, Fujieda Shun, Kondo Toshiki, Kikuchi Shin, Kargl Florian, Ohishi Yuji
International Journal of Thermophysics 45 (2024) 11 (doi) 10.1007/s10765-023-03302-2

Lattice Defects Underneath Hydrogen-induced Intergranular Fracture Surface of Ni-Cr Alloy Evaluated by Low-energy Positron Beam
Tomatsu Kota, Omura Tomohiko, Aoki Takahiro, Yabuuchi Atsushi, Kinomura Atsushi
ISIJ International 63(11) (2023) 1889-1896 (doi) 10.2355/isijinternational.ISIJINT-2023-080

Transient positron annihilation spectroscopy under light irradiation at liquid nitrogen temperature: evaluation of defect states in single-crystal ZnO
Nakajima Makoto, Kinomura Atsushi, Xu Qiu, Kuriyama Kazuo
Japanese Journal of Applied Physics 63(3) (2024) 038005 (doi) 10.35848/1347-4065/ad3007

Hydrogen Trapping Behavior at Vacancies Introduced by Electron Irradiation in B2 Ordered Fe Base Alloys
F. Hori, Y. Sumikura, K. Sugita, Y. Kaneno, K. Ohsawa, Q. Xu, M. Maekawa, A. Kawasuso, Y. Saito
JJAP Conference Proceedings 9 (2023) 011107 (doi) 10.56646/jjapcp.9.0_011107

Planar defects-induced low thermal conductivity in a superhard material SiB_6
Tanusilp Sora-at, Kumagai Masaya, Ohishi Yuji, Ishimaru Manabu, Sadayori Naoki, Kurosaki Ken
Journal of Alloys and Compounds 939 (2023) 168744 (doi) 10.1016/j.jallcom.2023.168744

Thermal shock behaviors of W/Cu joints with different structures
Wei Bangzheng, Chen Ruizhi, Xu Dang, Li Gemin, Yang Guang, Wang Bing, Chen Pengqi, Xu Qiu, Cheng Jigui
Journal of Alloys and Compounds 967 (2023) 171770 (doi) 10.1016/j.jallcom.2023.171770

Helium irradiation-induced swelling resistance of heterogeneous nanoparticles in an iron-based multi-principal element alloy
Ye Feng Jiao, Zhu Te, Song Ya Min, Wang Qian Qian, Zhang Peng, Kuang Peng, Liu Fu Yan, Yu Run Sheng, Xu Qiu, Wang Bao Yi, Cao Xing Zhong
Journal of Alloys and Compounds 939 (2023) 168643 (doi) 10.1016/j.jallcom.2022.168643

Study on the affecting factors of material removal mechanism and damage behavior of shear rheological polishing of single crystal silicon carbide
Chen Hongyu, Wu Zhengchao, Hong Binbin, Hang Wei, Zhang Peng, Cao Xingzhong, Xu Qiu, Chen Pengqi, Chen Heng, Yuan Julong, Lyu Binghai, Lin Hua-Tay
Journal of Manufacturing Processes 112 (2024) 225-237 (doi) 10.1016/j.jmapro.2024.01.040

Compositional dependence of intensity tensor and electric field gradient tensor for Fe^{2+} at *M*2sites of enstatites by single crystal Mössbauer spectroscopy
SHINODA Keiji, ONOUE Keita, KOBAYASHI Yasuhiro
Journal of Mineralogical and Petrological Sciences 118(1) (2023) 221015 (doi) 10.2465/jmps.221015

Atomic structure of ZrO_2-doped Li_2O–SiO_2-based multi-component glasses revealed by molecular dynamics–reverse Monte Carlo modeling
Toyoda R., Usui K., Hirota T., Kimura K., Onodera Y., Cicconi M.R., Belli R., Brehl M., Lubauer J., Lohbauer U., Tajiri H., Ikeda K., Hayakawa T., de Ligny D., Kohara S., Hayashi K.
Journal of Non-Crystalline Solids 616 (2023) 122472 (doi) 10.1016/j.jnoncrysol.2023.122472

Si promotes nano-clusters and α phase separation in early-stage neutron irradiated low activation ferritic/martensitic steel
Huang Shaosong, Xu Qiu
Journal of Nuclear Materials 582 (2023) 154485 (doi) 10.1016/j.jnucmat.2023.154485

Creep deformation and rupture behavior of 9Cr-ODS steel cladding tube at high temperatures from 700°C to 1000°C
Imagawa Yuya, Hashidate Ryuta, Miyazawa Takeshi, Onizawa Takashi, Ohtsuka Satoshi, Yano Yasuhide, Tanno Takashi, Kaito Takeji, Ohnuma Masato, Mitsuhara Masatoshi, Toyama Takeshi
Journal of Nuclear Science and Technology (2024) 1-16 (doi) 10.1080/00223131.2023.2269178

Cohesive/Adhesive strengths of CsOH-chemisorbed SS304 surfaces
Li Nabaichuan, Sun Yifan, Nakajima Kunihisa, Kurosaki Ken
Journal of Nuclear Science and Technology 61(3) (2024) 343-353 (doi) 10.1080/00223131.2023.2231447

A multiclass classification model for predicting the thermal conductivity of uranium compounds
Sun Yifan, Kumagai Masaya, Jin Mingyu, Sato Eriko, Aoki Masako, Ohishi Yuji, Kurosaki Ken
Journal of Nuclear Science and Technology 61(6) (2024) 778-788 (doi) 10.1080/00223131.2023.2269974

Extraction of ^{99}Mo hot atoms made by a neutron capture method from α-MoO_3 to water
Quach N. M., Ngo M. C., Yang Y., Nguyen T. B., Nguyen V. T., Fujita Y., Do T. M. D., Nakayama T., Suzuki T., Suematsu H.
Journal of Radioanalytical and Nuclear Chemistry 332(10) (2023) 4057-4064 (doi) 10.1007/s10967-023-09125-7

Feasibility Study of Thin Film Surface Analysis Using Synchrotron Low-Angle Incidence Conversion Electron Mössbauer Spectroscopy
Mitsui Takaya, Fujiwara Kosuke, Mibu Ko, Masuda Ryo, Kobayashi Yasuhiro, Seto Makoto
Journal of the Physical Society of Japan 93(3) (2024) 034705 (doi) 10.7566/JPSJ.93.034705

Direct observation of voids decorated with transmuted rhenium atoms in neutron-irradiated tungsten by correlative use of TEM and APT
Inoue Koji, Yamashita Taiki, Nogami Shuhei, Hasegawa Akira, Toyama Takeshi, Nagai Yasuyoshi
Materialia 32 (2023) 101963 (doi) 10.1016/j.mtla.2023.101963

Irradiation effects on binary tungsten alloys at elevated temperatures: Vacancy cluster formation, precipitation of alloying elements and irradiation hardening
Jing Wang, Yuji Hatano, Takeshi Toyama, Tatsuya Hinoki, Kiyohiro Yabuuchi, Yi-fan Zhang, Bing Ma, Alexander V. Spitsyn, Nikolay P. Bobyr, Koji Inoue, Yasuyoshi Nagai
Materials & Design 229 (2023) 111899 (doi) 10.1016/j.matdes.2023.111899

Homogeneous solid-solution formation in Fe_2O_3–Al_2O_3 system observed by TEM, XAFS, and Mössbauer spectroscopy
Nakaishi Hayato, Yabutsuka Takeshi, Yao Takeshi, Kitao Shinji, Seto Makoto, Chen Wen-Jauh, Shimonishi Yuta, Yoshida Shuhei, Takai Shigeomi
Materials Chemistry and Physics 303 (2023) 127764 (doi) 10.1016/j.matchemphys.2023.127764

Microstructural evolution of graded W-Cu materials under repeated thermal shocks
Wei Bangzheng, Yang Guang, Tai Yunxiao, Xu Dang, Chen Ruizhi, Zhou Rui, Chen Pengqi, Xu Qiu, Cheng Jigui
Materials Today Communications 35 (2023) 106268 (doi) 10.1016/j.mtcomm.2023.106268

Microstructure Evolution and Effect on Deuterium Retention in TiC- and ZrC-Doped Tungsten under He+ Ion Irradiation
Ding Xiaoyu, Fang Jiahui, Xu Qiu, Zhang Panpan, Zhang Haojie, Luo Laima, Wu Yucheng, Yao Jianhua
Metals 13(4) (2023) 783 (doi) 10.3390/met13040783

Evolution of Irradiation Defects in W and W-Re Systems: A Density Functional Theory and Rate Theory Study
Xin Tianyuan, Yang Yiying, Wang Yuexia, Wu Lu, Pan Rongjian, Xu Qiu, Wu Xiaoyong
Metals 12 (2023) 1990 (doi) 10.3390/met13121990

Atomic and electronic structures of an Ag-containing 4A zeolite
Hosokawa Shinya, Kobayashi Kentaro, Koura Akihide, Shimojo Fuyuki, Tezuka Yasuhisa, Adachi Jun-ichi, Onodera Yohei, Kohara Shinji, Tajiri Hiroo, Chokkalingam Anand, Wakihara Toru
Microporous and Mesoporous Materials 359 (2023) 112662 (doi) 10.1016/j.micromeso.2023.112662

Recent progress in research on bonding technologies of W/Cu monoblocks as the divertor for nuclear fusion reactors
Xu Dang, Cheng Jigui, Chen Pengqi, Fu Kaichao, Wei Bangzheng, Chen Ruizhi, Luo Laima, Xu Qiu
Nuclear Materials and Energy 36 (2023) 101482 (doi) 10.1016/j.nme.2023.101482

The neglected activation of tantalum in reduced activation materials
Zhang Lei, Du Yufeng, Han Wentuo, Yi Xiaoou, Liu Pingping, Yoshida Kenta, Toyama Takeshi, Xu Chi, Zhan Qian, Nagai Yasuyoshi, Ohnuki Somei, Wan Farong
Nuclear Materials and Energy 35 (2023) 101432 (doi) 10.1016/j.nme.2023.101432

Amorphization of gold film on silicon single crystal by hardness indentation at room temperature
Hatakeyama Akira, Yoshiie Toshimasa
Philosophical Magazine 103(21) (2023) 1968-1979 (doi) 10.1080/14786435.2023.2255973

Study of Vacancy Clusters and Antisite Defects in Titanium Beryllide $Be_{12}Ti$ Using Positron Annihilation Spectroscopy
Xu Qiu, Yang Qigui, Popov Evgeni, Yabuuchi Atsushi, Shibayama Tamaki, Kim Jaehwan, Nakamichi Masaru, Cao Xingzhong
physica status solidi (b) 261(3) (2024) 2300489 (doi) 10.1002/pssb.202300489

Cubic-type Heusler compound Mn_2FeGa thin film with strain-induced large perpendicular magnetic anisotropy
Bentley Phillip David, Li Songtian, Masuda Keisuke, Miura Yoshio, Du Ye, Mitsui Takaya, Fujiwara Kosuke, Kobayashi Yasuhiro, Guo Tengyu, Yu Guoqiang, Suzuki Chihiro, Yamamoto Shunya, Zheng Fu, Sakuraba Yuya, Sakai Seiji
Physical Review Materials 7(6) (2023) 64404 (doi) 10.1103/PhysRevMaterials.7.064404

Combinatorial characterization of metastable luminous silver cations
Masai Hirokazu, Koshimizu Masanori, Kawamoto Hiroki, Setoyama Hiroyuki, Onodera Yohei, Ikeda Kazutaka, Maruyama Shingo, Haruta Naoki, Sato Tohru, Matsumoto Yuji, Takahashi Chika, Mizoguchi Teruyasu
Scientific Reports 14 (2024) 4638 (doi) 10.1038/s41598-024-55014-8

X-ray free electron laser observation of ultrafast lattice behaviour under femtosecond laser-driven shock compression in iron
Sano Tomokazu, Matsuda Tomoki, Hirose Akio, Ohata Mitsuru, Terai Tomoyuki, Kakeshita Tomoyuki, Inubushi Yuichi, Sato Takahiro, Miyanishi Kohei, Yabashi Makina, Togashi Tadashi, Tono Kensuke, Sakata Osami, Tange Yoshinori, Arakawa Kazuto, Ito Yusuke, Okuchi Takuo, Sato Tomoko, Sekine Toshimori, Mashimo Tsutomu, Nakanii Nobuhiko, Seto Yusuke, Shigeta Masaya, Shobu Takahisa, Sano Yuji, Hosokai Tomonao, Matsuoka Takeshi, Yabuuchi Toshinori, Tanaka Kazuo A., Ozaki Norimasa, Kodama Ryosuke
Scientific Reports 13 (2023) 13796 (doi) 10.1038/s41598-023-40283-6

Effect of intergranular connectivity of $NaAlB_{14}$ on Na^+ extraction
Iwasaki Suguru, Hoshino Mihiro, Morito Haruhiko, Kumagai Masaya, Katsura Yukari, Nishii Junji, Fujioka Masaya
Solid State Sciences 144 (2023) 107308 (doi) 10.1016/j.solidstatesciences.2023.107308

Tribological performance of a surfactant derived from its structure of molecular aggregates in water
Gu Haiyang, Hirayama Tomoko, Yamashita Naoki, Okano Tomoaki, Xu Jimin, Sato Nobuhiro, Yamada Masako
Tribology International 188 (2023) 108881 (doi) 10.1016/j.triboint.2023.108881

Positron annihilation spectroscopy of thermally annealed hydrogenated amorphous carbon films
Nakao Setsuo, Kinomura Atsushi, Ikeda Keisuke, Nakajima Makoto, Yabuuchi Atsushi, Suzuki Kohtaku
Vacuum 215 (2023) 112255 (doi) 10.1016/j.vacuum.2023.112255

Characterization of δNi_2Si Precipitates in Cu–Ni–Si Alloy by Small Angle X–Ray Scattering, Small Angle Neutron Scattering and Atom Probe Tomography
Hirokazu Sasaki, Syunta Akiya, Kuniteru Mihara, Yojiro Oba, Masato Onuma, Jun Uzuhashi, Tadakatsu Ohkubo
Journal of Japan Institute of Copper 62(1) (2023) 85-89 (In Japanese)

Proceedings

Investigation of doping effect on the local structure and photocatalytic activity of $SrTiO_3$
Komatsuda Sayaka, Kawakami Miyuki, Sato Wataru, Taniguchi Akihiro, Tanigaki Minoru, Ohkubo Yoshitaka
HYPERFINE 2023 Nara, Japan (Mar. 13-17, 2024) 1-10 (doi) 10.1007/s10751-024-01868-3

Advanced Nuclear Fuel Discovery with Machine Learning
Yifan Sun, Masaya Kumagai and Ken Kurosaki
Proceedings of the 58th KURNS Scientific Meeting Kumatori, Japan/Online (Jan. 31- Feb. 1, 2024) 7

Development of isotope-specific studies by multi-element Mössbauer spectroscopy
Shinji Kitao, Yasuhiro Kobayashi, Takumi Kubota, Masayuki Kurokuzu, Hiroyuki Tajima, Hiroyuki Yamashita, Hidetoshi Ota, Keiji Shinoda, Hiroshi Fujii, Yoko Akiyama, Izumi Mashino, Yuki Matsushi, Hironori Ohashi,

Takafumi Kitazawa, Hiroki Wadachi, Yoichi Kamihara, Ryo Masuda, Kotaro Yonezu, Mitsuharu Tabuchi, Kyoko Okada, Makoto Seto
Proceedings of the 58th KURNS Scientific Meeting Kumatori, Japan/Online (Jan. 31- Feb. 1, 2024) 10-12 (In Japanese)

High efficiency of slow positron beam line source using KURNS-LINAC
Yuichiro Kawakami, Atsushi Kinomura
Proceedings of the 58th KURNS Scientific Meeting Kumatori, Japan/Online (Jan. 31- Feb. 1, 2024) 50

Interaction of defects with hydrogen and helium in austenitic stainless steel
Tsuyoshi Hanamitsu, Hidetsugu Tsuchida, Qiu Xu
Proceedings of the 58th KURNS Scientific Meeting Kumatori, Japan/Online (Jan. 31- Feb. 1, 2024) 49

Physics and engineering of unstable nuclei
Daisuke Niwa, Tomohiro Mishima, Koji Nakanishi, Kazuhiro Kanda, Naoki Fukumuro, Atsushi Kinomura, Atsushi Yabuuchi, Fuminobu Hori
Proceedings of the 58th KURNS Scientific Meeting Kumatori, Japan/Online (Jan. 31- Feb. 1, 2024) 21 (In Japanese)

Structual Evolution of Dynamically-compressed Amorphous Germanium Dioxide
Hiroto Araga, Yuhei Umeda, Yusuke Seto, Yonosuke Tarutani, Takuo Okuchi
Proceedings of the 58th KURNS Scientific Meeting Kumatori, Japan/Online (Jan. 31- Feb. 1, 2024) 13 (In Japanese)

Synthesis and structural analysis of hydrous SiO_2
Yonosuke Tarutani, Yohei Onodera, Tetsu Kogiso, Takuo Okuchi
Proceedings of the 58th KURNS Scientific Meeting Kumatori, Japan/Online (Jan. 31- Feb. 1, 2024) 16 (In Japanese)

Fabrication and characterization of BGaN diodes for nuclear instrumentation system
R. Kudo, T. Sakurai, S. Kawasaki, T. Kishishita, Y. Sakurai, H. Yashima, T.o Makino, T. Ohshima, Y. Honda, H. Amano, Y. Inoue, T. Aoki, and T. Nakano
The 14th International Conference on Nitride Semiconductors (ICNS-14) Fukuoka, Japan (Nov. 12-17, 2023)

プラズマ照射した Si 表面近傍の陽電子消滅法による評価
重定瑠士, 一宮正義, 番 貴彦, 薮内 敦, 木野村淳, 柳澤淳一
第 84 回応用物理学会秋季学術講演会 Kumamto city, Japan/Online (Sep. 19-23, 2023) 20p-A310-10 (In Japanese)

^{61}Ni Mössbauer Spectroscopy for 3D Coordination Polymers
K. Kitase, T. Kitazawa, Okada, D. Ueda, Y. Kobayashi, S. Kitao, T. Kubota, and M. Seto
Proceedings of the Specialists' Meeting on "Nuclear Spectroscopy and Condensed Matter Physics Using Short-Lived Nuclei IX" Online (Jan. 11, 2023) 4-8 (In Japanese)

Analysis of Chemical Species Formed by Nitrogen Ions injected into H_2O
M. Mihara, Y. Kimura, Y. Otani, T. Sugisaki, M. Fukutome, G. Takayama, R. Taguchi, K. Matsuta, M. Fukuda, T. Minamisono, S. Ishitani, R. Miyahara, K. Watanabe, S. Chen, H. Takahashi, D. Nishimura, T. Izumikawa, N. Noguchi, T. Ohtsubo, A. Ozawa, A. Yano, T. Nagatomo, A. Kitagawa, S. Sato, S. Momorta, M.K. Kubo, A.D. Pant, K. Shimomura, A. Koda, and S. Takeshita
Proceedings of the Specialists' Meeting on "Nuclear Spectroscopy and Condensed Matter Physics Using Short-Lived Nuclei IX" Online (Jan. 11, 2023) 44-47 (In Japanese)

Conversion electron Mössbauer spectroscopy (CEMS) of Bi-doped YIG
M.Yoshida, Y. Watanabe, and Y. Kobayashi
Proceedings of the Specialists' Meeting on "Nuclear Spectroscopy and Condensed Matter Physics Using Short-Lived Nuclei IX" Online (Jan. 11, 2023) 9-12 (In Japanese)

Magnetism and Its Time Variation of $Cd_{0.75}$ $Fe_{2.25}O_4$
W. Sato and T. Ito
Proceedings of the Specialists' Meeting on "Nuclear Spectroscopy and Condensed Matter Physics Using Short-Lived Nuclei IX" Online (Jan. 11, 2023) 17-19 (In Japanese)

Mössbauer Spectra of Graphene Oxide - Iron oxide Composites
S. Nakashima, B. S. Nugroho
Proceedings of the Specialists' Meeting on "Nuclear Spectroscopy and Condensed Matter Physics Using Short-Lived Nuclei IX" Online (Jan. 11, 2023) 1-3 (In Japanese)

Reviews

Analysis of Superconductors and Metals
Hirokazu Sasaki, Satoshi Yamazaki, Yojiro Oba, Masato Onuma
古河電工時報 143 (2024) 16 (In Japanese)

Books

^{197}Au Mössbauer Spectroscopy of Thiolate-protected Gold Clusters
Norimichi Kojima, Yasuhiro Kobaqyashi, and Makoto Seto
Mössbauer Spectroscopy: Applications in Chemistry and Materials Science
Yann Garcia, Junhu Wang, Tao Zhang
Wiley (2023) 195-211 (ISBN)978-3-527-34691-2

^{197}Au Mossbauer Spectroscopy of Gold Mixed-Valence Complexes, $Cs_2[Au^IX_2][Au^{III}Y_4]$(X, Y = Cl, Br, I) and $[NH_3(CH_2)_nNH_3]_2[(Au^I I2)(Au^{III}I_4)(I_3)_2]$ (n = 7, 8)
Norimichi Kojima, Yasuhiro Kobaqyashi, and Makoto Seto
Mössbauer Spectroscopy: Applications in Chemistry and Materials Science
Yann Garcia, Junhu Wang, Tao Zhang
Wiley (2023) 2013-250 (ISBN)978-3-527-34691-2

Others

金属間化合物合金における空孔型欠陥と水素原子の相互作用に関する研究
Fuminobu Hori
九州大学応用力学研究所共同利用研究成果報告書 26 (2023) 60 (in Japanese)

5. Geochemistry and Environmental Science

Papers

Technique for estimating the charge number of individual radioactive particles using Kelvin probe force microscopy
Shinke Yukimi, Mori Tatsuhiro, Iwata Ayumi, Mohd Nor Muhammad Aiman bin, Kurosawa Keiichi, Inagaki Makoto, Sekimoto Shun, Takamiya Koichi, Oki Yuichi, Ohtsuki Tsutomu, Igarashi Yasuhito, Okuda Tomoaki
Aerosol Science and Technology 57(8) (2023) 758-768 (doi) 10.1080/02786826.2023.2221726

Two metasomatic events recorded by noble gas characteristics in the Finero mantle wedge: Extreme fractionation (He, Ar) and seawater penetration into the mantle deformation zone
Fukushima Nanae, Sumino Hirochika, Kobayashi Masahiro, Kagi Hiroyuki
Chemical Geology 644 (2024) 121829 (doi) 10.1016/j.chemgeo.2023.121829

Electron flux is a key determinant of uranium isotope fractionation during bacterial reduction
Brown Ashley R., Molinas Margaux, Roebbert Yvonne, Sato Ataru, Abe Minori, Weyer Stefan, Bernier-Latmani Rizlan
Communications Earth & Environment 4(1) (2023) 329 (doi) 10.1038/s43247-023-00989-x

An intraoceanic juvenile arc of shoshonite and adakitic andesite in the Nemuro Belt, the Lesser Kuril Arc, across the K/Pg boundary
Yutani Taku, Hirano Naoto, Tanaka Hirotaka, Sumino Hirochika, Machida Shiki, Sekimoto Shun, Yoneda Shigekazu, Kato Yasuhiro
Cretaceous Research 147 (2023) 105510 (doi) 10.1016/j.cretres.2023.105510

Contribution of the nuclear field shift to kinetic uranium isotope fractionation
Brown A.R., Roebbert Y., Sato A., Hada M., Abe M., Weyer S., Bernier-Latmani R.
Geochemical Perspectives Letters 27 (2023) 43-47 (doi) 10.7185/geochemlet.2333

Magmatic Evolution of the Fossil Melanesian Island Arc: Evidence From Lower Miocene Lavas of Malekula Island (Vanuatu)
Haase K. M., Schneider K. P., Pelletier B., Ishizuka O.
Geochemistry, Geophysics, Geosystems 25(2) (2024) e2023GC011187 (doi) 10.1029/2023GC011187

Redetermination of Mass Fractions of Three Halogens (Cl, Br, I) for Seventeen USGS Geochemical Reference Materials
Ebihara Mitsuru, Shirai Naoki, Sekimoto Shun
Geostandards and Geoanalytical Research 47(4) (2023) 931-944 (doi) 10.1111/ggr.12516

The Conrad Rise Revisited: Eocene to Miocene Volcanism and Its Implications for Magma Sources and Tectonic Development
Sato H., Machida S., Meyzen C. M., Ishizuka O., Senda R., Bizimis M., Ashida K., Mikuni K., Sato T., Fujii M., Nogi Y., Kato Y.
Journal of Geophysical Research: Solid Earth 129(1) (2024) e2023JB027380 (doi) 10.1029/2023JB027380

Deformation microstructures in shock-compressed single crystal and powdered rutile
UMEDA Yuhei, NAGAI Yuma, TOMIOKA Naotaka, SEKINE Toshimori, MIYAKAWA Masashi, KOBAYASHI Takamichi, YUSA Hitoshi, OKUCHI Takuo
Journal of Mineralogical and Petrological Sciences 119(1) (2024) 230706 (doi) 10.2465/jmps.230706

Preliminary Analysis of Spherical Iron-rich Particles Extracted from Moto-Ujina Beach Sand as a Possible Tracer for the Hiroshima Black Rain
Satoru Endo, Tsuyoshi Kajimoto, Kenichi Tanaka, Hiroki Higuchi, Satoshi Fukutani, Koichi Takamiya, Makoto Maeda, Yasuhito Igarashi
Journal of Nuclear and Radiochemical Sciences 23 (2023) 5-13

Direct imaging of shock wave splitting in diamond at Mbar pressure
Makarov Sergey, Dyachkov Sergey, Pikuz Tatiana, Katagiri Kento, Nakamura Hirotaka, Zhakhovsky Vasily, Inogamov Nail, Khokhlov Victor, Martynenko Artem, Albertazzi Bruno, Rigon Gabriel, Mabey Paul, Hartley Nicholas J., Inubushi Yuichi, Miyanishi Kohei, Sueda Keiichi, Togashi Tadashi, Yabashi Makina, Yabuuchi Toshinori, Okuchi Takuo, Kodama Ryosuke, Pikuz Sergey, Koenig Michel, Ozaki Norimasa
Matter and Radiation at Extremes 8(6) (2023) 066601 (doi) 10.1063/5.0156681

Development of a dose estimation system for external exposure assessment at the late phase for individuals living in areas affected by the Fukushima nuclear accident
Yajima Kazuaki, Hasegawa Shin, Takahashi Tomoyuki, Aono Tatsuo
Radiation Protection Dosimetry 199(15-16) (2023) 2005-2009 (doi) 10.1093/rpd/ncac288

Transfer of ^{137}Cs and ^{90}Sr from soil-to-potato: Interpretation of the association from global fallout in Aomori to accidental release in Fukushima and Chornobyl
Tsukada Hirofumi, Takeda Akira, Takahashi Tomoyuki, Fukutani Satoshi, Akashi Makoto, Takahashi Junko, Uematsu Shinichiro, Chyzhevskyi Ihor, Kirieiev Serhii, Kashparov Valery, Zheleznyak Mark
Science of The Total Environment 899 (2023) 165467 (doi) 10.1016/j.scitotenv.2023.165467

Record of ^{3}H and ^{36}Cl from the Fukushima nuclear accident recovered from soil water in the unsaturated zone at Koriyama
Ohta Tomoko, Fifield L. Keith, Palcsu László, Tims Stephen G., Pavetich Stefan, Mahara Yasunori
Scientific Reports 13 (2023) 19672 (doi) 10.1038/s41598-023-46853-y

レイリー波とラブ波位相速度を併用した地下構造モデルの推定精度
吉田邦一, 上林宏敏
The 16th Japan Earthquake Enginnering Symposium (2023) C1-PA06 (In Japanese)

1995 年兵庫県南部地震時の「震災の帯」における 地震動評価と表面波各成分への分離
金山京香, 上林宏敏, 劉虹, 永野正行
The 16th Japan Earthquake Enginnering Symposium G417-25 (2023) (In Japanese)

京都盆地基準ボーリング地点における微動の位相速度と水平上下スペクトル比の全波動場モデリングによる評価
上林宏敏, 吉田邦一, 長郁夫, 新井洋, 大堀道広, 山田浩二, 小割啓史
The 16th Japan Earthquake Enginnering Symposium (2023) C1-PA05 (In Japanese)

Characterization of Ultra Fine Bubbles Using Various Measurement Techniques
UEDA Yoshikatsu, TOKUDA Yomei, TANIGAKI Minoru, AKAMATSU Shigenori, HATA Takashi
Vacuum and Surface Science 66(11) (2023) 654-659 (doi) 10.1380/vss.66.654 (In Japanese)

Proceedings

Evaluation of Tiron as a Silica Scale Inhibitor by Metal Plates Immersion Batch Experiment
R. TERASHI, K. YONEZU, S. JUHRI, K. MORI, S. SATO, E. WATANABE, T. YOKOYAMA
49th Stanford Geothermal Workshop 2024 Stanford, USA (Feb. 12-14, 2024)

Electrical conductivity measurements of iron-bearing enstatite glasses up to Mbar pressure: Insight into silicate melts at the bottom of the Earth's mantle
I. Mashino, T. Yoshino, S. Kitao, T. Mitsui, R. Masuda and M. Seto
AGU annual meeting 2023, San francisco, USA (Dec. 11-15, 2023) 1236467

Field Experiments for Evaluation of the Kinetics of Silica Scaling at well OW 707 in the Olkaria Geothermal Field,
E. WANYONYI, K. YONEZU, T. YOKOYAMA, A. IMAI, A. ITO and S. ODHIAMBO
International Symposium on Earth Science and Technology 2023, Fukuoka, Japan (Nov. 30 - Dec. 1, 2023) 225-231

6. Life Science and Medical Science

Papers

Self-Folding Macromolecular Drug Carrier for Cancer Imaging and Therapy
Gao Shan, Miura Yutaka, Sumiyoshi Akira, Ohno Satoshi, Ogata Keisuke, Nomoto Takahiro, Matsui Makoto, Honda Yuto, Suzuki Minoru, Iiyama Megumi, Osada Kensuke, Aoki Ichio, Nishiyama Nobuhiro
Advanced Science 11(7) (2024) 2304171 (doi) 10.1002/advs.202304171

Principles, Recent Developmentsand Perspectives in Boron NeutronCapture Therapy (BNCT) Sauerwein
Wolfgang A.G., Fischer Thomas, Sancey Lucie, Verry Camille, Matsuura Eiji, Moss Raymond L., Wittig Andrea
Bio-Algorithms and Med-Systems 19(1) (2023) 48-53 (doi) 10.5604/01.3001.0054.1824

Understanding the structural and functional changes and biochemical pathomechanism of the cardiomyopathy-associated p.R123W mutation in human αB-crystallin
Somee Leila Rezaei, Barati Anis, Shahsavani Mohammad Bagher, Hoshino Masaru, Hong Jun, Kumar Ashutosh, Moosavi-Movahedi Ali Akbar, Amanlou Massoud, Yousefi Reza
Biochimica et Biophysica Acta (BBA) - General Subjects 1868(4) (2024) 130579 (doi) 10.1016/j.bbagen.2024.130579

Genome-wide mapping and cryo-EM structural analyses of the overlapping tri-nucleosome composed of hexasome-hexasome-octasome moieties
Nishimura Masahiro, Fujii Takeru, Tanaka Hiroki, Maehara Kazumitsu, Morishima Ken, Shimizu Masahiro, Kobayashi Yuki, Nozawa Kayo, Takizawa Yoshimasa, Sugiyama Masaaki, Ohkawa Yasuyuki, Kurumizaka Hitoshi
Communications Biology 7 (2024) 61 (doi) 10.1038/s42003-023-05694-1

Optical Resolution of Carboxylic Acid Derivatives of Homoleptic Cyclometalated Iridium(III) Complexes via Diastereomers Formed with Chiral Auxiliaries
A. Kanbe, K. Yokoi, Y. Yamada, M. Tsurui, Y. Kitagawa, Y. Hasegawa, D. Ogata, J. Yuasa and S. Aoki
Inorganic Chemistry 62(29) (2023) 11325-11341 (doi) 10.1021/acs.inorgchem.3c00685

Design and Synthesis of Poly(2,2′-Bipyridyl) Ligands for Induction of Cell Death in Cancer Cells: Control of Anticancer Activity by Complexation/Decomplexation with Biorelevant Metal Cations
Balachandran Chandrasekar, Hirose Masumi, Tanaka Tomohiro, Zhu Jun Jie, Yokoi Kenta, Hisamatsu Yosuke, Yamada Yasuyuki, Aoki Shin
Inorganic Chemistry 62(36) (2023) 14615-14631 (doi) 10.1021/acs.inorgchem.3c01738

Unveiling the structural and functional consequences of the p.D109G pathogenic mutation in human αB-Crystallin responsible for restrictive cardiomyopathy and skeletal myopathy
Hosseini Jafari Mehrnaz, Shahsavani Mohammad Bagher, Hoshino Masaru, Hong Jun, Saboury Ali Akbar, Moosavi-Movahedi Ali Akbar, Yousefi Reza
International Journal of Biological Macromolecules 254(3) (2024) 127933 (doi) 10.1016/j.ijbiomac.2023.127933

Current trends in the promising immune checkpoint inhibition and radiotherapy combination for locally advanced and metastatic urothelial carcinoma
Sano Takeshi, Saito Ryoichi, Aizawa Rihito, Watanabe Tsubasa, Murakami Kaoru, Kita Yuki, Masui Kimihiko, Goto Takayuki, Mizowaki Takashi, Kobayashi Takashi
International Journal of Clinical Oncology 28(12) (2023) 1573-1584 (doi) 10.1007/s10147-023-02421-y

Large-scale column-free purification of bovine F-ATP synthase
Jiko Chimari, Morimoto Yukio, Tsukihara Tomitake, Gerle Christoph
Journal of Biological Chemistry 300(2) (2024) 105603 (doi) 10.1016/j.jbc.2023.105603

Preparation and in vitro evaluation of amphotericin B-loaded nano-formulations for both intravenous and ophthalmic administration using 3-aminophenylboronic acid-conjugated styrene-maleic acid copolymers
K. Banshoya, Y. Kaneo, M. Shirakawa, Y. Hieda, A. Machida, M. Ohnishi, T. Tanaka
Journal of Drug Delivery Science and Technology 90 (2023) 105176 (doi) 10.1016/j.jddst.2023.105176

Structural and Dynamic Changes of Nucleosome upon GATA3 Binding
Ishida Hisashi, Matsumoto Atsushi, Tanaka Hiroki, Okuda Aya, Morishima Ken, Wade Paul A., Kurumizaka Hitoshi, Sugiyama Masaaki, Kono Hidetoshi
Journal of Molecular Biology 435(23) (2023) 168308

Mechanistic Modeling of Amyloid Oligomer and Protofibril Formation in Bovine Insulin
Yuzu Keisuke, Imamura Hiroshi, Nozaki Takuro, Fujii Yuki, Badawy Shaymaa Mohamed Mohamed, Morishima Ken, Okuda Aya, Inoue Rintaro, Sugiyama Masaaki, Chatani Eri
Journal of Molecular Biology 436(6) (2024) 168461 (doi) 10.1016/j.jmb.2024.168461

Dynamic action of an intrinsically disordered protein in DNA compaction that induces mycobacterial dormancy
Nishiyama Akihito, Shimizu Masahiro, Narita Tomoyuki, Kodera Noriyuki, Ozeki Yuriko, Yokoyama Akira, Mayanagi Kouta, Yamaguchi Takehiro, Hakamata Mariko, Shaban Amina Kaboso, Tateishi Yoshitaka, Ito Kosuke, Matsumoto Sohkichi
Nucleic Acids Research 52(2) (2024) 816-830 (doi) 10.1093/nar/gkad1149

Internal dynamics of multidomain protein as revealed by an optimized neutron spin echo measurement and all-atom molecular dynamics simulation
Inoue Rintaro, Oroguchi Tomotaka, Oda Takashi, Farago Bela, Martel Anne, Porcar Lionel, Sato Mamoru, Sugiyama Masaaki
Physical Review Research 5(4) (2023) 043154 (doi) 10.1103/PhysRevResearch.5.043154

Site-specific relaxation of peptide bond planarity induced by electrically attracted proton/deuteron observed by neutron crystallography
Chiba Kaori, Matsui Takuro, Chatake Toshiyuki, Ohhara Takashi, Tanaka Ichiro, Yutani Katsuhide, Niimura Nobuo
Protein Science 32(10) (2023) e4765 (doi) 10.1002/pro.4765

Proximity estimation and quantification of ionizing radiation-induced DNA lesions in aqueous media using fluorescence spectroscopy
Ken Akamatsu, Katsuya Satoh, Naoya Shikazono, and Takeshi Saito
Radiation Research 201(2) (2024) 150-159 (doi) 10.1667/RADE-23-00145.1

Eye lens β-crystallins are predicted by native ion mobility-mass spectrometry and computations to form compact higher-ordered heterooligomers
Rolland Amber D., Takata Takumi, Donor Micah T., Lampi Kirsten J., Prell James S.
Structure 31(9) (2023) 1052-1064 (doi) 10.1016/j.str.2023.06.013

Characterization of K-binding factor involved in water-soluble complex of menaquinone-7 produced by *Bacillus subtilis natto*
Chatake Toshiyuki, Yanagisawa Yasuhide, Murakami Risa, Ohsugi Tadanori, Sumi Hiroyuki, Takata Takumi, Okuda Aya, Morishima Ken, Inoue Rintaro, Sugiyama Masaaki
The Journal of Biochemistry 174(4) (2023) 383-389 (doi) 10.1093/jb/mvad051

Detection of Circulating Tumor Cells in Blood Using Two-Step Random Forest
Hua Wei, Takahiro Natori, Tomohiro Tanaka, Shin Aoki, Sho Kuriyama, Takeshi Yamada, Naoyuki Aikawa
IEEJ Transactions on Electronics, Information and Systems 144(3) (2024) 121-126 (doi) 10.1541/ieejeiss.144.121 (In Japanese)

Proceedings

Crystal structure of dephospho-coenzyme A kinase from archaea.
Akiko Kita, Yuna Ishida, Takahiro Shimosaka, Yuta Michimori, Kira Makarova, Eugene Koonin, Haruyuki Atomi, and Kunio Miki
Proceedings of the 58th KURNS Scientific Meeting Kumatori, Japan/Online (Jan. 31- Feb. 1, 2024) 39

Development a fast scanner for bioimaging by HS-AFM
Masahiro Shimizu
Proceedings of the 58th KURNS Scientific Meeting Kumatori, Japan/Online (Jan. 31- Feb. 1, 2024) 54-56 (In Japanese)

Development of a novel purification method and structural analysis of mammalian FoF1ATP synthase
Chimari Jiko, Atsuki Nakano, Yuko Misumi, Eiki Yamashita, Genji Kurisu, Yukio Morimoto, Tomitake Tsukihara, Ken Yokoyama, Christoph Gerle,
Proceedings of the 58th KURNS Scientific Meeting Kumatori, Japan/Online (Jan. 31- Feb. 1, 2024) 60-62 (In Japanese)

DNA damage with the neutrons from reactor
Hiroaki Terato, Tadashi Hanafusa, Midori Isobe, Yoshinori Sakurai, Takushi Takata, Takeshi Saito
Proceedings of the 58th KURNS Scientific Meeting Kumatori, Japan/Online (Jan. 31- Feb. 1, 2024) 29 (In Japanese)

Multi-step protein ligation with the ligation enzyme, OaAEP
Aya Okuda
Proceedings of the 58th KURNS Scientific Meeting Kumatori, Japan/Online (Jan. 31- Feb. 1, 2024) 57 (In Japanese)

Non-equivalent out of the Equivalence – a limit for protein crystallography –
Yukio Morimoto
Proceedings of the 58th KURNS Scientific Meeting Kumatori, Japan/Online (Jan. 31- Feb. 1, 2024) 63-65 (In Japanese)

Structural analysis of clock protein complex in solution with small angle scatering and analytical ultracentrifugation
Ken Morishima, Masahiro Shimizu, Yasuhiro Yunoki, Liuonel Porcar, Anne Martel, Rintaro Inoue, Masaaki Sugiyama
Proceedings of the 58th KURNS Scientific Meeting Kumatori, Japan/Online (Jan. 31- Feb. 1, 2024) 26 (In Japanese)

Study of protein hydration
Toshiyuki Chatake, Tomoko Sunami, Satoru Fujiwara, Ichiro Tanaka, Katsuhiro Kusaka
Proceedings of the 58th KURNS Scientific Meeting Kumatori, Japan/Online (Jan. 31- Feb. 1, 2024) 35 (In Japanese)

Study of water-soluble vitamin K_2 from Bacillus subtilis natto
Toshiyuki Chatake, Yasuhide Yanagisawa, Takumi Takata, Aya Okuda, Ken Morishima, Rintaro Inoue, Masaaki Sugiyama
Proceedings of the 58th KURNS Scientific Meeting Kumatori, Japan/Online (Jan. 31- Feb. 1, 2024) 32 (In Japanese)

Study on the function and structure of Dpcd, the causative factor of primary ciliary dyskinesia
Masafumi Yohda, Hinako Koeda, Kentaro Noi, Masaaki Sugiyama, Rintato Inoue, Ken Morishima, Masato Kikumoto
Proceedings of the 58th KURNS Scientific Meeting Kumatori, Japan/Online (Jan. 31- Feb. 1, 2024) 15 (In Japanese)

The analysis of the solution structure and dynamics of multi-domain protein by integrated solution scattering
Naoki Aizawa, Takashi Oda, Ken Morishima, Masahiro Shimizu, Aya Okuda, Rintaro Inoue, Masaaki Sugiyama
Proceedings of the 58th KURNS Scientific Meeting Kumatori, Japan/Online (Jan. 31- Feb. 1, 2024) 23 (In Japanese)

The compactification of intrinsically disordered proteins from hyperthermophilic archaeon under high temperatures.
Takashi Oda, Rinntaro Inoue, Taiki Tominaga, Hiroshi Nakagawa, Ken Morishima, Hiroki Iwase, Tsuyoshi Konuma, Takahisa Ikegamim, Sonoko Ishino, Yoshizumi Ishino, Takayuki Oku, Mamoru Sato, Masaaki Sugiyama
Proceedings of the 58th KURNS Scientific Meeting Kumatori, Japan/Online (Jan. 31- Feb. 1, 2024) 36 (In Japanese)

アカモクフコイダンのアミロイド凝集抑制機構の解析
Masaru Hoshino, Ken Morishima, Rintaro Inoue, Masaaki Subiyama and Hisashi Yagi
Proceedings of the 58th KURNS Scientific Meeting Kumatori, Japan/Online (Jan. 31- Feb. 1, 2024) 14

Reviews

Oral Fibrinolytic Therapy : Nattokinase in Health and Disease Prevention
須見 洋行, 柳澤 泰任, 茶竹 俊行, 満尾 正, 井上 浩義, 島谷 和弘, 内藤 佐和, 矢田貝 智恵子
New food industry 66 (2024) 1-6 (In Japanese)

放射線損傷を利用した年代測定:開発と応用 金沢大学疾患総合モデル
Noriko Hasebe
Research Center for Experimental Modeling of Human Disease NEWS (2024) 6 (In Japanese)

Post-Translational Modifications of Amino Acid Residues in Lens Component Proteins
Takumi Takata
Journal of The Japanese Society for Cataract Research 35(1) (2023) 26-30 (In Japanese)

7. Neutron Capture Therapy

Papers

Tumor Eradication by Boron Neutron Capture Therapy with ^{10}B-enriched Hexagonal Boron Nitride Nanoparticles Grafted with Poly(Glycerol)
Zhang Yucai, Kang Heon Gyu, Xu Hua-zhen, Luo Honghui, Suzuki Minoru, Lan Qing, Chen Xiao, Komatsu Naoki, Zhao Li
Advanced Materials 35(35) (2023) 2301479 (doi) 10.1002/adma.202301479

Carcinogenesis Observed in the Spleens of Balb/c Mice After Head-neutron Irradiation
KINASHI YUKO, TAKATA TAKUSHI, SAKURAI YOSHINORI, TANAKA HIROKI
Anticancer Research 43(4) (2023) 1455-1461 (doi) 10.21873/anticanres.16294

Investigation of the usability of cone-beam computed tomography images using digital radiography equipment for boron neutron capture therapy treatment planning in the sitting position
Sato Hiroyuki, Takata Takushi, Sakurai Yoshinori
Applied Radiation and Isotopes 196 (2023) 110793 (doi) 10.1016/j.apradiso.2023.110793

Influence of lung physical density on dose calculation in boron neutron capture therapy for malignant pleural mesothelioma
Sato Hiroyuki, Takata Takushi, Suzuki Minoru, Sakurai Yoshinori
Applied Radiation and Isotopes 198 (2023) 110857 (doi) 10.1016/j.apradiso.2023.110857

Initial evaluation of accelerator-based neutron source system at the Shonan Kamakura General Hospital
Suzuki Shunsuke, Nitta Kazunori, Yagihashi Takayuki, Eide Paul, Koivunoro Hanna, Sato Naoki, Gotoh Shinichi, Shiba Shintaro, Omura Motoko, Nagata Hironori, Tanaka Hiroki
Applied Radiation and Isotopes 199 (2023) 110898 (doi) 10.1016/j.apradiso.2023.110898

Boron uptake of boronophenylalanine and the effect of boron neutron capture therapy in cervical cancer cells
Terada Shinichi, Tsunetoh Satoshi, Tanaka Yoshimichi, Tanaka Tomohito, Kashiwagi Hideki, Takata Takushi, Kawabata Shinji, Suzuki Minoru, Ohmichi Masahide
Applied Radiation and Isotopes 197 (2023) 110792 (doi) 10.1016/j.apradiso.2023.110792

Evaluation of the Effectiveness of Boron Neutron Capture Therapy with Iodophenyl-Conjugated closo-Dodecaborate on a Rat Brain Tumor Model
Fujikawa Yoshiki, Fukuo Yusuke, Nishimura Kai, Tsujino Kohei, Kashiwagi Hideki, Hiramatsu Ryo, Nonoguchi Naosuke, Furuse Motomasa, Takami Toshihiro, Hu Naonori, Miyatake Shin-Ichi, Takata Takushi, Tanaka Hiroki, Watanabe Tsubasa, Suzuki Minoru, Kawabata Shinji, Nakamura Hiroyuki, Wanibuchi Masahiko
Biology 12(9) (2023) 1240 (doi) 10.3390/biology12091240

Development and evaluation of dose calculation algorithm with a combination of Monte Carlo and point-kernel methods for boron neutron capture therapy
Nojiri Mai, Takata Takushi, Hu Naonori, Sakurai Yoshinori, Suzuki Minoru, Tanaka Hiroki
Biomedical Physics & Engineering Express 9(3) (2023) 035025 (doi) 10.1088/2057-1976/acc33c

Development of the Follow-Up Human 3D Oral Cancer Model in Cancer Treatment
Igawa Kazuyo, Izumi Kenji, Sakurai Yoshinori
BioTech 12(2) (2023) 35 (doi) 10.3390/biotech12020035

Strategies for Preclinical Studies Evaluating the Biological Effects of an Accelerator-Based Boron Neutron Capture Therapy System
Kondo Natsuko, Masutani Mitsuko, Imamichi Shoji, Matsumoto Yoshitaka, Nakai Kei
Cancer Biotherapy and Radiopharmaceuticals 38(3) (2023) 173-183 (doi) 10.1089/cbr.2022.0057

Systems Biology Approach to Investigate Biomarkers, Boron-10 Carriers, and Mechanisms Useful for Improving Boron Neutron Capture Therapy
Perico Davide, Di Silvestre Dario, Imamichi Shoji, Sanada Yu, Masutani Mitsuko, Mauri Pier Luigi
Cancer Biotherapy and Radiopharmaceuticals 38(3) (2023) 152-159 (doi) 10.1089/cbr.2022.0053

Optimizing Boron Neutron Capture Therapy (BNCT) to Treat Cancer: An Updated Review on the Latest Developments on Boron Compounds and Strategies
Monti Hughes Andrea, Hu Naonori
Cancers 15(16) (2023) 4091 (doi) 10.3390/cancers15164091

Proteomic Characterization of SAS Cell-Derived Extracellular Vesicles in Relation to Both BPA and Neutron Irradiation Doses
Perico Davide, Tong Ying, Chen Lichao, Imamichi Shoji, Sanada Yu, Ishiai Masamichi, Suzuki Minoru, Masutani Mitsuko, Mauri Pierluigi
Cells 12(12) (2023) 1562 (doi) 10.3390/cells12121562

Phospholipid-Coated Boronic Oxide Nanoparticles as a Boron Agent for Boron Neutron Capture Therapy
Kawasaki Riku, Hirano Hidetoshi, Yamana Keita, Oshige Ayano, Nishimura Kotaro, Kono Nanami, Sanada Yu, Bando Kaori, Tabata Anri, Yasukawa Naoki, Azuma Hideki, Takata Takushi, Sakurai Yoshinori, Tanaka Hiroki, Suzuki Minoru, Tarutani Naoki, Katagiri Kiyofumi, Nagasaki Takeshi, Ikeda Atsushi
ChemBioChem 24(15) (2023) e202300186 (doi) 10.1002/cbic.202300186

HER-2-Targeted Boron Neutron Capture Therapy with Carborane-integrated Immunoliposomes Prepared via an Exchanging Reaction
Kawasaki Riku, Oshige Ayano, Yamana Keita, Hirano Hidetoshi, Nishimura Kotaro, Miura Yamato, Yorioka Ryuji, Sanada Yu, Bando Kaori, Tabata Anri, Yasuhara Kazuma, Miyazaki Yusuke, Shinoda Wataru, Nishimura Tomoki, Azuma Hideki, Takata Takushi, Sakurai Yoshinori, Tanaka Hiroki, Suzuki Minoru, Nagasaki Takeshi, Ikeda Atsushi
Chemistry – A European Journal 29(72) (2023) e202302486 (doi) 10.1002/chem.202302486

Cover Feature: Rational Design, Multistep Synthesis and in Vitro Evaluation of Poly(glycerol) Functionalized Nanodiamond Conjugated with Boron-10 Cluster and Active Targeting Moiety for Boron Neutron Capture Therapy
Nishikawa Masahiro, Yu Jie, Kang Heon Gyu, Suzuki Minoru, Komatsu Naoki
Chemistry – A European Journal 29(63) (2023) e202303312 (doi) 10.1002/chem.202303312

Rational Design, Multistep Synthesis and in Vitro Evaluation of Poly(glycerol) Functionalized Nanodiamond Conjugated with Boron-10 Cluster and Active Targeting Moiety for Boron Neutron Capture Therapy
Nishikawa Masahiro, Yu Jie, Kang Heon Gyu, Suzuki Minoru, Komatsu Naoki
Chemistry – A European Journal 29(63) (2023) e202302073 (doi) 10.1002/chem.202302073

Pharmacokinetic Study of ^{14}C-Radiolabeled p-Boronophenylalanine (BPA) in Sorbitol Solution and the Treatment Outcome of BPA-Based Boron Neutron Capture Therapy on a Tumor-Bearing Mouse Model
Watanabe Tsubasa, Yoshikawa Tomohiro, Tanaka Hiroki, Kinashi Yuko, Kashino Genro, Masunaga Shin-ichiro, Hayashi Toshimitsu, Uehara Koki, Ono Koji, Suzuki Minoru
European Journal of Drug Metabolism and Pharmacokinetics 48(4) (2023) 443-453 (doi) 10.1007/s13318-023-00830-y

Boron neutron capture therapy anti-tumor effect of nanostructured boron carbon nitride: A new potential candidate Kaur Manjot, Meena Ramovatar, Nishimura Kai, Miura Kazuki, Nakamura Hiroyuki, Suzuki Minoru, Sharma Ram K., Kumar Akshay
Inorganic Chemistry Communications 157 (2023) 111318 (doi) 10.1016/j.inoche.2023.111318

Carborane-Containing Hydroxamate MMP Ligands for the Treatment of Tumors Using Boron Neutron Capture Therapy (BNCT): Efficacy without Tumor Cell Entry
Flieger Sebastian, Takagaki Mao, Kondo Natsuko, Lutz Marlon R., Gupta Yash, Ueda Hiroki, Sakurai Yoshinori, Moran Graham, Kempaiah Prakasha, Hosmane Narayan, Suzuki Minoru, Becker Daniel P.
International Journal of Molecular Sciences 24(8) (2023) 6973 (doi) 10.3390/ijms24086973

Efficient neutron capture therapy of glioblastoma with pteroyl-closo-dodecaborate-conjugated 4-(p-iodophenyl)butyric acid (PBC-IP)
Nishimura Kai, Kashiwagi Hideki, Morita Taiki, Fukuo Yusuke, Okada Satoshi, Miura Kazuki, Matsumoto Yoshitaka, Sugawara Yu, Enomoto Takayuki, Suzuki Minoru, Nakai Kei, Kawabata Shinji, Nakamura Hiroyuki
Journal of Controlled Release 360 (2023) 249-259 (doi) 10.1016/j.jconrel.2023.06.022

Feasibility study of one-dimensional imaging with an optical fiber for radiation dose-rate monitoring system in the decommissioning process
Matsukura Daisuke, Kurosawa Shunsuke, Fujiwara Chihaya, Yamaji Akihiro, Ohashi Yuji, Yokota Yuui, Kamada Kei, Sato Hiroki, Masao Yoshino, Hanada Takashi, Murakami Rikito, Horiai Takahiko, Yoshikawa Akira, Takata Takushi, Tanaka Hiroki
Journal of Instrumentation 19(2) (2024) C02053 (doi) 10.1088/1748-0221/19/02/C02053

Imaging of gamma photons from activated gold wire using a high-energy gamma camera after irradiation of neutrons from boron neutron capture therapy (BNCT) system
Yamamoto Seiichi, Hu Naonori, Kataoka Jun, Koshikawa Nanase, Kanai Yasukazu, Tanaka Hiroki, Ono Koji
Journal of Instrumentation 18(4) (2023) T04003 (doi) 10.1088/1748-0221/18/04/T04003

A characterization of dye gel dosimeters for boron neutron capture therapy - dose response to gamma rays
Narita Ryosuke, Sakurai Yoshinori
Journal of Physics: Conference Series 2630 (2023) 012016 (doi) 10.1088/1742-6596/2630/1/012016

Proposal of recommended experimental protocols for in vitro and in vivo evaluation methods of boron agents for neutron capture therapy
Hattori Yoshihide, Andoh Tooru, Kawabata Shinji, Hu Naonori, Michiue Hiroyuki, Nakamura Hiroyuki, Nomoto Takahiro, Suzuki Minoru, Takata Takushi, Tanaka Hiroki, Watanabe Tsubasa, Ono Koji
Journal of Radiation Research 64(6) (2023) 859-869 (doi) 10.1093/jrr/rrad064

Experimentally determined relative biological effectiveness of cyclotron-based epithermal neutrons designed for clinical BNCT: in vitro study
Hu Naonori, Suzuki Minoru, Masunaga Shin-ichiro, Kashino Genro, Kinashi Yuko, Chen Yi-Wen, Liu Yong, Uehara Koki, Mitsumoto Toshinori, Tanaka Hiroki, Ono Koji
Journal of Radiation Research 64(5) (2023) 811-815 (doi) 10.1093/jrr/rrad056

The effects of BPA-BNCT on normal bone: determination of the CBE value in mice
Iwasaki Ryota, Yoshikawa Ryutaro, Umeno Ryo, Seki Azusa, Matsukawa Takehisa, Takeno Satoshi, Yokoyama Kazuhito, Mori Takashi, Suzuki Minoru, Ono Koji
Journal of Radiation Research 64(5) (2023) 795-803 (doi) 10.1093/jrr/rrad054

Relative biological effectiveness for epithermal neutron beam contaminated with fast neutrons in the linear accelerator-based boron neutron capture therapy system coupled to a solid-state lithium target
Nakamura Satoshi, Imamichi Shoji, Shimada Kenzi, Takemori Mihiro, Kanai Yui, Iijima Kotaro, Chiba Takahito, Nakayama Hiroki, Nakaichi Tetsu, Mikasa Shohei, Urago Yuka, Kashihara Tairo, Takahashi Kana, Nishio Teiji, Okamoto Hiroyuki, Itami Jun, Ishiai Masamichi, Suzuki Minoru, Igaki Hiroshi, Masutani Mitsuko
Journal of Radiation Research 64(4) (2023) 661-667 (doi) 10.1093/jrr/rrad037

Development of optimization method for uniform dose distribution on superficial tumor in an accelerator-based boron neutron capture therapy system
Sasaki Akinori, Hu Naonori, Matsubayashi Nishiki, Takata Takushi, Sakurai Yoshinori, Suzuki Minoru, Tanaka Hiroki
Journal of Radiation Research 64(3) (2023) 602-611 (doi) 10.1093/jrr/rrad020

Out-of-field dosimetry using a validated PHITS model and computational phantom in clinical BNCT
Kakino Ryo, Hu Naonori, Tanaka Hiroki, Takeno Satoshi, Aihara Teruhito, Nihei Keiji, Ono Koji
Medical Physics 51(2) (2024) 1351-1363 (doi) 10.1002/mp.16916

Feasibility study of optical imaging of the boron-dose distribution by a liquid scintillator in a clinical boron neutron capture therapy field
Maeda Hideya, Nohtomi Akihiro, Hu Naonori, Kakino Ryo, Akita Kazuhiko, Ono Koji
Medical Physics 51(1) (2024) 509-521 (doi) 10.1002/mp.16727

Development of a Gadolinium–Boron-Conjugated Albumin for MRI-Guided Neutron Capture Therapy
Okada Satoshi, Nishimura Kai, Ainaya Qarri, Shiraishi Kouichi, Anufriev Sergey A., Sivaev Igor B., Sakurai Yoshinori, Suzuki Minoru, Yokoyama Masayuki, Nakamura Hiroyuki
Molecular Pharmaceutics 20(12) (2023) 6311-6318 (doi) 10.1021/acs.molpharmaceut.3c00726

Organosilica nanoparticles containing sodium borocaptate (BSH) provide a new perspectives for boron neutron capture therapy (BNCT): efficient cellular uptake and enhanced BNCT efficacy
Laird Mathilde, Matsumoto Kotaro, Higashi Yuya, Komatsu Aoi, Raitano Art, Morrison Kendall, Suzuki Minoru, Tamanoi Fuyuhiko
Nanoscale Advances 9 (2023) 2537-2546 (doi) 10.1039/D2NA00839D

Development of a prompt gamma-ray detector with an 8×8 array $LaBr_3(Ce)$ scintillator and a multi-pixel photon counter for boron neutron capture therapy
Okazaki Keita, Tanaka Hiroki, Takata Takushi, Kawabata Shinji, Hu Naonori, Matsubayashi Nishiki, Mukawa Tetsuya, Sakurai Yoshinori, Suzuki Minoru

Nuclear Instruments and Methods in Physics Research Section A: Accelerators, Spectrometers, Detectors and Associated Equipment 1055 (2023) 168546 (doi) 10.1016/j.nima.2023.168546

Feasibility of multilayer neutron spectrometer with Backus and Gilbert approach using moderator-combination selection for energy-resolution optimization in Boron Neutron Capture Therapy irradiation field
Prateepkaew Jakkrit, Matsubayashi Nishiki, Takata Takushi, Tanaka Hiroki, Sakurai Yoshinori
Nuclear Instruments and Methods in Physics Research Section A: Accelerators, Spectrometers, Detectors and Associated Equipment 1059 (2024) 168948 (doi) 10.1016/j.nima.2023.168948

Estimation of internal-exposure contribution in radiation dose exposure for boron neutron capture therapy
Narita Ryosuke, Sakurai Yoshinori
Radiation Protection Dosimetry (2024) ncae073 (doi) 10.1093/rpd/ncae073

Development of DynamicMC for PHITS Monte Carlo package
Watabe Hiroshi, Sato Tatsuhiko, Yu Kwan Ngok, Zivkovic Milena, Krstic Dragana, Nikezic Dragoslav, Kim Kyeong Min, Yamaya Taiga, Kawachi Naoki, Tanaka Hiroki, Haque A K F, Islam M Rafiqul, Shahmohammadi Beni Mehrdad
Radiation Protection Dosimetry (2023) ncad278 (doi) 10.1093/rpd/ncad278

Advanced Boron Neutron Capture Therapy Targeting Cancer Stem Cells by Selective Induction of LAT1 Overexpression
Toshiaki Tani, Tomoya Fujita, Masaki Misawa, Naomi Tojo, Naoto Shikano, Minoru Suzuki, Ken Ohnishi
Radiation Research 200(1) (2023) 21-31 (doi) 10.1667/RADE-22-00195.1

5-Aminolevulinic acid increases boronophenylalanine uptake into glioma stem cells and may sensitize malignant glioma to boron neutron capture therapy
Fukumura Masao, Nonoguchi Naosuke, Kawabata Shinji, Hiramatsu Ryo, Futamura Gen, Takeuchi Koji, Kanemitsu Takuya, Takata Takushi, Tanaka Hiroki, Suzuki Minoru, Sampetrean Oltea, Ikeda Naokado, Kuroiwa Toshihiko, Saya Hideyuki, Nakano Ichiro, Wanibuchi Masahiko
Scientific Reports 13(1) (2023) 10173 (doi) 10.1038/s41598-023-37296-6

Proceedings

Development of Albumin Nano Particles Installed with Gd(III)-Thiacalixarene Complex for Gd-NCT ― Investigation of installing method and in vitro assay
Kohei Ohama, Miku Komiya, Ryota Sawamura, Ryunosuke Karashimada, Minoru Suzuki, Nobuhiko Iki
Proceedings of the 58th KURNS Scientific Meeting Kumatori, Japan/Online (Jan. 31 - Feb. 1, 2024) 20 (In Japanese)

Development of neutron dosimeters for accelerator-based BNCT irradiation field
ZHAO LIANG, Nishiki Matsubayashi, Mai Nojiri, Naonori Ko, Takushi Takata, Hiroki Tanaka,
Proceedings of the 58th KURNS Scientific Meeting Kumatori, Japan/Online (Jan. 31 - Feb. 1, 2024) 19 (In Japanese)

Measurement method with acrylic phantom for BNCT
Nishiki Matsubayashi, Naonori Hu, Takushi Takata, Yoshinori Sakurai, Hiroki Tanaka
Proceedings of the 58th KURNS Scientific Meeting Kumatori, Japan/Online (Jan. 31 - Feb. 1, 2024) 2

Chordoma Treatment with Boron Neutron Capture Therapy (BNCT): Experimental Insights
Y. Fujikawa, S. Kawabata, K. Tsujino, R. Kayama, H. Kashiwagi, Y. Fukuo, R. Hiramatsu, H. Tanaka, N. Hu, S-I. Miyatake, T. Takami and M. Wanibuchi
The 4th International Electronic Conference on Cancers Online (Mar. 6-8, 2024)

Evaluation of the safety of folate receptor-targeted boron carrier in boron neutron capture therapy (BNCT) for malignant gliomas using CED administration
K. Tsujino, H. Kashiwagi, R. Kayama, Y. Fujikawa, Y. Fukuo, R. Hiramatsu, N. Nonoguchi, T. Takata, H. Tanaka, M. Suzuki, N. Hu, M. Wanibuchi, K. Nakai, K. Nishimura, H. Nakamura and S. Kawabata
The 4th International Electronic Conference on Cancers Online (Mar. 6-8, 2024)

Exploring BNCT as a Novel Approach for Metastatic Spinal Tumor Management
Y. Fujikawa, S. Kawabata, K. Tsujino, R. Kayama, H. Kashiwagi, Y. Fukuo, R. Hiramatsu, T. Takata, H. Tanaka, M. Suzuki, N. Hu, S-I. Miyatake, T. Takami and M. Wanibuchi
The 4th International Electronic Conference on Cancers Online (Mar. 6-8, 2024)

Reviews

Strategies for Preclinical Studies Evaluating the Biological Effects of an Accelerator-Based Boron Neutron Capture Therapy System
Kondo Natsuko, Masutani Mitsuko, Imamichi Shoji, Matsumoto Yoshitaka, Nakai Kei
Cancer Biotherapy and Radiopharmaceuticals 38(3) (2023) 173-183

Systems Biology Approach to Investigate Biomarkers, Boron-10 Carriers, and Mechanisms Useful for Improving Boron Neutron Capture Therapy
Perico Davide, Di Silvestre Dario, Imamichi Shoji, Sanada Yu, Masutani Mitsuko, Mauri Pier Luigi
Cancer Biotherapy and Radiopharmaceuticals 38(3) (2023) 152-159

特集 新たに注目される頭頸部癌治療 BNCT BNCT の原理と基礎
Minoru Suzuki
JOHNS 39(11) (2023) 1403-1405 (In Japanese)

The Combination Therapy Effects on Brain Tumor Cells and the Transplanted Mice Incorporated as a New Radio-photosensitizer and by Laser Light and Xrays (Hard- & Ionized-X-rays and Thermal Neutron Beam) in the Radiation Field
Miyoshi Norio, Okazaki Shigetoshi, Kondo Natsuko, Tanaka Hiroki, Sakurai Yoshinori
The Journal of Japan Society for Laser Surgery and Medicine 44(1) (2023) 2-15 (In Japanese)

ホウ素中性子捕捉療法(BNCT)の生物学研究の近況
Yu Sanada, Tsubasa Watanabe
放射線生物研究 58 (2) (2023) 175-184 (In Japanese)

8. Neutron Radiography and Radiation Application
Papers

Li_2HfBr_6 scintillator for neutron and gamma-ray dual detection
Fujiwara Chihaya, Kurosawa Shunsuke, Yamaji Akihiro, Yoshikawa Akira
Applied Physics Express 16(10) (2023) 102005 (doi) 10.35848/1882-0786/ad03ab

Introduction to Neutron Radiography Facilities at the Japan Research Reactor-3
Kurita K, Iikura H, Tsuchikawa Y, Kai T, Shinohara T, Odaira N, Ito D, Saito Y, Matsubayashi M
Journal of Physics: Conference Series 2605 (2023) 012005 (doi) 10.1088/1742-6596/2605/1/012005

Cooling rate of reactant solution in a flow-type supercritical hydrothermal reactor estimated using neutron radiography
Sasaki Ryosuke, Sato Kosei, Xie Bo, Takami Seiichi, Kubo Masaki, Tsukada Takao, Sugimoto Katsumi, Odaira Naoya, Ito Daisuke, Saito Yasushi
Journal of Physics: Conference Series 2605 (2023) 012029 (doi) 10.1088/1742-6596/2605/1/012029

Proceedings

Activation imaging of drugs using wide-band X-rays and gamma rays
Nanase Koshikawa, Yuka Kikuchi, Jun Kataoka, Yuichiro Kadonaga, Atsushi Toyoshima, Koichi Takamiya
Proceedings of the 58th KURNS Scientific Meeting Kumatori, Japan/Online (Jan. 31 - Feb. 1, 2024) 18 (In Japanese)

Development of High-Dose Rate Real-Time Monitors with an Optical Fiber
Shunsuke Kurosawa, Hiroki Tanaka, Takushi Takada, Daisuke Matsukura, Yusuke Urano, Chihaya Fujiwara, Akihiro Yamaji, Shohei Kodama
Proceedings of the 58th KURNS Scientific Meeting Kumatori, Japan/Online (Jan. 31 - Feb. 1, 2024) 48 (In Japanese)

Properties of Photo-detector with micro vacuum electron sources under gamma-ray irradiation
Yasuhito Gotoh, Yoichiro Neo, Nobuhiro Sato, Masayoshi Nagao, and Tamotsu Okamoto
Proceedings of the 58th KURNS Scientific Meeting Kumatori, Japan/Online (Jan. 31 - Feb. 1, 2024) 27 (In Japanese)

Development of imaging method using β -ray nuclear magnetic resonance
Fukuda, Y. Otani, M. Fukutome, R. Taguchi, S. Chen, S. Ishitani, R. Miyahara, K. Watanabe, T. Izumikawa, N. Noguchi, K. Takatsu, T. Otsubo, D. Nishimura, H. Takahashi, A. Yano, H. Seki, K. Matsuta, A. Kitagawa, S. Sato, and S. Momota
Proceedings of the Specialists' Meeting on "Nuclear Spectroscopy and Condensed Matter Physics Using Short-Lived Nuclei IX" Online (Jan. 11, 2023) 20-25 (In Japanese)

9. TRU and Nuclear Chemistry

Papers

Direct Measurement of the Internal Pressure of Ultrafine Bubbles Using Radioactive Nuclei
Tanigaki Minoru, Yamakura Takuya, Hayashi Daiju, Ueda Yoshikatsu, Taniguchi Akihiro, Ohkubo Yoshitaka, Tokuda Yomei
Chemical Engineering & Technology 46(9) (2023) 1773-1781 (doi) 10.1002/ceat.202300070

Edge-Driven Convection Melting Before the Emplacement of the Afar Mantle Plume Head Inferred From $^{40}Ar/^{39}Ar$ Dating
Yoshimura Yutaka, Ishizuka Osamu, Yamazaki Toshitsugu, Ahn Hyeon-Seon, Kidane Tesfaye, Yamamoto Yuhji, Sekimoto Shun, Sano Takashi, Otofuji Yo-ichiro
Geophysical Research Letters 50(8) (2023) e2022GL102560 (doi) 10.1029/2022GL102560

A quantitative description of the compatibility of technetium-selective chromatographic technetium-99m separation with low specific activity molybdenum-99
Jang Jaewoong, Sekimoto Shun, Ohtsuki Tsutomu, Tatenuma Katsuyoshi, Tsuguchi Akira, Uesaka Mitsuru
Journal of Chromatography A 1705 (2023) 464192 (doi) 10.1016/j.chroma.2023.464192

Reduction of radioactive impurities in liquid scintillator by using metal scavengers
Kamei Y., Shimizu I., Teraoka Y., Yamamura T., Shirasaki K.
Journal of Instrumentation 18 (2023) P08002 (doi) 10.1088/1748-0221/18/08/P08002

Crystallographic and/or magnetic properties of neutral and cationic uranium(IV) sandwiched phthalocyanine complexes
Tabata Chihiro, Watanabe Hirohito, Shirasaki Kenji, Sunaga Ayaki, Fukuda Takamitsu, Li Dexin, Yamamura Tomoo
Journal of Molecular Structure 1277 (2023) 134870 (doi) 10.1016/j.molstruc.2022.134870

Dissolution behavior and aging of iron–uranium oxide
Tonna Ryutaro, Sasaki Takayuki, Okamoto Yoshihiro, Kobayashi Taishi, Akiyama Daisuke, Kirishima Akira, Sato Nobuaki
Journal of Nuclear Materials 589 (2024) 154862 (doi) 10.1016/j.jnucmat.2023.154862

Experimental production of Ac-225 using an electron linear accelerator: Scaling up the production to MBq level and improving the quality
Mizuho Maeda, Takahiro Tadokoro, Yuichiro Ueno, Yuko Kani, Kento Nishida, Takuma Koiwai, Takahiro Sasaki, Takahiro Watanabe, Mitsuyoshi Yoshimoto, Kazunobu Ohnuki, Hirohumi Fujii, Hidetoshi Kikunaga, Shigeru Kashiwagi, Kenji Shirasaki, Shun Sekimoto, Tsutomu Ohtsuki, Makoto Inagaki, Satoshi Fukutani and Yuji Shibahara
Journal of Nuclear Medicine 64(SUPP1) (2023) 24

Neutron total and capture cross-section measurements of ^{155}Gd and ^{157}Gd in the thermal energy region with the Li-glass detectors and NaI(Tl) spectrometer installed in J-PARC·MLF·ANNRI
Kimura Atsushi, Nakamura Shoji, Endo Shunsuke, Rovira Gerard, Iwamoto Osamu, Iwamoto Nobuyuki, Harada Hideo, Katabuchi Tatsuya, Terada Kazushi, Hori Jun-ichi, Shibahara Yuji, Fujii Toshiyuki
Journal of Nuclear Science and Technology 60(6) (2023) 678-696 (doi) 10.1080/00223131.2022.2134224

Measurements of capture cross-section of ^{93}Nb by activation method and half-life of ^{94}Nb by mass analysis
Nakamura Shoji, Shibahara Yuji, Endo Shunsuke, Kimura Atsushi
Journal of Nuclear Science and Technology 60(11) (2023) 1361-1371 (doi) 10.1080/00223131.2023.2198526

Utilization of different radionuclides for high-energy extended efficiency calibration of a HPGe for improved determination of calcium and sulfur using k0-INAA
Soliman Mohamed, Mindil Ahmed, Takamiya Koichi
Journal of Radioanalytical and Nuclear Chemistry 332(6) (2023) 1687-1693 (doi) 10.1007/s10967-023-08859-8

Enhancement of Parity-Violating Energy Difference of CHFClBr, CHFClI, and CHFBrI by Breaking the Cancellation among Valence Orbital Contributions
Kuroda Naoya, Sunaga Ayaki, Senami Masato
Journal of the Physical Society of Japan 92(12) (2023) 124301 (doi) 10.7566/JPSJ.92.124301

An Evaluation of Three Halogens (Cl, Br, and I) Data from a Geological Survey of Japan Geochemical Reference Materials by Radiochemical Neutron Activation Analysis
Shirai Naoki, Sekimoto Shun, Ebihara Mitsuru
Minerals 14(3) (2024) 213 (doi) 10.3390/min14030213

Electron-capture decay rate of 7Be in cluster and crystal forms of beryllium: A first-principles study Be7 in cluster and crystal forms of beryllium: A first-principles study
Kuwahara Riichi, Ohno Kaoru, Ohtsuki Tsutomu
Physical Review C 109(2) (2024) 024609 (doi) 10.1103/PhysRevC.109.024609

Proceedings

Radium Separation from Thorium and Manufacturing of Targets by Precipitation Method
Feng Yin, Satoshi Fukutani, Mari Toyama, Tomoo Yamamura, Suzuki Tatsuya
11th International Conference on Isotopes Saskatoon, Canada (Jul. 23-27, 2023)

A direct conversion method for the separation and temporary storage of MA
Tomoo Yamamura
Actinide Separations Conference Idaho Falls, ID INL Meeting Center (May 16-18, 2023) 30

Crystallographic and Magnetic Properties of Neutral and Cationic Uranium (IV) Phthalocyanine double-decker Complexes synthesized down to mg samples from g
Takumi Saito, Mari Toyama, Kenji Shirasaki, Chihiro Tabata, Takamitsu Fukuda, Dexin Li, Tomoo Yamamura
Actinides 2023 Denver, Colorado, USA (Jun. 5-8, 2023) 134

First structural study on Thorium(IV) complexes with long-chained and cyclic polyethylenediamine (methylphosphonate)；EDTMP and DOTMP for nuclear medicine
Mari Toyama, Kenji Shirasaki, Chihiro Tabata, Koshin Washiyama, Tomoo Yamamura
Actinides 2023 Denver, Colorado, USA (Jun. 5-8, 2023) 149

Electrochemical investigation of complex formation between vanadium ion and benzoic acid
Takuma Mototani, Akihiro Uehara, Chizu Kato, Renki Sugiyama, Yuki Yokoyama, Yoshino Ikeda, Kim Taejune, Toshiyuki Fujii
Proceedings of the 58th KURNS Scientific Meeting Kumatori, Japan/Online (Jan. 31 - Feb. 1, 2024) 30 (In Japanese)

Fundamental experiments for the formation of radionuclide endohedral fullerenes
Makoto Inagaki, Hiroki Nakada, Kazuhiko Akiyama, Tsutomu Ohtsuki
Proceedings of the 58th KURNS Scientific Meeting Kumatori, Japan/Online (Jan. 31 - Feb. 1, 2024) 45 (In Japanese)

Gallium concentrations in GSJ standard materials
Chizu Kato, Satoshi Fukutani, Toshiyuki Fujii
Proceedings of the 58th KURNS Scientific Meeting Kumatori, Japan/Online (Jan. 31 - Feb. 1, 2024) 42 (In Japanese)

Isotope fractionation of zinc using a chemical exchange method with Aza-crown ether
Seiya Akamatsu, Satoshi Fukutani, Shigeyuki Wakaki, Ryoichi Nakada, Kazuya Nagaishi
Proceedings of the 58th KURNS Scientific Meeting Kumatori, Japan/Online (Jan. 31 - Feb. 1, 2024) 31

Prediction and extraction experiments of alkaline earth metal toward the chiemical study of nobelium
Yudai Itakura, Yoshitaka Kasamatsu, Koichi Takamiya, Masashi Kaneko, Kojiro Nagata, Ruilin Wang, Miyu Konno, Kyosuke Shibamoto, Eisuke Watanabe, Saki Otaka, Ryohei Nakanishi, Atsushi Shinoahara
Proceedings of the 58th KURNS Scientific Meeting Kumatori, Japan/Online (Jan. 31 - Feb. 1, 2024) 17

Solubility and solid phases of trivalent lanthanide oxides and hydroxides
Taishi Kobayashi, Takayuki Sasaki
Proceedings of the 58th KURNS Scientific Meeting Kumatori, Japan/Online (Jan. 31 - Feb. 1, 2024) 43

Solvent extraction characteristics of Europium using new extractants, and separation and recovery by extraction chromatography
Kosuke Otsu, Chizu Kato, Masaya Ikeno, Chuya Saiga, Yuya Nihei, Satoshi Fukutani, Tatsuro Matsumura, Toshiyuki Fujii
Proceedings of the 58th KURNS Scientific Meeting Kumatori, Japan/Online (Jan. 31 - Feb. 1, 2024) 41 (In Japanese)

Structural studies of Th(IV) complexes with cyclic polyethylenediamine (methylphosphonate) for nuclear medicine
Mari Toyama
Proceedings of the 58th KURNS Scientific Meeting Kumatori, Japan/Online (Jan. 31 - Feb. 1, 2024) 4-6 (In Japanese)

Study of Isotope Separation via Chemical Exchange Reaction
Ryuta Hazama, Takaaki Yoshimoto, Kumsut Pantiwa, Anawat Rittirong, Yoichi Sakuma, Toshiyuki Fujii, Satoshi Fukutani, Yuji Shibahara
Proceedings of the 58th KURNS Scientific Meeting Kumatori, Japan/Online (Jan. 31 - Feb. 1, 2024) 47 (In Japanese)

Structural studies of mononuclear Th(IV) complexes with cage-shaped acyclic or cyclic chelate ligands possessing a polyethylenediamine(methylphosphonate) moiety; EDTMP and DOTMP for nuclear medicine
Mari Toyama, Kenji Shirasaki, Tomoo Yamamura
The 73rd Conference of Japan Society of Coordination Chemistry Mito City, Japan (Sep. 21-23, 2023) 73 2B-06

遊離イオンに基づくコバルトキュバン型錯体の架橋ハロゲンの配列制御
Mari Toyama, Soichiro Uchida, Kenji Nagao, Tomoo Yamamura
The 73rd Conference of Japan Society of Coordination Chemistry Mito City, Japan (Sep. 21-23, 2023) 2Aa-01 (In Japanese)

10. Health Physics and Waste Management

Papers

STEAM Educational Development of Risk Management Education Framework for Secondary School Students
SHUHARA Ai, MORIMOTO Ayako, NAKAYAMA Jo, HAYASHI Rumiko, TAKASHIMA Ryuta, IIMOTO Takeshi **Japanese Journal of Health Physics 58(1) (2023) 5-9 (doi) 10.5453/jhps.58.5**

A Source-Related Approach for Discussion on Using Radionuclide-Contaminated Materials in Post-accident Rehabilitation
Miwa Kazuji, Iimoto Takeshi
Journal of Radiation Protection and Research 48(2) (2023) 68-76 (doi) 10.14407/jrpr.2022.00045

Proceedings

Mass balance of radioactive cesium and stable cesium accumulated in wild animal bodies living in difficult-to-return zones in Fukushima Prifecture
Michiko Fukushima, Hitoshi Komatsu, Yuto Iinuma, Yamato Tsuji, Yuya Sugawara, Shota Mochizuki, Takashi Sakata, Kimie Murakami, Kousuke Kanda
Proceedings of the 58th KURNS Scientific Meeting Kumatori, Japan/Online (Jan. 31 - Feb. 1, 2024) 25 (In Japanese)

プラスチックに基づく波長変換材に関する先駆的研究 ～環境レベルの放射線照射中における分子内電子状態その場計測の実現に向けて～
Hidehito Nakamura
Proceedings of the 58th KURNS Scientific Meeting Kumatori, Japan/Online (Jan. 31 - Feb. 1, 2024) 1 (In Japanese)

Reviews

日本保健物理学会「エックス線被ばく事故検討 WG」経過報告書（前半）
日本保健物理学会「エックス線被ばく事故検討 WG」（飯本武志他）
ESI-NEWS 41(1) -2023 3-10 (In Japanese)

The Combination Therapy Effects on Brain Tumor Cells and the Transplanted Mice Incorporated as a New Radio-photosensitizer and by Laser Light and Xrays (Hard- & Ionized-X-rays and Thermal Neutron Beam) in the Radiation Field
Norio Miyoshi, Shigetoshi Okazaki, Natsuko Kondo, Hiroki Tanaka, Yoshinori Sakurai
The Journal of Japan Society for Laser Surgery and Medicine 44(1) (2023) 45337 (In Japanese)

Review of Articles Related to the Accident of TEPCO's Fukushima Daiichi Nuclear Power Station Published on Japanese Journal of Health Physics: Risk Communication
Takeshi IIMOTO, Masahiro KATO, Nobuyuki HAMADA, Tsuyoshi MAEDA, Akira YOSHIDA
Japanese Journal of Health Physics 58(2) -2023 59-62 (In Japanese)

11. Accelerator Physics

Papers

Long-Axis Uniform Magnetic Field Generation Using Permanent Magnets
Iwashita Yoshihisa, Kuriyama Yasutoshi, Fuwa Yasuhiro
IEEE Transactions on Applied Superconductivity 5 (2024) 1-4 (doi) 10.1109/TASC.2024.3380588

Design Improvement of Bipolar Correction Magnet With Permanent Magnets
Kuriyama Yasutoshi, Iwashita Yoshihisa, Fuwa Yasuhiro, Terunuma Nobuhiro
IEEE Transactions on Applied Superconductivity 5 (2024) 1-5 (doi) 10.1109/TASC.2024.3365099

Electric field in the RF cavity with large beam duct for high current beam acceleration
Sako T., Ishi Y., Uesugi T., Kuriyama Y., Mori Y., Tsumori K., Ando A., Yonemura Y.
Journal of Instrumentation 18(11) (2023) P11019 (doi) 10.1088/1748-0221/18/11/P11019

Technical note: Application of an optical hydrophone to ionoacoustic range detection in a tissue-mimicking agar phantom
Sueyasu Shota, Kasamatsu Koki, Takayanagi Taisuke, Chen Ye, Kuriyama Yasutoshi, Ishi Yoshihiro, Uesugi Tomonori, Rohringer Wolfgang, Unlu Mehmet Burcin, Kudo Nobuki, Yokokawa Kohei, Takao Seishin, Miyamoto Naoki, Matsuura Taeko
Medical Physics 2023 (2023) 1-12 (doi) 10.1002/mp.16892

Neutron-production double-differential cross sections of ^{nat}Pb and ^{209}Bi in proton-induced reactions near 100 MeV
Iwamoto Hiroki, Meigo Shin-ichiro, Satoh Daiki, Iwamoto Yosuke, Ishi Yoshihiro, Uesugi Tomonori, Yashima Hiroshi, Nishio Katsuhisa, Sugihara Kenta, Çelik Yurdunaz, Stankovskiy Alexey
Nuclear Instruments and Methods in Physics Research Section B: Beam Interactions with Materials and Atoms 544 (2023) 165107 (doi) 10.1016/j.nimb.2023.165107

Benchmark Experiments for Bulk and Maze Shielding Using Activation Detectors with 24-GeV/c Protons at CERN/CHARM
Nakao Noriaki, Sanami Toshiya, Kajimoto Tsuyoshi, Froeschl Robert, Bozzato Davide, Iliopoulou Elpida, Infantino Angelo, Yashima Hiroshi, Lee Eunji, Oyama Takahiro, Hagiwara Masayuki, Nagaguro Seiji, Matsumoto Tetsuro, Masuda Akihiko, Uwamino Yoshitomo, Roesler Stefan, Brugger Markus
Nuclear Science and Engineering 198(2) (2023) 336-347 (doi) 10.1080/00295639.2023.2196228

Heavy Ion Injection of Fixed-Field Alternating Gradient Accelerator
Yonemura Yujiro, Arima Hidehiko, Nishibata Hiroki, Teranishi Takashi, Wakasa Tomotsugu, Ikeda Nobuo, Watanabe Kenichi, Shigyo Nobuhiro, Iwamura Tatsunori, Adachi Kyosuke, Takamatsu Koki, Kotani Motoki, Tanaka Hisato, Matsunaga Rintaro, Matsumoto Taichi, Takenaka Kyohei, Kajihara Takafumi, Matsunaga Sotaro, Shinohara Yusuke, Mori Yoshiharu
Progress of Theoretical and Experimental Physics 2024(2) (2024) 023G01 (doi) 10.1093/ptep/ptae017

Development of a non-destructive depth-selective quantification method for sub-percent carbon contents in steel using negative muon lifetime analysis
Ninomiya Kazuhiko, Kubo Michael Kenya, Inagaki Makoto, Yoshida Go, Chiu I-Huan, Kudo Takuto, Asari Shunsuke, Sentoku Sawako, Takeshita Soshi, Shimomura Koichiro, Kawamura Naritoshi, Strasser Patrick, Miyake Yasuhiro, Ito Takashi U., Higemoto Wataru, Saito Tsutomu
Scientific Reports 14 (2024) 1797 (doi) 10.1038/s41598-024-52255-5

Proceedings

A conceptual design of FFA ring for super heavy element production adopting the ERIT mechanism
Yoshihiro Ishi, Uesugi Tomonori, Mori Yoshiharu
14th International Particle Accelerator Conference, Venice, Italy (May 7-12, 2023) 955-957

Development of EPICS-based data acquisition system for beam loss monitor and sX-Map
Y. Kuriyama, Y. Iwashita, Y. Fuwa, H. Hayano
14th International Particle Accelerator Conference, Venice, Italy (May 7-12, 2023) 4011-4013

Short pulsed beam extraction from Kurns FFAG
Uesugi Tomonori, Ishi Yoshihiro, Mori Yoshiharu
14th International Particle Accelerator Conference, Venice, Italy (May 7-12, 2023) 952-954

Updates of high-density temperature and X-ray mapping
Y. Iwashita, H. Tongu, Y. Kuriyama
14th International Particle Accelerator Conference, Venice, Italy (May 7-12, 2023) 3056-3058

12. Other

Papers

Experimental Evaluation of Energy Resolutions for Pulsed Neutron Beam in the KURNS-LINAC
Matsuo Yasunori, Jun-ichi Hori, Takahashi Yoshiyuki, Yashima Hiroshi, Terada Kazushi, Kanda Takashi, Sano Tadafumi
EPJ Web of Conferences 284 (2023) 06003 (doi) 10.1051/epjconf/202328406003

Best thermoelectric efficiency of ever-explored materials
Ryu Byungki, Chung Jaywan, Kumagai Masaya, Mato Tomoya, Ando Yuki, Gunji Sakiko, Tanaka Atsumi, Yana Dewi, Fujimoto Masayuki, Imai Yoji, Katsura Yukari, Park SuDong
iScience 26(4) (2023) 106494 (doi) 10.1016/j.isci.2023.106494

Alpha-ray imaging with alkali copper halide scintillator
Urano Y., Kurosawa S., Yamaji A., Yoshikawa A., Wu Y.
Journal of Instrumentation 18(12) (2023) C12009 (doi) 10.1088/1748-0221/18/12/C12009

^{99m}Tc generator using molybdenum nanoparticles
Naruto Takahashi, Mamoru Fujiwara, Maki Kurosawa, Masoto Tamura, Yoshiaki Kosuge, Takumi Kubota, Naoya Abe, Toshiharu Takahashi
Journal of Radioanalytical and Nuclear Chemistry 333 (2024) 17-22 (doi) 10.1007/s10967-023-09173-z

Adsorption Characteristics and Mechanical Responses of Lubricants Containing Polymer Additives under Fluid Lubrication with a Narrow Gap
Hirayama Tomoko, Yamashita Naoki, Yamamoto Waka, Shirode Kenta, Okada Akira, Hatano Naoya, Tsuchiya Toshiyuki, Yamada Masako
Langmuir 40(12) (2024) 6229-6243 (doi) 10.1021/acs.langmuir.3c03725

An Intensity Tensor and Electric Field Gradient Tensor for Fe^{3+} at *M*1 Sites of Aegirine–Augite Using Single-Crystal Mössbauer Spectroscopy
Shinoda Keiji, Kobayashi Yasuhiro
Minerals 13(11) (2023) 1452 (doi) 10.3390/min13111452

Development of neutron resonance fission neutron analysis for nondestructive fissile material
J. Lee, Y. Kodama, F. Rossi, K. Hironaka, M. Koizumi, J. Hori, T. Sano
第 43 回 日本核物質管理学会 年次大会論文集 (2023) 442

Feasibility Study on One-Dimensional Dose Rate Distribution Measurement Using Fiber Noise Data from the Fiber-Optic Radiation Dose Rate Monitoring System
Daisuke Matsukura, Shunsuke Kurosawa, Akihiro Yamaji, Hiroki Tanaka, Takushi Takata
Ionizing Radiation 49(1) (2024) 18-22 (In Japanese)

Proceedings

Overview of the New Research Reactor at the “Monju” Site and Its Experimental Facilities
Nobuhiro Sato, Makoto Inagaki, Koichi Takamiya, Masahiro Hino, Yuji Kawabata, Masaaki Sugiyama
Proceedings of the 58th KURNS Scientific Meeting Kumatori, Japan/Online (Jan. 31 - Feb. 1, 2024) 28

Plan for the equipments related to neutron activation analysis at the new research reactor to be constructed on the "Monju" site Makoto Inagaki, Koichi Takamiya, Masahiro Hino, Masaaki Sugiyama, Yuji Kawabata, Nobuhiro Sato
Proceedings of the 58th KURNS Scientific Meeting Kumatori, Japan/Online (Jan. 31 - Feb. 1, 2024) 44 (In Japanese)

Nuclear Spectroscopy Experiments at KISS
Y.X. Watanabe, Y. Hirayama, M. Mukai, P. Schury, T. Niwase, J.Y. Moon, T. Hashimoto, M. Rosenbusch, H. Ishiyama, S. Kimura, S. Iimura, M. Oyaizu, S.C. Jeong, A. Taniguchi, H. Miyatake, M. Wada, and KISS collaboration
Proceedings of the Specialists’ Meeting on "Nuclear Spectroscopy and Condensed Matter Physics Using Short-Lived Nuclei IX" Online (Jan. 11, 2023) 32-38 (In Japanese)

Books

建築学会内委員会メンバーによる共著
地盤震動研究とその応用 5章 / 地下構造モデルと堆積地盤での増幅特性,7章/ 入力地震動と建物応答,資料編 I
近年の日本の被害地震 日本建築学会（発行所：丸善） (2023) 978-4-8189-0674-7 （In Japanese）

Others

広帯域 X 線・ガンマ線による薬剤可視化へ向けた新技術
Nanase Koshikawa, Miho Masubuchi, Jun Kataoka
応用物理学会放射線分科会会誌 48(1) (2023) 14 (In Japanese)

薬物動態を可視化する放射化イメージング：宇宙の元素合成を医療に応用
Nanase Koshikawa, Jun Kataoka
月刊化学/Chemistry 178(5) (2023) 33 (In Japanese)

ダイバーシティ＆インクルージョン
Ken Kurosaki
Journal of the Atomic Energy Society of Japan 65(5) (2023) 307 (In Japanese)

KURNS Progress Report 2023

Issued in July 2024

Issued by the Institute for Integrated Radiation and Nuclear Science,
Kyoto University
Kumatori-cho, Sennan-gun, Osaka 590-0494 Japan

Tel. +81-72-451-2300
Fax.+81-72-451-2600

In case that corrections are made, overwrite the modified version
in the following webpage:
https://www.rri.kyoto-u.ac.jp/PUB/report/PR/ProgRep2023/ProgRep2023.html